Development of a decision support tool in uncertain conditions for the maintenance of reinforced concrete structures subjected to corrosion

Paulo Claude

THÈSE

En vue de l'obtention du

DOCTORAT DE L'UNIVERSITÉ DE TOULOUSE

Délivré par l'Institut National des Sciences Appliquées de Toulouse

---

Présentée et soutenue par

Paulo CLAUDE

Le 20 septembre 2023

Development of a decision support tool in uncertain conditions for the maintenance of reinforced concrete structures subjected to corrosion

---

Ecole doctorale : **MEGEP - Mécanique, Energétique, Génie civil, Procédés**

Spécialité : **Génie civil**

Unité de recherche :
LMDC - Laboratoire Matériaux et Durabilité des Constructions de Toulouse

Thèse dirigée par
Frederic DUPRAT et Thomas DE LARRARD

Composition du Jury

Frédéric DUPRAT	LMDC - INSA Toulouse	Directeur de thèse
Emilio BASTIDAS-ARTEAGA	LaSIE - Université de La Rochelle	Rapporteur
Stéphanie BONNET	GeM - Université de Nantes	Rapportrice
Ouali AMIRI	GeM - Université de Nantes	Examinateur
Jonathan MAI-NHU	Cerib	Examinateur
Franziska SCHMIDT	EMGU – Université Gustave Eiffel	Examinatrice
Thomas STABLON	Arcadis	Examinateur
Stéfanie VON GREVE-DIERFELD	TFB AG	Examinatrice
Thomas DE LARRARD	LMDC - INSA Toulouse	Invité
Patrick ROUGEAU	Cerib	Invité

REMERCIEMENTS

La liste est évidemment très longue, et je pense que la plupart n'auront pas l'occasion/motivation d'ouvrir ce document. Cependant, il faut bien rendre à César… comme dirait mon directeur de thèse Frédéric Duprat qui mérite bien d'être nommé en premier dans ce passage. Je tiens à remercier l'ensemble de mes (nombreux) encadrants : Frédéric, Thomas, Jonathan, Patrick, Louis, Pascal et Pierre. Votre accompagnement durant cette thèse, vos conseils, remarques et critiques m'ont permis d'acquérir en connaissances ainsi qu'en maturité et en confiance en moi. Merci pour vos relectures et le temps que vous avez pu me consacrer.

Merci aux nombreux membres de mon jury de thèse pour avoir accepté cette tâche et de me permettre d'accéder au rang de docteur.

Merci aux équipes du LMDC ! A Pierre Morenon pour les devoirs de maths. Merci aussi à Aurélie Papon pour sa gentillesse, à Alain Sellier et Jean-Paul Balayssac pour leurs précieux conseils.

J'ai passé le plus clair de mon temps au CERIB, avec les équipes de DMEC. Merci pour votre accueil et pour les bons moments passés avec vous tous. Merci à CCU et PBY pour l'aide dans la réalisation des essais chimiques. Merci à BLO pour les gros coups de pouce et son humeur que j'apprécie tant. Merci à YPN et VOU pour les blagues, à LI pour les sourires et les conseils de rangement, et à toute l'équipe de LEM pour les aides apportées.

Merci à DO pour mon intégration, à MVD ma co-bureau pour sa présence et pour les nombreux échanges ! Merci à TPN pour les covoits (et accident), les conseils et le soutien. Merci à CC pour son aide précieuse sur le manuscrit (surtout à la fin) et pour les encouragements à la salle ! PME, je te dois beaucoup (genre 25 vol.% du manuscrit), ma coloc, collègue et amie. Merci de m'avoir supporté, surtout dans les derniers moments cruciaux. Merci de me laisser t'écraser à la plupart des jeux de société/activité physique et de rire à mes blagues de merde.

En parlant de grand soutien, merci à LMO pour m'avoir précédé et avoir partagé mes joies comme mes peines. Merci pour les pintes et les trop nombreux passages à la Bella Rosa. Merci aussi à TDL (Dieu) pour des raisons évidentes.

Merci aux équipes de la Com' et du SI pour leur investissements et encouragements.

Je pense que cette thèse n'aurait pas pu être réalisée sans l'appui de mes amis et de ma famille. Chlothilde, Jules, j'ai adoré nos week-ends passés dans les trois coins de la France. Fabien, Célia, Jules, et tous les anciens de l'EEIGM, vous avez été avec moi très souvent en pensée.

Merci Lucie Schmitt, de m'avoir pris en stage de fin d'étude, et de m'avoir permis d'avoir cette thèse. J'aurais adoré t'avoir à mes côtés pendant ces trois années.

Merci à Luc et Aurélien (et Julien), mes colocataires de la rue Labrouste, pour tous ces moments incroyables comme pour les leçons de maths et de français. Merci à tous les anciens de Nancy, LK, LF, HC, SG, VD, JM, RV, BP, LC, FB, BS, TS et AL.

Merci à ma mère qui partage mon stress (même à distance) et qui me soutien à chaque seconde. A ma sœur qui m'encourage et me nargue en m'envoyant des photos de pingouin. A mon père qui m'a inculqué une culture scientifique et sera à jamais avec moi par l'esprit. A mon grand-père pour ses histoires répétées sur la 2ème guerre. Merci aux Malacarne, aux Favre et aux Martin qui ont toujours été là pour m'épauler.

Enfin, merci à Amandine, qui m'a supporté pendant cette dernière année et est entrée dans ma vie sans aucune hésitation. Tu m'as permis de tenir et de toujours aller plus loin. Merci aussi aux deux petits monstres qui t'accompagnent.

RÉSUMÉ

L'optimisation et la supervision des structures en béton constituent l'un des principaux défis pour les parties prenantes du secteur de la construction dans un contexte fort de transition écologique. Les enjeux se situent en particulier au niveau de la réduction de l'empreinte environnemental des ouvrages en béton et intègrent la nécessité de maitriser leur durabilité. Pour les ouvrages existants, cela se traduit par la nécessité de maintenir la continuité de service en allongeant leur durée d'utilisation. Pour les ouvrages neufs, les leviers d'actions concernent à la fois la conception et le dimensionnement optimisés des ouvrages, les process de mise en œuvre et les solutions matériaux à travers l'utilisation de bétons décarbonés, par exemple en utilisant des liants à moindre teneur en clinker. La durabilité des bétons décarbonés constitue donc un enjeu majeur pour les acteurs de la construction et le sujet de nombreuses études.

Ce travail de thèse vise à contribuer à l'étude et la prédiction de la phase d'initiation de la corrosion de l'acier dans les structures en béton armé, anciennes ou neuves, en intégrant les contraintes technico-économiques et les enjeux associés à la réduction de l'empreinte carbone associés à la construction et à l'entretien des infrastructures routières et maritimes. Par conséquent, les objectifs de cette thèse de doctorat sont multiples. Tout d'abord, une campagne expérimentale a permis d'acquérir les indicateurs de durabilité de bétons à base de liants décarbonés. La carbonatation, la pénétration des ions chlorure et les transferts hydriques ont été étudiés grâce à des essais naturels et accélérés. Les données obtenues ont été utilisées pour calibrer un modèle par éléments finis développé lors de deux précédentes thèses (Mai-Nhu, 2013), (Schmitt, 2019). Ce modèle, appelé SDReaM-Crete, est capable de prendre en compte l'interaction des trois phénomènes mentionnés ci-dessus. La charge de calcul associée à un tel modèle complique cependant son utilisation dans un contexte opérationnel. Par conséquent, des modèles de substitution basés sur des développements en chaos polynomiaux (Crestaux et al., 2009) ont été créés à partir des résultats du modèle d'origine afin de réduire le temps d'exécution tout en conservant un niveau de précision compatibles avec les besoins des utilisateurs. Ils ont ainsi été introduits à un outil opérationnel d'évaluation de la durée de vie d'ouvrages en béton armé, et d'aide à la planification d'opérations d'entretien et de réparation.

Cette application se compose d'une interface graphique développée en Python, permettant à l'utilisateur d'exécuter et de visualiser les résultats des modèles de substitution. D'autres modèles de la littérature sont également intégrés, offrant ainsi une base de comparaison plus large et la possibilité de considérer la propagation de la corrosion. Parallèlement, une méthode de fiabilité du premier ordre (FORM) (Ardillon, 2014) est intégrée et permet à l'utilisateur d'adopter une approche probabiliste pour l'évaluation de la durée de vie. Une base de données de résultats expérimentaux a été construite au cours de ces travaux à partir de la littérature et adjointe à l'application afin de faciliter la transition entre les données de formulation des bétons et les données d'entrée des méta-modèles. Un travail a notamment été réalisé concernant l'évaluation des incertitudes liées à la méthode d'obtention des données Ainsi, un indice de confiance traduit la répercussion des incertitudes des méthodes sur les prédictions probabilistes finales. Différentes validations de l'outil ont été réalisées sur des données obtenues dans le cadre d'inspection d'ouvrages, et ont permis d'éprouver les différents modèles intégrés à cette application. Celle-ci constitue un véritable outil d'aide à la décision pour les constructeurs et des gestionnaires d'ouvrages.

ABSTRACT

Optimization and supervision of concrete structures present significant challenges for stakeholders in the construction sector, particularly in the context of ecological transition. The primary focus is on reducing the environmental impact of concrete structures and ensuring their durability. In the case of existing structures, this entails the need to extend their service life while maintaining continuity of service. In the case of new structures, the key actions involve optimized design, dimensioning, implementation processes, and material solutions using decarbonized concrete, for instance, by utilizing binders with lower clinker content. The durability of decarbonized concrete is an important concern for industry players, leading to numerous studies.

This doctoral thesis aims to contribute to the study and prediction of the initiation phase of steel corrosion in both existing and new reinforced concrete structures, considering the technical-economic constraints and challenges associated with reducing the carbon footprint in the construction and maintenance of road and maritime infrastructures. Consequently, the objectives of this thesis are multifaceted. Firstly, an experimental campaign has been conducted to acquire durability indicators for concrete based on decarbonized binders. Carbonation, chloride ion penetration, and water transfers have been investigated via natural and accelerated tests. The obtained data has been used to calibrate the SDReaM-Crete finite element model, which was developed in two previous theses (Mai-Nhu, 2013; Schmitt, 2019). This model enables the consideration of the interaction among the precedingly mentioned phenomena. However, the computational load associated with this model complicates its operational use. In order to minimize execution time while maintaining the desired level of precision, substitution models based on polynomial chaos expansions (Crestaux et al., 2009) were developed using the results from the original model. These models were then integrated into an operational tool for assessing the service life and planning maintenance and repair operations of reinforced concrete structures.

The tool consists of a Python-based graphical interface, enabling users to execute and visualize the substitution model results. Additionally, other models from the literature were included, providing a broader basis for comparison and consideration of corrosion propagation. To incorporate a probabilistic approach for service life evaluation, a first-order reliability method (FORM) (Ardillon, 2014) was integrated into the tool. During the development process, an experimental results database was constructed using literature data to facilitate the transition from concrete formulation data to input data for the metamodels. Emphasis was placed on evaluating uncertainties associated with the data acquisition method. As a result, a confidence index was established to quantify the impact of uncertain methods on the final probabilistic predictions. Validation of the tool was performed using data obtained from structural inspections, which enabled thorough testing of the various integrated models. This tool serves as a valuable decision support for builders and asset managers.

CONTENT

REMERCIEMENTS II
RÉSUMÉ III
ABSTRACT IV
CONTENT V
GLOSSARY OF TERMS XIII
Acronym: XIII
Recurrent notations: XIV
General: XIV
Composition: XV
Thermal: XVI
Hydrologic: XVI
Durability: XVI
Carbonation: XVII
Chloride: XVII
Corrosion: XVIII
INTRODUCTION 19
I. State of the art 22
I.1. Concrete composition 24
I.1.1. Aggregates 24
I.1.1.1. Type and properties 25
I.1.1.2. Recycled Concrete Aggregate (RCA) 26
I.1.2. Cements and mineral additions 27
1.1.2.1. Inert additions – Type I 27
1.1.2.2. Pozzolanic and latent hydraulic additions – Type II 27
1.1.2.3. NF EN 197-1 cements 30
1.1.2.4. NF EN 197-5 cements 31
I.1.3. Water 32
I.1.4. Admixture 32
I.2. Hydration mechanisms 33
I.2.1. Portland cement 33
I.2.2. Pozzolanic and latent hydraulic additions 34
I.3. Durability of reinforced concrete structures 38
I.3.1. Carbonation 38
I.3.2. Chloride ions penetration 43

I.3.2.1 Chloride induce corrosion initiation 44
I.3.2.2 The road environment (XD classes of the NF EN 206+A2/CN (2022)) 47
I.3.3. Carbonation-Chlorides coupling 47
I.3.4. Corrosion propagation 48
I.3.4.1. Passivation layer 48
I.3.4.2. Corrosion process in reinforced concrete 53
I.3.4.3. Pitting corrosion 56
I.4. Modelling – state of the art 57
I.4.1. Carbonation 57
1.4.1.1. Finite element model for heat transfer, moisture transport and carbonation in concrete [212] 60
1.4.1.2. pH computation 63
1.4.1.3. Artificial Neuron Network (ANN) from Kellouche and Al. work [213] 64
I.4.2. Chloride ions exposure 65
1.4.2.1. Physical models – Ion transport model of Ukrainczyk et al. [237] 68
1.4.2.2. Physical models – Non-saturated Conditions 69
1.4.2.3. Boundary conditions 70
1.4.2.4. Binding isotherm modelling 71
I.4.3. Carbonation-Chloride ions pairing 72
I.4.4. Corrosion 73
I.4.4.1. Models for carbonation induced corrosion 74
I.4.4.2. Models for chloride-induced corrosion 77
1.4.4.3. Laplace equation-based models [264], [275] 78
I.4.5. Mechanical, Microstructure and durability parameters assessment 79
1.4.5.1. Mechanical resistance computation 79
1.4.5.2. Porosity models 80
1.4.5.3. Hydration models 81
1.4.5.4. Diffusion coefficient of chloride ions 83
1.4.5.5. Ageing factor 84
1.4.5.6. Critical concentration for chloride initiation $Ccrit$ 85
1.4.6. Conclusion 87
I.5. Mathematical processing 87
I.5.1. Learning-based models 88
I.5.1.1. Polynomial chaos expansion 88
I.5.1.2. Artificial Neural Network 90
I.5.2. Probabilistic approach 91

I.5.2.1. Monte Carlo method 96
I.5.2.2. First and Second Order Reliability Method (FORM/SORM) 97
I.6. Standardization context 99
I.6.1. Standardization context and prevention 99
I.6.2. Prescriptive approach 99
I.6.3. Performance-based approach 100
Study test 105
I.6.4. Cover sizing 105
I.6.5. Expert Group “Low Carbon Solution”, French concrete normative commission P18B AFNOR 108
II. Experimental campaign: material, methods, and results 109
II.1. Introduction – Context and goals 109
II.2. Concrete mixes and experimental plan 110
II.2.1. Materials and designations 110
II.2.2. Tests and modelling purposes 113
II.2.3. Conservation and pre-conditioning 114
II.2.4. Carbon footprint computation 116
II.3. Methods and results 117
II.3.1. Mechanical resistance 118
II.3.1.1. Flexural and compressive strength on mortars 118
II.3.1.2. Compressive strength on concrete 119
II.3.2. Porosity accessible to water 123
II.3.3. Gas permeability 124
II.3.4. Mass loss monitoring 126
II.3.5. Accelerated carbonation 128
II.3.6. Natural carbonation 133
II.3.7. Chloride ions migration under electric field 136
II.3.8. Electric resistivity 141
II.3.9. Thermogravimetric analysis (TGA) 145
II.3.9.1. Hydration kinetics 146
II.3.9.2. CO2 storing capacity and buffer capacity 151
II.4. Discussions and conclusions 153
II.4.1. Pozzolanic additions and conservation conditions 153
II.4.2. Prescriptive approach [1] and Performance-based approach described in FD P 18-480 (2022) 158
II.4.3. Carbon footprint indicator 162

III. SDReaM-Crete model 167
III.1. Introduction 167
III.2. Model input 167
III.2.1. Chemical, physical, and mathematical constants 167
III.2.2. Environmental parameters 168
III.3. Finite Element Modelling with Comsol 170
III.3.1. Relative humidity (RH, -) 171
Mass balance equation: 171
Boundary conditions – surface of concrete: 173
III.3.2. Partial pressure of CO_2 ($PCO2$, Pa) 173
Mass balance equation: 173
Boundary conditions – surface of concrete: 173
III.3.3. Carboxyl ions CO_3^{2-} ($[CO32-]$, mol/m^{3}sol) 174
Mass balance equation: 174
Boundary conditions – surface of concrete: 175
III.3.4. Chloride ions Cl- ($[Cl-]$, mol/m^{3}sol) 175
Mass balance equation: 175
Boundary conditions – surface of concrete: 176
III.3.5. Temperature (T, Kelvin) 176
Conservation equation: 177
Boundary conditions – surface of concrete: 177
III.3.6. Portlandite ($CaCH$, mol/m$^3_{concrete}$) 177
Mass balance equation: 177
III.3.7. Hydrated calcium silicate C-S-H ($CaCSH$, mol/m$^3_{concrete}$) 177
Mass balance equation: 178
III.3.8. Monosulfoaluminates ($CaAfm$, mol/m$^3_{concrete}$) 178
Mass balance equation: 178
III.3.9. Ettringite ($CaAft$, mol/m$^3_{concrete}$) 178
Mass balance equation: 178
III.3.10. Friedel' salts ($CaFS$, mol/m^{3}concrete) 178
Mass balance equation: 178
III.3.11. Calcite ($CaCO3$, mol/m$^3_{concrete}$) 178
Mass balance equation: 178
III.3.12. Other functions 179
III.4. Previous developments 179
III.4.1. Model initiation and fitting – SDReaM-Crete 1.0 [7] 179

III.4.2. Surrogate model and probabilistic approach implementation [6] 180
III.5. Model improvements – New binders and environment considerations 182
III.5.1. Hydrologic transfers 182
III.5.1.1. Sorption isotherm determination and verifications 182
III.5.1.2. Mass loss monitoring in dry conservation environment 185
III.5.1.3. Mai-Nhu data [7] 187
III.5.1.4. Water permeability estimation 187
III.5.2. Carbonation rate 188
III.5.2.1. Hyvert's work on carbonation kinetic dependence on partial pressure of CO_2 [105] 188
III.5.2.2. Mai-Nhu accelerated carbonation results [7] 190
III.5.2.3. Schmitt accelerated and natural carbonation results [6] 191
III.5.2.4. Accelerated and natural carbonation results of Sections II.3.5 and II.3.6 193
III.5.2.5. Bucher accelerated carbonation results [102] 196
III.5.2.6. National project PerfDuB – Natural carbonation on laboratory scale [2] 197
III.5.2.7. National project PerfDuB – On field carbonation tests [2] 203
III.5.3. Chloride ingress 204
III.5.3.1. Earlier results on chloride natural diffusion [6] 204
III.5.3.2. Gao's experimental results in tidal zone [393] 205
III.5.3.3. Case study proposed by Bastidas on chloride convection [236] 206
III.6. Surrogate model creation 212
III.6.1. Environments consideration and input preparation 212
III.6.2. Polynomial chaos expansion 216
III.6.2.1. Carbonation-induced corrosion exposure classes (XC) 217
III.6.2.2. Marine chlorides induced corrosion (XS) 219
III.6.2.3. Non-marine chlorides-induced corrosion (XD) 222
III.6.2.4. Surrogate model for saturation computation 224
III.6.3. Artificial neural network 225
Conclusion 228
IV. A tool for deterministic and probabilistic computations of corrosion initiation 229
IV.1. Introduction and goals 229
IV.2. Python-based graphic interface 229
IV.3. Input data and transformations 230
IV.3.1. Operational context 231
IV.3.1.1. Materials 231
IV.3.1.2. Environment 233
IV.3.1.3. Geometry and design 235

IV.3.2. Literature models 236
IV.3.2.1. Mechanical resistance computation 237
IV.3.2.2. Porosity accessible to water models 239
IV.3.2.3. Hydration models 241
IV.3.2.4. Ageing factor 243
IV.3.2.5. Conclusion 245
IV.3.3. Experimental results database 245
IV.3.3.1. Learning-based models 246
IV.3.3.2. Closest Formulations Selection Algorithm (CFSA) 250
IV.3.3.3. Tendencies observed 255
IV.3.4. Confidence index ω 267
IV.3.4.1. Definition and use 267
IV.3.4.2. Experimental measurements 269
IV.3.4.3. Literature model 269
IV.3.4.4. Regression and Artificial Neural Network 270
IV.3.4.5. Closest formulation selection algorithm 270
IV.4. Engineering modelling 270
IV.4.1. Model selection and deterministic results 270
IV.4.1.1. Carbonation models 271
IV.4.1.2. Chloride penetration models 276
IV.4.1.3. Corrosion models 287
IV.4.2. Probabilistic approach 295
IV.4.2.1. Carbonation induced corrosion (XC) – depassivation probability 296
IV.4.2.2. Carbonation-induced corrosion (XC) – Corrosion-induced cracking probability 302
IV.4.2.3. Chloride induced corrosion (XS) – Depassivation probability 305
IV.5. Conclusion and recommendations 307
GENERAL CONCLUSIONS AND PERSPECTIVES 309
BIBLIOGRAPHY 315
ANNEXES 339
Annex 1 – Constituents (Section II) 339
Annex 2 – Numerical values (Sections II – III – IV) 347
Experimental measurements (Sections II.3.4 – III.5.1) 347
Experimental results database (Section IV.3.3) 347
Input data used for carbonation depth computation (Section IV.4) 348
Data associated to probabilistic computations (Section IV.4.2) 352
Carbonation-induced depassivation 352

Chloride-induced depassivation 352
Annex 3 – Sensitivity analyses (Section IV) 353
Literature models for input parameters calculations (Section IV.3.2) 354
Mechanical resistance computation 354
Water porosity models 354
Hydration models 355
Learning-based models for properties computation (Section IV.3.3) 356
Compressive strength fc 356
Carbonation depth 357
Electrical resistivity 358
Models for carbonation depths computation (Section IV.4.1) 360
Models for chloride penetration computation (Section IV.4.1) 361
Annex 4 – Literature and models (Sections I – III – IV) 361
Analytic models for carbonation-induced corrosion (Section IV.4) 361
Model of Von-Greve and Gehlen [199] 361
Demis model [27] 362
Carbonation model of the Japan Society of Civil Engineers (JSCE) [196] 363
Carbonation model of Parrott [194] 363
PerfDuB Model [266] 364
Analytic models for chloride-induced corrosion (Section IV.4) 365
fib code model [20] 365
PerfDuB and ANR Modevie model [2], [229] 365
Analytic model for carbonation-induced corrosion propagation (Section IV.4) 366
PerfDuB model for carbonation induced corrosion propagation [2] 366
Morinaga [193] 367
Maaddawy [430] 368
Analytic model for chloride-induced corrosion propagation (Section IV.4) 368
Balafas and Burgoyne [270] 368
Yalcyn and Ergun [271] 369
PerfDuB model for chloride induced corrosion propagation [2] 369
Stewart and Suo [441] 370
Analytical models for concrete properties estimation (Sections III.5 – IV.4) 371
Porosity 371
Hydrate contents 373
Statistical methods (Sections III.6 – IV.3.2) 373
Latin Hypercube Sampling (LHS) 374

Principal Component Analysis (PCA) 374
Sensitivity analysis (Section III.6 – IV.3 – IV.4) 376
Morris sensitivity analysis 376
Sobol sensitivity analysis 378

GLOSSARY OF TERMS

Acronym:

Afm: Monosulfoaluminates ($C_4A\bar{S}H_{12}$)
Aft: Ettringite ($C_6A\bar{S}_3H_{32}$)
ANN: Artificial Neural Network
C_3A: Tricalcium aluminate
C_4AF: Tetracalcium aluminogerrite
CC: Consequence of Failure
CFSA: Closest Formulation Search Algorithm
CH: Portlandite
CoV: Coefficient of Variation
CPE: Constant Phase Element
CPT: Critical Pitting Temperature
C-S-H: Calcium Silicate Hydrate
D: Schist
DC: Dry curing
DPL: Dense Product Layer
EC: External curing
EIS: Electrochemical Impedance Spectroscopy
fib: Fédération International du Béton (French)
FORM: First Order Reliability Method
GDP: Gross Domestic Product
GGBS: Ground Granulated Blastfurnace Slag
HPC: High Performance Concrete
ITZ: Interfacial Transition Zone
JSCE: Japan Society of Civil Engineers
L, LL: Filler, limestone-based additions
LPR: Linear Polarization Resistance
M: Metakaolin
MAE: Mean Absolute Error
MC: Moist curing
MEC: "Modèle d'Empilement Compressible" (French)
MRE: Mean Relative Error
OCP: Open-Circuit Potential
OPC: Ordinary Portland Cement
P: Pozzolan
PCE: Polynomial Chaos Expansion
PerfDuB: Approche Performantielle de la Durabilité des Bétons – National Project in France (2015-2021)
P_f: Probability of failure
PM/ES: "Prise Mer/Eau Sulfatée" (French)

PR: Polynomial Regression
PREN: Pitting Resistance Equivalent Number
Qz: Quartz, Silicious-based additions
UHPC: Ultra High Performance Concrete
ULS: Ultimate Limit State
RC: Reliability Class
RCA: Recycled Concrete Aggregate
RH: Relative Humidity
SCM: Supplementary Cementitious Material
SEM: Scanning Electron Microscope
SLS: Service Limit State
SORM: Second Order Reliability Method
TGA: Thermogravimetric analysis
TG-DTA: Thermogravimetric and Differential Thermal Analysis
TM: Transformed Medium
V: Fly ash
WA: Water Absorption
W/B: Water-to-Binder ratio
W/C: Water-to-Cement ratio
XRD: X-Ray Diffraction

Recurrent notations:

General:

t: Time (years, s)
t_c: is the curing time (days)
t_0: Time of test realization (days)
t_{ini}: Time of corrosion initiation (years)
t_{prop}: Time of corrosion propagation (years)
$t_{prop,cr}$: Time of corrosion propagation until cover cracking (years)
R: Gas law constant (8.314 J.mol^{-1}.K^{-1})
F: Faraday constant (96485 C.mol^{-1})
f_{cem}: Cement characteristic resistance measured at 28 days (MPa)
f_{c,t_0}: Compressive strength at t_0 (MPa)
f_t: Tensile strength (MPa)
E_c: The elastic modulus (MPa)
v: Poisson' ratio of concrete (0.18)
ψ_{cr}: Creep coefficient of concrete (2.35)
ε_{air}: Volume fraction of entrapped air in concrete (%, -)
$WA_{agg,i}$: Water absorption of aggregate after 24h (%, -)
φ_{agg}^{w}: Aggregate porosity accessible to water (%, -)
φ_{p}^{w}: Cementitious paste porosity accessible to water (%, -)

$\varphi_{p,car}^{w}$: Carbonated cementitious paste porosity accessible to water (%, -)
φ_c: Total concrete porosity (%, -)
$\varphi_{c,car}$: Total porosity of carbonated concrete (%, -)
φ_c^w: Concrete porosity accessible to water (%, -)
φ_c^{Cl}: Effective porosity for chloride diffusion in concrete (-)
CC: Concrete cover (mm)
C_{nom}: Nominal concrete cover (mm)
D_{rebar}: Reinforcing bar diameter (mm)
D_{max}: Maximal diameter of aggregates (mm)

Composition:

CH: Portlandite content (kg/m^3)
Ca_{CH}: Quantity of Calcium able to carbonate in CH (mol/L, mol/m^3, kg/m^3)
CSH: Calcium silicate hydrate content (kg/m^3)
Ca_{CSH}: Quantity of Calcium able to carbonate in C-S-H (mol/L, mol/m^3, kg/m^3)
Afm: Monosulfoaluminate content (kg/m^3)
Ca_{Afm}: Quantity of Calcium able to carbonate in Afm (mol/L, mol/m^3)
Aft: Ettringite and hexahydrate content (kg/m^3)
Ca_{Aft}: Quantity of Calcium able to carbonate in Aft (mol/L, mol/m^3)
F_{paste}: Volume fraction of paste in the material (-)
F_{agg}: Volume fraction of aggregates in the material (-)
ρ_{agg}: Bulk density of aggregate (kg/m^3)
C: is the cement content (kg/m^3)
ρ_{cem}: Bulk density of cement (kg/m^3)
ρ_c: Bulk density of concrete (kg/m^3)
B: Content of binder (kg/m^3)
Q_{agg}: Content of aggregate (kg/m^3)
ρ_w: Water bulk density (981 kg/m^3)
W_{eff}: Effective water content (kg/m^3)
W_{eff}/B_{tot}: Effective water to total binder content ratio (-)
W_{eff}/C: Effective water to cement ratio (-)
A/C: Aggregate-cement ratio (-)
α: Hydration rate of cementitious material (-)
C_3S: Tricalcium silicate content (-, mol/kg of cement)
CaO: Calcium oxide content (-, mol/kg of cement)
CaO_r: Amount of reactive CaO (kg/m^3)
SO_3: Sulphur oxide content (-, mol/kg of cement)
SiO_2: Silicon oxide content (-, mol/kg of cement)
Al_2O_3: Aluminum oxide content (-, mol/kg of cement)
Fe_2O_3: Iron oxide content (-, mol/kg of cement)
MgO: Magnesium oxide content (-, mol/kg of cement)
C/S: Molar ratio of CaO/SiO2 in C-S-H (-)

Q_{SCM}: SCMs contents (kg/m^3)
Q_P: Pozzolan content (kg/m^3)
ρ_P: Pozzolan bulk density (kg/m^3)
Q_K: Clinker content (kg/m^3)
Q_{SF}: Silica fume content (kg/m^3)
F_{SF}: Silica fume weight ratio (-)
Q_V: Fly ash content (kg/m^3). Low calcium $Q_{V,L}$ and high calcium $Q_{V,H}$ are sometimes differentiated.
F_V: Fly ash weight ratio (-)
Q_S: Slag content (kg/m^3)
F_S: Slag weight ratio (-)
Q_M: Metakaolin content (kg/m^3)
F_M: Metakaolin weight ratio (-)
Q_L: Filler content (kg/m^3)

Thermal:

T_{env}: Temperature of the environment (K)
T: The temperature of the concrete (K, °C)
k_{therm}: Thermal conductivity of concrete (W/m.K)
c_{therm}: Specific heat of concrete (J/kg.K)
σ: Stefan-Boltzman constant (5.669 x 10^{-8} W/m^2.K^4)

Hydrologic:

RH_{ref}: Relative humidity of reference (65%)
RH_{env}: Relative humidity of the environment (%)
RH: Relative humidity in the concrete material (%, -)
RH_s: Relative humidity of the concrete surface (%, -)
D_h: Effective moisture diffusion coefficient (m^2/s)
$D_{app,h}$: Apparent moisture diffusion coefficient (m^2/s)
Pv_{sat}: Saturation vapor pressure (atm)
Pv: Vapor pressure (atm)
w_e: Evaporable water (-)

Durability:

k_e: Environmental factor (-). Different values are proposed for carbonation and chloride penetration models. *Ccrit*
k_{RH}: Relative humidity factor (-)
k_c: Curing factor (-). Different values are proposed for carbonation and chloride penetration.
k_t: Test influence factor (-). Different values are proposed for carbonation and chloride penetration.
k_a: CO_2 concentration factor (-)
k_p: Thermal treatment factor (-)
k_T: Temperature factor (-)
k_{O_2}: Oxygen factor (-)

$k_{C/A}$: Cathode – anode ratio factor (-)
k_{Cl}: Chloride contamination factor (-)
k_{SCM}: SCMs factor (-)
k_f: Finishing and coating factor (-)

Carbonation:

x_c: Carbonation depth (mm)
x_c^{exp}: Carbonation depth (mm)
D_{CO2}: CO_2 diffusion coefficient in concrete exposed to natural conditions (m^2/s)
D_{air}: Air permeability coefficient in concrete (10^{-16} m2/$years^{-1}$)
K: Carbonation rate ($mm.year^{-0.5}$)
K_{nat}: Natural rate coefficient ($mm.year^{-0.5}$)
R_{NAC}: Effective carbonation resistance of concrete (kg/m^3)($years/mm^2$)
$ToW_{2.5}$: Ratio of annual day number with rain superior to 2.5 mm (-)
ToW_{10}: Ratio of annual day number with rain superior to 10 mm (-)
p_{dr}: Probability of driving rain (-)
$[CO_2]_{env}$: Carbon dioxide concentration in the environment (kg/m^3)
$[CO_2]$: Carbon dioxide concentration in the concrete (kg/m^3)
P_{CO_2}: Partial pressure of carbon dioxide in the environment (%.vol, Pa)
$P_{CO_2 ref}$: Carbon dioxide concentration of reference (0.04%.vol, 415 Pa)
P_{atm}: Carbon dioxide concentration of reference (101325 Pa)
$t_{cr,carbo}$: Critical time of carbonation (s)
t_{eff}: Effective time of carbonation (years)

Chloride:

Cl_t: Total chloride concentration (kg/m^3 of concrete, mol/m^3 of concrete)
Cl_0: Initial total chloride concentration (kg/m^3 of concrete)
Cl_S: Total chloride concentration at the concrete surface (kg/m^3 of concrete)
$Cl_{S,\Delta x}$: Total chloride concentration at the depth Δx (kg/m^3 of concrete)
Cl_f: Free chloride concentration (kg/m^3 of solution, mol/m^3 of solution, wt.% of binder)
$Cl_{f,sat}$: Free chloride concentration in saturated concrete (kg/m^3 of solution)
$Cl_{f,env}$: Free chloride concentration in the environment (kg/m^3 of solution, wt.% relative to the binder mass)
Cl_b: Bound chloride concentration (kg/m^3 of concrete)
C_{crit}: Critical concentration (wt.% of binder)
Δx: Depth of the convective zone (mm)
D_1: Diffusion coefficient of the 1st Fick law (m^2/s)
D_2: Diffusion coefficient of the 2nd Fick law (m^2/s)
D_m: Average diffusion coefficient (m^2/s)
D_{eff}: Effective diffusion coefficient (m^2/s)
D_{app}: Apparent diffusion coefficient (m^2/s)
D_{rcm,t_0}: Accelerate migration coefficient measured at t_0 (m^2/s)

ae: Ageing factor (-)

t_{th}: threshold time beyond which the diffusion coefficient is supposed constant (years)

t_{salt}: Annual days number where deicing salts are applied on the structure (days)

Corrosion:

i_{corr}: Corrosion current (µA.cm^{-2}, A.m^{-2})

i_0: Initial corrosion current density (µA.cm^{-2})

Re_{sat}: Lineic electrical resistivity in saturated concrete (Ω.m)

Re: Lineic electrical resistivity in concrete (Ω.m)

R_{Ohm}: Electrical resistivity in concrete (Ω)

V_{corr}: Corrosion rate (µm.year^{-1})

M_{Fe}: Molar mass of iron (55.845 g/mol)

ρ_s: Bulk density of steel (7.85 g/cm^3)

z_{Fe}: Valence of iron cation (2)

L_a: Anodic length (mm)

X_{crit}: Critical section lost (mm)

i_c: Anodic current density (A.m^{-2})

i_a: Cathodic current density (A.m^{-2})

$[O_2]$: Oxygen concentration (Pa)

D_{O_2}: Oxygen diffusion coefficient (m^2/s)

H: Henry constant (7.47.10^4 Pa.m^3/mol).

Δe_{tot}: total growth of the corrosion product (m)

INTRODUCTION

Global warming and ecosystem contamination are omnipresent topics of discussion, concerns and debate in our society. The measurable impacts and future consequences of these issues are becoming increasingly evident, shaping our understanding and guiding decision-making to reduce global emissions and achieve carbon neutrality in the coming decades.

One sector that makes a significant contribution to carbon dioxide emissions is the building and construction industry, which accounted for 39% of CO2 emissions in 2019 (236 Mt eq CO_2/an) [1]. Concrete, a commonly used material in construction, has a substantial carbon footprint due to the clinker used in the cement production. Cement industry is responsible for 2.5% of the French emissions and 12% of the industry emissions (10 Mt eq CO_2/year) [2], [3]. Thus, it is imperative for the concrete sector to swiftly adapt and mitigate its impact by transitioning towards more sustainable practices that address current ecological challenges. Several feasible solutions have been proposed to achieve this goal, including incorporating supplementary cementitious materials (SCMs) to replace clinker (either mineral produced for this purpose, or by-products of other industries) or reutilizing construction debris instead of aggregates [4]. It is crucial for the concrete sector to embrace these proposed solutions and make significant advancements towards "decarbonizing" the industry. Optimising the construction system by using fewer materials is another important lever to consider this aspect. The reduction of the material volume used for a functional unit can sometimes be more advantageous than formulating a concrete with lower environmental impact that will require higher thickness of material to ensure the safety of the structural system. Hence, the measures adopted need to consider the whole ensemble of possibility to find the optimal option.

On the other hand, the prediction of the durability, as well as the desire of structure managers to lengthen the service life of existing structures, correspond to circular economy principles. It explains the decisive position of the structure durability in the French and European standards. The goal of these regulations is to ensure the reliability of the structures in specifics environments and for a given service life. In fine, the compliance with these rules, and the manufacture of resilient structure also plays an important part in reducing of the environmental impact of the concrete sector.

Many structures that were built in the twentieth century now require inspections and maintenance due to their potential level of degradation. The corrosion of reinforced structures represents a major cause of degradation and leads to substantial repair costs each year [5]. Therefore, there is a growing demand to accurately predict the optimal timing for inspections, maintenance, and repair operations on specific structures or areas to achieve the highest economic and environmental benefits. Additionally, accurately predicting structural failure is crucial for preventing harm to persons and damage to the structures themselves.

To address the aforementioned challenges, models can be utilised, in complement with experimental approaches, to accurately predict the degradation of a structure. Some mechanical phenomena can be accurately modelled with the assumption that the reinforced concrete has an elastic behaviour. It can be noted that the consideration of the mechanical degradation, with visco-elasto-plastic behaviour, is much more complicated to predict. Durability may also be predicted adequately in certain situations allowing the use of some assumptions. Modelling is always a simplification of the real phenomena, which sometimes leads to significant misestimations and requires much attention in verifying its consistency. Durability in reinforced concrete pertains to the interaction between various physical and chemical phenomena (liquid and gaseous diffusion, convection, chemical reactions, heat transfer, corrosion, etc.), representing the interactions between a complex medium (concrete and its cementitious matrix) and its environment which depends on many parameters such as the temperature,

relative humidity, chloride concentration, and CO_2 concentration. This complexity is therefore inherent to the modelling of durability in reinforced concrete. This is particularly true for new and alternative binders, whose behaviours with regard to durability are being progressively understood at the moment. Moreover, the developed models are typically based on laboratory studies rather than actual structural outcomes, which may limit their practical applicability.

Hence, engineers use modelling tools to design structures and formulating materials complying with regulation and standards. These standards serve as solid basis and essential safeguard to ensure the reliability of reinforced concrete systems. Due to the current evolution of the concrete construction sector, these standards evolve, leading to renewal durability requirements that need to be met by the structural project designer helped by adequate prediction tools. Hence, the models and tools developed must be flexible and adapt to the specific needs of the engineers, while giving reliable predictions.

The need for comprehensive and complete methodologies for predicting operational durability has been the primary motivation behind this Ph.D. thesis. The objective of this thesis is to develop a comprehensive methodology that accurately predicts the durability of reinforced concrete structures exposed to carbonation or chloride ingress. Ultimately, the aim of this methodology is to assist users in making decisions at four levels:

1. For the construction of new structures, including the selection of an appropriate concrete mix for a specific situation and its optimal design.

2. For predicting the optimal inspection time to enhance prediction accuracy and ensure reliable results. Non-destructive testing methods should be preferred over destructive tests whenever feasible.

3. To allow the prediction of the optimal operation and maintenance time.

4. For estimating critical times for depassivation, crack formation, and failure.

To meet these operational points, different scientific requirements have been established for this work:

A. The methodology must consider both new and ancient structures, incorporating concrete materials formulated up to 70 years ago as well as novel concrete mixes developed using the performance-based approach defined in the recent FD P18-480 (2022). It implies the capability to predict the degradation of reinforced concrete structures with sometimes a few available data.

B. It must account for carbonation and chloride ingress in all exposure classes defined in the NF EN 206/CN+A2 (2022), together with recent subclasses defined in the FD P18-480 (2022).

C. The methodology must possess high flexibility to adapt to restricted input parameters, which are often limited for ancient structures. In particular, three main difficulties can be identified:

- The appraisal of the initial condition state of the structure (generally unknown and relying on the composition of the material used and the manufacturing process).
- The knowledge of the exposure conditions and the degradation that impacted the structure.
- The estimation of the present condition state, which is either based on testing (non-destructive or destructive) used to directly measure this aspect, or predictions based on models or assumptions on the exposure and initial state of the structure.

Additionally, the tool should provide reliable predictions for new concrete mixes even in the absence of inspection data.

D. The implementation of probabilistic computations must enable considering uncertainties that affect material properties, geometrical dimensions and environmental actions impacting the structure. Lack of precise knowledge of the quantities of interest, random variability, inherent approximation in their appraisal or estimation from various methods contribute to render them uncertain. Beyond evaluating

the uncertainties, target reliability levels imposed by design codes for new structures, or more specifically recommended for existing ones, must be checked against the actual levels by appropriate reliability estimates. Nevertheless, deterministic computations can also be performed for comparison with experimental measurements.

E. The tool must enable simple verifications of the results. The idea is to establish a database of experimental feedback that can be employed for comparison with the user's case study. This database should be modifiable and continuously updated using the methodology.

This work consists of four main chapters aimed at investigating the durability of reinforced concrete in a scientific context. In the first chapter, a comprehensive overview of reinforced concrete durability is provided, including a discussion of fundamental phenomena such as concrete hydration, carbonation, chloride ingress and corrosion. Various existing methods for modelling these phenomena are explored, with a focus on mathematical approaches used to facilitate the analysis of databases and probabilistic computations. Additionally, an examination of the main standards used for concrete mix regulations is presented.

The second chapter details an experimental plan used to thoroughly investigate specific types of low-carbon binders. This includes an analysis of mechanical and microstructural parameters, as well as resistance to carbonation and chloride penetration. To conduct these investigations, six different concrete mixes are proposed, including CEM III/B, CEM V/A (S-V), and CEM VI (S-V)-based concretes.

The third chapter focuses on utilizing the experimental results to enhance the SDReaM-Crete finite element model predictions. This model, developed through previous PhD studies [6], [7] to account for carbonation and chloride ingress, is improved to consider various types of concretes, including CEM I, filler, slag, fly ash, and metakaolin-based concretes. To reduce the computational time required by the finite element model and enable its use for operational predictions, surrogate models are developed using the polynomial chaos expansion method.

The fourth and final chapter describes the first version of the tool and methodology for operational predictions, which integrates various models and mathematical methods based on the exploitation of an experimental database. This methodology allows for the prediction of reinforced concrete durability in carbonating and chlorinating environments. It offers a flexible approach with a reduced number of inputs and considers the variability of average parameters and uncertainties introduced by each method. Hence, a confidence index associated to each predicted parameter is computed and used to account for the uncertainty on the final probabilistic computations, which are used to estimate the remaining service life of the reinforced concrete structure.

I. State of the art

Nowadays, society inevitably relies on the use of concrete for the construction of buildings, civil engineering structures and roads among other things. The average annual production of cement was 4.1 billion tonnes in 2019 [8] while the annual production of concrete was already superior to 18 billion tonnes in 2008 [9]. This production represents around 8% of the man-made carbon emissions and 6% of the greenhouse gases [10]. The production of cement depends on the country and on the availability of the materials. Figure I-1 shows that China dominates most of the market today [11].

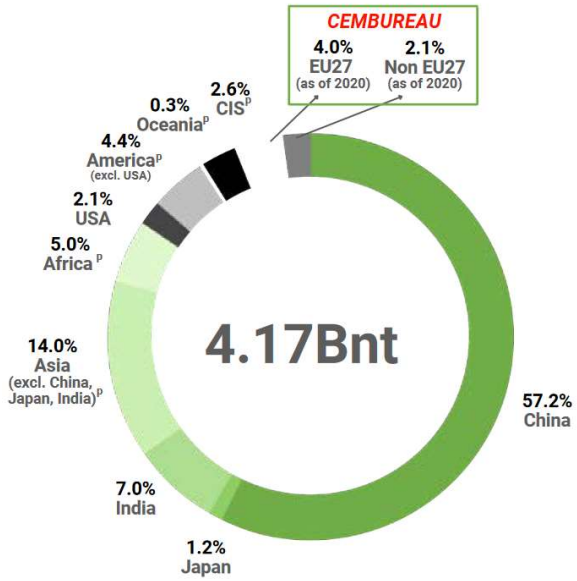

Figure I-1 World cement production in 2020, by region and main country [12].

The Ordinary Portland Cement (OPC), which is the primary cement used in the concrete industry, accounts for approximately 6% of all man-made carbon emissions [13]. Addressing challenges such as global warming and ecosystem destruction, the focus of the construction industry is shifting towards ecological transition, with efforts to reduce the environmental impact of structures. This transition applies to both the construction and public works sectors. Public authorities in France have initiated efforts to define the French Energy and Climate Strategy ("Stratégie Française Énergie Climat" in French), including the National Low-Carbon Strategy. Within this context, major construction stakeholders have various tools and solutions to reduce CO_2 emissions from concrete structures:

- The first approach involves designing the different components according to structural requirements and environmental considerations. For example, thinner walls can be used on higher floors of a building if lower weight is applied. Avoiding oversized concrete cover is crucial to minimize the quantity of material used. Manufacturing more compact concrete can significantly enhance durability, and thus lead to thinner concrete cover to sustain in aggressive environments.
- The selection of locally produced materials also helps to reduce the carbon footprint associated with transportation.
- Reusing materials from previously demolished structures is another strategy to decrease the consumption of natural resources and minimize waste resulting from deconstruction. Additionally, capturing carbon during cement production may offer an alternative method to reduce the overall environmental impact [14].
- Regarding the binder of the concrete, substituting the traditional OPC with suitable additions can be pursued to achieve this goal.

However, the global clinker (main constituent of OPC) to cement ratio has increased in recent years (from 2014 to 2018) at an average of 1.6% per year, leading to an increase in CO_2 release due to cement production [8].

Controlling the durability of concrete structures contributes to reducing their carbon impact, not only for new structures but also for existing structures, for which extending the service life and maintaining continuity of service are major challenges for all owners of building and infrastructures. Maintenance of structure is also an ecological and financial key factor. The cost of structure maintenance and repair vary in a non-linear way over time (see example in Figure I-2), which means that a good prediction of the material state and evolution gives economic advantages. Proactive interventions are generally cheaper than the extensive repairs potentially needed following the traditional approach based on visual inspection. This last aspect is of importance for the manufacturers since the corrosion of steel bars, used to reinforce concrete structures, leads to an annual cost ranging between 3 and 4 % of the GDP (Gross Domestic Product, PIB in French) in developed countries [15], [16]. In China, the cost of reinforcement corrosion exceeded $2 trillion in 2021 while the American Society of Civil Engineering considers that infrastructural repair will cost $2 trillion by 2025 in the US [17], [18]. To assure the structural integrity of a system, while achieving optimal economic and ecological outcomes, accurate anticipation of environmental influences on construction materials, such as concrete and steel, is paramount. This enables the optimization of their design, both in terms of geometry and composition. Many techniques and models were developed to predict the behaviour of the reinforced concrete, according to its properties, its environment, and the quality of the structure manufacture. The importance of these predictive tools is to help the designer acquiring:

- The best knowledge to build efficiently in terms of materials (cements, additions, aggregates, durability properties…), and cost (carbon footprint, reduction of transport distance, maintenance prediction…).
- Safeguards to ensure the safety of the structure for the required service time (Concrete cover, performance-based approach application, reliability index for the structure). The application of durability models in predicting the performance of structures aids in achieving optimized designs by effectively accounting for external aggressions. These predictions assist users in making informed decisions and improving design durability.

Additionally, the utilization of predictive models enables the implementation of semi-probabilistic or probabilistic methodologies. These methodologies vary from deterministic approaches as they take into account the significant variability inherent in concrete materials. The utilization of these methods permits the assessment of the failure probability of a specific structure, along with its long-term reliability. The use of semi-probabilistic approach is defined in [19], [20] and [6]. International standards also deal with this subject [21], [22].

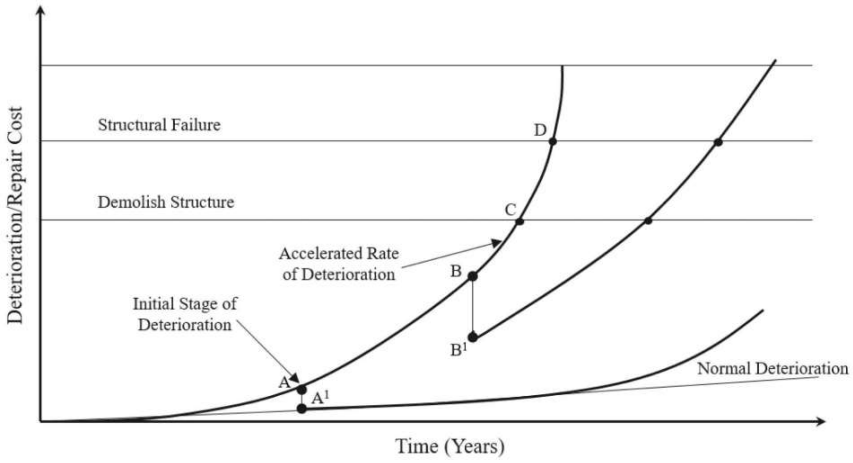

Figure I-2 Relations among maintenance costs, repair and damages within the building life cycle [23].

The study of concrete structures' durability generally implies the study of the reinforcing steel bar corrosion. Indeed, rebar corrosion is to a large extent the prominent phenomenon of degradation of these structures. It is a complex mechanism which relies on numerous parameters such as the type of cement used, the transfer properties of concrete, the environment, but also the nature and electrochemical state of the steel used as reinforcement [24]–[26]. Corrosion is generally initiated when a critical quantity of chloride ions is reached in the vicinity of the steel, or when the pH is reduced below a critical value by the carbonation phenomenon. The propagation of the corrosion also depends on the moisture condition state in the cementitious matrix and the oxygen quantity available on the steel surface [7].

To this day, the literature shows few complete methodologies able to consider the entire determination of a structure failure probability, from inputs determination to results interpretations [27]. There is a growing need in the civil engineering sector to possess and master tools for the computation of reinforced concrete structures durability, when exposed to diverse environments. This statement holds a growing significance as novel concrete constituents are being actively employed to optimize the appeal of reinforced concrete material in terms of its carbon footprint and environmental impact. The diversity of supplementary cementitious materials, or the use of recycled concrete aggregate, involve higher uncertainties of the concrete material properties, and requires more complex and advanced models to consider precisely the phenomena impacting the structure durability. For this reason, the present work aims at giving a complete documentation for durability prediction in the case of carbonation induced corrosion and chloride induced corrosion, from concrete properties determination to service life computation.

This section thus provides an overview of the current state of research in this field. To ensure the most accurate replication of the literature results, the PlotDigitizer software was used [28] for extracting graphical data. Further post-processing was performed using Python [29], primarily employing the Matplotlib library [30].

I.1. Concrete composition

Traditional concrete is mainly constituted of sand and gravel, between 60 and 80 % in volume [31]. The second main constituent of concrete is cement. It reacts with the mixing water to form the cementitious paste. This phenomenon is the cement hydration and consists of exothermic reactions which lead to the hardening of the concrete cementitious paste. Various admixtures can also be added to the blend to modify the final properties of fresh and hardened concrete. These different components and their importance for concrete material are one of the subjects of this section.

In recent decades, several strategies have been devised to attenuate the environmental repercussions of concrete, primarily attributed to clinker production. This section provides an account of mineral additions and recycled concrete aggregate deployment as viable alternatives.

Another bias that can be used to reduce the carbon footprint of a structure construction is the use of local constituents for the production. The availability of the constituent and their proximity from the manufacturing site need to be considered by the project manager. The mineral resources in France have been evaluated in different reports and works [32].

I.1.1. Aggregates

Sand and gravel are the principal constituents of concrete in terms of mass and volume. They compose the "stone skeleton" of the concrete. Their properties thus impact greatly the overall concrete material properties. Different methods have been established to optimize the properties of concrete with the adequate aggregate and granular skeleton. An important example is the formulation method developed by De Larrard and detailed in [33]. Among many parameters, the compressible stacking model theory (MEC, "Modèle d'Empilement Compressible" in French) included in [33] shows the importance to

consider the particle size distribution of the different constituents to optimize the concrete mechanical capacity.

When assessing the corrosion resistance of concrete materials, various parameters are utilised to evaluate the effectiveness of gravels and sands, such as the porosity or the water absorption capacity. This section provides an overview of the different types of aggregates employed in concrete production and their properties crucial for classification.

I.1.1.1. Type and properties

From a general point of view, an aggregate is characterized by its origins, the way it was produced, its shape, size, and microstructure among other properties. Four main categories of aggregates can be defined considering the manufacturing process used, as shown in Table I-1.

Table I-1 Presentation of the different aggregate types and shaping.

Aggregate type	Origin	Shaping process
Natural rounded	Mineral, loose rock	Erosion
Natural crushed	Mineral, solid rock	Mechanical
Synthetic	Inorganic, organic or vegetal	Complex (thermal or mechanical treatment)
Recycled	Demolished concrete	Mechanical

The French standard NF EN 18-545 (2011) defines different classifications for aggregate size, which are summarized in Table I-2.

Table I-2 Classification of aggregates used in concrete production [34].

	Fine	Sand	Gravel	Coarse
Diameter range	< 63 µm	0-4 mm	4 – 12 mm	12 – 45 mm

Concerning the properties of the aggregate, the main and most pertinent ones are [35]:

- The density (ρ): The dry density (ρ_{dry}), generally expressed in kg/m^3, is obtained by drying the aggregate until reaching a constant mass. The saturated density (ρ_{sat}) is obtained by immersing the aggregate in water until obtaining a constant mass value. It ranges from 2400 kg/m^3 to 2900 kg/m^3 for standard aggregates [33].
- The water absorption (WA): It represents the amount of water absorbable in the aggregate. It can be computed using the Equation I.1. Technical sheet of aggregate generally gives the water absorption obtained after 24h of immersion (WA_{24h}). In [33], De Larrard explains that in the case of rheological parameter of fresh concrete estimation, it can be wise to consider the water absorption obtained after one hour. In the investigation of long-term durability, the water absorption value obtained after 24 hours or beyond is strongly recommended, as it accounts for extended durations [36].

$$WA = 100 \times \left(\frac{\rho_{sat}}{\rho_{dry}} - 1 \right) \quad \text{Eq (I.1)}$$

- The porosity accessible to water (φ_{agg}^{w}): It can be computed simply from WA and ρ_{dry}:

$$\varphi_{agg}^{w} = \rho_{dry} \times WA \quad \text{Eq (I.2)}$$

- The granularity: It holds significant importance due to its inherent variability and potential impact on the mechanical properties. The granular distribution is generally assessed using a sieving method [37].
- The residual compactness, which is controlled by the geometry and textural surface of the aggregate. It represents the virtual capacity of the grains to stack with each other. It is notably linked to the density and mechanical properties of the concrete.

I.1.1.2. Recycled Concrete Aggregate (RCA)

Recycled concrete aggregates consist in demolition waste of old roads and buildings mechanically crushed. Extensive research has been conducted on both fine and coarse RCAs to investigate their influence on diverse concrete properties. [38]–[42].

One issue regarding the study of RCA is connected to the considerable variability of their properties. They are influenced by various factors such as the crushing technique employed during their extraction, the initial concrete composition, the exposure environment, and the duration of exposure. These factors have a significant impact on the final properties of RCA, making it challenging to accurately predict and account for the durability of concrete structure integrating them.

The main reason of incorporating RCA in concrete manufacturing is to prevent the harvesting of natural resources while reusing the waste material (circular economy) [43]. It also helps reducing the carbon footprint, even if natural aggregates production is associated to low carbon emission. The Fastcarb project [14] even focused on the capacity to store CO_2 from cement manufacturing plant in RCAs to optimize their environmental impact.

Because of their nature, the properties of recycled concrete aggregates differ from the one of natural aggregates. The density is generally lower for RCA while the porosity and water absorption of RCA have significantly higher values. The difference is attributed to the residual mortar that composes the concrete waste [43]. Because of the impacts of the aggregate's parameters on the final concrete properties and the consequently lower attributes of RCA, their content is often limited in concrete mix [19]. It was reported that the crushing process has an important influence on the final shape of the RCA. The residual mortar of recycled concrete aggregates (RCA) exhibits smoother and more spherical shaped aggregates compared to natural aggregates [44], [45]. This affords better rheological properties of fresh concrete. The mechanical properties of concrete containing RCA is generally lower while durability resistance is also degraded because of higher diffusions properties [38], [43]. Another important factor that needs to be considered is the crack formation. Maruyama et al. report greater crack width on RCA based beam as well as smaller crack spacing even if the difference remains limited with standard natural aggregate based concrete [46]. An explanation proposed is the presence of a second Interfacial Transition Zone (ITZ) region (between the residual mortar and the new mortar) in the case of RCA-based concretes, creating a weaker point for crack initiation and propagation [43].

In conclusion, the use of Recycled Concrete Aggregates (RCAs) presents a high interest from the environmental point of view, but their use can be complex in certain situations, where reinforced concrete structures are exposed to aggressive environment or important mechanical solicitations. Incorporation of Recycled Concrete Aggregate (RCA) is generally effectively managed when the substitution ratio falls within the range of 5 to 30 vol.%, ensuring efficient utilization of the available stock of RCA.

I.1.2. Cements and mineral additions

Cement and mineral additions compose the binder of the concrete material. It ensures the structural binding of the aggregates and is one of the key parameters concerning the final concrete properties.

Historically, binder consisted in Portland cement, which is composed of clinker (around 95% in average) and gypsum (generally around 3%). This latter constituent is added to the clinker to allow the reaction of one anhydrous specie of the clinker (C_3A) as detailed in Section I.2.1. Other constituents can be found in low quantities in this type of cement, now defined by the NF EN 206/CN+A2 (2022) as CEM I.

The clinker reacts with water (and gypsum) to form the different hydrates that compose the cementitious matrix, including the portlandite responsible for the alkalinity of the interstitial solution. These reactions play a crucial role in the acquisition of concrete's physical and chemical properties. The different reactions are detailed in Section I.2.

Several studies have been conducted in the past decade on the replacement of clinker material. Because of its manufacturing process and mainly the dehydration step involving a heating at 1450°C, the production of clinker is responsible for an important part of the man-made carbon-dioxide emissions. This section details some of the Supplementary Cementitious Materials (SCMs) available to replace the clinker in concrete [32], generally separated in two categories of additions: type I and type II. This section then resumes the definition of the different blended cement defined by the NF EN 197-1 (2012) standard recently completed by the NF EN 197-5 (2022).

1.1.2.1. Inert additions – Type I

Type I additions refer to inert additions that have minimal impact on the hydration process, aside from reducing the available reactive material by replacement. Their primary function is to occupy space, as they are not intended to undergo any significant reactions.

In this category, two types of additions are found: limestone-based additions (defined in France by the NF P18-508 (2012) standard – L and LL) and silicious-based additions of Qz mineralogy (defined in France by the NF P18-509 (2012) standard – Qz). These additions are generally mineral materials such as limestone and silica, finely crushed and used in the form of powder.

1.1.2.2. Pozzolanic and latent hydraulic additions – Type II

Type II additions refer to reactive additions, generally defined as pozzolanic additions or latent hydraulic additions. Due to their nature, these additions will impact the final nature of the cementitious matrix, notably by modifying the hydrate nature and content, by replacement and reaction. The name “pozzolanic” is associated to the reaction they cause, which is detailed in Section I.2.2, and is responsible for the portlandite consumption produced by the clinker hydration. The degree of portlandite consumption depends on the additions properties and is sometimes defined by the pozzolan reactivity index (expressed in mg of portlandite consumed for the hydration of 1 g of addition). Values measured in the literature are shown in Table I-4.

The use of type II additions shows the interest to reduce the final carbon footprint of the concrete production since they generally are by-products of other industries (wastes) and are therefore considered as less environmentally impacting components. Some of the most used type II additions are described with more details in the following paragraphs.

Metakaolin (NF P 18-513 (2012)) is a powder with a large specific surface obtained by calcination-griding or grinding-calcination of clay mainly composed of kaolinite. This addition is an amorphous aluminium silicate with high pozzolanic properties (reactive SiO_2 and Al_2O_3) [47]. Its particles are porous and lamellar and have an average size comprised between 1 and 20 µm. Depending on the source of extraction, metakaolin composition may exhibit significant variability [48]. The use of metakaolin in concrete can have a small impact on the interstitial solution pH value (see Figure I-4). Due to its high

pozzolan reactivity index (see Table I-4) and the modification of the mechanical properties it causes, the replacement of clinker by metakaolin is generally limited to values inferior to 30 wt.%, while an optimum replacement percentage of 20 wt.% is generally found [49], [50]. In fact, metakaolin utilization can help improving the general properties of the formulated concrete, especially for low Water/Binder (W/B) ratio [51].

Fly ash (NF EN 450-1 (2012)) is made during coal combustion which produces gases at the thermal power plant outlets. They are present in the form of spherical particles with a diameter ranging from 10 to 100 micrometres. They are essentially composed of SiO_2, Al_2O_3, Fe_2O_3 and CaO under amorphous (glassy) phases (60 to 90%) as detailed in Table I-3. Fly ashes reduce the temperature required for the hydration of cement and refine the cementitious matrix pores. They can also be used in the manufacture of Ultra High and High Performance Concretes (respectively UHPC and HPC) [52], [53]. Different classifications exist according to country. The ASTM-C618 (2023) [52] categorizes fly ash in two categories according to its chemical composition [48]:

- Class F: For this category, the chemical requirement is expressed by $SiO_2+Al_2O_3+Fe_2O_3 > 70\%$. This addition is essentially pozzolanic, and the predominant specie is amorphous silica.
- Class C: The chemical requirement for this class is $SiO_2+Al_2O_3+Fe_2O_3 > 50\%$. This type of fly ash has pozzolanic and cementitious properties. They are generally used when early strength of concrete is required.

Fly ash may contribute to a decrease of the pH value of some tenth compared to a classic OPC [54]. However, results showed in [55] seem inconsistent with pH value of some FA-PC blended pastes higher than for the control. Numerous studies on the properties of fly-ash based concretes are available in the literature, certainly because of the high availability of this addition [39], [41], [42], [54]. They are generally used in higher content in the concrete formulation than metakaolin.

Blast-furnace slags (NF EN 15167-1 (2006)) are by-products of the steel industry. They exhibit a glass phase due to the violent cooling that they undergo that can be related to quenching. This mineral addition is mainly composed of CaO, SiO_2, Al_2O_3 and MgO [56], [57]. Its particle shape depends on the technique used to refine it. The mean particle size ranges between 14 and 22 µm for this addition [48]. It was shown that this SCM consumes alkaline species and essentially portlandite. However, interstitial solutions analysis only show a pH difference of 0.8 between a CEM I and a CEM III/B as shown in Figure I-4 [7], [58]. The reactions of slags differ from the pozzolanic reactions in the sense that water is involved directly in the reaction (refer to Section I.2.2.). For this reason, slags are defined as latent hydraulic additions. Ordinary slags alone have very little cementing properties. They require an activator that can either be alkaline (Portlandite, NaOH, KOH, etc.) or a sulphate activation (gypsum, hemihydrate, anhydrite, etc.) [59].

Silica fumes (NF EN 13263-1 (2009)) are by-products of the silicon production (made with electric arc furnaces). More precisely, the reduction of high-purity quartz into silicon produces vapor of silicon dioxide, which then oxidizes and condenses to produce silica fume. For this addition, particles have a mean size ranging from 0.1 to 0.3 µm and are spherically shaped. Because of its fineness, silica fume can be difficult to handle from a practical viewpoint. For this reason, alternative forms such as water-based slurry are sometimes used instead of the initial product [48]. Silica fume is generally used as substitute to cement in a replacement ranging from 5 to 15 wt.%. For higher content, this SCM can have an elevated impact on the pH of the interstitial solution (see Figure I-4). Silica fume is sometimes used in HPC and UHPC to help obtaining high performance [60]–[62].

Bauxite residue (or red mud) is inevitably generated during the extraction of alumina from bauxite (see Bayer process [63]). Since no advantageous alternative exists to the Bayer process, (or likely to emerge within the next 50 years [64]) the generation of this by-product should continue at a high level for some time (160 million tonnes in 2017). Bauxite residue is already used for both Portland cement clinker and special cements production (because of its high concentration in iron and aluminium) [65]. Its use as an SCM is at the centre of numerous investigations [64]. Calcinated bauxite is also regarded as a potential

candidate. However, there currently does not exist a standardized regulation for the use of this product as a supplementary cementitious material in concrete production.

As detailed above, the origin of the different type II mineral additions can be very different. It leads to different mineralogical compositions and properties. The Figure I-3 and Table I-3 show the place of the different type II additions in terms of oxide contents compared to the ordinary Portland cement and the type I limestone addition. An important precision is that the CaO content displayed includes inert $CaCO_3$ as well as free CaO able to react.

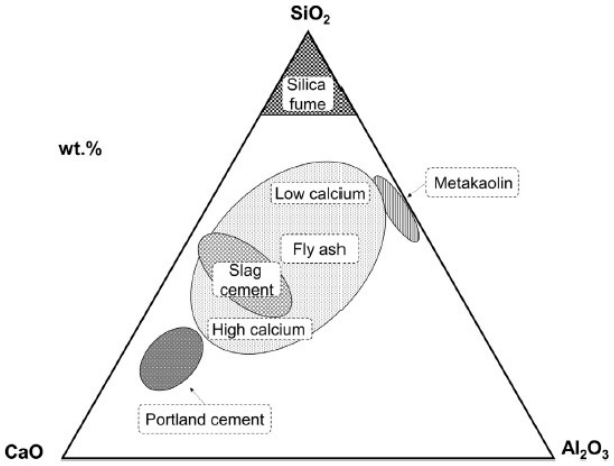

Figure I-3 Ternary diagram of Portland cement and supplementary cementing materials [48].

Table I-3. Chemical composition of classic cementitious additions (wt.%).

Component	SiO_2	Al_2O_3	Fe_2O_3	CaO	MgO	Na_2O	K_2O	TiO_2	SO_3	LOI
CEM I [66], [67]	15.4-25	3-8	0.5-6	60-67	0.1-4	0.21	0.8	-	1-3.1	0.86-2.84
Limestone filler [67], [68]	0.1-2.5	0.04-0.6	0.01-0.9	36-55	0.2-15.3	0.01-0.06	0.01-0.05	0.02	0.5	42-47
Blast furnace slag [67], [69]	30.5-42.2	5.9-17.6	1.5-3.8	30.9-46.1	1.7-4.7	0.1-1.7	0.1-1.5	0.1-3.7	0-1.5	0.8
Pozzolan [67]	46.4	17.5	10.5	10.5	3.8	3.4	1.5	-	0.4	4.31
Silica fume [66], [67]	89-90.9	0.3-1.1	0.9-1.46	0.36-0.69	1.5	0.6	1.7	-	0.3-0.38	3
Metakaolin [70]–[72]	50-55	40-45	0.5-5	0 – 0.5	0-0.05	0.2-0.8	0.2-0.8	0-1.7	-	-
Class F Fly ash [73], [74]	47.9-59.7	24-32.5	4.5-11.6	1.69-12	1.1-1.6	0.6--1.3	1.62-3.18	0.88-1.25	0-0.9	0.79-6.34
Class C Fly ash [75]	38.4-40	17-18.7	5.1-6	15-30	5	1.7	0.6	1.5	1.4-3	0.26
Calcinated bauxite [76]	12.11	77.92	2.12	0.68	0.55	0.09	0.41	4.93	0.04	-
Bauxite residue [64]	3-50	5-30	5-60	2-14	-	1-10	-	0.3-15	-	1.5-7.25

Due to their different natures, the different SCMs influence the physical and chemical properties of concrete in different ways. An example is given in Figure I-4, where the influence of different SCM replacement ratios on the reduction of the interstitial solution pH is shown [55], [77], [78]. This property can have an importance when considering the passivation and corrosion initiation of the reinforcing steel bar. It highlights the intricate nature of the domain of concrete durability research.

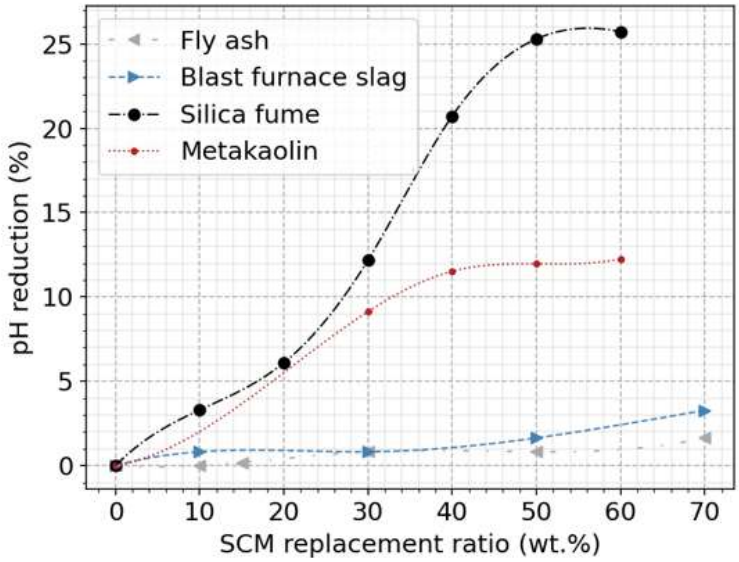

Figure I-4 Reduction of equilibrium pH of concrete interstitial solution for different SCM (Fly Ash [55], [77]; Blast furnace slag [78]; Silica fume [55], [77]; Metakaolin [77]).

Other characteristics of the different SCMs and of Portland cement are exposed in Table I-4. Unavailable data are signified by the symbol "-".

Table I-4. Physical and mineralogic characteristics of classic cementitious additions.

Component	Bulk density (kg/L)	Blaine's specific surface (cm^2/g)	Pozzolan reactivity (mg of $Ca(OH)_2$/g of material) [79]	Glass percentage (%)	Carbon footprint (kg_{eq} CO_2/t, Dec 2022) [32], [80]
Portland cement [67]	3.1	4000	-	-	765
Filler [67], [81]	2.7	3400	0	-	30-60
Silicious addition (Qz)	-	-	0	-	120
Blast furnace slag [67], [48], [81]	2.8	3500-6500	200-450	80	100
Pozzolan [67], [81]	2.8	3200	980	15	-
Silica fume [67], [81]	2.24	130000-300000	425-1800	-	354
Metakaolin [70]–[72]	2.5-2.54	70000-120000	1000	-	139-239
Fly ash [71], [81]	1.3-2.9	3000-5000	400-875	-	47.5
Calcined bauxite [71]	-	-	534	-	-

To regulate the incorporation and optimize the utilization of such additions in concrete production, the NF EN 197-1 (2012) and NF EN 197-5 (2021) standards have been established, defining various categories of cement that encompass these additions.

1.1.2.3. NF EN 197-1 cements

The standard NF EN 197-1 (2012, [82]) defines different types of cement and their compositions. Each constituent defined in this standard has an equivalence denomination which is recalled in Table I-5. The primary objective of this document is to establish consistent regulations for cement production and the inclusion of SCMs.

A total of 27 different types of cement have been classified into five distinct categories.

- CEM I is the standard Portland cement composed with clinker (95-100 wt.%).
- CEM II category integrates 17 "Portland cement" types depending on the addition type and content. First, the standard differentiates CEM II/A and CEM II/B types for SCM replacement ratio of 6-20 and 21-35 wt.% respectively (for L, LL, S, P, Q, V, W and T). An exception is made for silica fume-based cement, only defining CEM II/A-D with a replacement ratio ranging from 6-10 wt.%. Finally, the CEM II/A-M and CEM II/B-M categories are composed Portland cement where the clinker replacement is done using various SCMs of the Table I-5.
- CEM III category is composed of 3 blast furnace slag-based cements: CEM III/A cement integrates between 36 and 65 wt.% of slag, CEM III/B between 66 and 80wt.% while CEM III/C has a slag content ranging between 81 and 95 wt.%.
- CEM IV are called pozzolanic cements. The clinker replacement is realised using pozzolanic additions, namely D, P, Q, V and W. CEM IV/A cement integrates between 11 and 35 wt.% of SCMs while CEM IV/B has between 36 and 55 wt.%.
- CEM V category integrates two composed cements integrating slag (S) up to 49 wt.% and P, Q or/and V additions up to 49 wt.%.

Table I-5 Equivalence letters of the different NF EN 197-1 (2012) constituents.

Constituent	Clinker	Limestone	Slag	Silica fume	Pozzolan	Fly ash	Calcined schist
Letters	K	L, LL	S	D	P, Q	V, W	T

1.1.2.4. NF EN 197-5 cements

The recent standard NF-EN 197-5 (2021, [83]) adds five new different types of cements to the definition of the NF EN 197-1 (2012):

- CEM II/C-M composed with a clinker content ranging from 50 to 64 wt.% and a SCM content ranging from 36 and 50 wt.%. Any of the additions defined in Table I-5 can be used.
- CEM VI (S-X) category includes 4 different cements composed with slag in proportion ranging from 35 and 49 wt.% and another addition X (either P, V, L or LL) which content is comprised between 6 and 20 wt.%.

Their definitions are linked to the growing need to replace clinker in higher proportions. Using the carbon footprint values of Table I-4, it is possible to compute the theoretical carbon footprint values of certain cements. The values obtained considering minimal and maximal ranges of clinker replacement are displayed in Figure I-5.

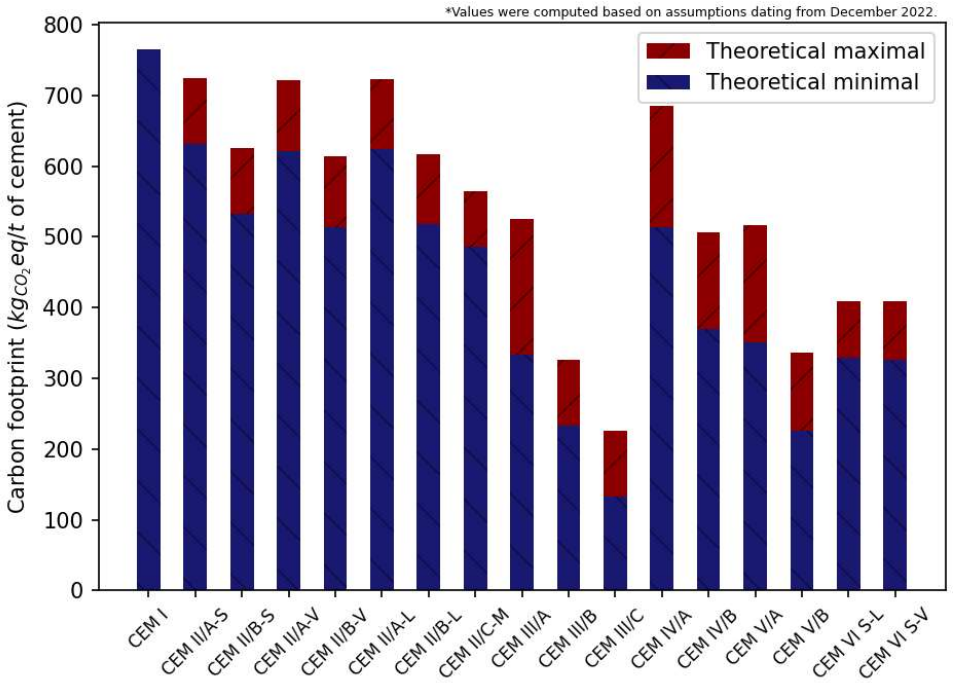

Figure I-5 Minimal and maximal theoretical carbon footprint value (expressed in kg of CO2 eq/t of cement, refer to values of Table I-4) of some cements defined by the NF EN 197-1 (2012) and NF EN 197-5 (2021) standards.

I.1.3. Water

Water is an essential component of concrete production. Its content in the concrete is generally expressed in terms of Water to Cement or Water to Binder ratio when considering addition and cement (respectively W/C and W/B). Water allows both the obtaining of the adequate rheological properties of fresh concrete during its mixing and the hydration. In scientific literature, it is widely acknowledged that an elevated water-to-binder ratio adversely affects the mechanical properties and durability of concrete. This negative impact is primarily attributed to the excess water that does not actively participate in the hydration process and ultimately evaporates after the cementitious paste sets, resulting in voids within the cementitious matrix. The presence of these voids creates open porosity, leading to a decrease in mechanical properties and increased diffusional properties, which often correlates with diminished durability. Accordingly, it is essential to minimize the water content in concrete, while ensuring acceptable rheological properties for proper setting. One viable approach involves incorporating water reducing admixtures in the concrete formulation.

I.1.4. Admixture

Concrete admixtures can be natural or manufactured chemicals added during concrete mixing to enhance specific properties of the fresh or hardened concrete. They belong to different categories based on their intended purpose, with each category focused on enhancing specific properties. The application and utilization guidelines for these admixtures are described in the NF EN 480-1 (2014) standard document.

Water-reducing admixtures are used to reduce the water content and optimize the final properties of concrete while keeping a satisfying workability of the fresh concrete. In this category are found the plasticizers and superplasticizers.

Accelerators facilitate rapid setting and hardening of concrete materials. These admixtures enhance the hydration kinetics of hydraulic cement, serving to achieve improved early mechanical properties and

ease the demoulding process. Employing accelerators becomes particularly important in scenarios where the low temperature hampers the concrete material's setting.

Set retarder admixtures extend or delay the setting time of the cement. They are generally used for the manufacturing of concrete in environment with high temperature, or when a relatively long transport of the fresh concrete is required. Generally, they are composed of anions and molecules absorbed on the cement particles surfaces that will prevent the access to water.

Air entrained admixtures are used to entrap small quantities of air during the mixing of fresh concrete. It causes the formation of closed porosity in the cementitious matrix. These admixtures are surfactants, acting by changing the surface tension of water. They allow the obtaining of higher resistance to freeze-thaw cycle and change the rheological properties of fresh concrete.

I.2. Hydration mechanisms

I.2.1. Portland cement

This section provides a concise overview of the hydration reactions occurring in concrete. Numerous factors can affect the hydration process, predominantly the composition of cement and the amount of water combined with the mixture. Cement and additions primarily consist of oxides. The designated symbols for the principal oxides found in cementitious materials are:

- $C = CaO$
- $S = SiO_2$
- $A = AlO_2$
- $F = Fe_2O_3$
- $H = H_2O$
- $\bar{S} = SO_3$

These oxides are contained in anhydrous compounds. The main ones are shown in the left list of the Figure I-6. Firstly, the hydration of the calcium silicates C_3S and C_2S leads to the formation of two different hydrates, which are the calcium silicate hydrates (C-S-H) and the portlandite (CH), of raw formula $Ca(OH)_2$. This hydration process is summarized in Equation I.3.

$$C_\alpha S + \alpha H \rightarrow CSH + \beta CH \qquad \text{Eq (I.3)}$$

With $\beta = \alpha - 1.7$ if the ratio C/S equals 1.7 [7] and α equal to 2 or 3.

This reaction, once detailed, can be expressed as:

$$Ca_3SiO_5 + 3H_2O \rightarrow 3Ca^{2+} + H_2SiO_4^{2-} + 4OH^- \qquad \text{for } C_3S$$

$$Ca_2SiO_4 + 2H_2O \rightarrow 2Ca^{2+} + H_2SiO_4^{2-} + 2OH^- \qquad \text{for } C_2S$$

$$xCa^{2+} + H_2SiO_4^{2-} + 2(x-1)OH^- + yH_2O \rightarrow xCaO, SiO_2, yH_2O \qquad \text{for CSH}$$

$$Ca^{2+} + 2OH^- \rightarrow CaO, 2OH \qquad \text{for CH}$$

Tricalcium aluminate (C_3A) reacts with the gypsum contained in cement to form the ettringite (Aft), of raw formula $C_6A\bar{S}_3H_{32}$:

$$C_3A + 3C\bar{S}H_2 + 26H \rightarrow AFt \qquad \text{Eq (I.4)}$$

Once all the gypsum is consumed, tricalcium aluminate reacts with the Ettringite to form the monosulfoaluminates (Afm) of raw formula $C_4A\bar{S}H_{12}$:

$$2C_3A + AFt + 4H \rightarrow 3AFm$$ Eq (I.5)

Tetracalcium aluminoferrite (C_4AF) also reacts with the gypsum:

$$C_4AF + 3C\bar{S}H_2 + 30H \rightarrow AFt + CH + FH_3$$ Eq (I.6)

And the same way as tricalcium aluminate, once gypsum is consumed, Tetracalcium aluminoferrite and ettringite react to form monosulfoaluminates:

$$2C_4AF + AFt + 12H \rightarrow 3AFm + 2CH + 2FH_3$$ Eq (I.7)

The hydrations of C_3S and C_3A quickly take place while C_2S and C_4AF may require several months or even years to be fully hydrated. In its hardened state, the cementitious matrix of traditional concrete contains 65 vol.% of calcium silicate hydrate (C-S-H) and 20 vol.% of portlandite (CH). The 15 vol.% left are composed of Afm and Aft (see Figure I-6 Schematic representation of the hydration process in Ordinary Portland Cement.).

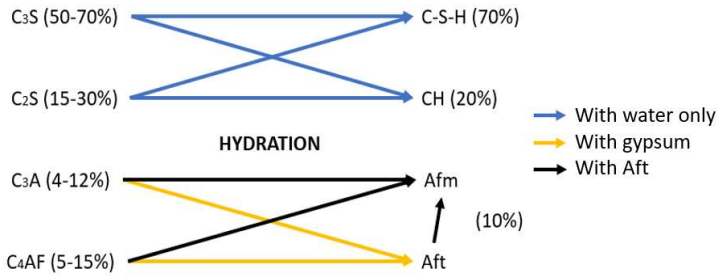

Figure I-6 Schematic representation of the hydration process in Ordinary Portland Cement.

Calcium silicate hydrates are mainly amorphous products. They are present in the cementitious matrix under the form of leaves where they ensure the mechanical strength of concrete. The portlandite is present under a different structure depicted as hexagonal plates whose size can vary from a few micrometres to a few hundred micrometres. Finally, calcium monosulfoaluminates are also present under the form of hexagonal plates while the ettringite formed during the hydration of cement produces hexagonal needle structures.

Hydrates (mainly portlandite) and alkaline species contribute to the pH stabilisation of clean concrete at a value close to 13.5 [84]. Solubility of portlandite in water is close to 22 mmol.L^{-1} (1.6 g.L^{-1}) for a temperature of 25°C [85]. This phenomenon alone should ensure a pH of 12.6. It is the presence of alkali-sulphates in cement which ensures the remaining part of pH increase by reacting with portlandite:

$$Ca(OH)_2 + K_2SO_4 \rightarrow CaSO_4 + 2KOH$$ Eq (I.8)

$$Ca(OH)_2 + Na_2SO_4 \rightarrow CaSO_4 + 2NaOH$$ Eq (I.9)

This way, the concentration of alkaline bases increases progressively in the interstitial solution, furnishing the hydroxyl ions responsible for the pH value of about 13.5.

The reaction equations presented above are valid in the case of portlandite hydration. When other pozzolanic or latent hydraulic additions are used, other reactions take place and need to be considered for the estimation of the hydrate types and contents.

I.2.2. Pozzolanic and latent hydraulic additions

Different aspects need to be considered in the case of pozzolanic and latent hydraulic hydration. First, these additions required an activator to hydrate, which is the portlandite (lime) formed during the clinker hydration in the case of hydraulic cement. Therefore, hydration of binder formulated using Type

II additions will lead to cementitious matrix with lower CH content than portlandite cement alone. The pozzolanic reactions and the one of slag essentially lead to the formation of C-S-H, which will be present in higher quantity. It was shown in the literature that a lower CaO/SiO_2 ratio (C/S) is obtained when pozzolanic and latent hydraulic additions are part of the blend than when clinker hydrates alone. This C/S ratio may vary from 1.5 to 2 for a CEM I cement, while for slag cement or other pozzolanic cements, this ratio is lower (see Table I-6) [86], [87].

Table I-6. C/S and Al_2O_3/SiO_2 (A/S) ratio change according to the wt.% of different SCM in binder [87].

Ref	Addition	wt.%	C/S	A/S
[88]	Nano-silica	2.5	1.69	0.14
	Metakaolin	15	1.24	0.24
[89]	Silica fume	10	1.25	0.052
[66]	Silica fume	5	1.48	-
		10	1.43	-
		15	1.28	-
[55]	PC control	0	2.03	0.12
	Fly ash	40	1.01	0.21
	Slag	40	1.62	0.71
[90]	PC control	0	1.63	-
	MK	25	1.29	-
[87]	Slag	0	1.76	0.027
		25	1.78	0.032
		50	1.55	0.05
		75	1.37	0.065
		100	1.14	0.095

The modification of the portlandite quantity within the material is a significant aspect to account for when modelling the concrete durability. Other species may be formed (see Figure I-7), such as C-A-S-H, and may also impact the durability of the final concrete material. The formula and stoichiometry of C-A-S-H will also depend on the initial species and composition of the binder, leading to different Al_2O_3/SiO_2 (A/S) ratio (see Table I-6).

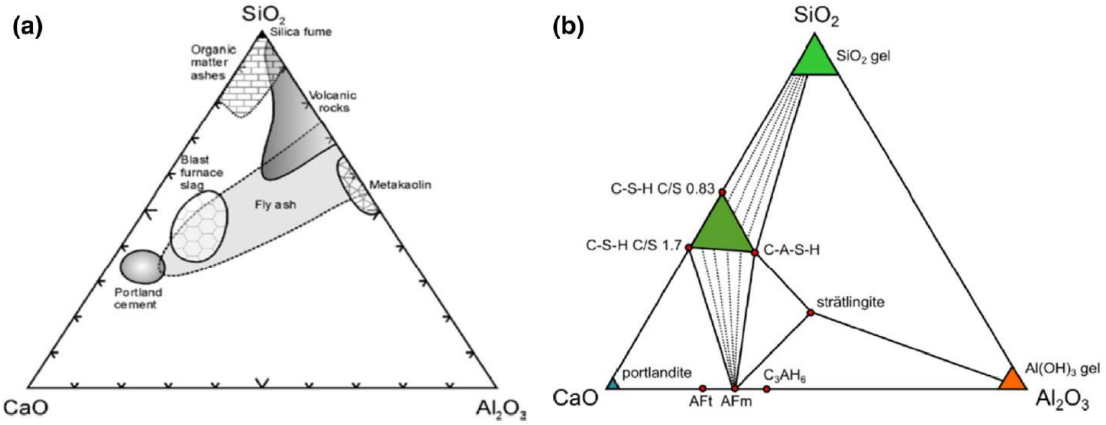

Figure I-7. Ternary diagrams expressed in wt% (a) of the main SCM groups and OPC [91] in [92], (b) Hydration diagram of the system CaO – Al2O3 – SiO2 – H2O in absence of gypsum [93] in [92].

The pozzolanic reactivity values (presented in Table I-4) are also different depending on the addition considered. It leads to a different consumption of the portlandite content and explains why certain SCM with higher pozzolanic reactivity index can only be used in lower quantity in the binder formulation. Using various references of the literature, it was possible to build the Figure I-8, showing the impact of different SCM content for clinker replacement on the lime consumption [55], [77], [88], [89], [94], [95].

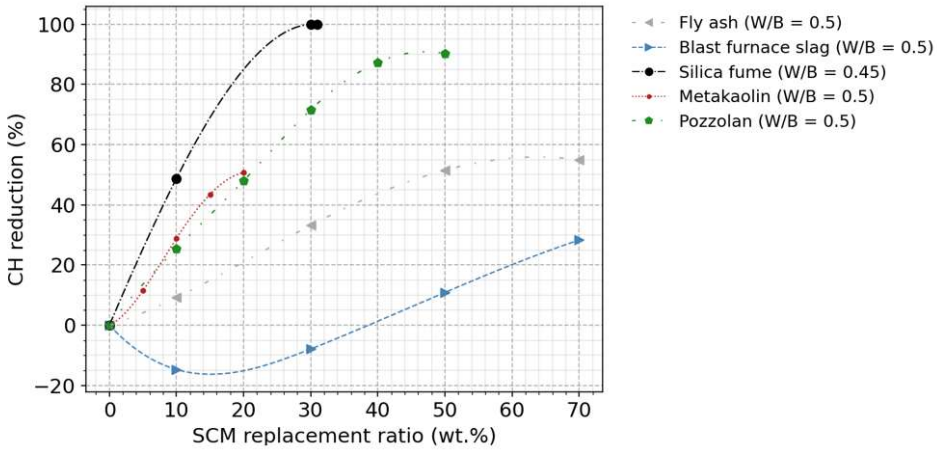

Figure I-8 Portlandite reduction (wt.%) versus clinker replacement by SCM (wt.%) for different additions in mix with W/B close to 0.5.

It is important to note that there are two effects that contribute to the reduction of portlandite content in the cementitious matrix when SCM are used as a replacement for clinker. Firstly, the lower quantity of clinker leads to a decrease in the formation of portlandite. Secondly, as the quantity of pozzolanic additions in the binder increases, there is a greater consumption of portlandite in the formation of C-S-H.

Pozzolanic additions possess relatively high contents in silicon dioxide and aluminium trioxides (refer to Table I-3). In presence of water and quicklime (in ordinary conditions of temperature), they react to form hydrated calcium silicate, calcium aluminate or calcium aluminium silicate hydrate depending on the oxides availability and equilibrium (see Figure I-7) [96].

$$Ca^{2+} + 2(OH^-) + SiO_2 \rightarrow C-S-H \qquad \text{Eq (I.10)}$$

$$Ca^{2+} + 2(OH^-) + Al_2O_3 \rightarrow C-A-H \qquad \text{Eq (I.11)}$$

$$Ca^{2+} + 2(OH^-) + Al_2O_3 + SiO_2 \rightarrow C-A-S-H \qquad \text{Eq (I.12)}$$

During cement hydration, pozzolanic reaction occurs after the initiation of the Portlandite hydration. This is due to a slower hydration kinetic (see Figure I-9). As shown in Equations I.10 to I.12, the reactions taking place lead to the consumption of CH. As explained earlier, the portlandite is the main component in the cementitious matrix responsible for the basic pH stabilization. Therefore, pozzolanic reaction might lead to cementitious matrix less able to durably protect steel rebar from aggressive species. This is especially the case regarding carbonation phenomenon because carbonation rate is strongly influenced by the portlandite content.

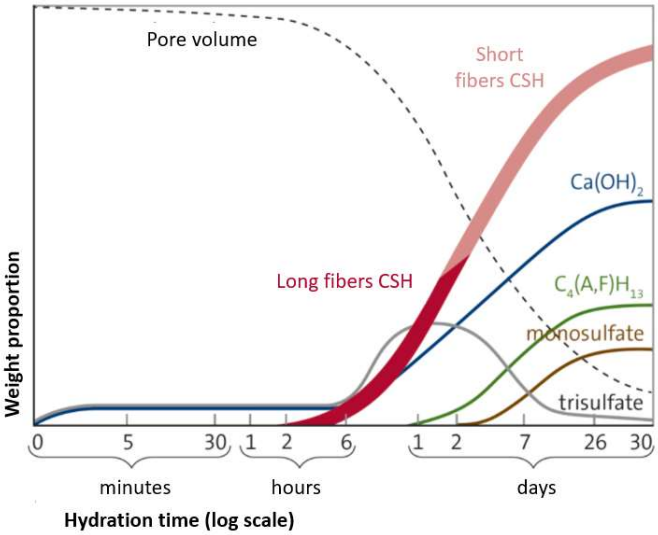

Figure I-9. Schematic representation of the different hydrate phases temporal evolution for an environmental temperature of 20°C [97].

Other factors influence the pozzolanic reactivity index measure for the different additions. The Figure I-10 shows that, for the same type of pozzolanic addition, properties such as granulometry, which impacts the surface area of the addition, influences greatly the ability to react and consume lime. This aspect, among others, may also explain the difference of results obtained by different authors on the same addition type in Table I-6. The "shaking" of the mix also shows an influence on the results, even if it does not concern the case of concrete hydration. Higher temperature, up to 60°C in [98] can increase the pozzolanic reaction and lead to higher reacted lime content at early age.

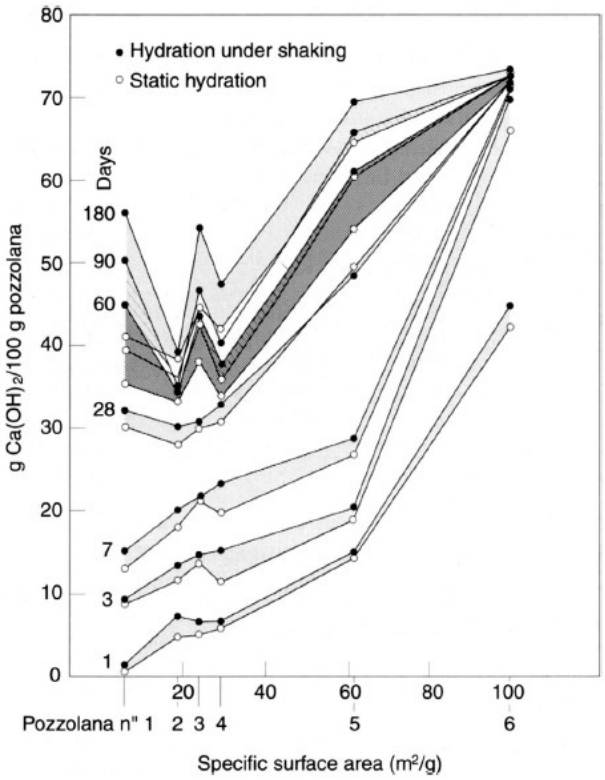

Figure I-10 Influence of the curing time, the specific surface area of the pozzolanic material and shaking on the combine calcium hydroxide content [55].

Slag activation can be achieved using different activator than Portland cement or lime. Literature reports two different types of activation:

- **Alkaline activation** that can be done using NaOH, KOH, waterglass (Na_2SiO_3 $5H_2O$), or lime (contained in clinker for instance). This type of activation leads to the formation of C-S-H, C-A-H and C-A-S-H species. Hydrotalcite can also be observed in slag with high MgO content.
- **Sulphate activation** is either performed using gypsum, hemihydrate, anhydrite or phosphogypsum. The species formed are Ettringite, C-A-S-H and C-S-H. Hydrotalcite like Mg-Al product are also reported [59].

Table I-7 Species reported in the case of alkaline activation of blast furnace slag in [59]

Hydrates	Raw formula	Shorted name
Monosulfoaluminates	$Ca_4Al_2(SO_4)(OH)_{12}{\cdot}6H_2O$	Afm
Calcium silicate	$CaO \cdot xSiO_2 \cdot (Yh_2O)$	C-S-H
calcium tetra-aluminate	C_4AH_{13}	C-A-H
Gehlenite	C_2ASH_8	C-A-S-H
Hydrogarnet	C_3ASH_4	C-A-S-H
Hydrotalcite	$Mg_6Al_2CO_3(OH)_{16}.4H_2O$	-

Pozzolanic additions activated with lime lead to the formation of similar species. It is reported in [55] by McCarthy et al. that hydrates formed in natural pozzolana-portlandite mixes are essentially C-S-H (with lower C/S ratio than in Portland cement hydration), Hydrogarnet, Gehlenite and carboaluminate ($C_3A\bar{C}H_{12}$).

This section showed the main differences in terms of hydration products between clinker-based concrete and mixes including pozzolanic and slag. These variations will impact the different parameters of concrete, notably the durability against corrosion, and need to be controlled to perform precise prediction of the reinforced concrete service life.

I.3. Durability of reinforced concrete structures

I.3.1. Carbonation

Concrete carbonation is a natural phenomenon which consists in the dissolution of the carbon dioxide contained in the air within the interstitial solution of the cementitious matrix and its reaction with the calcium ions contained in the hydrates of the cementitious matrix. The volume fraction of the CO_2 in the air is 0.04 vol.% (400 ppm) on average (in the 2010s) but can be up to 1% in certain confined places such as a subterranean garage. Anthropic activities will inevitably lead to an increase of this average value, and subsequently increase the carbonation phenomenon [99]. CO_2 can penetrate concrete under a dissolved form if the material is saturated in water, or under gaseous form if the concrete is only partially saturated. Once in solution, CO_2 reacts with the concrete hydrates such as portlandite and C-S-H to form calcite ($CaCO_3$). During those reactions, hydroxyl ions OH^- are consumed which causes a reduction of the interstitial solution pH and subsequently the depassivation of the reinforcing bar once the CO_2 reaches the zone close to the steel. This aspect may lead to the corrosion of the reinforcing bar and impair the durability of the reinforced concrete structure. For this reason, the phenomenon must be considered to prevent irreversible deterioration of the material.

Concrete carbonation also causes modifications of the cementitious matrix which may present advantages such as the reduction of the porosity in certain cases [66], [90], [92]. Numerous studies and modelling focused on this phenomenon during the three last decades due to its importance and influence on concrete properties.

The penetration mechanisms of CO_2 into the cementitious matrix can be summarised based on three reaction steps:

- The first one is the dissolution of the CO_2 in the interstitial solution which leads to the carbonic acid formation (H_2CO_3), The carbonic acid is then transformed into a bicarbonate ion (HCO_3^-) and finally into a carbonate ion (CO_3^{2-}). The consumption of the hydroxyl ion OH^- during the reaction causes a reduction of the interstitial solution's pH.

$$CO_2 + H_2O \leftrightarrow H_2CO_3 \quad \text{Eq (I.13)}$$

$$H_2CO_3 + OH^- \leftrightarrow HCO_3^- + H_2O \quad \text{Eq (I.14)}$$

$$HCO_3^- + OH^- \leftrightarrow CO_3^{2-} + H_2O \quad \text{Eq (I.15)}$$

- The second step is the carbonation of the portlandite, which begins with its dissolution. This reaction helps to maintain a basic pH in the concrete interstitial solution but also causes the calcium ions to liberate which react with carbonate ions to form calcite.

$$Ca(OH)_2 \leftrightarrow Ca^{2+} + 2OH^- \quad \text{Eq (I.16)}$$

- Calcite formation is the final step of the carbonation process.

$$CO_3^{2-} + Ca^{2+} \leftrightarrow CaCO_3 \quad \text{Eq (I.17)}$$

In literature, carbonation is often summarised as one global equation (see Equation I.18):

$$Ca(OH)_2 + CO_2 \rightarrow CaCO_3 + H_2O \quad \text{Eq (I.18)}$$

This reaction shows the water formation during carbonation, which also implies a modification of the interstitial solution equilibrium. However, calcium ions formation does not appear in this reaction. Carbonation process is summed up in Figure I-11.

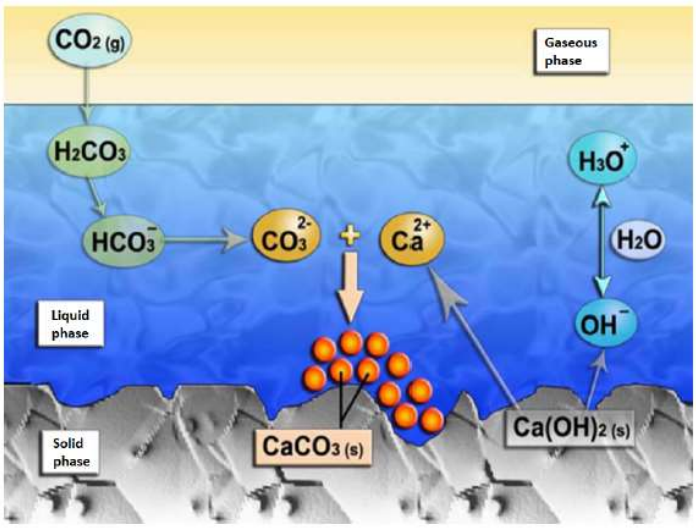

Figure I-11. Corrosion mechanisms in the case of carbonation [100].

More recently, Von Greve et al. [92] have depicted the different steps of the carbonation phenomenon for OPC concrete. They are summarized in order below:

1) A reduction of the Afm solid volume is first observed, as monosulphate (of molar volume equal to 285 cm^3/mol) and hemicarbonate (332 cm^3/mol) phases destabilise into monocarbonate-Afm (262 cm^3/mol).
2) Secondly, the portlandite starts carbonating. It leads to a reduction of the overall porosity because a 12% volume variation is observed. The pH drops to 12.5 and is then kept stable around this value while the portlandite content remains high enough.

3) Once all accessible portlandite is transformed, C-S-H begins to decalcify. The C/S ratio is reduced from 1.75 to 1.3. No significant volume change is observed during this stage, but a marginal decrease of the pH is signalled.
4) The monocarbonate-Afm (262 cm^3/mol) decomposes into stratlingite (216 cm^3/mol) while C-S-H are consumed without further change of the C/S ratio.
5) Once all Afm is consumed, decalcification of C-S-H brings the C/S ratio down to 0.75. The largest drop of pH is observed (down to a value close to 11).
6) Stratlingite and ettringite dissolve one after another when pH reaches a value of 10. C/S ratio of C-S-H drops to a value of 0.67.
7) While carbonation goes on, C-S-H dissolves entirely and forms calcite and hydrated amorphous silica. The pH value goes rapidly from 10 to 8.5.
8) The last specie decomposing is hydrotalcite.

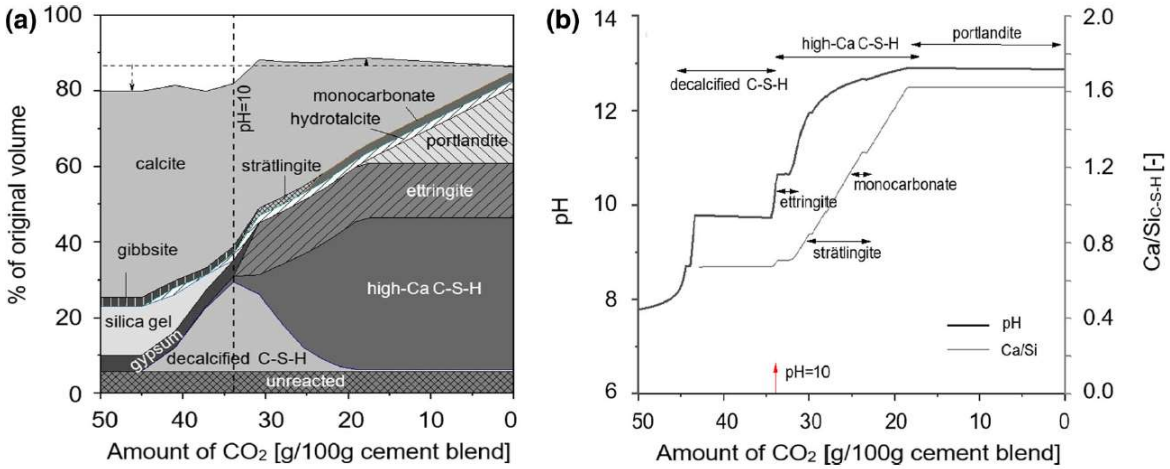

Figure I-12 Thermodynamic modelling of the hydrates buffering capacity of a OPC (w/b = 0.5) considering a hydration degree of 90% (a), and variations of pH and C/S ratio of the C-S-H (b) [92].

The overall phenomena are detailed in Figure I-12 [92] for CEM I-based concrete. Shi et al. showed (using the open source model CSHQ of Kulik [101] and experimental results) in [90] how the presence of additions leads to change in the C/S ratio (Figure I-13 (a)) and pH evolution (Figure I-13 (b)) during carbonation. Four cement pastes with a ratio w/b equal to 0.5 were manufactured. P corresponds to the reference OPC, L contains 31.9 wt% of limestone, M 31.9 wt% of metakaolin while ML contains 25.5 wt% of metakaolin and 6.4 wt% of limestone. A CO_2 concentration of 1% was applied for 90 days.

The $Ca(OH)_2$ and calcite contents were assessed at 28 and 90 days for different depths to check the model data. First, the thermodynamical model highlights a lower buffer capacity of the cement pastes M and ML containing metakaolin. This is essentially due to a lower portlandite content responsible for the first barrier to pH decrease. It explains partially why carbonation kinetics are higher for those cement pastes compared to the reference when considering similar formulation and granular skeleton [102].

Another important observation that can be made of Figure I-13 (b) concerns the phenolphthalein bar represented on the right. The turning point of this product is comprised between 8 and 9, when an important part of the hydrates, including the portlandite, is consumed. For this reason, and because of the transition zone observed (that can be superior to 10 mm in certain cases [103]) [104], the depth of carbonation measured experimentally with phenolphthalein and the real depth reached differ. It causes additional uncertainties on the kinetic value that need to be considered when realising predictions of the time before depassivation.

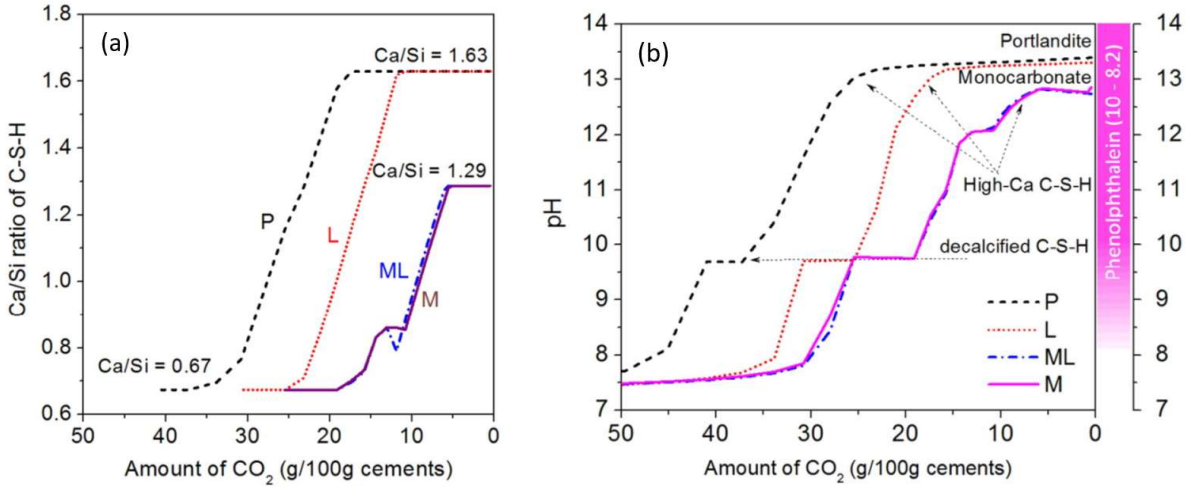

Figure I-13 Evolution of C/S ratio of C-S-H (a) and pH evolution (b) during carbonation [90].

The difficulties linked to the prediction of the carbonation are also due to the various factors influencing the concrete resistance toward this phenomenon. Material and environmental parameters are concerned.

First, an increase of the water cement ratio, which leads to an increase of the paste porosity and the capillarity interconnections, reduces the carbonation resistance of the material [105], [106]. On the contrary, an increase of the cement content generally leads to a higher compactness of the cement paste and therefore reduces the diffusion coefficient of the carbon dioxide. It also leads to a higher content in portlandite, increasing the pH stability of the interstitial solution.

The binder type may also have an influence on the carbonation resistance of the concrete material. Indeed, pozzolanic additions consume portlandite during their hydration processes which causes higher carbonation depths. It can be noted that for certain pozzolanic additions, other phenomena may compete with the latter. For example, the use of silica fume generally leads to a higher density of the material, thus to a better carbonation resistance [107], [108].

Among the environmental parameters, one of the most influent variables is the relative humidity. Indeed, according to authors [7], [109], carbonation will reach its maximum for a relative humidity (RH) close to 65%. For lower values of RH, the reduced water content contained in the interstitial solution will reduce the carbon dioxide capacity to dissolve in water and thus reduce the quantity of carbonate able to consume the hydrates. For higher relative humidity values, the diffusion of the carbon dioxide, which is 10^4 times higher in air than in water [7], is limited by high saturation level. The impact of the relative humidity is represented in Figure I-14. It can be noted that variations of these values are expected due to different sorption equilibria according to the composition of the material, leading to different optimum for carbonation according to the concrete mix.

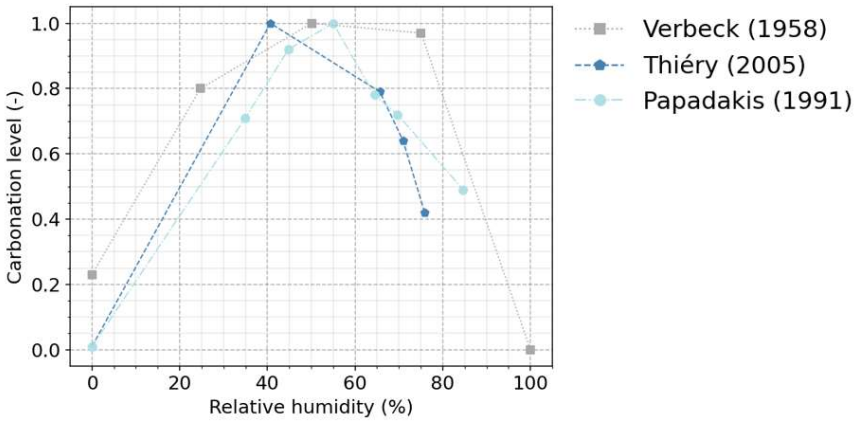

Figure I-14. Influence of relative humidity on carbonation level in concrete [110].

The CO_2 partial pressure has an evident impact on the carbonation. For higher values, the CO_2 content will increase as well as the carbonation speeds up to a certain point. According to the results obtained by Hyvert [105] on clinker and slag-based mortars, carbonation rate stops increasing with the partial pressure of CO_2 for partial pressure higher than 25 vol.% (see Figure I-15).

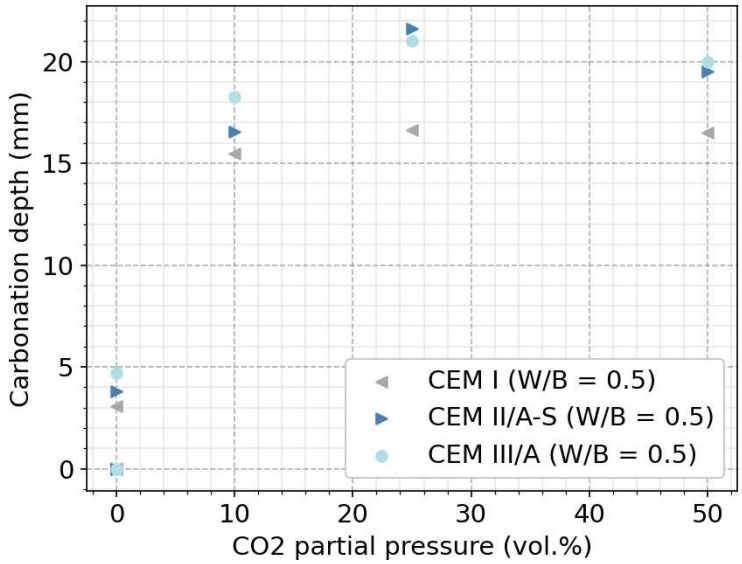

Figure I-15 Influence of CO2 partial pressure on carbonation depth according to the results of Hyvert [105].

Temperature has a more complex influence on carbonation. Carbon dioxide diffusion is enhanced for higher temperature conditions. A rise of temperature accelerates the gas diffusion but also eases the pore drying, which can lead to higher carbonation depth up to a certain temperature [111], [112]. Since carbonation needs liquid water to proceed, too elevated temperatures will certainly slow down the process by causing water evaporation. In [113], Drouet et al. investigated the temperature effect on the carbonation of a CEM I and a CEM V/A based pastes. They found that the carbonation rate increases "linearly" from 20°C to 80°C in the case of the CEM I cement, but that a maximum is reached for a temperature around 50°C in the case of the CEM V/A cement. The authors associate this difference to the mineralogical variations between the two mixes, notably the inferior portlandite content and C/S ratio of C-S-H.

I.3.2. Chloride ions penetration

Chloride ions penetration into the cementitious matrix is the principal cause of steel corrosion in reinforced concrete past carbonation [6]. This phenomenon especially affects concrete structures exposed to marine environments or deicing salts. When penetrating the concrete, chloride ions may damage the protective layer of reinforcing bars, and if certain conditions are gathered, lead to the steel corrosion initiation. Globally, the exposed small zone of the steel due to the depassivation by the erosion of chloride acts as the anode, while the remaining steel area passivated by the alkaline medium acts as cathode. This electrochemical system thus created with a large cathodic zone and little anodic zone leads to the aggravated corrosion of the steel, known as pitting corrosion [114].
In a porous cementitious medium, chlorides are present in two forms:

Free chlorides, which are the principal actors in the corrosion process of reinforced concrete. Their movements in the liquid phase are due to a concentration gradient between the heart and skin of concrete.

Bound chlorides, which are formed when free chlorides react with the hydrates contained into the cement. The number of chloride ions that can be bound depends on the cement composition among other parameters. Within this state, two different kinds of bound chlorides can be distinguished.

First, chlorides can be chemically bound by the aluminates or aluminoferrites and form the hydrated calcium chloroaluminates of empirical formulas $3CaO.Al_2O_3.3CaCl_2.32H_2O$ or $3CaO.Al_2O_3.CaCl_2.10H_2O$, which are also called Friedel's salts [115]. It can also be noted that Ferrite may bind chloride and thus form compound similar to Friedel's salts. However, in classic OPC cement, this form of binding is not considered to be important because of the slow hydration of ferrite phase [116].

Secondly chlorides are physically bound. The phenomenon responsible for their formation consists in the adsorption of chlorides by the C-S-H through the substitution of the hydroxyl ion. Indeed, cationic species such as Na^+, form a condensed layer on the SiO_4 sites of the C-S-H. This layer is called "intern Stern layer" and has a high charge density. The electric compensation is ensured by the SiO_4 and an external layer composed of anions hydroxides. This external layer is less rigid and enables ionic exchanges with the interstitial solution, leading to the adsorption of chloride ions [117].

According to the literature, the quantity of physical binding is often higher than the chemical binding [118]–[120]. This could be due to the frequent use of PM/ES cements, especially in XS2 and XS3 environments where their use is mandatory in France. The use of these cements leads to a low quantity of Afm in the cementitious matrix, and thus, to a low quantity of chemical binding of chlorides [19]. PM cement stands for underwater cement (or "Ciment Prise Mer" in French) while ES stands for sulphated water ("Eau Sulfatée" in French). PM/ES cements possess a low C_3A content to confer to the concrete a higher resistance to sulphate and chloride ions aggression [121].

It is then possible to define the term "total chlorides", being the sum of the free and bound chlorides. The proportion of chloride in both states can be determined by chemical tests [122] allowing the obtention of mathematical relations. Thus, different ways to compute the equilibrium between free and bound chlorides have been defined in the literature (refer to Section I.4.2.4).

Like carbonation, various parameters influence the chloride ions infiltration into concrete. Concerning the material properties, the effect of the W/B ratio and the binder content on the porosity and permeability are similar to the one on carbonation. An increase of the binder content leads to higher quantity of hydrates able to fix free chlorides, and thus to slow their ingress in the cementitious material [6], [7].

The cement type has also an impact on the chloride ions ingress since the aluminates quantity highly influences the binding capacity of chlorides. Therefore, the presence of higher quantity of C_3A reduces the quantity of free chlorides [105]. This is the case with the use of blast-furnace slag which increases the concrete resistance to chloride penetration. Moreover, this addition also contributes to the

reduction of the pore size while enhancing the formation of C-S-H (responsible for the physical binding of free chloride) during the hydration process. In a general way, pozzolanic additions can change the product types formed during the hydration and lead to the formation of C-S-H in the cementitious matrix through pozzolanic reactions. For this reason, the use of pozzolanic additions can increase the chloride binding capacity and reduce the chloride diffusion coefficient. Moreover, they are responsible for the portlandite content reduction in the hydrates formed, that causes a refinement of the pores and thus a decrease of the concrete permeability. Depending on the scale, refinement of pores may also facilitate the condensation of vapour and consequently ease chloride diffusion. Thus, the chloride diffusion which is enhanced by the presence of humidity (up to a certain point), can be impacted positively or negatively in that case depending on the initial properties of the material. Fly ash impact on the concrete behaviour with respect to the chloride penetration is both physical and chemical as explained above. However, its impact seems to be limited to a cement substitution rate of 50% [123], [124]. It was also shown that the use of fly ash in cement production reduces the chloride critical concentration (C_{crit}) value, but that this phenomenon is compensated by the good behaviour of fly ash concrete respecting to the chloride ingress [125], [126]. On the opposite, it was demonstrated that silica fume can alter the chloride binding capacity of cement [127]–[129]. This is also due to a higher quantity of aluminate formed. However, chloride diffusion in silica fume-based concrete is inferior to the one of a CEM I based concrete due to the reduction of the pores size and the subsequent cementitious matrix permeability. It can also be noted that the corrosion initiation time is longer despite a C_{crit} value inferior to a CEM I based concrete [130]–[132]. Finally, it has been shown that ternary binding agents, which consist in a mix of three components such as cement, fly ash and silica fume, can drastically reduce the pore size within the cementitious matrix compared to a standard CEM I. These mineral additions would then have a positive impact on the concrete durability properties.

The environment also influences the chloride ingress and its impact on the concrete material. It has been shown that, under cyclic drying-wetting conditions, a deeper penetration of aggressive chloride ions is observed [133]–[136]. It can also be added that cyclic drying-wetting action can lead to the creation of a convective zone, meaning that the chloride content reaches a local maximum in a zone close to the surface. This is mainly due to the limitation of the moisture influencing depth, ranging from 5 to 15mm for sound concrete [136]. In these conditions, chloride ions penetrate concrete by convection with the liquid phase and then by diffusion process in the pore solution beyond the convective zone, where the continuity of the liquid phase is reached [134]. Thus, the exposure of the concrete to water plays an important role on the chloride ingress.

Manufacturing parameters also impact the concrete durability. In the case of chloride ingress, thermal curing may alter the cement microstructure by densifying the C-S-H or reducing the inter-granular porosity [105]. The realisation of the curing treatment is also of importance, especially for binder with low hydration kinetics such as blast-furnace slag-based cement. In general, an increase of the curing length and water intake improves the hydration process which increases the hydrates content.

I.3.2.1 Chloride induce corrosion initiation

Once a certain concentration in chloride ions is reached inside the interstitial solution, the passive layer which surrounds the reinforcing bar dissolves leaving the steel unprotected against corrosion. It was shown that chloride ions, for high pH values, were able to form aqueous chlorocomplex, enhancing the dissolution of the rebar iron [137]. The hydrolysis of the iron products leads to a local fall in pH through the consumption of hydroxyl ions to form iron oxides [138]. The low pH at the pit then keeps the corrosion products in solution leading to their diffusion in regions richer in hydroxides and oxygen. Finally, solid corrosion products such as iron(III)hydroxide will form. An elevated danger is associated to the chloride induced corrosion because the attacks are concentrated in very small areas and may take place unnoticed for a long time. Moreover, because of the solubility of the corrosion products associated to the local pH fall of the pit, spalling and cracking of the concrete cover do not happen directly [139].

This chloride concentration value, called critical concentration and noted C_{crit} can be used to define two distinctive states [140], [141]:

- The ionic concentration for which the rebar steel depassivation starts.
- The chloride ions concentration reached when the structure aspect is affected by the migration of the corrosion products towards the concrete surfaces.

Those two different definitions lead to very different critical concentration values. Indeed, when the definition of this threshold value is based on the aesthetic deterioration of the structure, the propagation phase of the corrosion has already begun since long. Therefore, the chloride concentration value obtained is sufficient to cause the reinforcing bars depassivation and lead to their corrosion. Hence, this definition is less appropriate than the first one in the case of the durability study, whose goal is to prevent corrosion. The critical concentration is often expressed in terms of a ratio of total chloride quantity versus the binder mass. It could seem logical to express this concentration in terms of free chlorides content because this quantity represents the available chlorides in solution which can initiate corrosion. However, in certain conditions, some bound chlorides are prone to dissolve in the solution and thus to participate in the corrosion mechanism [128], [142], [143]. Indeed, some authors argued that bound chlorides might have a corrosion potential close to the one of free chlorides [142], [144]. When pit nucleation occurs, a drop of the pH value can generally be observed. Many of the cementitious matrix compounds can resist pH fall. These compounds dissolve and release hydroxyl ions in the process, which subsequently increases the pH value. Within these compounds, Friedel's salts and C-S-H, which can bind chloride, can be found. Therefore, when dissolving in the process of resisting the pH fall, bound chlorides are released and turned into free chlorides. For this reason, bound chlorides may participate in the same way than free chlorides to the corrosion process. Thus, it might be interesting to express the threshold value of chlorides in terms of total chloride to integrate bound and free chlorides. It was shown that Friedel's salts dissolve for pH value ranging between 11.99 and 12.14 [115], while values corresponding to the C-S-H dissolution vary according to its interaction with other hydrates and species. [142] gives a range of value from 12.5 and 10.5 for the interstitial solution pH. Knowing that a pH value inferior to 8.5 [145] is necessary to maintain the passive film unstable, and that most of the acid soluble chlorides (more than 98%) are free after a relatively small pH reduction to 11.5, bound chlorides may participate to the pitting corrosion mechanism [142]. The results of a test to measure resistance of pH reduction performed on OPC concrete is shown on Figure I-16.

This aspect also explains the high rate of corrosion penetration in the local pit. In extreme cases, penetration rate of 5-10mm/year can be observed on the field [146]. The function of the reinforcing bar can be quickly lost while the overall corrosion rate is kept low [139].

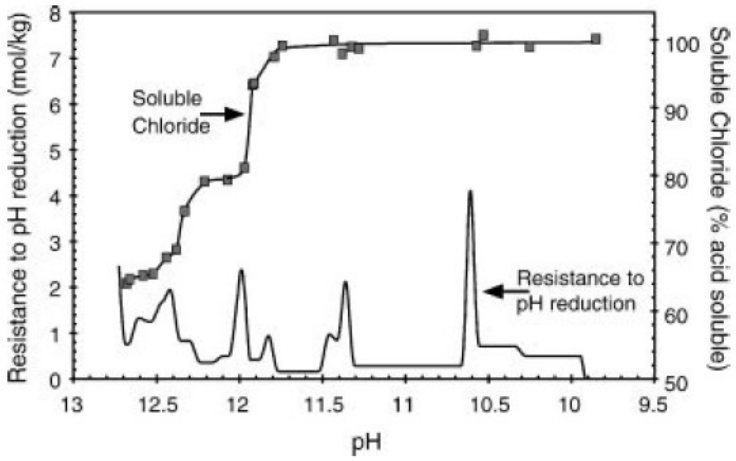

Figure I-16 The resistance to a reduction in pH and soluble chloride content determined on OPC concrete [142].

It can be noted that the value of C_{crit} varies considerably according to the sources in literature and can range from 0.03 % to 8.34 wt.% [64], [67]. In France, the NF EN 206/CN [19] standard imposes a maximal

chloride quantity of 0.4 wt.% of the cement mass which must not be exceeded during a CEM I based concrete manufacture. In the case of a slag concrete formulation, this value can be up to 0.65 wt.% of the cement mass. Various investigations are still in progress to identify in a more precise way the C_{crit} determination [2], [148]. Moreover, most of the values proposed originate from laboratory tests, which might not be representative of the on-field phenomenon. A small overview of the different variables impacting the value of C_{crit} are presented in this section to illustrate the challenges associated with its estimation.

The corrosion initiation critical value is influenced by various parameters such as the steel-concrete interface defects, concrete compactness, chloride ingress conditions as well as the cement type. In [149], Frederiksen realised a compilation of the threshold levels obtained in different publications. First, the type of exposure zone seems to impact greatly the threshold value C_{crit} . Measurements of critical concentrations for corrosion initiation in submerged zone and atmospheric zone are globally higher than in splash zone (with elevated relative humidity variation). It was shown by Pettersson [150] on OPC mortar that relative humidity has an effect on the threshold level, with a minimal chloride threshold level obtained for values around 90% (see Figure I-17).

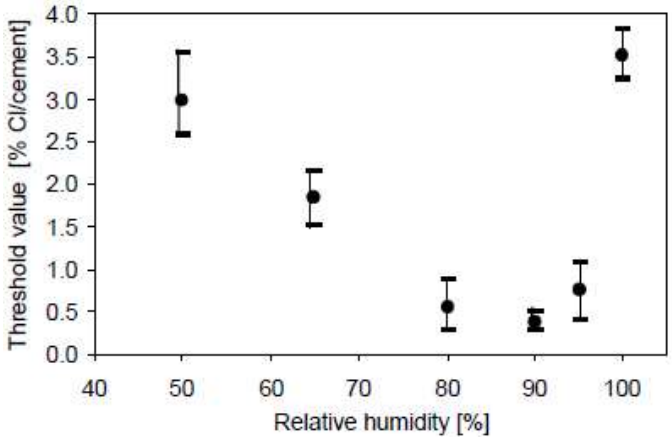

Figure I-17 The effect of relative humidity on the chloride threshold level in laboratory exposed mortars (with a W/C ratio of 0.5) [150].

Concerning the material parameters, it was highlighted that an increase of the water/binder ratio leads to a reduction of the chloride critical value required for the corrosion initiation (see Figure I-18, [150]).

This is certainly linked to the impact of the ratio on the microstructure, causing a difference in resistivity and in oxygen diffusion. Very low water-to-binder ratio would then lead to improper setting and an increased diffusion coefficient of gas and electrical conductivity, explaining the optimum value obtained in Figure I-18.

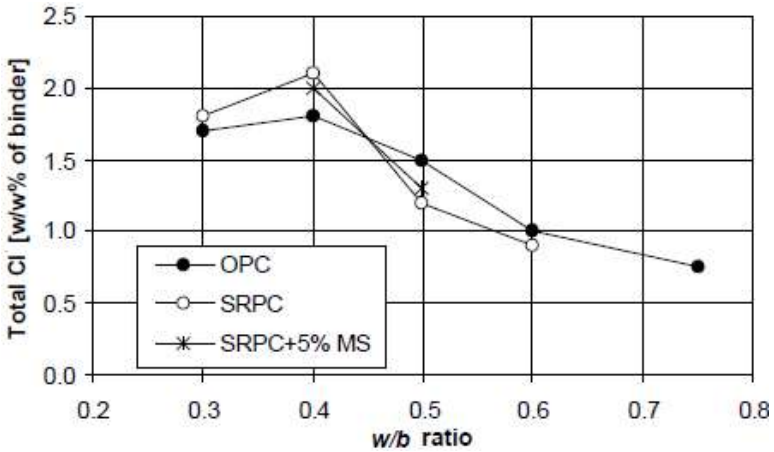

Figure I-18 Chloride threshold levels measured on submerged concretes and mortars with cover ranging from 15 to 20 mm [150].

The binder type also influences the critical value of chlorides. It is said in [125], [149], [151] that fly ash (up to 50 wt.%) and silica fume (up to 5 wt.%) reduce the concentration in chloride required to initiate corrosion. This negative impact on the chloride threshold level is attributed to the reduction of alkalinity within the interstitial solution of the cementitious matrix as well as a decrease in calcium hydroxide content at the steel-concrete interface [139]. It can be noted here that the use of mineral admixtures may have a positive impact on the propagation phase of corrosion by reducing the corrosion rate [149].

In addition to the high variability and uncertainties of the C_{crit} parameter, it has to be considered that the depassivation of the reinforcing bar is not irreversible [139]. Due to the non-uniform permeability of the concrete and the oxide layer, chloride ions concentrate in certain pits, leading to the formation of micro-piles and pitting corrosion. Each pit may again repassivate and reactivate following fluctuation of steel potential, oxygen availability and chloride availability (controlled by the micro-climate). The term of "electrochemical noise" emitted by the steel is used to define this transient corrosion. Sound concrete therefore possesses an ability to stop the corrosion propagation because of its heterogeneities [139].

I.3.2.2 The road environment (XD classes of the NF EN 206+A2/CN (2022))

Additional factors are to be considered in road environment concerning the chloride penetration. The source of salting is mainly due to the application of de-icing salts on the structure surface. Salt water then penetrates the concrete, by diffusion, convection (that can move the chloride inward and outward of the material), or capillarity. On one side, rainwater washes the surface free from chloride and may remove some [152]. On the other side, evaporation of the water contained in the pores increases the chloride concentration in the material.

The boundary conditions applied to bridges and road structures vary extensively with time. The seasonal conditions are generally less foreseeable than environmental conditions in marine environments (XS class of the NF EN 206+A2/CN (2022)). In wintertime, zones of the road structures are exposed to saturated salt solutions which are diluted with the melting of the ice and snow. Depending on the geographic zone, these exposures can be repeated frequently (up to once a day) or not. Rain, wind, sun radiation, impact in different ways the chloride ingress by modifying the saturation degree and temperature of the concrete material. Gases from motor vehicles can also impact the material by changing the pore solution pH. It was shown that more acidic water can be obtained in area close to traffic. This aspect can then affect the leaching of salts and cementitious species [152].

Principal transport processes from the road surface are defined in [152] as drainage, splash and aerosols. Drainage systems are designed to evacuate the water of the road or structure surface. Asphalt with open pore is for example used to drain the water through the road surface. Splash is mainly provoked by vehicles driving through water from wet snow. The majority of the flow created is directed towards the side of the road and is function of the vehicle design and speed. Finally, aerosols are transported in the air due to wind or dragging from vehicles.

In the conclusions of the the Hetek N°84 report [152], the author reports that a reasonable approach to describe the environments for road structures is to create two main groups: One for wet road structures (exposed to direct driving rain and direct splash) and the other for dry road structures (exposed to airborne chloride).

I.3.3. Carbonation-Chlorides coupling

Carbonation can affect chloride ions ingress in different ways:

- When penetrating the cementitious matrix, chloride ions can be bound on aluminates and form Friedel's salts. Because those species are sensible to carbonation, they may release

chloride ions into the interstitial solution by reacting with CO_2. This phenomenon can thus cause an increase in free chlorides concentration [153].

- At the same time, the chloride binding capacity of concrete is altered by the C-S-H carbonation. Indeed, carbonated C-S-H are no longer able to bind chlorides [117]. Therefore, the chloride ions diffusion is higher, and it is easier for chlorides to reach the steel vicinity.
- In contrast, it can be noted that the calcite production caused by carbonation reduces the concrete porosity, and thus reduces the chloride diffusion.

Additionally, from a theoretical point of view, if carbonation and chloride ingress reach the reinforcing bar at similar time, there should be a coupling effect of the steel depassivation. From a practical viewpoint, this kind of situation is not likely to occur, except in some case of punctual exposure to deicing salts.

I.3.4. Corrosion propagation

Corrosion is the main cause of degradation for reinforced concrete structures. Many researchers have devoted considerable endeavour to identify the most influencing factors as well as new ways to slow down this destructive process, and research is continuously carried out upon this topic. Iron, the main component of steel, is thermodynamically unstable in natural conditions. Being its main stable form in those conditions, iron oxide is obtained by the natural corrosion of iron. Usually, corrosion is caused by the formation of an electrochemical cell on the metal surface. The latter is formed when a potential difference between two points in the metal is created [154]. Electrochemical cells comprise an anodic and a cathodic zone connected by an electrolyte medium. The oxidation reaction takes place on the anodic zone, where the metal is transformed into an ion and releases electron(s) (see Equation I.19).

$$Me \rightarrow Me^{n+} + ne^{-} \qquad \text{Eq (I.19)}$$

At the same time, the reduction reaction takes place at the cathodic site and consumes the electron(s) released during the oxidation reaction (see Equation I.20).

$$xOx + qe^{-} \rightarrow yRed \qquad \text{Eq (I.20)}$$

In the context of reinforced concrete, the superficial atoms of metal at the anode surface release their electrons and then pass into the electrolyte solution as cations (see Equation I.21).

$$Fe \rightarrow Fe^{n+} + ne^{-} \qquad \text{Eq (I.21)}$$

The cathodic reaction is responsible for water reduction at the cathode surface. This reduction reaction differs according to the presence or absence of oxygen as the Equations I.22 and I.23 show.

$$2H_2O + 2e^{-} \rightarrow 2OH^{-} + H_2 \qquad \text{Eq (I.22)}$$

$$2H_2O + O_2 + 4e^{-} \rightarrow 4OH^{-} \qquad \text{Eq (I.23)}$$

However, embedded in concrete, the steel reinforcing bar is in an alkaline medium and thus in a passive state. It leads to the formation of a passive layer composed of oxides that protects the steel and limits corrosion.

I.3.4.1. Passivation layer

The passive film forming on ordinary steel in alkaline solutions is generally very thin (10-50 Å) [139]. Its microstructure and chemical composition depend on the chemical environment (pH, potential of the steel and oxygen pressure) at the time of formation. Solutions rich in O_2 favour the formation of oxides with higher content in oxygen: Fe_2O_3. The oxide film then thickens, and the oxygen concentration diminishes with a growing permeability to gas of the film. The steel potential drops, resulting in the formation of magnetite (Fe_3O_4) with lower content in O_2.

In concrete, the potential of the alloy and the oxygen pressure depends on the environment surrounding (moisture, temperature, microstructure, alkalinity of the interstitial solution…). However, the iron oxide layer is generally composed of a spinel Fe_3O_4-γ Fe_2O_3 solid solution, with sometimes clusters of $Ca(OH)_2$. The porosity of this layer is believed to favour the film growth in the passive state. During the cement hydration, calcium hydroxide precipitates at the steel-concrete interface and is likely to affect the passive layer composition.

The passive layer is generally known to be a thin and denser layer, but studies on old concrete structures have shown a hundred microns thick layers of iron oxide. A thicker layer often means a less efficient passivation, as it is associated to a higher ion permeability. The thickness and microstructure of the film is controlled by the rate of growth, which is in turn controlled by the oxygen and ferric ions permeability through the oxide layer.

Ordinary steel in concrete is in a "semi-passive" state, because only partly protected by the passive oxide film which is thick but inhomogeneous and permeable. Corrosion products from active corrosion (rust) may be observed around the passive oxide film.

The separated layers exposed in Figure I-19, respectively the oxide layer from the hot rolling of ordinary steel (scale), the passive oxide film forming during the hydration of concrete and the rust phases initially found on most reinforcement, may evolve and fuse over time [139].

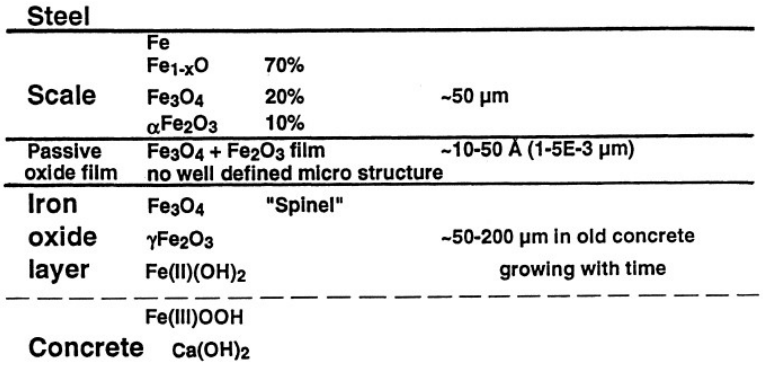

Figure I-19 Composition of the different iron oxide phases on ordinary steel in concrete at early ages [139].

The steel composition and microstructure have an influence on the passivation layer formation as well as the surrounding medium [155]. For example, the literature reports high pitting resistance for the use of descaled austenitic and duplex stainless steel. Ferritic stainless steels performed well in moderated environments against carbonation induced corrosion. Globally, stainless steel leads to high corrosion resistance because of the formation of a compact dual-layer passive layer on the steel surface, but the high alloy content (> 8wt.% of alloying elements) results in high cost and a bad weldability [156], [157]. Low alloy contents (< 8wt.% of alloying elements) performed well in alkaline medium but corrode if the medium pH is reduced. Interest has been given to medium alloy content steel [158]. Among the alloying elements, only the Copper (Cu), the Nickel (Ni), the Manganese (Mn), the Tungsten (W) and the Chromium (Cr) are reputed to increase the corrosion resistance [159]. Although the passive layer of stainless steel has been widely studied, the exact relationships between the alloying elements and the passive film properties are still subject to debate. It seems to be due to the participation of elements such as Chromium and Nickel in the oxide layer formation [159], [160].

In [157] the following Equations I.24 and I.25 are given in the case of an in-situ Fe-Cr oxide inner layer formation in alkaline concrete like medium (observed for high Cr content in steel). It is said that after long-time passivation, a crystalline inner layer of FeO-Cr_2O_3 forms.

$$Cr^{3+} + 3OH^- \rightarrow Cr(OH)_3 \qquad \text{Eq (I.24)}$$

$$2Cr(OH)_3 \rightarrow Cr_2O_3 + 3H_2O$$ Eq (I.25)

A value for chloride induced corrosion resistance is defined as the Pitting Resistance Equivalence Number (PREN) [158]. Different empirical formulas for this number can be found in the literature, where the more standard equation are the $PREN_{16}$ and the $PREN_{30}$ with variation on the coefficient α (ranging from 16 to 30) [161]–[164]. All % values of elements are expressed in wt.%.

$$PREN = \%Cr + 3.3\ (\%Mo + 0.5\ \%W) + \alpha\ \%N$$ Eq (I.26)

The ASTM G48 standard specifies a testing procedure to evaluate the PREN. It consists in immersing a steel sample in a 6 wt.% $FeCl_3$ solution for a time ranging from 24 to 72h at a given temperature. The result consists in the evaluation of the steel weight loss or the pit penetration depth. If this test is performed at different temperatures, it is also possible to obtain the Critical Pitting Temperature (CPT). The CPT can also be obtained following the ASTM G150 test recommendations, which consist in monitoring the current of a sample polarized to a potential in the high passive region while applying a temperature ramp. The CPT then corresponds to the temperature for which the current exceeds a critical value, which is usually 10 µA for more than 60 s. The ASTM G150 is reputed to be more precise but is generally less used than ASTM G48 immersion tests [163].

The determination of the passivation layer electrochemical properties is also at the centre of past decades and current investigations. The electrochemical method generally consists in measurements of open-circuit potential (OCP), linear polarization resistance (LPR) and electrochemical impedance spectroscopy (EIS).

For the Electrochemical Impedance Spectroscopy test interpretation, the corrosion resistance is quantified using the equivalent circuit in Figure I-20 in [157]. High frequency time constant is represented by the charge transfer resistance (R_t) and the admittance associated with the double layer capacitance (Q_{dl}). The low frequency time constant is represented by the passive layer resistance (R_f) and the passive film admittance (Q_f).

The computation of the impedance Z_{CPE} of the constant phase element (CPE) Q_f and Q_{dl} is obtained with Equation I.27.

$$Z_{CPE} = 1/Q(j\omega)^{\alpha}$$ Eq (I.27)

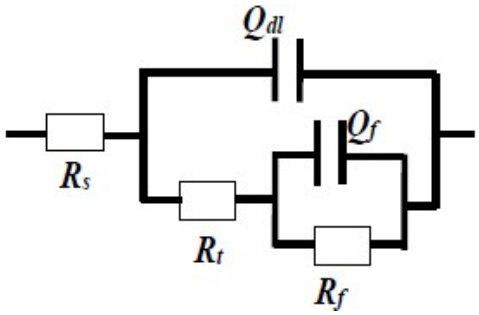

Figure I-20 Equivalent circuit proposed by [157] to fit the experimental EIS data.

It was shown in [157] that the passive film formation occurs in the first 24h passivation once the steel is embedded in concrete. In this study, the formation of the passivation layer is monitored using OCP and LPR. The measurements at the time of the layer formation will result in a sharp reduction of the corrosion current density (i_{corr}, A.cm^2), increase of the linear polarization resistance (Rp, Ω.cm^2) and

of the corrosion potential (E_{corr}, V). Once the 24h passed a slower increase of the E_{corr} and Rp takes place for time up to 250h, while i_{corr} variations are almost null.

The thermodynamic study of corrosion states that corrosion can only manifest if the potential of the metal surpasses the equilibrium potential ($E > E_{eq}$). E_{eq} is determined by the anode's potential E_a, which can be calculated using the Nernst equation:

$$E_a = E_a^0 + \frac{RT}{nF}\ln\left(\frac{[Fe^{2+}]}{[Fe]}\right) \quad \text{Eq (I.28)}$$

Where E_a^0 is the standard potential of the anode (-0.44V for iron relative to the standard electrode of hydrogen), R is the gas law constant (8.314 J.mol^{-1}.K^{-1}), T is the temperature (considered equal to 298 K), F is the Faraday constant (96487 C) and n is the number of electron released in the reaction (2 for iron). Hence, in the case of iron, the Equation I.28 reads:

$$E_a = -0.44 + 0.0296\log([Fe^{2+}]) \quad \text{Eq (I.29)}$$

With $[Fe] = 1$ because in solid form, and $\ln(x) = \ln(10).\log(x)$.

Nernst equation also defined the potential of the cathode E_c as:

$$E_c = E_c^0 + \frac{RT}{nF}\ln\left(\frac{[O_2].[H_2O]^2}{[OH^-]^4}\right) \quad \text{Eq (I.30)}$$

Where E_c^0 is the standard potential of the cathode (-0.401V for iron relative to the standard electrode of hydrogen). The Equation I.30 can then be written:

$$E_c = 1.229 + 0.0148\log([O_2]) - 0.0519pH \quad \text{Eq (I.31)}$$

Therefore, the electromotive force of corrosion (e) which defines the current in the electrolyte from the anode to the cathode can be written as:

$$e = E_c - E_a \quad \text{Eq (I.32)}$$

$$e = 1.67 + 0.0148\log10([O_2]) - 0.0519pH - 0.0296\log10\,(Fe^{2+}) \quad \text{Eq (I.33)}$$

This equation is given for a constant temperature of 298K.

A thermodynamic analysis of corrosion provides essential information on the necessary conditions for the initiation of the electrochemical process. However, these conditions alone are insufficient to start corrosion. By performing a kinetic study of the corrosion process, it becomes possible to calculate the corrosion rate, which must reach a certain threshold to induce significant corrosion. The current density (i, A.m^{-2}) represents the electron flux resulting from the oxidation-reduction reaction. Under equilibrium potential conditions and with identical anodic and cathodic exchange surfaces, the expression for current density can be written as:

$$i_a = -i_c = i_0 \quad \text{Eq (I.34)}$$

Where i_a is the anodic exchange current, i_c is the cathodic exchange current, and i_0 is the free exchange current.

Conditions outside of equilibrium result in the generation of a consistent internal entropy, in accordance with the second law of thermodynamics. There exists a potential difference between E and E_{eq}, denoted as η (system surge). The simplified Butler-Volmer equation establishes a connection between the exchange current and the system potential, as given by:

$$i = i_0\left(\exp\left(\frac{(1-\alpha)nF\eta}{RT}\right) - \exp\left(\frac{-\alpha nF\eta}{RT}\right)\right)$$ Eq (I.35)

Where α is the coefficient of charge transfer.

In the case of an anodic surge, the cathodic reaction becomes negligible relative to the anodic reaction, leading to Equation I.36, while a cathodic surge leads to Equation I.37:

$$i = i_a = i_0 \exp\left(\frac{\alpha nF\eta_a}{RT}\right)$$ Eq (I.36)

$$i = i_c = i_0 \exp\left(\frac{(\alpha-1)nF\eta_c}{RT}\right)$$ Eq (I.37)

A linear equation between the surge (η) and the logarithm of the exchange current (i) is highlighted by the Butler Volmer equations. It corresponds to the Tafel relation that defines the anodic and cathodic Tafel lines with Equations I.38 and I.39 respectively:

$$\eta_a = \frac{RT}{\alpha nF}\ln\left(\frac{i_a}{i_0}\right) = \beta_a \ln\left(\frac{i_a}{i_0}\right)$$ Eq (I.38)

$$\eta_c = \frac{RT}{(\alpha-1)nF}\ln\left(\frac{i_c}{i_0}\right) = \beta_c \ln\left(\frac{i_c}{i_0}\right)$$ Eq (I.39)

β_a and β_c are called Tafel coefficients. The previous relations are generally used to plot the Tafel lines and determine the corrosion potential E_{corr} and the exchange current of corrosion i_{corr}. An example is given in [165] and showed in Figure I-21.

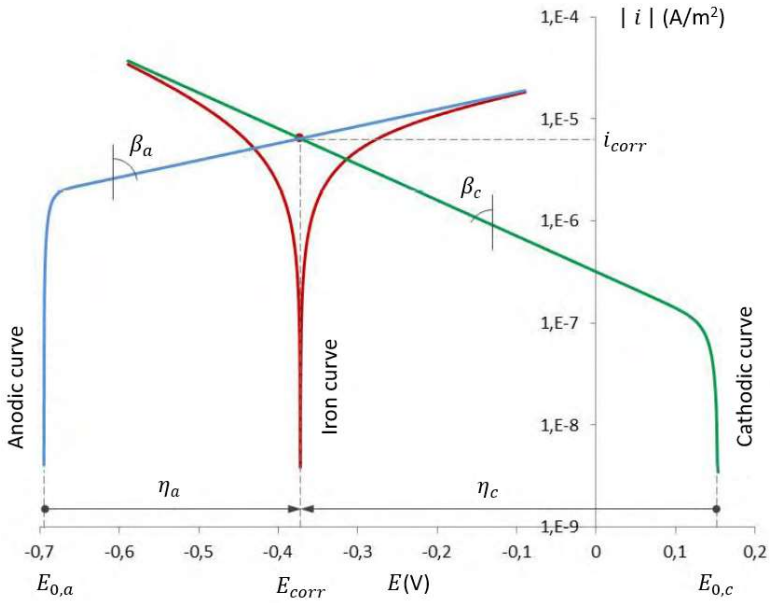

Figure I-21 Tafel lines representation defined in [165]

The intersection of the cathodic and anodic Tafel lines allows the acquisition of E_{corr} and i_{corr} at the equilibrium by extrapolation.

Finally, Faraday law can be used to correlate the current density (i_{corr}, expressed here in A.m^{-2}) to the metal weight loss (Δm, g):

$$Q = i_{corr} t = \frac{nF\Delta m}{AM} \quad \text{Eq (I.40)}$$

Where Q is the coulombs quantity, t is the time (s), A the polarized metal surface (m^2) and M the molar weight of the metal considered (55.85 g/mol^{-1} in the case of iron). The corrosion rate can thus be computed with Equation I.41:

$$v_{corr} = \frac{\Delta m}{t} = \frac{i_{corr} AM}{nF} \quad \text{Eq (I.41)}$$

It is then admitted that for a uniform dissolution of iron, a current density of 1 $\mu A.cm^{-2}$ corresponds to an average section loss rate of 11.6 $\mu m.an^{-1}$. This assumption holds true for carbonation-induced corrosion, which leads to a uniform phenomenon. However, in the case of chloride-induced corrosion, a non-uniform process occurs, requiring more intricate calculations for thorough analysis.

In reinforced concrete structures, the i_{corr} values measured in the literature are shown in Table I-8.

Table I-8 Corrosion risk in reinforced concrete according to the current density (i_{corr}) and corrosion rate (v_{corr}) [166].

i_{corr} (µA/cm²)	v_{corr} (mm/an)	Corrosion risk
< 0.1	< 0.001	Negligible
0.1 – 0.5	0.001 – 0.005	Low
0.5 – 1	0.005 – 0.01	Moderate
> 1	> 0.01	High

I.3.4.2. Corrosion process in reinforced concrete

The medium containing the rebar exhibits a pH approximately equal to 13.6 [167], indicating its alkalinity. This characteristic renders it an ideal environment for the protection of steel through chemical means, as the passivation layer formed provides natural protection. Corrosion initiation occurs only when aggressive elements succeed in damaging this protective layer. As a result, the corrosion process in reinforced concrete can be divided into two distinct stages, as illustrated in Figure I-22. It is important to note that this diagrammatic representation oversimplifies the process, as depassivation does not invariably correspond to propagation. A period may exist between depassivation and propagation, contingent upon variables such as the presence of oxygen, moisture content, and various other parameters [168], [169].

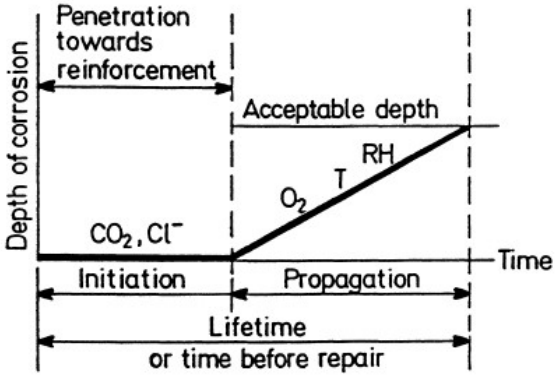

Figure I-22. Schematic representation of steel corrosion steps in concrete [170].

The initiation stage describes the corrosion phenomenon at a passive state, while the rebar steel is still passivated. During this period, reinforcing bars are still protected by the interstitial concrete solution which is basic due to the presence of portlandite and alkaline species. Chloride ions and/or carbon dioxide have not yet reached the steel in a sufficient quantity. As these aggressive substances penetrate

the concrete, the physiochemical equilibrium of the rebar cover is gradually disrupted, leading to the depassivation of the reinforcing bars. During these initial stages, the corrosion rate is negligible.

The last stage of the phenomenon is called corrosion propagation. The concentration of aggressive species which have reached the reinforcing bar is high enough to cause partial to complete depassivation of the steel. Then, a drop of the rebar material corrosion potential is observed, and corrosion propagation may take place if the relative humidity and the oxygen availability are elevated enough.

The Pourbaix diagram [171] of iron is presented in Figure I-23. This diagram defines the stability domain of the different species produced by iron corrosion according to the pH and potential conditions. It also shows the nature of the products allowing the formation of the passivation layer.

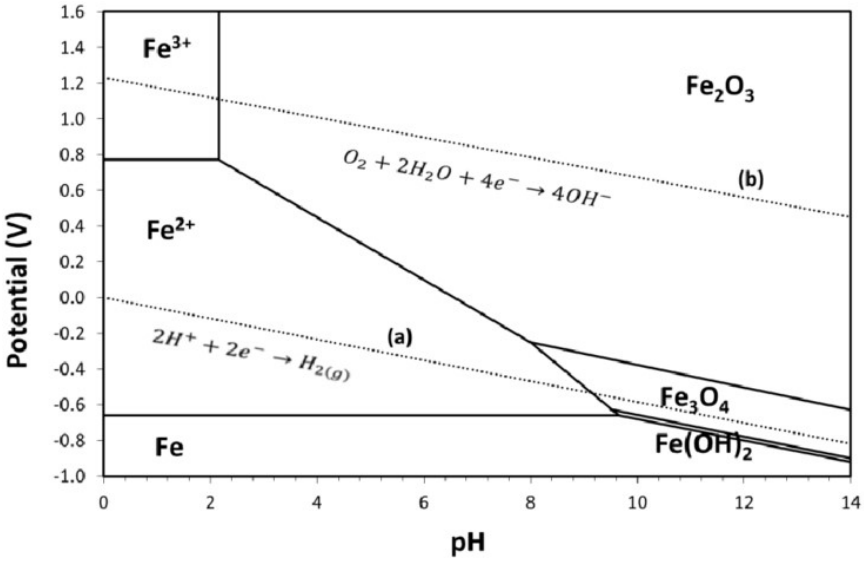

Figure I-23. Simplified Pourbaix diagram of iron (25°C) [172].

The corrosion products formed possess a higher volume than the initial material volume (see Figure I-24), which causes internal stresses to develop within concrete during the corrosion process. Therefore, after a certain time, cracks may form and become preferential channels for oxygen and aggressive species. This phenomenon contributes widely to enhance the rebar corrosion and thus to the structure's deterioration. This is the propagation phase of the corrosion mechanism. These corrosion products may also migrate through the cementitious matrix and cause the appearance of stains on the cladding. It can be noted here that, in the case of high strength concrete, corrosion may develop without leading to the formation of cracks, hindering its detection.

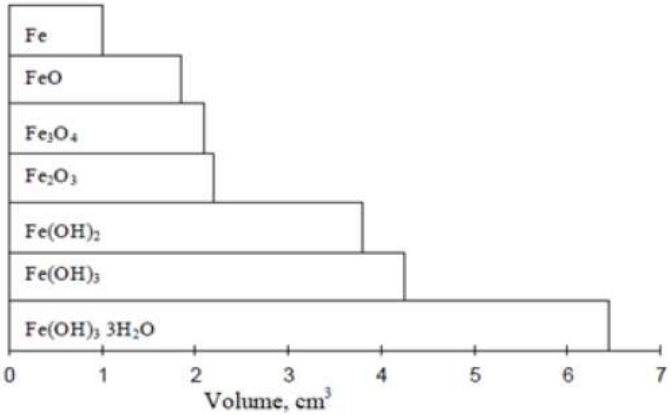

Figure I-24. Representation of the corrosion products volumes [173].

Numerous investigations have demonstrated that the composition of the binder interstitial solution does not affect the characteristics of the corrosion products. Instead, the environment plays a crucial role in governing the formation process, depending on the presence of aggressive species, primarily carbon dioxide and chloride ions, which will be discussed in this work.

Different types of corrosion may happen in the case of reinforced concrete [140]:

Galvanic corrosion: this corrosion happens when two materials with different natures and/or electrochemical potentials are in contact. The corrosion of the least noble metal is then accelerated while the corrosion of the other, nobler, is highly reduced.

Uniform corrosion: this corrosion consists of a uniform alteration of the metal.

Pitting corrosion: this corrosion is localised at a precise point and on a very small area and its propagation is essentially in-depth with a high velocity.

Crevice corrosion: this corrosion occurs when the oxygen accessibility on the rebar steel surface differs according to the zones, which causes a potential difference.

Intergranular corrosion: this corrosion takes place at the grain boundaries.

Stress corrosion cracking: it is the result of the combined action of mechanical stress and environmental aggression of the reinforcing steel bar.

In various forms of aggression, it is consistently observed that two layers of corrosion products are formed. The initial layer, situated proximate to the reinforcing bar, is referred to as the Dense Product Layer (DPL). It is characterized by its dark and compact structure. The subsequent layer, known as the Transformed Medium (TM), exhibits a brighter appearance and higher porosity (refer to Figure I-25). These corrosion products have the potential to propagate up to several millimetres within the cementitious matrix surrounding the steel reinforcement [174].

It can also be noted that the type of corrosion products formed also depends on the aggression underwent by the concrete:

- In the case of carbonation, the DPL is essentially composed of iron under the form of ferric oxy-hydroxide (FeO(OH)) and magnetite under the form of mottling. The TM is composed of ferric oxy-hydroxide poorly crystallised [175], [176].
- In the case of chloride ions aggression, DPL is composed of goethite and akageneite ($Fe^{3+}O(OH, Cl)$) while the TM is mainly constituted of maghemite (γ-Fe_2O_3) with a small quantity of goethite [6].

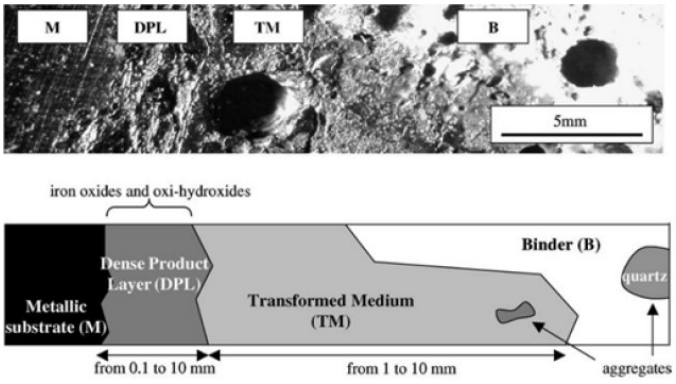

Figure I-25. Photography and schematic representation of the two corrosion products layers, surrounded by the rebar steel and the binder [176].

I.3.4.3. Pitting corrosion

Pitting corrosion is a highly localised phenomenon. Its initiation is fast and of the nanoscale magnitude order. The three representative models for pit initiation discussed in the literature are the following [163]:

- Penetration of anions to the film/metal interface (initiating disbanding).
- Film breaking, where a sudden rupture of the film gives direct access of anions to the metal surface.
- Film thinning, where passivity breakdown is initiated by an increased material transport.

For common steel, pit initiation may be related to the presence of singularities on the steel surface.

They can consist of the presence of manganese sulfide, or other sensitizations. However, pit initiation is generally considered as a random phenomenon for practical reason for the evaluation of time-to-initiation experiments. The interface between steel and concrete may also be responsible as demonstrated in [177] with the “top bar effect”. This effect consists in a steel-concrete interface debonding which may lead to the presence of void at the steel interface [178].

The pitting zone normally turns acidic due to the metal hydrolysis once the corrosion initiated. The propagation of corrosion becomes generally self-sustained because cations dissolved in the solution attract chlorides or other anions. However, if the pit opens, or if the solution within and around the pit get saturated by metal cations, the pit can repassivate. This is due to the necessity for pit propagation to reunite a series of factors to proceed. The pit needs to present an occluded geometry, an elevated concentration of chlorides and a high solubility of metal salts in the pit solution [163].

I.4. Modelling – state of the art

In the models addressing the phenomena studied in this research, different levels of complexity can be observed, based on the selected modelling method. Essentially, two distinct types of models can be identified:

- Analytical models which are possibly based on:
  1. One or a limited set of equations partially describing the phenomenon, focusing only on the most significant aspects. These equations are solved analytically while considering specific mathematical assumptions that align with the conditions under which the phenomenon occurs. As a result, an explicit expression of the solution is provided.
  2. An expression that mimics the result of the phenomenon, based on a mathematical expression adjusted to fit various experimental measurements.
- Numerical models utilize the same set of equations as analytical models, or an expanded set that accounts for additional accompanying phenomena. These models solve equations using numerical methods such as finite element or finite volume resolutions.

The validation of these models is typically accomplished with experimental measurements, thus categorizing them as empirical.

In this section, a brief overview of the various models developed for estimating the durability of reinforced concrete subjected to carbonation or chloride ions is given. Subsequently, models utilised to forecast the corrosion process are outlined. Finally, models used to compute the different properties of concrete are detailed in the last section.

I.4.1. Carbonation

Due to the importance of the carbonation impact on reinforced concrete structures, numerous models were developed to estimate the associated time to depassivation. It is important to highlight that not all models consider the same inputs, owing to their utilization of different equations. Consequently, these models often yield diverse outcomes when applied to the same scenario. Consequently, it becomes crucial to fully comprehend the various inputs, outputs, and application domains of the models in order to make an appropriate selection for a specific application. Nevertheless, in scientific literature, carbonation is typically characterized as a function of the square root of time, as denoted by Equation I.42.

$$x_c(t) = K\sqrt{t} \qquad \text{Eq (I.42)}$$

Where x_c is the carbonation depth (mm), t the time (years) and K a constant referred to as carbonation rate (mm. years$^{-0.5}$) which depends on the material, environmental and manufacturing factors. This latter parameter remains nowadays the source of numerous investigations.

A vast array of models is available in the literature, with Table I-9 and Table I-10 providing a summary of analytical and numerical models, respectively.

Table I-9 Analytical carbonation models of the literature [7], [179], [180]

Reference	Nat/Acc	Environmental parameter	Material parameter	Information on additions considered
Papadakis et al. [66], 1999	N-A	K		All
Khunthongkeaw et al. [181], 2006	N	P_{CO_2}, RH	$x_{c,acc}$	All
Niu et al. [182], 1999	N/A	T, RH, P_{CO_2}	k_c, f_c	
Zhang et al. [183], 2013	N/A	P_{CO_2}, RH	K_{gas}	Slag
Zhu et al. [184], 1992	N	RH, rain	W_{eff}, C	Fly ash (<15%), Consider cement type
Jiang et al. [185], 1996	N/A	RH, P_{CO_2}	W_{eff}, C, α	Consider cement type
Jiang et al. [186], 2000	A	RH, P_{CO_2}	$W_{eff}, C, \alpha, \varphi, Q_V$	Fly ash in high volume
Wang and Lee [187], 2009	N/A	P_{CO_2}, RH	$\varphi^w_{c,car}, Q_V$, W, $C, CH, CH, \rho_{cem}, \rho_V$	Fly ash
Wang and Lee [188], 2009	N/A	P_{CO_2}, RH	$\varphi^w_{c,car}, Q_V, W_{eff}, C, CH, CH, \rho_{cem}, \rho_{SF}$	Silica fume
Papadakis et al.[189], 1991	N/A	P_{CO_2}	$CH, CSH, C_2S, C_3S, D_{CO_2}$	
Hyvert et al.[104], 2010	A/N	P_{CO_2}, P_{atm}	F_{paste}, D_{CO_2}	
Sisomphon and Lutz [190], 2007	A	P_{CO_2}	K, D_{CO_2}, binding capacity	
fib code model [191], [192], 2006	N	k_e, Weather, P_{CO_2}, RH	R^{-1}_{NAC}	
Morinaga [193], 1988	A/N	P_{CO_2}, RH, T	W_{eff}/B_{tot}	
Thomas and Matthews [73], 1992	N	RH, T	f_c	Considers cement type
Parrott [194], 1994	N	RH	B, D_{air}	
Bamforth [195], 2004	N	RH	B	Considers cement type
JSCE [196], 2007	N	-	B, W_{eff}	Considers cement type
Czarnecki and Woyciechowski [197], 2012	N/A		B, W_{eff}	Considers cement type
Silva et al. [198], 2014	N/A	P_{CO_2}, RH	f_c	
	N/A	P_{CO_2}, RH	B, f_c	
Von-Greve Dierfled and Gehlen [199], 2016	N	RH, Rain	?	
Hills et al. [200], 2015	N	?	?	Considers cement type
	N	?	f_c	
Schiessi [201], 1976	N	P_{CO_2}	Binding capacity, D_{CO_2}	
Tuuti [170], 1982	N	P_{CO_2}	B, C, Binding capacity, D_{CO_2}, α	
Papadakis et al [189], 1991	N/A	P_{CO_2}	Binding capacity, D_{CO_2}	
Bouquet [202], 2004	N/A	P_{CO_2}, RH, rain	Binding capacity, D_{CO_2}, α	
Andrade and Andrea [203], 2010	N	P_{CO_2}	Binding capacity, Re	
Salvoldi et al. [204], 2015	A	P_{CO_2}, RH, rain	Binding capacity, D_{O_2}	

Based on a comprehensive analysis of the existing analytical models in the literature, it is evident that certain key parameters significantly influence the carbonation process. These parameters must be taken into account while developing a model that can accurately predict this phenomenon in various environmental and concrete conditions:

- The temperature, relative humidity (considering the rain frequency) and the partial pressure of CO_2 seem sufficient to consider the environment. Accelerated and natural conditions can be modelled by modifying the value of P_{CO_2}. However, the initial hydrologic conditions of the sample are never considered in analytical model, which sometimes explains the difference of results when compared to numerical models able to consider this aspect.
- The identification of the most relevant material parameters is difficult. The existing literature provides a general overview of the factors to consider. Firstly, the ability of the concrete to bind CO_2 and retard the diffusion process is crucial in terms of carbonation resistance. This is primarily influenced by the type and amount of binder (hydrates or anhydrous), as well as the water content and hydration rate. Secondly, the concrete's capacity for CO_2 diffusion must be taken into account, either directly through D_{CO_2}, or by considering other parameters such as φ, K_{gaz}, and the alternative gaseous diffusion coefficient. Some models also consider additional parameters like the compressive strength (f_c) or the electrical resistivity (Re), which are not directly connected to the carbonation process, but offer an overall assessment of concrete quality and enable correlation with the carbonation rate K. However, it should be noted that these models require the use of constants specifically tailored to certain types of concrete, limiting their applicability in predicting carbonation for all binder types.
- The manufacturing and curing conditions are sometimes considered because they impact the final carbonation resistance. The curing time t_c is frequently used to consider this aspect.

Table I-10 Numerical carbonation models of the literature [7], [180]

Reference	Heat transfer	Moisture transfer	Specific kinetics	Microstructure evolution	Output
Steffens et al [205], 2002	x	x			
Saetta and Vitaliani [206], 2004	x	x	Chemical reaction rates		
Bary and Sellier, 2004 [24]		x	CH, CSH, C_3S, C_2S	Porosity, hydration	$CaCO_3$
Bary and Mügler [207], 2006		x	Different carbonation kinetics for each hydrates		
Morandeau et al. [208], 2014		x			
Saetta, Schurefler et Vitaliani [7], [209]	x	x	CH	Hydration	$CaCO_3, pH, CH$
Miragliotta [210], 2000	x	x	CH, CSH, C_3S, C_2S	Hydration, porosity	x_c
Thiéry [211], 2011		x	CH, CSH	Porosity, hydration	$CH, CaCO_3, pH$
Papadaki et al. [66], 1990		x	CH, CSH		x_c

Numerical models offer superior precision for analysing phenomena, allowing for a more accurate consideration of carbonation kinetics and various reactions (e.g., CO_2 dissolution in the interstitial solution, hydrate dissolution based on pH). Unlike analytical models, which only provide information on carbonation depth, numerical models provide multiple outputs that enhance the understanding of

material evolution during carbonation. For instance, estimating the pH of the interstitial solution can be utilised to predict steel depassivation using a probabilistic approach.
However, the complexities associated with input requirements often necessitate the use of additional models to predict the initial state of the concrete material (refer to Section I.4.5). The added uncertainties introduced by these models should be taken into account during the prediction analysis.

Several models are described in greater detail in Annex 4 in order to provide alternative examples or because they are applied in subsequent sections of this document (refer to Section IV.4). Furthermore, these models are incorporated into the final tool to provide alternative methods for calculating carbonation depth, which may be more readily applicable in specific cases compared to the developed numerical model.
Hence, five analytical models are described:

- A model developed by Von Greve and Gehlen [199].
- A model developed by Demis and al. [27].
- The model developed by the Japan Society of Civil Engineers (JSCE) [196].
- A model developed by Parrott [194].
- The model developed in the recent project PerfDuB [2].

A concise description of a finite element is provided in the following section due to its relevance, particularly in the context of integrating carbonation with heat and hydrologic transfer [212]. Furthermore, the various methods in the literature used to approximate the pH value are summarized, as their inclusion is frequently crucial in finite element models that consider carbonation. Lastly, an alternative approach is introduced, whereby the estimation of carbonation depth is achieved through the utilization of a neural network [213].

1.4.1.1. Finite element model for heat transfer, moisture transport and carbonation in concrete [212]

In their paper, the authors presented a finite element model that accurately simulates the dynamic interactions between heat transfer, moisture transport, and the carbonation process in concrete structures. This model, unlike the previously discussed analytical models, employs a more sophisticated approach by incorporating complex and differential equations, which are effectively solved using numerical methods.

The transportation mechanism of carbon dioxide within the concrete matrix is effectively governed by the Equation I.43 that captures the intricate dynamics of this process:

$$\frac{\partial}{\partial x}\left(D_{CO_2}\frac{\partial[CO_2]}{\partial x}\right)+\frac{\partial}{\partial y}\left(D_{CO_2}\frac{\partial[CO_2]}{\partial y}\right)+Q_{CO_2}=\frac{\partial[CO_2]}{\partial t} \qquad \text{Eq (I.43)}$$

Where:

- D_{CO_2} is the diffusion coefficient of CO_2 (m^2/s) computed following the expression proposed by Papadakis et al. [214] with Equation I.44
- $[CO_2]$ is the concentration of CO_2 (kg/m^3 of pore solution).
- Q_{CO_2} is the sink term representing the reduction of CO_2 concentration due to the carbonation reaction.

$$D_{CO_2} = 1.64 \times 10^{-6} \varphi_c(t)^{1.8} (1 - RH\,(t))^{2.2}$$ Eq (I.44)

With $\varphi_c(t)$ the time dependant porosity of the concrete material (-) and $RH(t)$ the time dependent relative humidity in the concrete pores (-).

In this study, the heat transfer phenomenon is being modelled using Fourier's law, which accurately considers thermal conduction. By applying this law, the corresponding differential Equation I.45 is obtained:

$$-\frac{\partial}{\partial x}\left(-k_{therm}\frac{\partial T}{\partial x}\right) - \frac{\partial}{\partial y}\left(-k_{therm}\frac{\partial T}{\partial y}\right) + Q_{therm} = \rho_c c_{therm}\frac{\partial T}{\partial t}$$ Eq (I.45)

Where:

- k_{therm} is the thermal conductivity of the concrete material (W/m.°C).
- T is the temperature of the concrete (°C).
- ρ_c is the density of concrete (kg/m^3).
- c_{therm} is the specific heat (J/kg.°C).
- t is the time (s).
- Q_{therm} represents the heat source/sink term.

In this study, the authors aim to analyse the various parameters that influence the boundary conditions for heat transfer. Specifically, they focus on the impact of wind, solar radiation, and ambient temperature on the net heat flow across a concrete surface. The mathematical expression for the calculation of net heat flow is denoted as Equation I.46:

$$q_s - q_c - q_r - q_y = 0$$ Eq (I.46)

Where:

- q_s represents the total radiation absorbed, computed with the Equation I.47.
- q_r is the total amount of radiation emitted by the concrete surface (obtained from Stefan-Boltzman law with Equation I.48).
- q_c is the heat loss by convection, computed with Equation I.49.
- q_y is the heat conducted into the concrete material (computed using the Fourier's law with Equation I.50).

$$q_s = \alpha C_N G_Z e^{-\frac{\tau}{\cos(\beta)}}$$ Eq (I.47)

$$q_c = h_c(T_l - T_{sh})$$ Eq (I.48)

$$q_r = h_r(T_l - T_{sh}) + \varepsilon\sigma((T_{sh} + 273.15)^4 - (T_l + 273.15)^4)$$ Eq (I.49)

$$q_y = -k\left(n_x\frac{\partial T}{\partial x} + n_y\frac{\partial T}{\partial y}\right)$$ Eq (I.50)

Where:

- α is the absorptivity of concrete, generally comprised between 0.5 and 1.
- C_N is the clearness number, which depends on the location of the structure.
- β is the solar zenith angle.
- G_Z and τ are given by the trigonometric series shown in Equations I.51 and I.52 respectively.

- h_c is the convection coefficient of the concrete surface (W/m^2.°C). This coefficient is computed with the expression suggested by Priestley and Thurston [215] summarized in Equation I.53.
- T_{sh} is the shade air temperature (°C).
- T_l is the concrete surface temperature (°C).
- h_r is the radiation heat transfer coefficient (W/m^2 °C).
- ε is the emissivity of the concrete surface (-).
- σ is the Stefan-Boltzman constant (5.669 x 10^{-8} W/m^2.K^4)
- n_x and n_y are the direction cosines of the normal to the surface.

$$G_Z = 1162.4 + 77.4\cos(C_T) - 3.6\cos(2C_T) - 3.4\cos(3C_T) + 1.8\sin(C_T) - 0.6\sin(2C_T) + 0.9\sin(3C_T) \quad \text{Eq (I.51)}$$

$$\tau = 0.1717 - 0.0344\cos(C_T) + 0.0032\cos(2C_T) + 0.0024\cos(3C_T) - 0.0043\sin(C_T) - 0.0008\sin(3C_T) \quad \text{Eq (I.52)}$$

With $C_T = \frac{2\pi.n_d}{366}$ where n_d is the day of the year.

$$h_c = 13.5 + 3.88v \quad \text{Eq (I.53)}$$

With v being the average wind speed (m/s).

Finally, the moisture transfer is expressed using the Equation I.54. Moisture is examined through two distinct factors: the first factor, denoted as w_e , represents the amount of evaporable water (expressed in grams of water per gram of cementitious material), while the second factor, labelled as RH, characterizes the relative humidity.

$$\frac{\partial}{\partial x}\left(D_h\frac{\partial RH}{\partial x}\right) + \frac{\partial}{\partial y}\left(D_h\frac{\partial RH}{\partial y}\right) + \frac{\partial RH_s}{\partial t} + H\frac{\partial T}{\partial t} + Q_h = \frac{\partial w_e}{\partial RH}\frac{\partial RH}{\partial t} \quad \text{Eq (I.54)}$$

Where:

- The hygrothermal coefficient (H), expressed as °C^{-1}, determines the change in humidity resulting from a one-degree temperature change for a constant water content (w_e).
- Q_h represents the heat source that arises from carbonation and generates water.
- $\partial RH_s/\partial t$ represents the pore relative humidity change due to self-desiccation, which can be considered equal to 0 in normal strength concrete after a certain time.
- The moisture transport coefficient (D_h) accounts for the impact of temperature change on moisture transport. For practical purposes, the term $H(\partial T/\partial t)$ is replaced by D_h to incorporate the effect of temperature change on moisture transport.

The term $\partial w_e/\partial RH$ represents the moisture capacity, which indicates the relationship between evaporable water and pore water contents. The Brunauer, Skaklny and Bodor (BSB) model [216] is selected as the adsorption isotherm in this study, where the equation for w_e is expressed as:

$$w_e = \frac{Ck_mV_mRH}{(1-k_mRH)(1+(C-1)k_mRH)} \quad \text{Eq (I.55)}$$

Where:

- V_m is the amount of vapour required for monolayer formation (also called monolayer capacity) and is computed with the Equation I.56.
- C and k_m are parameters computed with the Equations I.57 and I.58.

$$V_m = \left(0.068 - \frac{0.22}{t_c}\right)\left(0.85 + 0.45\frac{W_{eff}}{C}\right) \quad \text{Eq (I.56)}$$

$$C = e^{\frac{855}{T}} \quad \text{Eq (I.57)}$$

$$k_m = \frac{\left(1-\frac{1}{n}\right)C-1}{C-1}$$ Eq (I.58)

The parameters n is a function whose computation depends on the equivalent hydration age (t_c, days) and the water-to-cement ratio (W_{eff}/C, -).

First:

- If $\frac{W_{eff}}{C} < 0.3: n = 0.99(2.5 + \frac{15}{t_c})$
- If $\frac{W_{eff}}{C} \geq 0.6: n = 1.65(2.5 + \frac{15}{t_c})$

Second, if $0.3 \leq \frac{W_{eff}}{C} < 0.6$:

- If $t_c > 5\ days: n = \left(2.5 + \frac{15}{t_e}\right)\left(0.33 + 2.2\frac{W_{eff}}{C}\right)$
- If $t_c \leq 5\ days: n = 5.5(0.33 + 2.2\frac{W_{eff}}{C})$

In addition to its complexity and the involvement of numerous equations, the numerical resolution of this model needs to be non-linear due to the heat transfer equation. This is particularly important because Equation I.49 applies an exponent of 4 to the temperature variable for the computation of the radiation heat term (q_r).

One advantage of such a modelling approach is the ability to accurately represent cracked concrete with a 2-dimensional mesh. The precise nature of the equations also allows for consideration of specific environmental factors, which is typically not possible with a traditional analytic model. This is especially relevant for the heat transfer equations, as they account for numerous environmental factors and are more reliable in extreme conditions.

The main drawback of this model is the high computational time and complexity, which is commonly associated with most finite element models. Additionally, the acquisition of values for the different settings further complicates its use, particularly in practical applications.

1.4.1.2. pH computation

In finite element models, the computation of carbonation depth is typically not performed directly. Instead, the determination of hydrates and/or calcite contents as a function of space and time is obtained. Consequently, it is necessary to establish a methodology to convert concentrations into carbonation depth. One approach is to assess the pH value, as carbonation leads to a decrease in pH by consuming the hydrates present in the cementitious paste. Multiple formulas have been developed for this purpose:

- In [217], the authors propose a simple function for the pH computation from the only knowledge of the dissolved calcium hydroxide content (CH_d, mol/m^3):

$$pH = \begin{cases} 14 + log10(2 \times 10^{-3} CH_d) & \text{For } CH_d \geq 1 \times 10^{-3} \\ 8.3 & \text{Otherwise} \end{cases}$$ Eq (I.59)

- In [218], a formula is proposed for calculating the pH in the transition zone, aimed at estimating its value without the inclusion of hydrate content. Instead, this equation directly utilizes the carbonation depth (x_c, mm) and the depth (x, mm) of the concrete cover. Consequently, it is not suitable for determining the carbonation depth, as it already necessitates this information as input in the first place. Nonetheless, this equation presents an alternative approach to evaluating carbonation, thereby enabling a distinct assessment of the pH that may result in the depassivation of the steel.

$$pH = 12.6\left[\frac{6.5}{12.6} + \frac{1 - 6.5/12.6}{1 + \left(\frac{1 - (x - x_c + 2.88)/4}{1 - 0.5}\right)^4}\right] \quad \text{Eq (I.60)}$$

In order to accurately compute the pH in the concrete pores, more complex methods involve the calculation of the chemical equilibrium of the interstitial solution, taking into account all ionic species present. Although this approach requires significant computational time, it provides a more precise estimation of pH. The necessary chemical constants for this computation can be found in [219], [220].

1.4.1.3. Artificial Neuron Network (ANN) from Kellouche and Al. work [213]

In their work, Kellouche and Al. [213] devised a neural network model for the prediction of carbonation depth. The model was specifically tailored for OPC and slag-based concrete. To construct, train, and verify the model's performance, a comprehensive dataset comprising 218 data points was collected from six sources in the literature. The study encompasses nine distinct input parameters alongside the recorded carbonation depths, as outlined in Table I-11, while adhering to predefined ranges of values.

Table I-11 Range value of data collected from the literature [213].

Parameter (Unit)	Average	Min	Max
Blast Furnace Slag (%)	45.29	0	85
Binder content (kg/m^3)	390.57	301	550
$\boldsymbol{W_{eff}/B_{tot}}$	0.25	0.25	0.6
Oxide ratio (%)	71.31	0	98.11
Finesse (m^2/kg)	367.75	0	600
$\boldsymbol{P_{CO_2}}$ (%)	13.81	6.5	50
RH (%)	64.52	60	70
Age (days)	8.74	1.73	19
Curing time (days)	98.16	28	540
Xc (mm)	9.03	0	36

The operation of the artificial neural network (ANN) is described in Section I.5.1.2. The architecture of the model developed by Kellouche et al. consisted of three layers:

- An input layer with the 9 parameters.
- A hidden layer composed of 15 neurons.
- An output layer with 1 neuron.

The authors utilised a tansig activation function with a training rate of 0.05 and conducted 100 training cycles. Once the ANN was constructed, the authors conducted an experimental campaign to assess its potential application. Carbonation depths were measured for 12 concrete formulations consisting of ordinary Portland cement (OPC) and slag substitution ranging from 0% to 60%.

To gauge the disparity between the model's predictions and the experimental measurements, the authors quantified the relative error using Equation I.61.

$$RE(\%) = 100 \times \frac{ABS\left(X_{exp} - X_{ANN}\right)}{X_{exp}} \quad \text{Eq (I.61)}$$

Samples used for validations were exposed to controlled conditions (CO_2 = 4 vol.%, RH = 65%, T = 20 °C) and carbonation depths were measured after 7, 28 and 90 days.

The Mean Relative Error computed with Equation I.62 is finally used to estimate the performance of the model.

$$MRE(\%) = \frac{\sum_{i=1}^{N} RE(\%)}{N}$$ Eq (I.62)

Where N is the number of samples. The MRE value obtained is 7.65%, which is low and proves that the model can adequately simulate the carbonation phenomenon for slag-based concretes.

I.4.2. Chloride ions exposure

Similar to carbonation, the exposure of reinforced concrete structures to chloride ions results in degradation. The pitting corrosion resulting from this phenomenon is usually more detrimental to the structural integrity compared to the uniform corrosion caused by carbonation. As a result, several models have been developed to calculate chloride penetration in concrete. These models are primarily based on an analytical solution of Fick's second law (referred to in Equation I.63 for a one-dimensional representation):

$$\frac{dCl_t}{dt} = D_2 \frac{d^2 Cl_t}{dx^2}$$ Eq (I.63)

Where Cl_t is the total chloride concentration (kg/m^3), t the time (s), x the depth (m) and D_2 the diffusion coefficient of the Fick's second law (m^2/s) associated to the total concentration. However, it is important to note that only free chlorides (Cl_f, kg/m^3 of liquid) are involved in the diffusion phenomenon.

Therefore, to accurately describe this phenomenon, the previous Equation I.63 needs to be modified using Fick's first law of diffusion (as stated in Equation I.64). This modification leads to the following Equation I.65:

$$J = -D_1 \left(\frac{dCl_f}{dx} \right)$$ Eq (I.64)

$$\frac{dCl_t}{dt} = -\frac{dJ}{dx} = -\frac{d}{dx}\left(-D_1 \left(\frac{dCl_f}{dx} \right) \right)$$ Eq (I.65)

Where J is the flux of chloride (kg/m^{2}s), D_1 the diffusion coefficient of the Fick's first law (m^2/s) associated to the free chloride concentration. Finally, the Equation I.65 can be rearranged in terms of free and bound chlorides, giving the Equation I.66 and the Equation I.67 if D_1 and dCl_t/dCl_f are independent with respect to x.

$$\frac{dCl_t}{dt} = \frac{d}{dx}\left(\frac{D_1}{\frac{dCl_t}{dCl_f}} \frac{dCl_t}{dx} \right)$$ Eq (I.66)

$$\frac{dCl_t}{dt} = \frac{D_1}{\frac{dCl_t}{dCl_f}} \frac{d^2 Cl_t}{dx^2}$$ Eq (I.67)

Finally, the comparison of the Equations I.63 and I.67 helps to define the relationship between the diffusion coefficients used in the two laws:

$$D_2 = \frac{D_1}{\frac{dCl_t}{dCl_f} \frac{1}{\varphi_c^w . Sr}}$$ Eq (I.68)

The term dCl_t/dCl_f represents the chloride binding capacity, expressed in (kg Cl/m^3 of concrete) / (kg Cl/m^3 of solution). To maintain homogeneity and a coherent equation, an operation needs to be

performed on Cl_f ensure it has the same unit as Cl_t. This involves incorporating the term $\varphi_c^w . Sr$ into the equation, which corresponds to the volume of solution within one m^3 of concrete.

The solution of the Fick second law reads:

$$Cl_t\,(x,t) = Cl_0 + (Cl_S - Cl_0)\mathrm{erf}\,(\frac{x}{\sqrt{4D_2 t}}) \qquad \text{Eq (I.69)}$$

Where Cl_0 is the initial chloride concentration in concrete (kg/m^3 of concrete), Cl_S the chloride concentration on concrete surface (kg/m^3 of concrete). erf is the Gauss error function which is computed as:

$$\mathrm{erf}(x) = \frac{2}{\sqrt{\pi}}\int_0^x e^{-t^2}dt \qquad \text{Eq (I.70)}$$

The use of the second Fick law solution is only valid under the assumption that:

- The medium is semi-infinite.
- The concrete material is saturated in liquid water.
- The chloride diffusion coefficient is independent of time and space.

This approach is simple and practical. However, it may lead to overestimations of the chloride content due to the consideration of a constant chloride diffusion coefficient. Therefore, an additional equation is typically included to calculate the evolution of the chloride diffusion coefficient over time [221], [222]. Various adaptations for this purpose are detailed in [223].

In the case of a coupling with hydrologic transfer, an additional phenomenon that induces chloride ingress needs to be considered alongside diffusion. The convection of chloride occurs when the hydrological state of the concrete material's porous network is different than that of the surrounding environment. Chloride ions displace with the water content and move inward and outward. The variation of relative humidity generally impacts the first millimetres of the material to a great extent. In this zone, the convective phenomenon controls the chloride concentration if hydrologic variations occur (e.g., in reinforced structures in tidal zones or those subjected to sea spray, deicing salts, and rain).

In modelling, convection can be accounted for using different methods. Firstly, an offset Δx of the maximal concentration can be added to the diffusion modelling using the second Fick's law (this approach is employed in models such as the *fib* code model and the PerfDuB model). The other method involves modifying Equation I.69 (Second Fick's law solution) and is generally used for more complex models solved using finite element methods. An example of the expression used for the coupled diffusion/convection of chloride ions is presented in Equation I.71 [224].

$$\frac{\partial Cl_t}{\partial t} = \frac{\partial}{\partial x}\left(D_2\frac{\partial Cl_t}{\partial x} - Cl_t(v_p + v_c)\right) \qquad \text{Eq (I.71)}$$

Where v_p and v_c are the flow velocity of the pore fluid under the action of the pressure permeability and the capillary action respectively. However, it is important to note that there are various factors that can cause water movement, which need to be considered in addition to these two terms. Therefore, the inclusion of convection in the model implies considering the transfer of water within the material, increasing the complexity of the model.

In terms of the existing literature, there are fewer analytical models available for pore fluid flow compared to carbonation studies; however, a similar number of numerical models have been developed. The Table I-12 and Table I-13 provide examples and specific details of these models.

Table I-12 Analytical model for chloride penetration in concrete [6].

Reference	Chloride type Free/Total	Environmental parameter	Material parameter	Other parameters	Additions considered
fib code model [20]	F	$Cl_{f,env}$, k_e	Cl_0, D_{rcm}, t_0, ae, Δx		ae and D_{rcm} can be used to consider most materials
Mejlbro-Poulsen [225] [6]	F	Cl_s	Cl_0, D_{app}, ae		Test needs to be carried on for pozzolanic material to fit the parameters
Selmer [226], 1999	F	$Cl_{f,env}$, Cl_s	D_m, ae	t_c	
Duracrete [227], [228] 2000	F	k_e, $Cl_{f,env}$, T	D_{rcm}, t_0, ae, Cl_0, Δx	k_t, k_c, C_{crit}	ae and D_{rcm} can be used to consider most materials
Modevie model [2], [229]	F	$Cl_{f,env}$, T	D_{rcm}, t_0, ae, Cl_0, Δx, φ_c^w, B	T_{ref}	ae and D_{rcm} can be used to consider most materials

The parameters shown in Table I-12 demonstrate the similarities inherent to the analytical modelling of chloride ingress. Indeed, although there are some differences among the five models presented, consistent parameters can be observed due to the initial assumption based on the solution of the second Fick law that was utilised to create these models. These consistent parameters include the chloride concentration in the environments, the initial chloride content, the diffusion coefficient, and the ageing factor, which are commonly utilised in most models, albeit sometimes represented in different forms. These parameters play a crucial role in governing the diffusion process of chloride in the models.

However, the differences between the various models can be found in the definition of certain factors on:

- Environmental conditions: These encompass considerations such as temperature, with the diffusion coefficient evolving in accordance with the Arrhenius law.
- Material preconditioning: This involves parameters such as k_c, which takes into account the effects of curing treatment on the material.
- Convection of chloride: This factor is characterized by the offset of the depth at which the maximal chloride concentration is present (Δx).

The numerical models generally include additional physics and parameters, even when they are based on the second Fick's law.

Table I-13 Numerical model for chloride ingress in concrete

Reference	Heat transfer	Moisture transfer	Chloride binding	Chloride type	Convection	Electro-coupling
ClinConc [230], [231], 1996	X	X	X	F/T		
HETEK-Conv [152], 1997	X	X	X	F/T	X	
Cerema [232]			X	F/T	X	X
LEO 2000			X	F	X	
Life 365 DAL [233], 2000	X			F		
Li et Page [234], 2000			X	F/T		X
STADIUM [235], 2007	X		X	F/T		X
Bastidas [236], 2010	X	X	X	F/T	X	
Tuutti [170], 1982			X	F/T		
Ukrainczyk et al. [237]			X	F/T		X
Mejlbro [225]			X	F/T		
ERFC [238]	X	X			X	
Liu et al. [239], 2012	X		X	F/T		X
Benkemoun et al. [240], 2017			X	F/T		

The preceding table demonstrates a significant variability among existing models for chloride ingress in concrete. Nearly all these models take into account the binding of chloride and the equilibrium between free and total chloride. However, they differ in the inclusion of other phenomena such as moisture and heat, which are crucial factors in modelling chloride penetration. The consideration of chloride convection requires precise computation of the hydrological state of the material. Additionally, some models also incorporate the electro-coupling of chloride with other ionic species, thereby enhancing the computation of diffusion capacity. Nevertheless, this method often imposes a substantial computational load.

Other numerical models are presented in the next section, including the pairing between chloride ingress and carbonation.

Two analytic models, based on the second Fick law solution, are presented in Annex 4: the *fib* code model [20] and the PerfDuB model [2]. Each model provides a unique perspective on the diffusion process.

Two numerical models are described, referencing publications [237], [241]. These models are based on distinct assumptions and utilize different phenomenological approaches to accurately capture the behaviour of the diffusion process. Their aim is to provide a deeper understanding of the complex nature of chloride-induced corrosion and to explore different possibilities for modelling this phenomenon.

The consideration of boundary conditions including the convection of chloride is then presented. Subsequently, a concise overview of the currently available approaches for assessing chloride binding is provided.

1.4.2.1. Physical models – Ion transport model of Ukrainczyk et al. [237]

The complexity of the chloride ions penetration necessitates the utilization of more intricate equations to ensure accurate predictions. The Nernst-Planck equation is frequently employed to elucidate a multi-species system involving the transportation of multiple ions.

The Equation I.72 outlines the flux J_i (kg/m^{2}s) of the ionic species i. It is important to note that this equation assumes the material is saturated in water, which implies that unsaturated concrete is not encompassed within this framework.

$$J_i = -D_{1,i}\left(\frac{\partial^2 c_i}{\partial x^2} + c_i \frac{\partial ln a_i}{\partial x} + \frac{z_i F}{RT} c_i \frac{\partial \psi}{\partial x}\right) \quad \text{Eq (I.72)}$$

Where $D_{1,i}$ is the diffusion coefficient of ion i (m^2/s), c is the concentration (kg/m^3 of liquid), a is the activity coefficient (-), ψ the electrical potential (V) and F the Faraday constant (96485 s.A/mol).

One of the challenges associated with utilizing the Nernst-Planck equations for describing ionic flux is the requirement to account for the electric field, or in some cases, make assumptions about its magnitude and influence. This issue arises in the models discussed in references [237], [239]. Ukrainczyk et al. tackle this problem by developing a multi-species ionic transport model using Equation I.73 derived from the Nernst-Planck equation:

$$\varphi . \frac{\partial\, c_i(x,t)}{\partial t} = -D_{eff,i}\left(\frac{\partial^2 c_i(x,t)}{\partial x^2} + \frac{c_i(x,t)}{\gamma_i(x,t)} \frac{\partial \gamma_{\,i}(x,t)}{\partial x} + \frac{z_i F}{RT} E(x,t) \frac{\partial c_i(x,t)}{\partial x}\right) - r_i \quad \text{Eq (I.73)}$$

Where:

- φ is the material porosity (-).
- c_i is the concentration of the species i in the bulk solution (mol/m^3).
- x is the concrete depth (m).
- t is the time (s).
- $D_{eff,i}$ is the intrinsic effective diffusion coefficient ($m^2.s^{-1}$).
- $\gamma_{\,i}$ is the chemical activity coefficient of the ionic species i (-).
- z_i is the valence number of the ionic species i (-).
- F is the Faraday constant (96485 $C.mol^{-1}$).
- R is the ideal gas constant (8.314 $J.mol^{-1}.K^{-1}$).
- T is the absolute temperature (K).
- E is the local (diffusion induced) electrical field ($Volt.m^{-1}$). The various approaches for evaluating this variable are outlined in [237]. However, in cases where the solution is electro-neutral and there is no application of external current, the diffusion coefficient for all species is similar and it can be assumed that $E(x,t)$ is equal to 0.
- r_i is the binding term for the ionic species i ($mol.m^{-3}.s^{-1}$).

The resolution of this type of equation necessitates a numerical implementation and imposes a high computational burden. The primary focus of a model based on Nernst-Planck equations lies in accounting for the interactions among various ionic species. For example, the inclusion of sulphates or alkaline species is frequently disregarded, despite its influence on chloride binding and diffusion capacity within the porous network. Hence, employing such a model could yield more precise predictions if the exact composition of the interstitial solution is known.

1.4.2.2. Physical models – Non-saturated Conditions

Non-saturated conditions in the context of ion transfer involve the simultaneous consideration of diffusion and convection processes. The overall diffusion coefficient is influenced by the transfer of water molecules, which is commonly quantified by the saturation degree of relative humidity. In physical models, it is important to account for the state of water, as the transport of chloride ions differs between the liquid and vapor phases. One approach to capturing the equilibrium between these phases is using saturation vapor pressure. It is worth noting that the relationship between relative humidity (RH, -), vapor pressure (Pv, atm) and saturation vapor pressure (Pv_{sat}, atm) can be expressed using Equation I.74.

$$RH = \frac{Pv}{Pv_{sat}(T)} \quad \text{Eq (I.74)}$$

The Rankine formula ([241], Equation I.75) expresses saturation vapor pressure at different temperatures (T, K).

$$\ln\left(Pv_{sat}/P_0\right) = 13.7 - \left(\frac{5120}{T}\right) \quad \text{Eq (I.75)}$$

This equation is a simplification of the Dupré formula ([241], see Equation I.76), which relies on the consideration that the vapor behaves as a perfect gas.

$$\mathrm{Ln}\left(\frac{Pv_{sat}}{P_0}\right) = \frac{MLv}{R}\left(\frac{1}{T_{eb}} - \frac{1}{T}\right) - \frac{Ma}{R}\ln\left(\frac{T}{T_{eb}}\right) \quad \text{Eq (I.76)}$$

The ebullition temperature T_{eb} of a substance (water), for a given pressure P_0 (atm) in atmospheres, is expressed in Kelvin (K). The variation of fluid enthalpy with temperature T is controlled by a factor (a). The molar mass of the substance is denoted as M (in kilograms per mole), while the latent heat (Lv) is measured in joules per kilogram (J/kg). The constant of ideal gases is represented by R (in joules per mole per Kelvin).

Including the computation of the saturation degree based on relative humidity enhances the precision of the model's consideration of hydrologic transfer. Consequently, when convective motion is taken into account, it becomes necessary to incorporate adsorption and desorption isotherms to refine the computation of chloride content.

One example of a finite element model that couples moisture transfer, chloride transport, and heat transfer is the model developed by Bastidas [236]. In this model, the transport of free chloride (represented by its concentration, Cl_f, expressed in kilograms per cubic meter of concrete) is considered using an equation that includes two terms: one referring to diffusion and the other to the convection of chloride ions:

$$\frac{\partial Cl_f}{\partial t} = div\left(D_{eff} w_e \vec{\nabla}\left(Cl_f\right)\right) + div\left(D_h w_e Cl_f \vec{\nabla}(RH)\right) \quad \text{Eq (I.77)}$$

With D_{eff} the effective diffusion of chloride ($m^2.s^{-1}$), D_h the effective moisture transport coefficient ($m^2.s^{-1}$), and w_e is the evaporable water (-). The author explains that considering the binding of the chloride, and a 2-dimensional space, the Equation I.77 can be rewritten as:

$$\frac{\partial Cl_f}{\partial t} = D_{app}\left(\frac{\partial^2 Cl_f}{\partial x^2} + \frac{\partial^2 Cl_f}{\partial y^2}\right) + D_{app,h}\left(\frac{\partial}{\partial x}\left(Cl_f \frac{\partial\, RH}{\partial x}\right) + \frac{\partial}{\partial y}\left(Cl_f \frac{\partial\, RH}{\partial y}\right)\right) \quad \text{Eq (I.78)}$$

Here, D_{app} and $D_{app,h}$ are the apparent chloride and humidity diffusion coefficients. They are both computed from the effective diffusion coefficients with the Equation I.79:

$$D_{app,x} = \frac{D_{eff,x}}{1 + \left(\frac{1}{w_e}\right)\left(\frac{\partial Cl_b}{\partial Cl_f}\right)} \quad \text{Eq (I.79)}$$

Where Cl_b represent the bound chloride concentration (kg/m^3 of concrete).

The moisture transport is modelled in terms of pore relative humidity using Equation I.80:

$$\frac{\partial w_e}{\partial t} = \frac{\partial w_e}{\partial RH}\frac{\partial RH}{\partial t} = div(D_h \vec{\nabla} RH) \quad \text{Eq (I.80)}$$

1.4.2.3. Boundary conditions

In analytical models computing chloride concentration, the main boundary conditions are the surface chloride concentration (Cl_s). This concentration depends on the environmental concentration of

chloride, which can be either from sea or ocean concentrations or from deicing salts. Additionally, Cl_s is influenced by the binding capacity of the material and, consequently, by the temperature. Lindvall [242] even demonstrated that Cl_s is more affected by sea temperature than by water salinity. Therefore, proper physical modelling should consider humidity and temperature as boundary conditions, in addition to the external chloride concentration.

In [236], Bastidas utilizes Robin's conditions to model the boundary conditions of chlorides in terms of flux. The chloride flux normal to the concrete surface J_{Cl}^s can be expressed using the following equation:

$$J_{Cl}^s = B_C\left(Cl_f^s - Cl_{f,env}\right) + Cl_{f,env}J_h^s \quad \text{Eq (I.81)}$$

Where :

- B_C is the surface chloride transfer coefficient which varies between 1 and 6 m/s.
- Cl_f^s is the concentration of free chloride at the concrete surface.
- $Cl_{f,env}$ is the environmental concentration of chloride.
- J_h^s is the normal flux of humidity defined with Equation I.82.

$$J_h^s = B_h(RH_s - RH_{env}) \quad \text{Eq (I.82)}$$

With B_h the surface humidity transfer coefficient (ranging from 2.43-4.17×10^{-7}), the pore relative humidity at the concrete surface noted RH_s (-) and the environmental relative humidity RH_{env} (-).

The use of a flux-based boundary condition allows for a more accurate representation of the natural phenomena occurring at the concrete surface. This is particularly important due to the significant influence of surface convection on chloride penetration into the material.

Additionally, the orientation of the reinforced concrete structure surface exposed to deicing salt may affect chloride penetration [243]. This can be accounted for by considering different exposure times to deicing salt in the modelling process.

1.4.2.4. Binding isotherm modelling

In order to enhance the realism of models, it is imperative to account for the interaction between chloride ions and the cementitious matrix. Many methods described in the literature involve the consideration of a binding isotherm, which establishes a mathematical relationship between the quantity of chlorides bound within a volume of material and the concentration of free chloride ions in the corresponding pore solution at a specific temperature.

For instance, Hiro et al. define the quantity of bound chloride (Cl_{bound} in mol.kg^{-1} of cement) within the cementitious matrix using the Equation I.83 [244].

$$Cl_{bound} = 0.62\frac{2.65[Cl]_{free}}{1 + 2.65[Cl]_{free}}\frac{CSH}{100} + 1.38(Cl_{free})^{0.58}\frac{Afm}{100} \quad \text{Eq (I.83)}$$

Where Cl_{free} is the free chloride concentration (expressed in mol.L^{-1}), CSH and Afm respectively the weight percentages of C-S-H and Afm present in the cement (wt.%). Hiro and al. [244] demonstrate that only Afm and C-S-H phases have the ability to bind chloride ions. This finding provides an explanation for the absence of portlandite and ettringite concentrations in Equation I.83, as these phases do not contribute to chloride binding.

Alternative approaches have been developed to quantify the relationship between free and bound chloride concentrations. Langmuir and Freundlich isotherms, represented by Equations I.84 and I.85, are commonly employed methods to describe this phenomenon [245], [246].

$$C_{bound} = \frac{\alpha C_{free}}{1 + \frac{\beta}{C_{free}}} \quad \text{Eq (I.84)}$$

$$C_{bound} = k\left(C_{free}\right)^{\frac{1}{n}}$$ Eq (I.85)

With C_{bound} and C_{free} expressed in mol.m^{-3} of concrete and mol.m^{-3} of solution respectively. α, β, k and n are constants that need to fit experimental results [247].

In these two equations, only a general representation of the bound chloride is included, without distinguishing between its physically and chemically binding characteristics.

On an over level, Glass and Al. [248] used an artificial neural network to model the chloride binding capacity of concrete material according to different factors. In Section I.5.1.2, artificial neural networks, which are nonlinear systems consisting of multiple layers of neurons, are further explained.

Among the inputs considered in a previous study [248], the following factors were identified as the most influential in terms of their percentage change on the results, ranked from strongest to weakest importance:

- **Tricalcium aluminate (C_3A) and tetracalcium aluminoferrite (C_4AF) contents**: Increasing the content of these compounds in the cementitious matrix has been found to enhance its binding capacity. This is attributed to the hydration capacity of these anhydrous compounds, which form Afm and subsequently react with free chlorides to produce Friedel's salts [249], [250].
- **Silica Fume (SF) content**: Increasing the SF content tends to decrease the binding capacity, despite lowering the pH value of the interstitial solution. This effect is likely due to a decrease in the C/S ratio, which influences the binding process. A decrease in solution pH leads to lower hydroxyl concentrations, creating a less competitive environment for chloride binding sites. Additionally, a lower CaO/SiO_2 ratio results in a less positively charged pore wall surface, reducing the tendency to absorb negative ions [137].
- **Water-to-cement ratio (W/C)**: Increasing the W/C ratio can enhance chloride binding in concrete. This is likely because it affects the porosity and water content in the cementitious matrix [127].
- **Ground Granulated Blastfurnace Slag (GGBS) content**: Increasing the GGBS content leads to greater binding capacity in concrete. This is attributed to its higher aluminate content and its tendency to lower pH [127], [251], as well as the higher content of C-S-H formed during the hydration of the latent hydraulic mineral.
- **Hydroxyl ion concentration ([OH-]):** Hydroxyl ions present in the interstitial solution compete with free chloride ions for binding sites. A higher alkalinity of the pore solution has been found to result in lower binding levels, indicating competition between anions for available adsorption sites [252], [253].
- **Cation type and concentration:** The type and concentration of cations in solution can influence the quantity of hydroxyl ions and, consequently, the binding capacity [253].

Physical models that aim to incorporate more realistic representations of binding processes must acknowledge the influence of additional parameters, such as pH fluctuations. In advanced multi-species models [254], [255], it is important to account for the interaction of other ionic species with the matrix, as they can impede the availability of binding sites for chloride ions. Furthermore, the effect of temperature on binding dynamics and its potential reversibility [256] should also be considered.

I.4.3. Carbonation-Chloride ions pairing

Fewer models have been developed to fully consider both carbonation and chloride ingress phenomena, as well as their interactions. Typically, the effect of carbonation on chloride ingress is examined by studying the changes in microstructure resulting from hydrate transformation. These changes influence the porosity, permeability, and binding capacity of the cementitious matrix, thereby affecting the diffusion and convection processes of chloride ions and the amount of chloride bound to the matrix.

Consequently, carbonation results in the release of chloride bound to Afm and CSH, increasing the concentration of free chloride in the material and leading to greater depth of penetration. The impact of chloride ingress on carbonation is often not accounted for in existing models, as it has not been clearly identified in the literature and is considered negligible. However, it is possible that the carbonation rate of Friedel's salts and chloride bound to CSH differs from that of Afm and CSH.

Four numerical models were found in the literature and are summarized in Table I-14. No analytical model considering this pairing was available. However, it can be said that, since most models are fitted on experimental results, an implicit consideration of carbonation is included through constants or other parameters adjusted based on measurements conducted in environments that cause carbonation and chloride ingress simultaneously (XS1, XS3, XD1, and XD3 exposure classes of the NF EN 206/CN+A2 (2022)).

Table I-14 finite element model for Chloride-carbonation pairing.

Reference	Heat transfer	Moisture transfer	Pore solution	Chloride binding	Solid phases	Microstructure evolution
Mai-Nhu [7], 2013 Schmitt [6], 2019	x	x	CO_3^{2-}, Cl_f	With Afm and CSH	$CH, CSH, Afm, Aft, SF, Cl_{CSH}$ $CaCO_3$	Porosity, binding capacity, water release
Achour et al. [257], 2017		x	CO_3^{2-}, $HCO_3^- H_2CO_3$, OH^-, Ca^{2+}, Cl_f, $Na^+, Al(OH)_4^-$, K^+	Langmuir	$CH, CSH, SF, Cl_{b,CSH}$, $C_3A, CaCO_3$	Porosity, binding capacity
Meijers et al. [258] 2004	x	x	Cl_f	Langmuir	Cl_b	Porosity
Puatatsananon and Saouma [259], 2005	x	x	Cl_f	Freundlich	$Cl_b, CaCO_3$	Binding capacity, water release, porosity
Conciatori et al. [218]	x	x	Cl_f	?	$CH, CSH, C_3S, C_2S, Cl_b$	Porosity
Shen et al. [260]	x	x	Cl_f	Langmuir	Cl_b	Binding capacity, Porosity

The finite element model utilised in this study is established upon the groundwork laid by Mai-Nhu [7] and Schmitt [6]. The model, outlined in Section III, incorporates rigorous details and comprehensive explanations.

I.4.4. Corrosion

Various approaches exist for synthesizing and simulating corrosion in concrete reinforcing bars. Since the type and characteristics of corrosion depend on the aggressive species that lead to depassivation, models typically focus on corrosion induced by a specific type of aggressive species (or propose different constant values according to the phenomenon considered). Therefore, carbonation-induced and chloride-induced corrosion are usually addressed separately in the models. These models are presented in two different subsections.

The general approach is similar in both cases. First, the corrosion current (i_{corr}) is calculated based on material and/or environmental parameters. Then, this corrosion current is used to determine the

propagation time that leads to a critical section loss or internal pressure, which can cause concrete cracking, spalling, or a significant reduction in the strength of the reinforcing bars.

I.4.4.1. Models for carbonation induced corrosion

Many models have been discussed in the existing literature. In Table I-15, a summary of some analytical models is provided. A focus on three specific models is presented in Annex 4, as they are utilised in Section IV.4 for performing predictions on various structures using probabilistic computations. A finite element model developed by Nguyen [261] is subsequently presented and will be discussed in this study.

Table I-15 Empirical time dependent models for corrosion propagation in carbonated concrete [180].

Reference	T	RH	O_2	CC	D_{rebar}	Dry-Wet cycles	Re	f_t, f_c	$\frac{W_{eff}}{B_{tot}}$	pH	Cl	Output
Alonso et al.[262], 1988							X					i_{corr}
Morinaga [193], 1990	X	X	X	X	X							i_{corr}
Gulikers [263], 2005							X					i_{corr}
Song [264], 2005			X							X	X	i_{corr}
Ghods et al. [265], 2007			X				X					t_{prop}
Parrott [194], 1994		X										t_{prop}
Bouquet [202], 2004				X		X						t_{prop}
Bamforth [195], 2004		X		X	X			X				t_{prop}
Andrade and Andrea [203], 2010							X					t_{prop}
PerfDuB model [266], 2020	X	X		X	X		X					i_{corr}, t_{prop}
Vu and Stewart's [267], 2000				X					X			i_{corr}

The preceding table demonstrates a high variability in the models developed for carbonation-induced corrosion propagation. Although certain parameters such as Re, CC, RH, and O_2 appear frequently, each model has its own unique characteristics, making it difficult to identify a clear trend. This variability likely reflects the challenges associated with studying the propagation phenomenon, which is influenced by multiple factors. Moreover, the difficulties in accurately measuring corrosion propagation in reinforced concrete have led to the development of accelerated testing methods with specific conditions. However, these methods sometimes overlook certain aspects of the phenomenon and neglect important parameters, leading to equations with few inputs.

The numerical model presented by Nguyen [261] below offers a more comprehensive approach to analyse corrosion propagation, considering the influence of oxygen diffusion and its interaction with various species formed during steel corrosion. This model provides improved representation and understanding of the corrosion process.

Finite element model of Nguyen [261]

Nguyen's model is a finite element model that enables the calculation of corrosion product quantities. The significance of this model lies in its ability to account for the growth of different layers. Specifically, the model distinguishes between a stable layer, denoted as e_1, which is a dense product layer, and an unstable layer made up of green rust, denoted as e_2.

To begin, the model takes into account the oxygen flux and consumption via Equations I.86 and I.87, respectively, based on the corrosion product layers formation. It assumes that the flux is zero at the steel surface.

$$\frac{\partial[O_2]}{\partial t} = D_{O_2,UL} div\left(\overrightarrow{grad}[O_2]_l\right) - k_{UL} S_{UL} \varphi_{UL} [O_2] \quad \text{Eq (I.86)}$$

$$\frac{\partial[O_2]}{\partial t} = D_{O_2,SL} div\left(\overrightarrow{grad}[O_2]_l\right) \quad \text{Eq (I.87)}$$

Where:

- k_{UL} is a kinetic constant (5.10^{-10} m/s).
- S_{UL} is the pore's specific surface of the oxides ($3.7.10^{7}$ m^{-1}).
- φ_{UL} is the porosity of the instable products layer (0.2 -).
- $D_{O_2,UL}$ Is the diffusion coefficient of oxygen in the instable products layer (10^{-9} m^2/s).
- $D_{O_2,SL}$ is the diffusion coefficient of oxygen in the stable layer of corrosion products ($1.3.10^{-10}$ m^2/s).

The resolution of the two precedent equation relies on the assumption that a continuity exists between the two layers of corrosion products. Hence the solutions of the Equations I.86 and I.87 can respectively be written with Equations I.88 and I.89:

$$[O_2]_{UL} = [O_2]_{concrete} \left[\cosh\left(\frac{x}{\lambda_{UL}}\right) + \gamma \lambda_{UL} [O_2]_{ext} \sinh\left(\frac{x}{\lambda_{UL}}\right)\right] \quad \text{Eq (I.88)}$$

$$[O_2]_{SL} = [O_2]_{concrete} \left[\frac{e_2}{\lambda_{UL}} \sinh\left(\frac{e_1}{\lambda_{UL}}\right) + e_2 \gamma \cosh\left(\frac{e_1}{\lambda_{UL}}\right) + \cosh\left(\frac{e_1}{\lambda_{UL}}\right) + \gamma \lambda_{UL} \sinh\left(\frac{e_1}{\lambda_{UL}}\right)\right] \quad \text{Eq (I.89)}$$

Where:

- $[O_2]_{concrete}$ is the oxygen concentration in the concrete material (boundary condition, Pa). A simplification assumption can be to consider the oxygen concentration of the environment directly.
- λ_{UL} is a parameter defined with Equation I.90.
- γ is a coefficient defined with Equation I.91.

$$\lambda_{UL} = \sqrt{\frac{D_{O_2,UL}}{k_{UL} s_{UL}}} \quad \text{Eq (I.90)}$$

$$\gamma = -\frac{1}{\lambda_{UL}} \frac{\left(\frac{[O_2]_{SL}}{k_{UL}} + e_2\right) \sinh\left(\frac{e_1}{\lambda_{UL}}\right) + \lambda_{UL} \cosh\left(\frac{e_1}{\lambda_{UL}}\right)}{\left(\frac{[O_2]_{SL}}{k_{UL}} + e_2\right) \cosh\left(\frac{e_1}{\lambda_{UL}}\right) + \lambda_{UL} \sinh\left(\frac{e_1}{\lambda_{UL}}\right)} \quad \text{Eq (I.91)}$$

Consumption of the oxygen may take place in the unstable layer (with the integration of Equation I.92) and at the steel surface with the Equation I.93.

$$\phi_{O_2,UL} = k_{UL} S_{UL} \varphi_{UL} \frac{RT}{H} \int_0^{e_1} [O_2]_{UL} dx \quad \text{Eq (I.92)}$$

$$\phi_{O_2,SL} = k_{SL} S_r \, \varphi_{SL} [O_2]_{SL} \frac{RT}{H} \quad \text{Eq (I.93)}$$

Where:

- k_{UL} and k_{SL} are kinetic constants for unstable and stable layers (5.10^{-10} and 10^{-5} m/s).
- φ_{UL} and φ_{SL} are the porosity of the unstable and stable layers (0.2 and 0.03, -).
- S_r is the saturation degree of the concrete (-).
- H is the Henry constant (7.47×10^4 Pa.m^3/mol).

Finally, Nguyen explains that it is possible to compute the growth of the corrosion products with the Equations I.94 and I.95 for each product type:

$$\Delta e_{UL} = P_{ac} \times \frac{4}{3} \frac{M_{Fe}}{\rho_{Fe}} \left[\phi_{O_2,UL}(1 - \alpha_{TM}) - \phi_{O_2,SL}\right] \Delta t \quad \text{Eq (I.94)}$$

$$\Delta e_{SL} = P_{ac} \times \frac{4}{3} \frac{M_{Fe}}{\rho_{Fe}} \phi_{O_2,UL} \Delta t \quad \text{Eq (I.95)}$$

Where:

- Δe_{UL} is the thickness of the unstable layer (m)
- Δe_{SL} is the thickness of the dense product layer (m)
- P_{ac} is the activation probability of the corrosion in the reinforcing bar (-).
- α_{TM} is the amount of corrosion product that migrates in the cementitious matrix (0.2 -).

Finally, the total growth of the corrosion product (Δe_{tot}, m) corresponds to the sum of the thickness and is expressed with Equation I.96.

$$\Delta e_{tot} = \Delta e_{SL} + \Delta e_{UL} \quad \text{Eq (I.96)}$$

The variation in the total thickness of corrosion products allows for the estimation of the average corrosion rate (V_{corr}, m/year) over a given duration of propagation (t_{prop}, years), which, in turn, enables the calculation of the corrosion current (i_{corr}, µA/cm^2). This calculation can be done using the Equations I.97 and I.98 in accordance with Faraday's law.

$$V_{corr} = \Delta e_{tot} / t_{prop} \quad \text{Eq (I.97)}$$

$$i_{corr} = 10^5 \frac{V_{corr}}{11.6} \quad \text{Eq (I.98)}$$

This model is thoroughly investigated in Section IV.4.1. It offers the advantage of considering the temporal evolution of the corrosion phenomenon, thereby providing more accurate predictions of the actual formation of corrosion products. Additionally, it takes into account the availability of oxygen in the material, which is a crucial factor often implicitly considered in analytical models rather than directly addressed. However, due to its numerical nature, the calculations conducted with this model require a higher computational load, which can pose challenges particularly when considering probabilistic applications.

I.4.4.2. Models for chloride-induced corrosion

Numerous studies have been undertaken to ascertain the extent of corrosion propagation induced by chloride. In Table I-16 , a comprehensive comparison of various analytical models documented in existing literature is presented. Three analytical models are emphasized in Annex 4 and are employed in Section IV.4 to calculate the critical propagation time, which ultimately results in the cracking of the concrete cover. Laplace equation-based finite element models are subsequently presented, showing the complexity of the overall propagation corrosion phenomena.

Table I-16 Analytical models for chloride induced corrosion propagation [266], [268].

Ref	T	RH	O_2	CC	D_{rebar}	Dry-Wet cycles	Re	f_t	pH	C	W_{eff}	Cl	C_{crit}	SO_2	i_0	Out put
Klinesmith et al. [269], 2007	x	x				x						x		x		i_{corr}
Balafas and Burgoyne [270]	x	x					x					x				i_{corr}
Yalcyn and Ergun [271]															x	i_{corr}
PerfDuB [272], 2020		x	x	x	x		x					x	x			i_{corr}, t_{prop}
Liu and Weyers [273], 1998	x						x					x				i_{corr}
Ahmad et al. [274], 2000										x	x	x				i_{corr}
Duracrete [227], [228], 2000	x	x					x					x				i_{corr}
El Farissi [266], 2020	x	x					x			x	x	x				i_{corr}, t_{prop}

Like carbonation induced corrosion propagation, the various models described in the literature for studying chloride induced corrosion propagation exhibit a wide range of input parameters. This diversity makes it difficult to identify a clear trend. However, upon examining the different inputs used in these models, it becomes apparent that chloride concentration at the reinforcing bar, electrical resistivity, temperature, and relative humidity are the most represented parameters. This observation suggests that these factors have a significant influence on the output variables i_{corr} and t_{prop}, and therefore, they must be taken into consideration when predicting corrosion propagation.

It is noteworthy that, similar to carbonation, most of the models in Table I-16 were derived from accelerated tests, and thus may not accurately represent the phenomenon under real structural conditions. This limitation arises from the challenge of monitoring corrosion and accurately measuring the corrosion current at the precise onset of corrosion propagation.

1.4.4.3. Laplace equation-based models [264], [275]

More advance corrosion rate prediction models are based on the resolution of the Laplace equation (represented in 2 dimensions with the Equation I.99) [275]–[277]. It allows the evaluation of the electric potential in the medium surrounding the steel and on the steel surface.

$$\frac{\partial^2 \phi}{\partial x^2} + \frac{\partial^2 \phi}{\partial y^2} = \nabla^2 \phi = 0 \qquad \text{Eq (I.99)}$$

From Equation I.99 and the hypothesis of electrical charge conservation and isotropic conductivity, the corrosion rate can be computed. In this equation, *x* and *y* are the Cartesian coordinates, ϕ the electrical potential and ∇ the Laplacian harmonic operator. The solving of this equation relies on the use of:

- Relevant boundary conditions on the different factors implied, essentially for the electrical field, the temperature, and the hydrologic conditions.
- A suitable mathematical technique, such as finite element method (among many others)

In [275], Burkan Isgor uses finite element modelling with Laplace relation (Equation 1.99) as governing equation. The author computes the potential distribution around the surface of the steel with the consideration of two boundary conditions representing the relationship between potential and current density. The first is used for the anodic zones and corresponds to the Equation I.100.

$$\phi_a = \phi_{Fe} + \beta_a \log\left(\frac{i_a}{i_{oa}}\right) \qquad \text{Eq (I.100)}$$

For the cathodic zone, the condition expressed with Equation I.101 is considered.

$$\phi_c = \phi_{O_2} + \beta_c \log\left(\frac{i_c}{i_{oc}}\right) - \frac{2.303RT}{z_{Fe}F} \log\left(\frac{i_L}{i_L - i_c}\right) \qquad \text{Eq (I.101)}$$

ϕ_{Fe} and ϕ_{O_2} corresponds to the non-standard equilibrium potential of Fe and O_2. β_a and β_c are the Tafel slope of the anodic and cathodic reaction respectively. i_a and i_c are the anodic and cathodic current densities while i_{oa} and i_{oc} are the exchange current density of the anodic and cathodic reactions. Finally, i_L is the limiting current density. The author also furnished a graphical representation of the physical system with Figure I-26.

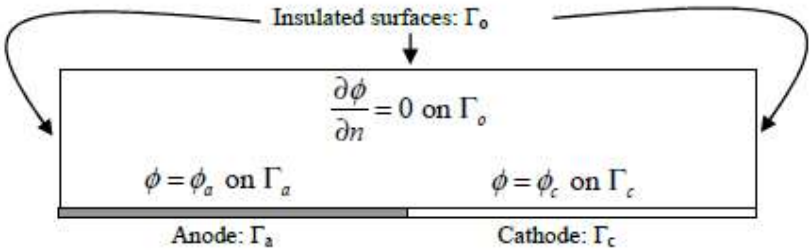

Figure I-26 Boundary conditions of a rebar corrosion problem [275].

Finally, it can be said that for more complex and precise modelling, charge transfer, oxygen and moisture transfer need to be considered in physical modelling using Butler-Volmer relation (see Equation I.102) and second Fick's law respectively. It expresses the boundary condition of the corrosion current at the cathode and the anode when a change of potential takes place.

$$i_{corr} = j_0 \left(\exp\left(\frac{\alpha z_{Fe} F(\phi - \phi_{eq})}{RT}\right) - \exp\left(-\frac{(1-\alpha) z_{Fe} F(\phi - \phi_{eq})}{RT}\right)\right) \qquad \text{Eq (I.102)}$$

Where :

- i_{corr} is the current density ($A.m^{-2}$).
- j_0 is the current density of exchange computed with the Equation I.103 ($A.m^{-2}$).

- ϕ is the electrode potential (V) (either ϕ_a or ϕ_c).
- ϕ_{eq} is the equilibrium potential (V) (either ϕ_{Fe} or ϕ_{O_2}).
- T is the temperature (K).
- z_{Fe} is the electron number exchanged in the reaction.
- F is the Faraday constant (96485 C.mol^{-1}).
- R is the ideal gas constant (8.314 J.K^{-1}.mol^{-1})
- α is the charge transfer coefficient.

$$j_0 = \frac{i_{corr,0}}{S} = zFk^0[C_{Ox}]_{sol}^{\alpha}[C_{Red}]_{sol}^{1-\alpha} \quad \text{Eq (I.103)}$$

With $i_{corr,0}$ is the initial current of corrosion (A), S is the surface of exchange (m^2), z the valence number (equal to 2 at the anode), k^0 the kinetic constant, $[C_{Ox}]_{sol}$ the oxidant specie concentration in solution and $[C_{Red}]_{sol}$ the reductant specie concentration in solution.

The first part of the Butler-Volmer relation corresponds to the forward (anodic) current while the second part corresponds to the reverse (cathodic) current.

I.4.5. Mechanical, Microstructure and durability parameters assessment

The functioning of the durability models exposed in Sections I.4.1 to I.4.4 relies on the knowledge of concrete properties among other parameters. These material properties can either be measured experimentally or estimated using empirical models and/or assumptions. Experimental measurements can be onerous in economical and temporal terms. For this reason, reliable methods for estimating material properties are of great importance in the framework of durability modelling. In this section, the methods used in this work for concrete properties assessment and originating from the literature are exposed.

Most of the models presented here and in Annex 4 are compared with each other and with experimental data in Section IV.3.2.

1.4.5.1. Mechanical resistance computation

Compressive strength of concrete is one of the major properties of concrete. It is used as a general indicator to assess the global mechanical behaviour of the material. Hence, it is always measured in parallel with concrete production and easy to obtain.

Although the compressive strength is not a straightforward durability property, it is at some extent related to the concrete capability to limit the ingress of pollutants. An approximate correlation between mechanical resistance and carbonation resistance was hence pointed out in different studies [180], [278]. Therefore, there is an interest in predicting accurately the mechanical resistance of cementitious material for durability prediction. Moreover, the mechanical strength of the concrete cover is generally a key parameter in the computation of the corrosion propagation time leading to the cracking (as shown in Table I-15).

Papadakis equation for f_c 28 days [278]

One relationship to estimate the 28-day compressive strength is proposed by Papadakis in [279] in [278]. Equation I.104 was fitted on experimental values obtained for CEM I-based concretes.

$$f_c = 7.84 \frac{f_{cem}}{\left(1 + \frac{W_{eff}}{C}\frac{\rho_c}{\rho_w} + \varepsilon_{air}\frac{\rho_c}{C}\right)^2} \quad \text{Eq (I.104)}$$

Where C and W_{eff} are the cement and effective water content respectively (kg/m3). ρ_c and ρ_w are the bulk density of cement and water (kg/m^3). f_{cem} is the cement characteristic resistance (MPa) while ε_{air}

is the air content brought in concrete during its manufacture. The authors give average values according to the maximal diameter of the aggregates (see Figure I-16).

Table I-17 Air content in concrete according to the aggregate maximal diameter [279] in [278].

D_{max} (mm)	ε_{air} (-)
31.5	0.015
16	0.023
8	0.035

It can be noted that this equation is adapted for CEM I-based concretes and does not consider SCM quantities or type.

De Larrard equation [280]

In his work, De Larrard [280] proposes an equation for the 28-day compressive strength of cement paste (see Equation I.105).

$$f_{c,28} = 11.4 f_{cem} \left(\frac{V_c}{V_c + V_w + V_{air}} \right)^{2.85} \quad \text{Eq (I.105)}$$

Where V_c, V_w and V_{air} represent the volume of cement, water, and air (m^3). f_{cem} is the characteristic cement resistance obtained at 28 days.

This equation does not consider the impact of aggregates; therefore, it is not directly possible to compute the mortar or concrete compressive strength. However, different improvement were added by De Larrard in [280] which are based on the compressible packing model and the Feret model [281]. The complexity and experimental data required for their computation diminish the interest of these additions for the present work and are thus not presented here.

1.4.5.2. Porosity models

The water accessible porosity of concrete has an important influence on the transfer and durability properties. First, this property influences greatly the moisture transfer in the material which impacts the carbonation and chloride ions ingress. This parameter is generally used as input in durability models [[2], [7], [236]] because of its clear signification and the relative simplicity of the experimental test required to measure it (see Section II.2.2).

This sub-section detailed the model of Powers, used to compute the porosity of the paste [282], as well as a simple method to account for the porosity relative to the aggregates. Two additional models for porosity computation are presented in Annex 4 [66], [283].

Powers' model for porosity accessible to water in CEM I-based concrete [282], [284]

In the absence of an experimental value, the model developed by Powers [282], [284] is used in the Section III and IV. It allows the determination of the cementitious paste porosity (see Equation I.106). The porosity provided by the aggregates is obtained from their water adsorption and their bulk density, data available on the technical sheet of the material. Concrete porosity is then estimated from the weighted average of the porosity provided by the cementitious paste and the aggregates. The proportions of paste and aggregate in concrete are specified in the formulation data.

$$\varphi_p^w = \frac{\frac{W_{eff}}{C}}{\frac{W_{eff}}{C} + 0.32} - 0.53\alpha\left(1 - \frac{\frac{W_{eff}}{C}}{\frac{W_{eff}}{C} + 0.32}\right) \quad \text{Eq (I.106)}$$

Where φ_p^w is the cementitious paste porosity accessible to water, α the hydration rate of the cementitious paste calculated from Waller formula [285] (see Equation I.107).

$$\alpha = 1 - \exp\left(-3.3\frac{W_{eff}}{C}\right)$$ Eq (I.107)

The Equations I.106 and I.107 are validated for CEM I based concrete by the author. However, Schmitt showed in her PhD that it was operational for slag and limestone concrete [6].

The impact of the aggregates microstructure on the concrete porosity needs to be considered. One method consists in computing the porosity accessible to water of each aggregate i used in the concrete formulation. The Equation I.108 relies on the knowledge of the bulk density ($\rho_{agg,i}$, kg/m^3) and the water absorption ($WA_{agg,i}$, %) to compute the porosity of one aggregate type ($\varphi^w_{agg,i}$, %):

$$\varphi^w_{agg,i} = WA_{agg,i}\frac{\rho_{agg,i}}{1000}$$ Eq (I.108)

The porosity brought by all aggregates (φ_{agg}, %) is then computed using the weighted sum which depends on the ratio of the aggregate content ($Q_{agg,i}$, kg) relative to the total content of aggregate (Q_{agg}, kg):

$$\varphi^w_{agg} = \sum_{i=0}^{n}\frac{Q_{agg,i}}{Q_{agg}}\varphi^w_{agg,i}$$ Eq (I.109)

Finally, the volumetric fraction of paste F_{paste} and of volumetric fraction of aggregates F_{agg} composing the concrete mix can be used to compute the overall concrete porosity accessible to water φ^w_c with the Equation I.110:

$$\varphi^w_c = F_{agg}\varphi^w_{agg} + F_{paste}\varphi^w_p$$ Eq (I.110)

1.4.5.3. Hydration models

The hydrates contents and type of the cementitious paste also play an important role in durability. The Portlandite as well as the remaining other hydrates are responsible for the carbonation resistance by reacting with the CO_2 dissolved in the interstitial solution and maintaining an alkaline pH. In the case of chloride ingress, C-S-H and Afm impact the diffusion rate of the ionic chloride either by physical or chemical binding respectively. For these reasons among others, the estimation of the cementitious matrix composition is essential to model concrete durability against carbonation and chloride induced corrosion. The main method used in the Section III and IV is presented subsequently [286]–[288], while two alternative methods are available in Annex 4 [109], [289].

Hydration model for CEM I and slag-based concrete, Lacarrière and Kolani

The works by Lacarrière [288] and then Kolani [287], based on the research carried out by Adenot [290] and [291], led to the development of a hydration model for CEM I and slag-based concretes.
The hydration products considered are the CH, C-S-H, Afm and Aft (regrouping Ettringites and hexahydrates) according to the sulphate quantity available. Table I-18 details the quantities of oxides required for the formation of the various hydrates.

Table I-18. Oxides molar balance for the hydration in clinker [287].

Hydrates		Oxides (mole)				
		CaO	SiO_2	Al_2O_3	SO_3	H_2O
CH		1				1
C-S-H		$(C/S)_c$	1			$(H/S)_c$
Afm		4		1	1	12
Enough SO_3	Aft_c	6		1	3	32
Insufficient quantity of SO_3	Hexa	3		1		6

$(C/S)_c$ and $(H/S)_c$ are the molar ratios of the C-S-H formed during clinker hydration [292]. In presence of blast furnace slag, new hydrates form in addition to those already formed with the clinker alone: Calcium silicates in a different form (C-S-A-H) where particular aluminates replace silica. Hydrotalcite and tetracalcium aluminates hydrates also form in addition to Ettringite (see Table I-19).

Table I-19 Oxides molar balance for the hydration products in binder containing slag [287].

Hydrates	Oxides (mole)					
	CaO	SiO_2	Al_2O_3	SO_3	MgO	H_2O
C-S-A-H	$(C/S)_s$	1	$(A/S)_s$			$(H/S)_s$
Hydrotalcique (M_5AH_{13})			1		5	13
Aft_l	6		1	3		12
Tetracalcite aluminate (C_4AH_{13})	4		1			13

$(C/S)_s$, $(A/S)_s$ and $(H/S)_s$ are the molar ratio of the C-S-A-H formed during the hydration of the binder with slag. The calcium present in C-S-A-H comes from both the CaO contained in the binder and the portlandite formed during the clinker hydration, in turn consumed during the slag hydration. Thus, the portlandite and calcium quantities available strongly evolve during the hydration process. Hydration Equations I.111 to I.116 result from the molar balances and are expressed in molar quantities (mol/kg of cement).

$$\alpha_c SiO_2 = CSH \quad \text{Eq (I.111)}$$

$$\alpha_c(CaO - (C/S)_c SiO_2 - SO_3 - 3Al_2O_3) = CH \quad \text{Eq (I.112)}$$

$$\alpha_c(0.5SO_3 - 0.5Al_2O_3) = Aft_c \quad \text{Eq (I.113)}$$

$$\alpha_c(1.5Al_2O_3 - 0.5SO_3) = Afm_c \quad \text{Eq (I.114)}$$

$$\alpha_c(Al_2O_3 - SO_3) = Hexa \quad \text{Eq (I.115)}$$

$$\alpha_c SO_3 = Afm_c \quad \text{Eq (I.116)}$$

Where α_c is the hydration rate of the clinker. The Equations I.117 to I.120 describe the hydration reaction of slag in presence of clinker.

$$\alpha_S SiO_2 = CSAH \quad \text{Eq (I.117)}$$

$$(1/5)\alpha_S MgO = M_5AH_{13} \quad \text{Eq (I.118)}$$

$$(1/3)\alpha_S SO_3 = Aft_S \quad \text{Eq (I.119)}$$

$$\alpha_S(Al_2O_3 - (A/S)_S SiO_2 - (1/5)MgO - (1/3)SO_3) = C_4AH_{13} \quad \text{Eq (I.120)}$$

Where α_S is the hydration rate of slag. In addition to the previous Equations I.111 to I.120, Lacarrière and Kolani's model accounts for the reaction kinetics according to the species in presence, slag reaction kinetic being lower than the clinker one [287], [288]. The model considers the $(C/S)_s$ ratio evolution over time and as a function of the available calcium quantity. It was validated for binders containing a quantity of slag ranging from 0 to 70 %, values corresponding to those used in the concrete industry. This model was used for all the concretes composed of CEM I, filler and slag-based cement.

1.4.5.4. Diffusion coefficient of chloride ions

The chloride ions diffusion coefficient depends on the microstructure of the material as well as the nature of the hydrates composing the cementitious matrix. The experimental methods for assessing it, based on accelerated or natural ingress, are defined in standards [225], [293]–[296].

However, in absence of experimental results, some equations exist in literature that allow to estimate it [218], [297], [298]. Two of them are detailed in this section.

Diffusion coefficient of chloride ions, Bentz [299]

In the frame of its work for the finite element modelling of the coupled diffusion/convection of chloride ions, Bentz proposed an equation to compute the effective chloride diffusion coefficient D_{eff} (m^2/s):

$$\begin{aligned} Log10\left(D_{eff}\right) = & -13.75 - 0.82\left(\frac{W_{eff}}{C}\right) + 32.55\left(\frac{W_{eff}}{C}\right)^2 + 8.374F_{SF} + 15.36F_{SF}^2 \\ & + 23.15F_{SF}\left(\frac{W_{eff}}{C}\right) + 5.79\alpha - 21.10\alpha\left(\frac{W_{eff}}{C}\right) - 43.15F_{SF}\alpha \\ & - 1.705F_{agg} \end{aligned} \qquad \text{Eq (I.121)}$$

Where F_{SF} is the weight fraction of silica fume in the binder (-), F_{agg} is the volumetric fraction of aggregates in the concrete (-) and α is a hydration coefficient ranging between 0 and 1.

This equation presents the advantage of considering pozzolanic additions among its inputs as well as the aggregate content. This latter parameter is often neglected in the equation, essentially because it has a lesser impact compared to the binder type and the water content. Hydration is also considered even if the choice of the parameter value can sometimes be complicated.

The Equation I.122 can be used in the absence of values:

$$\alpha = 1 - \exp\left(-3.15\frac{W_{eff}}{C}\right) \qquad \text{Eq (I.122)}$$

The consideration of different additions with this equation would certainly requires new constants fitted to different experimental measurements.

Intrinsic effective diffusivity of Cl- in concrete, Papadakis et al. [289]

A semi-empirical equation to compute the effective chloride diffusion coefficient for NaCl exposition is proposed by Papadakis for concrete respecting $0.5 < W_{eff}/C < 0.7$ and $0 < A/C < 6$.

$$D_{eff} = \frac{2.4 \times 10^{-10}}{\left(\frac{C + k_{SCM}Q_P}{\rho_c} + \frac{W_{eff}}{\rho_W}\right)^2}\left(\frac{W_{eff}}{\rho_W} - 0.226 \times 10^{-3}(C + k_{SCM}Q_P)\right)^3 \qquad \text{Eq (I.123)}$$

Where C, Q_P and W_{eff} are respectively the cement, SCMs and water content (kg/m^3). k_{SCM} represents the efficiency factor of the SCMs for chloride penetration (6 for silica fume, 3 for low-calcium fly ash and 2 for high calcium fly ash). ρ_c and ρ_w are the cement and water bulk density (kg/m^3).

In these equations, no parameter account for the impact of the aggregates on the chloride diffusion which certainly lead to misestimation for certain cases. The curing process is not included for a complete hydration is considered.

The apparent diffusion coefficient is generally used in the chloride ingress models instead of the effective diffusion coefficient. An equation is proposed in the GranDuBé documentation [122] to perform the transition:

$$D_{eff} = D_{app}\varphi_c^w + D_{app}\rho_c \frac{dCl_b}{dC_f}$$ Eq (I.124)

Where:

- φ_c^w is the porosity accessible to water (-)
- ρ_c is the bulk density of concrete (kg/m^3)
- $\frac{dCl_b}{dC_f}$ is the binding isotherm (with concentration in total and free chloride)

Schmitt [6] used this equation while neglecting the effect of the binding and only considering the first part. No further justification is given, however the results obtained in her modelling are satisfying.

Numerical model paired with artificial neural network [300]

In their work, Lizarazo-Marriaga and Claisse developed a method for ions diffusion coefficients estimation. This method relies on the pairing of modelling computation with an artificial neural network calibrated on an electrochemical test of chloride migration. The numerical model is based on the Nernst-Planck equation for different ionic species (Cl^-, OH^-, Na^+, K^+) resolved using FEM. The results of the numerical model serve as input parameters for the artificial neural network associated which then compute the diffusion coefficients of the different species for a given concrete material.

This method gives excellent results according to the author. However, its complexity makes its use difficult even for an expert user. Moreover, its manufacturing requires the fitting of the artificial neural network, which in turn requires the possession of a large database of results, not published by the authors in the case of this work.

1.4.5.5. Ageing factor

The ageing factor pertains to the evolution of both the chloride binding capacity and hydration of concrete over time and depends on the material formulation.

An equation to compute the ageing factor is proposed in the FD P 18-480 [301]. The hypothesis is that CEM I-based concretes possess an ageing factor equal to 0.3. Finally, the interest of this equation is the consideration of different pozzolanic and latent hydraulic additions through the slag (F_S), the fly ash (F_V), the metakaolin (F_M) and the silica fume (F_{SF}) weight ratios (-). A maximal added value is associated to each SCM.

$$ae = 0.3 + \min(0.2F_S; 0.15) + \min(1.1F_V; 0.3) + \min(1.1F_{SF}; 0.1) + \min(1.1F_M; 0.1)$$ Eq (I.125)

The lack of data on metakaolin, as underlined in the document, limits the use of this equation for mixes containing metakaolin of type A with a weight fraction inferior to 0.09.

Surprisingly, although its influence on the diffusion process and hydration is well established, the ratio W_{eff}/B_{tot} was not integrated in the expression of ae, assuming that W_{eff}/B_{tot} is approximately 0.5. In another document, the HETEK manual [152], a relationship was proposed for an OPC concrete mix (see Figure I-27).

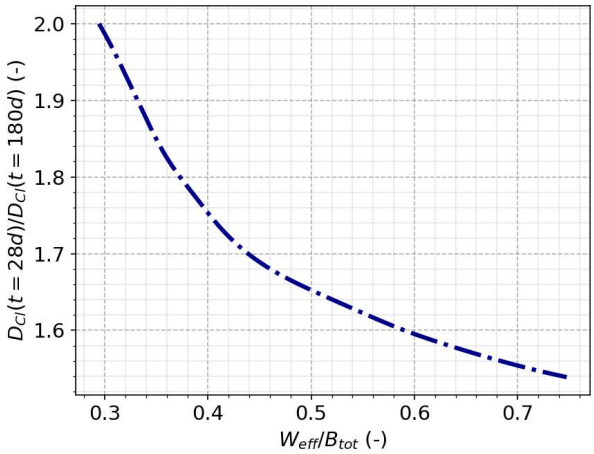

Figure I-27 Relation between the diffusion coefficient evolution and water-cement ratio [152].

1.4.5.6. Critical concentration for chloride initiation C_{crit}

The critical concentration is the threshold above which the steel depassivation is supposed to occur. The value of C_{crit} depends on both the material properties and the environment. Additionally, it is important to mention the influence of the steel - concrete interface quality and condition state in terms of microcracking, as well as the effect of the steel reinforcing cage in terms of electric connection between anodic and cathodic zones. The value of C_{crit} has been hence debating for three decades. The experimental assessment of C_{crit} is also affected by the type of indicator used to detect the steel depassivation (corrosion potential, polarisation resistance, etc.) and naturally the accuracy of the device employed [141]. Not surprisingly very few attempts to theoretically express C_{crit} have been undertaken in the literature.

The estimation presented by Frederiksen [149] is derived from [152]. The Equation I.126 was modified according to the critical values C_{crit} (total chloride content in wt.% of binder) recommended for Nordic exposure zones and black steel reinforcements. It should be noted that this expression is applicable solely to concrete devoid of macro cracks (> 0.1 mm) (refer to Table I-22).

$$C_{crit} = k_e \exp\left(-1.5\left(\frac{W_{eff}}{B_{tot}}\right)_{cr}\right) \quad \text{Eq (I.126)}$$

The equivalent ratio $\left(\frac{W_{eff}}{B}\right)_{cr}$ accounts for the mineral addition used through the factor k_{SCM} (refer to Equation I.127). The values of k_{SCM} were fitted on experimental values by the authors (of Table I-22).

Table I-20 k_{SCM} values for different mineral additions type and content.

Mineral addition (wt.%)	5% SF	10% SF	20% FA
k_{SCM}	1.605	2.29	1.94

$$\left(\frac{W_{eff}}{B_{tot}}\right)_{cr} = \left(\frac{W_{eff}}{B_{tot}}\right) k_{SCM} \quad \text{Eq (I.127)}$$

The parameter k_e is a constant depending on the environment. Three types of environmental classes are defined for road environments and three for marine environments:

1. Road environments
    a. **Wet Splash class (WRS)** concerns the structure parts exposed to direct rain with a distance to the traffic inferior to 4m (edge beams for example)

b. **Dry Splash class (DRS)** is defined for structural parts sheltered from direct rain but exposed to traffic splash with a distance to the traffic inferior to 4m (pillars for example).

c. **Distant Road Atmosphere class (DRA)** defined the zones outside the borders mentioned in the two other classes. Wet and dry environments are regrouped here when the distance to the traffic is superior to 4m (noise shelters or parts above road level).

2. Marine environments

a. **Submerged structures class (SUB)** regroups the structural parts placed below -3m with respect to the lowest minimum water level (caissons for example).

b. **Splash zone class (SPL)** concerns the structure parts placed above 3m with respect to the highest maximum level and below -3m with respect to the minimum water level (for example bridge pier shafts).

c. **Atmosphere class (ATM)** regroups the parts placed above 3m with respect to the maximum water level (bridge piers and underneath of decks are concerned).

Table I-21 Values of k_e for the different environment [152].

Environment	Road			Marine		
Class	WRS	DRS	DRA	SUB	SPL	ATM
Equivalent NF EN 206+A2/CN class	XD3	XD3	XD1-3	XS2	XS3	XS1/XS3
k_e	1	1.25	1.25	3.35	1.25	1.25

Table I-22 Suggested design values for chloride threshold levels (black steel) in various Nordic exposure zones [152].

Concrete type	submerged zone C_{crit} wt.%Cl$_t$ of binder	Marine splash zone C_{crit} wt.%Cl$_t$ of binder	De-icing salt splash zone C_{crit} wt.%Cl$_t$ of binder
Class	SUB	SPL	WRS
W_{eff}/B_{tot} = 0.5			
100% CEM I	1.5	0.6	0.4
5% SF	1	0.4	0.3
10% SF	0.6	0.2	0.2
20% FA	0.7	0.3	0.2
W_{eff}/B_{tot} = 0.4			
100% CEM I	2	0.8	0.6
5% SF	1.5	0.5	0.4
10% SF	1	0.3	0.2
20% FA	1.2	0.4	0.3
W_{eff}/B_{tot} = 0.3			
100% CEM I	2.2	1	0.8
5% SF	1.6	0.6	0.5
10% SF	1.2	0.4	0.3
20% FA	1.4	0.5	0.4

The use of Equation I.126 leads to an average absolute error of 0.055 wt.%Cl$_t$ of binder on the overall values presented in Table I-22.

1.4.6. Conclusion

The diversity of the models presented provides insight into the inherent complexity of carbonation and chloride-induced corrosion in reinforced concrete materials. First, concrete is a material with a wide range of properties that need to be considered in modelling durability. However, experimental measurement of these parameters is often challenging in operational contexts on structures, thus

highlighting the need for further development of computational methods. Therefore, different methods are presented in the precedent section for acquiring key parameters such as porosity, hydrate content, and diffusion coefficient. These models rely on certain assumptions regarding the material characteristics. However, it is crucial to update these models to account for new supplementary mineral additions, especially within the framework of reducing carbon footprint.

Secondly, the prediction of the initiation phase is well-represented in the literature, with a wide range of models enabling the prediction of chloride penetration and carbonation. However, the phenomena involved remain complex, and the analytical models developed for their predictions may not always adequately represent the underlying processes due to reliance on laboratory measurements instead of on-field measurements. Additionally, the consideration of relative humidity poses challenges in certain models, particularly for low relative humidity and the convection of chloride ions. Finite element models offer better performance in capturing precise and complex environmental conditions, but their use in maintenance prediction remains complex and time-consuming.

Lastly, estimation of corrosion propagation proves to be one of the most challenging prediction domains. This difficulty is inherent in the measurement of corrosion evolution in real structures and conditions, which often necessitates the use of accelerated tests that may not accurately represent reality. Consequently, a multitude of analytical models has been developed to predict corrosion propagation in specific cases, making it difficult to comprehensively understand the entire phenomenon. It is therefore challenging to compute propagation time accurately and reliably for most cases, which also highlights the variability of corrosion activation and propagation. Once again, the utilization of finite element models, such as those based on Laplace equations, allows for a better evaluation of specific cases, but they are more costly and often require more comprehensive knowledge of material parameters (steel and concrete) and the environment.

I.5. Mathematical processing

One of the main objectives of this research is to predict the durability of reinforced concrete system under various environmental aggressions. There are several methods available for estimating concrete durability, but this thesis primarily focuses on the following approaches:

- Employing analytical models to estimate the input parameters required for the finite element models.
- Building a database of experimental results for either validating the models' predictions or calculating the missing input parameters for the finite element models.
- Utilizing a numerical model (more precisely, a Finite Element Model (FEM)) to predict the initiation of carbonation and chloride-induced corrosion. This model is then implemented in an operational context by creating surrogate models based on the results of the FEM.
- The high uncertainties inherent to the concrete material and its durability, impose the use of computational methods able to consider them. Hence, probabilistic computations are finally performed using the surrogate models created and account for the input parameters variability.

The creation of these approaches is based on different mathematical assumptions and methods. Hence, this section details the different mathematical approaches utilised for:

- The generation of learning-based models (or surrogate models), specifically Polynomial Chaos Expansion (PCE) and Artificial Neural Network (ANN).
- The realisation of probabilistic computations with the First Order Reliability Method (FORM) and the Monte Carlo method.

In the Annex 4:

- Two statistical methods are presented for generating and analysing datasets. The acquisition of reliable data concerning concrete durability can be complicated, especially concerning novel concrete binder and material. Hence, two possibilities are investigated: generating data using models and optimizing the use of available experimental measurements. The utilization of both methods depends on the ability to assess the reliability of the results obtained.
- Following that, sensitivity analyses are described (Morris and Sobol). The aim of these methods is to give a more comprehensive view of the model functioning. They are used in the present work to alert on the behaviour of the models and identify the parameters responsible for the sensitivity.

I.5.1. Learning-based models

Unlike physical models, which rely on equations involving physical quantities, learning-based models, also known as meta-models or surrogate models, do not assume predetermined relationships but instead estimate them from available data. These models are particularly useful when physical models are complex, high-dimensional, or time-consuming to execute. In such cases, physical models are solely used for constructing the numerical experimental design.

The construction of learning-based models involves a "learning process" which includes fitting the new model to dataset values and validating it against a separate group of datasets. However, the size of the numerical experimental design is limited due to the trade-off between computational or experimental burden and the accuracy of the meta-model. Therefore, it is often necessary to conduct a preliminary step to analyse the database. For example, it is necessary to identify any erroneous values or outliers that could potentially disrupt the process. It is also important to ensure that the input data is adequately represented without any empty regions.

While some validation is performed on the meta-model, caution should be exercised, especially when input parameters are beyond or near the boundaries of the working dataset. Hence, database visualization also plays a crucial role in identifying the application range of the future surrogate model.

I.5.1.1. Polynomial chaos expansion

This type of meta-model has been extensively utilised in various engineering disciplines that heavily rely on finite element method (FEM) based numerical models [302]. The polynomial chaos expansion (PCE) offers an efficient representation of the output of a numerical model, denoted as M, wherein the inputs are treated as random variables [303]. This is achieved by employing orthogonal polynomial equations to determine coefficients, which are further fitted on datasets.

To develop a PCE metamodel, the m random variables regrouped in the vector X are assumed independent. The model output, noted Y, supposed being scalar herein, is expressed as:

$$Y = M(X) = \sum_{\alpha=0}^{m} a_\alpha \psi_\alpha(X) \qquad \text{Eq (I.128)}$$

Where ψ_α represents the multivariate polynomials, orthogonal with respect to the joint probability distribution function of X (refer to Table I-23 for some usual correspondence between polynomials and probability distribution functions [303]), and a_α the expansion coefficients to be determined. α is a multi-index (with $\alpha \in N^m$).

The selection of the polynomial order is typically conducted in a manner that guarantees the surrogate model's accurate representation of the true model. Nevertheless, it is important to highlight that opting for a higher polynomial order might lead to an accelerated over-fitting of the dataset [304]. Over-fitted models are prone to producing erroneous values and should be circumvented.

Two different approaches can be used to obtain the polynomial coefficients:

- The intrusive approach, that involves directly introducing the coefficients into the numerical model [305], [306].
- The non-intrusive approach, that allows for the determination of coefficients using the results from a database. This latter can be built using a numerical plan (without altering the physical model) or experimental measurements. It is also possible to associate both experimental and numerical results to create the required dataset.

The intrusive method has the advantage of requiring only one computation, but it can pose numerical difficulties, particularly in the case of nonlinear models, like the one considered in this study. For this reason, the non-intrusive approach is detailed in this section and was preferred for this research. The determination of polynomial coefficients (a_i) can be achieved using three main techniques: quadrature methods [307], stochastic collocation [308] or regression estimation [309]. In this study, the ordinary least squares regression was chosen due to its simplicity and reasonable efficiency [310]. To ensure practicality, a truncation scheme is applied to Equation I.128, which guarantees that the set of multi-indices remains finite. The rule is to retain multivariate polynomials with a total degree not exceeding a prescribed integer p. Hence, the set of multi-indices is defined as follows:

$$A^{m.p} = \left\{ \alpha \in N^m : \left|\left|\alpha\right|\right|_1 = \sum_{i=1}^{m} \alpha_i \leq p \right\} \quad \text{Eq (I.129)}$$

Where $A^{m.p}$ is the truncated set. The expression of the meta-model becomes:

$$Y_A = M_A(X) = \sum_{\alpha=0}^{\prod} a_\alpha \psi_\alpha(X) \quad \text{Eq (I.130)}$$

Where $\prod$ is the number of terms (coefficients to determine) [303]:

$$\prod = \frac{(m+p)!}{m!\,p!} \quad \text{Eq (I.131)}$$

Equations I.130 and I.131 demonstrate the exponential increase in the number of unknown coefficients as a function of p and m (curse of dimensionality), resulting in significant computational challenges.

To address this issue, a hyperbolic truncation set was proposed in [303]. This truncation set can be further improved by incorporating weighting factors that depend on sensitivity Sobol' indices (which is discussed in more detail in Annex 4). Furthermore, the truncation set enables consideration of anisotropic behaviour.

$$A^{m.p} = \left\{ \alpha \in N^m : \left|\left|\alpha\right|\right|_q \equiv \left(\sum_{i=1}^{m} (|w_i \alpha_i|^q) \right)^{\frac{1}{q}} \leq p \right\} \quad \text{Eq (I.132)}$$

Where w_i is the weight of the term i:

$$w_i = \frac{\sum_{j=1}^{m} S_j^T + max_{1 \leq k \leq m} S_k^T - S_i^T}{\sum_{j=1}^{m} S_j^T} \quad \text{Eq (I.133)}$$

With i ranging from 1 to m.

The anisotropic truncation method is utilised in order to reduce the number of terms and enhance the efficiency of the numerical model [309].

In addition to the truncation scheme, it is advantageous to consider the fact that numerous PCE coefficients often approach zero, leading to minimal influence on the PCE output. To address this, the

sparse regression technique can be employed to encourage coefficient sparsity, resulting in a sparse PCE as opposed to the full PCE. Various iterative algorithms, including the Least Angle Regression algorithm (LARS) [311], have been proposed for the identification of low-order interactions. For an extensive overview of pertinent literature, please refer to [312].

Table I-23 Correspondence between continuous distributions and orthogonal polynomials families.

Distribution	Supported data domain	Polynomial
Gaussian	R	Hermite
Uniform	[-1, 1]	Legendre
Gamma	[0, + ∞ [	Laguerre
Chebyshev	[-1, 1]	Chebychev
Beta	[-1, 1]	Jacobi

The software Openturns [313], which is implemented in Python, is utilised in this study. Other software packages, such as UQLab [314], also provide the capability to administer polynomial chaos.

The application of polynomial chaos expansion in this study and for the simplification of the SDReaM-Crete model offers two key advantages:

- Firstly, the meta-model requires less computational time compared to the exact model, making it suitable for industrial and probabilistic applications.
- Additionally, the selected input parameters are physical in nature and can be easily acquired through feasible industry tests, existing empirical formulas, and technical data sheets of the constituents.

I.5.1.2. Artificial Neural Network

Artificial Neural Networks (ANNs) are intricate systems comprising interlinked neurons that exhibit complex behaviour. These neurons are arranged in distinct layers, as depicted in Figure I-28. The initial layer, known as the input layer, consists of neurons associated with the model's input parameters. It is followed by the hidden layer(s) and ultimately the output layer. Each neuron of the output layer then corresponds to a result of the ANN-based surrogate model.

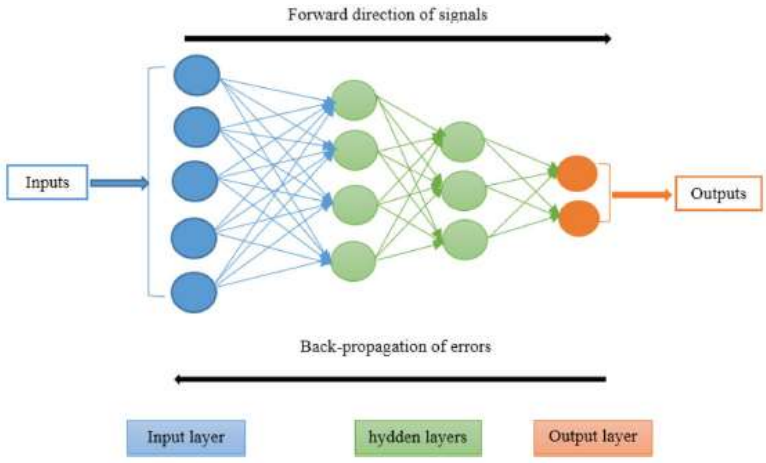

Figure I-28 Schematic representation of an ANN model architecture and functioning [213].

An artificial neuron can be defined as an integrator that calculates the weighted sum of its inputs and applies a transfer function to the result. The output of the neuron is determined by this transfer function. In most cases, the transfer function is a threshold value. If the weighted sum exceeds this value (referred to as the "bias" or "activation threshold" of the neuron), the neuron becomes active and produces a positive output. Otherwise, the transfer function returns 0, indicating that the neuron is inactive [248].

The training or learning process of an Artificial Neural Network (ANN) model involves finding the optimal weights and bias for the neurons to enhance the accuracy of output estimation. This is accomplished through an iterative technique known as "back-propagation of errors," which aims to minimize the overall error on a given dataset. The model is then validated using a separate dataset to assess its ability to provide accurate predictions beyond the training data. The training process is considered complete when further training does not yield improved results on the test dataset.

According to Glass et al. [248], preprocessing of the data, such as applying a logarithmic function to certain variables, can improve the accuracy of predictions made by the model. For instance, in the context of carbonation prediction, it is demonstrated in Section IV.3.3.1 that utilizing the square root of time produces superior results compared to using the raw time variable.

In this work, ANN-based models were built using two libraries implemented in Python:

- Scikit-learn [315]: It was used in Section III.6 for the creation of SDReaM-Crete-based surrogate models for carbonation.
- Keras [316]: This latter is used to create surrogate model for the acquisition of the different input parameters of the durability models, as detail in Section IV.3. It was used instead of Scikit-learn because it yielded better precision.

I.5.2. Probabilistic approach

The design criteria for concrete structures are established based on the concept of a limit state function, denoted as $G(X,t)$, which takes into account various input parameters such as material properties, geometrical dimensions, and environmental factors like temperature, pollutant contents, and applied loads. This approach aims to mitigate any potential unfavourable structural conditions through proper design considerations. In its simplest form, the limit state function is expressed as the disparity between the resistance $R(X,t)$ and the solicitation $S(X,t)$:

$$G(X,t) = R(X,t) - S(X,t) \quad \text{Eq (I.134)}$$

The structure performs if $G(X,t) > 0$ and fails if $G(X,t) \leq 0$ [23].

The use of alternative expressions, such as $G(X) = \ln(R(X)/S(X))$, can also be used. However, a simple difference can be easily seen as a safety margin and be comfortably handled in design calculations. In the context of concrete structure durability, it is possible to establish a limit state for the depassivation of rebars in relation to a specific aggressor. As a result, the variable R may be influenced by factors such as the thickness of the cover and the formulations used. The variable S, on the other hand, may represent the critical chloride concentration at the steel rebar surface or the depth of carbonation [227], [238].

Various factors, including material properties, environmental conditions, and geometrical parameters, are subject to uncertainties, which can sometimes be significant. The variability of these factors can be characterized using known distribution laws. Furthermore, there are certain quantities of interest, such as specific properties of concrete or other materials, that are either unknown or difficult to obtain. In such cases, estimation processes are used, introducing additional uncertainty to a certain extent. The deterministic approach, where input parameters are treated as predefined or average values, fails to account for these uncertainties in a rational manner.

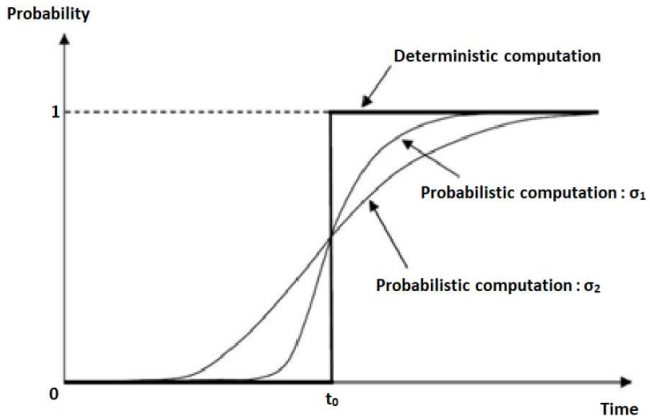

Figure I-29. Graphical representation of the deterministic and probabilistic computations (where σ1 and σ2 are two standard deviations and σ1<σ2) [105].

According to the deterministic approach, as illustrated in Figure I-29, it is assumed that the structure ceases to function when the deterministic end of service life t_0 is reached, or equivalently, when the design limit state expression becomes negative.

To incorporate uncertainties in a more scientific and rational manner, the probabilistic approach can be employed. This approach considers input parameters of $G(X,t)$ as random variables, following a specific joint probability distribution. Consequently, t_0 is no longer a deterministic value but becomes a random variable with a distribution function spread around the mean value (Figure I-29).

The failure probability P_f is the probability for $G(X,t)$ to be negative and is expressed (if t is not a random variable):

$$\mathrm{Pf} = \mathrm{P}(\mathrm{G}(\mathrm{X},\mathrm{t}) < 0) = \int_{\mathrm{G(X)}\leq 0} \mathrm{f_X}(x,t)\ \mathrm{d}x_1 \ldots \mathrm{d}x_n \qquad \text{Eq (I.135)}$$

Where X is the n-dimensional random vector, x the realisation of the random vector, x_i a component of the sample random vector x and $f_X()$ the joint probability density.

In the case of reinforced concrete structure failure probability computation, the variations of the model's input parameters listed below should be taken into consideration [317], [318]:

- Material properties.
- Structure sizing.
- Environmental and load constraints underwent by the structure.
- Manufacturing conditions.
- Models used to conceive the structure.

The reliability index (β) is a measure of the reliability level. Hasofer-Lind reliability index is directly correlated to the failure probability. However, all reliability indices are not directly correlated to P_f. The reliability index can be considered, in a simplified way, as the distance measured in standard deviation, which separates the median point of the variables from the most probable failure point, lying on the failure surface where $G(X) = 0$.

Further, the reliability index is the reference measure for the reliability level in design standards.

For the purpose of reliability differentiation, classes related to the consequence of failure (CCi for Consequences Classes) are defined in the EN 1990 [319]. These classes specifically address the potential effects on human life, as well as economic, social, and environmental implications. Three classes within this framework are specifically intended for mechanical applications:

- CC3 in case of high consequences (for example, a concert hall).
- CC2 in case of medium consequence (a residential building).
- CC1 in case of low consequence (for Agricultural buildings or greenhouses).

To each CCi is associated a Reliability Class (RCi). Reliability index (β) values are then associated to each RCi according to the ultimate limit state desired for the structure. The following Table I-24 shows the recommendation given in the EN 1990 [319].

Table I-24. Recommended minimum values for reliability index β (ultimate limit states) [319].

Reliability class	Minimum values for β	
	1 year reference period	50 years reference period
RC3	5.2	4.3
RC2	4.7	3.8
RC1	4.2	3.3

Other limit states are also considered. For RC2 structural members, the values given in the EN 1990 are available in Table I-25 for a 1 and a 50-year reference period.

Table I-25. Target reliability index β for class RC2 structural members [319].

Limit state	Target reliability index	
	1 year	50 years
Ultimate	4.7	3.8
Fatigue		1.5 to 3.8
Serviceability (irreversible)	2.9	1.5

Quantifying uncertainties associated with parameters, such as probability distributions, is a critical step in evaluating failure probabilities, as these probabilities are heavily influenced by the assumed distributions. In the context of mechanical service limit state, the selected failure probability $P_{f_{target}}$ typically falls between 2.28% and 6.68%, which corresponds to reliability indices β of 2 and 1.5, respectively [320]. Similarly, Schmitt utilised similar values in her work on the probabilistic approach to reinforced concrete durability [6]. For ultimate service limit state, a reliability index of 3.8 is often preferred to minimize associated risks.

The standards based on the limit state criteria, such as the Eurocodes [320], the ISO 2394 "General principals of the construction reliability" (2015) [321], as well as the pre-standard *fib* code model [191] define two types of limit state:

- SLS: Service Limit State (β_{SLS} in Figure I-30).
- ULS: Ultimate Limit State (β_{ULS} in Figure I-30).

A third limit state was proposed in the *fib* 34th bulletin [238] which corresponds to the time beyond which the aggressive species have reached the rebars. It is a durability limit state that represents the depassivation of the steel (β_{dep} in Figure I-30).

Finally, a fourth limit state is defined in [6] (β_{dur}) and corresponds to the probability to reach a threshold value of iron thickness loss.

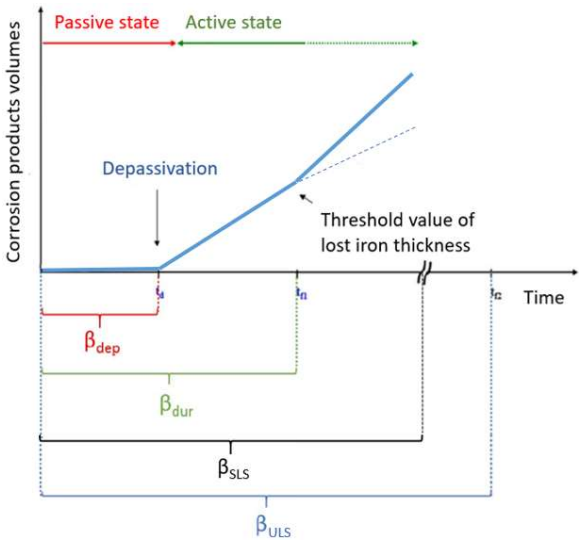

Figure I-30. Link between reliability indices and phases of a reinforced concrete structure lifespan [6].

As shown in Figure I-30, each of these limit states corresponds to a reliability index (β). To ensure a sufficient reliability level for a given limit state, it is required to obtain a reliability index superior or equal to a target reliability index. The Eurocodes and the *fib* 34th bulletin advise on the use of different values for these indices (see Table I-26 for the F65 [322] and EC2 [320] values).

Table I-26. Reliability indices for the different limit states according to the fib 34th bulletin [238].

Limit states	Reliability index for a 50 years lifespan
Durability ($\boldsymbol{\beta_{dur}}$)	1.3 [322] (and 1.0 [105])
Service (for a RC2 structure) ($\boldsymbol{\beta_{SLS}}$)	1.5
Ultimate (for a RC2 structure) ($\boldsymbol{\beta_{ULS}}$)	3.8

Most of the proposals concerning the durability are limited to a unique reliability index value (β_{dep}). It means that only depassivation is actively considered, while the propagation phase is not included in the computation. It assumes that the propagation time should be considered equal to 0, and thus reduce the service life predicted for the structure. Von-Greve and al. [199] proposed a dissociation of the mechanisms linked to the depassivation from those linked to the propagation. They propose different reliability indices threshold for the depassivation phase according to the durability classes XC2, XC3 and XC4. The proposed reliability indices take into account the cover thickness and the concrete formulation prescribed by the standards. This way, the reliability associated to the standard recommendations is computed for the depassivation stage, while the propagation can be considered deterministically. The corrosion propagation is however sometimes implicitly considered in the reliability index, accounting for a probabilistic propagation time defined for specific environments [323].

Different methods can be employed to conduct reliability assessment of a system by utilizing a failure criterion and a model. Two specific methods are elaborated in the subsequent subsections. Although they differ in approach, both methods typically necessitate multiple runs of the failure-describing model, which can consume significant time. Hence, to mitigate this issue when numerical models are concerned, it is advantageous to construct a surrogate model through a relatively conservative numerical experimental design, as it can expediently reduce the computational load.

The introduction of a limit state for durability has been a significant advancement compared to the prescriptive approach outlined in the EC2. This limit state specifically focuses on the depassivation of steel and is coupled with a simplified physical model for carbonation or chloride ions ingress. This approach has been improved by incorporating the modulation of the reliability index based on the exposure classes proposed by Von-Greve Dierfled and Gehlen [199] as well as the *fib,* [324] for the XC and XS classes respectively. By including feedback from normative development, this method provides

a more realistic understanding of corrosion development. However, to align with the current approach to durability, it is necessary to study the quantitative aspects of the corrosion propagation phase. Previous research has investigated the cracking phenomenon associated with corrosion [147], [325], [326] and developed simplified models [273], [327]. Despite this progress, integrating these findings into recommendations or design codes has been challenging due to the lack of an internationally recognized physical model. Therefore, instead of focusing on cracking and post-depassivation effects, it may be more relevant to consider the effective initiation of corrosion propagation without cracking. In this case, the estimation would solely rely on corrosion product quantities and would not consider any mechanical aspects in defining the limit state.

The expected service life of a given structure, chosen for the verification of durability limit states such as depassivation or corrosion effective propagation, may correspond to the reference design working life of the structure. For standard buildings, this is typically 50 years, while civil engineering structures have a reference lifespan of 100 years. In the specific case where the durability limit states are exceeded, it can be considered that there is no impact on the structural integrity limit states corresponding to the same time. However, this depends on the reliability level set for the durability limit states. If the reliability level is sufficiently high, there will be no incidence on the structural integrity limit states, but the initial cost of the structure would have been excessive. On the other hand, if the structural limit state is reached before the end of the reference lifespan, it is considered unacceptable and certainly endangered the population. Therefore, it is necessary to establish a link or at least correlate the reliability level aimed at the durability limit states with those obtained with the ultimate limit states (ULS).

In the field of civil engineering, Monte Carlo simulations and FORM/SORM (First/Second-Order Reliability Method) are the most commonly used reliability methods. These methods serve as the basis for many other techniques that have been derived from them in order to improve convergence, accuracy, and computational efficiency [328].

I.5.2.1. Monte Carlo method

Crude Monte Carlo sampling is one of the simplest ways to determine the probability of failure. Different method for its application can be found in the literature [303]. However the general pattern can be defined with the following steps [329]:

- It is first required to define the domain of the input parameters of the study.
- The second step consists in generating random inputs following a statistic distribution over the parameters' domains.
- Deterministic computations (using the studied model m) are then performed with all the generated dataset of inputs (X_i).
- Finally, the results obtained are used to compute a probability. In this study, it consists in enumerating the computations leading to values exceeding the criterion of depassivation ($Crit$), critical corrosion or failure according to the case. This number is then divided by the total number of computations N (see Equation I.136).

$$P_f = \frac{1}{N}\sum_{i=0}^{N} I(m(X_i) > Crit) \qquad \text{Eq (I.136)}$$

Where $I(m(X_i) > Crit)$ is a function equals to 1 if X supers $Ccrit$ (failure domain) and 0 otherwise.

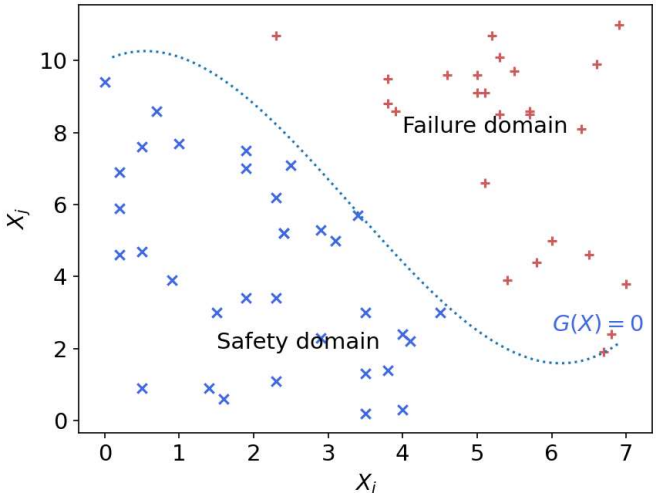

Figure I-31 Results of a Monte Carlo experiment.

This relatively simple method requires a high number of computations to obtain accurate results. The minimum number of simulations needed to achieve a stable and final probability value depends on several factors, such as the equations used in the model and the number of input parameters. Consequently, computational time can become a significant issue, for complex models especially. Generally, a variation of less than 10% in the computed probability is considered as the criterion for stability. Additionally, the Monte Carlo method is unable to determine the most likely point of failure. This advantage is exclusive to the FORM/SORM method, which is useful for identifying the input parameter that requires modification in order to more efficiently move away from the failure point [328].

I.5.2.2. First and Second Order Reliability Method (FORM/SORM)

FORM (First Order Reliability Method) and SORM (Second Order Reliability Method) are advanced techniques used to estimate the probability of an event occurrence. By utilizing the concept of the most probable failure point (MPP) and an assumed failure domain, FORM and SORM can evaluate the likelihood of failure. The coordinates of the MPP are sought in a standardized space of variables, where all variables are centred Gaussian and stochastically independent. The MPP represents the point on the limit state surface that is closest to the origin of the space. Therefore, determining the MPP involves minimizing a function under constraints, which can be solved using various algorithms. The most efficient algorithm for this purpose is derived from the Rackwitz-Fiessler algorithm [330], [331]. The norm of the corresponding vector is known as the Hasofer-Lind reliability index.

To facilitate the transition from the physical space to the standardized space, the Rosenblatt and Nataf transformations [332] can be applied (refer to Figure I-32 [333]). In the standardized space, the limit state function can be approximated using a Taylor series expansion according to Equation I.137:

$$g(U) = G(U_0) + J(U - U_0) + \frac{1}{2}(U - U_0)^t H(U - U_0) + \underset{U \to U_0}{\longrightarrow} [(U - U_0)^t (U - U_0)] \qquad \text{Eq (I.137)}$$

Where J is the Jacobian matrix and H the Hessian matrix of the limit state function at the point U_0. Depending on the desired or needed refinement, the first order (FORM) or second order (SORM) approximation is computed.

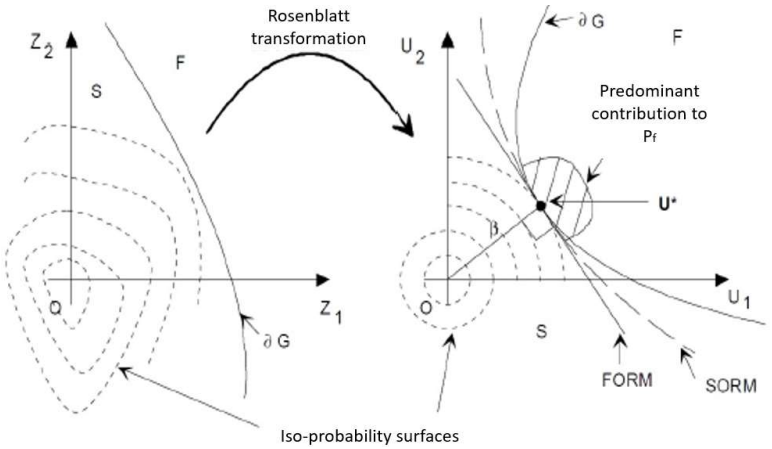

Figure I-32. Graphical representation of the Rosenblatt and Nataf transformation used for the transition of an ordinary space to a reduce centred space [333].

The failure surface is assumed to be a hyper-plane in FORM, and a hyper-paraboloid in SORM (Figure I-32). In the context of FORM, the failure probability is defined with Equation I.138:

$$P_{f,FORM} = \phi(-\beta) \qquad \text{Eq (I.138)}$$

Where ϕ is the standard Gaussian cumulative density and β the reliability index [333], [334]. As it can be seen in the equivalence graphic (see Figure I-33), in a case of a failure probability superior to 50%, the reliability index is negative.

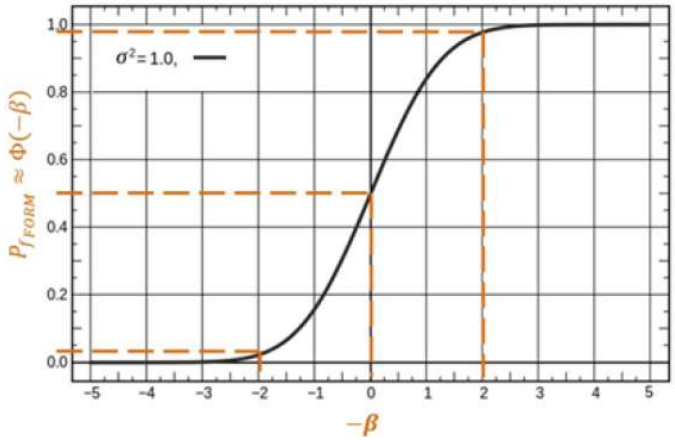

Figure I-33. Graphical representation of the failure probability obtained with the FORM method as a function of the reliability index [6].

Furthermore, FORM and SORM methods enable the determination of the sensitivity of failure probability or reliability levels through a few additional computations involving variables and parameters of their probability distributions. By recognizing that the probability density reaches its maximum at point P^* within the failure domain, the integration near P^* provides a close approximation to the P_f value as per Equation I.138. This justifies the favourable approximation achieved with the FORM method. However, in cases where the failure surface exhibits strong non-linearity, it is recommended to use the SORM method as it incorporates correction factors that are not applied in the case of the FORM method.

I.6. Standardization context

This section aims to present the standard framework relative to the concrete durability. This part also includes the main works in progress in standard committee to promote the development of low-carbon concrete.

I.6.1. Standardization context and prevention

The durability can be defined as the ability of a system to maintain its use-functions with a minimum reliability level as well as to preserve the aspect of a structure over time in a given environment. It also includes conventional maintenance operations. Thus, the Eurocode 2 [335] states that a durable structure shall meet the requirements of serviceability, strength, stability and reliability throughout its design service life, without significant loss of utility or excessive unforeseen maintenance. Durability is one of the stakes involved to justify the financial investment for a structure, but most of all to ensure user safety. The objectives of concrete durability must be specified as a function of the environment's aggressivity in which the structure is placed. Those objectives can then be used to adapt the formulation and the rebar concrete cover according to the desired lifespan. The surrounding environment properties are considered through exposure classes. In the present standards for concrete structures, the specifications comprise: the nature and minimal quantity of equivalent binder (B_{eq}), the minimal mechanical resistance, the maximal W_{eff}/B_{eq} ratio, the minimal cover of rebars and the maximal content of chlorides inside the concrete [19]. The present knowledge on cement and other compounds allows the concrete composition and formulation to be optimised and adapted to environmental constraints while respecting the mechanical performance criteria. European standards open the door to:

- The prescriptive or deemed-to-satisfy approach (obligation of means).
- The performance-based approach (obligation of performances) via the Exposure Resistance Classes system in development or national standard as the FD P18-480 (2022) in France.

Both can be used at the same time, as shown in [322], [336], [337].

I.6.2. Prescriptive approach

The prescriptive approach described in the NF EN 206/CN standard [19] represents the specification procedure for concrete currently used for structural applications. It ensures, in the normal use conditions and for an appropriate number of maintenance operations, a minimum lifespan of fifty years for a given environment, by giving the obligation of means and thresholds concerning the type and proportion of the constituents which can be used. A concrete is thus formulated according to the structure environment, this latter being characterised by the concept of exposure class. Six different families of exposure classes are described in the NF EN 206/CN standard:

- X0: no particular aggression
- XC: carbonation aggression
- XS: aggression due to the penetration of chloride ions of marine origin
- XD: aggression due to the penetration of non-marine salts
- XF: aggression caused by freeze-thaw cycles
- XA: aggression with chemical origin

Each exposure class is further subdivided into subclasses based on various environmental conditions, such as relative humidity, exposure to weather, and intensity of freeze-thaw cycles. The selection of exposure classes is based on environmental studies conducted at the implementation site. The requirements for a formulation corresponding to a specific exposure class can be found in the NA.F tables of the NF EN 206/CN standard.

These requirements primarily include:

- The minimum class of compression resistance of the concrete,
- The minimum equivalent binder content and the maximal quantity of additions that can be considered in the equivalent binder,
- The minimal percentage of entrained air,
- The maximal W_{eff}/B_{eq} ratio (where W_{eff} is the effective water responsible for the cement hydration, while B_{eq} is the equivalent binder, which corresponds to the cement and a part of the additions).

The equivalent binder B_{eq} value is obtained from the Equation I.139:

$$B_{eq} = C + kA \qquad \text{Eq (I.139)}$$

The variables C, A, and k represent different factors pertaining to cement (CEM I or CEM II/A, 42.5 or 52.5, R or N) and mineral additions. The quantity A refers to the amount of a mineral addition (limestone, siliceous, blast furnace slag, silica fume, etc.) that can be considered in the calculation of the equivalent binder. The coefficient k is dependent on the specific type of mineral addition being used. The maximum value of A authorized is determined by the ratio $A/(A+C)$, which varies depending on the exposure class being considered. If a higher quantity of mineral addition is added to the mixture, exceeding the maximum value defined by the standard, the excess amount is not taken into account in the calculation of the equivalent binder. This specific aspect raises questions from physical and chemical perspectives. The equivalent binder fails to consider the entire binder content. Therefore, certain modifications in the concrete compositions may be made without being measured by the equivalent binder. However, altering the mineral addition content typically affects the durability properties of the resulting concrete. Elevating the binder content might enhance compactness, and increasing reactive addition content reduces the portlandite content. Using the total binder content may be more suitable to account for the overall effect induced by the composition.

For civil engineering structure or important structure for which the minimal lifespan required is a hundred years, the procedures to follow in France are those of the leaflet F65 (2018) [322] which completes the Eurocodes as well as the standards NF EN 206/CN and NF EN 13369 [19], [338]. The cover thickness is also adapted for this greater lifespan [320].

The NF EN 206/CN+A2 (2022) and the leaflet F65 (2018) thus define the prescriptive approach for structures with 50 and 100 years of service life respectively. Despite the consideration of the binder quantity, the ratio W_{eff}/B_{eq} and the characteristic compressive strength, the requirements concerning the concrete formulation only partially consider the binder chemistry or the solid skeleton chemistry [339]. Thus, this approach can sometimes become a brake for innovation, especially in a context of carbon footprint reduction where industries look to produce materials for construction less impacting for the environment.

I.6.3. Performance-based approach

Like all materials, concrete has an important part to play in the reduction of carbon dioxide emissions as well as energy and material use reduction (with development of circular economy process for instance). To this end, the standardization context evolves towards the more frequent use of performance-based approaches. With this type of method, a greater choice is left to the means, while strict criteria must be fulfilled to conclude on performance and durability requirements. Hence, designers and engineers have wider choices and a clear liability for the constituent types and contents.

Finally, this approach enables the formulation of innovative concretes while ensuring the safety and quality level for the final users. First, the standard NF EN 206/CN [19] incorporated the performance-based approach as a compliant one with recommendations but its use remained limited in practice.

Indeed, only a few paragraphs referred to it, without providing a methodology for its practical implementation.

In France, two distinct ways to implement the performance-based approach were defined:

- Performance-based approach **based on the comparison of concrete properties with threshold values**: it consists in qualifying the durability performances of a concrete composition by directly using durability indicators and threshold values.
- Performance-based approach **based on the comparison to a reference concrete**: this method aims at qualifying a concrete composition from its durability according to a comparative approach with a reference concrete.

More recently, the leaflet FD P18-480 (2022) was developed to define more precises boundaries for the application of the performance-based approach based on the comparison with thresholds. This document defines a methodology for the performance justification associated to a concrete mix. The equivalence of performance is stated thanks to durability indicators and performance tests. On one hand, durability indicators are general parameters, intrinsic, which are fundamental for the evaluation and prediction of the material and structural durability against the degradation process considered.

These parameters are easily measurable from reproducible laboratory tests, such as porosity accessible to water, chloride ions migration coefficient, electrical resistivity, and the accelerated carbonation rate. On the other hand, performance tests can allow the evaluation of the concrete behaviour under physicochemical constraints peculiar to the environment in which the structure is placed. These tests are carried out to classify different concretes according to their resistance against specific aggressions: for instance, the accelerated carbonation test, chloride ions migration under an electric field test, scaling test (for freeze-thaw cycles) or leaching test (for chemical aggression).

The performance-based approach defined in the FD P18-480 (2022) [340] for the exposure classes XC, XS and XD is briefly described in this section. It consists of a comparison of the concrete performances with threshold values. This fascicule allows the definition of concrete formulations that derogate to the table NA.F. of the NF EN 206/CN+A2 (2022) used for the prescriptive approach. Despite the high degree of freedom, the application of the performance-based approach implies the use of standard constituents, which restrain the use of the authorized material but guarantees a higher security.
First, **three categories of structure** are defined:

- **N1**: Corresponds to a category of structure 1 (non-structural part, provisional structure …). Exceptions are made for class 2 structures exposed to XC1 environment that can be considered with N1 and class 1 structures exposed to XA environments that need to be considered with N2.
- **N2**: Corresponds to a category of structure 2 (Building and certain basic civil engineering structures conceived for a 50-years lifetime). Moreover, structure class 3 exposed to XC1 and structural class 1 and 2 exposed to XA environments are also categories as N2.
- **N3**: Corresponds to a category of structure 3 (Structures conceived for a 100-years lifetime and exceptional structures) except for XC1 environment.

This section only focuses on the class N3 which concerns most of the structures addressed in this PhD and is the more constraining. For the other application levels, different recommendations are given in the fascicule.

The realisation of the performance-based approach consists in **three successive studies**:

- The first is the **study test** and is performed on concrete manufactured and tested in laboratory.
- The second is the **convenience test** It consists in testing in manufactory, the same concrete mix, this time manufactured in industrial context, with the same mixer than the one used for the concrete production.
- The final step, called **control test**, escort the manufacturing process, and consists in controlling the concrete produced on field.

The study test is detailed with the consideration of the exposure classes XC and XS/XD.

Three types of indicators are defined:

- Mechanical indicators which consist in the compressive strength obtained after 28 days of water conservation, and the determination of the cement characteristic strength (on mortar). This latter is used to assess the quality of the cement. The results of compressive strengths are considered satisfying if they respect the two following conditions:

$$f_{CE} \geq f_{CK} + \lambda(C_E - C_{min}) \quad \text{Eq (I.140)}$$

$$f_{CE} \geq f_{CK} + 2\sigma \quad \text{Eq (I.141)}$$

With f_{CE} the average value of compressive strength measured according to the NF EN 12390-3 (2019), f_{CK} the characteristic compressive strength, λ a coefficient equal to 1 except in the presence of compelling justification, C_E the observed 28 days compressive strength of the mortar, C_{min} the minimal 28 days compressive strength of the cement and σ the minimal standard deviations (3 MPa).

- General indicators which are the electrical resistivity and the porosity accessible to water measured after 28 days of water conservation. For a precast concrete, it is possible to replace the test of porosity accessible to water by a measurement of the water absorption, except if the performance-based approach validates a XC exposure class using the φ_c^w / F_{paste} indicator.
- Durability indicators depend on the exposure class to validate. They are normally computed after 90 days of conservation in water. The durability indicators relative to the exposure classes for carbonation (XC) and chloride (XS/XD) induced corrosion are explained below:
    - For XC classes, it is either possible to verify the concrete mixes with the evaluation of the accelerated carbonation rate (XP P 18-458 where the characteristic values computed with Equation I.142 need to comply with the Table I-27), or with the ratio Porosity accessible to water on the fraction of paste volume φ_c^w / F_{paste} (NF P 18-459 Where the characteristic values computed need to comply with the Table I-27). Lastly, if the exposure class XC3 or XC4 are considered, it is required to add the measurement of the accelerated carbonation on one of the "nominal" batches to verify that the concrete may comply with the aggression of the environment. In both cases, the electrical resistivity needs to be measured (XP P 18-481). The value of the electrical resistivity is used to modulate the threshold values of the Table I-27 for the characteristic values of K_{acc} and the ratio φ_c^w / F_{paste} respectively.
    - For XS and XD classes, the durability indictor correspond to the accelerated migration coefficient D_{rcm} measured according to the XP P 18-462 and used to compute the characteristic values with the Equation I.142 that will be compared to the threshold value of Table I-28. This latter table is modulated by the ageing factor computed according to the Equation I.125 which depends on the relative composition of the concrete mix.

Table I-27 Threshold values of durability indicators for the validation of XC exposure classes [340].

Exposure class	Modulation with Re_{90d} (Ohm.m, XP P 18-481)	$K_{acc,90d}$ (mm.j$^{-0.5}$)	$\varphi^{w}_{c,90\ days}/F_{paste}$ (%)
		100 years	100 years
XC1	< 100	4	65
	100 to 175		
	> 175		
XC2	< 100	2.6	60
	100 to 175	3	65
	> 175		
XC3	< 100	1.8	50
	100 to 175		
	> 175		
XC4	< 100	1.8	50
	100 to 175		50
	> 175	2.2*	55

Table I-28 Threshold values of durability indicators for the validation of XS and XD exposure classes [340].

Modulation with ae (-, Equation I.125)	XS exposure class	$D_{rcm,90d}$ (m^2.s^{-1})	XD exposure class	$D_{rcm,90d}$ (m^2.s^{-1})
		100 years		100 years
0.3 to 0.39	XS1	9 (16*)	XD1	16 (22*)
0.4 to 0.49		22		28
0.5 to 0.59				
0.6 and higher				
0.3 to 0.39	XS2	3 (5*)	XD2	9
0.4 to 0.49		5		16
0.5 to 0.59		9		22
0.6 and higher				
0.3 to 0.39	XS3e	5	XD3f	9
0.4 to 0.49		9		16
0.5 to 0.59		16		22
0.6 and higher		22		
0.3 to 0.39	XS3m	2	XD3tf	5
0.4 to 0.49		3		9
0.5 to 0.59		5		16
0.6 and higher		9		

The values compared in Table I-27 and Table I-28 are characteristic values of the durability indicators ($X_{k,90j}$) computed according to the Equation I.142 with the average measured value ($X_{moy,90}$) and the provisional standard deviation $\sigma_{provisional}$.

$$X_{k,90d} = X_{moy,90d} - 1.5.\sigma_{provisional} \quad \text{Eq (I.142)}$$

The provisional standard deviation is computed with the equation with the mean value ($X_{moy,90}$) and the minimal acceptable coefficient of variation (CoV_X) whose value depends on the durability indicator considered (see Table I-29).

$$CoV_X = \frac{\sigma_{provisional}}{X_{moy,90d}} \quad \text{Eq (I.143)}$$

Table I-29 Minimal acceptable coefficient of variation [340].

Durability indicator X	Porosity accessible to water ($\varphi^{w}_{c,90\ days}$, %)	Chloride migration coefficient ($D_{rcm,90d}$, 10^{-12} m²/s)	Accelerated carbonation rate ($K_{acc,90d}$, mm.d$^{-0.5}$)
CoV_X (%)	3%	20%	20%

In addition, in the case of the validation of XC3 and XC4 exposure classes with the ratio Phi_{90d}/fV_{paste} as durability indicator, the results must comply with the following inequation:

$$K_{acc,90d} \leq 0.08 \frac{\varphi^{w}_{c,90\ days}}{F_{paste}} - 2.2 \qquad \text{Eq (I.144)}$$

Other tables are proposed in the FD P18-480 (2022) with more constraining values that allow the reduction of the structural classes of 1 or 2 levels. The structural classes are described in the EC2 [320].

Study test

During the realisation of this step, three "nominal" batches of the desired concrete mixes are manufactured in laboratory. In addition, two derived mixes are manufactured with a variation of the water content of + and – 10L. In the case of self-compacting concrete, this value can be reduced to 5L. Other derivate mixes can be added, with variation on the value of binder (+ and – 20kg/m^3), admixture (generally to test the winter and summer variations) and aggregate contents (+ and – 10%).

On the "nominal" concrete are measured:

- The mechanical indicators (Compressive strength at 28 days is measured for each batch while characteristic resistance is measured once on mortar at 28 days).
- The general indicators.
- The durability indicators which depend on the exposure class(es) and the method chosen to validate it(them).

On the derivate mixes are only measured:

- The compressive strength at 28 days as mechanical indicator.
- The durability indicators which depend on the exposure class(es) and the method chosen to validate it(them).

I.6.4. Cover sizing

The Eurocode 2 (2005) [335] gives the minimal values of the concrete cover. The 4th section of this standard discusses the cover durability and cover manufacture quality. It also refers to the exposure classes as defined in the table NA.F.1 and NA.F.2 of the NF EN 206/CN+A2 (2022). To satisfy the durability requirement during the whole lifetime of the structure, the designer must obey dedicated provisions for concrete cover. The determination of the cover value according to the NF EN 206/CN+A2 (2022) standard considers [19]:

- The exposure class depending on the environmental actions on the structure parts.
- The expected service life.
- The resistance class of the concrete.
- The type of control system used to ensure the performance regularity of the concrete.
- The rebar nature.
- The control level of the rebar positioning and layout.

This way, the EC2 defines the nominal value of the cover (C_{nom}) with the following Equation I.145:

$$C_{nom} = C_{min} + \Delta C_{dev} \qquad \text{Eq (I.145)}$$

Where C_{min} is the minimal cover and ΔC_{dev} a margin of calculation for the execution tolerance. The value used as C_{min} considers the bond and the environmental conditions at the same time with the use of Equation I.146.

$$C_{min} = max\{C_{min,b};\ C_{min,dur} + \Delta C_{dur,y} - \Delta C_{dur,st} - \Delta C_{dur,add};\ 10mm\} \quad \text{Eq (I.146)}$$

Where $C_{min,b}$ is the minimal cover due to the bond requirement (mechanical behaviour), $C_{min,dur}$ the minimal cover due to the environmental conditions, $\Delta C_{dur,y}$ the safety margin (in France the recommended value by the national standard is 0 mm), $\Delta C_{dur,st}$ the minimal cover reduction in the case of stainless steel use (in France the recommended value by the national standard is 0 mm) and $\Delta C_{dur,add}$ the reduction of the minimal cover value in the case of additional protection (in France the recommended value by the national standard is 0 mm). The value of $C_{min,b}$ is not considered in this work in which only the durability aspects are considered. This latter is defined to ensure the binding between the steel and the concrete and to ensure the sufficient cover of the steel to results in the mechanical integrity of the composite material.

The value of ΔC_{dev} for a given country is obtained with the national annex (NA) of the EC2. The French national annex recommends the use of 10 mm, except in case of high process control. In the case of precast concrete, its value ranges from 0 to 10 mm. The minimal value of the cover allows the good transmission of the adherence forces, the steel protection against corrosion and better flame resistance. It is worth noting that provisions taken to ensure the structure durability are defined in European standards and often completed in national annexes. Indeed, according to the country, the annexes give different requirements on the w/c ratio, the binder content or the cover thickness may change.

As presented in the previous sections, concrete is formulated in compliance with the recommendations of one exposure class defined in the standard NF EN 206/CN [19]. The cover is then prescribed in Eurocode 2 according to a structural class (see Table I-30) in turn adaptable as function of the materials and manufacture process [320]. Structures designed for 50 years-service life correspond to a S4 class while S6 is used for 100 years-service life when no reduction is applied.

Table I-30. $C_{min,dur}$ values (mm) according to the exposure classes [320].

Environmental exigences for $C_{min,dur}$ (mm)							
Structural classes	Exposure classes according to table 4.1 of the EC2						
	X0	XC1	XC2/XC3	XC4	XD1/XS1	XD2/XS2	XD3/XS3
S1	10	10	10	15	20	25	30
S2	10	10	15	20	25	30	35
S3	10	10	20	25	30	35	40
S4	10	15	25	30	35	40	45
S5	15	20	30	35	40	45	50
S6	20	25	35	40	45	50	55

A more recent approach was discussed along with the definition of the performance-based approach. Indeed, in the synthesis report "Definition of performance thresholds according to exposure classes" [323], the author defined the notion of Exposure Resistance Classes (ERC) for the different exposure classes. The same durability indicators are considered for the classes XC, XS and XD to define concrete values as a function of the concrete performances. The goal is to propose a modulation of the concrete cover thickness values through the performance-based approach.

First, the work on XC environment is based on analytic modelling results obtained using the Equation I.147 to compute the carbonation depth x_c (mm) as function of the time t (years).

$$x_c(t) = K\ k_e\ t^{\alpha_e} \quad \text{Eq (I.147)}$$

Where:

- K is the nominal average carbonation rate expressed in mm.year$^{-0.5}$ and assumed constant with time.
- k_e is an environmental coefficient accounting for the relative humidity.
- α_e is an exponent dependant on the relative humidity.

It is assumed that the service life (t_{SL}, years) respects Equation I.148 where t_{prop} is the time of corrosion propagation (function of the electrical resistivity and expressed in years) and t_{ini} is the time of corrosion initiation (function of the carbonation kinetic and the concrete cover).

$$t_{SL} = t_{ini} + t_{prop} \quad \text{Eq (I.148)}$$

The computations were then realised using the values of Table I-31, allowing the computation of the concrete cover for each situation (service life of 50 and 100 years, electrical resistivity class and exposure classes).

Table I-31 Values defined for t_{prop} and the environmental parameters for the carbonation induced environments [323].

		t_{prop}			
Risk of failure	Re_{90} (Ohm.m)	XC1	XC2	XC3	XC4
Low	< 100	45/48 – 90/96	10	20	5
Intermediate	100-175	45/48 – 90/96	15	25	20
High	> 175	45/48 – 90/96	20	30	30
α_e		0.5	0.4	0.45	0.4
k_e		1	0.5	0.87	0.83

The concrete values definitions are based on these assumptions and the values obtained are summarized in Table I-32.

Table I-32 Recommended $C_{min,dur}$ values (mm) for the three classes of electrical resistivity (<100/100-175/>175) and XRC classes.

K_{acc}	XRC	XC1		XC2		XC3		XC4	
mm.d$^{-0.5}$		50y	100y	50y	100y	50y	100y	50y	100y
	0.5	10	10	10	10	10	10	10	10
	1	10	10	10	15	10	20	10	20/20/15
1	2	10	10	10	20	15	25	15	25
1.4	3	10	15	15	20	20/20/15	30	20/20/15	30
1.8	4	10	15	15	25	25/20/20	40/35/35	25/25/20	40/35/35
2.2	5	10	20	20	30	30/25/25	45	30/30/25	45/40/40
2.6	6	10	20	25/20/20	35	30	50	35/30/30	50/50/45
3	7	15	20	25	40/35/35	35/35/30	60	40/35/30	60/55/55
3.5	8	15	25	30/30/25	45/40/40	40/40/35	70/65/65	50/40/35	70/65/60
4	9	15	25	35/30/30	50/45/45	50/45/40	75/75/70	55/45/40	75/70/70

The equivalent study is performed for chloride induced corrosion environments with the definition of the XRDS classes. The model used for the computation is based on the solution of the second Fick law (see Equation I.69 detailed in Section I.4.2).

$$C(x,t) = C_i + (C_S - C_i)\,\mathrm{erfc}\left(\frac{\mathrm{x} - \Delta\mathrm{x}}{2}\left(D_{app}(t)\,t\right)^{0.5}\right) \quad \text{Eq (I.149)}$$

The different assumptions made for the computation, notably concerning the environmental conditions at the critical chloride values are described at [323].

I.6.5. Expert Group “Low Carbon Solution”, French concrete normative commission P18B AFNOR

Reflections are currently underway regarding new methodologies and requirements to enlarge the low carbon concrete possibilities for concrete structures.

The French standardization commission for concrete (P18B), mirror committee of TC104/SC1, has decided in 2021 to create an expert group in order to verify that "low carbon" concrete formulas, of interest to the market, are allowed by NF EN 206/CN (2022), and if not, what amendment to French national annex to NF EN 206/CN (2022) could be done, if these formulas meet the essential requirements of constructive performance, safety of use and durability.

This group named « Low Carbon Solutions » relies on six task forces:

- Task Force n°1: **“New additions and new binders”**. The goal of the TF1 is to write a standard (technical report) describing the methodology to validate the suitability of use in concrete of new additions and new binders.
- Task Force n°2: **“Terminology and indicators”**. The mission of the TF2 is to propose terms and definitions to clarify the concepts relating to low-carbon concrete solutions and to define, for low-carbon concrete, reference levels for each kind of concrete depending on the strength and exposure classes.
- Task Force n°3: **"Binders, aggregates and concrete formulation according to an evolution of the prescriptive approach"**. The goal of the TF3 is to identify in the prescriptive approach of the NF EN 206/CN (2022) what limits the use of low carbon solutions and to propose possible changes to the current rules of the prescriptive approach related to the definition and use of binders, in particular to the concepts of use of standardized additions.
- Task Force n°4: **“Low Carbon Solutions database”**. The mission of the TF4 is to create a database (concrete CO_2 footprint, performance, durability properties, data on constituent’s footprint according to NF EN 15804) on concretes leading to lower carbon footprints.
- Task Force n°5 deals with the: **"Non-structural concrete and concrete for temporary works"**.
- Task Force n°6 concerns the **"Contribution to the structural design with low carbon concrete solutions"**. The missions of TF6 are as to propose evolutions of Eurocode 2 national annex rules in order to accompany the evolutions on the material (NF EN 206/CN (2022)).

II. Experimental campaign: material, methods, and results

II.1. Introduction – Context and goals

An experimental campaign was planned for this work. It aims to improve the understanding of the behaviour of different low carbon footprint concretes regarding durability in aggressive environment, namely carbonation and chloride ingress. The results obtained are used to enhance the predictive modelling of these phenomena for the maintenance policy of reinforced concrete structures. In this aim, six concrete formulations were proposed (see Table II-1). The specific objectives of the campaign cover two distinct aspects:

- The investigation of the hydration process, particularly in fly ash and metakaolin-based binders, carried out with a primary focus on formulations F3 and F4. The objective is to assess the influence of these pozzolanic additions on the hydrate contents, and subsequently, the carbonation rate and chloride resistance. The preceding Section I's literature review identified deficiencies in the current models for considering certain reactive additions, thus validating the need to explore this aspect.
- The investigation of the durability of reinforced concrete against carbonation and chloride ions ingress, with a specific emphasis on a novel low carbon impact binder. The concrete mixes F2, F5 and F6 are formulated to address this aspect using a CEM III/B, a CEM V/A (S-V) and a CEM VI (S-V) recomposed using a blend of two cements. Durability data are gathered on these concrete mixes in order to develop a model for their behaviour in Section III.

The structural context driving the methodology established in this study is to examine both road and maritime structures. Furthermore, the concrete mixtures formulated in this section were determined within the range commonly utilised for various types of structures, such as bridges and maritime constructions. Boulonnais sand and gravel were chosen based on their representative properties within the industry. These are Visean hard compact limestone aggregates of code A according to the NF P18-545 (2011) standard. The technical specifications for the constituents can be found in Annex 1.

It should be noted that the actual compositions of the different mixtures varied from the predetermined target values (refer to Table II-1).

Almost all results from this study are utilised for modelling purposes, either to gather input data for the evaluation of new binder materials or to provide a basis for comparing the model's outcomes. In order to ensure the accuracy of the test measurements and results, the data obtained from the National Project PerfDuB [2] are systematically examined. The variations in composition between different concrete mixes are clearly illustrated in figures to better understand the potential fluctuation in the results. It is important to note that this comparison is solely employed to observe the overall trends associated with each type of concrete. The objective is not to obtain identical results, as the initial compositions of the individual mixes differ.

The experiments were conducted at the CERIB in Epernon. This section primarily focuses on the methodologies employed and the corresponding results obtained. The discussions and conclusions, along with the application of the prescriptive approach (NF EN 206/CN+A2 (2022)) and performance-based approach (FD P18-480 (2022)) to the six different concrete mixes, are presented in Section II.4.

II.2. Concrete mixes and experimental plan

II.2.1. Materials and designations

Six mixes are designed for this work. They are detailed in Table II-1. The technical sheets of the different constituents are shown in Annex 1.

The concrete blends were prepared using a Skako concrete mixer with a maximum capacity of 80L. The mixing procedure remained consistent during the overall plan:

1. Initially, the aggregates were introduced into the mixer and blended for 2 minutes at a rotational speed of 25 rpm. This step aimed to ensure the homogenization of sand and gravel.
2. The motor was then stopped to facilitate the addition of cement(s) and any other necessary components. The mixture was further blended for 2 minutes at a speed of 25 rpm.
3. Water was slowly added to the blend without interrupting the rotation. Prior to this, the plasticizer was mixed with water to ensure an even distribution of the admixture within the mixture.
4. Subsequently, an additional 2 minutes of mixing was carried out at a rotation speed of 50 rpm. After this, the slump measurement was conducted on the fresh concrete. In cases where the desired slump was not achieved, admixture was added to the mixture once again, followed by 1 minute of mixing. The slump measurement was then repeated. This process was repeated a maximum of two times within the scope of this study.
5. Apart from slump measurement, the entrapped air and bulk density were also measured on fresh concrete immediately after pouring it out of the mixer. These measurements facilitated an initial comparison between different batches of the same concrete formulation. The average values obtained from these measurements are presented in Table II-1.

The formulations used in this study all employ identical sand and gravel types. Consequently, the influence of the aggregates on the various concrete mixes should be uniform and disregarded when comparing the concretes for each property. Similarly, the W_{eff}/B_{tot} ratio has been selected to approximate a value of 0.5, and the total binder content is approximately 380 kg/m^3 of concrete. These values have been chosen based on those employed in structures erected nowadays, facilitating a direct comparison between the laboratory findings and those obtained from structures (primarily bridges).
To assert the comparison between field and experimental measurements:

- The second curing class defined by the NF EN 13670/CN (2013) standard is applied, which imposes the gain of 35% of the compressive strength at 28 days prior to demoulding the material.
- The targeted slump falls under the S4 category, as per the requirements of the NF EN 206/CN+A2 (2022). This category is determined by conducting the Abrams cone measurement on fresh concrete. The specified slump for this category ranges from 160 to 210 mm.

It is crucial to clarify the distinction between curing time, referring to the duration prior to demoulding of the sample, and conservation time, denoting the duration of storage before conducting the test. Conservation time includes periods of storage in moist, dry, and external environments (defined subsequently).

To assert the manufacturing quality of the concrete material, entrapped air and bulk density measurements are conducted on fresh concrete.

Finally, the maximal diameter of aggregates is limited to 12 mm. This restriction was decided to accommodate the dimensions of reinforced concrete samples and reduce the experimental burden. The results obtained on reinforced samples were not exploited in this document. It is necessary to note that this value differs from the regular industry practice. The decision to use 12 mm was based on the

inequation $C_{nom} \geq 1.5D_{max}$, which ensures the presence of cementitious paste in the concrete cover and provides more realistic measurements.

The applied nomenclature is close to the one used in the PerfDuB project. It enhances the comprehension of the concrete mix composition and properties upon initial observation. This notation functions as follows:

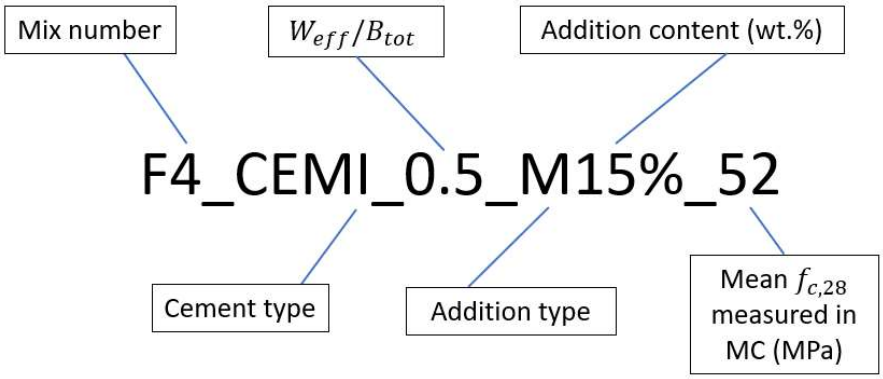

Figure II-1 Example of PerfDuB notation applied to F4.

Table II-1 Compositions of the six concrete mixes defined for the experimental part of the PhD.

N°	1	2	3	4	5	6
Name	F1_CEMI_0.49_55	F2_CEMIII/B_0.49_35	F3_CEMI_0.52_V15%_52	F4_CEMI_0.49_M15%_53	F5_CEMV/A_0.49_51	F6_CEMVI_0.5_48*
Cement type (quantity kg/m³)	CEM I 52,5 N – SR 5 CE PM-CP2 Lafarge (**383**)	CEM III/B 32,5 N-LH/SR CE PM-CP1 NF "SPM" Calcia Rombas (**377**)	CEM I 52,5 N – SR 5 CE PM-CP2 Lafarge (**319**)	CEM I 52,5 N – SR 5 CE PM-CP2 Lafarge (**320**)	CEM V/A (S-V) 42,5 N CE PM-ES-CP1 NF « PMF3 » Calcia Rombas (**377**)	CEM V/A (**187**) + CEM III/B (**187**)
Addition type (quantity kg/m³)	-	-	Fly ash Gardanne Surschiste (k = 0,60) (**56**)	Metakaolin Argicem Argeco (k = 1) (**56**)	-	-
Boulonnais sands 0/4 (kg/m³)	943	929	923	927	930	924
Boulonnais aggregates 4/12 (kg/m³)	870	857	853	855	859	853
Admixture Glenium sky (kg/m³)	1.6**	2.9***	1.3***	3.4**	2.5**	2.0**
W_{eff}/B_{tot}	0.49	0.49	0.52	0.49	0.49	0.5
Slump (mm)	18.7	19.6	20.3	17.8	17	18
Entrapped air (%)	1.6	1.1	1.3	1.4	1.0	1.4
Bulk density (kg/m³)	2384	2365	2364	2360	2378	2351
Paste volume (L/m³)	323	324	320	329	328	329

N°	1	2	3	4	5	6
Name	F1_CEMI_ 0.49_55	F2_CEMIII/B_ 0.49_35	F3_CEMI_0.52_ V15%_52	F4_CEMI_0.49_ M15%_53	F5_CEMV/A_0 .49_51	F6_CEMVI_0.5_ 48*
Clinker (wt.% binder)	99	29	74	74	56	42
Slag (wt.% binder)	0	71	0	0	22	46.5
Fly ash (wt.% binder)	0	0	15	0	22	11
Metakaolin (wt.% binder)	0	0	0	15	0	0
Total carbon footprint ($kg_{CO_2}eq/m^3$)	296	128	255	260	189	158.5
Demoulding time (day)	1	2	1	1	2	3

*This formulation was recomposed using two different cements to obtain an equivalent of CEM VI (S-V) in terms of proportions.
** Glenium sky 537.
*** Glenium sky 841.

The equivalent mortar formulations are designed for evaluating the characteristic compressive strength of the cement and performing the thermogravimetric analysis. The compositions of these mortars are detailed in Table II-2 following the recommended guidelines of NF EN 196-1 (2016) [341].

Additionally, two mortar mixes (M7 and M8) were prepared using CEM II/A-LL. These mortars are also used to determine the portlandite and calcite contents through thermogravimetric analysis. The obtained data from these mixes is utilised to validate the performance of hydration models in Section IV.3.2.3.

Table II-2 Compositions of the eight mortar mixes.

N°	1	2	3	4	5	6	7	8
Name	M1_CEMI_0. 5	M2_CEMIII/B _0.5	M3_CEMI_ 0.5_V15%	M4_CEMI_0. 5_M15%	M5_CEMV/A _0.5	M6_CEMVI_0 .5*	M7_CEMII/A-LL_ 0.5	M8_CEMII/B-M_ 0.5**
Cement type (quantity g)	CEM I 52,5 – - SR 5 CE PM-CP2 Lafarge (**450**)	CEM III/B 32,5 N-LH/SR CE PM-CP1 NF "SPM" Calcia Rombas (**450**)	CEM I 52,5 – - SR 5 CE PM-CP2 Lafarge (**382.5**)	CEM I 52,5 – - SR 5 CE PM-CP2 Lafarge (**382.5**)	CEM V/A (S-V) 42,5 N CE PM-ES-CP1 NF « PMF3 » Calcia Rombas (**450**)	CEM V/A (**225**) + CEM III/B (**225**)	CEM II/A-LL 42.5 R CE CP2 NF Calcia Couvrot (**450**)	CEM V/A (**225**) + CEM II/A-LL (**225**)
Addition type (quantity g)	-	-	Fly ash Gardanne Surschiste (k = 0,60) (**67.5**)	Metakaolin Argicem Argeco (k = 1) (**67.5**)	-	-	-	-
Standard sand 0/2 (g)	**1350**							
W_{eff}/B_{tot}	0.5							

N°	1	2	3	4	5	6	7	8
Name	M1_CEMI_ 0.5	M2_CEMIII/ B_0.5	M3_CEMI_ 0.5_V15%	M4_CEMI_0. 5_M15%	M5_CEMV/A _0.5	M6_CEMVI_ 0.5*	M7_CEMII/A- LL_ 0.5	M8_CEMII/B- M_ 0.5**
Clinker (wt.% binder)	99	29	74	74	56	42	87	72
Filler (wt.% binder)	0	0	0	0	0	0	12	6
Slag (wt.% binder)	0	71	0	0	22	46.5	0	11
Fly ash (wt.% binder)	0	0	15	0	22	11	0	11
Metakaolin (wt.% binder)	0	0	0	15	0	0	0	0

* and ** These formulations were recomposed using two different cements, in order to obtain an equivalent of CEM VI (S-V) and CEM II/B-M in terms of constituents' proportions.

II.2.2. Tests and modelling purposes

All the tests conducted on the various formulations are presented in Table II-3. The primary objective of these tests is, along with the characterization of their durability behaviour, to gather the essential data required for the development of modelling. Consequently, the investigations focus on the hydrologic transfer properties of the concrete materials, including measurement of the porosity accessible to water and liquid permeability. The resistance against carbonation is assessed using both natural and accelerated testing methods, while the ability to restrict chloride ingress is evaluated through natural diffusion and accelerated migration tests.

To provide valuable insights into the material capability to limit the corrosion of embedded steel reinforcement, the measurement of resistivity is also performed. This parameter is also necessary to apply the performance-based approach defined in the FD P 18-480 (2022).

The microstructure was investigated by conducting X-ray diffraction (DRX) and thermogravimetric analysis to determine the types and contents of hydrates present. Gas permeability measurements were also performed to obtain comparative values alongside other experimental parameters.

Lastly, the compressive strength of the various mixtures was measured to assess mechanical resistance and provide a rapid and efficient basis for comparison between different batches of the same mixture.

Most of the tests are carried out within different conservation conditions prior to testing. The specific conditions related to each of the three conservation types are detailed in the subsequent section.

Table II-3 Experimental tests planned on the six formulations defined for the experimental part of the PhD.

Test	Standard	Goal/parameter	Conservation type	Conservation time(s) (day)	Measurement time(s) (day)
Gaz permeability	XP P18-463 (2011)	K_{gaz} (m^2)	Moist, dry and outdoor conditions	90	7, 28, dry
Porosity accessible to water and bulk density	NF P18-459 (2022)	φ_{water} (%), $\rho_{concrete}$ (kg/m^3)	Moist, dry and outdoor conditions	90	-
Cl- migration in non-stationary regime	XP P18-462 (2022)	Chloride migration coefficient D_{rcm} (m2/s)	Moist, dry and outdoor conditions	28, 90, 365	-
Resistivity	XP P18-481 (2022)	Ohmic resistance (Re, Ohm)	Moist, dry and outdoor conditions	1*, 7, 28, 60, 90, 120, 180, 240, 300, 365	-
Compressive strength	NF EN 12390-3 (2019)	f_c (MPa)	Moist, dry and outdoor conditions	1*, 7, 28, 90	-
TGA	-	Portlandite content (hydration monitoring)	Moist condition	7, 28, 90	-
DRX	-	Hydrate types and contents	Moist condition	7, 28, 90	-
Accelerated carbonation	XP P 18-458 (2022)	K_{acc}	Moist, dry and outdoor conditions	90	0, 28, 42, 70
Natural carbonation	NF EN 12390-10 (2018)	K_{nat}	Outdoor and dry conditions	0	365, 730
Weight loss monitoring	[342]	Liquid permeability (K_{liq}, m^2)	Moist, dry and outdoor conditions	90	Monitoring up to 90 days

*Realised directly after demoulding (35% of the 28 days compressive strength reached)

II.2.3. Conservation and pre-conditioning

Three different conservation methods were applied to the samples of the different mixes. The statistical values of the environmental conditions measured during this study are summarized in Table II-4. Having different conservation conditions serves two purposes in this research:

- The first goal is purely experimental and involves measuring the impact of the conservation conditions on hydration and various properties measured in this study. Different results are expected based on the type of binder used.
- The second goal is to gather data for calibrating the models, which allows for a better consideration of concrete quality in relation to the binder type and its conservation. This aspect is often neglected in modelling, despite its significant influence on durability. This is particularly true for concrete with high supplementary cementitious materials (SCMs) contents, which require longer time to complete their hydration.

Table II-4 Statistic values environment conditions for the three conservation conditions.

Parameters	Statistical value	Moist Conservation (MC)	Dry Conservation (DC)	External Conservation (EC)
RH (%)	Average	99	37	80
	CoV (%)	2	19	23
	Percentile 1	97	22	32
	Percentile 99	100	61	100
	Imposed or measured	Imposed	Measured	Measured
T (°C)	Average	20.1	20.3	10.8
	CoV (%)	3.7	2.6	62.1
	Percentile 1	17.4	17.3	-3.1
	Percentile 99	21.8	26.0	27.6
	Imposed or measured	Imposed	Imposed	Measured
Measurement time	Start	11/05/2020	11/08/2021	24/09/2020
	End	11/01/2023	02/07/2022	30/11/2021
Measurement apparatus		Rotronic (HC2-S)	Rotronic (HL-1D-SET)	Weather station (NEW WMS-25-NEMA)

The relative humidity is controlled only for Moist Conservation (MC), while the temperature is controlled for both MC and Dry Conservation (DC). Due to variations in manufacturing periods for different batches of the same concrete mix, the defined conservation conditions of DC and External Conservation (EC) cannot be assumed as constant. This variability may result in differences in the measured values.

The samples in EC were sheltered from rain but exposed to wind. Wind exposure can cause the concrete surface to dry out and affect the hydration process by reducing water content [343]. Consequently, this hydration gradient may have an impact on the overall properties of the samples. The wind direction predominantly originated from the south and west, as influenced by the building's proximity to the storage area. While this aspect is not extensively addressed in this study, it may account for certain observed variations between the results obtained in EC. The samples manufactured for each concrete mix were not exposed to the same wind intensity, and their conservation processes differed accordingly, certainly impacting the measured properties. Furthermore, within the same batch, the samples were subjected to varying wind exposures (some were protected by other samples, while others were directly exposed), resulting in variations in the conservation process of the different samples conserved in EC.

As expected, the values presented in Table II-4 suggest a higher degree of concrete hydration for samples stored in MC as compared to the other two conditions. A lower relative humidity in the DC and EC conditions is expected to have an impact on the hydration process, as well as the lower average temperature in EC. The EC conditions replicate the environmental conditions of a rain-sheltered structure, making it easier to compare laboratory and field measurements.

For the main general results, two sets of concrete samples were produced in two batches for each concrete formulation. The first set was used to determine the porosity accessible to water, the gas permeability, the electrical resistivity, and the chloride migration coefficient. The second set was used to determine the liquid permeability, the accelerated and natural carbonation rates.

The two batches were both manufactured within the same week, with the aim of minimizing variations in conservation conditions between the DC and EC. Hence, it can be reasonably assumed that the samples from both batches underwent similar conservation treatments.

Table II-5 displays the average values of relative humidity (RH_{env}) and temperature (T_{env}) measured during the 90-day conservation period for each concrete mix.

Table II-5 Mean values of relative humidity and temperature measured during the 90 days of conservation.

Mix name	EC		DC	
	RH_{env}	T_{env}	RH_{env}	T_{env}
F1_CEMI_0.49_55	78	6	35	21
F2_CEMIII/B_0.49_35	73	16	40	24
F3_CEMI_0.52_V15%_52	85	12	37	20
F4_CEMI_0.49_M15%_53	91	6	35	20
F5_CEMV/A_0.49_51	89	5	36	21
F6_CEMVI_0.5_48*	71	14	42	24

*This formulation was recomposed using two different cements (50 wt.% of CEM III/B and 50 wt.% of CEM V/A).

A preliminary analysis of the data presented in Table II-4 and Table II-5 reveals that the variability of conditions in DC are comparatively lower than those in EC. As a result, the focus of the next section will primarily revolve around comparing the values obtained from concretes conserved in MC with those obtained from DC.

II.2.4. Carbon footprint computation

The development of new cements incorporating supplementary cementitious materials (SCMs) is associated with an ecological approach. The primary objective of reducing clinker content in the binder is to minimize the carbon footprint of concrete production. Evaluating the environmental impact of a specific mix, particularly the carbon emission resulting from its manufacturing process, has become crucial in the field of structural engineering. Against this backdrop, the advancement in the design approach for reinforced concrete structures, as outlined in the recent standard FD P 18-480 (2022) [301], allows greater flexibility in terms of mix composition for structure designers and construction companies. This approach presents opportunities for reducing carbon emissions, provided that certain parameters meet the threshold values specified in the fascicule (refer to Section II.4.2).

In this study, the carbon footprint of the different mixes was estimated under various assumptions. Firstly, universal values for the carbon footprint linked to the raw materials were utilised (refer to Table II-6). Secondly, the transportation of the components was disregarded due to lack of information.

Table II-6 Carbon footprint ($kgCO_2eq/m^3$) of the different constituents and reference used.

Constituent	Carbon footprint ($kg_{CO_2}eq/m^3$, December 2022)	Reference
CEM I	765	[344]
CEM III/B	325	
CEM V/A – (S-V)	484	
Fly ash	27	[345]
Metakaolin flash	139	[346]
Superplasticizer	1530	[347]
Sand	2.74	[348]
Aggregate		
Water	0.132	[349]

In this study, the selection of binder compositions was also driven by the consideration of the carbon footprint, especially concerning the cements used. When including F3 and F4, the purpose was to assess the influence of fly ash and metakaolin on durability and hydration, while F2, F5, and F6 were included to evaluate the ability of CEM III/B, CEM V/A (S-V), and CEM VI (S-V) to limit carbonation and chloride ingress. The main objective of this research is to enhance the modelling of standardized cements and

binders that comply with current standards, specifically NF EN 206/CN+A2 (2022) and FD P18-480 (2022). Hence, a comparison of the equivalent carbon footprint is conducted to classify each mix relatively to its environmental impact.

Using the values presented in Table II-6, it is possible to calculate the carbon footprint associated with each blend in this experimental plan. These calculated values can be found in Table II-7. The carbon footprint for the F6_CEMVI_0.5_48 blend was determined by considering an average value of the F2_CEMIII/B_0.49_35 and F5_CEMV/A(S-V)_0.49_51 formulations.

Table II-7 Carbon footprint ($kg_{CO_2}eq/m^3$) computed for each formulation of the experimental plan.

Formulation Name	Carbon footprint ($kg_{CO_2}eq/m^3$)
F1_CEMI_0.49_55	296
F2_CEMIII/B_0.49_35	128
F3_CEMI_V15%_0.52_52	254
F4_CEMI_M15%_0.49_53	260
F5_CEMVA_0.49_51	189
F6_CEMVI_0.5_48*	158.5

*This formulation was recomposed using two different cements to obtain an equivalent of CEM VI (S-V) in terms of constituent proportions.

New discussions in the field have recently raised towards defining the carbon footprint associated with a functional unit of a given concrete formulation, rather than only the formulation itself. The second task force (TF2) of the standardization commission AFNOR P18B/GE SBS, which focuses on low carbon solutions, is actively working on this issue. By considering the mechanical properties and structural design, a more comprehensive analysis can be achieved. The optimization of concrete cover is a part of structural design. This approach is further explored in Section II.4.3 following the presentation of durability results, which are essential for determining the optimal design of a component exposed to a specific environment.

II.3. Methods and results

This section presents the different experimental procedures and results obtained on mortars and concretes. The verification of the characteristic compressive strength of the cements declared by the suppliers required the production of mortar as it allows for proper evaluation. Consequently, the same batch of mortar was used to obtain samples for thermogravimetric analysis in order to minimize imprecisions compared to using concrete. Although the manufacture of an equivalent cement paste could have been preferred for this purpose, it was not undertaken. The mortar samples were conserved in water (WC), as it is considered more suitable than MC for the completion of hydration.

The figures depict the average values obtained from three samples. The error bars displayed correspond to the minimum and maximum values obtained when only three results are available for calculating the mean. In cases where more results are provided, the Pearson standard deviation is represented. The variation of the measurements is assessed by computing the Coefficient of Variation (CoV) using Equation II.1:

$$CoV = 100\frac{\sigma_{pearson}}{\mu} \qquad \text{Eq (II.1)}$$

Where $\sigma_{pearson}$ corresponds to the Pearson standard deviation and μ to the average value computed on the different values.

II.3.1. Mechanical resistance

II.3.1.1. Flexural and compressive strength on mortars

To determine the specified strength provided for the cement in the technical data sheet, flexural and compressive strength tests were conducted on mortar samples in accordance with the NF EN 196-1 (2016) [341] standard after 28 days of water immersion. The composition of the eight mortar mixes used is detailed in Table II-2.

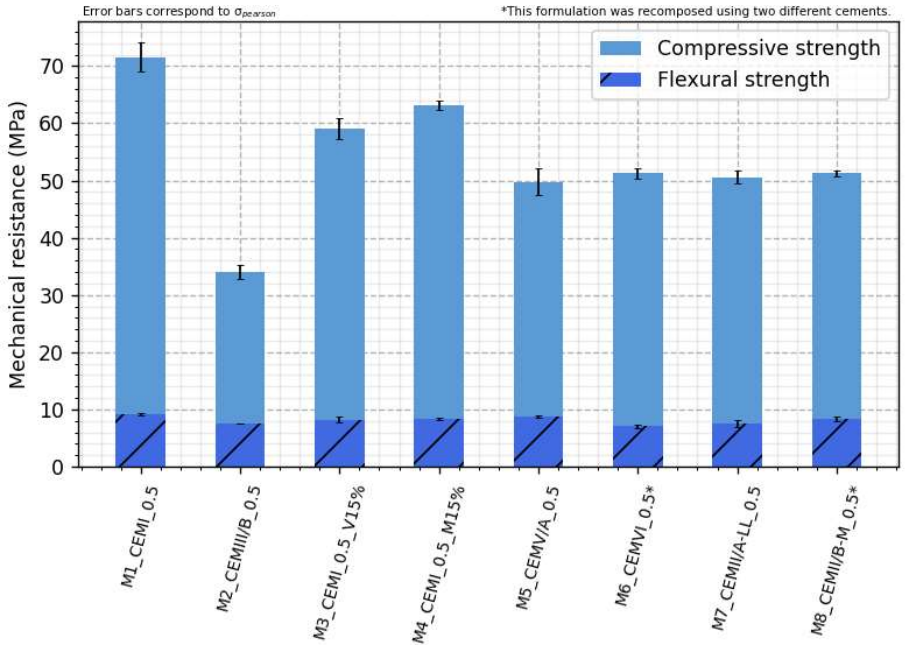

Figure II-2 Compressive and flexural strength measured on mortars after 28 days of Water Conservation (WC).

Compressive and flexural strengths are depicted in Figure II-2. Some variations are visible among the different mix compositions. Notably, the highest mechanical strengths are observed in mix M1, followed by M4 and M3. This outcome was foreseeable due to the utilization of CEM I 52.5N in the production of these mixes, while the remaining cements possess characteristic strengths of 42.5 MPa or 32.5 MPa. Consequently, formulations based on CEM I 52.5N are expected to exhibit superior final mechanical resistance, even with the inclusion of 15 wt.% metakaolin and fly ash. Mixes M5 and M7 consist of CEM V/A 42.5 N and CEM II/A-L 42.5 R, respectively, while mix M2 employs a CEM III/B 32.5 N cement. Hence, this disparity in results can be attributed to the specific cement types employed in each formulation.

However, mixes M6 and M8 were formulated using two types of cement each. Two cements with a characteristic strength of 42.5 MPa (N and R) are used for M8, which justifies the obtained compressive strength value, similar to that of M5 and M7. In contrast, the M6 mix is composed of CEM III/B 32.5 N (used for M2) and CEM V/A 42.5 N (used for M5). The compressive strength achieved is equivalent to that of M5, M7, and M8, rather than falling between M2 and M5 as expected. One possible explanation for the increased potential mechanical resistance could be the difference in slag hydration between M2 and M6. Slag hydration requires an activator, typically the clinker (which forms portlandite) in the case of slag-based concrete. In the M2 mix, the clinker content is limited to 29 wt.%, while in M6, the CEM V/A cement contributes to a total clinker content of 42 wt.%. As a result, the pozzolanic and latent hydraulic additions content in M2 exceeds that of M6. Therefore, if the clinker content in M2 is insufficient to facilitate the hydration of all the slag, M6 provides a higher hydration potential. A higher compacity of the granular skeleton could also justify the higher mechanical resistance of M6 compared to M2, potentially due to the difference of fineness of the two cements used.

Only a few differences are observable in the bending test. However, it appears that mixes M2 and M6 result in lower flexural strength. This suggests that despite an increase in compressive strength for M6, the flexural strength remains lower than the mixes utilizing cement 42.5. The highest values are achieved with M1, attributed to the use of cement with a characteristic resistance of 52.5 MPa. All cements exhibit a normal hardening time denoted by the letter N, except for the CEM II/A-LL cement utilised which has a faster hardening time (R). However, this aspect does not impact the results obtained at 28 days.

The standard NF EN 197-1 (2012) [82] is used to compute the characteristic values (x_c) for the compressive strength with the following Equation II.2. The values obtained are compared to the threshold values of 32.5 MPa, 42.5 MPa and 52.5 MPa of the technical sheets in Figure II-3.

$$x_c = \bar{x} - \sigma\, k_A \qquad \text{Eq (II.2)}$$

Where $\bar{x}$ is the average value, σ the standard deviation and k_A the acceptability constant equals to 2.4 (and corresponding to a percentile of 5% according to the NF EN 197-1 (2012), when 20 measurements are realised).

The application of this method requires a minimal of 20 measurements. In the present study, only 6 measurements were realised for each mortar mix. Hence, the results presented below cannot be considered statistically significant.

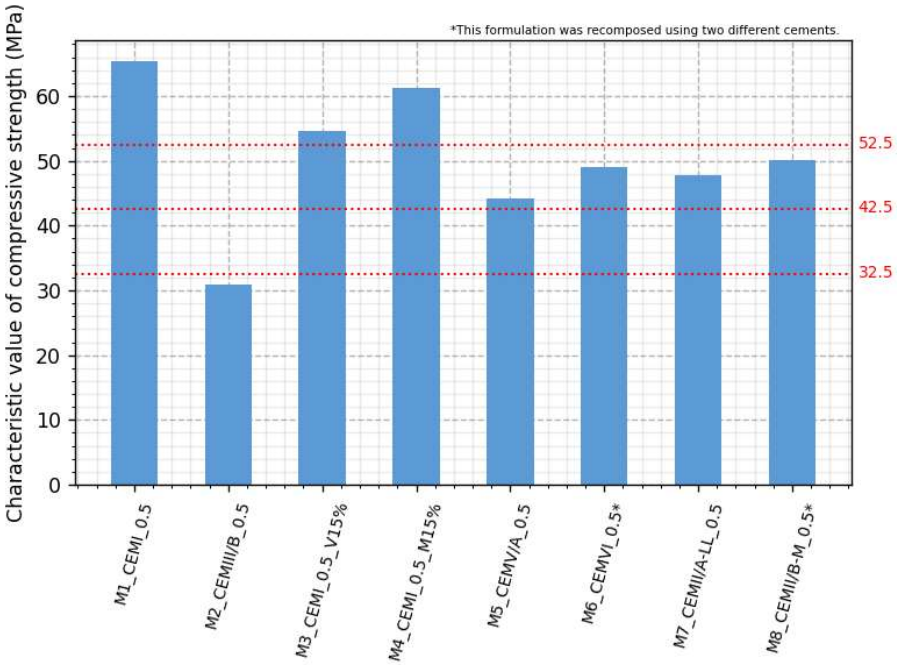

Figure II-3 Characteristic compressive strength measured on mortars after 28 days of water conservation according to the NF EN 197-1 (2012).

Three mixes comply with the requirement, namely M1 (CEM I 52.5 N), M5 (CEM V/A 42.5 N), and M7 (CEM II/A-LL 42.5 R). However, the specified characteristic resistance of 32.5 for M2 (CEM III/B 32.5 N) is not met using this test. Even the characteristic values obtained are not statistically reliable (6 measurements are not enough to define adequately the characteristic value), the results could highlight an issue regarding this latter cement. This discrepancy could be attributed to either a defective batch of cement or manufacturing issues during the production of these mortars.

II.3.1.2. Compressive strength on concrete

Compressive strengths (f_c) were measured for each concrete mixture under different conservation conditions, in accordance with the guidelines provided by NF EN 12390-3 (2019) [350]. The compressive

strength tests were conducted on 100 mm cubic samples at either 1 or 2 days, depending on the demoulding date. Furthermore, compressive strength evaluations were performed on 110/220 mm cylinders at 7, 28, and 90 days of conservation. The primary objective of these tests is to establish comparative values for various batches of the same formulation, thereby assessing the resemblance in composition and properties.

The values are adjusted to consider the influence of geometry on the compressive strength (R_c) following the recommendations of NF EN 206/CN (2022) [19].

Figure II-4 illustrates the average f_c values obtained from these samples after a 28-day conservation period. These values are calculated from different batches of samples manufactured for the study. It is important to note that certain formulations may exhibit higher variation in compressive strength under exterior and dry conservation conditions, as discussed in Section II.4.1.

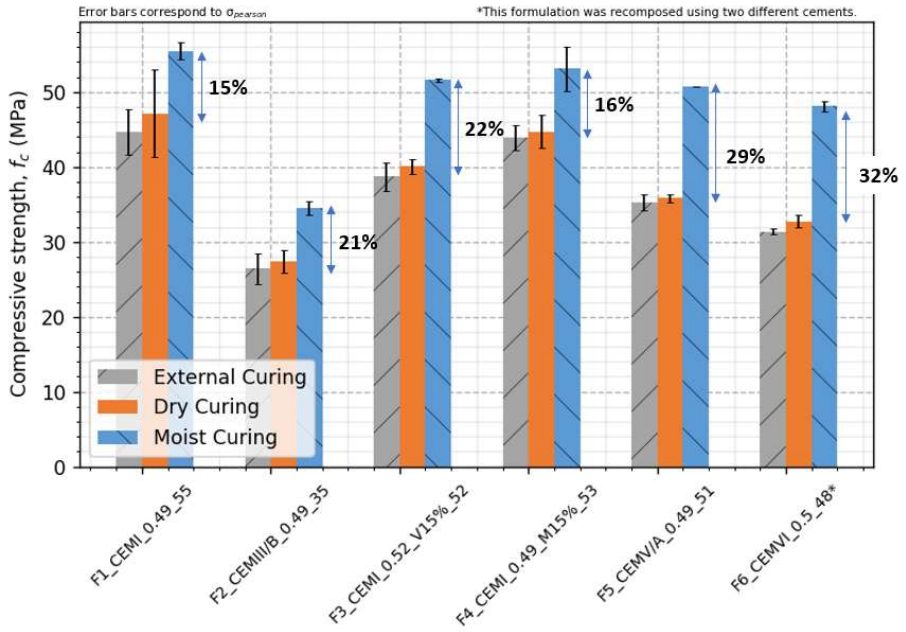

Figure II-4 Average compressive strength f_c values obtained for each formulation and conservation condition after 28 days.

In general, it is observed that moist conservation leads to higher values for f_c. Dry conservation yields slightly higher average values than exterior conservation, although DC is not always more favourable for hydration than EC.

The difference between the values obtained in moist conservation and the other two conservation methods varies for different mixes. Higher differences are obtained for F5 and F6, which is likely due to a high content of pozzolanic addition. This suggests that, even though water does not directly participate in the pozzolanic reaction, it is necessary for dilution, motion, and reaction of the different reactants. Thus, with a lesser amount of water in the concrete material, the hydration of slag, metakaolin, and fly ash is limited, leading to a limited increase in mechanical strength. This difference in gaps observed between F3 (22%) and F4 (16%) could also indicate that fly ash requires more water than metakaolin in these conditions. This may be attributed to a slower hydration kinetic of fly ash compared to metakaolin [94], [95], [291]. However, the difference between the two values is low, and other factor such as the different values of W_{eff}/B_{tot} could also be responsible, complicating the analysis.

In the case of F2, the difference in conservation between MC and the other two conditions remains relatively low, despite the high slag content. This can be attributed to the insufficient presence of portlandite, which becomes the limiting factor in the slag addition's hydration process. Another

explanation is that the mechanical resistance of this concrete is less controlled by the cementitious matrix, leading to a lesser sensitivity to the conservation conditions.

The overall trend of the values obtained in MC conditions is similar to the ones obtained in the previous Section II.3.1.1, which focused on mortars. Figure II-5 illustrates the variations in f_c for all mixes conserved under MC conditions.

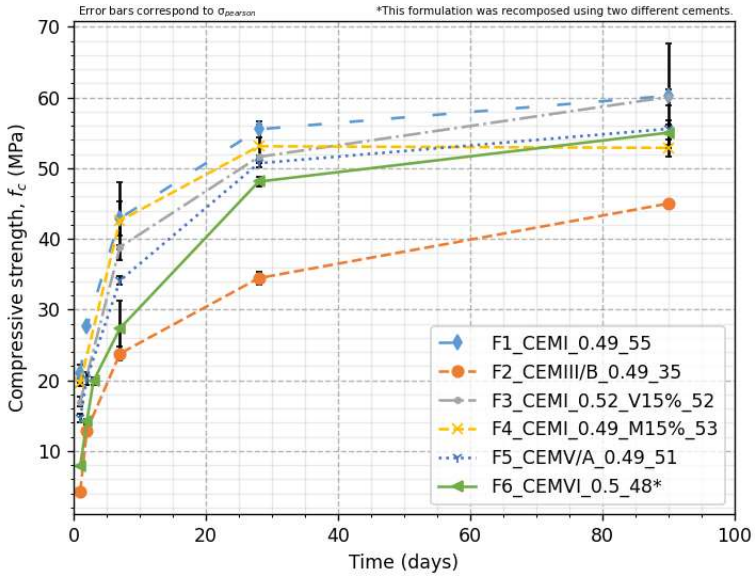

Figure II-5 Compressive strengths evolutions for the different mix stored in moist conservation conditions.

Figure II-5 shows a slower hydration of the fly ash in comparison to the metakaolin (F3 and F4, respectively), with the F3 values surpassing F4 after 90 days of moist conservation. This further confirms that fly ash requires longer exposure to water, as depicted in Figure II-4. Moreover, the high reactivity rate of metakaolin is already demonstrated in the literature [72], [94].

In general, formulations with lower clinker content and without specific chemical admixture (set accelerator) exhibit a slower increase in mechanical strength. This is particularly manifest in F2 and F6, where a noticeable difference can be observed between the two mixes after 7 days of conservation. Notably, the compressive strength value of F6 almost reaches that of F5 after 28 and 90 days of conservation. As mentioned in Section II.3.1.1, the improvements seen in F6 compared to F2 are likely attributable to a higher portlandite content, enabling the hydration of the slag introduced by the 50 wt.% of CEM III/B. It would be valuable to investigate if F2 can catch up with F6 after a longer conservation period.

It is well known that the conservation conditions play a significant role in the development of mechanical properties, particularly in concretes with low clinker content [351]. This correlation is glaring in Figure II-4 with the difference in compressive strength obtained between DC and MC for the concrete mixes F6 (42.5 wt.% clinker, 32%), F5 (56 wt.% clinker, 29%), F3 (85 wt.% clinker, 22%) and F1 (100 wt.% clinker, 15%). It can also be seen in Figure II-5, that mixes with lower clinker content require higher conservation time to achieve maximum compressive strength.

Subsequently, the results obtained are compared to several similar mixes of the PN PerfDuB [2] , as depicted in Figure II-6 for 28 days of DC and Figure II-7 for 28 days of MC.

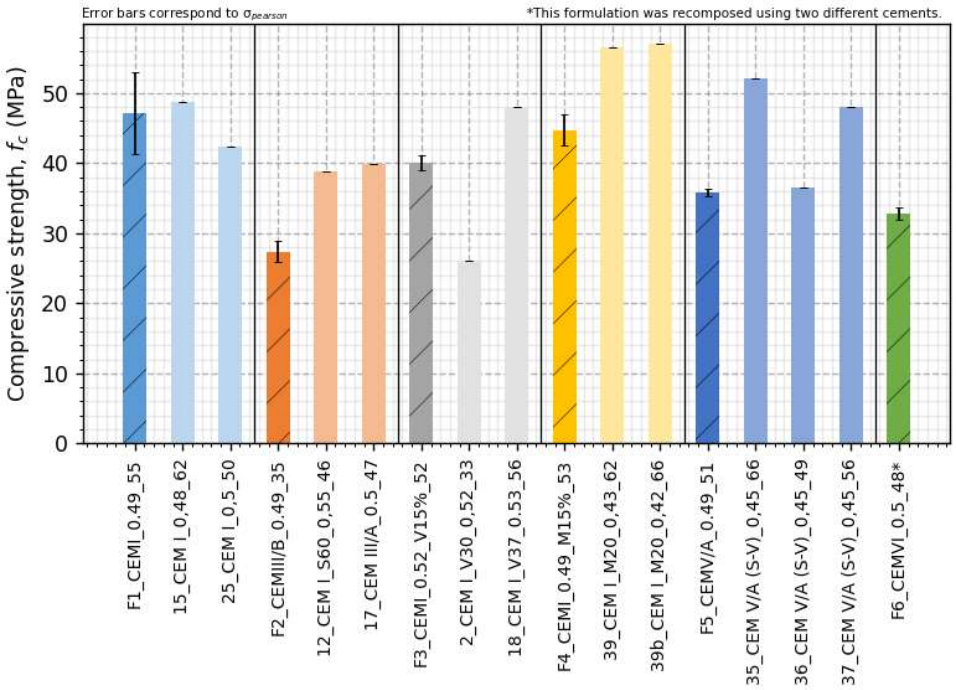

Figure II-6 Compressive strength values obtained after 28 days in dry conservation for the PhD mixes and the closest formulations presented in the National project PerfDuB.

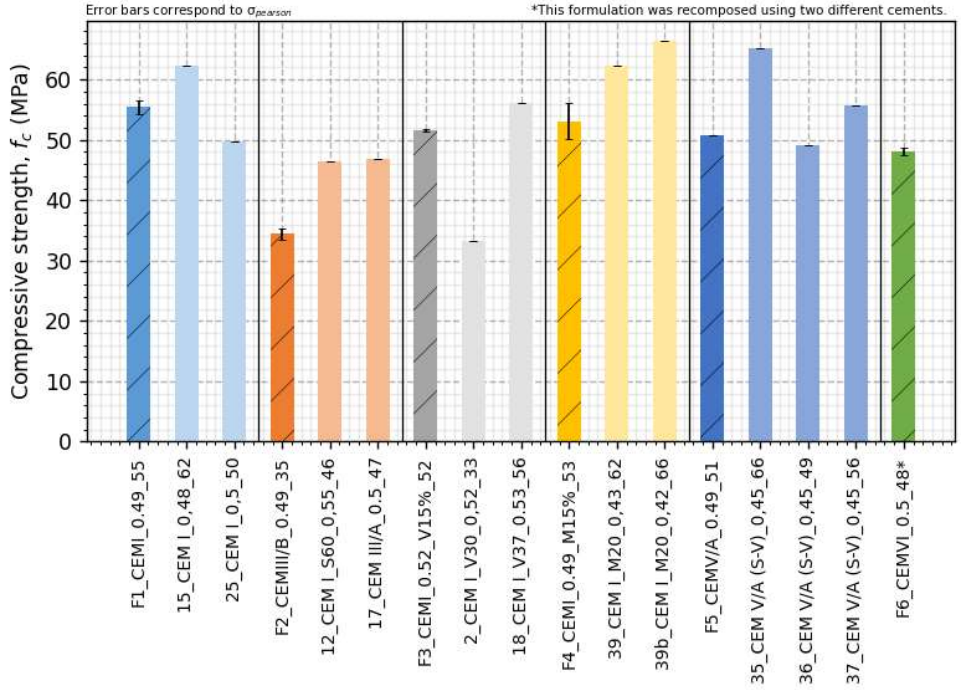

Figure II-7 Compressive strength values obtained after 28 days in moist conservation for the PhD mixes and the closest formulations presented in the National project PerfDuB.

Close similarities clearly appear between the formulations employed in this work and those utilised in the PerfDuB project. The F2 mix exhibits reduced mechanical strength, likely attributed to the higher slag content and the inherent lower characteristic strength of the cement used (a CEM I 52.5 and CEM III/A 42.5 for formulations 12 and 17, respectively, in the PerfDuB project). The low resistance observed in F4 and F5, when compared to the PerfDuB concretes, can be due to a higher water-cement ratio. Lastly, the mechanical strength of mix 2 in PerfDuB is lower than F3, primarily related to the greater fly ash content.

For the calculation of characteristic strengths and classification of each mix, the mean compressive strength (f_c) is utilised in Section II.4.2, according to the prescriptive approach outlined in the NF EN 206/CN+A2 (2022).

II.3.2. Porosity accessible to water

The assessment of water-accessible porosity (φ, %) was conducted on the six different concrete formulations after a 90-day conservation period. The procedure used was in accordance with the NF P18-459 (2022) standard [352].

The porosity accessible to water plays a significant role in assessing concrete durability, serving as relevant indicator, even if its pertinence is controversial. It influences the diffusion of pollutants and offers insights into the material's water transfer capabilities. Furthermore, this property can be utilised to estimate the concrete's resistance to carbonation and corrosion (divided with the volume fraction of paste, F_{paste}), as outlined in the performance-based approach described by FD P 18-480 (2022). Therefore, it is crucial for determining the exposure classes that the different formulations presented in this study can withstand.

Values obtained for the three conservation conditions are represented in Figure II-8.

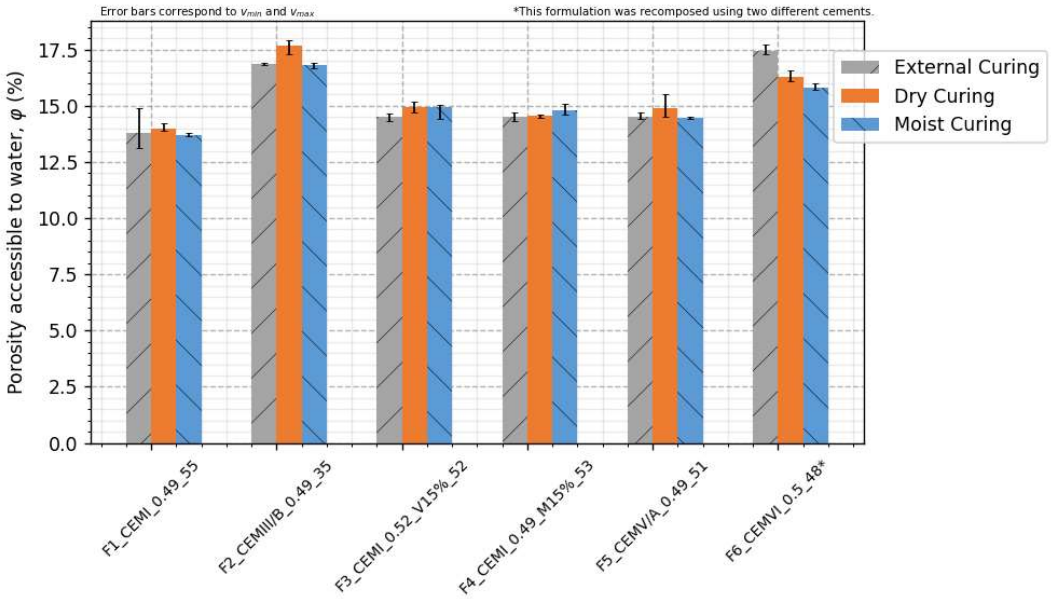

Figure II-8 Values of porosity accessible to water obtained for the different formulations and conservation conditions.

The results obtained reveal different trends when compared to the mechanical resistance data. The conservation condition does not exert a substantial influence on the water-accessible porosity, even for mixtures with a high proportion of mineral additions. One reason is that the porosity provided by the aggregates is unaffected by the conservation conditions, explaining in part the low difference between the different treatments. It is noteworthy that only F6 exhibits a reduced level of water-accessible porosity in the specimens conserved in MC.

The Figure II-8 displays higher values of porosity accessible to water for the mixes F2 and F6. This can be attributed to the use of CEM III/B cement and a lack of slag hydration. The paste volumes of the different mixes are close and certainly not responsible for this deviation (refer to Table II-1). The decrease in water accessible porosity in MC for F6 may be a result of the combined effect of water and clinker presence, allowing for greater slag hydration. Additionally, the type of cement used in F2 and F6, which has a lower characteristic strength compared to the other cements used, may contribute to the higher values observed. On the other hand, F1 exhibits slightly lower values, which could be attributed

to the higher fineness of the cement and the absence of mineral addition for clinker replacement in its composition. These measured values are utilised in Section II.4.2 to classify the concrete according to the FD P18-480 (2022) for the XC exposure classes.

Figure II-9 illustrates the comparison of the results obtained in the six formulations with the PerfDuB project mixes.

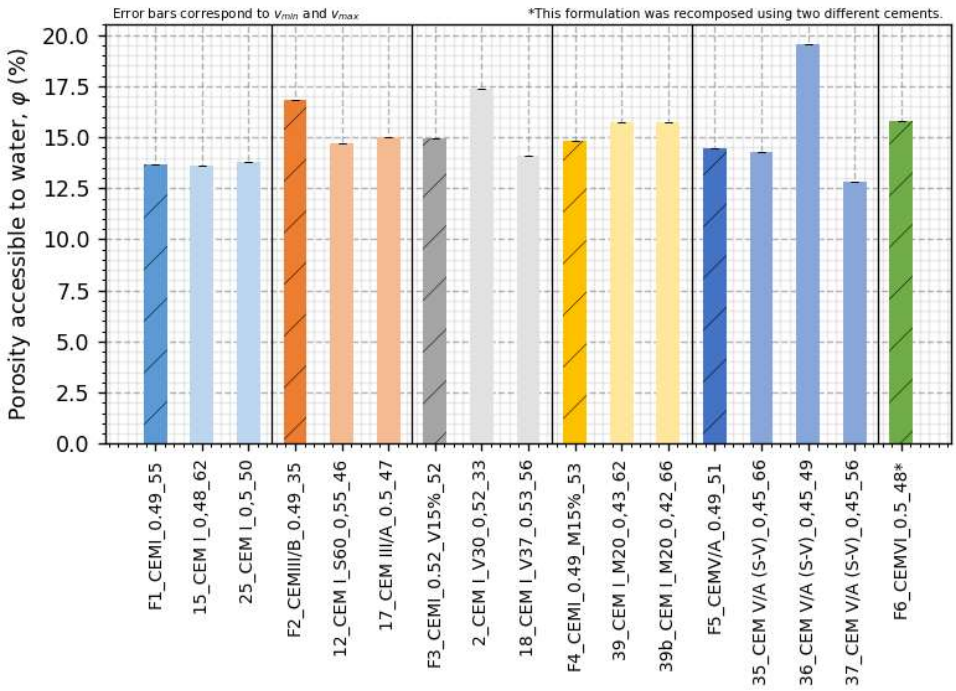

Figure II-9 Comparisons of the values of porosity accessible to water obtained in MC with the PhD and PerfDuB mixes.

Most of the tested mixtures exhibit similar values of porosity accessible to water. An exception is observed in the case of F2, which displays a higher value due to a lower cement fineness and a lower clinker content (resulting in a higher slag quantity). The higher values of porosity observed in mixes 2 and 36 of PerfDuB in comparison to their respective mixes F3 and F5 can be due to the following factors:

- Mix 2 has a granular skeleton of lower quality and a higher fly ash content, leading to increased porosity accessible to water compared to F3.
- Mix 36 of PerfDuB contains aggregates with higher water absorption coefficient compared to F5, resulting in an increase in the overall porosity accessible to water.

II.3.3. Gas permeability

Gas permeability is measured on the six concrete formulations for each of the three conservation conditions. The testing procedure utilised follows the guidelines outlined in XP P 18-463 (2011). This section only presents the results obtained from the dry samples (K_{dry}, dried at 105°C until reaching a constant weight). This value corresponds to the intrinsic permeability of the material (measured with a pressure of 8 Bar). Figure II-10 illustrates the values obtained from the six different mixes under the three different conservation conditions.

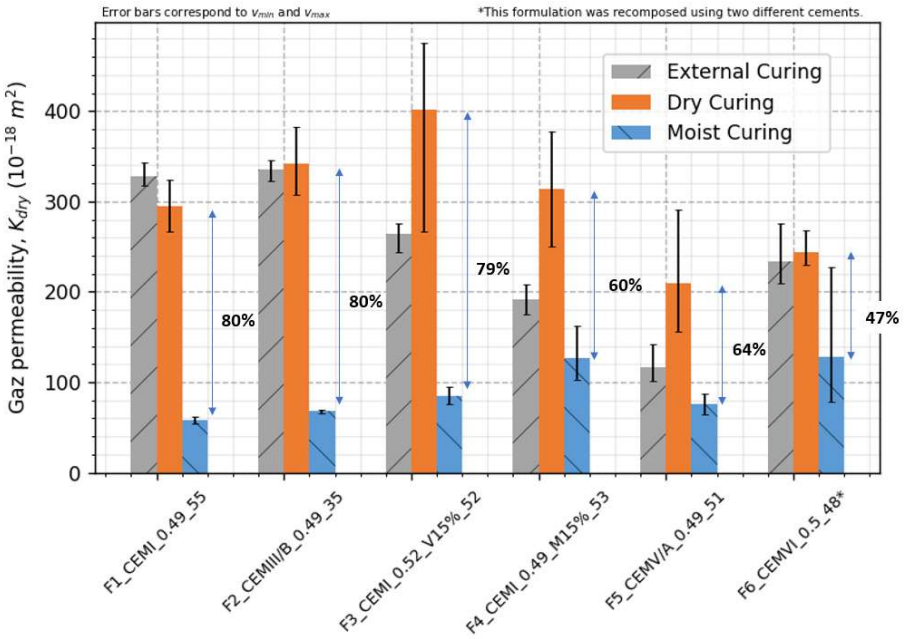

Figure II-10 Gas permeability values measured on dry concrete (K_{dry}) in each conservation condition.

The observed uncertainties in gas permeability measurement surpass those obtained for water-accessible porosity and mechanical strength. This aspect raises doubts regarding the actual utility of this measurement technique. Additionally, this test was not taken into consideration in the FD P 18-480 (2022), for similar reasons.

The observed differences between the three conservation conditions demonstrate that MC consistently leads to lower gas permeability values compared to DC and EC across all mixes. Notably, the disparity between MC and DC is more pronounced for mixtures F1, F2, and F3, which contrasts with the compressive strength results depicted in Figure II-4. In the figure, the disparity was more significant for mixtures F5 and F6 compared to the remaining mixtures. This discrepancy suggests that the impacts of clinker, slag, metakaolin, and fly ash hydration on the small porosity (inaccessible to water), tortuosity and the connectivity degree of the pores differ from their influence on mechanical strength.

The environmental conditions associated with DC and EC, as indicated in Table II-5, may explain certain variations. Firstly, the higher mean relative humidity in EC, to which F3, F4, and F5 have been exposed (85%, 91%, and 89% respectively), favours the hydration and then lowers the gas permeability compared to the results observed during dry conservation.

The results of F6, which consists of a mixture of CEM III/B and CEM V/A, are not within the range observed for F2 and F5. Perhaps the outcomes could be attributed to varying levels of hydration or the arrangement of particles. This discrepancy could also be attributed to an error in the testing procedure, explaining the significant difference between the minimum and maximum values.

Globally, gas permeability appears more influenced by the conservation conditions than the porosity accessible to water indicator. These results could signify that the conservation conditions have a greater impact on certain aspect of the microstructure (small scale microstructure, tortuosity, pore connectivity) than on the overall value of water accessible porosity (certainly more controlled by the composition of the concrete mix). The effect on the tortuosity of water porosity is investigated in Section II.3.4 by determining the liquid permeability through weight loss monitoring.

However, it is important to note that the initial state of the samples just before testing varied depending on the conservation method employed (EC, DC, or MC). Despite the pre-conditioning for this test, it is

likely that the values obtained for the parameter K_{dry} were influenced by this aspect. Therefore, it could be a contributing factor influencing the results and exacerbating the difference between MC and the other conservation methods. In addition, the concrete material is likely to develop internal cracks if it is completely dried out, which also explains the higher values observed in DC and EC samples.

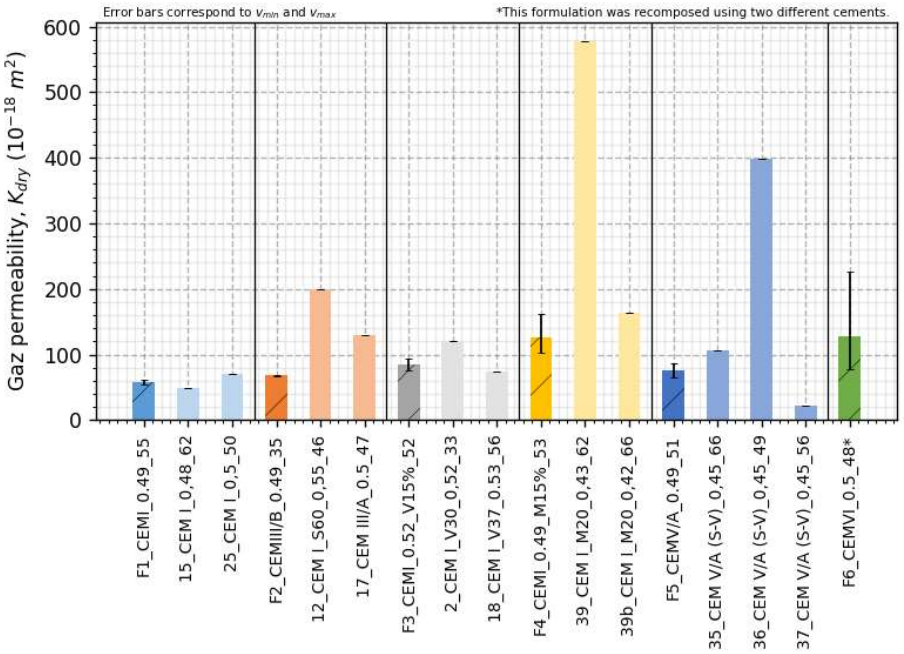

Figure II-11 Comparisons of the values of gas permeability of dry concrete obtained in MC for the PhD and PerfDuB mixes.

The comparison between the results from the PerfDuB project and the current study is presented in Figure II-11. The obtained results indicate lower values for the mixes of this study, on average. The higher value obtained for mix 39 can be attributed to the use of a different type of metakaolin compared to F4 and 39b. It could also be the result of internal cracking, explaining the difference of magnitude order, like mix 36. Differences between mix F5 and mix 36 can also be attributed to the lower quality of aggregates used in the PerfDuB mix. Of particular interest is the lower value obtained for mix F2 compared to its equivalent PerfDuB mixes 12 and 17. Conversely, the mechanical strength and water-accessible porosity results exhibit an opposite trend, suggesting a distinct behaviour of the microstructure in binders with a high slag content and low clinker content.

II.3.4. Mass loss monitoring

The test described in this section aimed at estimating the liquid permeability using the SDReaM-Crete model (refer to Section III.5.1). The experimental procedure was conducted according to previous studies [7], [342]. It involved saturating the samples with water and evaluating the unidirectional permeability under controlled environmental conditions.

After a conservation period of 90 days, cylindrical samples measuring 110/50 mm were extracted from a cylindrical sample of 110/220 mm. To promote unidirectional diffusion of water, an aluminium scotch coating was applied to circular face of the cylindrical samples. The samples were then saturated following the same pre-conditioning procedure described in the NF P 18-459 (2022) standard [352]. Following a 44-hour exposure to water under vacuum, the samples were placed in an environment identical to the one used for Dry Conservation (DC). Temperature and relative humidity were monitored using a Rotronic apparatus (HL-1D-SET). Daily weight measurements were taken to determine the weight loss resulting from water evaporation. Figure II-12 illustrates the average values obtained from three samples for each mixture and each conservation treatment.

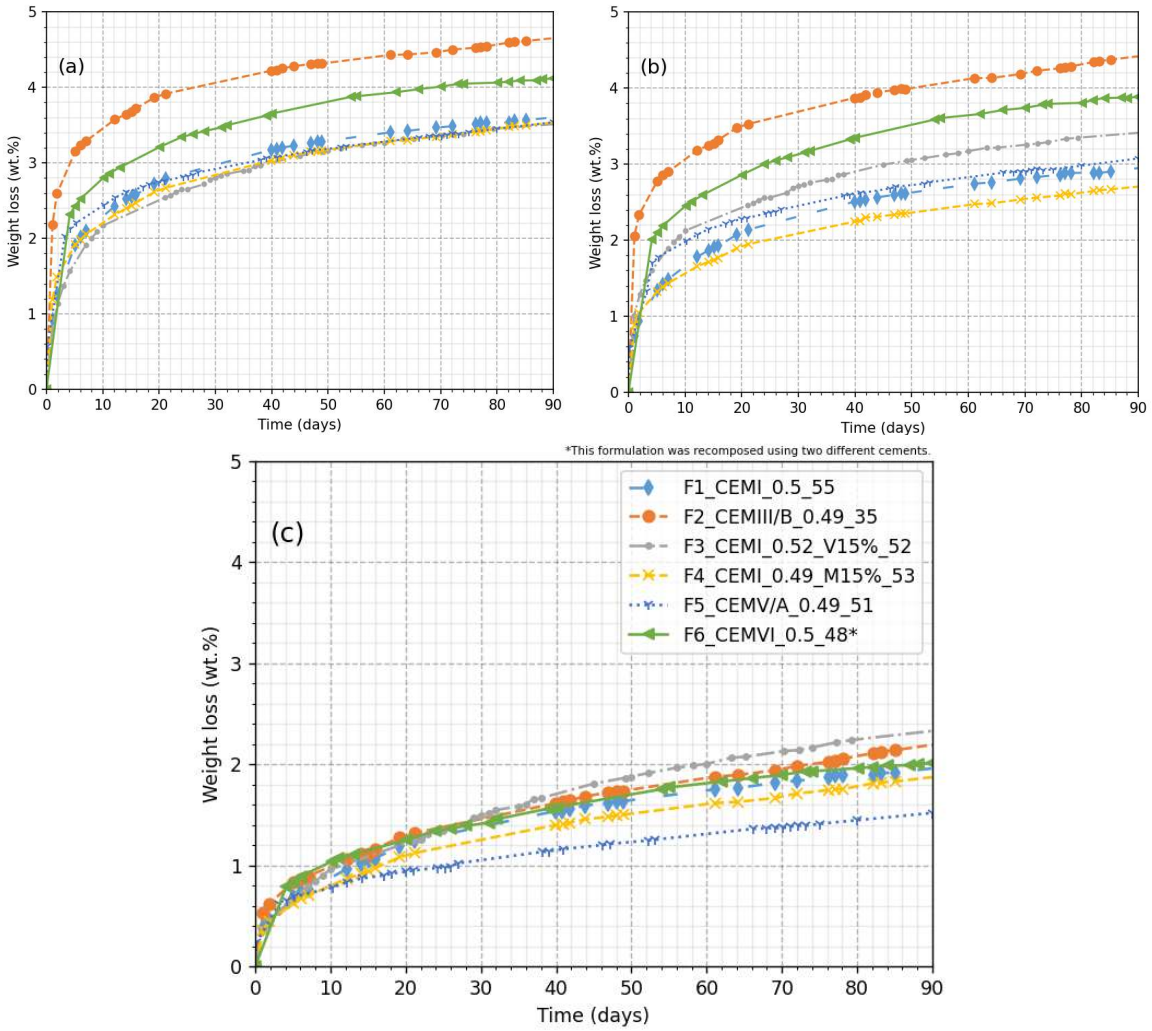

Figure II-12 Average value of the mass loss monitoring for the samples conserved in DC (a), EC (b) and MC (c).

The statistical values of relative humidity and temperature measured throughout the 90-day mass monitoring period are presented in Annex 2. Notably, the temperature recorded during the monitoring of F3 exhibited a lower average compared to the other mixes. This variation is likely to have resulted in a slower drying rate of the sample and a reduced apparent liquid permeability.

The monitoring results depicted in Figure II-12 reveal a significant distinction between the concretes conserved in MC and the other two conditions. As a fundamental observation, conservation conditions have a substantial impact on the hydrologic transfer capacity of the concrete material. This finding differs from the outcomes of water-accessible porosity obtained in Section II.3.2. It may suggest that although conservation conditions exert minimal influence on the overall macro porosity value, their effects on the porous network, as indicated by parameters like tortuosity or pore connectivity degree, give rise to distinct water transportation capability.

The weight loss differences observed after 90 days of monitoring between the samples conserved in MC and DC are presented in Table II-8. The largest differences (both absolute and relative) were observed in the mixes containing higher amounts of mineral additions (F2, F5 and F6). This suggests that the conservation conditions play a significant role in the hydrologic transfer properties of such binders.

For DC and EC, it is obvious that F2 exhibits the highest liquid permeability, resulting in quicker weight loss, followed by F6. This can be attributed to the usage of CEM III/B cement, which requires longer exposure to a wet environment for complete hydration. Additionally, the higher porosity accessible to

water in such mixes leads to a higher water content loss (refer to Figure II-8). In contrast, in MC, the differences among the various mixes are less pronounced, indicating a more uniform microstructure and likely a higher tortuosity compared to DC and EC.

Table II-8 Difference of weight loss after 90 days of drying obtained between MC and DC.

Mix name	F1_CEMI_ 0.49_55	F2_CEMIII/B_ 0.49_35	F3_CEMI_0.52 _V15%_52	F4_CEMI_0.49_ M15%_53	F5_CEMV/A_ 0.49_51	F6_CEMVI_0.5 _48*
Relative difference between MC and DC (%)	45	53	33	47	57	51
Absolute difference between MC and DC (wt.%)	1.64	2.45	1.16	1.66	2.02	2.10

*This formulation was recomposed using two different cements.

The comparison of mixes F1, F3, and F4 can yield different conclusions regarding the influence of fly ash and metakaolin on liquid permeability. Firstly, the curve of F4 consistently remains below that of F1 and F3, irrespective of the conservation conditions. This implies that the addition of metakaolin (at a 15 wt.% content) reduces the overall water permeability of the material. Secondly, the analysis of F3 is slightly more intricate. Apart from the DC conditions, the weight loss values of F3 are always higher than those of F1. Additionally, the test environmental conditions of F3 exhibit a higher average relative humidity and a lower average temperature compared to the test conditions of F1 and F4 (refer to Annex 2). This suggests that under the same conditions, the weight loss of F3 would likely have been higher than that of the other two mixes. Consequently, fly ash likely causes an increase in water permeability for this particular composition.

Finally, a low water permeability value can be observed for the F5 mix, particularly in the case of the samples conserved in MC. This could be attributed to the environmental conditions, as a higher mean relative humidity value was recorded during the test on F5 compared to the other mixes.

The results and measurements obtained under these conditions are utilised in Section III.5.1 for the purpose of modelling hydrologic transfer and determining the water permeability parameter k_{liq}.

II.3.5. Accelerated carbonation

Accelerated carbonation tests were conducted according to the XP P18-458 (2022) standard recommendations [353]. Cylindrical samples 11 cm diameter x 22 cm length were halved after a 90-day conservation period. To assure a radial diffusion of CO2, aluminium scotch was applied to the flat surfaces. Preconditioning involved drying the samples at 45°C for 14 days, followed by a 7-day exposure to laboratory conditions (65% relative humidity, 20°C). It is important to note that samples conserved in DC were not immersed in water for 48 hours prior being placed in the heat chamber. As a result, the initial saturation level of the concretes differed between DC and MC. This aspect undoubtedly affects the carbonation rate and must be taken into consideration.

The carbonation depth for t = 0 day was assessed on one cylinder, while the remaining samples were placed in a carbonation chamber with an atmosphere containing 3% CO_2, 65% RH, and 20°C. Subsequently, the carbonation depth was measured on three samples at specific time intervals: 28, 42, and 70 days. The assessment of carbonation depth was conducted using phenolphthalein and following the methodology outlined in XP P18-458 (2022).

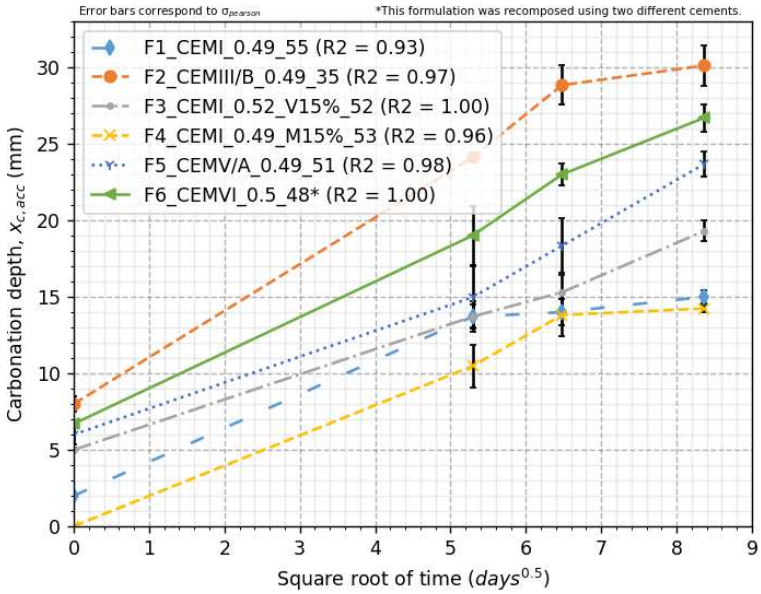

Figure II-13 Carbonation depth vs. square root of time for the different mixes conserved in DC.

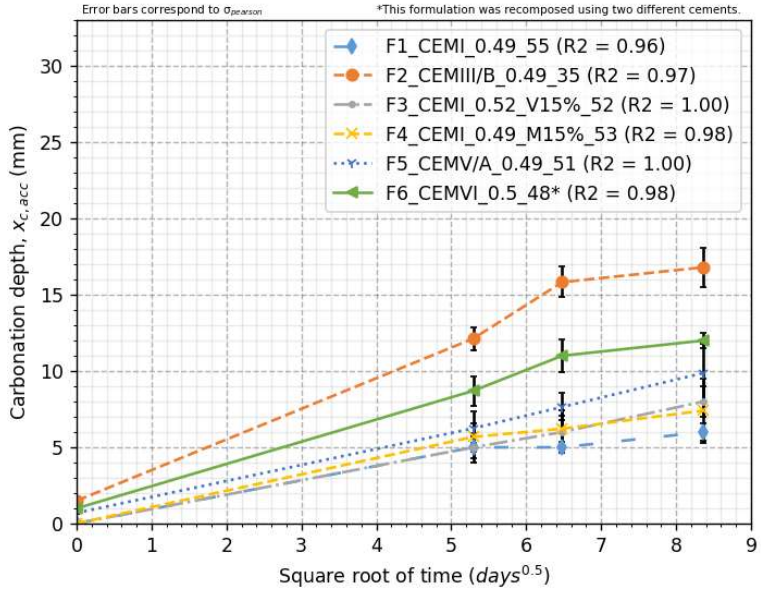

Figure II-14 Carbonation depth vs. square root of time for the different mixes conserved in MC.

The carbonation depth of the various samples is presented in Figure II-13 and Figure II-14 for DC and MC, respectively. The carbonation rate is determined through regression analysis, assuming that the kinetics of carbonation is proportional to the square root of time. The regression results can be found in Table II-9. It is noteworthy that all determination coefficients (R2) exceed 0.92, confirming the goodness of this assumption.

Table II-9 Carbonation rate K_{acc} (mm.day-0.5) obtained by regression for MC and DC.

Mix name	F1_CEMI_0.49_55	F2_CEMIII/B_0.49_35	F3_CEMI_0.52_V15%_52	F4_CEMI_0.49_M15%_53	F5_CEMV/A_0.49_51	F6_CEMVI_0.5_48*
K_{acc}, MC (mm.day$^{-0.5}$)	0.79	1.93	0.95	0.91	1.09	1.38
R2	0.96	0.97	1.00	0.98	1.00	0.98
K_{acc}, DC (mm.day$^{-0.5}$)	1.65	2.8	1.68	1.82	2.05	2.42
R2	0.93	0.97	1.00	0.96	0.98	1.00
Relative difference (%)	52	31	43	50	47	43
Absolute difference (mm.day$^{-0.5}$)	0.86	0.87	0.73	0.91	0.96	1.04

*This formulation was recomposed using two different cements.

The results presented in Table II-9 demonstrate that, irrespective of the conservation treatment applied, the carbonation rates are significantly lower for concretes based on CEM I. This can be attributed to the higher quantity of clinker and content of portlandite, which is the predominant hydrate species in concrete enhancing the resistance to carbonation (as discussed in Section II.3.9). The sequence of mixtures in terms of carbonation rate corresponds to the ranking of the added components. Mix F5, composed of 22 wt.% slag and 22 wt.% fly ash, exhibits the fourth highest carbonation resistance. It is followed by F6, composed of 11 wt.% fly ash and 46.5 wt.% slag, and F2 with 71 wt.% slag.

Carbonation rate is a property of concrete that is affected differently by conservation conditions in comparison with other parameters such as liquid permeability and compressive strength. The use of MC (moist conservation) seems to have a similar effect on carbonation for CEM I-based concretes (F1, F3, F4) and mixes with higher amounts of pozzolanic or latent hydraulic additions (F2, F5, F6). The differences in carbonation rates, as shown in Table II-9 , range from a reduction of 0.73 to 1.04 mm.day$^{-0.5}$ between dry conservation and moist conservation. Among these mixes, the F6 mix exhibits the greatest improvement, indicating that it has a higher potential for hydration compared to the F2 mix due to a higher clinker content, allowing for greater hydration of the slag from the CEM III/B. However, it should be noted that the carbonation rate (K_{acc}) is calculated by excluding the initial carbonation depth measured after preconditioning. Therefore, in the case of DC, where natural carbonation occurs at a faster rate than in MC, the concrete materials are already affected before the start of the test.

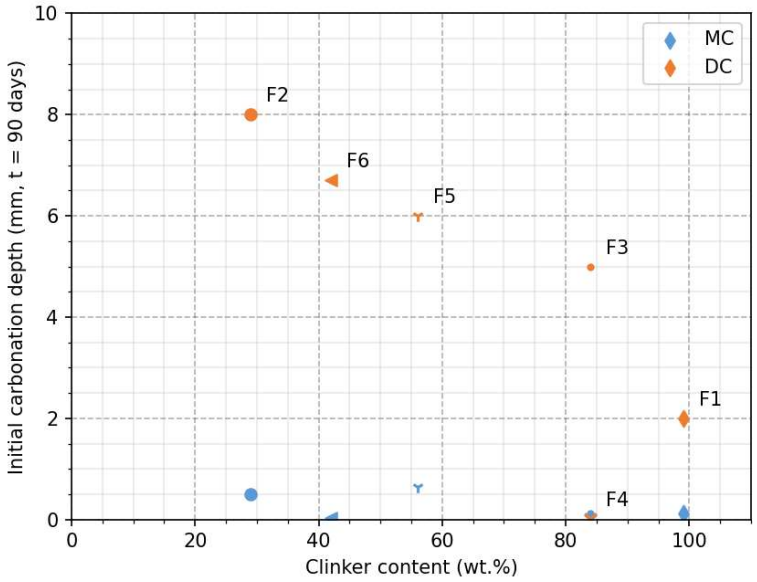

Figure II-15 Initial carbonation depth vs. clinker content of samples conserved in MC and DC.

The initial carbonation depths assessed are presented in Figure II-15 as a function of the clinker content. It is evident that, regardless of the binder composition, samples stored in MC consistently display an initial carbonation depth close to 0 mm. In contrast, a clear trend emerges for concrete stored in DC. The substitution of clinker with SCMs results in an increase in the measured carbonation depths, except for F4, which exhibits a significantly lower depth. The resistance of the concrete material to carbonation is evidently dependent on the initial clinker content, a finding that aligns with the results obtained in this study and those reported in the literature. Additionally, it is observed that the different concrete mixes are not in the same initial state before the beginning of the accelerated carbonation test. This difference in initial state impacts the values of accelerated carbonation rates and elucidates the small benefit of conservation in MC compared to other conservation. Mixes with lower clinker contents, when conserved in MC, experience greater advantage than mixes with higher clinker content. This could be verified by comparing specimens conserved in DC, which are not exposed to CO_2, with their counterparts conserved in MC, where carbonation proceeds slowly due to high relative humidity, leading to concrete saturation. However, since natural carbonation occurs in DC, the concrete skin is already carbonated over a few millimetres, and this depth increases with decreasing clinker content. Consequently, the first millimetres of the material exhibit lower total porosity, possibly a lower CO_2 diffusion coefficient, and certainly a longer distance that must be crossed by the accelerated carbonation atmosphere to reach the uncarbonated zone. This aspect leads to surface curing through carbonation, which is more pronounced in mixes with low clinker content compared to F3, F4, and F1. Finally, it can be inferred that the lower carbonation depth observed in F4 may be attributed to the higher compactness of the concrete material resulting from the inclusion of metakaolin in the binder. However, it is also plausible that this discrepancy is the consequence of an experimental error.

The same analysis was carried out using the blends from the PerfDuB national project. The corresponding results are presented in Figure II-16. The tendency in the results is not clear. The variation may be attributed to the fact that the experiments were conducted in different laboratories, resulting in potential differences in conservation conditions. Nevertheless, it is obvious that the sole determination of clinker content cannot accurately predict the initial carbonation depth observed in the samples following 90 days of dry storage. Factors such as compactness and environmental humidity conditions should also be taken into consideration.

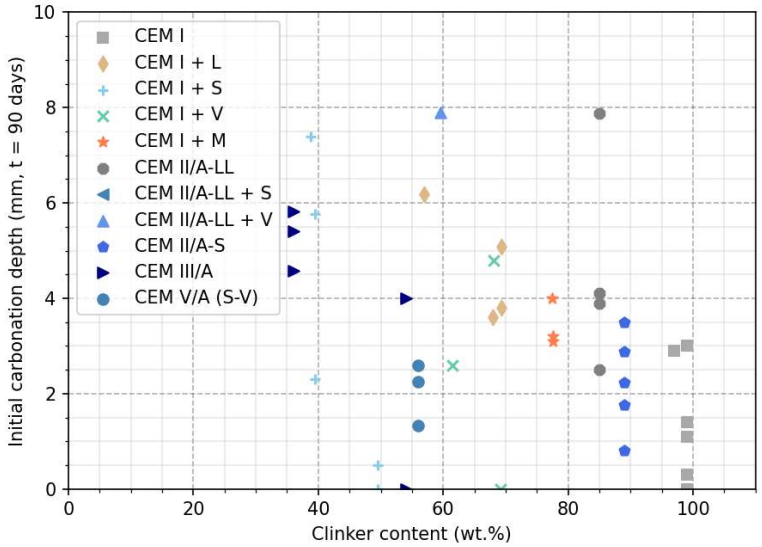

Figure II-16 Initial carbonation depth vs. clinker content of the PerfDuB concrete mixes conserved DC.

The carbonation rates are compared to those of the PerfDuB mixes in the Figure II-17 for DC, and in Figure II-18 for MC.

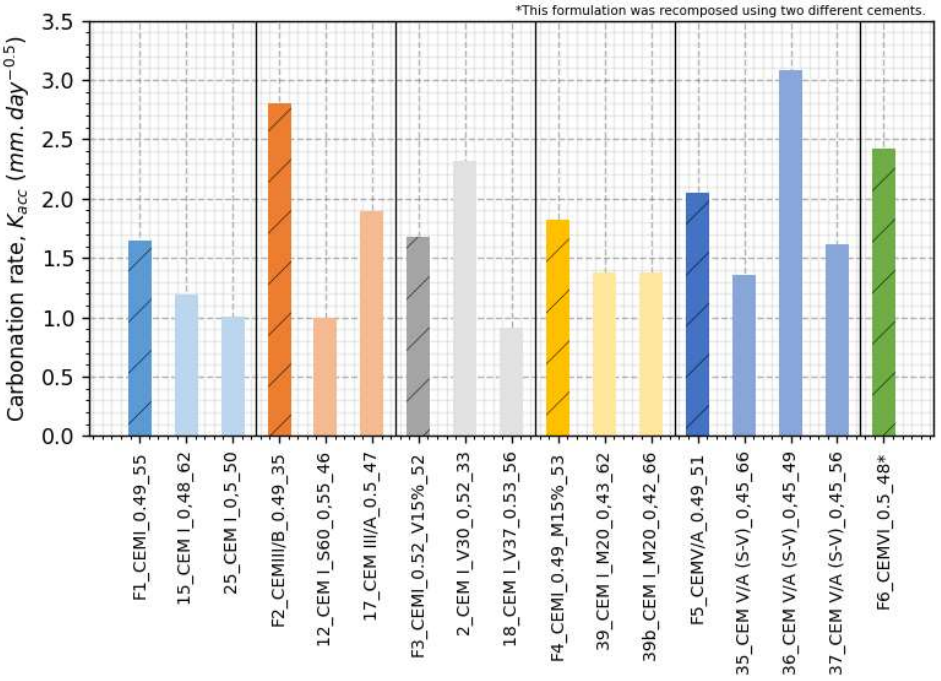

Figure II-17 Comparisons of the values of accelerated carbonation rate (K_{acc}) of concrete obtained in DC for the PhD and PerfDuB mixes.

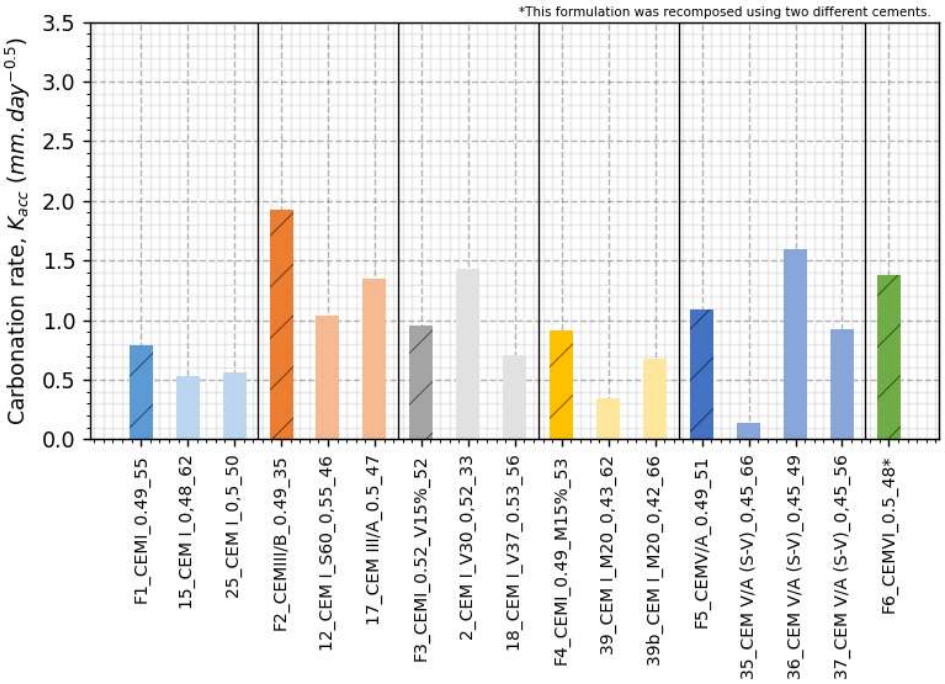

Figure II-18 Comparisons of the values of accelerated carbonation rate (K_{acc}) of concrete obtained in MC for the PhD and PerfDuB mixes.

Light differences between the mixes of this study and those of the PerfDuB project were observed. It was foreseeable that F2 would exhibit lower carbonation resistance compared to its two equivalent mixes, based on previous findings on water-accessible porosity and compressive strength. The higher carbonation rate observed for F4, in comparison to mixes 39 and 39b, can be attributed to the higher water-to-binder (W/B) ratio employed (0.5 compared to 0.43 and 0.42).

II.3.6. Natural carbonation

The natural carbonation depths are measured after one year of exposure. The samples were placed in two different environments that correspond to the EC and DC, directly after being demoulded. The variations in environmental parameters are described in Table II-4 of Section II.2.3. The carbonation conditions in each environment (DC or EC) are assumed to be similar for all mixes because the carbonation time covers one year. This assumption allows to consider that the different manufacturing dates only affect the conservation conditions of the concrete, described in Table II-5 of Section II.2.3.

The carbonation depths assessed ($x_{c,nat}$, mm) at the time t (year) for the different mixes are used to compute the natural carbonation rate K_{nat} expressed in mm.an$^{-0.5}$ with the Equation II.3:

$$K_{nat} = x_{c,nat}\sqrt{t} \qquad \text{Eq (II.3)}$$

The different values obtained for the six mixes in EC and DC conditions are exposed in Figure II-19.

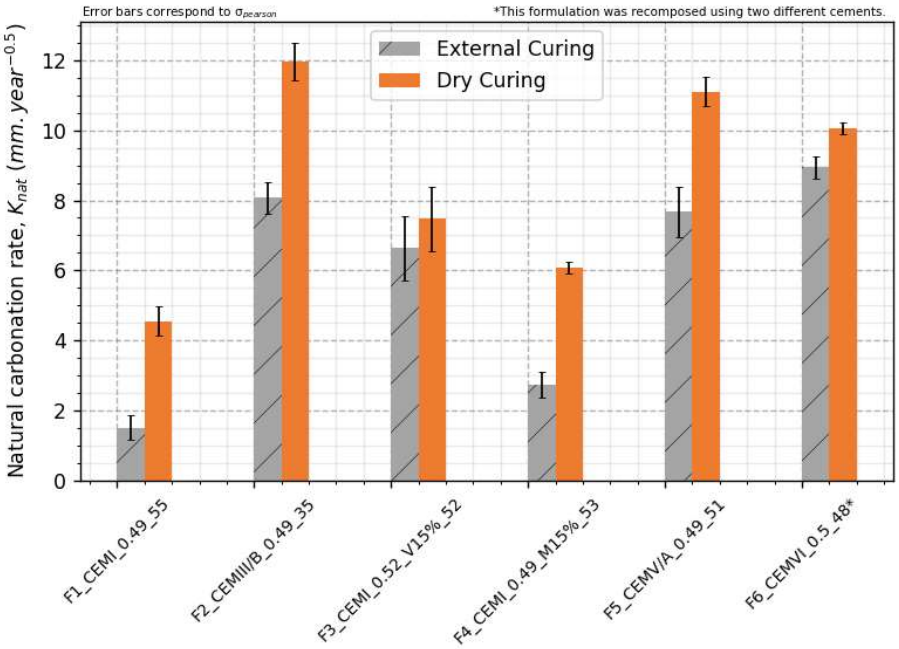

Figure II-19 Natural carbonation rate (K_{nat}, mm.year-0.5) obtained for the different mixes in DC and EC.

EC conditions resulted in lower carbonation rates compared to DC conditions. A comparison of the statistical values presented in Table II-4 reveals a lower average temperature (10.8°C for EC versus 20.3°C for DC) and a higher average relative humidity (79.7% versus 37.2%). These environmental parameters, along with the development of cement paste hydration, have the potential to reduce the progress of carbonation. Generally, carbonation increases with rising temperatures and is favoured in environments with a relative humidity of approximately 65% [92], [180]. Therefore, it is surprising to observe such high levels of carbonation in DC conditions. This unexpected result may be attributed to the initial saturation of the concrete samples, leading to an increase in carbonation depth as the material gradually desaturates. Additionally, significant variations in moisture content, up to 60%, are observed in the DC conditions, which further explains the elevated carbonation depths experienced under these storage conditions.

In comparison to the results obtained under accelerated conditions, the ranking of carbonation rate exhibits variations. Specifically, when considering the natural carbonation in EC, the carbonation level of F6 exceeds that of F2, which is contrary to the findings in accelerated conditions or natural carbonation in DC conditions. Conversely, in the case of natural carbonation in DC, F2 demonstrates a higher carbonation rate in comparison to F5 and F6. These opposing trends can potentially be explained by different underlying mechanisms. It is possible that the specific exposure conditions for the various samples within the same exposure category may have slightly varied, leading to discrepancies in conservation conditions and subsequently impacting carbonation. For instance, in the case of DC, some samples were stored at different heights while others were stored on the ground, depending on the available space. The same logic applies to EC.

In the context of the National project PerfDuB, the estimation of the natural and accelerated carbonation rates enabled the establishment of a correlation between these two parameters. The project participants defined the Equation II.4 that represents this relationship, which was based on the analysis of the 42 concrete mixtures involved in the project. It is noteworthy to emphasize the distinct units of measurement used for the carbonation rates, where K_{nat} is expressed in mm.year$^{-0.5}$ and K_{acc} in mm.day$^{-0.5}$.

$$K_{nat} = 3.01 K_{acc}$$ Eq (II.4)

Table II-10 Ratios of natural carbonation rate (EC and DC) on accelerated carbonation rate (DC).

Mix name	F1_CEMI_0.49_55	F2_CEMIII/B_0.49_35	F3_CEMI_0.52_V15%_52	F4_CEMI_0.49_M15%_53	F5_CEMV/A_0.49_51	F6_CEMVI_0.5_48*	Average
$K_{nat,EC}/K_{acc,DC}$	0.91	2.88	3.95	1.5	3.74	3.69	2.78
$K_{nat,DC}/K_{acc,DC}$	4.99	4.15	1.89	4.05	2.97	2.72	3.46

*This formulation was recomposed using two different cements.

The obtained values of the ratio differ from the average value of 3.01 from the PerfDuB project. These variations in the ratio can be attributed to differences in the preconditioning of the test samples. In the PerfDuB project, for accelerated carbonation test, the samples were immersed in water for 48 hours before being dried at 45°C, while in this study, the samples were directly placed in the heat chamber. This difference likely resulted in varying degrees of saturation at the beginning of the accelerated carbonation test, the PerfDuB samples being more saturated.

The fluctuation of ratios around 3 can be attributed to this difference in test preconditioning, as well as the annual fluctuations in environmental conditions in the DC and EC environments.

In a previous study by El Farissi [266], a value of 3.66 was proposed for samples conserved in DC, which is closer to the results obtained in this present work.

Figure II-20 compares the values obtained in natural carbonation with exposure to the DC environment to the values measured on the PerfDuB mixes under similar conditions.

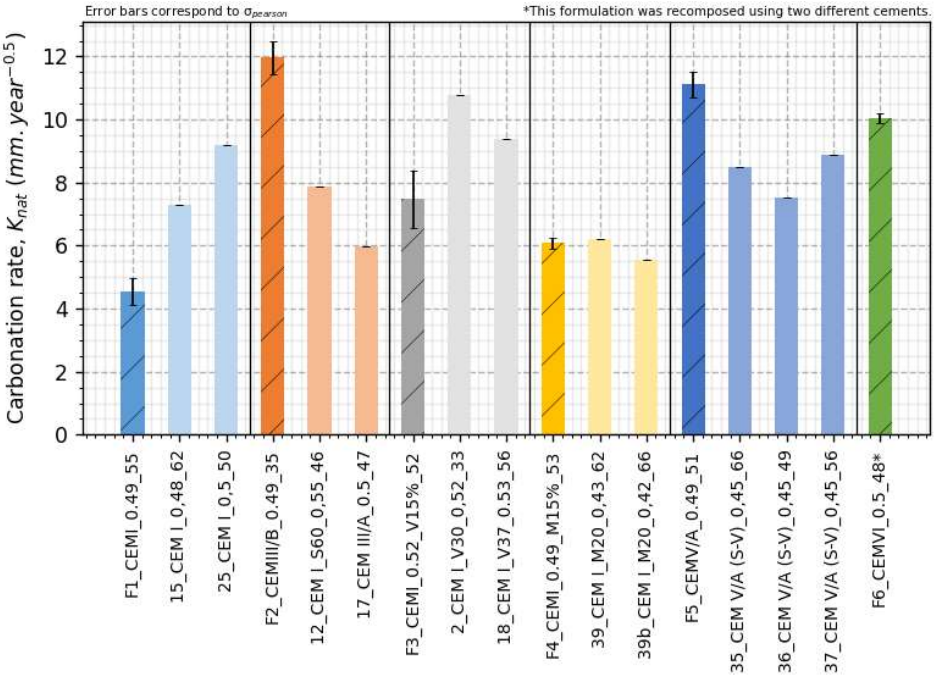

Figure II-20 Comparison of the PhD and PerfDuB natural carbonation rate obtained in DC.

These deviations between the mixes of the present study and the PerfDuB project can be attributed to differences in mix composition and carbonation exposure conditions. However, the values obtained in this study remain within the same order of magnitude as those obtained in the PerfDuB project.

II.3.7. Chloride ions migration under electric field

Accelerated chloride migration tests were conducted in a non-stationary regime according to the XP P18-462 (2022) standard [354]. Initially, cylindrical samples with dimensions of 220/110 mm were cut into 50/110 mm specimens. One day prior to the preconditioning stage, the cylindrical surfaces of the samples were coated with silicon to ensure the unidirectional diffusion of chloride ions and avoid leakage. The samples were then placed in a glass desiccator and subjected to a vacuum. After 4 hours, a solution of NaOH, concentrated at 0.1 mol/L, was introduced, and another round of vacuum treatment was performed. The resistivity of each sample was measured after 68 hours (refer to Section II.3.8) prior to mounting the diffusion cell.

The diffusion cell consisted of two chambers, each connected to a face of the sample. The first chamber was filled with a 0.1 mol/L NaOH solution, while the second chamber contained a solution of 0.1 mol/L NaOH + 0.5 mol/L NaCl. An electric generator was used to apply a potential difference of 30V to the installation. The testing duration was adjusted based on the concrete sample's resistance to chloride penetration. Upon completion of the test, the sample was split perpendicularly to the surface, and a solution of silver nitrate ($AgNO_3$) with a concentration of 0.1 mol/L was applied to the fractured surface, following the recommendations of XP P18-462 (2022). The depth of penetration was measured and corresponds to a chloride concentration of 0.07 mol/L [294], [355].

Testing is performed after conservation times of 28 and 90 days for each mix and conditions. The results are shown in Figure II-21 and Figure II-22.

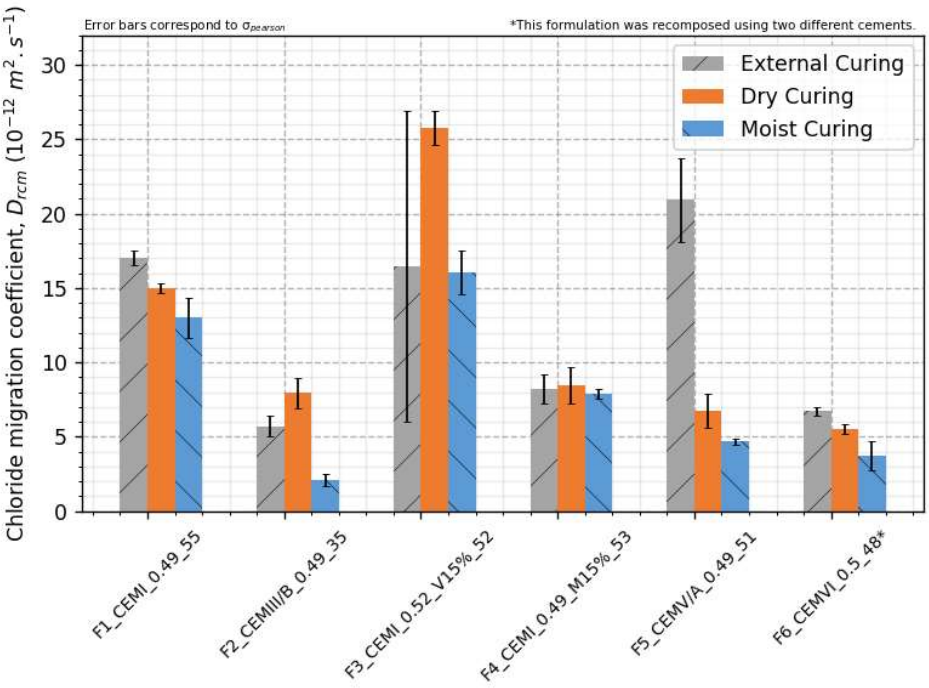

Figure II-21 Chloride migration coefficient values obtained after 28 days of conservation.

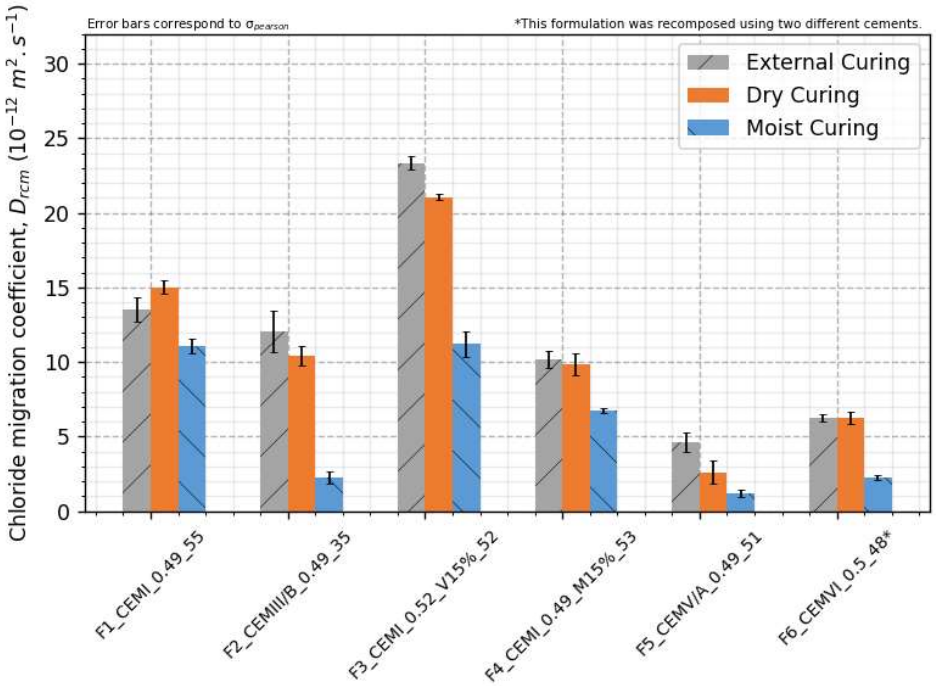

Figure II-22 Chloride migration coefficient values obtained after 90 days of conservation.

The results obtained from the six formulations demonstrate improved performance (lower chloride migration coefficients) when conservation is done in the MC compared to DC and EC. When comparing the two more stable treatments (MC and DC), it is evident that the MC treatment is more beneficial for mixtures containing a high content of mineral additions for clinker replacement. Table II-11 contains the relative and absolute differences of values obtained under the two conservation conditions. The table shows that the mixes F2, F5, and F6 exhibit a higher relative reduction compared to the other three mixes. The F5 mix displays the lowest diffusion coefficient, indicating the positive effect of incorporating fly ash and slag in concrete for resistance against chloride-induced corrosion. This supports the notion that conservation conditions play a significant role, particularly in the case of new cements with a high ratio of clinker replacement by pozzolanic and latent hydraulic additions.

When comparing F1, F3, and F4 it is possible to observe that:

- Fly ash alone appears to have a negative effect on chloride migration when stored in DC or EC, as F3 exhibits lower properties than the reference F1. This is likely due to the hydration kinetics and possibly the higher water demand of fly ash. Similar values are observed in MC for F1 and F3, particularly after 90 days, when the slower hydration of fly ash is complete.
- The inclusion of metakaolin enhances the properties of the concrete with respect to the chloride migration coefficient, as F4 demonstrates increased resistance to chloride penetration compared to F1 for all conservation conditions.
- Metakaolin appears to be less affected by conservation conditions in comparison to fly ash in the current formulation conditions. Notably, the relative and absolute differences between MC and DC (refer to Table II-11) are more pronounced for F3 than for F4.
- The chloride migration resistance of F1 profits less from ideal conservation conditions than the other mixes.

Table II-11 Comparison of the chloride migration coefficients obtained in MC and DC after 90 days of conservation.

Mix name	F1_CEMI_ 0.49_55	F2_CEMIII/B_ 0.49_35	F3_CEMI_0.52 _V15%_52	F4_CEMI_0.49 _M15%_53	F5_CEMV/A_ 0.49_51	F6_CEMVI_0.5 _48*
D_{rcm}, MC (10^{-12} m^2.s^{-1})	11.08	2.25	11.21	6.77	1.2	2.24
D_{rcm}, DC (10^{-12} m^2.s^{-1})	15.02	10.40	21.05	9.86	2.6	6.22
Relative difference (%)	26.2	78.4	46.7	31.3	53.8	64.0
Absolute difference (10^{-12} m^2.s^{-1})	3.94	8.15	9.84	3.09	1.4	3.98

*This formulation was recomposed using two different cements.

A general observation of Table II-11 reveals that higher performances are achieved in mixes that contain increased levels of pozzolanic and slag additions compared to CEM I-based concretes. This phenomenon is likely attributed to the nature of the cementitious matrix, which comprises more hydrates capable of binding chlorides (such as C-S-H and C-A-S-H) in the case of formulations F2, F5, and F6 [127], [129]. The increased binding capacity of these hydrates assists in reducing the diffusion capacity of the material. This effect is particularly prominent in concrete conserved in MC, as a more complete hydration process results in higher hydrate contents.

The Figure II-23 illustrates the progression of the chloride migration coefficient obtained for the 6 different mixes.

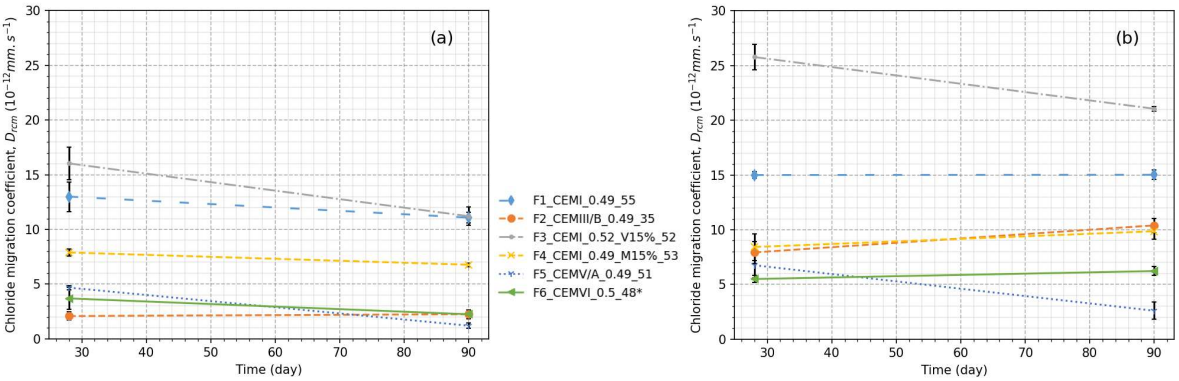

Figure II-23 Evolution of the chloride migration coefficient (D_{rcm}) for the different mixes in MC (a) and DC (b).

A reduction in the apparent diffusion coefficient over time is commonly observed in scientific literature on concrete [356], [357]. This improvement in concrete properties is influenced by various factors, including its composition. In this context, an ageing factor (ae, -) is frequently defined, representing a dimensionless coefficient ranging from 0 to 1. The ageing factor can be determined by measuring the D_{rcm} coefficient at different time intervals. Equation II.5, presented in [238], describes the time-dependent evolution of the diffusion coefficient and can be utilised to derive Equation II.6:

$$D(t) = D(t_0)\left(\frac{t_0}{t}\right)^{ae} \quad \text{Eq (II.5)}$$

Where D is the diffusion coefficient (m^2/s) measured at a given time, t or t_0 (days).

$$ae = \frac{ln\big(D(t)\big) - ln\big(D(t_0)\big)}{ln(t_0) - ln(t)} \quad \text{Eq (II.6)}$$

Due to the financial and time constraints associated with conducting migration coefficient measurements, alternative methods have been suggested for assessing the ageing factor coefficient. In the FD P 18-480 [301], a formula has been proposed to calculate the ageing factor based on the additions present in the mixture:

$$ae_{480} = 0.3 + \min(0.2S; 0.15) + \min(1.1V; 0.3) + \min(1.1D; 0.1) + \min(1.1MK; 0.1) \quad \text{Eq (II.7)}$$

Where S is the weight fraction of blast furnace slag (-), V is the weight fraction of fly ashes (-), D is the weight fraction of silica fume (-) and MK the weight fraction of metakaolin (A type) (-).

The values obtained at 28 and 90 days can be used to calculate the ageing factor for different conservation conditions using Equation II.6. It is important to note that caution should be paid when using a small-time difference of 62 days, as this may result in inaccuracies in the estimation of the ageing factor value. Typically, chloride diffusion coefficients measured after extended exposure periods (over one year) are utilised to estimate this parameter.

The method of the FD P18-480 (2022) is used as a comparison basis.

Table II-12 Ageing factor (ae) computed from experimental values and using the FD P18-480 (2022) method.

Mix name	F1_CEMI _0.49_55	F2_CEMIII/B_ 0.49_35	F3_CEMI_0.52_ V15%_52	F4_CEMI_0.49_ M15%_53	F5_CEMV/A_ 0.49_51	F6_CEMVI_0.5 _48*
ae_{EC}	0.2	-0.64	-0.3	-0.18	1.3	0.06
ae_{DC}	0	-0.23	0.17	-0.14	0.82	-0.11
ae_{MC}	0.14	-0.07	0.31	0.13	1.17	0.43
ae_{480}	0.3	0.44	0.47	0.4	0.59	0.59

*This formulation was recomposed using two different cements.

The ageing factors displayed in Table II-12 exhibit significant variations. It can be observed that:

- The ageing factors obtained in the MC condition are generally higher than those in the DC and EC conditions, excluding F1 and F5. This indicates the greater effectiveness of the MC conservation treatment in improving chloride migration properties, even after 28 days.
- Negative values of ageing factors can be obtained when utilizing the experimental method, particularly in the DC and EC conditions. This may be ascribed to various factors that can influence the chloride diffusion capacity, such as alterations in the porous network due to carbonation. It is also possible that this parameter is more sensitive to heterogeneities among the samples resulting from the manufacturing process, leading to variations in values. The uncertainties of the test may also contribute to the apparent decrease in chloride-induced corrosion resistance over time. In the case of F2, the low mechanical resistances observed in the DC and EC conditions at 28 days (as shown in Figure II-4) and presumed to be similar after a conservation time of 90 days (based on the minimal evolution of F2 in MC as shown in Figure II-5) , could explain the high negative values of ae_{DC} and ae_{EC} obtained. It is possible that the cutting process affects the integrity of the material, which then results in the appearance of random micro-cracks that adversely affect its properties.

- The ageing factors computed using Equation II.7 of the FD P18-480 (2022) are higher than those obtained experimentally, except for the F5 mix. Substantial differences can be observed, and it is challenging to draw conclusions about the accuracy of this equation in estimating the values obtained in this experimental campaign. The results clearly indicate that the proximity of measurements of the two chloride diffusion results quickly leads to errors in the estimation of the ageing factor.

In PerfDuB, similar conclusions were reached, indicating that the computation of the aging factor from D_{rcm} values was challenging. This complexity likely arises from the acquisition method employed. Therefore, it is more advisable to employ D_{app} values measured on structures or concrete samples that have been exposed to chloride over an extended duration to apply the ageing factor computation method (refer to Equation II.6).

The values obtained on the mixes of the PhD after 90 days of MC are compared to the PerfDuB mixes in Figure II-24.

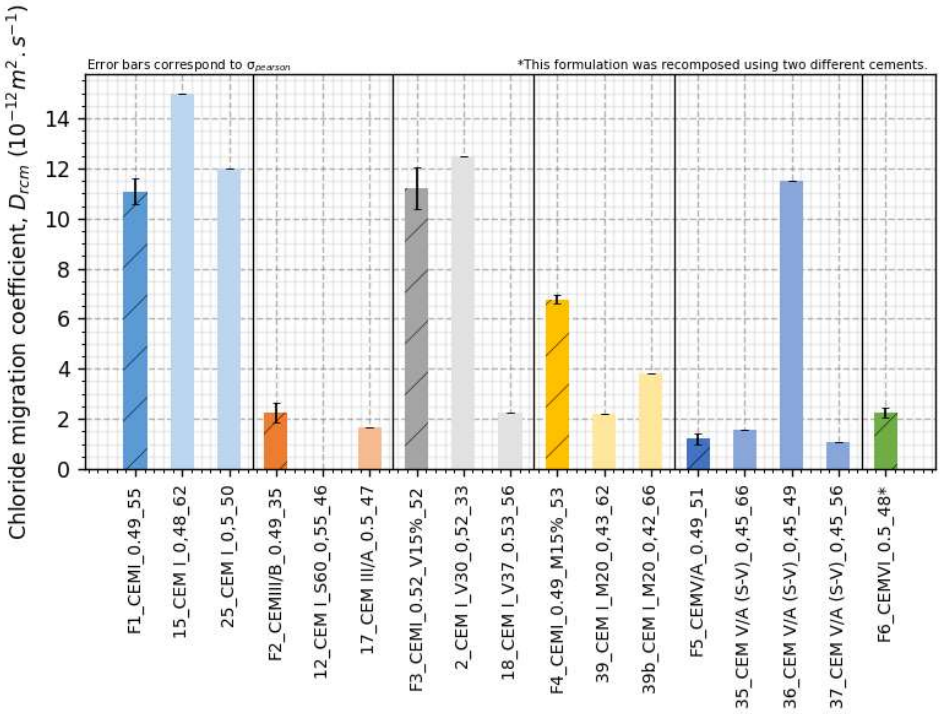

Figure II-24 Comparisons of the values of chloride migration coefficient (D_{rcm}) for the concretes conserved in MC in the PhD and PerfDuB mixes.

The obtained values demonstrate a comparable magnitude order of results among the similar mixes. Notably, there are discernible significant differences between F4 and the mixes 39 and 39b, which can be attributed to the denser matrix achieved through a lower W/B ratio in the case of PerfDuB mixes. Additionally, a distinction is observed between F5 and mix 36, which is attributed to the utilization of aggregates with higher porosity in the PerfDuB mix formulation.

II.3.8. Electric resistivity

Electric resistivity is measured following the XP P18-481 (2022) standard recommendations [358]. The preconditioning is identical to the one described in the previous section II.3.7. The results obtained on the different mixes and conservations are shown in Figure II-25 for time of 7, 28, and 90 days.

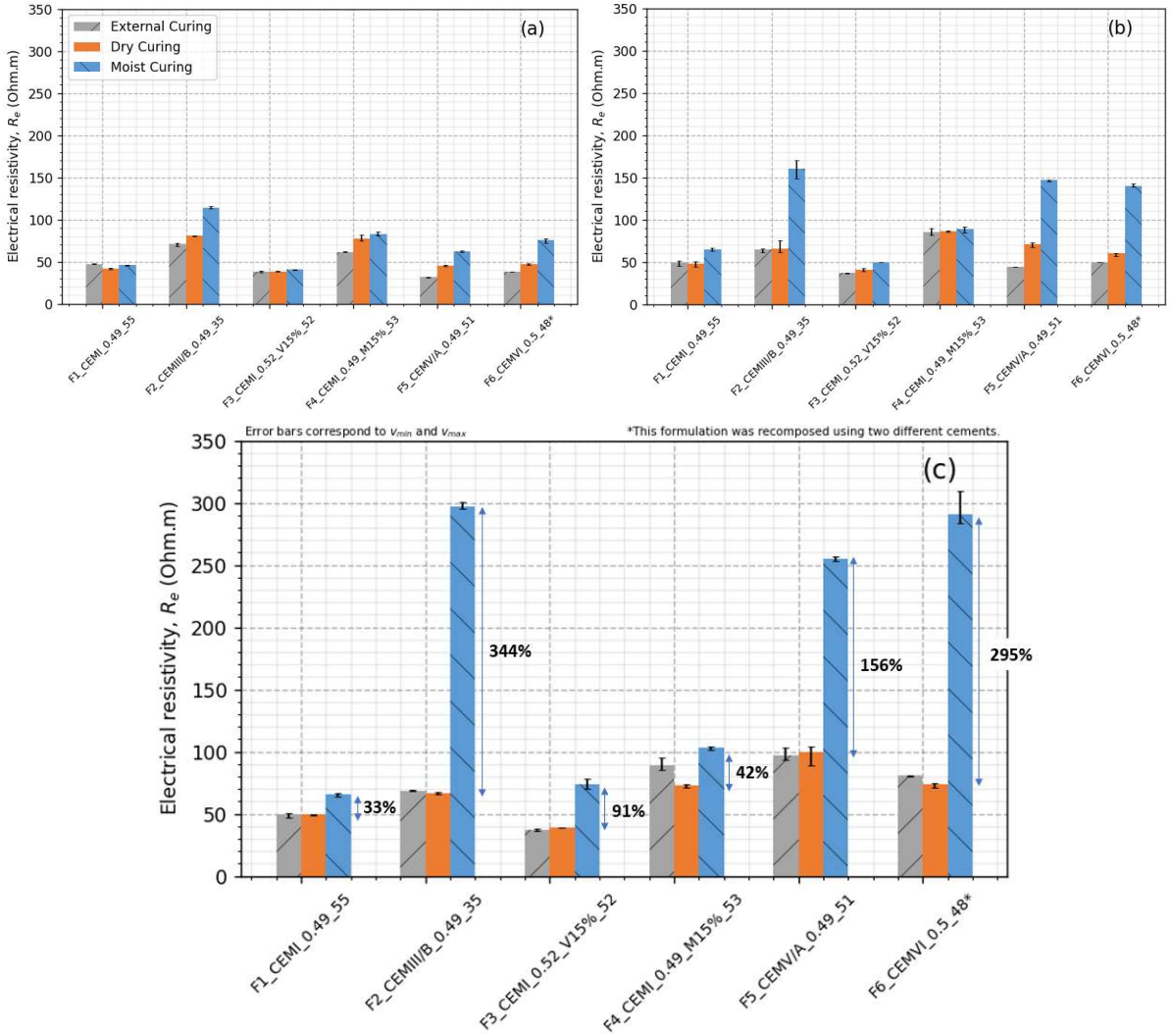

Figure II-25 Electrical resistivity measurement for conservation time of 7 (a), 28 (b) and 90 days (c).

The evolutions of the electrical resistivity of the 6 mixes are also represented in Figure II-26 for DC and MC conditions.

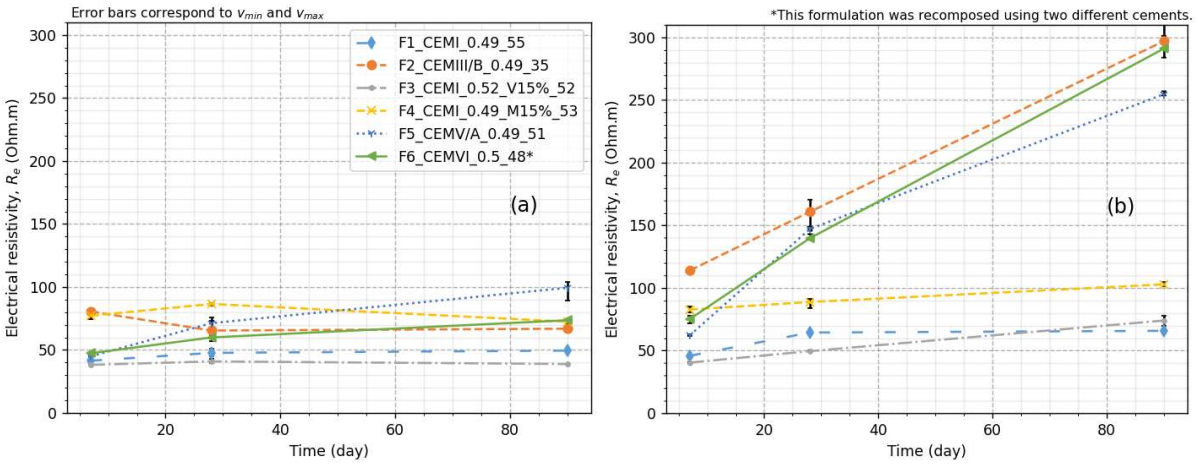

Figure II-26 Evolution of the electrical resistivity in DC conditions (a) and MC conditions (b).

Clear differences between MC and DC are observable:

- First, a significant increase in electrical resistivity is measured in concrete containing high levels of fly ash and/or slag exposed to MC conditions. This suggests that binders with high clinker content have lower potential in terms of their electrical parameters when efficient hydration is achieved. It should be noted that the increase in resistivity appears to be linear over time for F2 and F6, as observed in Figure II-26. This suggests that further increase in electrical resistivity may be possible with longer conservation periods.
- Second, the increase in electrical resistivity value of F1 is only observed up to 28 days. This can be attributed to the quicker hydration mechanism of clinker compared to other mineral additions. Consequently, the final 90-day resistivity values of mixes F3 and F4 are almost reached after 28 days. However, it is worth noting that the slope of the resistivity evolution is higher for F3 compared to F4. This suggests that fly ash requires a longer water-exposure duration for its hydration compared to metakaolin.
- The Table II-13 summarises the relative and absolute differences between the R_e values obtained in MC and DC after a 90-days period of conservation. It shows that:
    - The CEM I-based mixes (F1, F3, and F4) yield the lowest values. Fly ash, despite producing lower electrical resistivity values than metakaolin, exhibits a larger relative increase between DC and MC. It is worth noting that in DC, F1 exhibits higher electrical resistivity than F3, despite lacking other mineral constituents apart from clinker. These two observations serve as evidence that fly ash necessitates more favourable conditions to complete its hydration compared to metakaolin.
    - The CEM V/A and CEM III/B based mixes yield the highest electrical resistivity values. The difference between the values in DC and MC increases with the addition's content. Starting with F2 (71 wt.% slag), its value increases by 230.1 Ohm.m (344 %), followed by F6 (46.5 wt.% slag, 11 wt.% fly ash) with an increase of 217.4 Ohm.m (295 %). Lastly, the value of F5 (22 wt.% slag, 22 wt.% fly ash) increases by 155.2 Ohm.m (156 %). Consequently, higher addition contents result in higher electrical resistivity in MC, whereas the trend is reversed in DC, with F5 exhibiting the highest electrical resistivity value.

Table II-13 Comparison of the electrical resistance values obtained in MC and DC after 90 days of conservation.

Mix name	F1_CEMI_0.49_55	F2_CEMIII/B_0.49_35	F3_CEMI_0.52_V15%_52	F4_CEMI_0.49_M15%_53	F5_CEMV/A_0.49_51	F6_CEMVI_0.5_48*
R_e, MC (Ohm.m)	65.8	297	74	102.8	254.6	291
R_e, DC (Ohm.m)	49.5	66.9	38.8	72.5	99.4	73.6
Relative difference (%)	33	344	91	42	156	295
Absolute difference (Ohm.m)	16.3	230.1	35.2	30.3	155.2	217.4

*This formulation was recomposed using two different cements.

Andrade et al. [359] proposed a methodology to compute the ageing factor using electrical resistivity values. They describe the evolution of the electrical resistivity with the Equation II.8, defining the ageing factor q (-) associated to the electrical resistivity Re (Ohm.m).

$$Re(t) = Re(t_0)\left(\frac{t}{t_0}\right)^q \quad \text{Eq (II.8)}$$

$$Re = \frac{ln\big(Re(t)\big) - ln\big(Re(t_0)\big)}{ln(t) - ln(t_0)} \quad \text{Eq (II.9)}$$

They find the following correlation between ae and q:

$$q = 0.798\,ae - 0.0072 \approx 0.8\,ae \quad \text{Eq (II.10)}$$

The validity of this equation has been confirmed through its application on different concrete mixes consisting of CEM I, CEM II/A-P, and CEM II/B-V, which were previously conserved in a humid chamber with a relative humidity (RH) exceeding 95%.

Table II-14 displays the ageing factor (ae) associated with the chloride migration coefficient computed using the ageing factor q and Equation II.10. The measurement realised after 7 and 90 days of conservation were used.

Table II-14 Ageing factors obtained using experimental measurements of R_e, D_{rcm} and Equation (II.7).

Mix name	F1_CEMI_0.49_55	F2_CEMIII/B_0.49_35	F3_CEMI_0.52_V15%_52	F4_CEMI_0.49_M15%_53	F5_CEMV/A_0.49_51	F6_CEMVI_0.5_48*
$ae_{q,EC}$	0.02	-0.01	0	0.17	0.57	0.37
ae_{EC}	0.2	-0.64	-0.3	-0.18	1.3	0.06
$ae_{q,DC}$	0.08	-0.08	0	-0.04	0.39	0.22
ae_{DC}	0	-0.23	0.17	-0.14	0.82	-0.11
$ae_{q,MC}$	**0.17**	0.48	**0.30**	**0.11**	0.68	0.67
ae_{MC}	**0.14**	-0.07	**0.31**	**0.13**	1.17	0.43
ae_{480}	0.3	0.44	0.47	0.4	0.59	0.59

*This formulation was recomposed using two different cements.

Different conclusions can be derived from these findings. Initially, concretes conserved in MC consistently resulted in higher ae_q values compared to EC and DC. However, this was not the case for the ageing factor calculated from the chloride migration coefficient (ae).

Only similar values of the ageing factor were observed when employing both experimental methods for mixtures containing low addition contents (F1, F3, and F4) conserved in MC. These values are highlighted in bold in Table II-14. This observation strongly suggests that a distinct relationship between q and ae ought to be applied for mixtures with higher addition contents or those conserved under different conditions.

The $ae_{q,MC}$ values acquired for mixes containing high clinker contents (F1, F3, and F4) exhibit lower values compared to those computed using Equation II.7 from the FD P18-480 (2022). Conversely, for all mixes with high mineral additions contents, the values obtained using this experimental method in MC are higher than the estimation provided by the FD P18-480 (2022). This discrepancy could potentially be attributed to the fitting of the aforementioned equation based on results acquired under different conditions (such as varying conservation, water to binder ratio, or granular skeleton), consequently resulting in misestimation for the six mixes studied here. Another possible factor contributing to this discrepancy between theoretical and experimental values is the relatively low age of the concrete material.

A comparison with the results of PerfDuB is exposed in Figure II-27.

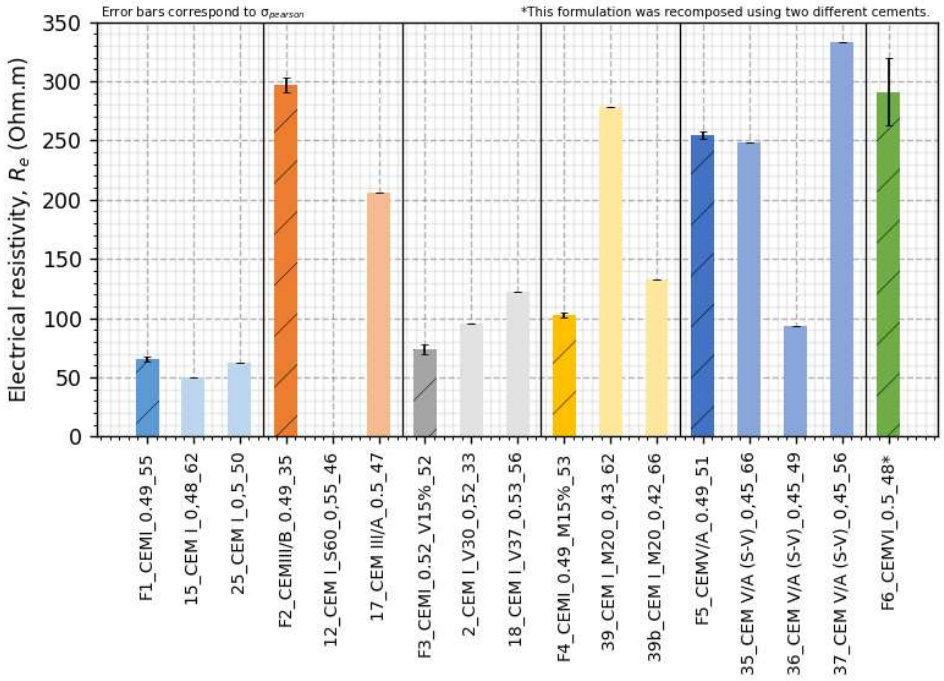

Figure II-27 Comparisons of the values of electrical resistivity (Re) for the concretes conserved 90 days in MC in the PhD and PerfDuB mixes.

The Figure II-27 displays some differences in results:

- F2 leads to higher electrical resistivity compared to the PerfDuB mix 17 which can be attributed to a higher slag content in F2.
- F3 exhibits a lower value than its PerfDuB counterparts, potentially due to a lower fly ash content in mixes 2 and 18.
- The mix 39 achieves a high value, likely attributed to the utilization of a different type of metakaolin compared to mixes F4 and 39b. In the meantime, the higher value of Re obtained for the mix 39b can be explained by a lower W/B ratio compared to F4.
- Lastly, the low value of PerfDuB mix 36 can be ascribed to the inferior properties of the aggregates incorporated in this formulation.

II.3.9. Thermogravimetric analysis (TGA)

Thermogravimetric analysis (TGA) involves monitoring the mass loss of a powdered sample while it is exposed to a temperature range of 20 to 1000°C. In order to prepare the material for analysis, a concrete sample is dried at 80°C. Once the sample is completely dry, it is crushed until particles with a diameter smaller than 315 µm are obtained. One gram of the resulting powder is then placed in the crucible of the TGA device. The temperature is then increased at a rate of 10°C per minute. The results of the analysis are represented in the form of a thermograph, which illustrates the successive weight loss resulting from the release of water bound to various hydrates and the decarbonation of $CaCO_3$. Additionally, the decomposition of the hydrates may also contribute to the weight loss observed.

Various works deal with the temperature ranges of dehydroxylation and decomposition of the different species. Figure II-28 is a cartography that summarize them.

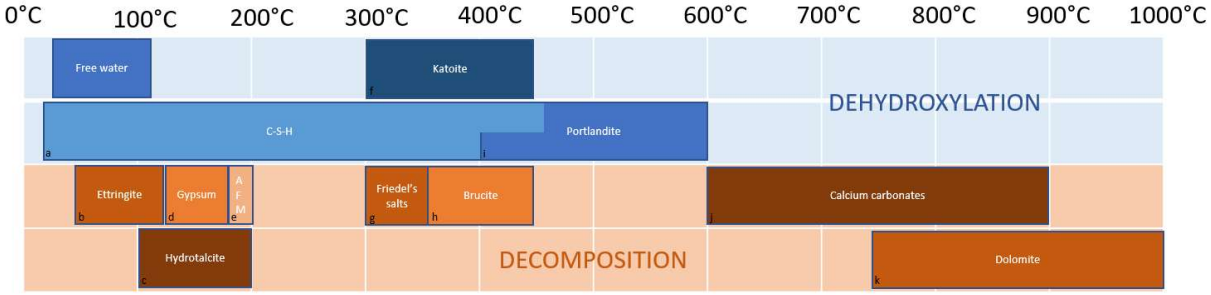

Figure II-28 Cartography of the dehydroxylation and decomposition temperature associated to the different species in cementitious material.

a. C-S-H **[360]**
b. Ettringite **[361], [364]**
c. Hydrotalcite **[366]**
d. Gypsum **[362]**
e. Afm **[361]**
f. Katoite **[365]**
g. Friedel's salts **[362]**
h. Brucite **[366]**
i. Portlandite **[362], [363]**
j. Calcium carbonates **[362], [363]**
k. Dolomite **[367]**

In Figure II-28, an overlapping of decomposition or dihydroxylation is observed for certain species. This phenomenon may complicate the analysis of thermographs. The following assumptions were employed for the experimental tests conducted in this research.

The temperature range for the dihydroxylation of portlandite is documented to occur between 450 and 550°C. The weight ratio of portlandite can be calculated using Equation II.11.

$$\%m_{Ca(OH)_2} = \frac{|\Delta m_{450°C-550°C}| M_{Ca(OH)_2}}{M_{H_2O}} \quad \text{Eq (II.11)}$$

With $M_{Ca(OH)_2}$ the molar mass of portlandite (74 g/mol) and M_{H_2O} the molar mass of water (18g/mol).

To determine the content of bound water in the sample, the weight loss observed between the temperature range of 20 to 550°C can be considered, assuming that the decomposition of ettringite is negligible. This characteristic can serve as an indicator for evaluating the hydration level of the cementitious matrix.

The decomposition of $CaCO_3$ occurs within the temperature range of 550 to 900°C. The Equation II.12 is used to calculate the amount of CaCO3 present in the material:

$$\%m_{CaCO_3} = \frac{|\Delta m_{550°C-900°C}| M_{CaCO_3}}{M_{CO_2}} \quad \text{Eq (II.12)}$$

With M_{CaCO_3} the molar mass of calcium carbonate (100g/mol) and M_{CO_2} the molar mass of carbon dioxide (44g/mol).

Finally, it can be said that the parameter known as loss on ignition corresponds to the global mass loss measured between 20 and 975°C.

In the scope of this study, the objective of thermogravimetric analysis is to evaluate the hydration of various binders and determine the CO_2 storage capacity of different mixtures. Given the complex nature of concrete materials and the presence of numerous species, it is expected that uncertainties may arise in the obtained results. However, these uncertainties can be reduced by comparing the results with those obtained from X-ray diffraction analysis, enabling a partial quantification of the errors.

II.3.9.1. Hydration kinetics

Thermogravimetric measurements are conducted on the eight mortars described in the Table II-2 of Section II.2.1. The mortars were produced in accordance with the recommendations outlined in the NF EN 196-1 standard (2016) [341]. All samples were conserved in water. The hydration process was monitored through measurements taken after three conservation periods of 7, 28, and 90 days. In addition to thermogravimetric analysis, X-ray diffraction analysis was performed on the same powder to validate the obtained values. Details regarding the methodology can be found in [368]. To replicate the measured portlandite content, the hydration model based on the work of Lacarrière [288] and Kolani [287], described in Section I.4.5.3, is also used. Further information regarding this aspect and the assumptions made for the different supplementary cementitious materials is provided in Section IV.3.2.3.

The portlandite contents obtained for the different times are shown in Figure II-29, Figure II-30 and Figure II-31 while the calcite contents obtained are shown in Figure II-32, Figure II-33 and Figure II-34.

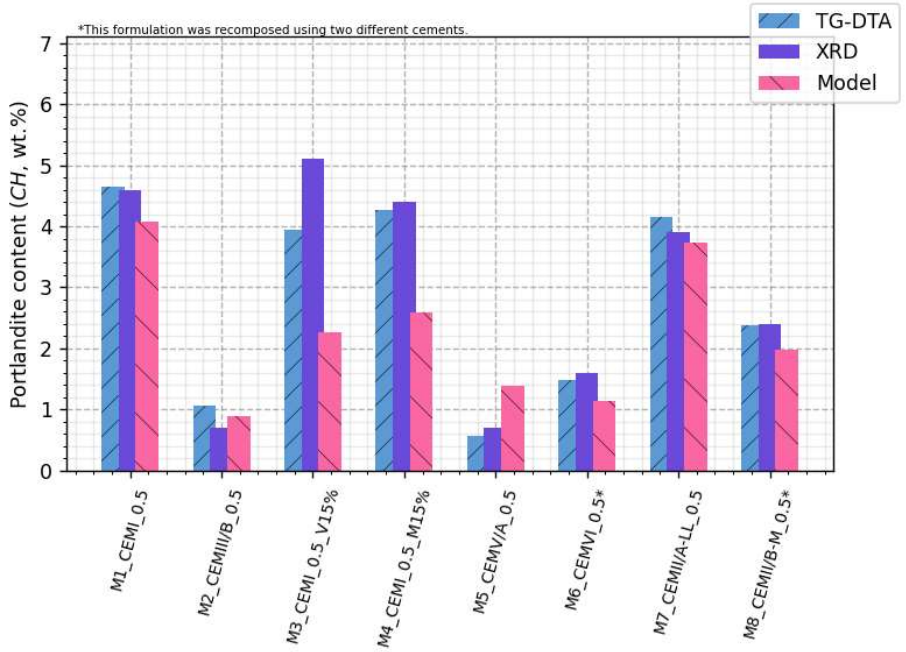

Figure II-29 portlandite content (wt.% of sample) obtained after 7 days of water conservation by means of thermogravimetric analysis, X-ray diffraction and modelling.

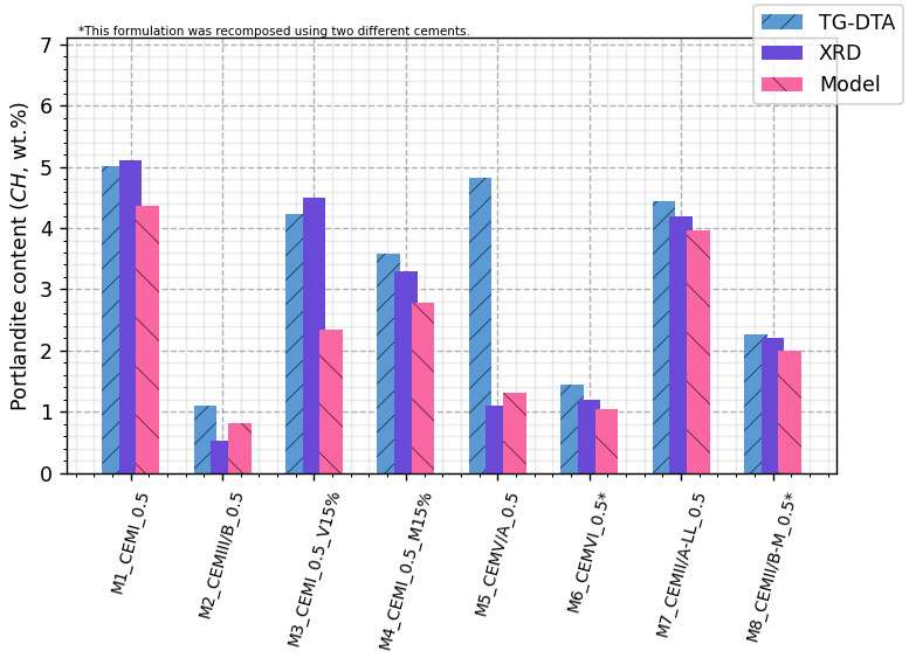

Figure II-30 portlandite content (wt.% of sample) obtained after 28 days of water conservation by means of thermogravimetric analysis, X-ray diffraction and modelling.

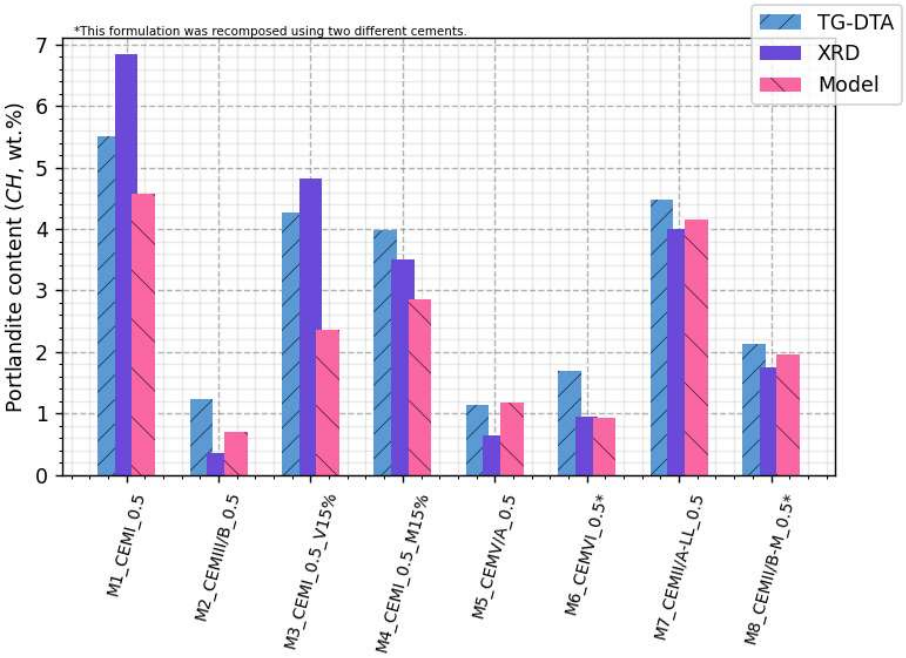

Figure II-31 portlandite content (wt.% of sample) obtained after 90 days of water conservation by means of thermogravimetric analysis, X-ray diffraction and modelling.

Discrepancies in values obtained using TG-DTA and XRD techniques are observed. The average absolute difference is 0.54 wt.% and the average absolute relative difference is 20.52 %. On average, TG-DTA results show slightly higher portlandite content compared to XRD. One possible explanation is that the concrete powder, exposed to air for longer periods before XRD analysis, undergoes carbonation prior to testing. This could result in lower portlandite content and higher calcium carbonate content.

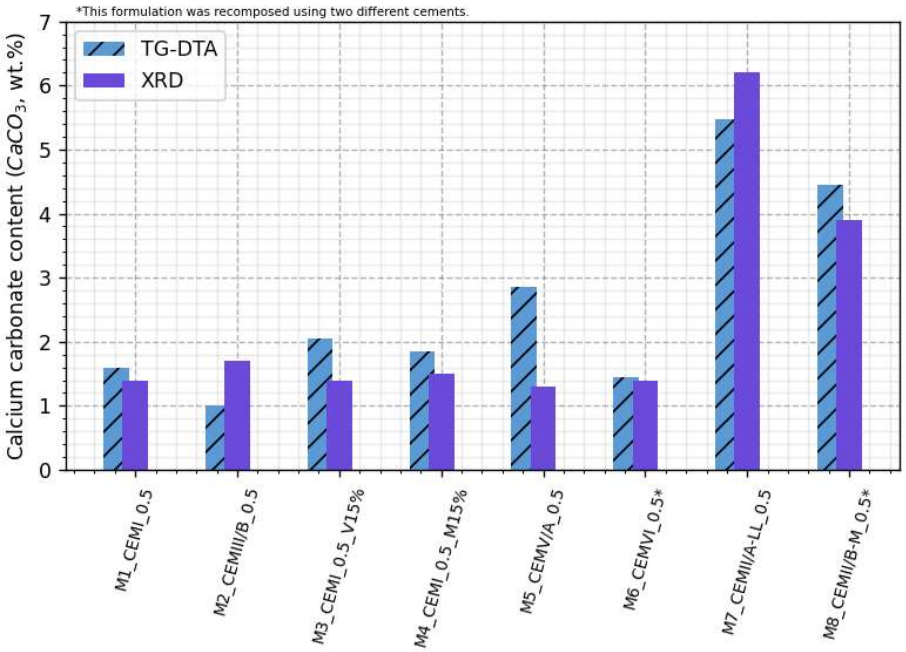

Figure II-32 Calcite content (wt.% of sample) obtained after 7 days of water conservation by means of thermogravimetric analysis, X-ray diffraction and modelling.

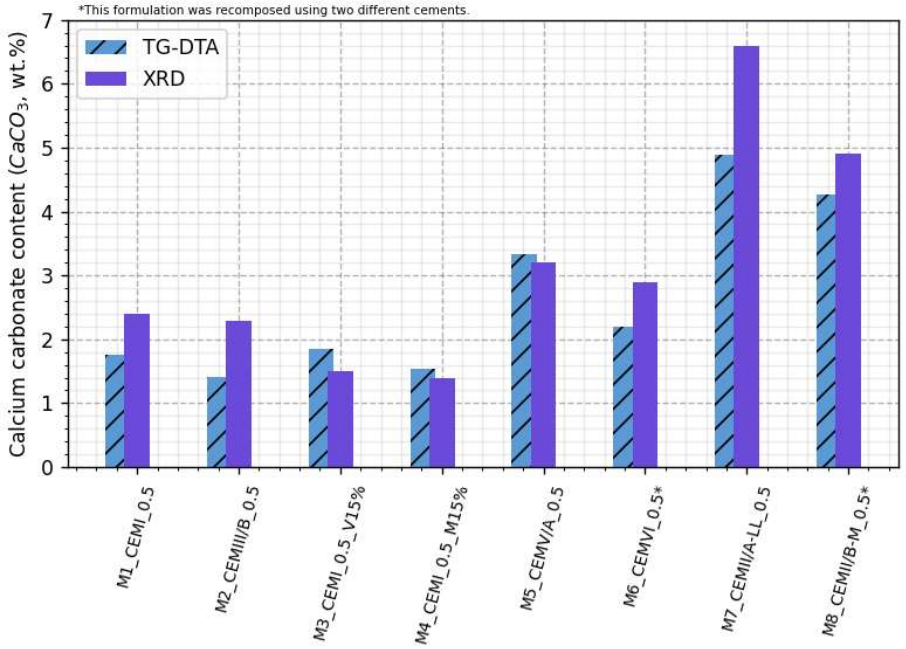

Figure II-33 Calcite content (wt.% of sample) obtained after 28 days of water conservation by means of thermogravimetric analysis, X-ray diffraction and modelling.

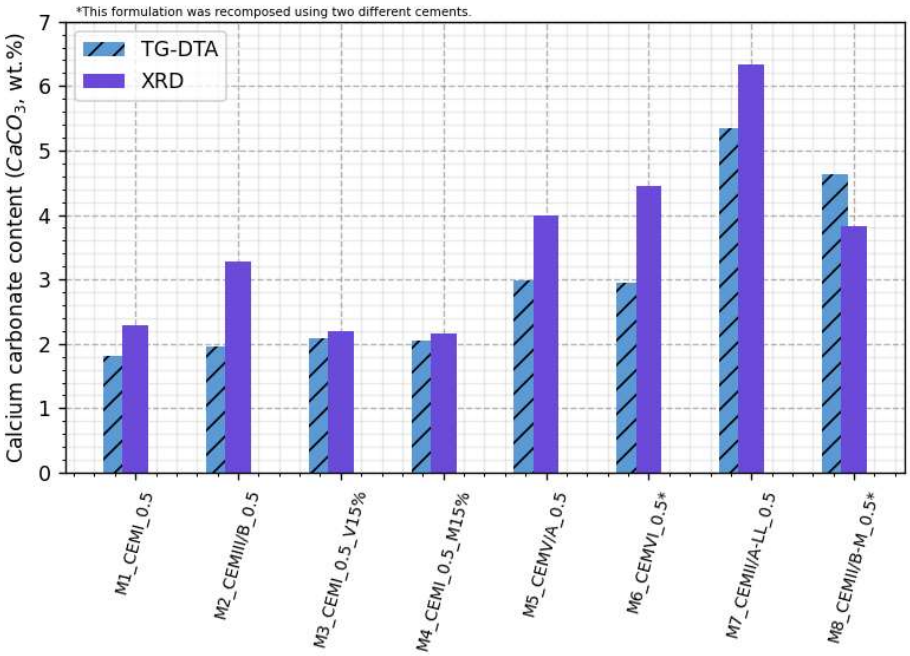

Figure II-34 Calcite content (wt.% of sample) obtained after 90 days of water conservation by means of thermogravimetric analysis, X-ray diffraction and modelling.

For the evaluation of calcite content, the mean absolute difference was found to be 0.68 wt.% and the mean absolute relative difference was 21.2%. TG-DTA analysis yielded lower values for calcite content compared to XRD, which supports the hypothesis of a higher degree of carbonation in the sample analysed using XRD.

The values obtained from TG-DTA analysis were used for the remainder of this work, except for the M5_CEMV/A_0.5 mix at 28 days, where the value obtained from XRD measurement was used instead.

The evolutions in portlandite and calcite contents over time are illustrated in Figure II-35.

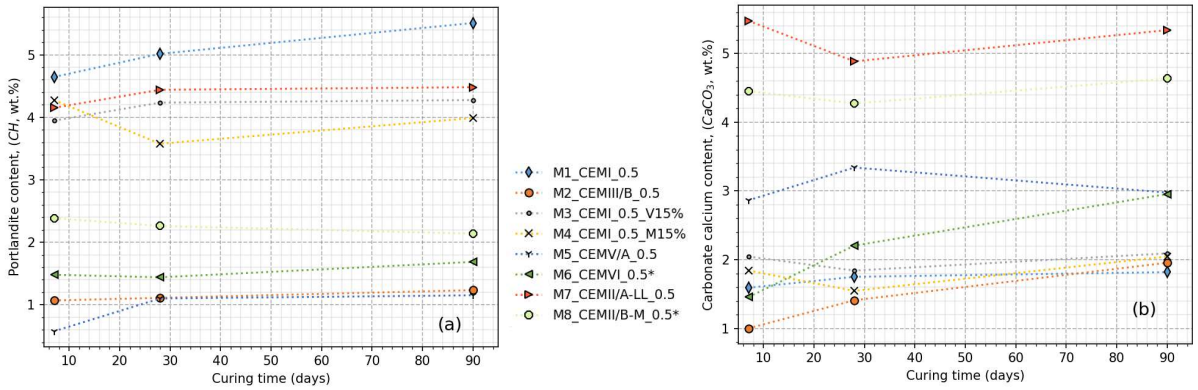

Figure II-35 Portlandite (a) and calcite (b) contents evolutions measured with TG-DTA.

The results on Figure II-35 show that:

- M1_CEMI_0.5 is the mixture that yields the highest concentration of portlandite. This can be attributed to its elevated clinker content, which primarily contributes to the formation of portlandite. The hydrate content increases as the conservation time lengthens, indicating that although a significant portion of portlandite formation occurs during the initial stages, cement hydration continues for at least 90 days.

- In terms of portlandite content, M7_CEMII/A-LL_0.5 ranks second. This reduction can be attributed to the lower clinker content, which is substituted by a filler (12 wt.%). Consequently, an increased $CaCO_3$ content is observed. Regarding the hydration kinetics, it appears that portlandite formation is predominantly completed within a 28-day conservation period. This can be attributed to the use of CEM II/A-LL 42.5 R, which exhibits a faster hardening time compared to the CEM I 52.5 N used for M1 (R denotes "Rapide" while N denotes "Normale" in French).
- For the mixes M3_CEMI_V15%_0.5 and M4_CEMI_M15%_0.5, two phenomena explain the lower amount of portlandite produced compared to the M1 mix. Firstly, 15 wt.% of additions are used to replace the CEM I, resulting in a lower clinker content. Secondly, both Fly ash and Metakaolin are pozzolanic additions. The anhydrous species that compose them consume the portlandite to form C-S-H and other hydrates such as C-A-S-H (see Section I.2.2). The formation of C-S-H is delayed compared to the hydration of portlandite. This delay may explain the significant drop in portlandite content between 7 and 28 days for M4. Carbonation cannot be responsible for the portlandite consumption in the sample, as the $CaCO_3$ content found for M4 at 28 days is lower than for 7 and 90 days. M3 does not exhibit the same behaviour. A possible explanation could be a lower rate of C-S-H formation, leading to a delayed consumption of portlandite. This delayed consumption could explain why the portlandite content stops increasing at 28 days for M3, while it continues to increase for M1 and M4 (which have compositions based on the same Portland cement). The kinetics of the pozzolanic reactions differ depending on the addition and other parameters (see Section I.2.2), as well as the amount of consumable portlandite. For these formulation conditions (W/B close to 0.5), fly ash leads to a lower consumption of portlandite than metakaolin, which is consistent with the findings in the literature (Figure I-8, Section I.2.2).
- The M8_CEMII/B-M_0.5* cement consists of 72 wt.% clinker, 11 wt.% slag, and 11 wt.% fly ash. The gradual decrease in portlandite over time can be attributed to the continuous consumption resulting from pozzolanic reactions and potentially varying carbonation ratios. The latter possibility is supported by the higher calcium carbonate content observed at 90 days of conservation.
- The replacement of clinker with higher amounts of pozzolanic and latent hydraulic additions is responsible for the reduced levels of portlandite in the three other mixes. The respective clinker contents for mixes M6, M2, and M5 are 42 wt.%, 29 wt.%, and 56 wt.%. It is possible that a minimal value of portlandite content be necessary for the pozzolanic hydration to proceed. This could explain the stagnation of portlandite content in M2_CEMIIIB_0.5 and M5_CEMV/A_0.5. However, a question arises regarding M6_CEMVI_0.5*, which essentially combines M2 and M5. Based on its composition, one would expect its values to fall between the one of the other two mixes. Surprisingly, the obtained values are higher, possibly due to the measurement method's uncertainty. Nevertheless, Figure II-31, which might prove the observation of a different phenomenon.

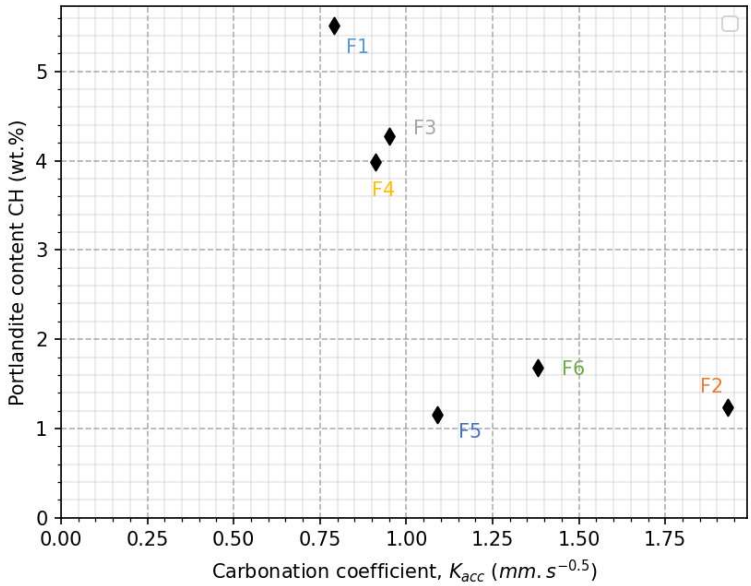

Figure II-36 Portlandite content obtained on mortars vs. carbonation rate obtained in MC after 90 days.

The Figure II-36 shows the relationship between the portlandite contents acquired in various mortars and the carbonation rate (K_{acc}, $mm.day^{-0.5}$) obtained with the equivalent concrete mixes conserved in MC (see Figure II-18 in Section II.3.5).

The results indicate a correlation between these two parameters, wherein a decrease in portlandite content leads to lower carbonation resistance. The relatively reduced K_{acc} value observed for F5, despite its lower portlandite content (according to the measurements realised on M5), can be attributed to its lower porosity and gaseous permeability. This explanation aligns with the findings presented in Figure II-10 of Section II.3.3, which display lower K_{dry} values for F5 in comparison to F2 and F6.

II.3.9.2. CO2 storing capacity and buffer capacity

The remaining concrete powders manufactured for analysis after a duration of 90 days were subsequently subjected to a carbonation chamber for a period of 10 days. The carbonation chamber was maintained at a relative humidity of 65%, a temperature of 20°C, and contained 3% CO_2. Following carbonation, thermogravimetric analysis was performed on the fully carbonated powders in order to determine their CO_2 storage capacity. The resulting $CaCO_3$ content of the different mixes is presented in Figure II-37.

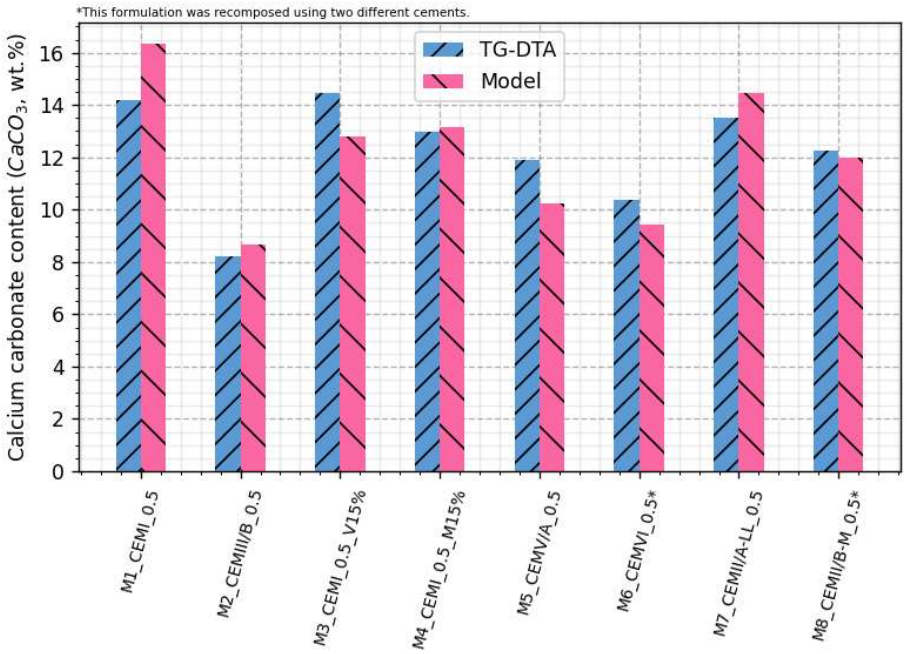

Figure II-37 $CaCO_3$ contents originated from carbonation of the different mix powders measured using TG-DTA and computed with the hydration model.

It should be noted that the initial $CaCO_3$ content of the sound material has been removed from these results (considering the values obtained after 90 days of conservation in water). Therefore, the complete content of $CaCO_3$ available in M7 and M8 is not shown in Figure II-37.

The results indicate different capacities of the cements to sequester CO_2. The representation of the $CaCO_3$ content appears to increase almost linearly with the clinker content in the binder, as depicted in Figure II-38.

The measurement of the $CaCO_3$ content in the mortar M3 may be inaccurate, as it yields a value higher than that obtained for M1. These findings demonstrate that the hydrates formed during clinker hydration have a greater ability to carbonate and store CO_2, thus impeding the progress of carbonation depth. Portlandite, which is transformed into C-S-H (or C-A-S-H) in concrete with pozzolanic and slag additions, is the main type of hydrate involved in this process. When pozzolanic and latent hydraulic are used, the presence of calcium in the material persists, albeit in a form that is less prone to carbonate, resulting in lower levels of $CaCO_3$.

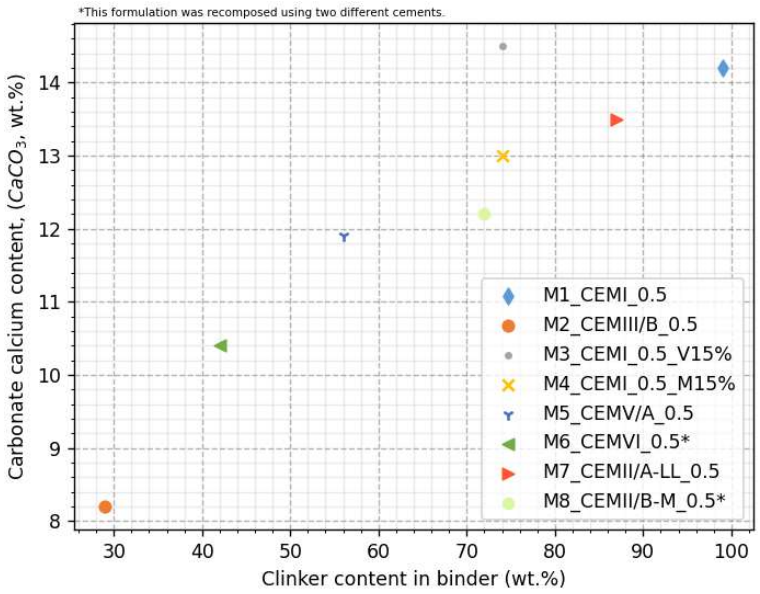

Figure II-38 $CaCO_3$ contents produced by the carbonation vs. initial clinker content in binder.

The results obtained from the Lacarrière and Kolani model exhibit minimal discrepancies when compared to the experimental measurements (refer to Figure II-37). A mean absolute difference of 1.03 wt.% is observed alongside a mean relative difference of 8.24%.

II.4. Discussions and conclusions

II.4.1. Pozzolanic additions and conservation conditions

The experimental campaign conducted on the six mixes generated a significant amount of data, encompassing various conservation conditions. This section presents a concise summary of the conclusions derived from this study.

First, the classification of the different properties measured during the experimental campaign is realised in Figure II-39 for each condition of conservation. It shows the following results:

- CEM I-based mixes demonstrate the highest mechanical resistance after 28 days. This can be attributed to the use of a cement with a characteristic resistance of 52.5 N, compared to CEM III/B 32.5 N used for F2 and F6, and CEM V/A 42.5 N used for F5 and F6. It is worth noting that all three conservation conditions show the same order of classification. These results are supported by similar classifications for compressive strength in mortars (refer to Figure II-2). Additionally, it is important to mention that the characteristic value of mechanical resistance obtained with CEM III/B is lower than the value provided by the supplier, explaining also why F2 exhibits the lowest mechanical properties. A different ranking is observed for compressive strength after 90 days of MC. F4 is surpassed by F3, F5, and F6, indicating the hydration limitation of metakaolin in these formulation conditions.
- An overall examination of the microstructure of the mixtures, along with assessment of the water-accessible porosity (φ, 90 days), gas permeability (K_{dry}), and liquid permeability (K_{liq}), reveals that the mixes F1, F5, and F4 exhibit less permeable microstructures, followed by F3. It is also evident that there is a decrease in microstructure quality associated with the use of CEM III/B in mixtures F2 and F6, particularly during early-age hydration stages, or in unfavourable hydration conditions (EC and DC).
- As expected, the use of mixes with high clinker content demonstrates better performance in both natural and accelerated carbonation. F1 and F4 exhibit the lowest carbonation rate, followed by F3. Conversely, F5 and F6 exhibit superior properties compared to F2. As

described in Section II.3.9.1, for similar physical transfer properties there is a correlation between carbonation kinetics and the presence of portlandite. This correlation explains the lower performance of mixes with higher slag and fly ash contents. Notably, after 90 days of conservation in water, mortar M5 exhibits a lower portlandite content compared to M2 and M6. Therefore, the higher resistance to carbonation in F5, compared to F2 and F6, can be attributed to the denser and less permeable microstructure of the concrete. Furthermore, the comparison between F3 and F4 reveals that metakaolin performs better than fly ash in terms of carbonation resistance, regardless of the conservation and carbonation exposure conditions. The higher W_{eff}/B_{tot} ratio of F3 (0.52), compared to F4 (0.49), could also explain these results. Despite the results obtained in this study, it has been demonstrated that concrete incorporating supplementary cementitious materials (SCMs) can exhibit favourable performance in carbonating environments under specific conditions. For instance, reducing the water-to-binder ratio enhances the carbonation resistance of these mixes, resulting in acceptable resistance to carbonation [73], [369], [370]. As a result, the incorporation of high levels of SCMs in the formulation can be justified using the FD P18-480 (2022) methodology.

- The results of chloride migration coefficients exhibit a distinct trend. Firstly, the mixes with the highest content of pozzolanic and latent hydraulic additions demonstrate the best performance, despite having a more permeable matrix in the case of F6 and F2. This phenomenon can be attributed to the ability of the hydrates present in these concretes, namely C-S-H and Afm, to attract and bind chloride ions. These findings are consistent with previously reported research on the topic, as outlined in Section I.3.2 [248], [371], [372]. This observation partially explains the superior resistance of slag and pozzolanic-based concretes in preventing chloride penetration, largely due to the favourable chemical properties of these cementitious matrices [373], [374].
- The results obtained on electrical resistivity also reveal similar observations. The mixes F2, F5, and F6 exhibit the highest values, particularly when conserved in MC. Additionally, F4 demonstrates relatively high electrical resistivity during the early stages of concrete age, even under unfavourable conservation conditions. It can be observed that higher values of electrical resistivity are certainly associated with the composition of the interstitial solutions of the concrete mixes. The results of liquid permeability and water-accessible porosity indicate that F1 exhibits a denser matrix. However, the compacity of its cementitious matrix appears to be insufficient in achieving high electrical resistivity values. Consequently, the electrical resistivity values obtained for F2, F5, and F6 are the outcome of pozzolanic and latent hydraulic reactions, leading to the formation of different species compared to clinker hydration.

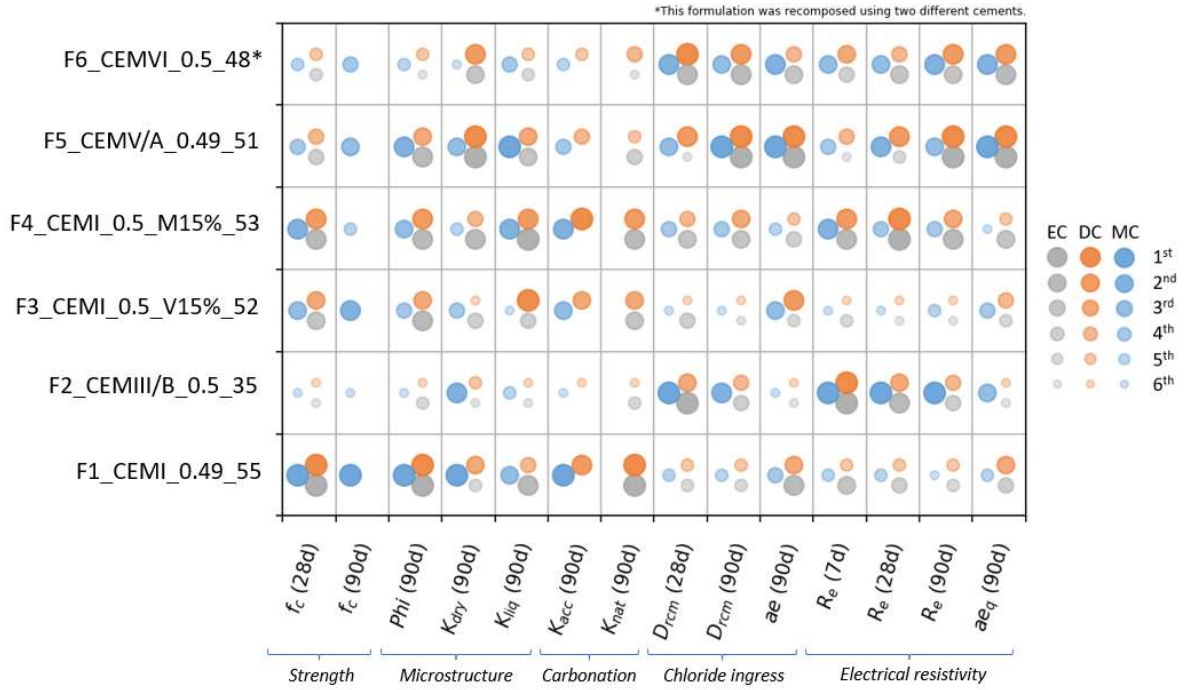

Figure II-39 Classification of performance order of the six mixes for each parameter and conservation.

For nearly all parameters, the moist conservation (MC) environment results in optimized values for all properties, albeit impacting them differently. Table II-15 summarizes the relative differences observed between the parameters of concretes conserved in MC and concretes conserved in dry conditions (DC) for each parameter measured in this study.

Table II-15 Relative difference (%) between the results obtained in MC and DC for the six mixes for each parameter.

	F1_CEMI_ 0.49_55	F2_CEMIII/B_ 0.49_35	F3_CEMI_0.52_ V15%_52	F4_CEMI_0.49_ M15%_53	F5_CEMV/A_ 0.49_51	F6_CEMVI_ 0.5_48*
f_c (28d)	15	21	22	16	29	32
Porosity (90d)	2	5	0	1	3	3
K_{dry} (90d)	80	80	79	60	64	47
K_{liq} (90d)	45	53	33	47	57	51
K_{acc} (90d)	52	31	43	50	47	43
D_{rcm} (28d)	13	74	38	6	31	33
D_{rcm} (90d)	26	78	47	31	54	64
R_e (7d)	11	41	6	7	38	59
R_e (28d)	35	147	21	3	106	133
R_e (90d)	33	344	91	42	156	295

*This formulation was recomposed using two different cements.

In order to analyse the tendencies associated with different properties and mixes, a preliminary representation of the results is shown in Figure II-40 . This figure shows the ratio of relative differences to the maximum relative difference obtained across the six mixes. All parameters evaluated in both MC and DC for each of the six mixes are presented according to this ratio.

The graphics allow for a comparison of the different mixes with regards to the impact of conservation on each parameter. It is obvious that mixes F2, F5, and F6 have a significantly larger area covered compared to the CEM I-based mixes. This indicates that conservation treatment has a greater influence on concretes with a high content of additions as opposed to concretes with a high clinker content. In order to achieve the desired durability of pozzolanic and latent hydraulic-based concretes, it is imperative to carry out a conservation process under suitable conditions and for an extended duration. Additional factors that can contribute to enhanced performance include minimizing the W_{eff}/B_{tot} ratio and implementing thermal treatment. These measures are crucial for attaining superior qualities in these types of concretes. It is important to note that the concrete specimens studied in this research have a water-to-binder ratio of approximately 0.5. It can be anticipated that the amount of clinker will have a lower impact on concrete specimens with lower water content. The higher density of the matrix in these specimens should ultimately enhance their performance, counterweighting the chemical effect linked to the binder nature.

Regarding the mixes F1, F3, and F4, Figure II-40 reveals that although the overall benefit of the conservation treatment is lower compared to mixes with higher addition contents, certain properties remain dependent on the conservation treatment. Specifically, the permeabilities to gas (K_{dry}) and liquid (K_{liq}), as well as the accelerated carbonation rate (K_{acc}), exhibit a ratio of 0.6 or higher for all mixes. This implies that the conservation treatment has an equivalent impact on these three parameters for all types of concrete in this study. This observation is also supported by Figure II-41 which illustrates the average relative difference between CEM I-based concretes and fly ash or/and slag-based concretes. Moreover, this graphic confirms that the differences in impact on water-accessible porosity and compressive strength (after 28 days) are minimal compared to other parameters.

F3 appears to be more affected by the conservation conditions, despite having a similar clinker content to F1 and F4. The values obtained for the D_{rcm} parameters and the compressive strength f_c in Figure II-40 are equal to or greater than 0.5, indicating a larger increase in parameter values from DC to MC conditions. This suggests that fly ash addition is more dependent on conservation conditions compared to other mineral additions like metakaolin in this specific composition. This is further supported by the higher "average" parameter value shown in Figure II-40 , which is lower for F1 and F4 compared to F3.

The obtained areas for the formulations F2, F5 and F6 indicate that the increase in global conservation impact is closely associated with the addition content. Notably, the smallest area among the three is observed for F5 (22 wt.% of slag and 22 wt.% of fly ash), followed by F6 (11 wt.% of fly ash and 46.5 wt.% of slag), and finally F2 (71 wt.% of slag). This finding reflects the growing demand for extended humidity exposure as the content of pozzolanic and latent hydraulic additions increases, due to their longer hydration time compared to clinker.

Figure II-40 Ratio of relative differences between MC and DC compared to the maximum obtained on the six formulations for F1 (a), F2 (b), F3 (c), F4 (d), F5 (e) and F6 (f).

The benefits of conservation concretes in high relative humidity conditions on the various parameters investigated in this study are presented in Figure II-41, comparing clinker-based formulations to concrete with high fly ash and slag contents. In mixtures with high clinker contents, the parameters exhibited increases ranging from 1% (water-accessible porosity) to 73% (gas permeability), with an average increase of 32%. Conversely, mixtures with high slag and fly ash contents displayed increases up to a maximum of 265% for electrical resistivity measured at 90 days, and an average relative increase of 74%. Notably, a significant improvement in conservation was observed for chloride migration coefficients (D_{rcm}) at 28 and 90 days, as well as electrical resistivity values (R_e) at 7, 28, and 90 days. Furthermore, it is worth mentioning that these benefits increase as the conservation period for measurement lengthens.

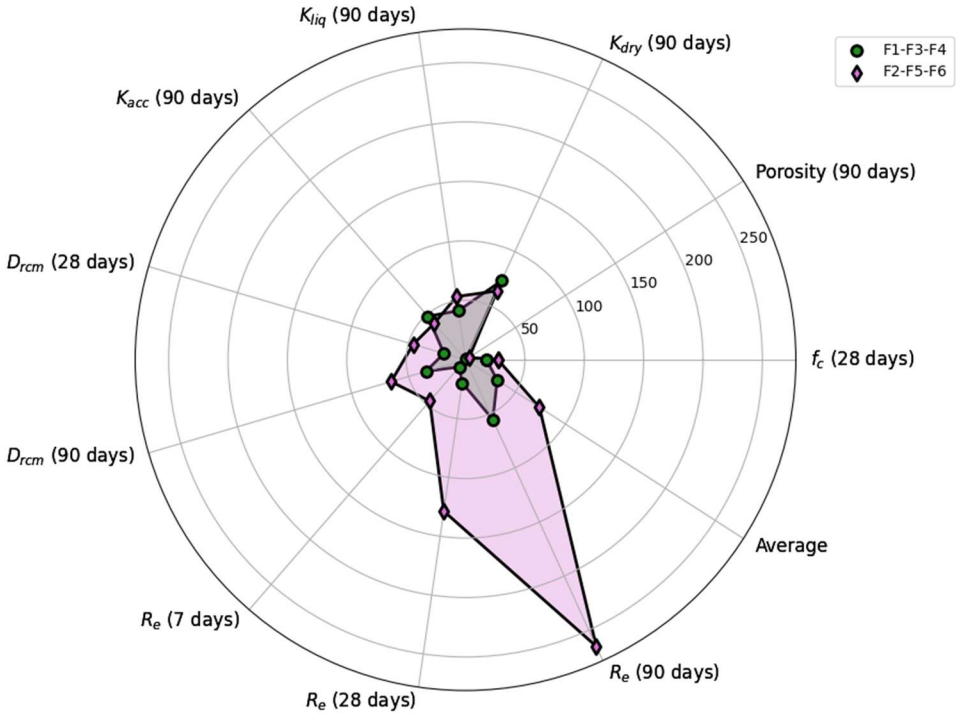

Figure II-41 Average relative difference obtained on CEM I based-mixes (F1-F3-F4) and on mixes with high clinker replacement ratio (F2-F5-F6).

The differences observed between unfavourable conservation treatments (DC and EC) and favourable conservation treatment (MC) can be significant, particularly in the case of low carbon concrete containing high levels of pozzolanic and latent hydraulic additions. In order to classify the concrete materials, especially within a performance-based approach, it is important to consider the conservation treatment applied to the entirety of the concrete components. The following section compares the outcomes of the prescriptive approach with those of the performance-based approach, using the results obtained from concrete conserved in MC and concrete conserved in DC. This analysis focuses on carbonation and chloride exposure classes (XC, XS and XD).

II.4.2. Prescriptive approach [1] and Performance-based approach described in FD P 18-480 (2022)

The outcomes obtained during this experimental study are utilised for classifying the six concrete mixes. The two methods outlined in Section I.6 are employed and juxtaposed. Firstly, the performance-based approach as described in the FD P18-480 (2022) is implemented by utilizing the outcomes of:

- Accelerated carbonation rate (K_{acc}, mm.days$^{-0.5}$) measured following the recommendation of the XP P18-458 (2022).
- Porosity accessible to water (Phi, %) measured according to the NF P18-459 (2022).
- Chloride migration coefficient (D_{rcm}, mm^2.s^{-1}) measured according to the XP P18-462 (2022).
- Electrical resistivity (R_e Ohm.m) measured according to the XP P18-481 (2022).
- The values of ageing factor computed with the Equation II.7 given in the FD P18-480 (2022) are used (see Section II.3.7).

According to the FD P18-480 (2022), the measurements of various parameters are conducted on specimens that have been conserved in a humid environment with a relative humidity (RH) exceeding 95%. However, this practice raises doubts, particularly because prefabricated concrete and cast-in-place concrete typically undergo a brief curing and conservation periods. To address this concern and facilitate comparisons, the present study aims to examine the parameter values obtained under two alternate

conservation conditions in addition to the moist conditions. This analysis intends to investigate the impact of different conservation methods on the validation of exposure classes and acceptance criteria.

The validation is presented in Figure II-42. The application of the performance-based approach to the mixes and results of this study leads to various conclusions:

- Firstly, significant differences are observed between the results of a single mix conserved under different conditions. This observation applies to all mixes, including the ones with CEM I as well as those with high pozzolanic and slag contents. For instance, mix F1 conserved in MC meets the requirements for its use in subclasses XC3, XC4, and XD1. However, when the same mix is conserved in EC or DC, its properties fall short of the criteria for these subclasses. A total of 34 cases were identified where the concrete met the requirements for subclasses when conserved in MC but not when conserved in DC. This discrepancy is even more pronounced for the mixes F3 and F4, where 8 and 6 differences were found, respectively. It is worth noting that the moist conservation (MC) is employed to classify the mixes according to FD P18-480 (2022).
- Secondly, the same conservation treatments result in different concrete cover reductions. Results obtained in MC lead to higher possibilities in terms of structural class reduction for concrete cover determination than DC and EC. 25 cases were observed across the six mixes.
- Finally, the two methods for classifying concrete materials according to their carbonation resistance do not yield the same results, despite considering the same concrete formulation and conservation conditions. 4 cases were observed where validation based on porosity accessible to water accepts the concrete material, but validation based on carbonation rate criteria deems the use of the concrete material in the same subclass invalid. The criteria of the performance-based approach defined in FD P18-480 (2022) were established based on the results of the PerfDuB project and its database of results obtained on 42 concretes. A comparison was made between the results obtained for accelerated carbonation rate and porosity accessible to water to establish a conservative relationship. This resulted in the definition of two criteria to validate a concrete formulation in XC environment. However, the more conservative criteria and the most valid method for XC classes validation should be the one based on the accelerated carbonation rate evaluation. The values of porosity and accelerated carbonation rate obtained for mixes F2 (MC for XC4 and DC for XC2), F5 (DC for XC2), and F6 (DC for XC2) show a different trend. Differences in structural class reduction can also be observed depending on the validation method used. It explains why the measurement of the accelerated carbonation is forced by the fascicule when a concrete is being validated in XC3 or XC4 with the porosity accessible to water criteria.

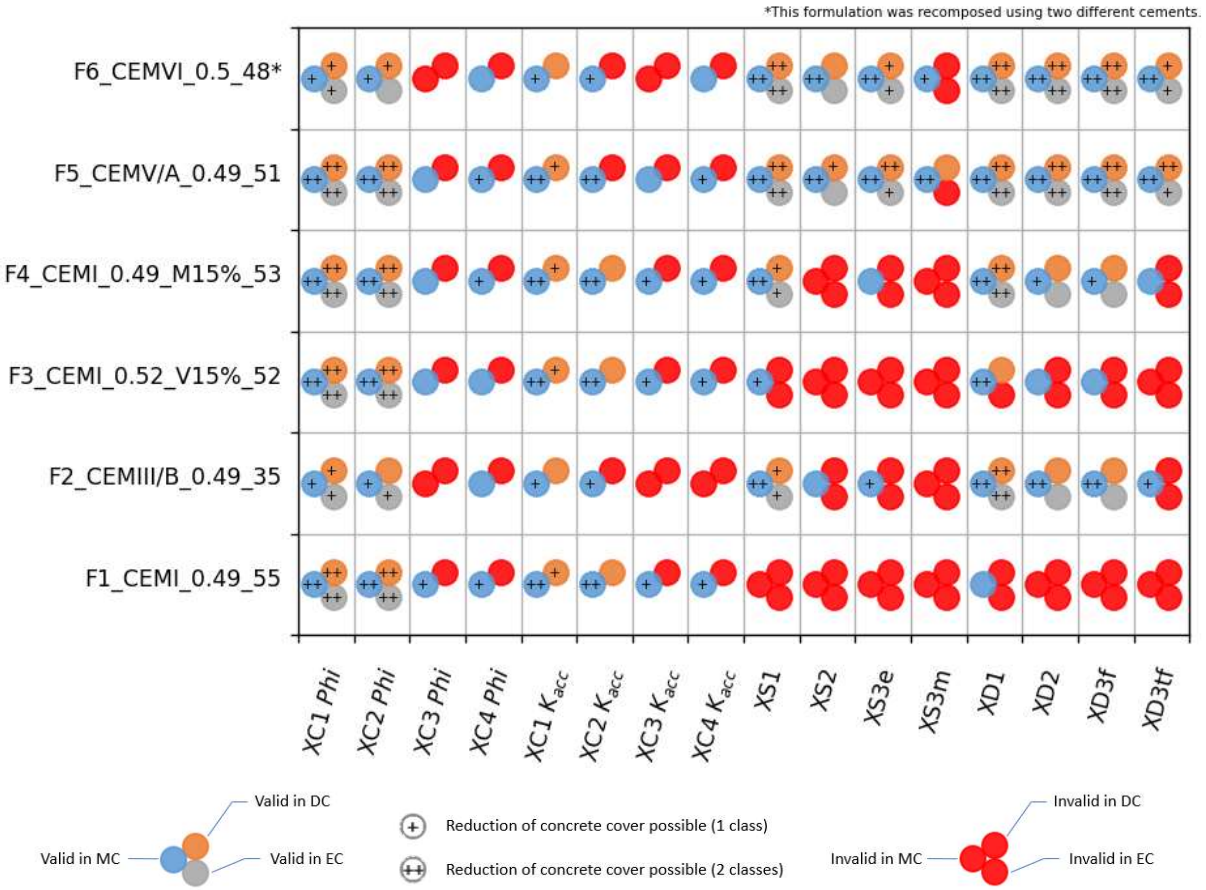

Figure II-42 Validation of the different exposure classes according to the performance-based approach described in the FD P18-480.

The findings presented in this study highlight potential shortcomings of the performance-based approach outlined in the FD P18-480 (2022). One issue is the failure to consider the curing class of the structure when determining the appropriate curing treatment for the specimens. This study, specifically Section II.4.1, demonstrates the significant impact of conservation conditions on concrete properties, particularly on mixes with higher levels of SCMs. Consequently, validating a low-carbon concrete with a high content of pozzolanic or latent hydraulic additions using the current method may yield distorted results.

The fascicule's recommendation for conservation with elevated relative humidity would likely result in artificially improved results compared to those that would be obtained under less favourable conservation conditions on the actual structure. Therefore, basing decisions about reducing concrete cover on results obtained through moist conservation could lead to premature deterioration of the reinforced concrete structure due to early initiation of deterioration.

A more appropriate approach would be to use the same conservation conditions throughout the different steps of the performance-based approach (study, convenience, and control). This would better simulate the real durability of the chosen concrete material.

In order to implement the prescriptive approach outlined in the NF EN 206/CN+A2, the characteristic strengths (f_{ck}) are determined based on the mean values of compressive strength obtained after a 28-day conservation period ($f_{c,28}$).

Equation II.13 is utilised for this purpose and is applicable when the average compressive strength is derived from cylindrical specimens with dimensions of 110/220 mm [320]:

$$f_{ck} = f_{c,28} - 8 \text{ MPa} \quad \text{Eq (II.13)}$$

The Table II-16 presents the various equivalent resistance classes. It is crucial to note that these classes are typically determined after a conservation period of 28 days in a wet environment with a relative humidity (RH) exceeding 95%. Nevertheless, to enable comparison with the previous performance-based approach undertaken on various conservation treatments, the values acquired from samples conserved in EC and DC are also included in the analysis.

Table II-16 Characteristic resistance classes of the different mixes conserved in the different conditions of the PhD.

f_{ck} (MPa)	F1_CEMI_0.49_55	F2_CEMIII/B_0.49_35	F3_CEMI_0.52_V15%_52	F4_CEMI_0.49_M15%_53	F5_CEMV/A_0.49_51	F6_CEMVI_0.5_48*
EC	C35/45	C20/25	C30/37	C35/45	C25/30	C20/25
DC	C35/45	C20/25	C30/37	C35/45	C25/30	C20/25
MC	C40/50	C25/30	C40/50	C40/50	C40/50	C40/50

*This formulation was recomposed using two different cements.

The eligibility of the different concrete mixes in each conservation for their use in various exposure classes can be determined by referring to the tables NA.F1 and NA.F3 of the NF EN 206/CN+A2 (2022). The outcomes are then presented in Table II-17. A colour code is used. A green "N" indicates a case where a concrete mix is not valid for a specific subclass based on the prescriptive approach but can be justified by the performance-based approach. In the case of subclasses XS3 and XD3, a blue colour is used for the letter "N" to indicate that the less aggressive equivalent subclass (XS3e and XD3f respectively) can be justified through the performance-based approach. When the conditions to use the concrete mix are met according to the prescriptive approach but not valid in the performance-based approach, a red "Y" is used. A blue "Y" is used when only one subclass of XS3 or XD3 is validated by the performance-based approach.

Table II-17 Prescriptive approach according to the tables NA.F1 and NA.F3 of the NF EN 206/CN+A2 (2022).

	F1			F2			F3			F4			F5			F6		
	NA.F1			NA.F3			NA.F1			NA.F1			NA.F1			NA.F3		
	MC	EC	DC	MC	EC	DC	MC	EC	DC	MC	EC	DC	MC	EC	DC	MC	EC	DC
XC1	Y	Y	Y	Y	Y	Y	Y	Y	Y	Y	Y	Y	Y	Y	Y	Y	Y	Y
XC2	Y	Y	Y	Y	Y	Y	Y	Y	Y	Y	Y	Y	Y	Y	Y	Y	Y	Y
XC3	Y	Y	Y	N	N	N	Y	Y	Y	Y	Y	Y	Y	Y	Y	Y	N	N
XC4	Y	Y	Y	N	N	N	Y	Y	Y	Y	Y	Y	Y	Y	Y	Y	N	N
XS1	Y	Y	Y	N	N	N	Y	Y	Y	Y	Y	Y	Y	N	N	Y	N	N
XS2	Y	Y	Y	N	N	N	Y	Y	Y	Y	Y	Y	Y	N	N	Y	N	N
XS3	Y	Y	Y	N	N	N	N	N	N	Y	Y	Y	Y	N	N	Y	N	N
XD1	Y	Y	Y	N	N	N	Y	Y	Y	Y	Y	Y	Y	N	N	Y	N	N
XD2	Y	Y	Y	N	N	N	Y	Y	Y	Y	Y	Y	Y	N	N	Y	N	N
XD3	Y	Y	Y	N	N	N	N	N	N	Y	Y	Y	Y	N	N	Y	N	N

The results demonstrate that the behaviour of the method varies depending on the type of concrete under consideration. Specifically, there is a notable occurrence of cases where the prescriptive approach is validated and the performance-based approach is invalidated for CEM I-based mixes (F1, F2, and F4) (36 instances of "Y" and 3 of "Y"). Conversely, for mixes with a high content of slag and fly ash (F2, F5, and F6), the opposite trend is observed, with many cases showing validation by the performance-based approach that cannot be achieved using the prescriptive approach (33 instances of

"N" and 6 of "N"). This highlights the interest of the performance-based approach, as it allows for more flexibility in material usage.

Concretes with higher levels of pozzolanic additions exhibit lower mechanical strength in relation to their ability to resist chloride ingress or carbonation, when compared to traditional Portland cement-based concrete. Consequently, considering durability indicators (D_{rcm}, ae, K_{acc}, and φ_c^w) directly leads to a higher ranking for these concretes and enhances their potential for various applications.

According to the findings of this study, the validation of a project utilizing concrete with a higher clinker content is more likely to be achieved through the prescriptive approach rather than the performance-based approach. Conversely, the validation of low carbon concrete with a higher concentration of pozzolanic or slag additions is more likely to be accomplished through a performance-based approach.

Furthermore, Table II-18 displays the maximum exposure classes (XC, XS, and XD) that the various concrete mixes can withstand. The initial values correspond to the prescriptive approach outlined in NF EN 206/CN+A2 (2022), while the second set of values represents the performance-based approach presented in FD P18-480 (2022).

Table II-18 Exposure classes respected by the different mixes for each conservation treatment.

206/18-480		F1	F2	F3	F4	F5	F6
XC	DC	XC3/XC2	XC2/XC2	XC3/XC2	XC3/XC2	XC3/XC2	X0/XC2
	MC	XC3/XC3	XC2/XC3	XC3/XC3	XC3/XC3	XC3/XC3	XC3/XC4**
XS	EC	XS3/X0	X0/XS1	XS2/X0	XS3/XS1	X0/XS3e	X0/XS2*
	DC	XS3/X0	X0/XS1	XS2/X0	XS3/XS1	X0/XS3m	X0/XS2*
	MC	XS3/X0	X0/XS2*	XS2/XS1	XS3/XS3e	XS3/XS3m	XS3/XS3m
XD	EC	XD3/X0	X0/XD3f	XD2/X0	XD3/XD3f	X0/XD3tf	X0/XD3tf
	DC	XD3/X0	X0/XD3f	XD2/XD1	XD3/XD3f	X0/XD3tf	X0/XD3tf
	MC	XD3/XD1	X0/XD3tf	XD2/XD3f	XD3/XD3tf	XD3/XD3tf	XD3/XD3tf

**XS2 considered more aggressive than XS3e in the FD P18-480 (2022).*

*** XC3 considered more aggressive than XC4.*

II.4.3. Carbon footprint indicator

The computation of the carbonation footprint conducted in Section II.2.4 (refer to Table II-7) is determined for a volume of 1 m^3 of concrete, allowing for comparisons at equivalent volumes. However, in the design of reinforced concrete structures, the volume of concrete used is dependent on various variables. If a prescriptive approach is applied, the design of the structure will be influenced by the desired lifetime and the exposure conditions it will face. In the case of a performance-based approach, the characteristics of the concrete may also result in changes to the required concrete cover. It has been demonstrated in previous sections that the different concrete mixes developed in this study were not able to withstand the same exposure classes and aggressive phenomena equally. The main objective of the performance-based approach is to assist structural engineers in optimizing the economic and ecological costs of their materials. This approach allows for the use of mineral additions with lower carbon footprints and also enables a reduction in the minimum concrete cover required if the performance of the concrete material meets the necessary criteria. As a result, there are two avenues available to reduce the overall carbon footprint of a reinforced concrete structure or component: altering the components used in its production and minimizing the quantity of material utilised. For this reason, ongoing standardization efforts, particularly those undertaken by the 2nd task force (TF2) of the AFNOR P18B/GE SBS standardization commission (low carbon solution), are shifting towards a functional unit perspective (with a value expressed in $kg_{CO2}eq/m^2$) rather than solely considering concrete volume ($kg_{CO2}eq/m^3$).

The mixes in this study were compared across three exposure classes, following the performance-based approach outlined in FD P18-480 (2022). The exposure classes considered were XC4 and XD1 for all six mixes, and XS2 for mixes F2, F5, and F6. Table II-19 provides a summary of the results obtained from the performance-based approach for these exposure classes. The results used in this study were acquired with samples conserved in MC.

Table II-19 Performance-based approach for the justification of the mixes use in the exposure classes XC4, XS2 and XD1.

N3	F1	F2	F3	F4	F5	F6
XC4 – Porosity	Y+	Y	Y	Y+	Y+	Y
XS2	N	Y	N	N	Y++	Y++
XD1	Y	Y++	Y++	Y++	Y++	Y++

The concrete cover prescribed by the NF EN 1992-1-1 was utilised in this study. A lifespan of 100 years was assumed for the structure. The concrete cover values obtained for various exposure classes and mixes are presented in Table II-20.

Table II-20 Concrete cover prescribed according to the performance-based approach and the NF EN 1992-1-1.

CC (mm)	F1	F2	F3	F4	F5	F6
XC4 – Porosity	35	40	40	35	35	40
XS2	-	50	-	-	40	40
XD1	45	35	35	35	35	35

The same reasoning is applied using the prescriptive approach of the NF EN 206/CN+A2. Table II-21 presents a summary of the outcomes obtained through this approach for the three evaluated exposure classifications.

Table II-21 Prescriptive approach (NA.F1/NA.F3) for the justification of the mixes use in the exposure classes XC4, XS2 and XD1.

N3	F1	F2	F3	F4	F5	F6
XC4	Y	N	Y	Y	Y	Y
XS2	Y	N	Y	Y	Y	Y
XD1	Y	N	Y	Y	Y	Y

The resistance classes computed in the Table II-16 of Section II.4.2 facilitate the reduction of the structural class for all mixes, with the exception of F2 due to its insufficient resistance class. In order to meet the required concrete cover, the corresponding values prescribed using this methodology are presented in Table II-22.

Table II-22 Concrete cover prescribed according to the prescriptive approach and the NF EN 1992-1-1

CC (mm)	F1	F2	F3	F4	F5	F6
XC4	35	-	35	35	35	35
XS2	45	-	45	45	45	45
XD1	40	-	40	40	40	40

The computation of carbon footprint associated with a part having a surface area of one square meter is performed for each concrete mix, taking into consideration the concrete covers specified in Table II-20 and Table II-22, along with the equivalent CO_2 values obtained from Table II-7, as calculated in Section II.2.4. The computed results are presented in Table II-23.

Table II-23 Equivalent CO_2 ($kgCO_2eq$) obtained prescribed according to the performance-based approach/the prescriptive approach and the NF EN 1992-1-1 recommendation.

$kgCO_2eq$	F1	F2	F3	F4	F5	F6
XC4	10.4/10.4	5.1/-	10.2/8.9	9.1/9.1	6.6/6.6	6.3/5.5
XS2	-/13.3	6.4/-	-/11.4	-/11.7	7.6/8.5	6.3/7.1
XD1	13.3/11.8	4.5/-	8.9/10.2	9.1/10.4	6.6/7.6	5.5/6.4

The results demonstrate that:

- In 6 out of 18 cases, the performance-based approach results in lower final equivalent CO_2 values by allowing the use of a lower concrete cover. However, the opposite trend is observed in 3 cases (F1 in XD1 and F3, F6 for XC4), indicating the limitations of the performance-based approach for certain scenarios. These limitations are specifically observed in cases with high clinker content in exposure classes susceptible to chloride-induced corrosion, and high reactive mineral addition contents in exposure classes prone to carbonation-induced corrosion.
- The mix F2, which is prohibited under the prescriptive approach, exhibits the lowest CO_2 equivalent in terms of volume (refer to Table II-7). Despite having a higher concrete cover compared to other mixes, it also leads to the lowest values for exposure classes XD1 and XC4. However, its carbon footprint exceeds that of the F6 mix for exposure class XS2. This highlights the importance of considering accurately the impact of a component rather than solely focusing on the volume of concrete. The overall impact associated with the use of a given concrete in a structure depends on the design (concrete cover) permitted for it, necessitating compliance with the recommendations of various standards and approaches, as demonstrated in this section.
- Nonetheless, the mixes F1, F3, and F4 consistently yield higher equivalent CO_2 values compared to the mixes F2, F5, and F6. This indicates a limited influence of geometry on CO_2 emissions in comparison to that of concrete formulations, creating a distinction between different cement types.

The evaluation of concrete's carbon impact is of significant interest, as illustrated above. In Daminelli's research [375], various metrics were calculated by combining the equivalent CO_2 emissions of a concrete mixture with the values of the concrete performance. This allowed Daminelli to assess the eco-efficiency of a specific concrete based on its compressive strength (f_c, MPa) and electrical resistivity (Re, Ohm.m). For the former, the indicator $f_{cCO_2,i}$, which represents the ratio of the equivalent CO_2 emissions from the binder to the mechanical strength (f_c) after 28 days of conservation, is determined using Equation II.14. Similarly, the second indicator $Re_{CO_2,i}$ is obtained by using Equation II.15 to calculate the ratio of the equivalent CO_2 emissions of the binder to the electrical resistivity (Re) achieved after 28 days of conservation.

$$f_{cCO_2,i} = \frac{equivalent\ CO_2\ emissions}{f_c} \quad \text{Eq (II.14)}$$

$$Re_{CO_2,i} = \frac{equivalent\ CO_2\ emissions}{Re} \quad \text{Eq (II.15)}$$

The values obtained for the six mixes are represented in the Figure II-43 for $f_{c\,CO_2,i}$ and Figure II-44 for $Re_{CO_2,i}$, each time with the results obtained in DC and in MC.

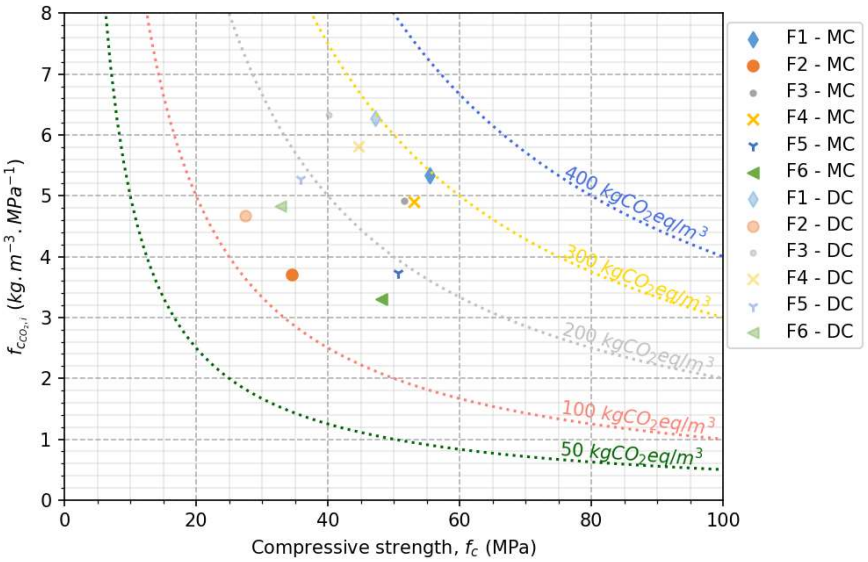

Figure II-43 CO_2 emissions relative to the compressive strength ($f_{c\,CO_2,i}$, $kgCO_2eq.m^{-3}.MPa^{-1}$) vs. 28 days compressive strength values (f_c, MPa).

The results presented in Figure II-43 demonstrate the efficiency of mixes F5 and F6 when subjected to a favorable conservation treatment. These mixes exhibit a relatively high mechanical strength of approximately 50 MPa, while maintaining a reduced carbon impact of less than 200 $kg_{CO2}eq/m^3$ of concrete. In comparison, mix F2, which has a lower carbon footprint, only reaches 35 MPa, limiting its overall suitability. Compositions with higher clinker contents unsurprisingly show less promise due to their higher carbon footprint of approximately 300 $kg_{CO2}eq/m^3$.

The use of a dryer conservation method, which is less conducive to the hydration process, significantly affects the overall results. Mixes with higher additions contents (F2, F5, and F6) experience greater reduction in their mechanical properties compared to compositions with higher clinker contents (F1, F4, and F5). Consequently, the desirability of mixes F5 and F6 diminishes due to their lower achieved mechanical strength.

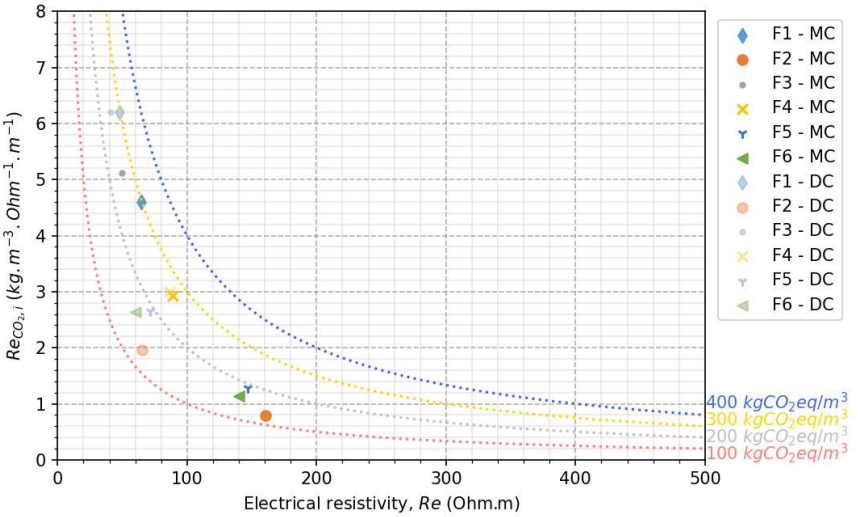

Figure II-44 CO_2 emissions relative to the electrical resistivities ($Re_{CO_2,i}$, $kgCO_2eq.m^{-3}.Ohm^{-1}.m^{-1}$) vs. the 28 days electrical resistivity values (R_e, Ohm.m);

The results presented in the second graph Figure II-44 indicate a greater interest in mixes with a high content of fly ash and/or slag conserved in MC. Specifically, F2, F5, and F6 exhibit a lower carbon footprint and higher electrical resistivity compared to mixes with higher clinker contents (F1, F3, and F4). Furthermore, this disparity between the two types of concrete is expected to increase when considering the electrical resistivity achieved after 90 days of conservation (refer to the values in Section II.3.8).

The results obtained in DC also demonstrate that higher eco-efficiency is achieved in mixes F2, F5, and F6, despite the lower difference in electrical resistivity. These findings highlight the benefits of using pozzolanic and latent hydraulic additions in general, as they enhance concrete resistance against corrosion and reduce the carbon footprint associated with its production.

A more comprehensive comparison of the results obtained in this study with those reported in the literature is conducted in Section IV.3.3.3, using the database of experimental results.

III. SDReaM-Crete model

III.1. Introduction

The model SDReaM-Crete (Serviceability, Durability and ReliAbility Modelling for reinforced Concrete structure) was originally developed at the LMDC and the CERIB by Jonathan Mai-Nhu during his PhD [7] and later by Lucie Schmitt [6]. This section presents the results of their research as well as the improvement made in the present work.

SDReaM-Crete is a Finite Element Model (FEM) that is based on solving several non-linear, coupled mass conservation equations, which are described in more detail in this section. The primary objective of the model is to simulate the degradation of concrete due to its interaction with the environment, specifically the penetration of CO_2 and chloride ions. In order to consider the influence of temperature and saturation degree on durability, the heat and hydrologic transfer processes are implemented in the model.

Furthermore, the model takes into account the combined effects of carbonation and chloride penetration, with the influence of carbonation on the microstructure of concrete and the binding capacity of hydrates (C-S-H and Afm).

III.2. Model input

SDReaM-Crete requires a minimum of 50 input parameters. The numerical values in question vary depending on the specific case study, mainly influenced by the defined boundary conditions and initial conditions. They are presented in the following tables. They can be classified in three categories:

- Physicochemical and mathematical constants (Table III-1).
- Environmental parameters (Table III-2).
- Material parameters (Table III-3).

III.2.1. Chemical, physical, and mathematical constants

The various physical quantities and mathematical constants utilised in the model are documented in Table III-1. These inputs primarily originate from established literature, earlier developed models, or fundamental assumptions. Certain quantities have been empirically adjusted during the current study to enhance the model's treatment of low carbon binders. Consequently, these adjusted values may exhibit variation within a specified range provided in the table.

Table III-1 Constants of the SDReaM-Crete model.

Parameter	Symbol	Unit	Value	Source
Reference temperature	T_{ref}	K	293.15	-
Reference saturation level for the sorption homothety calculation	Sr_{ref}	-	0.55	-
Gas law constant	R	$J.mol^{-1}.K^{-1}$	8.314	-
Dynamic viscosity of water at reference temperature	$\eta_{l,0}$	Pa.s	$1.002 \cdot 10^{-3}$	-
Activation energy of the water viscosity	Ea_{η_l}	$J.mol^{-1}$	-15700	-
Molar mass of water	M_{H_2O}	$kg.mol^{-1}$	$1.8 \cdot 10^{-2}$	-
Bulk density of water	ρ_{H_2O}	$kg.m^{-3}$	1000	-
Molar volume of water	Vm_{H_2O}	$m^3.mol^{-1}$	$1.8 \cdot 10^{-5}$	-
First constant for vapour diffusion in porous medium	a_{H_2O}	-	1.2	[7]
Second constant for vapour diffusion in porous medium	b_{H_2O}	-	2.7	[7]

Parameter	Symbol	Unit	Value	Source
Van Genuchten parameter	m	-	0.22 – 0.5	[376]
Van Genuchten parameter to account for connectivity	l	-	0.5	[376]
Proportionality factor for the hydrates' carbonation	$Kt1_0$	s^{-1}	10^{-5}	[7]
Activation energy of the hydrates' dissolution during carbonation	Ea_{Kt1}	$J.mol^{-1}$	-40000	-
Equivalent carbonates constant	$Kt4$	-	$1.9639 \cdot 10^{-3}$	[7]
Proportionality factor for the carbonates' formation	$Kt5$	s^{-1}	$5 \cdot 10^{-3}$	[7]
Diffusion coefficient of carbonate ions in saturated medium	$D_{CO_3^{2-}(S_r=1)}$	$m^2.s^{-1}$	$9.55.10^{-10}$	-
Diffusion coefficient of carbon dioxide in a non-porous medium	$D_{CO_2,0}$	$m^2.s^{-1}$	$1.6.10^{-5}$	-
Activation energy of the carbon dioxide diffusion coefficient	Ea_{DCO_2}	$J.mol^{-1}$	39000	-
First constant for gas diffusion in porous medium	a_{CO_2}	-	1.2	[377]
Second constant for gas diffusion in porous medium	b_{CO_2}	-	3.3	[377]
Molar volume of portlandite	Vm_{CH}	$m^3.mol^{-1}$	$3.321 \cdot 10^{-5}$	-
Molar mass of C-S-H	M_{CSH}	$kg.mol^{-1}$	$1.965 \cdot 10^{-1}$	-
Molar volume variation of the C-S-H during carbonation	ΔVm_{CSH}	-	$2.3 \cdot 10^{-5}$	[7]
C-S-H carbonation kinetic constant	n_1	-	1.5	[7]
Molar volume of calcite	Vm_{CaCO_3}	$m^3.mol^{-1}$	$3.693 \cdot 10^{-5}$	-
Proportionality factor of the chemical chloride binding	$Kt2$	s^{-1}	$4.25 \cdot 10^{-12}$	[7]
Proportionality factor of the physical chloride binding	$Kt3$	s^{-1}	$3.33 \cdot 10^{-8}$	[7]
Constant of the chemical chloride binding	Icl_1	-	0.8586	[244]
Second constant of the chemical chloride binding	Icl_2	-	0.58	[244]
Constant of the physical chloride binding	Icl_3	-	0.1218	[244]
Second constant of the physical chloride binding	Icl_4	-	0.3339	[244]
Activation energy of the chloride ions diffusion coefficient	Ea_{DCl}	$J.mol^{-1}$	40000	[20]
Constant accounting for the ionic diffusion resistance	Rl	-	6	[378]

III.2.2. Environmental parameters

The model incorporates four parameters, namely relative humidity, temperature, carbon dioxide concentration, and chloride concentration, to account for the environmental factors. These parameters, as depicted in Table III-2, play a crucial role in determining the boundary conditions within the model.

The environmental data presented in Table III-2 serve as illustrative examples, and it should be emphasized that, depending on the modelled conditions, either constant values or temporal functions can be employed. In this study, two common types of function, namely sinusoidal (or cosinusoidal) functions ($X_{env,sin}$) and conditional functions ($X_{env,cond}$), are utilised to represent the environmental

variables. These functions are defined by specific equations based on the time range, specifically by Equations III.1 or III.2 for any environmental parameter X.

Table III-2 Environmental parameters of the SDReaM-Crete model (computed with Equations III.1, III.2 or constant).

Parameter	Symbol	Unit	Value	Source
Environmental humidity	RH_{env}	%	Depends on the environment	-
Chloride concentration in the environment	$[Cl^-]_{env}$	mol.m^{-3}	Depends on the environment	-
Carbon dioxide concentration in the environment	$P_{CO_2,env}$	Pa	Depends on the environment and the hypothesis for global warming	A minimum value of 40.53 Pa, equivalent to 0.04%.vol is considered when in contact with air
Environment temperature	T_{env}	K	Depends on the environment	-

$$X_{env,sin}(t) = X_{mean} + \Delta X_{an} \sin\left(\frac{t}{365 \times 86400}\right) + \Delta X_{mon} \sin\left(\frac{t}{30 \times 86400}\right) + \cdots \quad \text{Eq (III.1)}$$

X_{mean} is the average value of the parameter X, ΔX_{an} is the amplitude of the annual variation, ΔX_{mon} is the amplitude of the monthly variation. The time t is expressed in second. For enhanced temporal precision, additional sinusoidal functions can be incorporated, such as to account for daily variations.

$$X_{env,cond}(t) = \begin{cases} X_{min}, & t \in [t_1; t_2] \\ X_{max}, & t \in [t_2 + \Delta t, t_1 - \Delta t] \\ X_{max} - (X_{max} - X_{min})\dfrac{(t - (t_1 - \Delta t))}{\Delta t}, & t \in [t_1 - \Delta t, t_1] \\ X_{min} + (X_{max} - X_{min})\dfrac{(t - t_2)}{\Delta t}, & t \in [t_2, t_2 - \Delta t] \end{cases} \quad \text{Eq (III.2)}$$

X_{max} and X_{min} are the maximal and minimal value reached. A periodicity of one year is commonly employed for this function, enabling, for instance, the modelling of chloride boundary conditions in the event of deicing salt utilization.

III.2.3. Material parameters

The material parameters outlined in Table III-3 are utilised to characterize the properties of the concrete. These parameters correspond to properties evaluated through experimental measurements or through the models detailed in Section I.4.5 and Annex 4.

Table III-3 Material parameters of the SDReaM-Crete model.

Parameter	Symbol	Unit	Value	Source
Bulk density of concrete	$\rho_{concrete}$	kg/m^3	Depends on concrete	From concrete
Initial concrete porosity	φ_0	-	Depends on concrete	From experience
Liquid water permeability	k_{l1}	m^2	Depends on concrete	From experience
Desorption isotherm polynomial coefficient (5 terms)	Iso_i	-	Depends on concrete	From experience
Calcium quantity able to carbonate contained in CH	Ca_{CH}	mol.m^{-3} of concrete	Depends on concrete	[287]
Calcium quantity able to carbonate contained in C-S-H	Ca_{CSH}	mol.m^{-3} of concrete	Depends on concrete	[287]

Parameter	Symbol	Unit	Value	Source
Calcium quantity able to carbonate contained in Aft	Ca_{Aft}	mol.m^{-3} of concrete	Depends on concrete	[287]
Calcium quantity able to carbonate contained in Afm	Ca_{Afm}	mol.m^{-3} of concrete	Depends on concrete	[287]
C/S ratio of C-S-H	C/S	-	1.65	[287]
Initial concentration of chloride in the material	Cl_{mat}	mol/m^3$_{solution}$	Depends on concrete composition	From technical sheets
Chloride effective diffusion coefficient	D_{Cl_0}	m^2.s^{-1}	Depends on concrete	From experience
Lifetime desired	t_{final}	Years	Depends on the specifications	-
Concrete cover	CC	m	Depends on the standards or measurements	[320]

III.3. Finite Element Modelling with Comsol

The SDReaM-Crete model comprises multiple sets of differential equations that encapsulate the mass conservation principles for different species within the concrete material. This section provides a comprehensive description of each equation, as well as the analytical expressions employed for variable computation. The significance of each constant parameter is documented in the Table III-1, Table III-2 and Table III-3, and therefore is not reiterated within this section.

Due to the intricate relationships and cross-interactions among multiple species, the equations involved in this study exhibit a non-linear nature. Hence, an implicit schematic approach is adopted to solve these equation sets. The resolution of these equations is accomplished using the PARDISO solver within the Comsol environment, employing the constant method (Newton) as the chosen non-linear computation technique.

Different mass conservation equations are integrated in the model and utilised to represent different physical quantities. The latter are summarized in Table III-4, along with the corresponding equations that represent them.

Table III-4 Different species considered in the model SDReaM-Crete.

Specie		Unit	Equation	Boundary conditions at the concrete surface	Default initial conditions
Relative humidity ($\boldsymbol{RH}$)		-	Eq (III.4)	Eq (III.17)	1
Partial pressure of CO_2 ($\boldsymbol{P_{CO_2}}$)		Pa	Eq (III.18)	Eq (III.24)	0.4
Carboxyl ions concentration ($[\boldsymbol{CO_3^{2-}}]$)		mol.m^{-3}$_{solution}$	Eq (III.25)	Eq (III.3)	0
Chloride ions concentration ($[\boldsymbol{Cl^-}]$)		mol.m^{-3}$_{solution}$	Eq (III.33)	Eq (III.43)	Cl_{mat}
Temperature ($\boldsymbol{T}$)		K	Eq (III.45)	Eq (III.46)	T_{env}
Calcium available for carbonation	CH (Ca_{CH})	mol.m^{-3}$_{concrete}$	Eq (III.47)	Eq (III.3)	$Ca_{CH,0}$
	C-S-H (Ca_{CSH})		Eq (III.48)		$Ca_{CSH,0}$
	Afm (Ca_{Afm})		Eq (III.49)		$Ca_{Afm,0}$
	Aft (Ca_{Aft})		Eq (III.50)		$Ca_{Aft,0}$
Friedel's salts ($\boldsymbol{Ca_{FS}}$)			Eq (III.51)		0 mol/m^3
Calcite ($\boldsymbol{CaCO_3}$)			Eq (III.52)		0 mol/m^3

The boundary conditions of the various differential equations correspond either to the surface of the material or to the inner core of the material at a specified depth (represented by x_{hea}). For the former case, this section specifies the boundary conditions for each species that undergo diffusion. As for the latter case, the Neuman condition, expressed with Equation III.3, is utilised for all considered species (X).

$$\frac{\partial X(x_{heart}, t)}{\partial t} = 0 \qquad \text{Eq (III.3)}$$

The introduced equation facilitates the incorporation of symmetry considerations in the system, such as the application of identical conditions on all concrete surfaces. The Neuman condition (Equation III.3) is employed on the concrete surface for all species that are assumed to be immobile within the material. Adhering to these assumptions, the presented model effectively prevents leaching and washout of the species, except for chloride.

III.3.1. Relative humidity (RH, -)

Mass balance equation:

Relative humidity is modelled to represent the moisture condition and liquid water motion in the material and the exchange with the environment. The significance of its consideration is twofold. Firstly, its effect on diffusion must be taken into account for adequate modelling of chloride and carbon dioxide transfers. Additionally, the convection of chloride (and to a lesser extent carboxyl ions) cannot be modelled without considering hydrologic transfer.

The mass conservation equation is stated by Equation III.4, where no convective term is included.

$$C_{p,h}\frac{\partial RH}{\partial t} = div\left((D_L + D_V)\overrightarrow{grad}(RH)\right) + \beta_{H_2O} \qquad \text{Eq (III.4)}$$

Where the capacitive term $C_{p,h}$ is expressed with the Equation III.5.

$$C_{p,h} = \rho_l \varphi \frac{\partial S_r}{\partial RH} + \frac{p_{vsat} M_{H_2O}}{RT}\varphi(1 - S_r - RH\frac{\partial S_r}{\partial h}) \qquad \text{Eq (III.5)}$$

The determination of the liquid and vapor diffusion coefficients at each time step, denoted as D_L and D_V respectively, is performed using Equations III.6 and III.7.

$$D_L = \frac{\rho_l k_l k_{rl} RT}{\eta_l M_{H_2O} RH} \qquad \text{Eq (III.6)}$$

$$D_V = \frac{M_v R_{dg} p_{vsat} D_0}{RT} \qquad \text{Eq (III.7)}$$

The saturation degree (S_r) of the concrete material can be determined as a function of RH by employing an approximate desorption isotherm, expressed as a polynomial whose coefficients $iso0$ to $iso4$ depend on the concrete mix and conservation conditions. A polynomial equation is utilised in this study instead of a more commonly employed isotherm (such as BET, Pickett, Van Genuchten, etc.) due to its ease of solvability and the convenience of computing its derivative.

$$S_r = iso4\ RH^4 + iso3\ RH^3 + iso2\ RH^2 + iso1\ RH + iso0 \qquad \text{Eq (III.8)}$$

φ is the porosity accessible to water of the concrete material. This parameter is time dependent and accounts for the impact of the carbonation on the porous network. The Equation III.9 is used to compute its value from the initial porosity to water φ_0 and the evolution of C-S-H and CH content.

$$\varphi(t) = \varphi_0 - \begin{pmatrix} Vm_{CaCo_3}\left(CaCO_3(t) - \left(Ca_{CSH,0} - Ca_{CSH}\right)\right) \\ -Vm_{CH}\left(\left(Ca_{CH,0} - Ca_{CH}\right)\right) \\ +\Delta Vm_{CSH}\left(Ca_{CSH,0} - Ca_{CSH}\right) \end{pmatrix} \quad \text{Eq (III.9)}$$

p_{vsat} represents the saturation vapor pressure and is calculated using the Rankine formula [241]:

$$p_{vsat} = 101325exp\left(13.7 - \left(\frac{5120}{T}\right)\right) \quad \text{Eq (III.10)}$$

The dependence of liquid water viscosity on temperature can be expressed using the Equation III.11, which is based on the Arrhenius law.

$$\eta_l = \eta_{l,0} \exp\left(-\frac{Ea_{\eta_{l,0}}}{R}\left(\frac{1}{T} - \frac{1}{T_{ref}}\right)\right) \quad \text{Eq (III.11)}$$

k_{rl} is the parameter of Van Genuchten-Mualem accounting for the resistance to liquid permeability. It is computed with the Equation III.12 [379], [380].

$$k_{rl} = {S_r}^l\left[1 - \left(1 - S_r^{\frac{1}{m}}\right)^m\right]^2 \quad \text{Eq (III.12)}$$

$R_{dg_{H2O}}$ represents the diffusion resistance of vapor in the porous material, and it is defined according to the Millington' law, which depicts the influence of porosity and saturation degree on vapor transfer, as discussed by [381]:

$$R_{dg_{H2O}} = \varphi^{a_{H2O}}(1 - S_r)^{b_{H2O}} \quad \text{Eq (III.13)}$$

Finally, Equation III.14 represents the release of liquid water β_{H_2O} as a result of carbonation of Portlandite. The source term's format aligns with a linearized representation of a thermodynamic model utilised to study the process of portlandite dissolution in an environment containing carbonate ions. It assumes that all bound water is released during the carbonation process. Consequently, the carbonation of 1 mol of calcium in Portlandite releases 1 mol of water.

$$\beta_{H_2O} = -\frac{\partial Ca_{CH}}{\partial t}\frac{M_{H_2O}}{\rho_l} = -Kt_1 Ca_{CH}\left[{CO_3}^{2-}\right]M_{H_2O} \quad \text{Eq (III.14)}$$

The other hydrates were not considered in the work conducted by Schmitt, despite their potential in releasing water. Therefore, their inclusion is realised in this research. It should be mentioned that the significance of this aspect is quite restricted and holds little importance when examining durability parameters such as carbonation depth. However, for the sake of accuracy, the Equation III.15 incorporates the variables associated with the three additional hydrate species present in the model.

$$\beta_{H_2O} = -Kt_1\left(\left(Ca_{CH} + 3Ca_{Afm} + 5.33Ca_{Aft}\right)\left[{CO_3}^{2-}\right] + 2Ca_{CSH}\left[{CO_3}^{2-}\right]^{n1}\right)M_{H_2O} \quad \text{Eq (III.15)}$$

The variable Kt_1 represents the carbonation kinetic of various hydrates. Its calculation is based on Equation III.16, which incorporates a value obtained through laboratory experiments conducted at specific temperature conditions of 20 °C (Kt_{1_0}) and an Arrhenius law to ensure accuracy and reliability in determining the variable for different temperatures.

$$Kt_1 = Kt_{1_0} exp\left(-\left(\frac{Ea_{Kt_1}}{R}\right)\left(\frac{1}{T} - \frac{1}{T_{ref}}\right)\right) \quad \text{Eq (III.16)}$$

Boundary conditions – surface of concrete:

The boundary condition of relative humidity at the surface of the concrete material is expressed using a Dirichlet condition. While the specific value of the condition (RH_{env}) may vary depending on the environment under consideration, the Equation III.17 is commonly utilised as a general expression to represent the boundary condition:

$$RH\left(x = x_{surf}, t\right) = RH_{env} \quad \text{Eq (III.17)}$$

III.3.2. Partial pressure of CO_2 (P_{CO_2}, Pa)

Mass balance equation:

The mass conservation equation for the partial pressure of CO_2 is calculated according to the following Equation III.18, which characterizes the diffusion of CO_2 within the porous network and its subsequent dissolution in the interstitial solution, resulting in its transformation into carboxyl ions CO_3^{2-}. The equation does not take into account any convective term.

$$C_{p,CO_2}\frac{\partial P_{CO_2}}{\partial t} = -div\left(-\frac{D_{CO_2}R_{dg_{CO_2}}}{RT}\overrightarrow{grad}P_{CO2}\right) - \beta_{CO_3{}^{2-}} \quad \text{Eq (III.18)}$$

Where the capacitive term for P_{CO_2} (C_{p,CO_2}) is computed with Equation III.19.

$$C_{p,CO_2} = \frac{\varphi(1 - S_r)}{RT} \quad \text{Eq (III.19)}$$

D_{CO_2} is the diffusion coefficient of the carbon dioxide which is computed following an Arrhenius law based on the work of [6] and expressed with Equation III.20.

$$D_{CO_2} = D_{CO_{2_0}} exp\left(-\left(\frac{Ea_{CO_2}}{R}\right)\left(\frac{1}{T} - \frac{1}{T_{ref}}\right)\right) \quad \text{Eq (III.20)}$$

$R_{dg_{CO_2}}$ is the diffusion resistance coefficient expressed with the Millington law in the Equation III.21.

$$R_{dg_{CO_2}} = \varphi^{a_{CO_2}}(1 - S_r)^{b_{CO_2}} \quad \text{Eq (III.21)}$$

$\beta_{CO_3{}^{2-}}$ represents the sink term that accounts for the dissolution of carbon dioxide (CO_2) in the interstitial solution and its subsequent transformation into cation form. In this model, the calculation of $\beta_{CO_3{}^{2-}}$ is based on the following Equation III.22. The thermodynamic equilibrium is considered in this equation with the term $\left[CO_3{}^{2-}\right]_{eq}$ computed using Equation III.23.

$$\beta_{CO_3{}^{2-}} = \frac{\partial[CO_3{}^{2-}]}{\partial t} = Kt_5\left(\left[CO_3{}^{2-}\right]_{eq} - \left[CO_3{}^{2-}\right]\right) \quad \text{Eq (III.22)}$$

$$\left[CO_3{}^{2-}\right]_{eq} = \frac{Kt_4}{RT}P_{CO_2} \quad \text{Eq (III.23)}$$

Boundary conditions – surface of concrete:

The boundary condition of the carbon dioxide is considered using a condition of Dirichlet with the Equation III.24:

$$P_{CO_2}\left(x = x_{surf}, t\right) = P_{CO_2,env} \quad \text{Eq (III.24)}$$

For the same reasons, the value of $P_{CO_2,env}$, which can be represented as either a constant or a function of time (refer to Equations III.1 and III.2), relies on the specific environmental factors under consideration.

III.3.3. Carboxyl ions CO_3^{2-} ($[CO_3^{2-}]$, mol/m³sol)

Mass balance equation:

The carboxyl ions are regarded as important species in this model due to their involvement in the carbonation reaction between carbon dioxide and calcite. The assumption is made that the successive transformation of CO_2 into H_2CO_3, HCO_3^-, and CO_3^{2-} can be considered as a single step. This simplification is supported by the fact that the dissolution of CO_2 is the limiting reaction in the overall reactive equations under these specific pH and temperature conditions [382]. The conversion of acidic species is assumed to occur nearly instantaneously, leading to the direct formation of CO_3^{2-} [382]. The mass balance equation for this system can be expressed by Equation III.25.

$$C_{P,CO_3^{2-}} \frac{\partial [{CO_3}^{2-}]}{\partial t} = -div\left(-D_{{CO_3}^{2-}} \overrightarrow{grad}[{CO_3}^{2-}] + \overrightarrow{\varphi_l}[{CO_3}^{2-}]\right) - \beta_{CaCO_3} + \beta_{{CO_3}^{2-}} \quad \text{Eq (III.25)}$$

Where the capacitive term $C_{P,CO_3^{2-}}$ is computed with Equation III.26:

$$C_{P,CO_3^{2-}} = \varphi S_r \quad \text{Eq (III.26)}$$

$D_{{CO_3}^{2-}}$ is the diffusion coefficient of the carboxyl ions and is computed using Equation III.27:

$$D_{{CO_3}^{2-}} = D_{{CO_3}^{2-}(S_r=1)} R_{dl} \quad \text{Eq (III.27)}$$

R_{dl} is the coefficient accounting for the liquid diffusion resistance of CO_3^{2-} and is computed as a function of the saturation degree with the Equation III.28:

$$R_{dl} = {S_r}^{Rl} \quad \text{Eq (III.28)}$$

$\overrightarrow{\varphi_l}$ represents the velocity field of the water flux in the material. This variable is used to represent the convective flux of cations. The Equation III.29 is used to compute its value from the relative humidity content and variation.

$$\overrightarrow{\varphi_l} = V_{wx} F_L C_{P,CO_3^{2-}} \quad \text{Eq (III.29)}$$

Where V_{wx} is the flux of water computed with Equation III.30. By analogy with the heat flux transfer, this term will represent the conductive flux of the relative humidity in the direction x. F_L is the fraction related to the liquid transport in the material (-) computed with the Equation III.31.

$$V_{wx} = (D_L + D_V)\frac{\partial RH}{\partial x} \quad \text{Eq (III.30)}$$

$$F_L = \frac{D_L}{D_L + D_V} \quad \text{Eq (III.31)}$$

β_{CaCO_3} represents the sink term accounting for the reaction between carboxyl ions and calcium in various hydrates. In the model, it is postulated that carbonate ions undergo a reaction with the calcium component found in different hydrates, leading to the creation of calcite. These reactions can be combined and simplified into a unified equation, drawing inspiration from the principles of thermodynamic chemistry. Its calculation involves the use of the Equation III.32 and encompasses the entirety of carbonation phenomena, including the carbonation of Friedel's salts.

$$\beta_{CaCO_3} = \frac{\partial CaCO_3}{\partial t} = Kt_1\left([{CO_3}^{2-}](Ca_{CH} + Ca_{AFt} + Ca_{AFm} + Ca_{FS}) + Ca_{CSH}[{CO_3}^{2-}]^{n_1}\right) \quad \text{Eq (III.32)}$$

Boundary conditions – surface of concrete:

The process of leaching is not considered by the model for this specie. Furthermore, only the aerial diffusion of CO_2 has been taken into account. This assumption is based on data from the literature, which indicates that the aerial diffusion capacity is 10^4 times higher than that of CO_2 dissolved in solution (in the form of CO_3^{2-}) [7]. Consequently, the boundary conditions at the surface for $[{CO_3}^{2-}]$ is expressed using the same Equation III.3 (Neumann), which imposes the absence of exchange with the environment.

III.3.4. Chloride ions Cl- ($[Cl^-]$, mol/m^{3}sol)

Mass balance equation:

The mass balance equation of chloride ions can be expressed as follows:

$$C_{P,Cl}\frac{\partial[Cl^-]}{\partial t} = -div\left(-D_{Cl^-}\overrightarrow{grad}[Cl^-] + \overrightarrow{\varphi_l}[Cl^-]\right) - \beta_{CSH} - \beta_{SF} \qquad \text{Eq (III.33)}$$

Where the capacitive term $C_{P,Cl}$ is defined with Equation III.34. It can be noted that this term intervenes in the computation of $\overrightarrow{\varphi_l}$ and replaces $C_{P,CO_3^{2-}}$ in the Equation III.29.

$$C_{P,Cl} = \varphi S_r \qquad \text{Eq (III.34)}$$

D_{Cl^-} is the chloride ions diffusion coefficient in the material for a specific saturation degree. The Equation III.35 uses the diffusion coefficient in fully saturated concrete and the diffusion resistance induced by the saturation degree in the material R_{dl} (refer to Equation III.28) to compute its value.

$$D_{Cl^-} = D_{Cl^-(S_r=1)}R_{dl} \qquad \text{Eq (III.35)}$$

$D_{Cl^-(S_r=1)}$ is expressed with Equation III.36 to consider the temperature influence:

$$D_{Cl^-(S_r=1)} = D_{Cl_0^-}\,exp\left(-\left(\frac{Ea_{DCl}}{R1}\right)\left(\frac{1}{T}-\frac{1}{Tref}\right)\right) \qquad \text{Eq (III.36)}$$

β_{CSH} is the sink term that accounts for the physical binding of chlorides on the calcium-silicate-hydrate (C-S-H). It incorporates the carbonation process of the C-S-H, as the term representing the equilibrium of C-S-H with chloride ions ($[Cl^-{}_{CSH}]_{eq}$) is calculated at each time step using Equation III.38. Hence, this term represents the maximum extent of physical binding achievable in the material at a given time.

$$\beta_{CSH} = Kt_3R_{dl}\left([Cl^-_{CSH}]_{eq} - [Cl^-_{CSH}]\right)\varphi S_r \qquad \text{Eq (III.37)}$$

$$[Cl^-_{CSH}]_{eq} = \frac{Icl_3\,Icl_4\frac{[Cl^-]}{1000}}{1+Icl_4\left(\frac{[Cl^-]}{1000}\right)}M_{CSH}\frac{Ca_{CSH}}{C/S} \qquad \text{Eq (III.38)}$$

Finally, the source term β_{SF} represents the chemical fixation of Afm. It also includes the formation of Friedel's salts and can be expressed as shown in the following Equation III.39:

$$\beta_{FS} = \frac{\partial Ca_{FS}}{\partial t} = 2Kt_2R_{dl}Ca_{AFm}\left(Ca_{FS_{eq}} - Ca_{FS}\right) + \beta_{FS}^{Carbonatation} \qquad \text{Eq (III.39)}$$

The chemical binding capacity of the material $[SF]_{eq}$ is determined using the Equation III.40 at each time step. This equation governs the maximum quantity of Friedel's salts that can be produced.

$$Ca_{FS_{eq}} = \left(Ca_{FS}/2 + Ca_{Afm}\right)Icl_1\left(\frac{[Cl^-]}{1000}\right)^{Icl_2} \qquad \text{Eq (III.40)}$$

Contrary to physical binding, Friedel's salts are considered as a distinct specie in the model. For this reason, carbonation is accounted through another source term $\beta_{SF}^{Carbonatation}$ defined with the Equation III.41.

$$\beta_{FS}^{Carbonatation} = -2Kt_1 Ca_{FS}[{CO_3}^{2-}] \quad \text{Eq (III.41)}$$

Boundary conditions – surface of concrete:

The boundary condition at the surface for chloride was originally defined with a Dirichlet condition (refer to Equation III.42) by Mai-Nhu and Schmitt, as stated in their previous work [6], [7]. However, in order to enhance the accuracy of the obtained results, especially when considering variations in moisture content (and consequently convection), it was decided to adopt the Robin conditions [383] in [236]. These conditions can be mathematically expressed by the Equation III.43.

$$[Cl^-](x = x_{surf}, t) = [Cl^-]_{env} \quad \text{Eq (III.42)}$$

$$\frac{\partial [Cl^-]}{\partial t}(x = x_{surf}, t) = B_C([Cl^-]_{surf} - [Cl^-]_{env}) + [Cl^-]_{env} J_h^s \quad \text{Eq (III.43)}$$

Where :

- B_C is the surface chloride transfer coefficient, comprised between 1 and 6 m/s [383] in [236].
- $[Cl^-]_{surf}$ is the concentration of free chloride ions at the concrete surface. In the model, the value of $[Cl^-]$ in the first zone of the mesh is directly used.
- J_h^s is the normal flux of humidity computed with Equation III.44.

$$J_h^s = B_h(RH_{surf} - RH_{env}) \quad \text{Eq (III.44)}$$

With :

- B_h the surface humidity transfer coefficient. Its value is comprised between 2.43×10^{-7} and 4.17×10^{-7} m/s [384] in [236],
- RH_{surf} the pore relative humidity at the concrete surface. In the model, the value of RH in the first zone of the mesh is used directly.

III.3.5. Temperature (T, Kelvin)

The temperature variable was initially incorporated into the SDReaM-Crete model by Mai-Nhu [7]. Initially, its influence was only taken into account in the variation of the saturation vapour pressure. Later, Schmitt introduced various Arrhenius laws to include the effects of temperature on different parameters [6]. Hence, temperature influence is considered on the chloride ions diffusion and the carbonate ions reaction kinetic. However, a comprehensive balance equation for this variable had not been considered yet. To address this limitation, a modification was made to the model by introducing a differential equation for temperature. This modification enables a more accurate representation of heat transfer within the material and allows for the inclusion of future advancements, such as the consideration of heat generated during hydration as well as radiation. The work of Lacarrière [288] and that of Burkan Isgor and Razaqpur [212] will certainly be used as references for these phenomena, respectively.

The inclusion of temperature conduction in this study is not supported by experimental results, which is a limitation of this research. The functioning of temperature in the model relies solely on information obtained from literature sources and requires further validation. Nonetheless, the rapid nature of temperature conduction in the material, compared to phenomena such as carbonation or hydrologic transfer, would necessitate an experimental timescale significantly smaller than what was used for the

present modelling. If modelling is performed with a lower timescale in the future, such as addressing the measurement of material temperature during hydration to prevent delayed ettringite formation, then additional verifications should be conducted.

Conservation equation:

The expression of the conservation equation for temperature is mathematically defined by the following equation:

$$\rho_{concrete} c_{therm} \frac{\partial T}{\partial t} = div[-k_{therm} \overrightarrow{grad}(T)] + Q_{therm} \quad \text{Eq (III.45)}$$

Where Q_{the} represents the heat source of the system. Since the heat due to the hydration is not yet considered and that no other source is considered in the concrete material, this term is equal to 0.

Boundary conditions – surface of concrete:

The boundary condition associated with the concrete surface is described by Equation III.46, as presented in [236].

$$\frac{\partial T(x = x_{surf}, t)}{\partial t} = B_T(T_{surf} - T_{env}) \quad \text{Eq (III.46)}$$

Where:

- T_{surf} is the temperature at the concrete surface. In the present model, the temperature computed in the first zone of the mesh close to the surface is used.
- B_T is the heat transfer coefficient comprised between 6.2 and 9.3 W/(m^2.K) according to [385] in [236].
- k_{therm} is the thermal conductivity of the concrete material considered equal to 0.8 W/(m.K) [386].
- c_{therm} is the specific heat at constant pressure considered equal to 880 J/(kg.K) [386].

III.3.6. Portlandite (Ca_{CH}, mol/m^3$_{concrete}$)

Mass balance equation:

The calcium present in Portlandite is estimated according to the Equation III.47. The diffusion of ions in the hydrates is assumed to be zero, based on the hypothesis that Ca^{2+} cations directly interact with carboxyl ions upon hydrate dissolution. This simplifies the equations significantly and reduces the computational burden of the model. However, this approach inhibits the potential for considering leaching of concrete.

$$\frac{\partial Ca_{CH}}{\partial t} = -Kt_1 Ca_{CH}[{CO_3}^{2-}] \quad \text{Eq (III.47)}$$

III.3.7. Hydrated calcium silicate C-S-H (Ca_{CSH}, mol/m^3$_{concrete}$)

A simplified equation is proposed for the consideration of C-S-H in this study. The model assumes that Portlandite governs the global carbonation kinetic process. This assumption was initially developed for CEM I-based concrete and materials with low addition content. Consequently, C-S-H is considered without distinguishing between different types, assuming a constant CaO/SiO_2 ratio regardless of the type of cement or SCMs used. Hence, improvements could be made to this part of the model by considering different chemical reactivities based on the binder type.

Mass balance equation:

The calcium contained in the C-S-H is considered with the equilibrium Equation III.48. The unique difference when compared to portlandite concerns the factor n_1 which expresses the difference of carbonation kinetic observed in the literature for this hydrate [104].

$$\frac{\partial Ca_{CSH}}{\partial t} = -Kt_1 Ca_{CSH}[{CO_3}^{2-}]^{n_1} \quad \text{Eq (III.48)}$$

The calcium available for carbonation is also considered for the physical binding of chloride. Further verifications are necessary to assess whether the percentage of calcium available for carbonation is comparable, or closely related, to the amount capable of binding chloride.

III.3.8. Monosulfoaluminates (Ca_{Afm}, mol/m^{3}concrete)

Mass balance equation:

The calcium contained in the Afm and available to carbonation is expressed with the Equation III.49.

$$\frac{\partial Ca_{AFm}}{\partial t} = -Kt_1 Ca_{AFm}[{CO_3}^{2-}] - Kt_2\, Rdl_1 Ca_{AFm}\left(Ca_{FS_{eq}} - Ca_{FS}\right) \quad \text{Eq (III.49)}$$

In addition to the sink term associated with the carbonation of hydrate, this equation also incorporates the sink term related to the reaction between Afm and free chloride, resulting in the formation of Friedel's salt (refer to Equation III.39).

III.3.9. Ettringite (Ca_{Aft}, mol/m^{3}concrete)

Mass balance equation:

Finally, the last hydrate species is considered, with the Equation III.50 representing the equilibrium for calcium present in Aft. This particular hydrate solely influences carbonation, resulting in the presence of only one sink term within the equation:

$$\frac{\partial Ca_{Aft}}{\partial t} = -Kt_1 Ca_{Aft}[{CO_3}^{2-}] \quad \text{Eq (III.50)}$$

III.3.10. Friedel' salts (Ca_{FS}, mol/m^{3}concrete)

Mass balance equation:

In this model, the carbonation of Friedel's salts is being considered. This phenomenon plays a significant role in the reversibility of binding and the effect of carbonation on chloride penetration. The mass balance of the Friedel's salts thus needs to be considered and is expressed using Equation III.51.

$$\frac{\partial Ca_{FS}}{\partial t} = -Kt_1 Ca_{FS}[{CO_3}^{2-}] + Kt_2\, Rdl_1\, \left(Ca_{FS_{eq}} - Ca_{FS}\right) Ca_{Afm} \quad \text{Eq (III.51)}$$

III.3.11. Calcite ($CaCO_3$, mol/m^{3}concrete)

Mass balance equation:

$CaCO_3$ is the product of carbonation and is commonly regarded as an inert specie that does not react or diffuse within the material. Consequently, its equilibrium, expressed through the Equation III.52, only includes a source term that accounts for the carbonation of other species. The difference in carbonation kinetics for C-S-H is also represented by the exponent n_1.

One criticism that can be raised about the model is the assumption of similar carbonation kinetics for all other species. In reality, there are likely variations in the carbonation rates among different hydrates and Friedel's salts that have not been taken into account. However, due to the higher presence of

calcium provided by portlandite and C-S-H compared to other species, this aspect was not defined as a priority. It is essential to consider the significance of this aspect and avoid undermining its importance without providing supporting references, especially when investigating concrete mixtures containing a low amount of portlandite. Hence, this section of the model necessitates further revision in future studies.

$$\frac{\partial CaCO_3}{\partial t} = Kt_1([{CO_3}^{2-}](Ca_{CH} + Ca_{Aft} + Ca_{Afm} + Ca_{FS}) + Ca_{CSH}[{CO_3}^{2-}]^{n_1}) \quad \text{Eq (III.52)}$$

III.3.12. Other functions

The pH in this model is determined using an approximation developed by Mai-Nhu in [7]. This equation is restricted to a minimal value of 7, and a maximal value of 14.

$$\begin{aligned} pH = -\frac{1}{log(10)}\Bigg(log\Bigg(max\Big(0.5\ [Cl^-] + [CO_3^{2-}] \\ + \left(\frac{1}{10^7}\right)(25 \times 10^{12}\ [Cl^-]^2 + 10^{14}\ [Cl^-][CO_3^{2-}] + 10^{14}\ [CO_3^{2-}]^2 \\ + 1)^{0.5}, Eps1\Big)\Bigg)\left(1 - \left(\frac{Ca_{CH}}{Ca_{CH,0}}\right)\right)\Bigg) \\ + \left(Ca_{CH}\frac{11.7 + 0.7exp(-8[Cl^-]) \times exp(-12[CO_3^{2-}])}{Ca_{CH,0}}\right) \end{aligned} \quad \text{Eq (III.53)}$$

The given equation approximates the pH tendency by considering only three species for computation: $[Cl^-], [CO_3^{2-}]$ and Ca_{CH}. It assumes that the concentrations of the other species in the material remain constant, although this may not always be true for reinforced concrete material. Incorporating the modelling of the alkaline species would add complexity to the model and increase the computational load. Hence, it was not considered in this work.

The equation employed may not offer an exact assessment of the pH, but it effectively facilitates the tracking of changes caused by carbonation and chloride penetration. The precise pH value is not necessary for quantifying phenomena like carbonation depth or depassivation within the model. Instead, the fluctuations in the pH value are adequate for defining these phenomena, considering the assumption that other species do not exert a noteworthy influence.

III.4. Previous developments

III.4.1. Model initiation and fitting – SDReaM-Crete 1.0 [7]

In [7], Mai-Nhu build the model on Comsol. The main species for corrosion initiation were integrated, as presented in Table III-4.

The constants of the equations were fitted using various experimental data obtained during the study on four different mixes. The compositions of these concretes can be found in Table III-5 , along with the input parameters utilised in SDReaM-Crete, either computed with other models or measured. In Mai-Nhu's research, the indicators that were measured and modelled using SDReaM-Crete are:

- The mass loss of initially saturated samples conserved during 380 days in an environment with constant conditions (RH = 50%, T = 20°C). 11x22 cm cylinder samples were fully saturated using the same modus operandi than the one detailed in Section II.3.4.

- Accelerated carbonation depths measured using two different protocols. The first protocol involved subjecting the samples to a constant relative humidity of 55%, a temperature of 20°C, and a partial pressure of CO_2 of 4%. In the second protocol, the samples experienced cyclic variations in relative humidity between 52% and 82%, a temperature of 20°C, and a constant partial pressure of CO_2 equal to 4%. Prior to conducting both tests, the concrete samples underwent a preconditioning process to achieve a uniform saturation degree of 55%.

Table III-5 Compositions and parameters of the mixes manufactured by Mai-Nhu [7].

Name	F1_MAI	F2_MAI	F3_MAI	F4_MAI
CEM I 52.5 N (Teil) (kg/m^3)	350	350	415	202
Filler limestone (kg/m^3)	79	79	0	0
GBFS (kg/m^3)	0	0	0	152
Sand 0/5 mm (Palvadeau) (kg/m^3)	794	794	844	841
Gravel 4/8 mm (Roulé de Loire) (kg/m^3)	828	828	844	841
$\boldsymbol{W_{eff}/B_{tot}}$ (-)	0.6	0.6	0.45	0.6
$\boldsymbol{Ca_{CH,0}}$ (mol/m^3)	1530	1530	1316	454
$\boldsymbol{Ca_{CSH,0}}$ (mol/m^3)	2269	2269	1951	1849
$\boldsymbol{Ca_{Afm,0}}$ (mol/m^3)	392	392	337	316
$\boldsymbol{Ca_{Aft,0}}$ (mol/m^3)	188	188	162	428
$\boldsymbol{\varphi_0}$ (%)	17.7	18.2	16	18.5
$\boldsymbol{kl_1}$ (10^{-18} m^2)	0.04	0.04	0.04	0.04
$\boldsymbol{D_{eff}}$ (10^{-12} m^2.s^{-1})	1.2	1.2	0.7	1.6

The results obtained by Mai-Nhu were utilised in Section III.5 to validate the performance of the modified version of the model.

III.4.2. Surrogate model and probabilistic approach implementation [6]

In the first phase, Schmitt conducted an experimental campaign on five different concrete mixes. The objective of the tests was to validate the durability model using new concrete formulations that have a reduced carbon footprint and incorporate a higher amount of slag. Table III-6 presents a summary of the composition of each concrete mix, including the main properties estimated or measured for their use in the subsequent modelling phase. The durability indicators measured and modelled during the study encompassed:

- The accelerated carbonation depth measured using the method outlined in the European standard prCEN/TS 12390-12 (2012). The prismatic samples, measuring 7x7x28 cm were kept under constant conditions (50% RH, 20°C) for 90 days. Subsequently, the samples were preconditioned in a different environment (65% RH, 20°C) for 14 days. The carbonation test was then conducted under high CO2 pressure (65% RH, 20°C, P_{CO_2} = 4%) for 70 days. Measurements of the carbonation depths were taken at 28, 56, 63, and 70 days of accelerated carbonation.
- The profiles of free and total chloride ions were determined using the Grandubé recommendation [122].

Table III-6 Compositions and parameters of the mixes manufactured by Schmitt [6].

Name	F1_SCH	F2_SCH	F3_SCH	F4_SCH	F5_SCH
CEM I 52.5 N PM (kg/m^3)	324	242	193	404	309
Filler limestone Betocarb HP OG (kg/m^3)	39	10	72	64	10
Slag (kg/m^3)	0	124	217	0	129
Sand 0/5 mm (Roulé de Loire) (kg/m^3)	943	940	904	937	923
Gravel 4/8 mm (Palvadeau) (kg/m^3)	771	769	740	767	755
$\boldsymbol{W_{eff}/B_{tot}}$ (-)	0.55	0.53	0.33	0.35	0.38
$\boldsymbol{Ca_{CH,0}}$ (mol/m^3)	1035.3	443.7	320.6	1185.7	583
$\boldsymbol{Ca_{CSH,0}}$ (mol/m^3)	1525.2	1959.5	1948.6	1746.9	2162.4
$\boldsymbol{Ca_{Afm,0}}$ (mol/m^3)	380.2	281.1	206.7	435.5	333
$\boldsymbol{Ca_{Aft,0}}$ (mol/m^3)	286.5	240.6	198.3	328.1	278.9
$\boldsymbol{\varphi_0}$ (%)	17	16.7	13.9	12	13.6
$\boldsymbol{kl_1}$ (10^{-18} m^2)	0.04	0.04	0.04	0.04	0.04
$\boldsymbol{D_{app}}$ (10^{-12} m^2.s^{-1})	29.4	3.6	2.9	5.8	2.2

The results obtained by Schmitt are subsequently utilised in Section III.5 to assess the performance of the updated model.

One part of Schmitt's work involves the simplification of the model to facilitate a probabilistic approach. The utilization of a polynomial chaos expansion is employed for the development of two surrogate models, specifically for considering chloride penetration and carbonation.

The selection of input parameters for these surrogate models was carried out using the Morris method, allowing for a comprehensive evaluation of their influence on the outcomes. The input parameters chosen for the chloride penetration surrogate model are presented in Table III-7 while those selected for the carbonation meta-model are outlined in Table III-8.

Table III-7 Retained parameters for the construction of the chloride penetration meta-model [6].

Input parameters	Unity	Variation range
Initial porosity of concrete (φ_0)	-	[0.11; 0.21]
Calcium quantity able to carbonate in CH ($Ca_{CH,0}$)	mol.m^{-3} of concrete	[300; 1500]
Calcium quantity able to carbonate in C-S-H ($Ca_{CSH,0}$)	mol.m^{-3} of concrete	[1450; 2200]
Calcium quantity able to carbonate in Aft ($Ca_{Aft,0}$)	mol.m^{-3} of concrete	[180; 350]
Calcium quantity able to carbonate in Afm ($Ca_{Afm,0}$)	mol.m^{-3} of concrete	[200; 450]
Desired lifespan (t_{tot})	Years	[30; 100]
Annual relative humidity (RH_{env})	%	[75; 100]
Effective diffusion coefficient of chloride (D_{Cl-})	m^2.s^{-1}	[5.10^{-14} ; 1.10^{-12}]
Environmental chloride concentration (Cl_{env})	mol.m^{-3}	[470 ; 630]
Critical chloride threshold (C_{crit})	mol.m^{-3}	[40 ; 440]

Table III-8 Retained parameters for the construction of the carbonation meta-model [6].

Input parameters	Unity	Variation range
Initial porosity of concrete (φ_0)	-	[0.11; 0.21]
Calcium quantity able to carbonate in CH ($Ca_{CH,0}$)	mol.m^{-3} of concrete	[300; 1500]
Calcium quantity able to carbonate in C-S-H ($Ca_{CSH,0}$)	mol.m^{-3} of concrete	[1450; 2200]
Calcium quantity able to carbonate in Aft ($Ca_{Aft,0}$)	mol.m^{-3} of concrete	[180; 350]
Calcium quantity able to carbonate in Afm ($Ca_{Afm,0}$)	mol.m^{-3} of concrete	[200; 450]
Desired lifespan (t_{tot})	Years	[30; 100]
Annual relative humidity (RH_{env})	%	[75; 92]
Ph critical threshold (Ph_{crit})	-	[7 ; 11]
Factor for the desorption isotherm (δ)	-	[-1; 1]

The variation ranges presented in Table III-7 and Table III-8 facilitate the simulation of various concrete compositions typically employed in XC2/XC3/XC4 and XS1/XS2 environments, as per the guidelines set by the standard NF EN 206/CN+A2 (2022) [19], as supported by [6].

In this study, a similar approach is employed to construct surrogate models based on the updated model. The effectiveness of these new surrogate models is then evaluated and compared against the surrogate models developed by Schmitt in her research.

III.5. Model improvements – New binders and environment considerations

In this section, various modifications and verifications are conducted on the SDReaM-Crete model for improved accuracy. This model relies on a significant number of input parameters, which are not always readily accessible in the literature.

Therefore, to evaluate the required inputs, several models from the existing literature are systematically employed:

- The water accessible porosity is computed using the model proposed by Powers [282], which takes into account the composition of the concrete mixes.
- To estimate the hydrate contents, the model developed by Lacarrière and Kolani [286] is utilised, incorporating the adjustments outlined in Section IV.3.2.3 to consider metakaolin and fly ash.
- The ageing factor of the concrete material is determined through the Equation II.7 provided in the FD P18-480 (2022) and explained in detail in Section II.3.7.

In Section IV, predictions are conducted on concrete with limited available data on its composition and properties. To address the data scarcity issue, alternative methods were introduced and integrated into the methodology to calculate the various missing inputs.

These models were also used to compute some of the values of Table III-5 and Table III-6.

III.5.1. Hydrologic transfers

This section focuses on two aspects. Firstly, the integration of desorption isotherm determination into the model as a function of the W/B ratio is investigated. The calibration data used for this analysis are extracted from existing literature [6], [7], [387]–[389].

Secondly, the relationships describing the hydrologic transfers are calibrated, and a correlation between the water permeability coefficient and the water accessible porosity is established. Two sets of data are utilised to fit the constants of these relationships. The first set of data used for calibration is obtained from the experimental plan, which is described in Section II.3.4. The second set of data, obtained by Mai-Nhu in [7], is used to verify the model's functionality.

III.5.1.1. Sorption isotherm determination and verifications

The finite element model SDReaM-Crete incorporates a desorption isotherm for characterizing the behaviour of concrete material. In [6], Schmitt developed a methodology to derive a modified desorption isotherm curve based on the specific concrete mix composition. In her approach, she introduced a parameter δ to create an offset allowing adaptation to different concrete mixes considered in her work. Nonetheless, the method lacks an explicit explanation for the relationship between the parameter δ and other compositional parameters. In order to enhance the usability of the model and facilitate its integration within probabilistic frameworks, it is desirable to establish a simple relationship to define the desorption isotherm in terms of another input parameter.

To achieve this, existing data from literature sources is utilised to calibrate a polynomial function that directly represents the desorption isotherm as a function of the water-to-binder (W/B) ratio. The selection of this parameter is motivated by its significant influence on the permeability and porosity characteristics of concrete. The scarcity of comprehensive results regarding the correlation between other material parameters impedes the development of more intricate relationships in this work.

Nevertheless, further research should concentrate on this subject as it holds paramount importance for considering hydrologic transfers and ensuring the long-term durability of reinforced concrete structures.

The initial step of this study involves developing a function capable of accurately representing isotherm curves. To capture the relationship between the saturation degree and relative humidity, sinusoidal and power functions have been selected:

$$Piso_1 = 1.66RH^3 - 1.34RH^2 + 0.60RH \quad \text{Eq (III.54)}$$

$$Piso_2 = Kiso\left(\sin^3\left(\pi(1.15 - RH)\right)\right) \quad \text{Eq (III.55)}$$

$$Kiso = -0.54(W/B)^2 - 0.27(W/B) + 0.61 \quad \text{Eq (III.56)}$$

Finally, Sr is defined by the following equation III.57:

$$Sr = Piso_1 + Piso_2 \quad \text{Eq (III.57)}$$

The results of this method are shown in the Figure III-1 for different CEM I-based concrete.

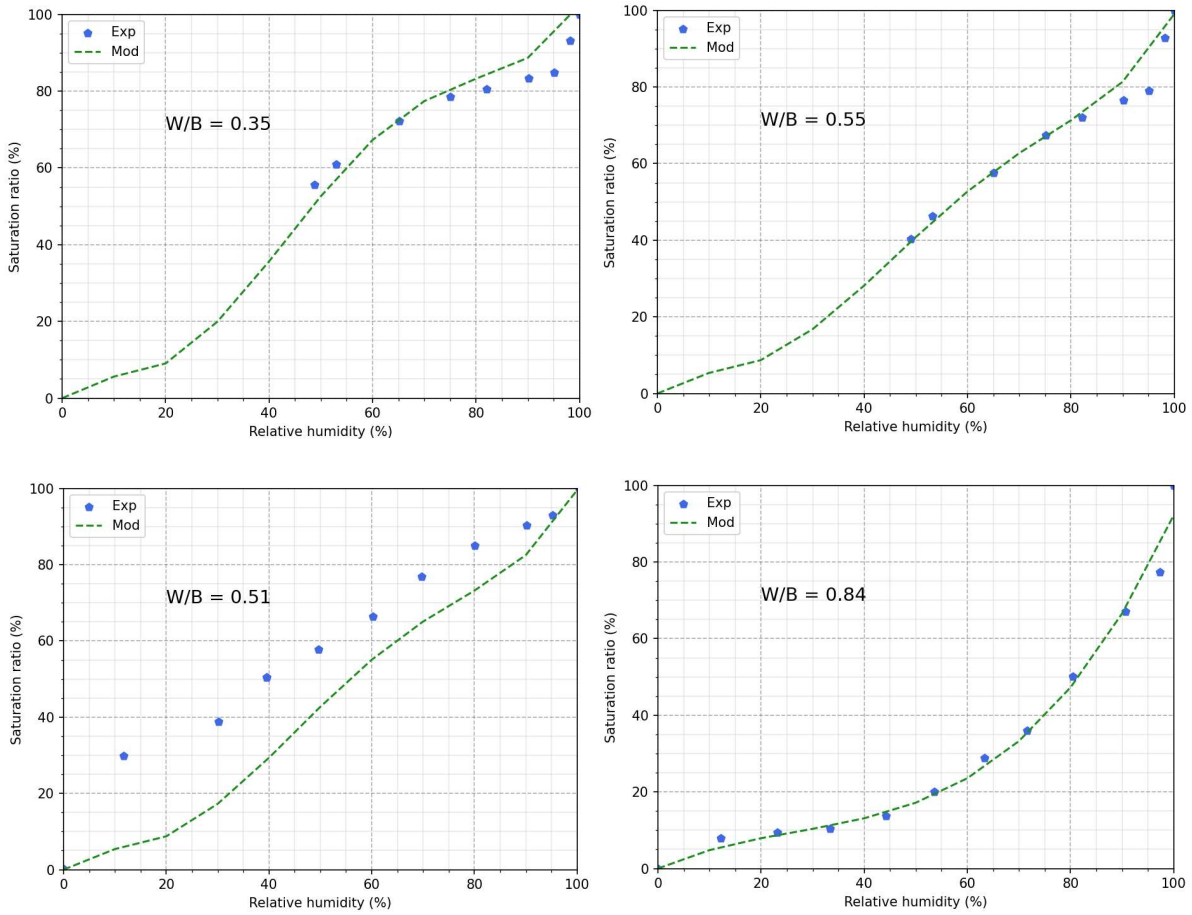

Figure III-1 Desorption isotherms obtained experimentally (blue curve, circle dot) and using the Equation III.57 (green curve, square dot) for different W/B ratios [6], [7], [387]–[389].

The experimental data shows a satisfactory fit with the equation. Notably, for each curve, there is an observable gap within a range of relative humidity values between 0.9 and 0.95. Limited verifications have been conducted for relative humidity values below 0.5. Nevertheless, environments where carbonation and chloride-induced corrosion are concerning exhibit higher relative humidity values (refer to Sections I.3.1 and I.3.2, respectively).

To integrate this method directly into the finite element model, the equation form was modified by fitting the curve with polynomial terms. Within the model, the computation of the derivative form of the equation governing the desorption isotherm (at each time step) is necessary to account for its variation (see Equation III.5). After conducting various computational tests, it was observed that polynomial equations impose a lower computational burden compared to the sinusoidal law described in Equation III.57. To transform the equation's form, the desorption isotherms were computed for various W/B ratios and fitted with fifth-order polynomial equations. Subsequently, each coefficient of the equation was determined as a linear function of the W/B ratio. This procedure resulted in the Equations III.58 to III.64. These equations are considered valid for W_{eff}/B_{tot} ranging from 0.35 and 0.65 and for relative humidity comprised between 10% and 96% (refer to Figure III-2)

$$Sr = \beta_5 RH^5 + \beta_4 RH^4 + \beta_3 RH^3 + \beta_2 RH^2 + \beta_1 RH + \beta_0 \quad \text{Eq (III.58)}$$

$$\beta_5 = -20.2 W_{eff}/B_{tot} + 17.2 \quad \text{Eq (III.59)}$$

$$\beta_4 = 39.53 W_{eff}/B_{tot} - 33.59 \quad \text{Eq (III.60)}$$

$$\beta_3 = -14.12 W_{eff}/B_{tot} + 13.67 \quad \text{Eq (III.61)}$$

$$\beta_2 = -7.95 W_{eff}/B_{tot} + 5.42 \quad \text{Eq (III.62)}$$

$$\beta_1 = 2.78 W_{eff}/B_{tot} - 1.77 \quad \text{Eq (III.63)}$$

$$\beta_0 = -0.21 W_{eff}/B_{tot} + 0.17 \quad \text{Eq (III.64)}$$

The variations and uncertainties associated with this method are accounted for in the probabilistic approach by considering the distribution of the W/B ratio. In the subsequent section, the presented model incorporates and utilizes this equation.

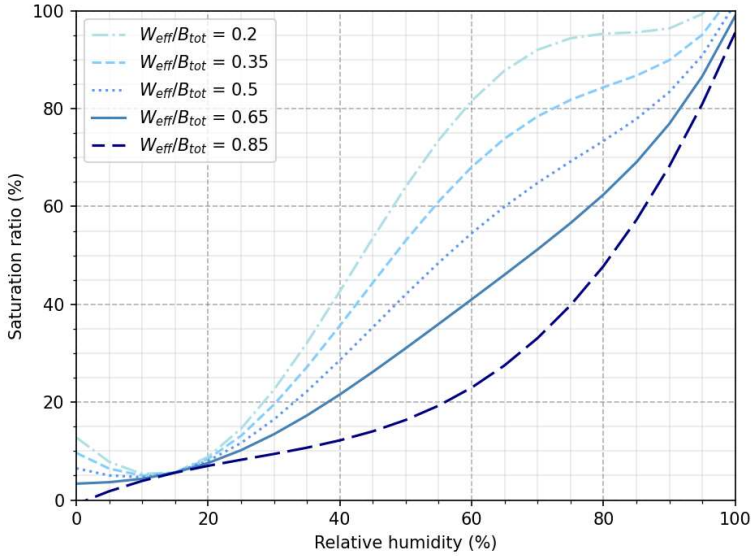

Figure III-2 Desorption isotherms obtained from the polynomial approximation for different W_{eff}/B_{tot}.

The validations are conducted on rather regular concrete mixes (OPC-based). It will be essential to conduct additional verifications on pozzolanic and slag-based concrete mixes when results become available.

III.5.1.2. Mass loss monitoring in dry conservation environment

The data obtained for the various mixes and conservation conditions were utilised to conduct modelling and fit the model version developed by Schmitt [6]. Table III-9 displays the material parameters input. Regarding the environmental parameters inputs (relative humidity and temperature), sinusoidal functions were chosen to represent the variations. Figure III-3 presents an example of the relative humidity for the F5_CEMV/A_0.49_51 mix, obtained using the Equation III.66.

Table III-9 Input parameters corresponding to the different mixes and conservation conditions for the hydrologic modelling.

Parameters	F1_CEMI _0.49_55	F2_CEMIII/B _0.5_35	F3_CEMI_0.5 _V15%_52	F4_CEMI_0.5 _M15%_53	F5_CEMV/ A_0.49_51	F6_CEMVI_0 .5_48*
$\boldsymbol{\varphi_0}$ Dry Conservation DC (-)	14	17.7	14.9	14.6	14.9	16.3
$\boldsymbol{\varphi_0}$ External Conservation EC (-)	13.8	16.9	14.5	14.5	14.5	17.4
$\boldsymbol{\varphi_0}$ Moist Conservation MC (-)	13.7	16.8	14.9	14.8	14.5	15.8
$\boldsymbol{Ca_{CH,0}}$ (mol/m^3)	1400	216	722	876	361	285
$\boldsymbol{Ca_{CSH,0}}$ (mol/m^3)	2063	1828	2031	1989	1988	1923
$\boldsymbol{Ca_{Afm,0}}$ (mol/m^3)	514	153	401	439	249	201
$\boldsymbol{Ca_{Aft,0}}$ (mol/m^3)	387	176	327	348	237	207
$\boldsymbol{W_{eff}/B_{tot}}$ (-)	0.49	0.5	0.5	0.5	0.49	0.5

*This formulation was recomposed using two different cements.

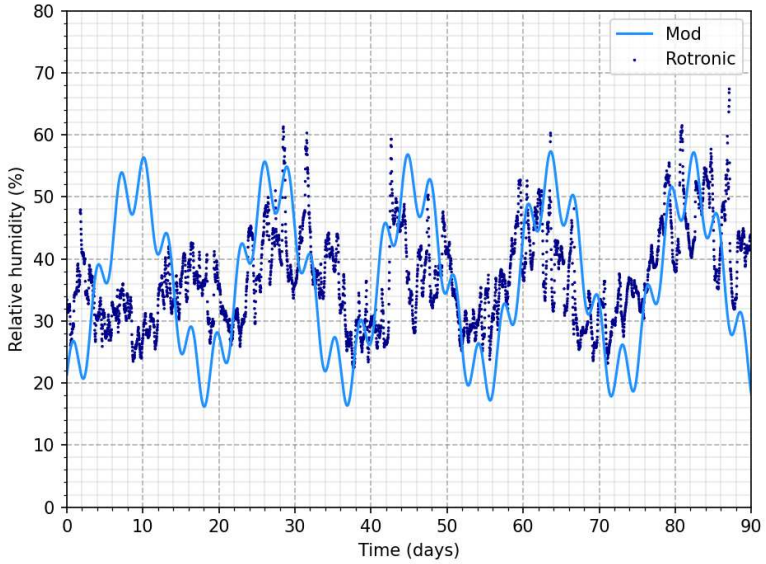

Figure III-3 Relative humidity evolution during the monitoring period of the formulation F5_CEMV/A_0.49_51 and modelling representation.

$$RH_{env} = \mu_{RH} + (CoV_{RH} - 5)\sin\left(\pi + \frac{2.9}{t}\right) + 5\sin\left(\frac{0.5}{t}\right) \quad \text{Eq (III.65)}$$

Where μ_{RH} is the average relative humidity (%) measured during the three months of monitoring (see values in Annex 2), CoV_{RH} the coefficient of variation (%) measured and t the time in days.

The same kind of equation is used for the temperature, while the partial pressure of CO_2 is considered constant and equal to 50 Pa (~ 0.05%).

In Figure III-4 , the results obtained from the dry conservation of formulation F1_CEMI_0.49_55 are presented. The orange curve represents the initial model as described in [6]. A noticeable deviation in the curve progression compared to the experimental results necessitated a modification of the hydrologic transfer equation. As a result, the Equation III.13 was adjusted by incorporating a constant multiplicator factor of 0.05, leading to the new Equation III.66.

$$Rd_{H_2O} = 0.05\varphi^{1.2}(1 - Sr)^{2.7} \quad \text{Eq (III.66)}$$

The outcomes acquired using the modified model are depicted in blue on Figure III-4. The revised version of the model is applied for the estimation of the water permeability parameter encompassing the 18 measurements.

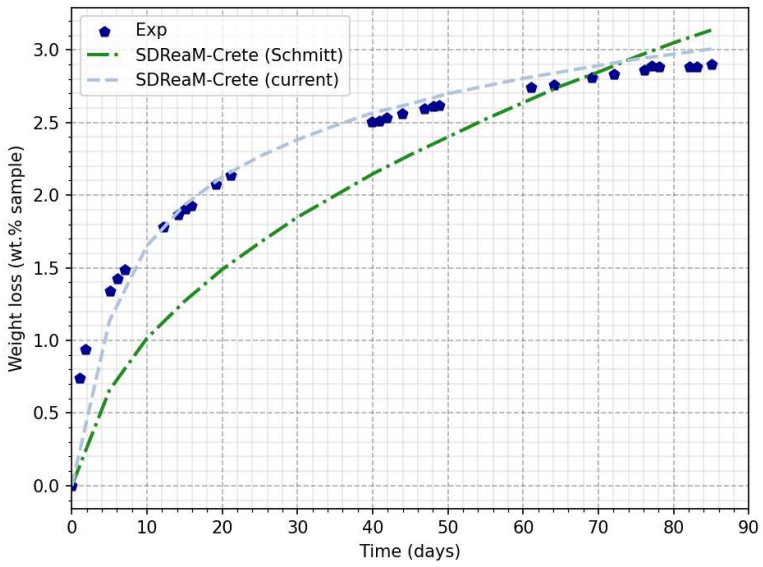

Figure III-4 Mass loss (wt.%) versus drying time obtained for F1_CEMI_0.49_55 in dry conservation.

The liquid permeability parameter (kl) for each formulation and conservation condition was determined using a bisection method to reduce the difference between experimental and modelling curves. The obtained values are presented in Table III-10. The method consisted in reducing the mean relative error on the different datasets, below a threshold of 5%, by adjusting the value of kl.

Table III-10 Water permeability coefficient (kl, 10-18m2) obtained by dichotomy.

Conservation type	F1_CEMI_0.49_55	F2_CEMIII/B_0.5_35	F3_CEMI_0.5_V15%_52	F4_CEMI_0.5_M15%_53	F5_CEMV/A_0.49_51	F6_CEMVI_0.5_48*
EC	5.0	40	10	9	5	10
DC	15.5	15	11	10	13	35
MC	0.6	0.5	0.95	0.85	0.3	0.5

Variations in the value of kl can be observed depending on the mixture composition and conservation conditions. The model's performance is validated using the data obtained by Mai-Nhu [7]. Subsequently, the entire dataset is utilised to establish a relationship for calculating liquid permeability.

III.5.1.3. Mai-Nhu data [7]

Mai-Nhu conducted a study in which he monitored the weight loss of cylindrical samples with dimensions of 11x22 cm in a controlled and constant environment. The study focused on three different concrete formulations. To ensure accuracy, the relative humidity and temperature of the environment were kept constant for a period of 380 days, with values of 50% and 20°C, respectively. The concrete mixes used in the study and the inputs of the model are detailed in Table III-5.

The obtained results are presented in Figure III-5 while the measurement values for liquid permeability are provided in Table III-11.

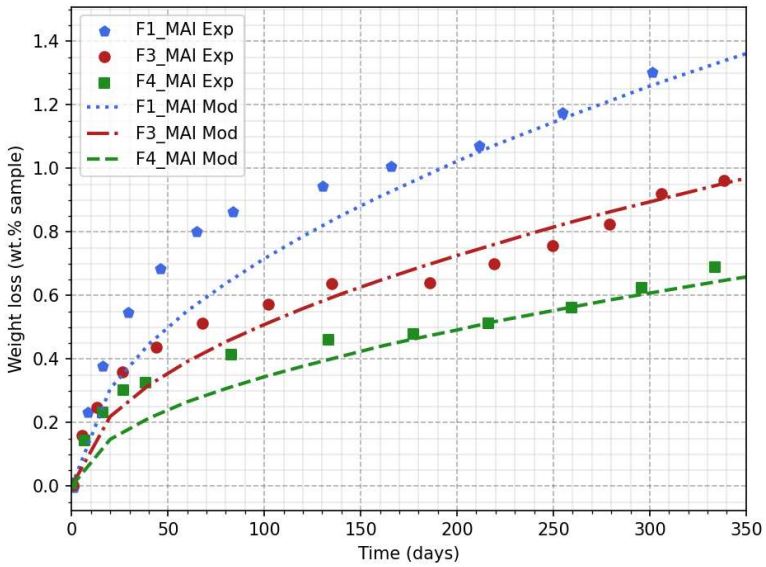

Figure III-5 Mass loss (wt.%) versus drying time obtained for Mai-Nhu's mixes.

Table III-11 Liquid permeability coefficient ($\boldsymbol{kl}$, 10^{-18} m²) of the concrete mixes extracted from Mai-Nhu's work.

Mix Name	F1_MAI	F3_MAI	F4_MAI
$\boldsymbol{kl}$ (10^{-18} m²)	1.3	0.5	0.2

The successful replication of the experimental findings confirms the validity of the model modification detailed in the preceding section. The implications of these modifications highlight the need to develop a methodology for calculating the liquid permeability based on concrete material properties, considering the time-consuming nature of the experimental procedure used to estimate it. Consequently, a methodology is proposed in the subsequent section.

III.5.1.4. Water permeability estimation

The realisation of mass loss monitoring and the estimation of the liquid permeability parameter is a time-consuming process. Additionally, one application of the finite element model is the development of surrogate models, which have limited input parameter capabilities. Therefore, there is a need to find an alternative way to estimate this parameter using a different input that is easier to obtain. In a study conducted by Lion et al. [390], the same experimental and modelling procedures as described in the previous section were employed to determine the water permeability for 17 concretes and 2 mortars. The accessible porosity to water was measured and compared to the liquid permeability values. These values are presented in Figure III-6, along with the values obtained in the current study and the mixes of Mai-Nhu [7].

The results obtained by Lion et al. indicate a correlation between liquid permeability and water porosity. However, this correlation is not observed in other studies. Nevertheless, the values obtained in moist conservation by Mai-Nhu and in the present study are of similar magnitude. On the other hand, a

discrepancy is observed in the results of dry and external conservation, where the liquid permeability increases without a corresponding increase in the water accessible porosity. This inconsistency may be attributed to the larger impact of moist conservation on the tortuosity of the material compared to the overall water porosity. As a result, the tortuosity of the material in external and dry conservation is lower than that in water conservation. To take these factors into account, two functions have been developed to estimate the liquid permeability based on the water accessible porosity, as shown in Figure III-6. These functions have been directly incorporated into the finite element model.

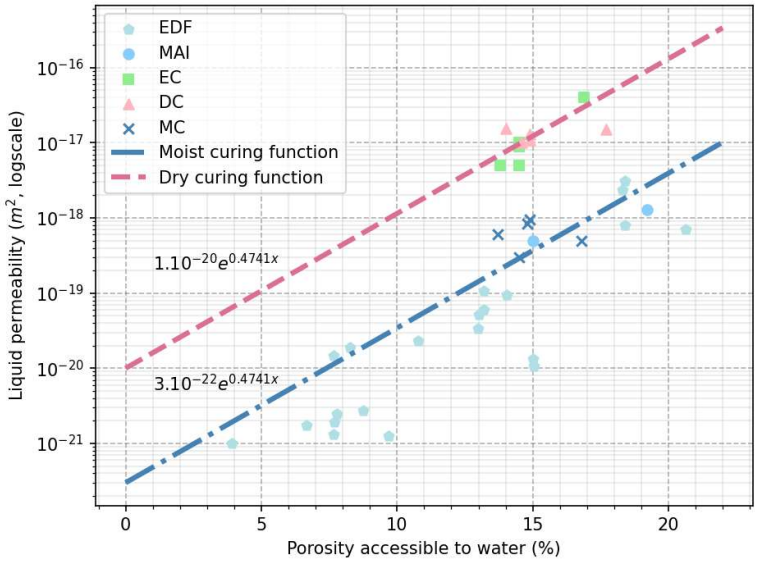

Figure III-6 Functions for liquid permeability coefficient kl (m2) estimation with porosity accessible to water (%).

The variability of these functions will be taken into account within the probabilistic approach by considering a distribution of water-accessible porosity.

III.5.2. Carbonation rate

The objective of this study is to investigate fly ash and metakaolin-based concretes and resolve any inconsistencies present. This research incorporates modifications to specific carbonation kinetic parameters, as suggested by Hyvert [105]. The model is subsequently adjusted using published data from [6], [7], [102]. Additionally, the accuracy of the calibrated model is evaluated by comparing it to the results obtained on the six mixes of the present work and the different concretes of the national project PerfDuB [2].

III.5.2.1. Hyvert's work on carbonation kinetic dependence on partial pressure of CO_2 [105]

The consideration of high partial pressure of CO_2 led to the need for changes in the parameter responsible for carbonation kinetics, referred to as $Kt1_0$ (see Equation III.16). In the previous version of the model (see Table III-1) this parameter maintains a constant value of 10^{-5}. However, in order to incorporate the influence of CO_2 partial pressure, it is essential for this parameter to be modified and become a function depending on environmental variables. To explore the impact of CO_2 partial pressures, Hyvert investigated the carbonation depths of three mortars, including CEM I and slag-based compositions, during his research [105]. The mortars were exposed to varying CO_2 partial pressures ranging from 0.03 to 50%. The results obtained from these tests are presented in Figure III-7.

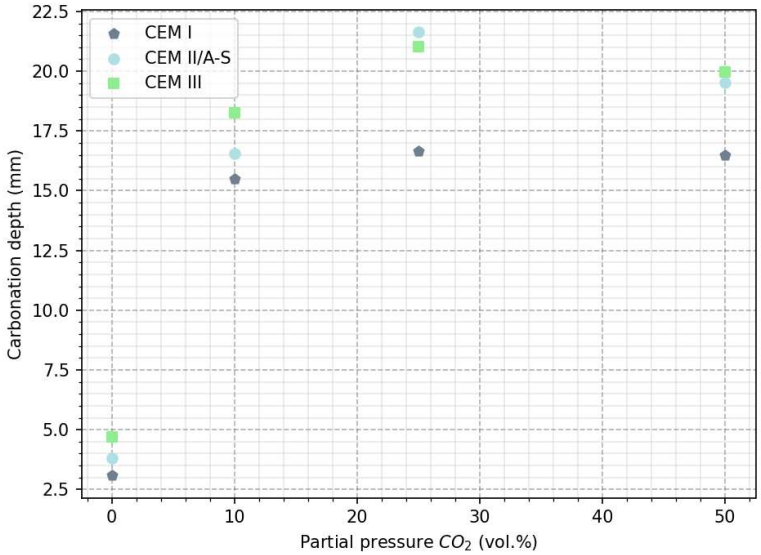

Figure III-7 Relation between carbonation depth (7 months) and partial pressure of CO2 for the different mortars [105].

An overall trend can be observed in the data, indicating a significant increase in carbonation depth with increasing partial pressure up to a maximum value of 25 vol.%. The coefficient $Kt1$ (mm.s$^{-0.5}$.Pa^{-1}) is determined by relating the carbonation rate K (mm.s$^{-0.5}$) using the Equation III.67. The resultant values are depicted in Figure III-8, representing the dependence on P_{CO_2}.

$$Kt1(P_{CO_2}) = \frac{K}{P_{CO_2}} \qquad \text{Eq (III.67)}$$

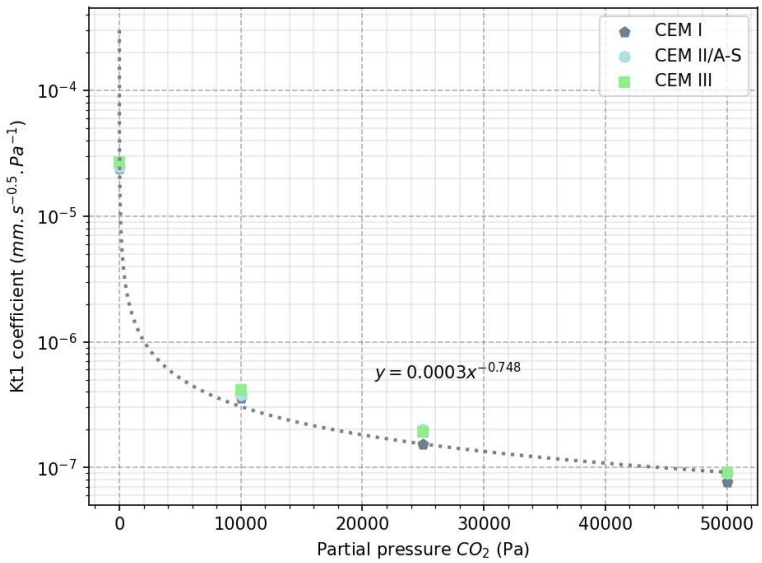

Figure III-8 $Kt1$ coefficient (log-scale, mm.s-0.5.Pa-1) versus partial pressure of CO_2 (Pa).

$$Kt1 = 0.0003\ P_{CO_2}^{0.748} \qquad \text{Eq (III.68)}$$

The new expression of $Kt1$ corresponds to Equation III.68. The hypothesis, particularly the consideration of mortars which may exhibit distinct behaviour from concrete, holds significant importance. Consequently, it is imperative to conduct a comprehensive analysis of this parameter and its implications on the model outcomes. The subsequent subsections are specifically devoted to the validation of the recent modification as well as the assumptions adopted from the hydration model proposed by Lacarrière and Kolani (refer to Section IV.3.2.3, [287], [288]).

III.5.2.2. Mai-Nhu accelerated carbonation results [7]

Mai-Nhu realised two distinct accelerated carbonation tests:

- The first test employed constant conditions of RH = 55%, 20°C, and 4% CO_2 concentration.
- The second test involved a cyclic variation of relative humidity, ranging from 52% to 82% RH, under constant temperature of 20 °C and 4% CO_2 concentration. To consider this particular test, the variation of relative humidity was modelled using a sinusoidal function dependent on time t (in seconds) and described by Equation III.69.

$$HR(t) = 0.77 + 15 \sin\left(\frac{t}{86400}\right) \quad \text{Eq (III.69)}$$

The compositions of the various concrete mixes and the model inputs are outlined in the initial section of Table III-5. The compositions adhere to standard practices with minimal use of mineral additions. The F1_MAI and F2_MAI mixes share the same composition, but the former undergoes an 18-hour thermal treatment at 55 °C (equivalent to 79 hours of regular conservation time).

Figure III-9 displays the outcomes achieved under constant relative humidity conditions over a period of 56 days, whereas Figure III-10 demonstrates the results obtained with cyclic variations for durations of 56 and 250 days.

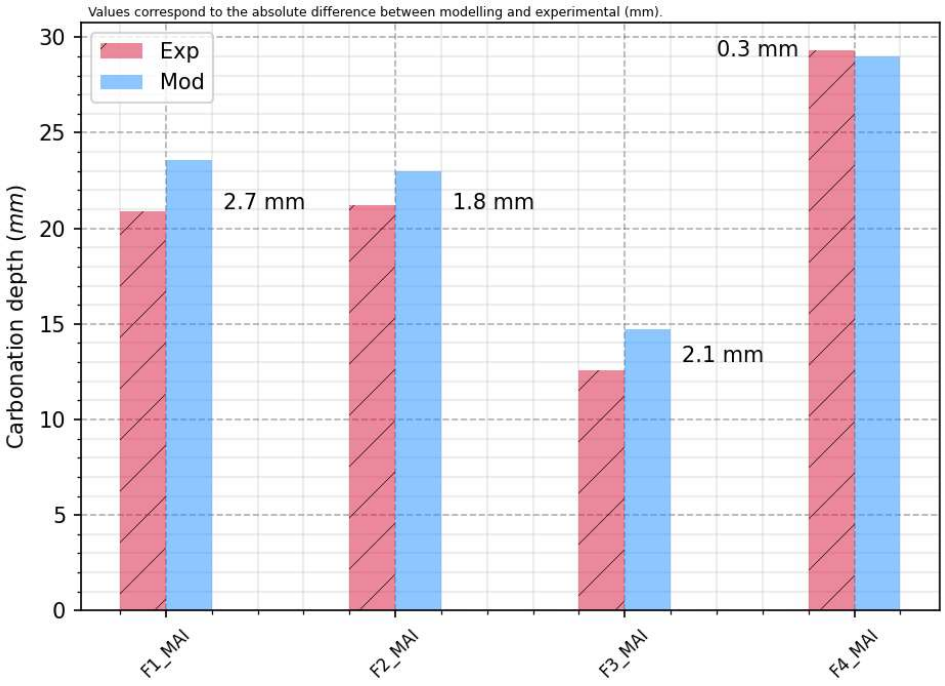

Figure III-9 Carbonation depths obtained after 56 days of accelerated carbonation in constant relative humidity [7].

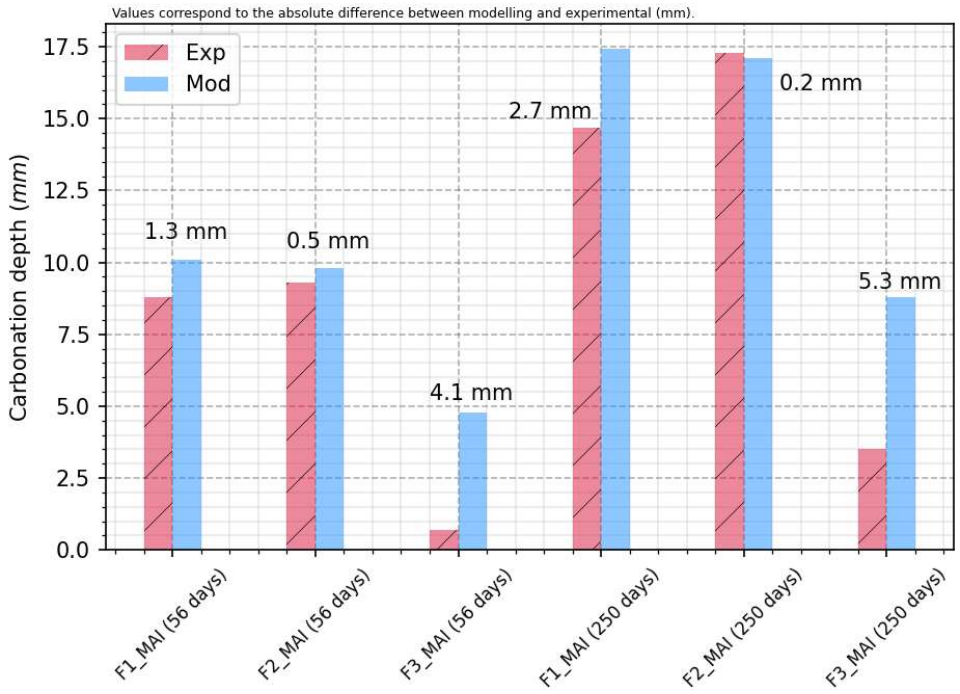

Figure III-10 Carbonation depths obtained for 56 and 250 days of accelerated carbonation with cyclic hydrologic variation [7].

The results obtained under constant conditions are highly satisfactory, despite slightly higher values obtained from the model overall. Initially, the second set of results were not favourable, which led to necessary adjustments in the impact of porosity and saturation degree on carbon dioxide diffusion resistance. As a result, the Millington law (refer to Equation III.21) underwent modifications in its exponent parameters. The porosity's exponent parameter was changed from 1.2 to 2.1, while the saturation degree's exponent parameter was altered from 3.3 to 3.1. After performing various computations and tests, the results presented in Figure III-9 and Figure III-10 were achieved. The difference observed between the experimental and modelling results for the mix F3_MAI can likely be attributed to an incorrect consideration of the desorption isotherm or the usage of a sinusoidal law to represent relative humidity. Both of these factors may result in a lower saturation degree, thereby increasing the diffusion of carbon dioxide for this particular mix.

III.5.2.3. Schmitt accelerated and natural carbonation results [6]

The results of accelerated carbonation considered in this section were obtained from [6]. Five different formulations were included in the experimental plan and summarized in Table III-6, along with the input parameters used for the simulations. These formulations were composed of CEM I, filler, and slag, but had a higher content of mineral additions compared to the mixes of Mai-Nhu. The objective of this study was to utilize the model for compositions with a more significant impact on carbon footprint.

The testing conditions remained constant at 65% relative humidity, 20 °C temperature, and 4% CO_2 concentration. The preconditioning and conservation (detailed in Section III.4.2) were also accounted for during the modelling. The depths of carbonation measured at 28, 56, 63, and 70 days are presented in Figure III-11, together with the corresponding model results.

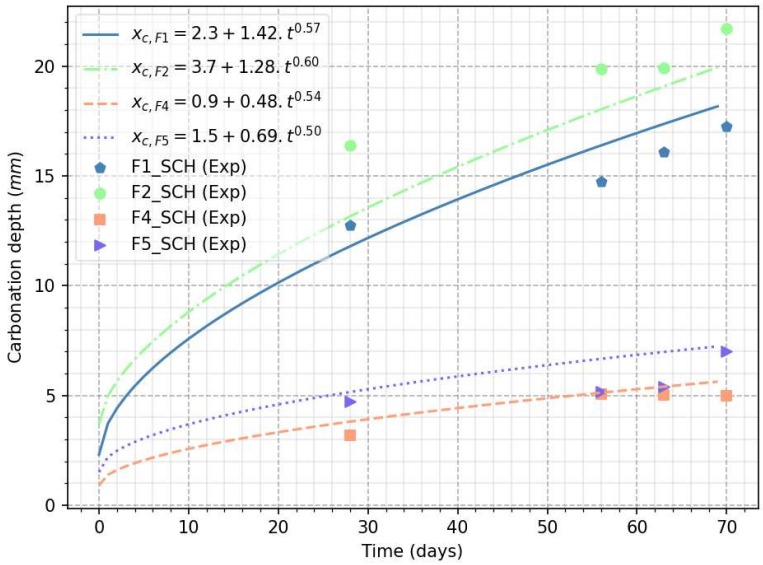

Figure III-11 Carbonation depth obtained in accelerated conditions [6].

The modelling results demonstrate good agreement with the experimental results. The modelling takes into account the carbonation that occurs prior to the initiation of the test. It is important to note that the evolution of carbonation depth does not always conform to a square root time law. The relationship with time will vary depending on various factors, including those associated with the calculation of the saturation degree. The dissimilarities in liquid permeability and desorption isotherm, which are computed based on the porosity accessible to water and the water-to-binder ratio, respectively, explain the variation in the exponents in the equations presented in Figure III-11.

In the frame of the present work, and after the end of Schmitt PhD, it was possible to assess the natural carbonation of the five formulations presented in Table III-6. Cylindrical 11x22cm samples of Schmitt's PhD stored in controlled atmosphere at the CERIB were broken to measure carbonation depth using phenolphthalein. The time of measurements were 1, 2 and 7 years, the average relative humidity 50% and the average temperature 20°C. The experimental and modelling results obtained are shown in Figure III-12.

Few differences were observed between the experimental and modelling results, except for the mix F3_LST. The increased concentration of slag in this formulation may be responsible for noticeable discrepancies. The influence of the higher slag content on the concrete can result in variations in the desorption isotherm, as the method used in this study was calibrated on CEM I-based mixes. Another potential source of deviation could be the equation utilised to compute the pH, obtained from Equation III.53, which was developed by Mai-Nhu and based on conventional formulations. Therefore, it may not be suitable to consider the carbonation impact on pH in slag-based concrete with elevated content in addition. This aspect is re-evaluated in this study by utilizing the PerfDuB results in a following section.

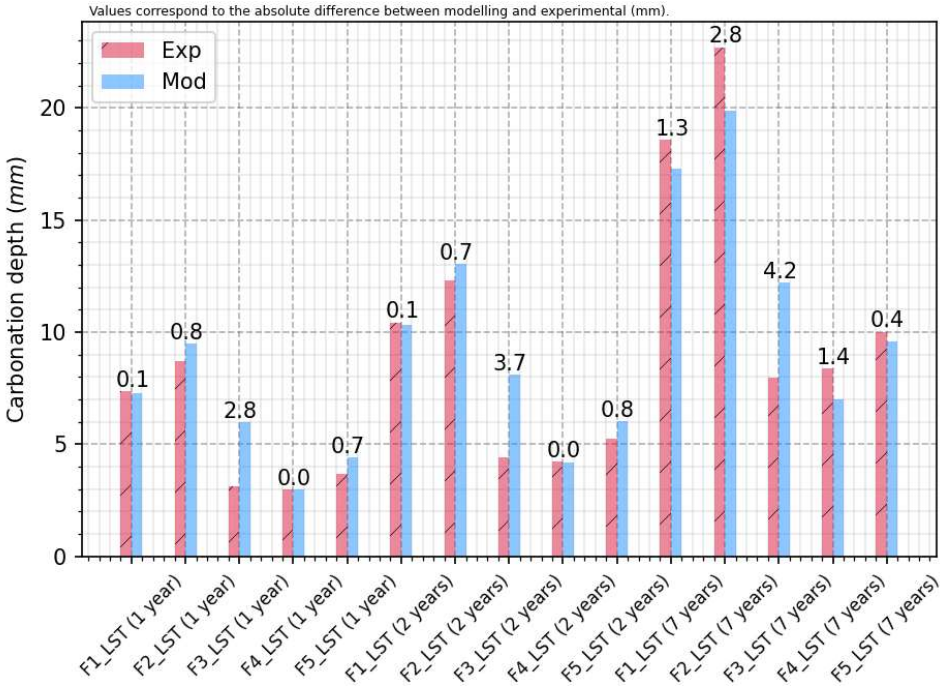

Figure III-12 Carbonation depths obtained in natural conditions.

III.5.2.4. Accelerated and natural carbonation results of Sections II.3.5 and II.3.6

The assessment of natural carbonation in exterior and dry conservation conditions (EC and DC) as well as accelerated carbonation are conducted in the present study. The results obtained from accelerated carbonation on samples under dry and moist conservation conditions are utilised in this section to determine the impact of conservation prior to carbonation exposure, through the incorporation of a curing parameter, Cu. Additionally, the precision of the model with metakaolin, fly ash, and high slag content is verified.

The parameter Cu is defined to be within the range of 0.5 to 1, representing unfavorable and favorable conservation, respectively. This factor redefines the values of the initial hydrate contents (with Equations III.70 to III.71) and the liquid permeability value using Equation III.72:

$$Ca_{Y_c} = (0.27\mathrm{Cu}^3 + 0.73)Ca_Y \quad \text{Eq (III.70)}$$

Where Y may correspond to CH_0, Afm_0, Aft_0.

$$Ca_{CSH_{0c}} = (0.58\mathrm{Cu}^4 + 0.42)Ca_{CSH_0} \quad \text{Eq (III.71)}$$

The distinction to be made between C-S-H and other hydrate species implies ensuring favourable conservation in order to facilitate CSH hydration, particularly when latent hydraulic and pozzolanic additions are utilised. The aforementioned equations are derived from the findings of [87], which investigated the hydration of slag-based paste, and [391], which examined the impact of relative humidity and temperature on hydration mechanisms for portlandite. These equations were subsequently adjusted to enhance the accuracy of results pertaining to carbonation depth and chloride ingress.

$$kl_c = \left(-1.01\left(\frac{Cu - 0.5}{0.5}\right)^2 + 1.04\right)10^{-20}exp(47.41\varphi_0) \quad \text{Eq (III.72)}$$

The estimation of liquid permeability in this study is based on the results obtained in Section III.5.1.4 (Figure III-6). Two linear functions, one for Dry Conservation (DC) and the other for Moist Conservation (MC), are presented. These functions are used to calibrate Equation III.72, which covers the area

between the two functions. A value of 1 for Cu corresponds to MC conditions, while DC corresponds to a Cu value of 0.5.

kl_c is considered independent on the material depth, while a dimensional function is used to represent the hydrates content. These considerations are made based on assumptions used to create the functions. The liquid permeability function is estimated using measurements obtained from an entire sample, while the functions for hydrates are based on results obtained at various depths.

The values calculated using Equations III.70 and III.71 are then incorporated into Equation III.73 to determine the initial calcium content as a function of the depth in concrete. This approach ensures a more appropriate and scientifically rigorous presentation of the research findings.

$$Ca_{Zx}(x) = min\left(Ca_{Z,0}, Ca_{Zc} + \left(\left(\frac{x}{x_{thre}}\right)^2\right)(Ca_{Z,0} - Ca_{Zc})\right) \quad \text{Eq (III.73)}$$

Where Z corresponds either to CH, Aft and Afm with x_{thre} = 25 mm, or to CSH with x_{thre} = 27.5 mm.

The composition of the different mixes is summarized in Table III-12 along with the modelling parameter used.

Table III-12 Compositions and modelling parameter of the concrete mixes designed in Section II.

Parameter	F1	F2	F3	F4	F5	F6
W_{eff}/B_{tot} (-)	0.49	0.5	0.5	0.5	0.49	0.5
Clinker (kg/m^3)	380	110.2	323	323	212.8	161.5
Slag (kg/m^3)	0	269.8	0	0	83.6	176.7
Metakaolin (kg/m^3)	0	0	0	57	0	0
Fly ash (kg/m^3)	0	0	57	0	83.6	41.8
$Ca_{CH,0}$ (mol/m^3)	1157	181.3	610	739.6	282	230
$Ca_{Afm,0}$ (mol/m^3)	429	127.3	338	371	193.8	161
$Ca_{Aft,0}$ (mol/m^3)	323	147.3	276	294	189	169
$Ca_{CSH,0}$ (mol/m^3)	1729	1818	1984	1937	1931	1891
φ (%, DC)	14	17.7	14.9	14.6	14.9	16.3
φ (%, MC)	13.7	16.8	14.9	14.8	14.5	15.8

The experimental and modelling results of the accelerated carbonation testing are illustrated in Figure III-13 , while the natural carbonation results are shown in Figure III-14 and Figure III-15.

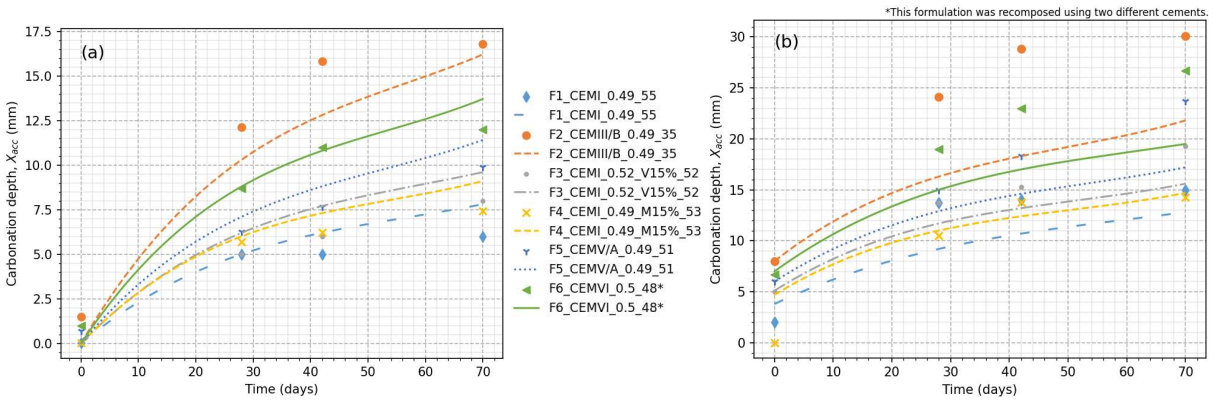

Figure III-13 Experimental and modelled carbonation depth obtained in accelerated condition for samples conserved 90 days in MC (a) and DC (b).

The accelerated carbonation results demonstrate a thorough analysis of the phenomenon in samples conserved in MC, with an average absolute error of 1.03 mm across the six mixes. However, the carbonation in samples preserved in DC is not adequately addressed for mixes F2_CEMIII/B_0.49_35, F5_CEMV/A_0.49_51, and F6_CEMVI_0.5_48*, likely due to shortcomings in the pH calculation for these types of binding agents. Nevertheless, the results obtained under natural conditions (depicted in Figure III-14 and Figure III-15) exhibit a good replication of the phenomenon by the model in both DC and EC, even for mixes with high slag and fly ash contents. This implies that only the accelerated carbonation process on these binding agents is not properly accounted for by the model, possibly due to a simplification in considering the pH evolution.

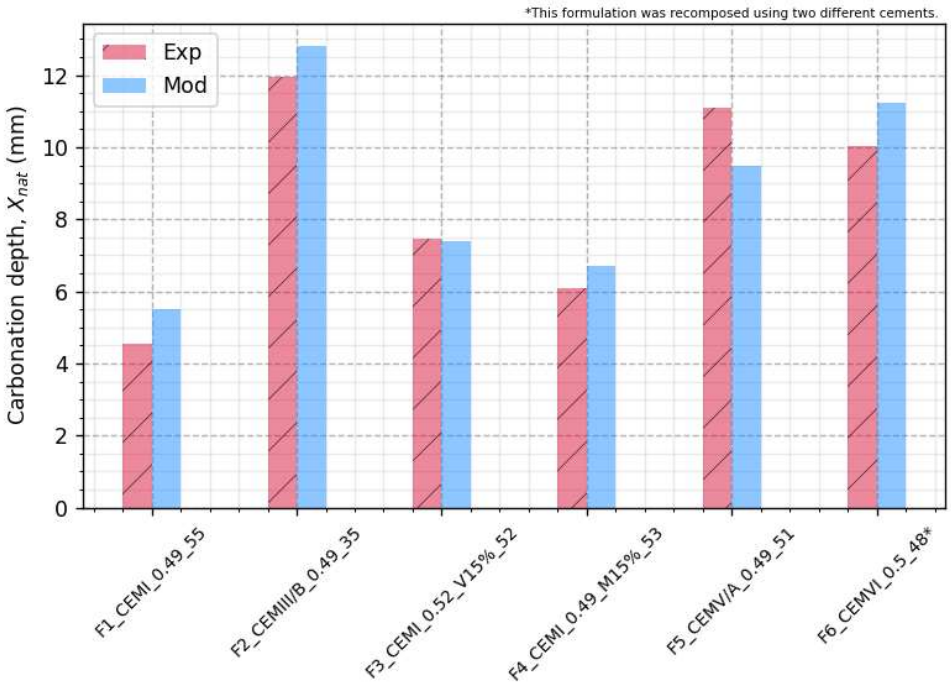

Figure III-14 Experimental and modelled natural carbonation depth obtained in DC.

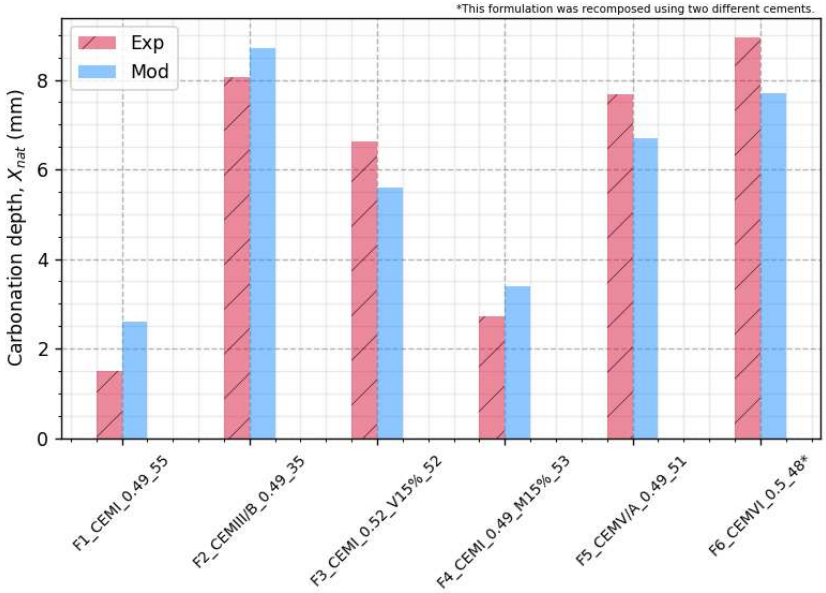

Figure III-15 Experimental and modelled natural carbonation depth obtained in EC.

It should be noted that this study only considers approximations of the environmental parameters, utilizing a sinusoidal function as described in Section III.2.2. This approach shows that focusing solely on monthly, rather than on daily variations of these parameters is rather accurate for this particular case.

III.5.2.5. Bucher accelerated carbonation results [102]

In the study conducted by Bucher et al. [102], the authors investigated the accelerated carbonation and quantities of hydrates in seven different concrete mixes. These mixes consisted of clinker, filler, slag, and metakaolin. The specific formulations and input parameters utilised in the model are presented comprehensively in Table III-13.

Table III-13 Composition and input parameters of Bucher's mixes.

Parameters	CEM I	CEM I M15	CEM I M20	CEM I M25	CEM III/A	CEM II/A-LL	CEM II/A-LL M15
Clinker (kg/m^3)	280	238	224	210	106.4	235.2	199.92
Filler (kg/m^3)	0	0	0	0	0	44.8	38.08
Slag (kg/m^3)	0	0	0	0	173.6	0	0
Metakaolin (kg/m^3)	0	42	56	70	0	0	42
$\boldsymbol{W_{eff}/B_{tot}}$ (-)	0.6	0.6	0.6	0.6	0.6	0.53	0.53
Sand 0-4 (kg/m^3)	738	755	733	733	733	732	753
Aggregate 4-20 (kg/m^3)	1149	1178	1145	1141	1142	1141	1174
Porosity (-)	0.145	0.131	0.138	0.136	0.135	0.114	0.111
$\boldsymbol{Ca_{CH}}$ (mol/m^3)	1510	565.75	392	318.75	684.32	1340	651
$\boldsymbol{Ca_{CSH}}$ (mol/m^3)	1370	1170.25	1071	962.5	1308.48	1050	829.25

The accelerated carbonation test was conducted on samples that were subjected to a 28-day water-immersion conservation. Prior to the test, the samples underwent preconditioning by being stored in an environment with 50% relative humidity and a temperature of 20°C. Subsequently, the samples were placed inside a carbonation chamber for a duration of 70 days. Within the chamber, the samples were exposed to an atmosphere characterized by a temperature of 20°C, 55% relative humidity, and 4% CO_2 concentration.

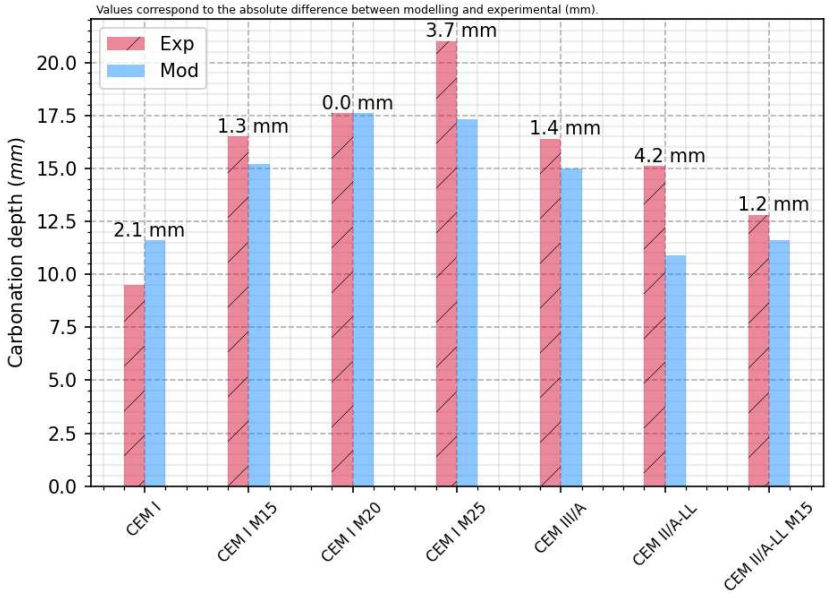

Figure III-16 Experimental and modelling results obtained on the different mixes of Bucher et al. after 70 days of accelerated carbonation.

The results depicted in Figure III-16 demonstrate an overall satisfactory outcome. However, the model failed to accurately fit two experimental measurements. The CEM I M25 mix exhibited a higher metakaolin content compared to the other mixtures. Consequently, the observed deviation of 3.7 mm may have arisen due to an inadequate consideration of metakaolin's influence on key parameters such

as liquid permeability and desorption isotherm. The discrepancy in the results obtained for CEM II/A-LL is more perplexing as the model should have adequately accounted for this particular composition. Possible explanations include suboptimal optimization of the concrete mix for unknown reasons, or the model's failure to incorporate one or more distinctive characteristics of this mix. The experimental measurement could also be erroneous.

III.5.2.6. National project PerfDuB – Natural carbonation on laboratory scale [2]

One of the tasks undertaken in the national project PerfDuB was the creation of a comprehensive database of durability test results. This database comprises data from a total of 42 concrete mixtures. However, for the purpose of this study, six formulations were excluded due to the presence of materials such as schist (D), quartz (Qz), or CEM I SR3, which cannot be accounted for in the current hydration model (refer to Section IV.3.2.3). Additionally, the assessment of the natural carbonation depth value for mix number 4 was not conducted as part of the project, thus it could not be included in the analysis. The composition of each remaining mixture can be found in Table III-14, while the input parameters of the model are summarized in Table III-15.

Table III-14 Composition (kg/m3) of the different PerfDuB's mixes.

Constituent (kg/m^3)	Clinker	Filler	Slag	Fly ash	Metakaolin	Sand	Aggregate
1_CEM I_0.59_43	280	0	0	0	0	830	906
2_CEM I_V30_0.52_33	216	0	0	95	0	782	946
3_CEM II/A-LL_0.6_41	238	42	0	0	0	894	914
5_CEM I_S60_0.58_26	115	0	179	0	0	798	940
6_CEM I_L30_0.46_34	245	108	0	0	0	820	891
7_CEM I_L41_0.39_42	262	190	0	0	0	831	761
8_CEM II/A-LL_V30_0.53_31	190	33	0	95	0	836	895
9_CEM II/A-LL_S45_0.57_31	137	24	132	0	0	869	904
10_CEM II/A-LL_0.61_32	238	42	0	0	0	897	904
11_CEM II/A-LL_0.54_50	285	50	0	0	0	832	1028
12_CEM I_S60_0.55_46	139	0	211	0	0	806	973
13_CEM I_L30_0.42_39	295	128	0	0	0	776	937
14_CEM I_0.55_38	327	0	0	0	0	820	990
15_CEM I_0.48_62	358	0	0	0	0	832	1033
16_CEM II/A-S_0.5_50	312	0	39	0	0	804	999
17_CEM III/A_0.5_47	189	0	161	0	0	815	983
18_CEM I_V37_0.53_56	202	0	0	120	0	781	968
19_CEM II/A-S_0.5_60	309	0	38	0	0	847	1036
20_CEM II/A-S_0.5_59	308	0	38	0	0	763	971
21_CEM I_L30_0.39_57	313	135	0	0	0	774	934
22_CEM II/A-LL_0.49_57	303	54	0	0	0	820	1020
23_CEM II/A-S_0.49_46	312	0	39	0	0	810	907
24_CEM II/A-S_0.5_44	304	0	38	0	0	786	1021
27_CEM I_S50_0.43_68	187	0	189	0	0	820	990
30_CEM I_V30_0.35_64	299	0	0	130	0	7966	961
31_CEM III/A_0.4_67	137	0	243	0	0	830	1005
32_CEM I_S50_0.33_90	198	0	200	0	0	845	1020
33_CEM III/A_0.45_52	200	0	170	0	0	817	986
34_CEM III/A_0.45_59	134	0	237	0	0	815	983
35_CEM V/A (S-V)_0.45_66	213	0	84	84	0	808	1003
36_CEM V/A (S-V)_0.45_49	207	0	81	81	0	746	988
37_CEM V/A (S-V)_0.45_56	207	0	81	81	0	826	1051
39_CEM I_M20_0.43_62	295	0	0	0	76	786	916
39b_CEM I_M20_0.42_66	295	0	0	0	76	791	921
41_CEM I_M20_0.35_93	293	0	0	0	76	793	1090

Table III-15 Input parameters for the different mixes of the PerfDuB project.

Input parameters	CH (mol/m³)	CSH (mol/m³)	Afm (mol/m³)	Aft (mol/m³)	Porosity (-)	W/B (-)
1_CEM I_0.59_43	868	1302	322	243	0.169	0.59
2_CEM I_V30_0.52_33	560	1629	296	237	0.174	0.53
3_CEM II/A-LL_0.6_41	775	1165	288	217	0.133	0.60
5_CEM I_S60_0.58_26	186	1547	139	142	0.186	0.58
6_CEM I_L30_0.46_34	794	1194	295	223	0.170	0.47
7_CEM I_L41_0.39_42	847	1272	315	237	0.168	0.40
8_CEM II/A-LL_V30_0.53_31	496	1530	271	218	0.198	0.53
9_CEM II/A-LL_S45_0.57_31	228	1480	166	155	0.164	0.57
10_CEM II/A-LL_0.61_32	776	1167	289	218	0.183	0.61
11_CEM II/A-LL_0.54_50	917	1374	340	257	0.146	0.54
12_CEM I_S60_0.55_46	225	1813	165	168	0.147	0.55
13_CEM I_L30_0.42_39	943	1413	350	264	0.134	0.43
14_CEM I_0.55_38	1023	1531	379	286	0.139	0.55
15_CEM I_0.48_62	1088	1627	403	304	0.136	0.49
16_CEM II/A-S_0.5_50	761	1752	358	279	0.137	0.50
17_CEM III/A_0.5_47	322	1834	217	199	0.150	0.50
18_CEM I_V37_0.53_56	522	1710	292	238	0.141	0.54
19_CEM II/A-S_0.5_60	754	1735	354	277	0.128	0.50
20_CEM II/A-S_0.5_59	753	1732	353	276	0.186	0.50
21_CEM I_L30_0.39_57	985	1475	365	276	0.119	0.39
22_CEM II/A-LL_0.49_57	961	1439	356	269	0.134	0.49
23_CEM II/A-S_0.49_46	758	1744	356	278	0.153	0.49
24_CEM II/A-S_0.5_44	744	1712	349	273	0.133	0.50
27_CEM I_S50_0.43_68	313	1858	205	193	0.131	0.43
30_CEM I_V30_0.35_64	699	1963	358	287	0.116	0.35
31_CEM III/A_0.4_67	225	1754	148	156	0.121	0.40
32_CEM I_S50_0.33_90	327	1760	196	184	0.122	0.33
33_CEM III/A_0.45_52	340	1879	223	204	0.140	0.45
34_CEM III/A_0.45_59	220	1791	151	159	0.134	0.45
35_CEM V/A (S-V)_0.45_66	447	1947	274	236	0.143	0.45
36_CEM V/A (S-V)_0.45_49	434	1891	266	229	0.196	0.45
37_CEM V/A (S-V)_0.45_56	434	1891	266	229	0.128	0.45
39_CEM I_M20_0.43_62	370	1907	235	212	0.157	0.44
39b_CEM I_M20_0.42_66	370	1898	234	211	0.157	0.43
41_CEM I_M20_0.35_93	360	1738	215	194	0.108	0.36

The natural carbonation depths were measured after one year of exposure in a controlled environment with a relative humidity of 50% and a temperature of 20°C. The samples were not subjected to a specific conservation process, and no preconditioning was applied. The results are presented in two distinct figures. Figure III-17 displays the experimental and modelling results for mixtures containing low contents (< 50 wt.% of binder) or no additional materials. Figure III-18, on the other hand, demonstrates the results obtained for mixtures in which the clinker is substituted by significant quantities of additional materials (> 50 wt.% of binder), as well as CEM V/A (S-V) and metakaolin-based concretes. This categorization aims to emphasize the challenges the model faces in accurately accounting for high concentrations of pozzolanic and latent hydraulic additions in its current state.

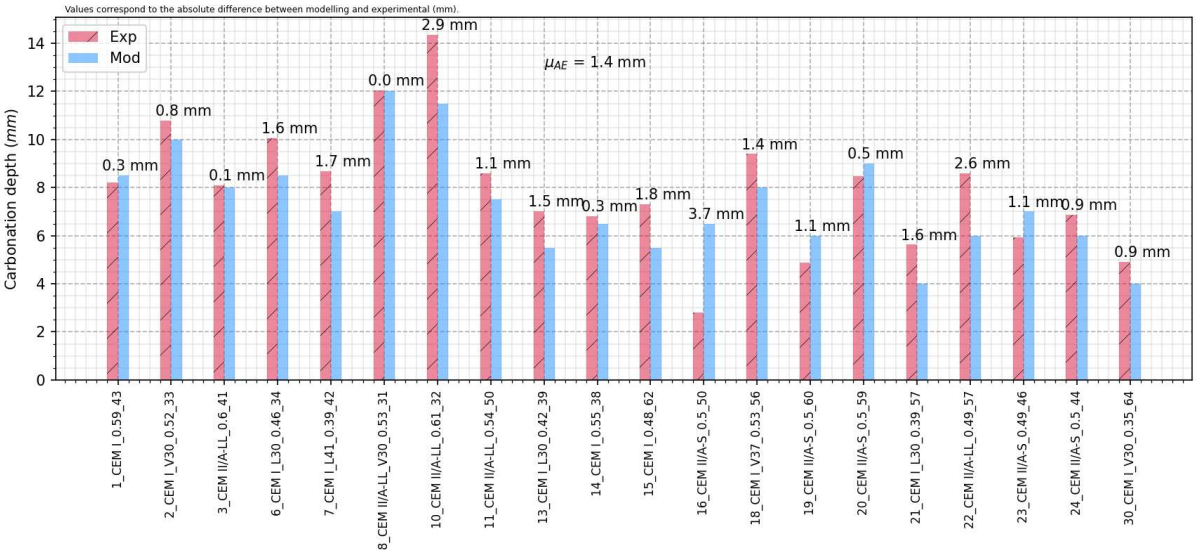

Figure III-17 Carbonation depths obtained on mixes with no or low contents (< 50 wt.% of binder) in SCMs.

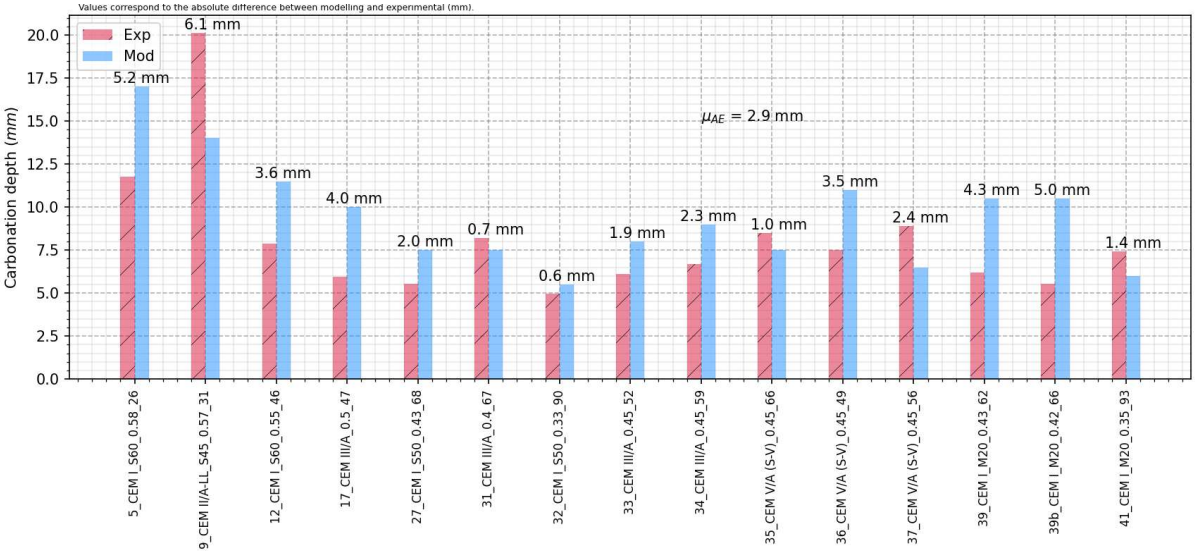

Figure III-18 Carbonation depths obtained on mixes with high contents (> 50 wt.% of binder) in SCMs and mixes containing CEM V/A (S-V) or metakaolin.

Figure III-17 demonstrates a high level of reproducibility of the carbonation phenomenon across the various concrete mixes analysed. The average absolute error of 1.4 mm obtained from the evaluation of 20 mixes is deemed satisfactory, thus substantiating the application of the model in practical scenarios. However, to fully validate the model, additional investigations are necessary to ensure the consistency of results when applied to current concrete structures, rather than laboratory specimens. Additionally, the majority of the predictions provided are conservative, which is preferable for determining the service life of structures.

Figure III-18 presents contrasting results, exhibiting an average absolute error of 2.9 mm, coupled with significant deviations reaching up to 6.1 mm for specific mixtures. The concrete mixes grouped in this figure have higher SCM contents. The previous works realised on the model did not investigate these types of concretes, which explains why the predictions obtained are less precise. Hence, this discrepancy is evidently attributable to certain aspects of the model that do not perform optimally when applied to

these particular formulations. The potential factors contributing to this disparity have been identified and are enumerated as follows:

- The pH calculation, developed by Mai-Nhu [7], is based on the chloride, carbonate, and portlandite concentrations, as explained in Section III.3.12 of this document. Its applicability has been verified for CEM I, filler, and slag-based concretes with addition content below 40 wt.%. However, the assumption made by the model that only portlandite contributes to pH reduction resistance is questionable, as previous research has demonstrated that all hydrates exhibit buffering capacity [92]. This observation is particularly relevant for concretes with high percentages of pozzolanic additions, which result in the formation of C-S-H and the consumption of portlandite.
- The computation of liquid permeability is conducted using Equation III.72 that requires the porosity accessible to water as an input parameter. These equations have been calibrated using experimental data, which display a high degree of variation, introducing a potential source of error.
- The polynomial equation used to account for the desorption isotherm is fitted based on results obtained from CEM I-based concretes. It is possible that the relationship between the water-to-binder ratio and liquid permeability may differ when higher levels of pozzolanic and latent hydraulic additions are used as clinker replacement.
- The estimation of hydrates using the models developed by Lacarrière [288] and Kolani [287] may present some challenges. Although these models have been tailored for use with slag, fly ash, and metakaolin (refer to Section IV.3.2.3), the terms "slag" and "fly ash" encompass materials with varying properties, such as particle size distribution and oxide contents (see Section I.2.2). Consequently, depending on the specific properties of an addition, the types and amounts of hydrates may differ, leading to potential inaccuracies in the models in certain cases.

A focus on the pH computation is addressed. In order to improve the existing equation established by Mai-Nhu [7], a modification is performed by incorporating the concentrations of the remaining hydrates. To calibrate the constant associated with these different hydrate quantities, a method of dichotomy was employed, based on the carbonation depths of the PerfDuB concretes with elevated SCMs contents exposed in Figure III-18. As a result, the Equations III.74 to III.79 were obtained for more accurate pH determination.

$$H_1 = 0.95[CH]_t + 0.15[CSH]_t + 0.125([Afm]_t + [Aft]_t) \quad \text{Eq (III.74)}$$

$$H_2 = 0.175[CSH]_0 + 0.95[CH]_0 + 0.125([Afm]_0 + [Aft]_0) \quad \text{Eq (III.75)}$$

$$pH_{p1} = 0.5[Cl^-] + [CO_3^{2-}] + \left(\frac{1}{10^7}\right)(25 \times 10^{12}[Cl^-]^2 + 10^{14}[Cl^-][CO_3^{2-}] + 10^{14}[CO_3^{2-}]^2 + 1)^{0.5} \quad \text{Eq (III.76)}$$

$$pH_{p2} = \frac{H_1}{H_2} \quad \text{Eq (III.77)}$$

$$pH_{p3} = \frac{(H_2)(11.7 + 0.7\exp(-8[Cl^-]).\exp(-12[CO_3^{2-}]))}{H_2} \quad \text{Eq (III.78)}$$

$$pH = \min\left(max\left(-\frac{1}{log(10)}log\left(max\left(pH_{p1}; 10^{-20}\right)\right)\left(1 - pH_{p2}\right) + pH3; 7\right); 14\right) \quad \text{Eq (III.79)}$$

The modifications resulted in the outputs depicted in Figure III-19 and Figure III-20. The carbonation depths achieved through both methodologies are succinctly summarized in Table III-16, including the calculation of absolute errors.

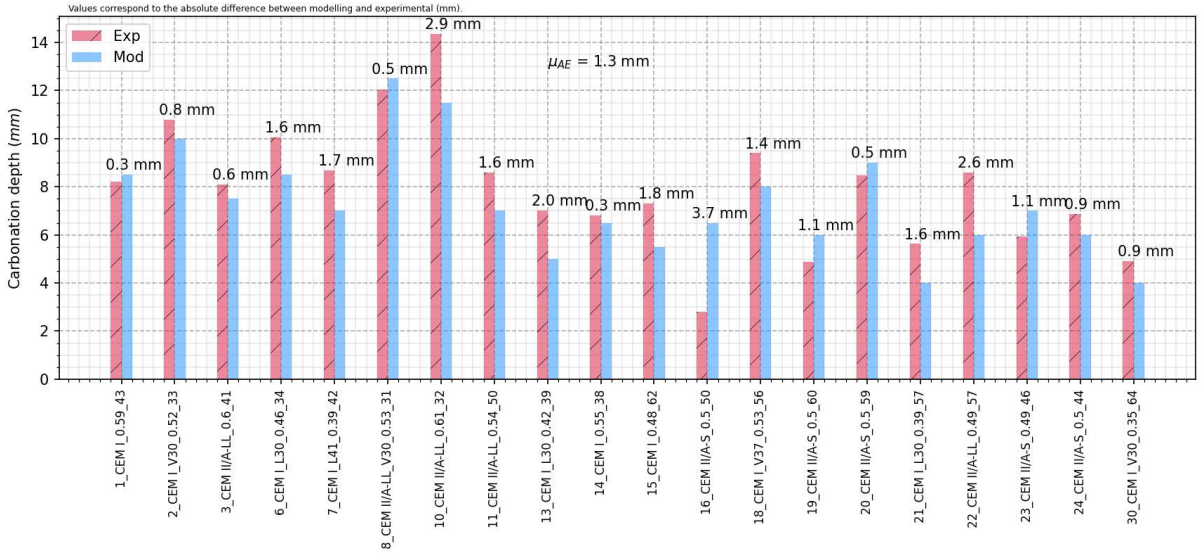

Figure III-19 Carbonation depths obtained on mixes with no or low contents (<50 wt.%) in SCM using the new pH equation.

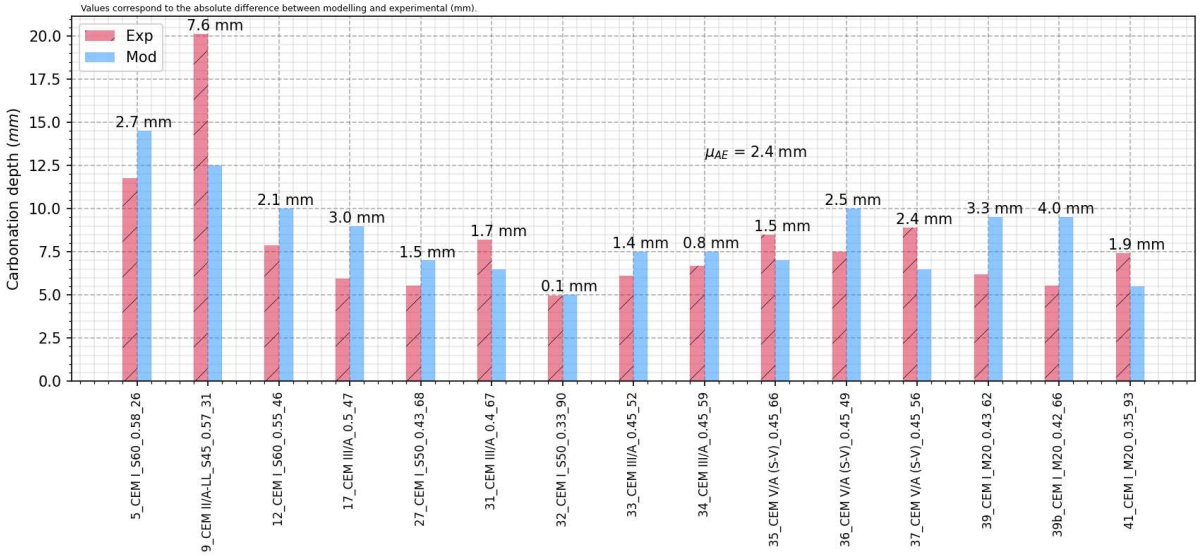

Figure III-20 Carbonation depths obtained on mixes with high contents (>50 wt.%) in SCM and mixes containing CEM V/A (S-V) or metakaolin using the new pH equation.

Table III-16 Carbonation depth (x_c) and absolute errors (AE) obtained on the different mixes using the different pH equations (AE values superior to 3 mm are shown in red).

Mix name	Xc (mm)	Xc (mm)	AE (mm)	Xc (mm)	AE (mm)
Method	Exp	pH equation of Mai-Nhu		New pH equation	
1_CEM I_0.59_43	8.2	8.5	0.30	8.5	0.30
2_CEM I_V30_0.52_33	10.8	10.0	0.79	10.0	0.79
3_CEM II/A-LL_0.6_41	8.1	7.5	0.60	8.0	0.10
5_CEM I_S60_0.58_26	11.8	17.0	5.23	14.5	2.73
6_CEM I_L30_0.46_34	10.1	8.5	1.56	8.5	1.56
7_CEM I_L41_0.39_42	8.7	7.0	1.69	7.0	1.69
8_CEM II/A-LL_V30_0.53_31	12.0	12.5	0.46	12.0	0.04
9_CEM II/A-LL_S45_0.57_31	20.1	14.0	6.12	12.5	7.62
10_CEM II/A-LL_0.61_32	14.4	11.5	2.86	11.5	2.86
11_CEM II/A-LL_0.54_50	8.6	7.0	1.60	7.5	1.10
12_CEM I_S60_0.55_46	7.9	11.5	3.64	10.0	2.14
13_CEM I_L30_0.42_39	7.0	5.0	2.02	5.5	1.52
14_CEM I_0.55_38	6.8	6.5	0.32	6.5	0.32
15_CEM I_0.48_62	7.3	5.5	1.80	5.5	1.80
16_CEM II/A-S_0.5_50	2.8	6.5	3.70	6.5	3.70
17_CEM III/A_0.5_47	6.0	10.0	4.03	9.0	3.03
18_CEM I_V37_0.53_56	9.4	8.0	1.40	8.0	1.40
19_CEM II/A-S_0.5_60	4.9	6.0	1.13	6.0	1.13
20_CEM II/A-S_0.5_59	8.5	9.0	0.53	9.0	0.53
21_CEM I_L30_0.39_57	5.6	4.0	1.63	4.0	1.63
22_CEM II/A-LL_0.49_57	8.6	6.0	2.60	6.0	2.60
23_CEM II/A-S_0.49_46	5.9	7.0	1.08	7.0	1.08
24_CEM II/A-S_0.5_44	6.9	6.0	0.88	6.0	0.88
27_CEM I_S50_0.43_68	5.5	7.5	1.97	7.0	1.47
30_CEM I_V30_0.35_64	4.9	4.0	0.92	4.0	0.92
31_CEM III/A_0.4_67	8.2	7.5	0.72	6.5	1.72
32_CEM I_S50_0.33_90	4.9	5.5	0.55	5.0	0.05
33_CEM III/A_0.45_52	6.1	8.0	1.89	7.5	1.39
34_CEM III/A_0.45_59	6.7	9.0	2.31	7.5	0.81
35_CEM V/A (S-V)_0.45_66	8.5	7.5	1.00	7.0	1.50
36_CEM V/A (S-V)_0.45_49	7.5	11.0	3.48	10.0	2.48
37_CEM V/A (S-V)_0.45_56	8.9	6.5	2.39	6.5	2.39
39_CEM I_M20_0.43_62	6.2	10.5	4.30	9.5	3.30
39b_CEM I_M20_0.42_66	5.5	10.5	4.97	9.5	3.97
41_CEM I_M20_0.35_93	7.4	6.0	1.43	5.5	1.93
Average	**8.02**	**8.22**	**2.07**	**7.84**	**1.78**
Standard deviation	**3.07**	**2.43**	-	**2.36**	-

At this stage, the carbonation depths values are recalculated for the mixes of Schmitt and Mai-Nhu to verify the new equation. The mean absolute errors obtained with Schmitt's mixes goes from 0.97 to 0.70 mm for natural carbonation (10 values) and 1.14 mm to 1.21 mm for the accelerated test (16 values). In the case of Mai-Nhu's results, the accelerated tests lead to an increase of the mean absolute error of 0.9 mm (10 values).

The fact that the new equation improves the results obtained in natural carbonation while increasing the deviations obtained for accelerated tests could be explained by the difference of carbonation kinetic of C-S-H. In the model, an exponent is used on Equation III.48 to reduce the kinetic of carbonation of C-S-H when compared to the other hydrates. In natural conditions, the partial pressure of CO_2 is relatively low with values close to 50 Pa. CO_2 diffusion is controlled by the diffusion resistance and by the CO_2

availability in the material in the carbonation process. Because the carbonation kinetic of CH, Afm and Aft is higher than that of CSH, the CO_2 is consumed essentially by those hydrates instead of C-S-H. When partial pressures superior to 3000 Pa are used in accelerated conditions, the content of CO_2 is too elevated to be consumed entirely during the carbonation of the hydrates. Therefore, CO_2 availability is no longer a limiting factor in the carbonation of C-S-H, leading to deeper carbonation depth estimated by the new equation.

The new equation leads to an imbalance of the pH value and errors in the carbonation depths estimations. For this reason, the new equation will only be used for natural carbonation assessment, while the initial equation will continue to be used for accelerated tests.

III.5.2.7. National project PerfDuB – On field carbonation tests [2]

The carbonation of a structure was studied as part of the national project PerfDuB. The palace of Iéna, located in France, underwent inspections after 80 years of service life. In order to model the carbonation process, the average relative humidity and temperature were taken into account. The average relative humidity used for the modelling was 76%, while the average temperature was 16 °C according to meteorological measurements [392]. To account for variations, sinusoidal laws with a period of 6 months were used, allowing for fluctuations of 10% in relative humidity and 10 °C in temperature.

The project focused on investigating the concrete of various zones within the palace. Specifically, the concrete cover, porosity, cement type, and quantity were determined for the pilasters and columns of the building. These values, along with the material input parameters of the finite element model, are summarized in Table III-17.

Table III-17 Composition and material input parameters for the two zones investigated.

Zone investigated	Pilasters	Columns
Cement (kg/m^3)	390	460
W/B (-)	0.63	0.58
Open porosity (-)	0.142	0.142
CH (mol/m^3)	1255	1460
CSH (mol/m^3)	1874	2175
Afm (mol/m^3)	465	540
Aft (mol/m^3)	350	407

The average values of carbonation depth measured on three core samples are presented in Table III-18. The accompanying modelling results demonstrate satisfactory outcomes, although they do not represent the full range of carbonation evolution. In order to account for this variability, a probabilistic approach, as detailed in Section I.5.2, could be employed to assess the impact of parameter variation on the durability of the material. This aspect is considered in Section IV.4.2 of this document.

Table III-18 Experimental and modelled carbonation depths (mm) of the two zones investigated.

	Min	Max	Average	Model value
Pilaster	21	27	23.3	23.5
Column	17	20	18.5	18.4

The model is deemed effective in simulating the phenomenon of carbonation for various scenarios, including:

- All natural conditions encompassed by the exposure classes XC1, XC3 and XC4 as defined in the NF EN 206/CN [19]. The suitability of the model for XC2 was validated by Schmitt; however, this aspect was not addressed in the current section. Further verifications are conducted in Section IV.4 using the surrogate model developed subsequently.

- Accelerated tests, with the incorporation of preconditioning. It can be noted that the model was not verified on accelerated test conducted with partial pressure of CO_2 exceeding 4 %.
- Concrete mixtures with different levels of mineral addition contents, namely filler, slag, fly ash, and metakaolin. Their consideration is intricately linked to the use of the hydration model of Lacarrière and Kolani [286]. The modifications performed on this model are detailed in Section IV.3.2.3.

The following section presents the calibration of the model for the penetration of chloride ions into the concrete material.

III.5.3. Chloride ingress

The part of the model responsible for chloride ions transport has been calibrated using various data found in the scientific literature. Initially, the equations governing the convection phenomenon were corrected (refer to Equation III.6 of Section III.3), and new boundary conditions were incorporated in order to better account for the influence of hydrologic variations on chloride penetration. The results obtained by Schmitt [6] , who employed the GranDuBé modus operandi, were used to assess the model's performance when diffusion is the primary mechanism driving chloride penetration. Measurements conducted in the natural tidal zone by Gao [393] were employed to validate the convective aspect of the model. Subsequently, chloride profiles on structures were evaluated through the implementation of the finite element model. Finally, the effects of deicing salt applications were considered, based on modelling results obtained by Bastidas during his Ph.D. research [236].

One modification of the model version developed by Mai-Nhu and Schmitt is to incorporate an ageing factor into the chloride's effective diffusion coefficient (D_{Cl}). The selection of the equation is influenced by the research conducted in the Modevie and PerfDuB project [2], [229]. Hence, two new parameters, namely D_{app} representing the apparent diffusion coefficient and ae denoting the ageing factor, are introduced. Consequently, D_{Cl} transforms into a temporal function characterized by Equation III.80:

$$D_{Cl}(t) = D_{app}\left(\frac{t}{t_0}\right)^{ae} \qquad \text{Eq (III.80)}$$

Where t is the time (in years) and t_0 the time of measurement for D_{app} (in years). In the finite element model, t_0 will always equal 90/365 to ease the creation of the surrogate model. If the measurement is done at a different time, the coefficient is recomputed to obtain the equivalent D_{app} value at 90 days.

III.5.3.1. Earlier results on chloride natural diffusion [6]

The experiment conducted by Schmitt [6] adhered to the guidelines suggested by GranDuBé [122]. Following 90 days of preservation in water, the specimens were submerged in a solution containing chloride ions (35 g/L) for a duration of 56 days. Subsequently, the level of free chloride was quantified.

The composition and the input parameters of the model are summarized in Table III-6. The results obtained experimentally and with the model are shown in Figure III-21.

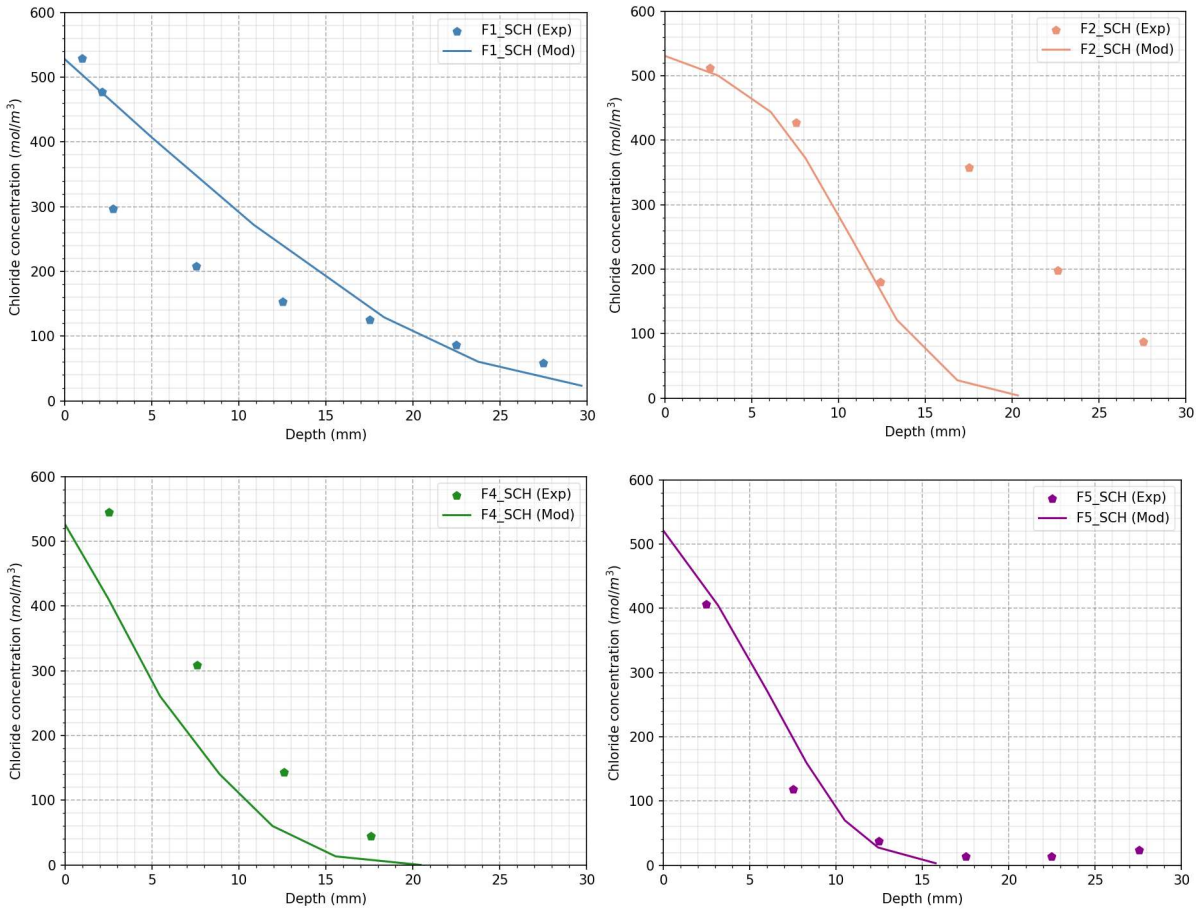

Figure III-21 Experimental and modelling results of the free chloride concentration profiles for the mixes of Schmitt.

The modelling results align with the experimental data for the majority of the mixtures. Schmitt also observed a similar deviation with the F2_SCH mixture, likely attributable to experimental inaccuracies. However, a slight discrepancy is obvious with the F4_SCH mixture, which can be attributed to a lower permeability assumed value than the current one.

III.5.3.2. Gao's experimental results in tidal zone [393]

In the study conducted by Gao et al., an investigation was carried out on the probability distribution of the convection zone in different concrete mixes. For this research, five concrete mixes were selected and utilised for modelling purposes. Their properties are shown in Table III-19. The distribution profiles of free chloride concentrations across these mixes can be observed in Figure III-22.

Table III-19 Compositions and input parameters of Gao's mixes.

Parameters	A1	A2	A3	A4	A5
PC32.5 (kg/m^3)	475	422	380	346	317
Aggregate (kg/m^3)	1174	1204	1229	1249	1269
Sand (kg/m^3)	552	567	578	589	597
W_{eff}/B_{tot} (-)	0.4	0.45	0.5	0.55	0.6
Porosity (-)	0.152	0.155	0.158	0.160	0.162
$\boldsymbol{D_{eff}}$ (10^{-12} m^2/s)	0.973	1.064	1.152	1.639	2.041
$\boldsymbol{Ca_{CH}}$ (mol/m^3)	1353	1254	1164	1084	1010
$\boldsymbol{Ca_{CSH}}$ (mol/m^3)	2017	1871	1739	1621	1512
$\boldsymbol{Ca_{Afm}}$ (mol/m^3)	500	464	431	402	375
$\boldsymbol{Ca_{Aft}}$ (mol/m^3)	377	350	325	303	282

The concrete samples were subjected to tidal environments for a duration of 600 days. In the model, daily variations in relative humidity are accounted for by incorporating a sinusoidal equation. A constant temperature of 13 °C is assumed for the computations. Furthermore, the partial pressure of CO_2 is considered by using a sinusoidal function, which accounts for the absence of CO_2 exposure when the concrete is immersed in water.

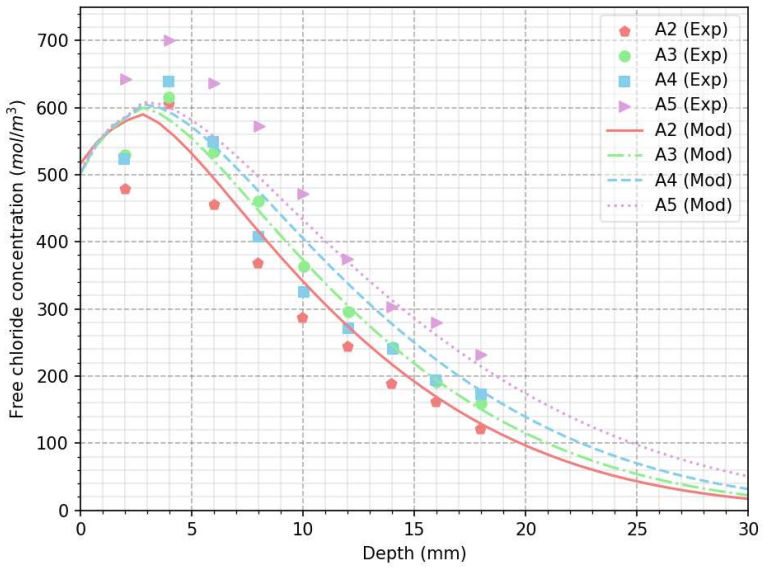

Figure III-22 Experimental and modelling results obtained on Gao's mixes.

The depth of the convective zone obtained through modelling deviates by approximately 1 to 2 mm compared to experimental results. Additionally, the model fails to accurately represent the difference in peak concentration values between different mixtures at around 4 mm. Certain mixtures also exhibit small deviations in their profiles, particularly the mix A4. However, the results depicted in Figure III-22 showcase a commendable understanding of the convective phenomenon in tidal environments.

III.5.3.3. Case study proposed by Bastidas on chloride convection [236]

The numerical results obtained by Bastidas were utilised to demonstrate the impact of convection on the penetration of chloride ions in concrete materials. Specifically, the study focused on a reinforced concrete bridge that was exposed to deicing salt. The bridge's surface experienced cyclic conditions, with variations in relative humidity and temperature following a sinusoidal function over a period of one year. Additionally, an annual salting occurred, resulting in an increase in chloride concentration represented by a triangle function. These environmental conditions were simulated for a duration of 25 years. In order to assess the influence of variations in environmental conditions on the structure's durability, a simulation with constant conditions was also conducted. The different functions used to represent the environmental boundary conditions are shown in Table III-20.

Table III-20 Exposure conditions used for the modelling.

Environmental parameter	Deicing salts exposition	Constant exposition
$[\boldsymbol{Cl^-}]$ (mol/m^3)	$C_{max}\ triangle(t_{salt})$	$\frac{C_{max}}{4}$
$\boldsymbol{RH_{env}}$ (-)	$(\frac{RH_{max}\ + RH_{min}}{2}) + (\frac{RH_{max} - RH_{min}}{2})sin(2\pi t)$	$(\frac{RH_{max}\ + RH_{min}}{2})$
$\boldsymbol{T_{env}}$ (K)	$(\frac{T_{max}\ + T_{min}}{2}) + (\frac{T_{max} - T_{min}}{2})sin(2\pi t)$	$(\frac{T_{max}\ + T_{min}}{2})$
$\boldsymbol{P_{CO_2}}$ (ppm)	0	0

The maximum chloride concentration (C_{max}) applied in this study was 451 mol/m^3. The maximum and minimum values of relative humidity (RH_{max} and RH_{min}) were set at 0.7 and 0.5, respectively. Additionally, the maximum and minimum values of temperature (T_{max} and T_{min}) were 298 K and 278 K, respectively. The time variable (t) is expressed in years in these equations, and the period of deicing salt use (t_{salt}) was set at 20 days.

Table III-21 presents the properties of the concrete used in this study. However, not all concrete properties were provided in [236]. Hence, the contents of hydrates and porosity were determined using formulas and models proposed in [282], [287], [288].

It should be noted that Bastidas' model only considers chloride ingress and assumes the partial carbon dioxide concentration to be zero.

Table III-21 Formulation and properties of the concrete [236]

Constituent/property	Value	Source
Ordinary Portland Cement (kg/m^3)	400	[236]
W/B (-)	0.5	
$\boldsymbol{D_{app}}$ (m^2/s)	3.10^{-11}	
Porosity (-)	0.18	[282]
$\boldsymbol{Ca_{CH}}$ (mol/m^3)	1130	[287], [288]
$\boldsymbol{Ca_{CSH}}$ (mol/m^3)	1825	
$\boldsymbol{Ca_{Afm}}$ (mol/m^3)	455	
$\boldsymbol{Ca_{Aft}}$ (mol/m^3)	452	

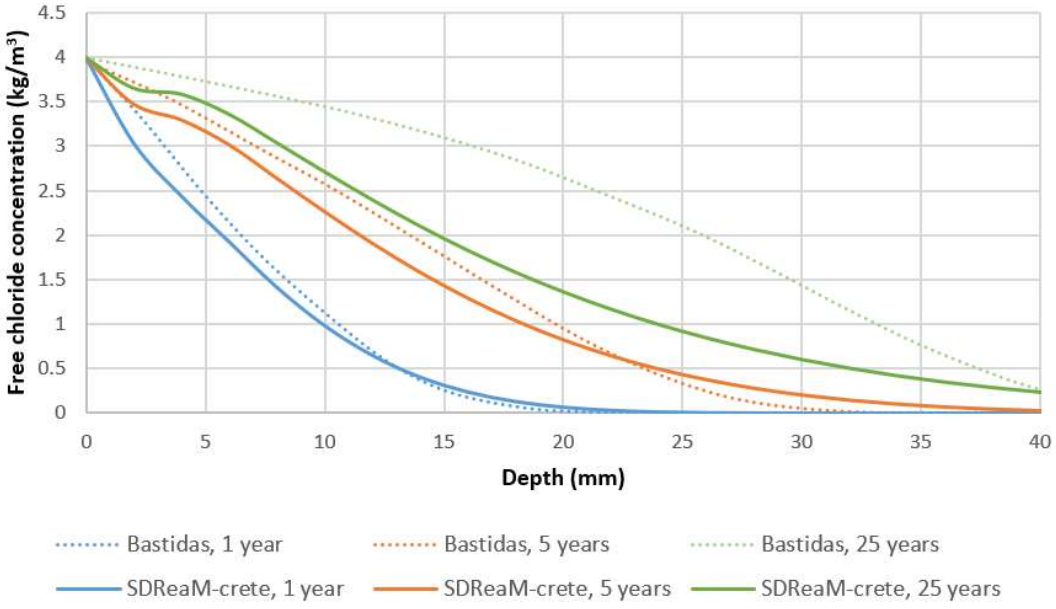

Figure III-23 Chloride content (kg/m3) after 1, 5 and 25 years considering constant environmental conditions.

In Figure III-23, it can be observed that both models yield quite comparable outcomes, assuming constant environmental conditions. This similarity can be attributed to the application of the second Fick's law, which governs the diffusion of chloride ions in both models.

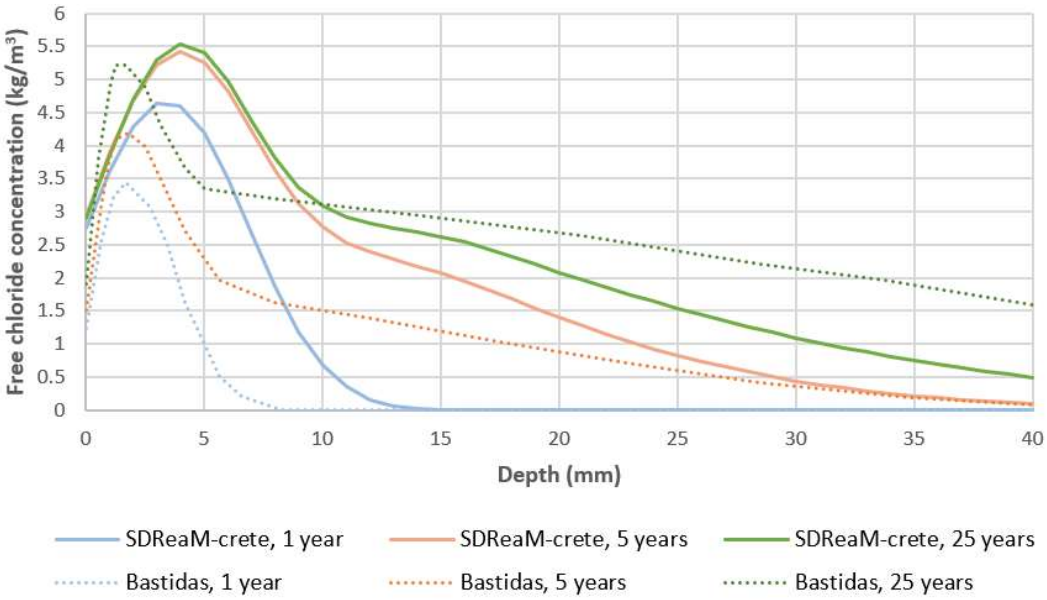

Figure III-24 Free chloride contents (kg/m3) after 1, 5 and 25 years considering variations of the environmental conditions.

In Figure III-24, it is obvious that the chloride content profiles vary between models when exposed to deicing salts. There is a notable discrepancy in the depth at which the maximum chloride content occurs, as well as the magnitude of this maximum, which is more pronounced in the SDReaM-Crete model compared to Bastidas' model. It is important to note that both models are governed by the same equations for the convection transport of chloride ions through water motion.

The observed deviation could potentially be attributed to differences in hydrologic transfer, including variations in isotherms and water permeability. Such disparities may lead to inconsistencies in how chloride ions are transported through the water medium.

To analyse chloride ingress exclusively, the previous comparison was conducted without considering carbonation. Now, a more realistic exposure condition is addressed by incorporating a partial pressure of carbon dioxide measured at 440 ppm. By considering this factor, any deviation from the previous results obtained with SDReaM-Crete would highlight the influence of carbonation.

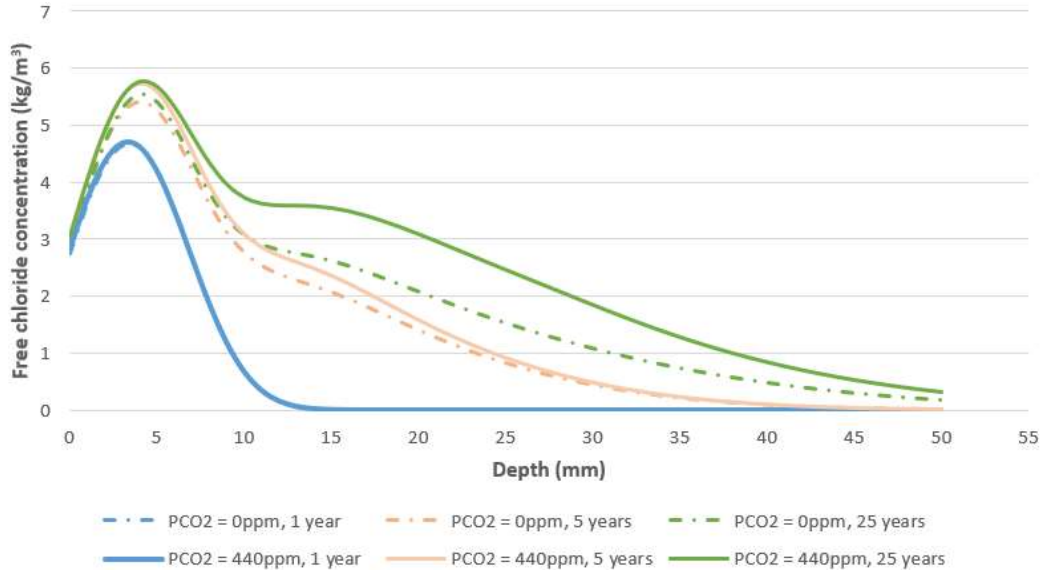

Figure III-25 Free chloride content (kg/m3) after 1, 5 and 25 years with or without carbonation.

In Figure III-25, it is shown that the disparity in free chloride concentration between the two scenarios (with or without carbonation) escalates gradually. This occurrence arises due to the carbonation process of Friedel salts and C-S-H minerals, leading to the liberation of previously bound chlorides into the interstitial solution. Additionally, it is obvious that the augmentation of free chloride concentration is non-uniform throughout the material, varying depending on the depth of carbonation.

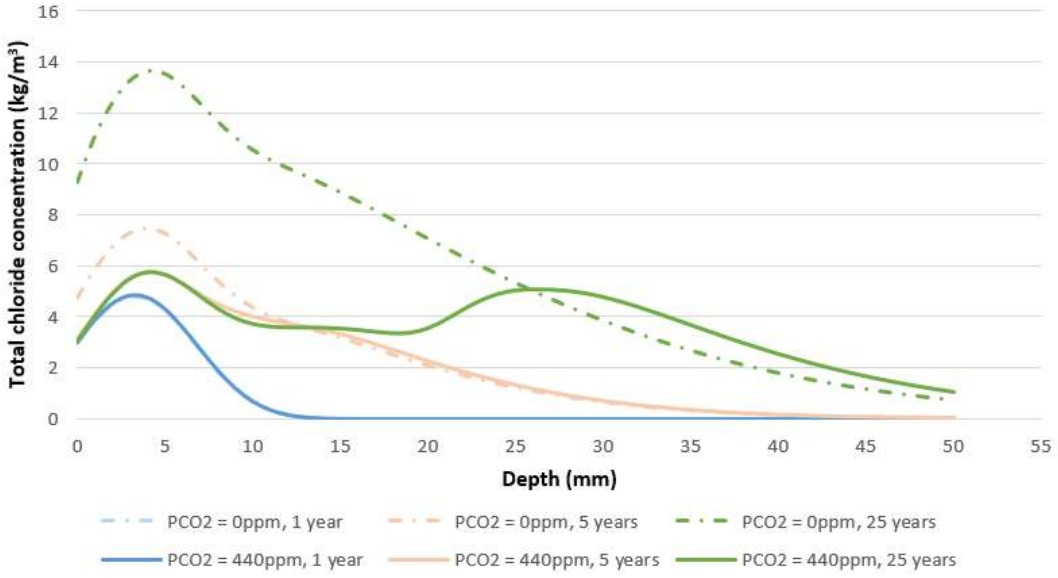

Figure III-26 Total chloride concentrations (kg/m3) after 1, 5 and 25 years with or without carbonation.

The total chloride profiles are illustrated in Figure III-26. As expected, the storage of chlorides without carbonation and their subsequent release upon carbonation of Friedel salts become increasingly noticeable with longer exposure times. Since the boundary conditions are solely dependent on the concentration of free chlorides (in terms of flux), the concentration of free chlorides in the initial

millimetres remains almost constant for both conditions (refer to Figure III-25). However, this rule does not hold for bound chlorides, thus accounting for the disparity in total chloride concentrations.

Regarding the curve obtained after 25 years of modelling with carbonation consideration, two peaks can be observed. The first peak is undoubtedly associated with the convection zone, as the value remains identical to that of free chloride concentration. However, the second peak corresponds to an increase in bound chlorides content. Specifically, when comparing the profiles of free and total chloride (refer to Figure III-27), bound chlorides are only present at depths beyond 18 mm after 25 years. The decrease in calcite content indicates that the carbonation depth should be between 20 and 30 mm, where the bound chloride content is significantly affected by hydrate carbonation. Therefore, the second peak of total chloride is located slightly ahead, where carbonation has just initiated. The subsequent decrease in content beyond the second peak is solely due to the diffusive process, which is more dominant than convective transport at this depth [393].

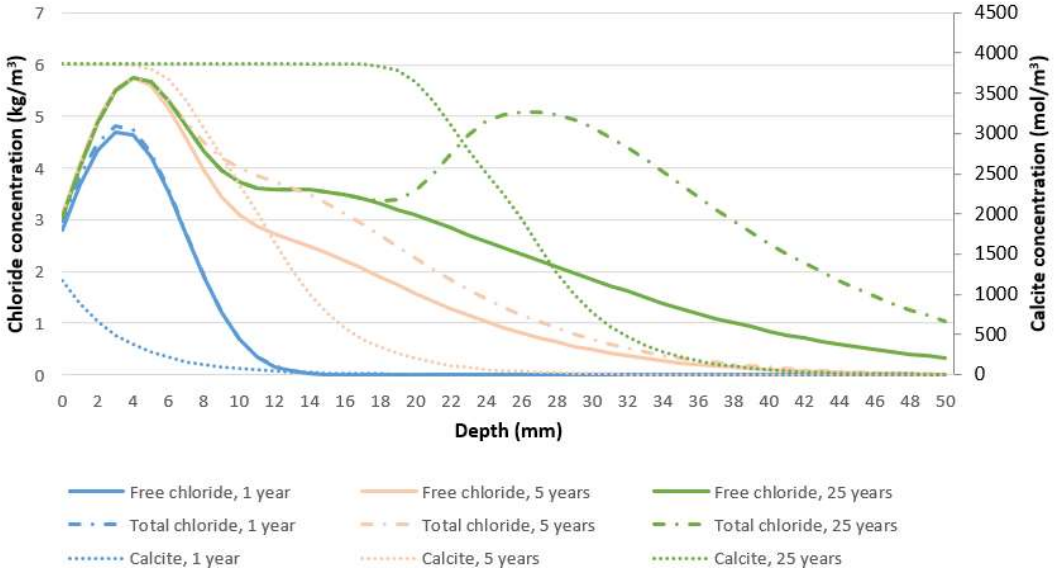

Figure III-27 Free and total chloride concentrations (kg/m3) compared to the calcite concentrations (mol/m3) in the material after 1, 5 or 25 years.

To enhance clarity and emphasize the capabilities of the SDReaM-Crete model, the profiles of Ca_{CSH} (mol/m3), Ca_{CH} (mol/m3), and Ca_{Afm} (mol/m3) obtained after 25 years of modelling, are illustrated in Figure III-28. The disparities in carbonation kinetics between C-S-H and other hydrates are evident. Additionally, this observation suggests that chloride chemically bound (by Afm) will be released before chloride physically bound (by C-S-H), as the carbonation kinetic of Friedel's salts is considered equivalent to that of Afm.

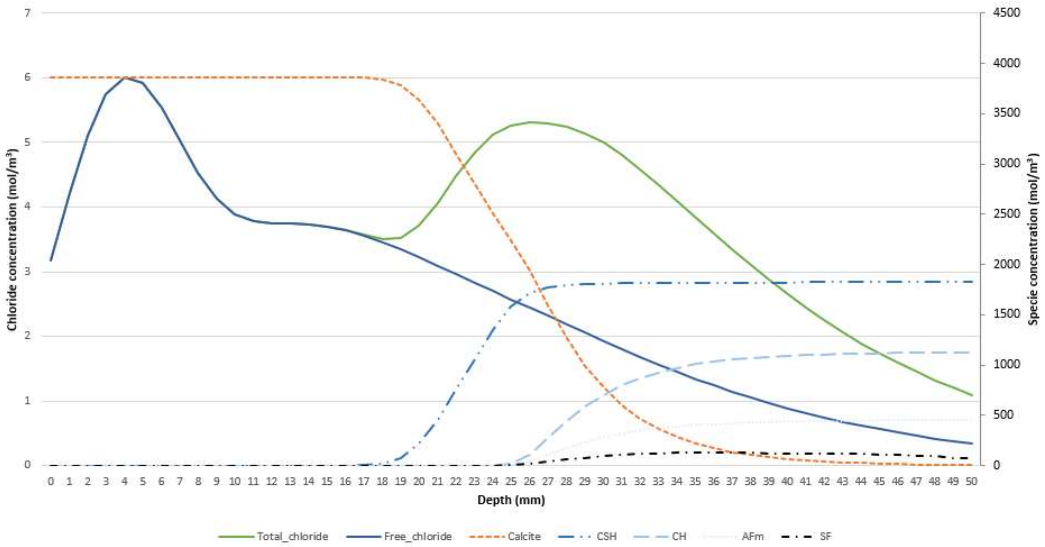

Figure III-28 Free chlorides (kg/m3), total chlorides (kg/m3), calcite (mol/m3), C-S-H (mol/m3), CH (mol/m3), Afm (mol/m3) and SF (mol/m3) after 25 years of exposure

Carbonation is known to significantly affect the microstructure of a material by reducing its porosity. In the present study, external conditions were applied, leading to a faster ingress of chloride than penetration of carbon dioxide. Therefore, it becomes challenging to differentiate the impact of porosity reduction from the release of bound chlorides due to carbonation of hydrates.

To address this issue, another modelling approach was employed, where the concrete was assumed to be fully carbonated. In this scenario, the binding capacity of the material is considered negligible, and therefore, no bound chlorides are expected to be released within the material.

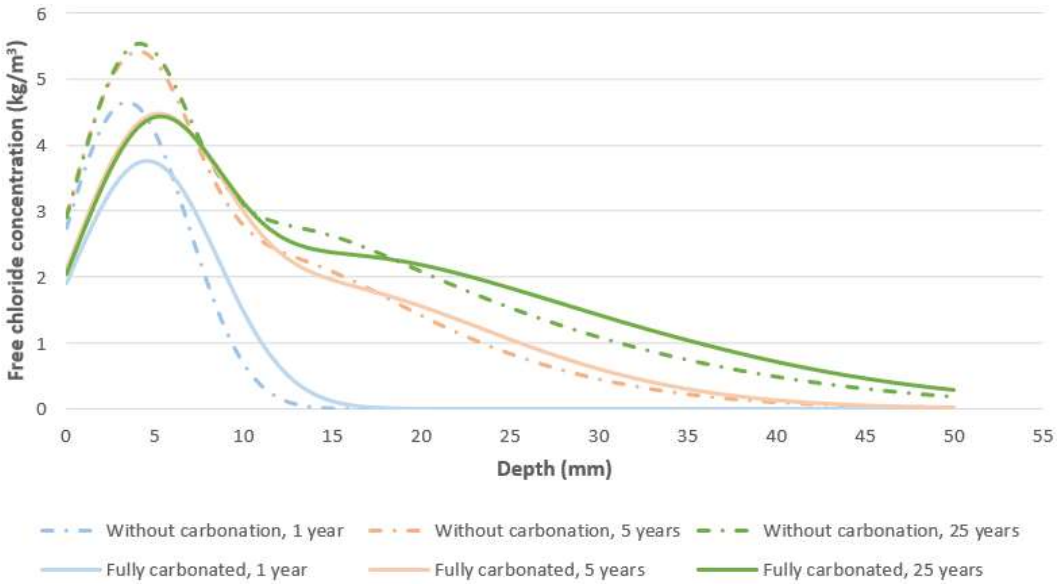

Figure III-29 Free chloride concentration (kg/m3) obtained after 1, 5 and 25 years for a carbonated concrete and for the consideration of chloride ingress alone.

The first observation from Figure III-29 pertains to the convective zone. There appears to be a slight deviation in the depth of the zone, along with a decrease in the maximum concentration value. This could be attributed to the absence of hydrates, which may impede the ingress of chloride ions. Consequently, it explains why the free chloride concentrations for fully carbonated concrete are higher

at depths of 20 mm and beyond, than sound concrete experiencing chloride ingress without carbonation.

Upon comparing Figure III-29 with Figure III-25, the impact of chloride release can be observed, further intensifying the concentration achieved under "real conditions" as compared to the modelling on carbonated concrete.

The latest findings indicate that the reduction in porosity has a lesser impact on the results than the consumption of hydrates. It is worth noting here that the effects of carbonation on water permeability or tortuosity of the material have not been considered. This approximation could potentially yield inaccurate outcomes.

III.6. Surrogate model creation

As explained earlier in this document, SDReaM-Crete is a finite element model. The nature of its differential equations, as well as the method used to solve them, lead to elevated computational time. Even if one dimensional space is considered, time and space steps, of respectively 0.5 mm and 3600 seconds, cause a high computational burden which is not acceptable for an operational use of the model. Hence, it is proposed to build surrogate models based on the initial FEM model to obtain precise results almost instantaneously. Hence, the final version of SDReaM-Crete described in the preceding sections is utilised to create the adequate databases of results.

The environmental conditions corresponding to the different exposure classes defined in NF EN 206/CN+A2 (2022) are considered for the creation of these meta-models [19]. Both Polynomial Chaos Expansion (PCE) and Artificial Neural Network (ANN) were envisaged. Full and sparse PCE techniques were also compared. The main finding derived from the comparison is that, for the sake of accuracy, full PCE should be selected. Therefore, full PCE was utilised to build four surrogate models for XC, XS1/XS3, XS2, and XD3 exposure classes, as explained in the following Section III.6.1. In addition, a fifth surrogate model was developed to estimate the saturation degree in the concrete material, which is subsequently used in Section IV.4.1 to calculate the probability of active corrosion in conjunction with existing literature models.

III.6.1. Environments consideration and input preparation

The NF EN 206/CN+A2 (2022) standard outlines the environmental classes for carbonation (XC) and chloride ingress (XS, XD). These classes signify different levels of exposure to specific environmental factors. A description of the definition of each class can be found in Table III-22, which provides comprehensive information on the exposure classes XC, XS, and XD.

Table III-22 Description of the exposure classes XC, XS and XD [19].

Exposure class	Environment description	Situation concerned
XC	Carbonation induced corrosion	Concrete containing reinforcing bar or metallic piece, exposed to air and humidity
XC1	Dry or wet permanently	
XC2	Wet, rarely dry	
XC3	Moderate humidity	
XC4	Alternation of low and high humidity	
XD	Chloride induced corrosion (origin other than marine)	Concrete containing reinforcing bar or metallic piece subjected to a contact with non-marine water containing chloride ions
XD1	Moderate humidity	
XD2	Wet, rarely dry	
XD3	Cyclic wet and dry	
XS	Chloride induced corrosion (marine origin)	Concrete containing reinforcing bar or metallic piece subjected to a contact with marine water or to air borne marine salt.
XS1	Exposed to air borne marine salt	
XS2	Permanently immerged	
XS3	Tidal, spray and splash zones	

In the FD-P18-480 [19], [301], 4 classes have been newly included. Furthermore, two additional specifications have been introduced for XD3, namely XD3f and XD3tf, which correspond to salting applications of frequent and very frequent nature respectively (denoted as "f" and "tf" in French). The XS3 category has been segregated into two subclasses: XS3e and XS3m for spray and tidal zones respectively (referred to as "embruns" and "marnage" in French). This modification ensures a more accurate representation and classification of the given scenarios.

The finite element model can consider environmental variations corresponding to the exposure classes XC, XS, and XD. Different surrogate models are then created to predict the time to reinforcing bar depassivation in each environment. Various approaches are chosen based on the specific occurring phenomenon.

For carbonation (XC), a single surrogate allows to consider all subclasses. However, for chloride-induced corrosion (XS and XD), specific surrogate models are built for certain subclasses. Firstly, the atmospheric content in CO_2 fluctuates similarly for each subclass of XC. In contrast, the chloride concentration in XS and XD varies significantly. Secondly, variations in water content do not impact the diffusion of CO_2 in the material (as only considered aerial in the model), in the same manner as chloride ions ingress. A diffusion resistance factor takes into account the impact of porosity and saturation degree onto CO_2 diffusion. However, environments with relative humidity variations are considered in the same way as environments with constant relative humidity. Regarding chloride penetration, two processes are considered: diffusion in liquid water and convection. Diffusion of chloride ions increases with the saturation degree and occurs regardless of relative humidity variations. Convective movements are directly affected by variations in water content and only occur if changes in the saturation degree take place. Due to these factors, the concentration of chloride ions obtained in the material will differ significantly depending on the subclasses considered. To facilitate the learning of the surrogate models and enhance their accuracy, the separation of certain classes is chosen. The variation ranges of each surrogate model are displayed in:

- Table III-23 for the XC classes
- Table III-24 for the XS2 subclass
- Table III-25 for the XS1, XS3e and XS3m subclasses
- Table III-26 for the XD3f and XD3tf subclasses for deicing salts applications.

The subclasses XD1 and XD2 are not considered in this study. Furthermore, the final surrogate model is developed to account only for structures exposed to periodic deicing salt application (as represented by the parameter t_{salt}, which denotes the number of days per year with deicing salts application). In the case of continuous exposure to non-marine salts, the surrogate models created for the XS classes should be utilised instead.

In order to ensure that the surrogate models encompass the conditions of the case studies, the parameters are selected to have high variation ranges.

Table III-23 Variations ranges of the XC class environmental parameters for the surrogate model construction.

Input parameters	Unity	Variation range
Annual relative humidity ($\boldsymbol{RH_{env}}$)	%	[45; 80]
Annual relative humidity variation ($\boldsymbol{\Delta RH}$)	%	[0; 25]
Annual temperature ($\boldsymbol{T_{env}}$)	Kelvin	[273; 303]
Annual CO_2 partial pressure ($\boldsymbol{P_{CO_2}}$)	Pa	[20; 80]

The pH_{dep} parameter was previously considered to account for the pH level that resulted in the depassivation of the rebar. In the current study, the surrogate model solely calculates the carbonation depth (pH < 8.3, corresponding to the inflection point of the commonly employed phenolphthalein for experimental carbonation depth evaluation). Consequently, the pH leading to corrosion initiation is deemed constant.

Table III-24 Variations ranges of the XS2 class environmental parameters used for the surrogate model construction.

Input parameters	Unity	Variation range
Annual temperature ($\boldsymbol{T_{env}}$)	Kelvin	[273; 303]
Annual [Cl^-] concentration ($\boldsymbol{Cl_{env}}$)	mol/m^3	[300; 800]
Concrete cover ($\boldsymbol{CC}$)	mm	[10; 250]

For the XS2 class, a constant relative humidity of 100% with no variation is considered. The concrete is not exposed to the air. Hence P_{CO_2} is kept constant at a value of 0 Pa.

Table III-25 Variations ranges of the XS1, XS3e and XS3m subclasses environmental parameters used for the surrogate model construction.

Input parameters	Unity	Variation range
Annual relative humidity ($\boldsymbol{RH_{env}}$)	%	[45; 90]
Relative humidity variation ($\boldsymbol{\Delta RH}$)	%	[0; 40]
Period of variation ($\boldsymbol{P_v}$)	days	[20; 90]
Annual temperature ($\boldsymbol{T_{env}}$)	Kelvin	[273; 303]
Annual CO_2 partial pressure ($\boldsymbol{P_{CO_2}}$)	Pa	[20; 80]
Annual [Cl^-] concentration ($\boldsymbol{Cl_{env}}$)	mol/m^3	[50; 800]
Concrete cover ($\boldsymbol{CC}$)	mm	[10; 250]

A singular surrogate model has been developed for the exposure classes XS1, XS3e, and XS3m. The divergence between the two subclasses of XS3 is characterized by variations in chloride concentration (lower for XS3e compared to XS3m), relative humidity (lower for XS3e than XS3m), and annual CO_2 partial pressure (higher for XS3e than XS3m). To ensure model convergence and prevent the inclusion of incorrect values, a threshold of 100% is imposed on RH_{env}.

Table III-26 Variations ranges of the XD3f and XD3tf subclasses environmental parameters used for the surrogate model construction.

Input parameters	Unity	Variation range
Annual relative humidity ($\boldsymbol{RH_{env}}$)	%	[50; 90]
Annual relative humidity variation ($\boldsymbol{\Delta RH}$)	%	[0; 25]
Annual temperature ($\boldsymbol{T_{env}}$)	Kelvin	[273; 303]
Annual CO_2 partial pressure ($\boldsymbol{P_{CO_2}}$)	Pa	[20; 80]
Annual [Cl^-] concentration ($\boldsymbol{Cl_{env}}$)	mol/m^3	[300; 800]
Concrete cover ($\boldsymbol{CC}$)	mm	[10; 250]
Salting period ($\boldsymbol{t_{salt}}$)	days	[5-30]

The XD3f and XD3tf subclasses are gathered using a unique surrogate model in this study. The main distinction between the two subclasses lies in the salting period, with XD3f having a shorter duration (around 15 days) compared to XD3tf (up to 30 days).

Finally, Table III-27 summarizes the material and modelling parameters, which remain consistent across exposure classes, except for the diffusion coefficient of chloride ions (D_{app}) and the aging factor (ae). These two parameters are not accounted for in the XC surrogate model. The selected parameter variation ranges are tailored to include the concrete mixes typically used in the industry over the past few decades. It is important to note that if the meta-models are employed beyond these predefined ranges, the results may yield inaccuracies, and alternative methods should be utilised for validation purposes.

Table III-27 Variations ranges of the material and modelling parameters used for the surrogate models' constructions.

Input parameters	Unity	Variation range
Initial porosity of concrete ($\boldsymbol{\varphi_c^w}$)	-	[0.05; 0.22]
($\boldsymbol{W_{eff}/B_{tot}}$)	-	[0.35; 0.65]
Apparent diffusion coefficient of Cl^- ($\boldsymbol{D_{app}}$)	m^2.s^{-1}	[10^{-15}; 10^{-11}]
Ageing factor ($\boldsymbol{ae}$)	-	[0.3; 0.6]
Curing factor ($\boldsymbol{Cure}$)	-	[0.5; 1]
Calcium quantity able to carbonate in CH ($\boldsymbol{Ca_{CH}}$)	mol.m^{-3} of concrete	[100; 2000]
Calcium quantity able to carbonate in C-S-H ($\boldsymbol{Ca_{CSH}}$)	mol.m^{-3} of concrete	[200; 2500]
Calcium quantity able to carbonate in Aft ($\boldsymbol{Ca_{Aft}}$)	mol.m^{-3} of concrete	[25; 600]
Calcium quantity able to carbonate in Afm ($\boldsymbol{Ca_{Afm}}$)	mol.m^{-3} of concrete	[25; 600]
Exposure time ($\boldsymbol{t_{tot}}$)	Years	[1; 100]

A Latin Hypersquare Sampling (LHS) technique is employed to optimize the distribution of the dataset used as input for creating and validating surrogate models (refer to Annex 4). Each parameter is assumed to follow a uniform distribution, with minimum and maximum values derived from the constraints presented in the previous tables. The objective is to minimize the number of simulations needed for constructing surrogate models by providing input samples that are distributed in a more efficient manner to the learning algorithms. In hindsight, considering the significant interactions observed among various parameters using the sensitivity analyses of Sobol (refer to Annex 4), it would have been more suitable to employ another method to construct the database of results, such as a pseudo-random sequences [394].

The minimal and maximal values were chosen using the experimental database (described in Section IV.3.3) for the material parameters and wide ranges for the environmental parameters. The goal is to enable the computation of most cases, including low carbon concretes, and the different exposure classes XC, XS and XD of the NF EN 206/CN (2022).

In addition, when conducting computations using the finite element model, results are recorded at four different time points: $\frac{1}{4}t_{tot}$, $\frac{1}{2}t_{tot}$, $\frac{3}{4}t_{tot}$ and t_{tot}. This approach increases the size of the dataset without adding to the computational burden.

The concrete material is assumed to be fully saturated at the start of each computation. Consequently, the initial time corresponds to either the demoulding process or the completion of conservation (in water or moist conditions) for the material.

III.6.2. Polynomial chaos expansion

A single scalar output is computed using surrogate models to determine the carbonation depth for carbonation-induced corrosion (XC) and the free chloride concentration at a given depth (CC) in the case of chloride-induced corrosion (XD and XS).

For the creation of each surrogate model, the input database is divided into two separate sub-databases. The first sub-database, which comprises 75% of the original database, is used to train the model. The second sub-database, containing the remaining 25%, is utilised for the meta-model verification. The distribution of datasets is randomized for each surrogate model creation.

A pre-treatment of the datasets acquired from the initial finite element model was performed to enhance the accuracy of the model. This pre-treatment involved the removal of datasets that resulted in a predicted depth of 0 mm, or those that exceeded the maximum depths used in the calculations, which were set at 100 mm for carbonation and 250 mm for chloride penetration. Figure III-30 (a) presents an example of this pre-treatment process, with the validation of a carbonation surrogate model trained on unprocessed data, while the validation of the selected surrogate model for carbonation is illustrated in Figure III-30 (b). It should be noted that the inclusion of extreme data to the training of the model increases the difficulty and reduces the precision of the predictions. It can be noted that around 30% of the initial data were discarded from each modelling results database while performing this pre-treatment.

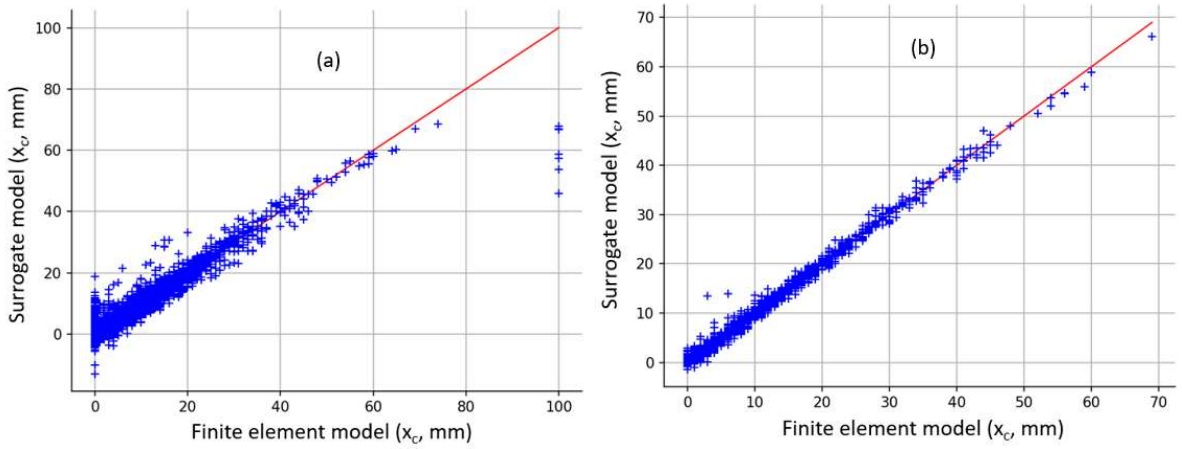

Figure III-30 Validation of a surrogate model for carbonation depth prediction trained on untreated data (a, R2 = 0.901) and on pre-treated data (b, R2 = 0.993).

The subsequent step involves checking the consistency and representativeness of the metamodel. This entails calculating and comparing the statistics (mean and standard deviation) of output for both the Finite Element Method (FEM) and the surrogate model. Furthermore, it is imperative to compute the mean absolute relative errors for each dataset utilised during the training and validation phases.

Moreover, an aspect inherent to this study is the computation of the first and total Sobol indices for every surrogate model. These indices serve as indicators of the influence exerted by each input on the resulting outcome.

III.6.2.1. Carbonation-induced corrosion exposure classes (XC)

All the exposure classes related to XC are evaluated using a single surrogate model. The dataset, consisting of 5424 data sets, is divided into two sub-databases for training (75%, 4068 data sets) and validation (25%, 1356 data sets). It proved challenging to determine the precise number of datasets needed to construct a complete Polynomial Chaos Expansion (PCE). Schmitt [6] used the following formula $n = (p+m)!/(p! \times m!)$, where p represents the maximum degree of the polynomial, and m represents the number of inputs incorporated in the surrogate model. In this study, this equation was also adopted as the minimal number of datasets for the surrogate model construction. This number was hence always exceeded.

The surrogate model developed predicts the carbonation depth. Two methods for creating the model are compared (refer to Section I.6.1):

- A full chaos method using the least square strategy.
- A sparse chaos method using the least square strategy.

The impact of the maximum degree on the results is assessed for degree values ranging from 1 to 10 for each method (refer to Figure III-31).

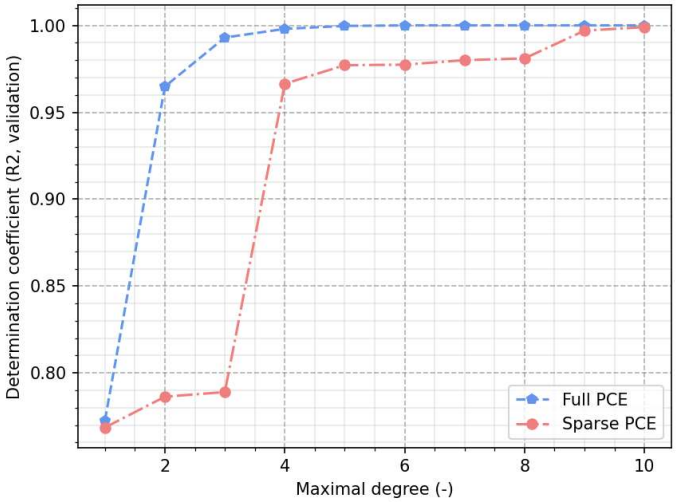

Figure III-31 Determination coefficient obtained for different polynomial maximal degree values.

The maximal degrees retained for each method are shown in Table III-28, along with the statistical results acting as verification values.

Table III-28 Statistical values for verification of the different PCE surrogate models.

	Total, least square	Sparse, least square
Maximal degree	4	9
R2 training	1.00	1.00
R2 validation	0.99	0.99
Mean FEM	9.190	9.131
Mean PCE	9.163	9.124
Error on mean	0.027	0.007
Standard deviation FEM	74.05	68.81
Standard deviation PCE	73.85	69.56
Error on standard deviation	0.20	-0.75

The Sobol indices derived from the meta-models are shown in Figure III-32. Some small variations can be observed depending on the method used. However, the most influential parameters remain consistent regardless of the chosen method.

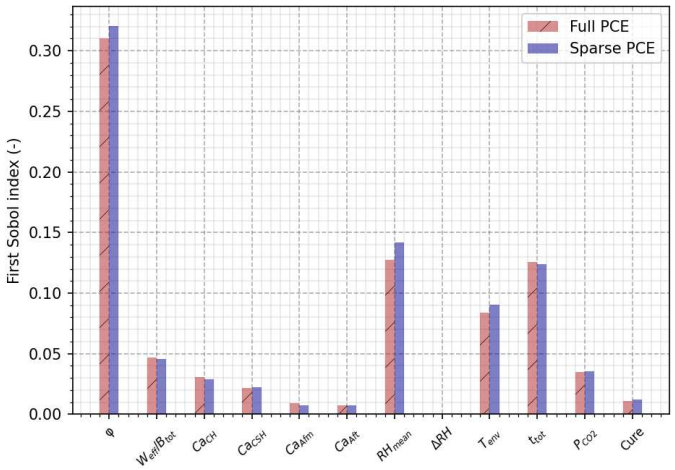

Figure III-32 First Sobol indices obtained for the PCE models.

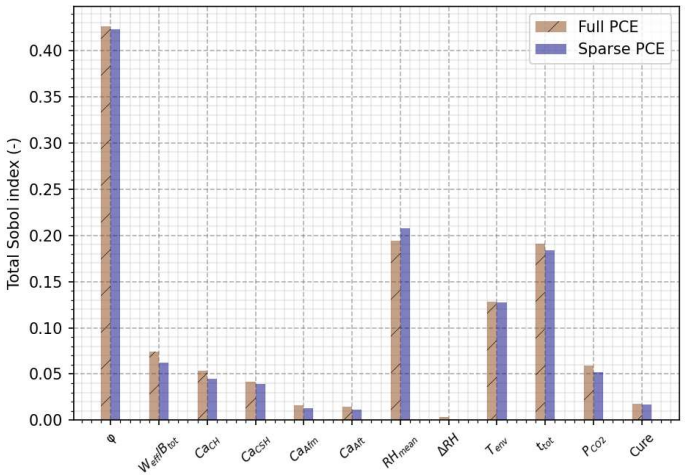

Figure III-33 Total Sobol indices obtained for the PCE models.

The carbonation depths of the PerfDuB mixes are computed using surrogate models in this study. The obtained results are then compared to those of the original finite element model. The input data utilised in the analysis were previously presented in Table III-15. The Mean Absolute Error (MAE), Mean Relative Error (MRE), mean, and deviation of the results are displayed for each created surrogate model in Table III-29. Additionally, the surrogate model proposed by Schmitt [6] for carbonation is employed to assess the improvement achieved on carbonation depth prediction in this research.

Table III-29 Verification of the PCE surrogate on the PerfDuB database.

	Experimental values	Total, least square	Sparse, least square	Finite element model	Schmitt surrogate model
Mean absolute error (mm)	-	2.07	2.05	1.79	2.60
Maximal absolute error (mm)	-	6.00	6.57	7.62	8.69
Mean (mm)	8.02	8.06	7.40	7.84	8.27
Deviation (mm)	3.07	3.07	3.10	2.36	1.88

The results obtained in this study demonstrate similar outcomes for the two surrogate models generated. However, the full chaos model requires a lower maximum order of polynomial to achieve the desired precision (4 compared to 9 for the sparse chaos model). Therefore, the metamodel that was selected for the creation of the tool and the computations in Section IV.4 is the full polynomial chaos expansion (PCE) model. For the same reason, the surrogate models for XS and XD environments were also created using the full PCE method. It is worth noting that sparse chaos exhibited a good trainability on a smaller dataset (25% of the dataset led to determination coefficient superior to 0.98), thereby enabling the development of a surrogate model with diminished finite element model computations. The selection of the full chaos methodology was solely motivated by the aim of circumventing higher polynomial orders. Hence, sparse PCE could demonstrate sufficient efficiency in generating prospective surrogate models and reducing computational workload.

Both surrogate models result in a slight decrease in precision when compared to the initial finite element model. This indicates that even with a large number of datasets used for training, it is challenging to accurately reproduce the behaviour of a complex model.

The more recent meta-model yields better results compared to the surrogate model created by Schmitt. This improvement is likely due to recent modifications made to the finite element model, which now allows for the consideration of a wider range of supplementary cementitious materials (SCMs) types and contents. Since the PerfDuB mixes include various SCMs, the results are consistent and verify the successful implementation of the PCE methodology. The modification of the PCE algorithm likely contributed to the enhancement of the predictions. Nevertheless, it should be noted that Schmitt utilised a distinct library in MATLAB, which makes it difficult to determine the precise discrepancies with the current algorithm.

III.6.2.2. Marine chlorides induced corrosion (XS)

As mentioned previously, in order to enhance the accuracy of the predictions, multiple surrogate models have been developed to account for the various exposure conditions in XS. Consequently, two surrogate models have been constructed using a complete PCE methodology:

- The first model is employed to account for reinforced concrete structures subjected to XS2 environments, specifically those fully submerged in sea water.
- The second model is utilised to address the exposure categories XS1 and XS3, where variations in moisture conditions are observed.

Each model incorporates the free chloride concentration in the computation of the outputs, while also implicitly considering the bound chlorides and their release through carbonation in XS1 and XS3 environments.

XS2 surrogate model

The surrogate model used in this study focuses on fully submerged reinforced concrete that is exposed to marine chlorides. A total of 4693 datasets were utilised, which were split into two subsets: 75% (3523 datasets) were used for training, and 25% (1173 datasets) were used for validation.

The developed surrogate model enables the determination of the free chloride concentration at a given depth (CC). To construct the complete polynomial chaos expansion (PCE), a maximum order of 3 was employed. Higher orders were found to result in overfitting of the model, resulting in a decrease in the determination coefficient obtained from the validation stage.

The results obtained from the validation of the meta-model are compiled in Table III-30, as shown below:

Table III-30 Statistical values for the verification of the surrogate model precision.

	Total, least square
Maximal degree	3
R2 learning	0.97
R2 validation	0.96
Mean database	388.6
Mean PCE	389.6
Error on mean	1
Deviation database	2974
Deviation PCE	2859
Error on deviation	115

The results of the sensitivity analysis performed using the method of Sobol are illustrated in Table III-34.

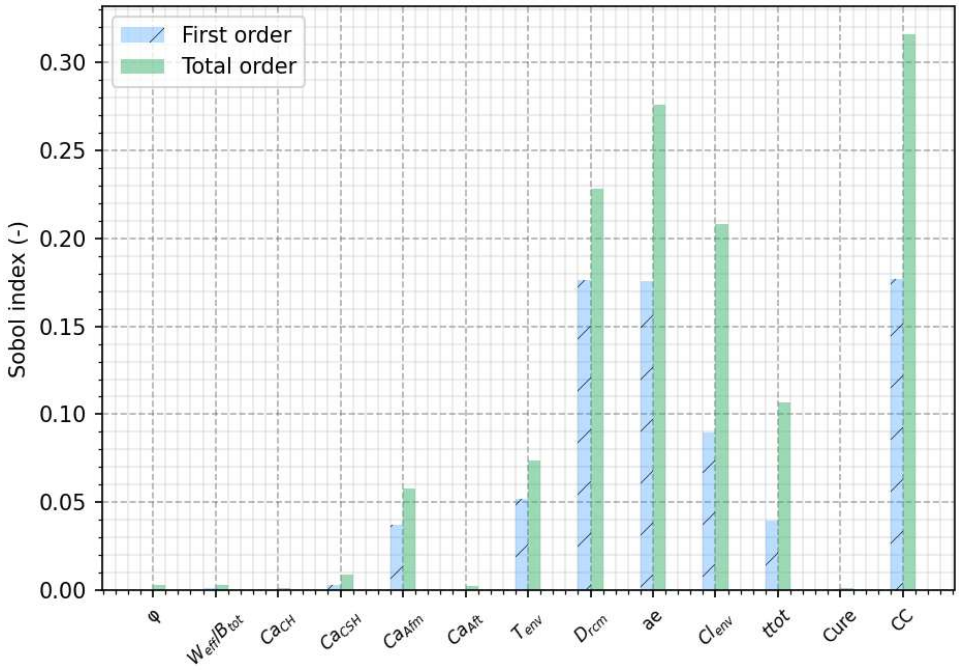

Figure III-34 First and total Sobol indices obtained for the XS2 surrogate model.

The results of the sensitivity analysis reveal a distribution of the main influences among 8 parameters. Notably, the concrete cover exerts the strongest impact on the outcome, which is expected as it defines the depth at which the concentration is computed. The model considers two significant environmental parameters, namely T_{env} and Cl_{env}. This inclusion is justifiable since the environmental chloride concentration directly affects the material's concentration, while temperature influences chloride

diffusion based on the Arrhenius law (refer to Equation III.36). As the structure remains submerged, relative humidity is not considered as an input. Consequently, chloride diffusion becomes the primary mode of transportation. This explains why the diffusion coefficient and aging factor have a significant influence on the results, while the impact of porosity and W_{eff}/B_{tot} ratio (utilised for computing water permeability and desorption isotherm respectively) is negligible. The quantities of Afm and CSH, which are responsible for chemical and physical binding, respectively, exhibit some influence on the output. However, it was expected that C-S-H would have a greater impact. Lastly, the duration of exposure greatly influences the computed concentration.

The analysis reveals that the total indices are higher than the first indices, indicating a cross-influence among different parameters. The fact that both first and total Sobol indices are close to 0 suggests that the direct and indirect impacts of porosity, water binder ratio, curing parameter, and CH and Aft contents are negligible on the variance in comparison with the other input parameters. This highlights the limited importance of considering these factors. It should be noted that this sensitivity analysis is representative only of the surrogate model and may not reflect a physical reality of the phenomenon. Hence, the sensitivity measured only corresponds to the phenomenon representation in the model.

The model developed is verified in Section IV.4.1 with the prediction of results measured on structures and is used to conduct probabilistic approaches in Section IV.4.2.

XS1/XS3e/XS3m surrogate model

The surrogate model developed for predicting chloride ion penetration in environments XS1 and XS3 is presented in this section. The full PCE is trained and validated using 2642 and 879 datasets, respectively. The verification values obtained during both steps are displayed in Table III-31 . It should be noted that lower determination coefficients are obtained compared to the surrogate model created for fully submerged structures (XS2). The difference between the determination coefficients obtained in the stages of training and validation is also higher than in the precedent case. This is likely due to the higher complexity of the chloride penetration phenomenon, which is influenced by variation in the moisture level. Consequently, convection is no longer negligible and actively contributes to chloride ingress. This aspect is further supported by the sensitivity analysis results depicted in Figure III-35.

Table III-31 Statistical values for the verification of the surrogate model precision.

	Total, least square
Maximal degree	3
R2 learning	0.89
R2 validation	0.85
Mean database	409.8
Mean PCE	409.6
Error on mean	0.2
Deviation database	3171
Deviation PCE	2885
Error on deviation	286

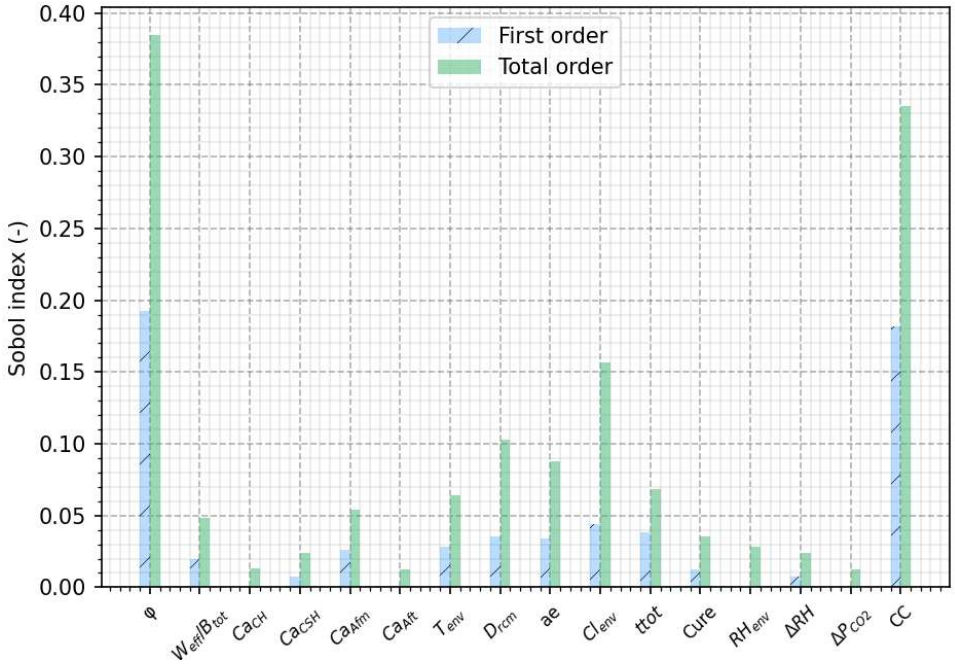

Figure III-35 First and total Sobol indices obtained for the XS1/XS3 surrogate model.

In the Figure III-35, the Sobol indices reveal a different pattern compared to the XS2 surrogate model. This difference can be attributed to the consideration of two additional phenomena in the calculations.

- Firstly, the convective transport of chloride due to variations in relative humidity plays a significant role. This phenomenon affects the porosity accessible to water, which in turn determines the liquid permeability in the model. The total Sobol indices for mean relative humidity (RH_{mean}) and its variation (ΔRH) are also influenced by this convective transport.
- Secondly, the carbonation of the cementitious paste hydrates is another important factor. The carbonation rate decreases with a higher hydrate content. Furthermore, the porosity and binding capacity of the concrete are affected by carbonation, resulting in the influence of ΔP_{CO_2} on the results, although its impact appears to be low.

These two phenomena contribute to a broader distribution of influences of the input compared to the previous model, particularly emphasized by the higher values of the total Sobol indices. This indicates cross-influences of the parameters. It can be pointed out that concrete cover remains one of the most influent factors.

Verifications of the model are realised in Section IV.4.1, while the model is used to realised probabilistic computations in Section IV.4.2.

III.6.2.3. Non-marine chlorides-induced corrosion (XD)

In this study, a singular surrogate model is developed to analyse the non-marine chloride induced corrosion in structures, specifically XD1 and XD3. This model distinguishes itself from previous models by incorporating an annual salting period, characterized by the parameter t_{salt}, which regulates the boundary conditions concerning the environmental chloride concentration. For the rest of the year, it is assumed that the structure remains unexposed to chloride ions. To represent this salting period, a periodic square function is employed, as depicted in Figure III-36.

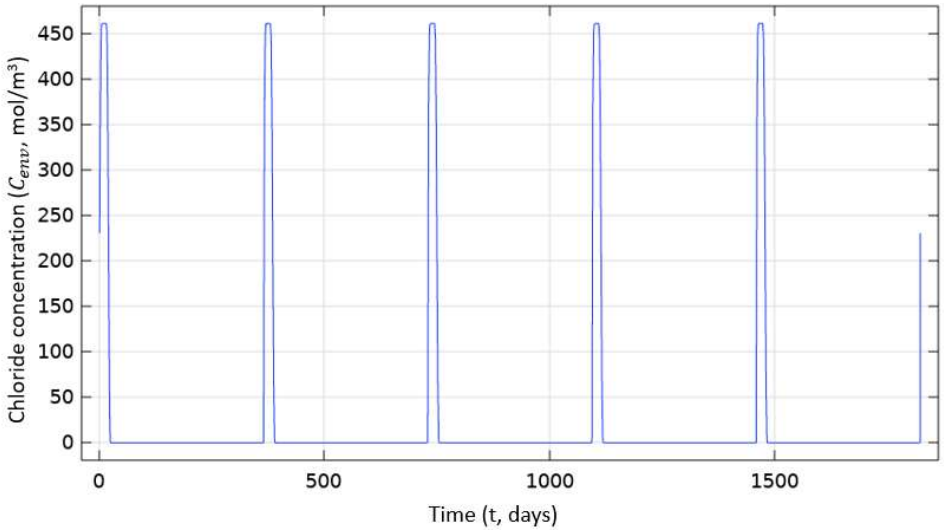

Figure III-36 Environmental chloride concentration (Cl_{env}) applied as boundary conditions for the XD surrogate model creation.

XD1/XD3f/XD3tf surrogate model

The present surrogate model developed for chloride-induced corrosion initiation specifically focuses on exposure to deicing salts. The construction methodology employed in developing this model is identical to the approaches used in previous studies. The training and validation processes were conducted using separate datasets, consisting of 2199 and 732 data points, respectively. A summary of the outcomes is presented in Table III-32. Furthermore, a sensitivity analysis was conducted using the Sobol method, resulting in the acquisition of Figure III-37.

Table III-32 Statistical values for the verification of the XD surrogate model precision.

	Total, least square
Maximal degree	3
R2 learning	0.903
R2 validation	0.852
Mean database	128.7
Mean PCE	130.0
Error on mean	1.3
Deviation database	8144
Deviation PCE	7770
Error on deviation	374

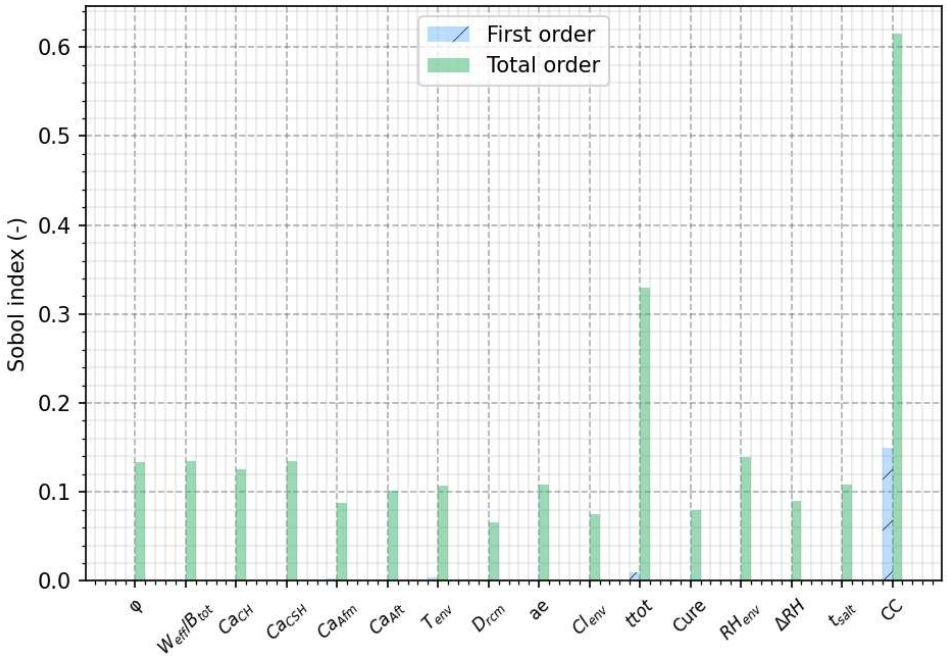

Figure III-37 First and total Sobol indices obtained for the XD1/XD3 surrogate model.

A different distribution of the influence is observed. Specifically, the majority of the influence is attributed to the concrete cover value. The second most influential parameter is the exposure time, although it is lower than the concrete cover value. It is worth noting that the total indices are significantly higher than the first indices, indicating a strong cross-influence among the various parameters. The disparities from the previous two models can be attributed to the modified phenomenon. In this model, the chloride boundary conditions are set to 0, except during the application of deicing salt. As a result, a washing of chloride ions on the surface is observed, which was not present in the other surrogate models. Moreover, the chloride concentration in this model tends to be lower than in marine exposure, explaining the rapid decrease in concentration in the concrete for high concrete cover values. Therefore, this parameter governs the outcome of the meta-model. However, the total Sobol indices demonstrate that all parameters exert an impact on the results.

The validation of the meta-model is performed in Section IV.4.1 to calculate chloride concentrations and estimate the time to corrosion initiation. Additionally, comparisons are made with other models.

III.6.2.4. Surrogate model for saturation computation

The saturation profiles were extracted from the modelling data used to create the various surrogate models in this study. These profiles are utilised to construct the final surrogate model. This model is then employed to quantify the probability of active corrosion, which is contingent upon the presence of water and oxygen. Initially, the surrogate model calculates the material saturation at a specific depth, followed by the utilization of a polynomial function (Equation III.81) based on the findings from [395] to compute the probability of active corrosion.

$$P_{a,corr} = -1.65 \times 10^{-5} Sr^3 + 0.0026 Sr^2 - 0.107 Sr + 1.653 \quad \text{Eq (III.81)}$$

Given these data acquired on soil [395], it is reasonable to expect similar outcomes in reinforced concrete, as supported by multiple studies in the literature that report comparable critical values of saturation degree and trends [396]–[398].

The same method of polynomial chaos expansion was utilised to obtain the results presented in Table III-33. This surrogate model incorporates fewer input variables compared to previous surrogate models. It is hypothesized that the parameters considered for chloride concentration and partial pressure of CO_2

have minimal influence on the saturation degree, consequently leading to neglect of water produced by carbonation in this analysis.

Table III-33 Setting and results of the surrogate model for saturation computation.

	Total, least square
Maximal degree	4
R2 learning	0.93
R2 validation	0.89
Mean database	0.797
Mean PCE	0.799
Error on mean	0.002
Deviation database	0.087
Deviation PCE	0.076
Error on deviation	0.011

The results of the Sobol sensitivity analysis are depicted in Figure III-38, demonstrating considerable cross-influences among the parameters. Notably, the three environmental parameters, namely HR_{mean}, T_{mean}, and ΔRH, exhibit a significant impact on the outcomes. Furthermore, the material parameters also play a vital role, particularly with regard to the porosity accessible to water (φ_c^w) and the W_{eff}/B_{tot} ratio, which govern the liquid permeability and the desorption isotherm, respectively. Conversely, the final exposure time scarcely affects the results, which can be reasonably expected since variations in moisture levels occur annually, and the exposure durations are typically long enough to attain material equilibrium at the concrete cover depth.

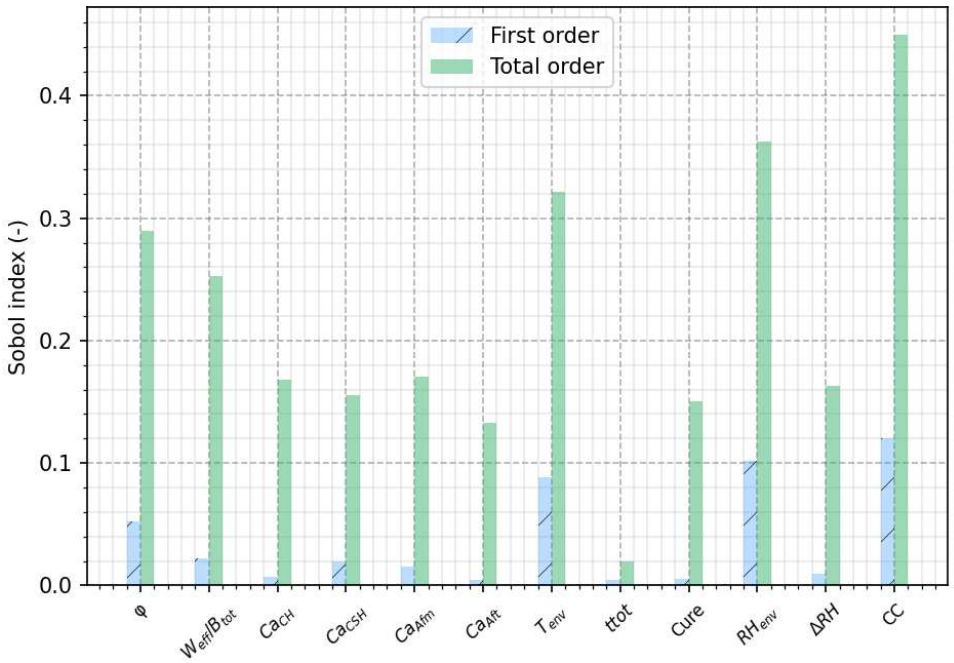

Figure III-38 First and total Sobol indices obtained for the surrogate model used for the saturation computation.

The methodology described here is used in Section IV.4.1 for deterministic computations of the propagation time.

III.6.3. Artificial neural network

An alternative method for the construction of the surrogate model was implemented. The goal was to compare the prediction results of the PCE-based meta-model for carbonation depth prediction. Artificial neural network (ANN, refer to Section I.5.1.2) was chosen for this comparison. The scikit-learn library is

utilised for the computation of the ANN surrogate models, employing the MLPRegressor class (Multi-Layer Perceptron Regressor) [315].

The precision of the ANN models is measured by computing the same statistical values as those used for the PCE-based models. Initially, determination coefficients are calculated for both the training and validation datasets. The mean and standard deviation are then computed using the validation sub-database and the results of the surrogate model. Finally, the mean absolute error and mean relative error are calculated using the validation sub-database. The values obtained are presented in Table III-34.

A study is conducted to investigate the architecture of the network. The influence of the number of layers on the determination results is analysed up to a maximum of 3 layers, along with the impact of varying the number of neurons within each layer up to a maximum of 50. The results of this investigation are depicted in the Figure III-39.

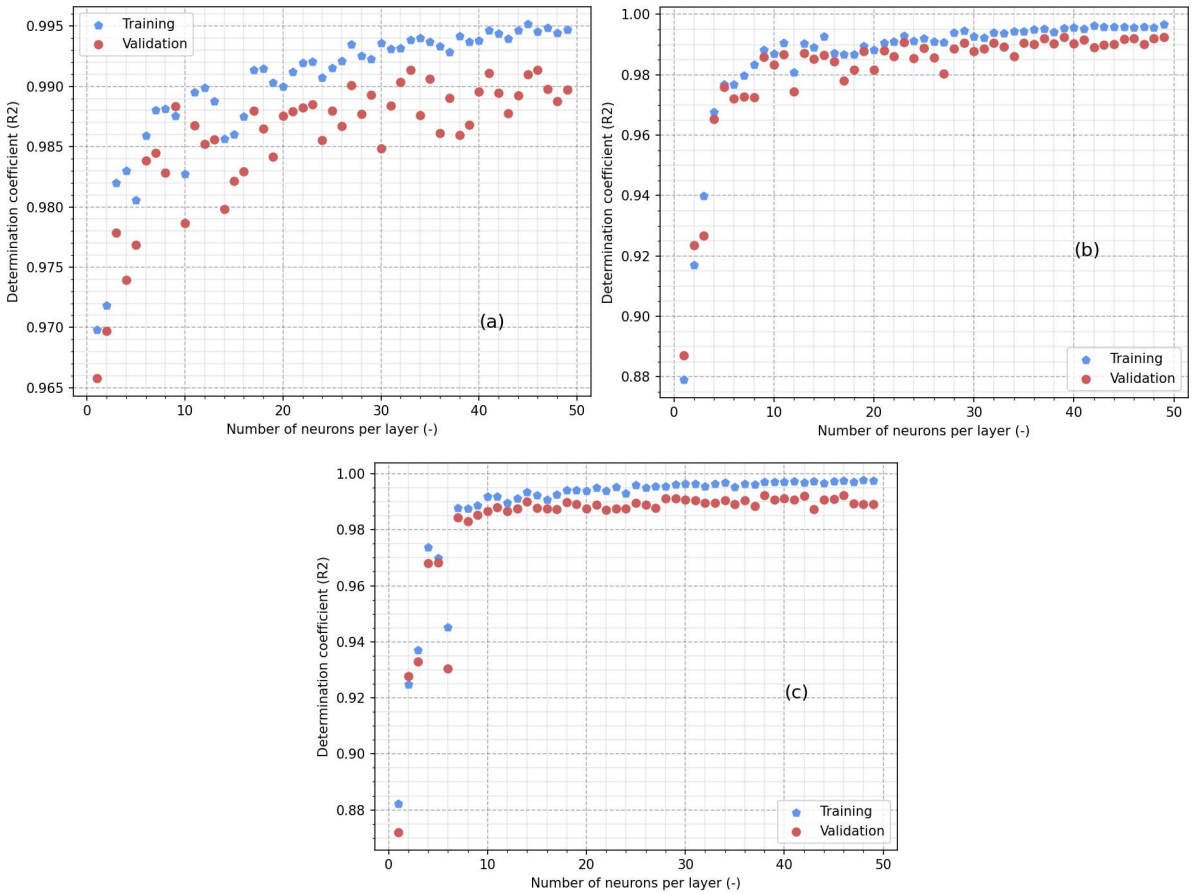

Figure III-39 Determination coefficients obtained for the validation of the surrogate models as a function of the neurons number for (a) one layer ANN models, (b) two-layers ANN models and (c) three layers ANN models.

Based on these result, three architectures are selected and compared:

- The first with 1 hidden layer and 50 neurons.
- The second with 2 hidden layers and 50 neurons in each layer.
- The third with 3 hidden layers and 30 neurons in each layer.

Table III-34 Results of the verifications performed on the three ANN surrogate models.

Architecture	1 layer; 50 neurons	2 layers; 50 neurons	3 layers; 30 neurons
R2 on learning	0.99	1.00	1.00
R2 on validation	0.99	0.99	0.99
Mean absolute error (mm)	0.6	0.6	0.6
Mean relative error (%)	14.5	13.9	14.7
Absolute error on mean (mm)	0.24	0.06	0.22
Absolute error on standard deviation (mm)	0.54	0.11	0.46

The sensitivity analysis of the models is conducted using the built-in permutation-importance function from the scikit-learn library [399]. This function performs a sensitivity analysis similar to the Morris method, evaluating the influence of each parameter by measuring the impact on the results caused by varying one parameter at a time. The permutation importance values are then compared to the first-order Sobol indices for considering the impact of each parameter individually. The obtained results, as depicted in Figure III-40, exhibit a similar trend to those obtained for the surrogate models generated using Polynomial Chaos Expansion (PCE) (refer to Figure III-32).

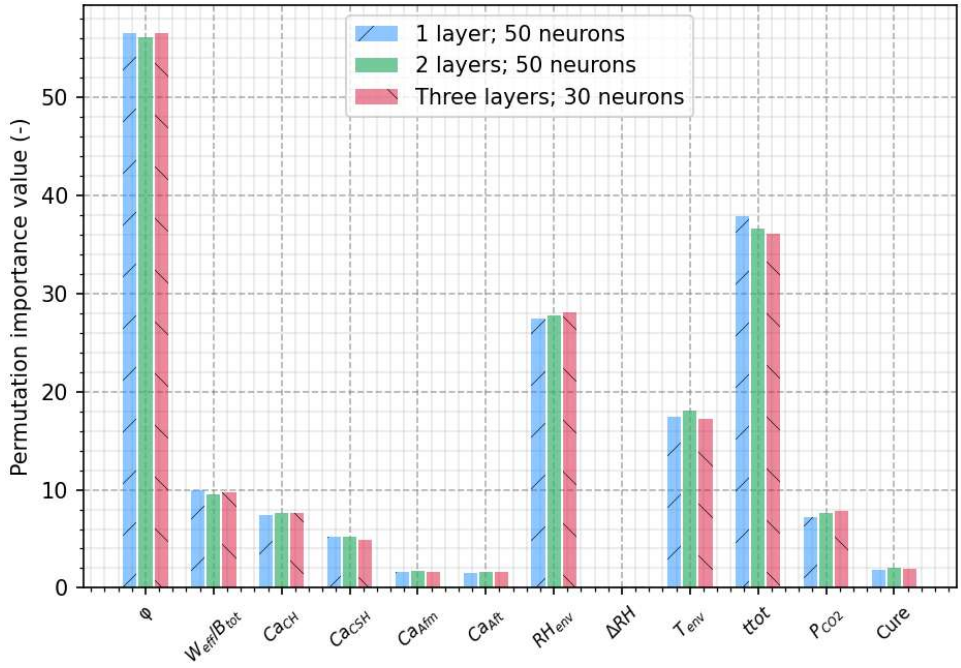

Figure III-40 Permutation importance of the input parameters obtained for the three ANN surrogate model.

The natural carbonation depths of the PerfDuB mixes were computed using three different models. The average outcomes are presented in Table III-35, along with the Mean Absolute Error (MAE) and Mean Relative Error (MRE).

Table III-35 Verification of the ANN-based surrogate models on the PerfDuB database.

	Experimental values	1 layer; 50 neurons	2 layers; 50 neurons	3 layers; 30neurons	Finite element model
Mean absolute error	-	4.76	4.96	4.99	1.79
Maximal absolute error	-	26.71	28.29	29.08	7.62
Mean	8.02	10.76	10.63	10.89	7.84
Deviation	3.07	8.07	8.52	8.51	2.36

Although the initial evaluation of the models conducted on the validation dataset indicates satisfactory performance (refer to Table III-34), the calculations of the carbonation depths for PerfDuB reveal significant errors. The effectiveness of the artificial neural network ANN-based surrogate models is inferior to that achieved by the PCE-based surrogate models (refer to values in Table III-29). The method was not applied to chloride ions concentration prediction because of the unsatisfactory results obtained for carbonation depth prediction.

Conclusion

This section outlines the development and validation of the surrogate models employed in the tool. Polynomial chaos expansion was found to be reliable for this purpose. The surrogate model obtained using artificial neural networks (ANN) for carbonation exhibited lower precision, thus, this approach was not further investigated. However, it is certainly possible to achieve similar results with improved settings, although limitations on time prevented further exploration. Monte Carlo simulation and kriging could also be considered as potential alternative solutions.

It was observed that the creation of surrogate models resulted in a loss of precision compared to the original finite element model. This was expected as polynomial chaos expansion inherently provides an approximation of the results. Nonetheless, the introduced imprecisions remained minimal when the inputs fell within the ranges utilised for surrogate model development.

It could be possible to enhance the accuracy of the surrogate model by modifying the properties of the polynomial chaos expansion utilised. A different distribution of the input data could be employed to allow for different polynomial families, such as Hermite or Laguerre, which may offer improved precisions for certain parameter ranges and cases. Furthermore, the use of full polynomial chaos expansion results in models with a heavier computational load compared to sparse polynomial chaos expansion, when considering the same maximum polynomial order [312]. Therefore, it would be interesting to optimize the utilization of sparse polynomial chaos expansion to reduce the computation time associated with the meta-model application.

Nevertheless, the created meta-models exhibit almost instantaneous functionality and provide the opportunity to obtain results more rapidly than the initial finite element model. This characteristic proves valuable in the context of the probabilistic approach employed in Section IV.4.2. Additionally, further testing is conducted on these meta-models utilizing data from structures' monitoring in the subsequent section. Modelling results obtained with analytic models are also presented and compared to the results of the surrogate models.

IV. A tool for deterministic and probabilistic computations of corrosion initiation

IV.1. Introduction and goals

This section presents a tool for predicting durability of the reinforced concrete structures submitted to reinforcement corrosion. It is specifically designed for civil engineers, who require assistance in assessing the condition state of such structures. The primary goal of this tool is to provide users with information on the remaining service life of a given structure that is subjected to exposure classes XC, XS, and/or XD.

In the context of corrosion, the initiation stage involves two aggressive phenomena: carbonation and chloride ingress. These two phenomena result in different forms of corrosion, namely uniform and pitting corrosion, respectively. Consequently, different methods are employed to consider the propagation of the induced corrosion.

From a broader perspective, this tool enables deriving concrete mix composition data into physical and chemical properties that are relevant to the durability. The tool relies on various models (most of them are empirical formulae) originated from the literature mentioned in Section I.4 and presented in Annex 4. The tool utilizes algorithms that make use of a database of experimental results generated during this work. The strength of this methodology lies in its ability to effectively incorporate new materials used in concrete formulations and address the concrete industry's growing concern for reducing its environmental impact. To meet this demand, the methodology was developed to offer maximum flexibility in terms of composition for concrete mixes. This aspect is elaborated upon in Section IV.3.1.

IV.2. Python-based graphic interface

A tool was developed using the Python library Tkinter [400] to facilitate the implementation of the methodology described in this section. This tool enables a graphical user interface, enhancing user interaction with various algorithms and models.

The application comprises multiple tabs, each corresponding to a specific step in the process. The initial screen, illustrated in Figure IV-1, serves as the home screen.

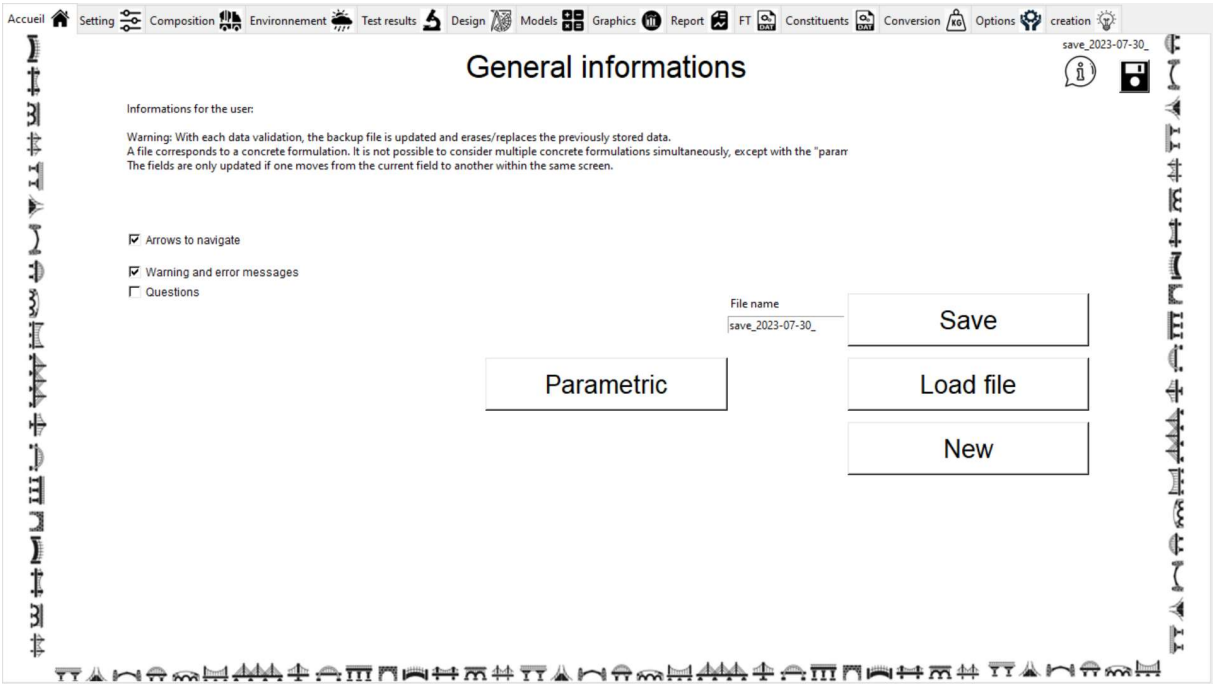

Figure IV-1 Screenshot of the application showing the home screen of the python-based tool.

To ensure a systematic and error-free procedure, a unique and dedicated tool has been developed for the methodology. This tool effectively guides the user throughout the entire process and provides timely feedback through popup messages. Two distinct types of messages have been defined for this purpose:

- **Error messages:** These messages are triggered when a value or setting is found to be unacceptable. They not only halt the execution of the subsequent steps but also necessitate the modification of the erroneous value before allowing the process to proceed.
- **Warning messages:** These messages serve to alert the user about an unusual setting value. However, they do not impede the execution of the subsequent steps of the application.

These messages play a crucial role in allowing users to promptly rectify errors and make informed decisions.

The different steps of the application are detailed in the following sections, allowing the user to go from the selection and adjustment of the different parameters to clear deterministic and probabilistic results of reinforced concrete structure durability.

The tool finally allows the automated creation of a .docx document (Word) with an extensive summary of the different input data, computation stages, models used, and results obtained. A clone .txt document is also generated, independent of any software licence or version and is used as a safeguard.

IV.3. Input data and transformations

Parameters generally known to the user are first asked and can be sorted in three categories: material properties, environmental conditions, and design quantities. Specific input parameters of durability models are then estimated by different methods and sources. Finally, because of the various methods available, a confidence index is defined in the last subsection, as a level of accuracy measure of each method.

Depending on the case study, the tool tends to ask for the lowest number of input data, while being able to benefit from the knowledge of additional measurements to increase the accuracy of the results.

Accordingly, the user is informed of the level of accuracy by a warning flag being raised each time a prediction implies the use of assumptions or simplifications.

IV.3.1. Operational context

The methodology defined in this study and the python-based tool associated aim to consider most of the maritime and road structures, either already in service or new, exposed to XC, XS and XD environments (according to the NF EN 206/CN+A2 (2022) recommendations).

IV.3.1.1. Materials

This subsection details the different parameters related to the constitutive materials: mix composition of the concrete, and steel type of the reinforcing bar (see Figure IV-2 and Figure IV-3) .

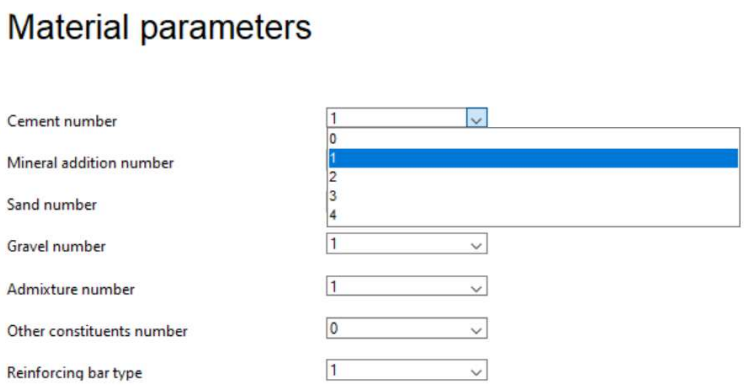

Figure IV-2 Screenshot of the tab allowing the general setting for the concrete mix.

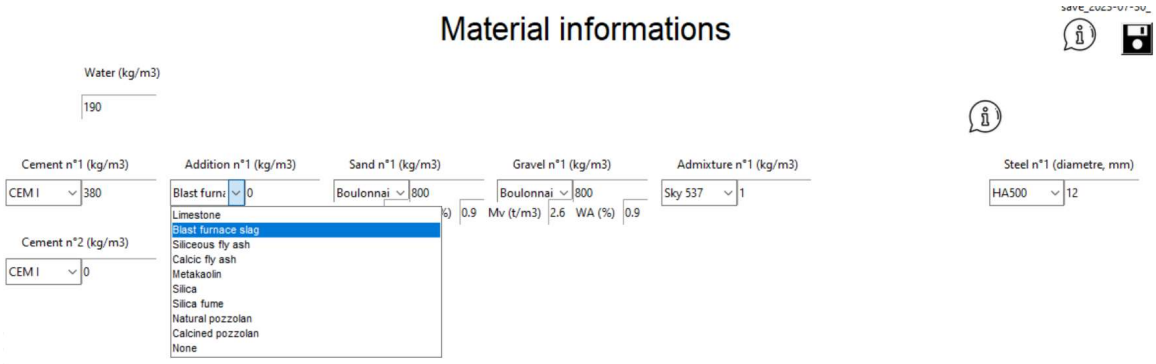

Figure IV-3 Screenshot of the tab allowing the specific setting of the concrete composition (example for 2 cements, 1 mineral addition, 1 sand, 1 gravel, 1 admixture and 1 steel type).

To ease the usage and reduce the probability of user mistakes, a technical datasheet for the different constituents with different associated parameters can be used. In the absence of technical datasheet, average values are considered for the different parameters of the constituents.

IV.3.1.1.1. Composition of concrete mix

The general composition of a concrete mix is detailed in Section I.1. The goal is to encompass most of the mixes of concretes used in the industry in the past decades, as well as the new materials used in the low-carbon concrete manufacturing, for their use will inevitably become usual in the future.

1) The binder formulation is defined by the user. For the sake of simplicity, it is assumed that the binder can be decomposed into clinker and mineral additions contents, implying that the fineness and the blending quality are not considered.

a. All the cements defined in the standards NF EN 197-1 (2012) and NF EN 197-5 (2021) can be used. They can also be blended for a particular concrete mix, especially in anticipation of potential future normative works. It is therefore possible to adjust the compositions of each cement, based on the standard recommendations, to consider the values of a specific technical sheet (see Figure IV-4).
b. To enable both the prescriptive and performance-based approaches, various mineral additions can be also used in the framework of the NF EN 206/CN+A2 (2022) and FD P18-480 (2022) recommendations. It is important to note that available mineral additions are those already included within the hydration model. The oxides content of each mineral addition (and clinker) can be adjusted to increase the accuracy of the hydrates computing, as shown in Figure IV-5.
c. The effective water content (or the water-to-binder ratio W_{eff}/B_{tot} ratio on option) is a crucial setting for the mix composition.
d. The admixture type(s) and content(s) are the last settings for the binder composition. These aspects are useful for searching in the database (see Section IV.3.3.2) and in certain learning-based models.

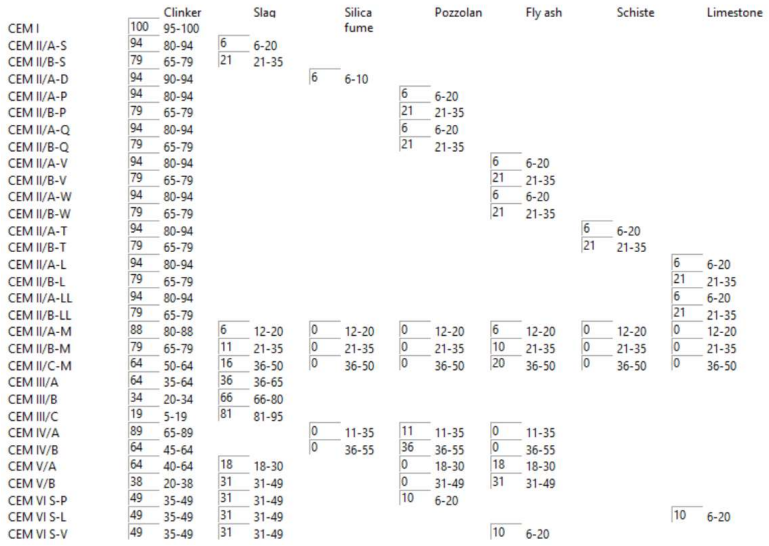

Figure IV-4 Screenshot of the tab responsible for the cements' compositions.

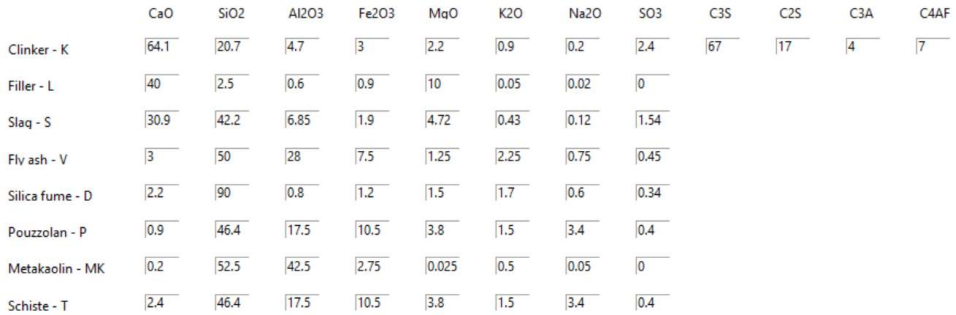

Figure IV-5 Screenshot of the tab dedicated to the setting of the oxide content for each constituent.

2) The aggregates' types and contents are also defined by the user. Only two parameters are asked in addition to the content: the bulk density (Mv_{agg}) and the water absorption (WA_{agg}) of the aggregates as shown in Figure IV-6. These two parameters are used in the porosity computation. Moreover, they will be used as a comparison basis for the search in the database. The

consideration of Recycled Concrete Aggregates (RCA) is authorized based on the assumption that the two previous parameter values are sufficient to account for their impact on the concrete durability. A perspective for further improvements would be to include diameter distribution which could enable the use of the granular stacking model of De Larrard [33], [280].

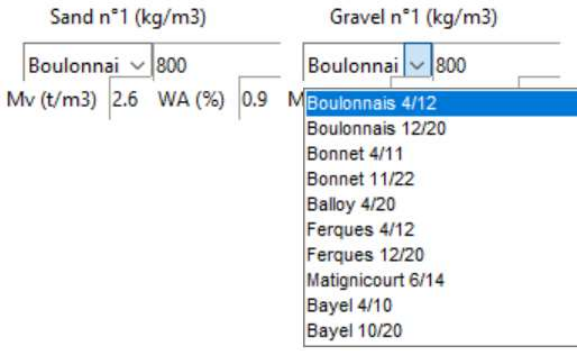

Figure IV-6 Application extract of the setting dedicated to the aggregates.

Once adjusted or simply chosen by the user, material parameters are checked with respect to the selected approach, either prescriptive or performance-based, according to NF EN 206/CN+A2 (2022) or FD P18-480 (2022) respectively, to comply with recommended thresholds or restrictions.

IV.3.1.1.2. Steel composition

The user is asked to select the type of steel used for the reinforcing bar (see Figure IV-7). This parameter will impact the initiation of corrosion (computation of the PREN number) and its propagation. It will also be used to warn the user on the potential gap between the model results (based on classic steel type) and the reality when unusual steels are used.

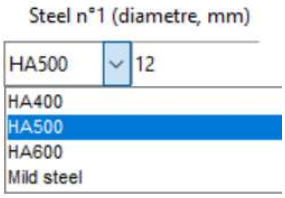

Figure IV-7 Screenshot of the setting dedicated to the reinforcing bar steel.

IV.3.1.2. Environment

The environmental parameters define the condition of carbonation and chloride exposure. The different exposure classes defined in the NF EN 206/CN+A2 (2022) and the new subclasses for XS3 and XD3 defined in the FD P18-480 (2022) are considered. Moreover, classes with no default parameters are also proposed under the name of XC0, XS0 and XD0, allowing the user to define his own conditions. The selection is first done in the tool with a system of checkboxes shown in Figure IV-8.

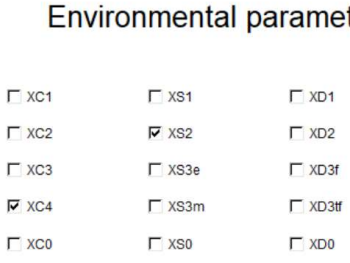

Figure IV-8 Screenshot of the checkboxes responsible for the exposure classes selection.

Different parameters are associated to each class, as shown in Figure IV-9. The values summarized in Table IV-1, Table IV-2 and Table IV-3 are used as default for the different exposure classes.

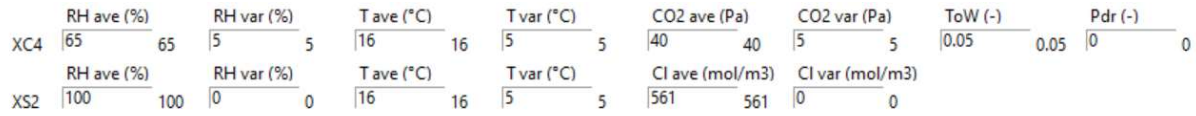

Figure IV-9 Screenshot of the different setting for the exposure classes.

Table IV-1 Default values of the parameters for the XC exposure classes.

Class	Mean relative humidity (%) [323]	Mean relative humidity variation (%)	Mean temperature (°C)	Mean temperature variation (°C)	Mean partial pressure of CO_2 (Pa) [6]	Mean CO_2 partial pressure variation (Pa)	ToW (days with rain > 10 mm) [229]	Pdr (Driving rain ratio) [191]
XC1	50	5	16	10	43	5	0	0
XC2	90	5	16	10	43	5	0	0
XC3	75	5	16	10	43	5	0	0
XC4	65	20	16	10	43	5	0.05	0.5
XC0	-	-	-	-	-	-	-	-

Table IV-2 Default values of the parameters for the XS exposure classes.

Class	Mean relative humidity (%)	Mean RH variation (%)	Mean temperature (°C) [20]	Mean temperature variation (°C) [20]	Mean Cl^- concentration (g/L) [323]	Mean Cl^- concentration variation (g/L)
XS1	75	10	16	5	16	10
XS2	100	0	16	5	22	0
XS3e	80	10	16	5	19	10
XS3m	83	20	16	5	22	10
XS0	-	-	-	-	-	-

Table IV-3 Default values of the parameters for the XD exposure classes.

Class	Mean relative humidity (%)	Mean RH variation (%)	Mean temperature (°C)	Mean temperature variation (°C) [20]	Mean Cl^- concentration (g/L) [323]	Mean Cl^- concentration variation (g/L)	Number of annual salting day [19]
XD1	75	5	16	8	-	10	15
XD2	90	5	16	8	-	10	-
XD3	75	20	16	8	10	5	5
XD3f	75	20	16	8	15	5	15
XD3tf	75	20	16	8	20	5	30
XD0	-	-	-	-	-	-	-

The default values proposed can be modified if the user has a more accurate knowledge of them. For instance, annual means of relative humidity and temperature can come from the measurements of a meteorological station. The tool also proposes a direct connection to an internet website [392] through an API to get data in real time. Although it does not allow to provide an annual database, it may help to acquire enough data to visualize the environment of a geographical zone. The website also proposes to sell complete database of results for different zones worldwide, with recording back to the 1980s.

Partial pressure of CO_2 can be modified, especially when considering new structures that will suffer the impact of human activity on the partial pressure of CO_2. Hence, higher values can be used in certain modelling which will then impact the carbonation results [401]. It could also be more accurate to

consider a lower partial pressure value when considering structures installed for decades, since values inferior to 35 Pa are reported in 1960 [401]. Finally, in some places like underground parking, the values can also be higher and exacerbate the concrete carbonation.

Regarding the salting period, a map of France is available in NF EN 206/CN+A2 and gives an overview of the salting frequencies according to the zone considered. This map can be used to refine the default number of annual salting days.

The previous parameters have an important impact on all the phenomena, although they are not considered in every durability models. Hence, the user needs to verify the input parameters of the selected models.

IV.3.1.3. Geometry and design

The main geometrical parameters are the concrete cover depth(s) and the reinforcing bar diameter(s). For the concrete cover, different methods are implemented and allow the consideration of:

A value or list of values: This method allows the selection of one or several values. Moreover, the values recommended by the different standards are also proposed as default after the specification of a concrete mix and the exposure classes considered. The values of the Eurocode 2 and of the Exposure Resistance Classes are proposed (see Section I.6.4).

A distribution of the concrete cover derived from measurements: This method allows the fitting of a probability distribution based on experimental measurements conducted on a structure zone, using the Kolmogorov-Smirnov test (implemented in Scikit-learn [402]) [403]. Beta distribution is frequently convenient and considered adequate when the p-value obtained is superior to 0.75. An example is given for three series of measurements in Figure IV-10 fitted.

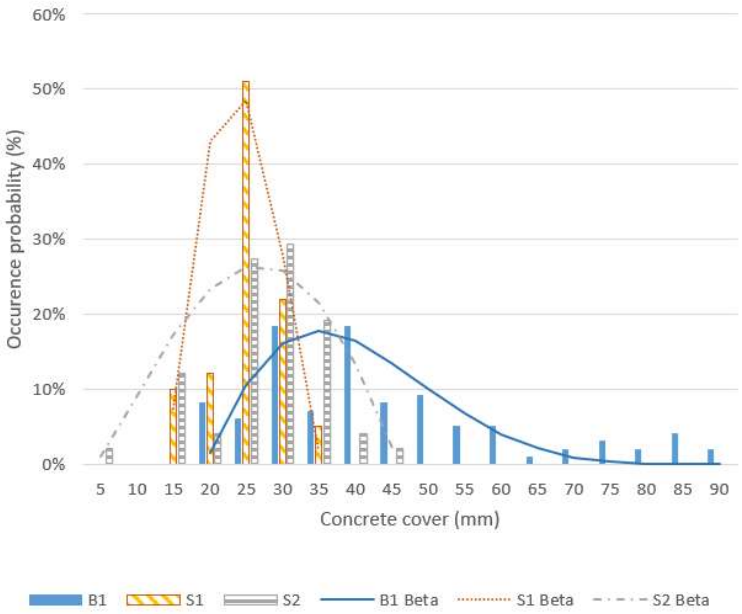

Figure IV-10 Beta distributions fitted on experimental measurements of concrete covers with pachometer on three structure zones (p-value = 0.76 for B1, p-value = 0.99 for S1, p-value = 0.96 for S2).

Different time scales must be set by the user:

The desired service-life: according to the durability issue, the service-life is the summation of the durations of corrosion initiation and propagation. The initiation stage of corrosion t_{ini} is either computed thanks to carbonation models or chloride penetration models. The propagation stage of

corrosion until concrete cover cracking t_{prop} is either computed from a corrosion model (refer to Section I.4 and Annex 4) or stated from the PerfDuB documentation [323] which defines the mean propagation time according to the exposure class (see Table IV-4 and Table IV-5 respectively). When the time exceeds $t_{ini} + t_{prop}$, the failure probability is deemed to be too high to consider that the structural service remains under safe condition. In this specific situation, the failure state corresponds to the formation of crack due to corrosion.

Table IV-4 Propagation times associated to each XC classes for different concrete electrical resistivity values [323].

	t_{prop} (years)			
Saturated resistivity (Ohm.m)	XC1	XC2	XC3	XC4
< 100	45 – 90	10	20	5
100 – 175	45 – 90	15	25	20
> 175	45 - 90	20	30	30

Table IV-5 Propagation time associated to each XS/XD exposure classes [323].

Class	XS1	XS2	XS3e	XS3m	XD1	XD2	XD3f	XD3tf
t_{prop} (years)	10	30	2	2	15	5	5	5

It should be noted that the values in Table IV-4 and Table IV-5 are based on specific on-site and laboratory measurements conducted on regular concrete materials commonly used in the construction sector. It is important to update these values, especially for concrete with low or very low clinker content. One potential approach could be to update these values based on electrical resistivity, using a more precise relationship than the values provided in Table IV-4. Additionally, the saturation level of the material and the access of oxygen to the reinforcing bar are crucial factors relatively to corrosion propagation. Therefore, it may be more effective to modify the propagation time value based on the average relative humidity instead of relying on exposure classes. However, it should be noted that the PerfDuB project is a recognized reference in the field of reinforced concrete durability and can serve as a stable foundation for this study.

The time(s) of inspection(s): For structures already in service, inspections may already have been carried out. If measurements are available, it is possible to use them for verifying and/or updating deterministic and/or probabilistic computations.

The time(s) of repair(s) and maintenance(s): These times ideally result from the developed tool. They have to be defined with respect to a triggering criterion and in accordance with the structural manager / owner. The criterion for triggering a repair (for example replacement of the concrete cover) may, for instance, correspond to exceeding a certain proportion of the surface area (of a part) of the structure for which the probability of corrosion initiation of the first bed of passive reinforcement reaches a certain threshold.

IV.3.2. Literature models

This section is dedicated to the examination of the empirical models available in the literature, sometimes altered, providing as output the input parameters of durability models (carbonation, chloride ingress, corrosion), and using input data furnished by the user. The quantities estimated by these empirical models may be erroneous at some extent. The goal is to identify the relevant context of their use to ensure their convenience in the tool and assess their strength and weakness.

Different methods are available to perform this work:

- It is first possible to use the initial literature reference to define the application field. Quasi-systematically, authors give information about the fitting data, and the initial goal of the model. This information is useful to define a first application range, with variability range for the input data.
- As part of this work, a database of experimental results was established from a literature review. The detail of this database is given in Section IV.3.3. It contains 1673 data sets on different properties originating from over 57 works at the time of writing, comprising both input and output data corresponding to empirical models. This data has hence been used on the one hand, to check some models in the domain defined by their authors, and on the other hand to possibly enlarge the application domain. This way, Schmitt showed that the porosity model developed by Powers [282], initially defined for CEM I-based materials, could be extended to filler and slag based concrete up to 45 wt.% of binder [6]. More globally, the database has also served to statistically characterize the uncertainties associated to the empirical models.
- Finally, a sensitivity analysis, such as the Morris method, may additionally help in this process by emphasizing the influence of the input data. For instance, if the sensitivity analysis shows that certain input data has a low impact on the output, it would indicate that extending the application range for this input could be done while likely avoiding a significant increase of the uncertainty. Conversely, it can be noted that input bearing strong sensitivity must be more strictly bounded.

The three described methods were applied to the selected empirical models. The final variation ranges defined are presented in Annex 3.

IV.3.2.1. Mechanical resistance computation

The model selected to obtain the 28-day compressive strength was initially proposed by Papadakis [278] for CEM I-based mixes and is detailed in Section I.4.5.1. The 5 input parameters are described in Annex 3, along with the variation ranges used for the sensitivity analysis. The density of water is considered constant and equal to 981 kg/m^3. In the Equation I.104, only the cement content is considered. For practical reason, this parameter is replaced by the total binder content if concrete is formulated with mineral addition. In Equation IV.1 the bulk density of cement is in the same way replaced by the bulk density of binder ρ_B:

$$f_c = 7.84 \frac{f_{cem}}{\left(1 + \frac{W_{eff}}{B}\frac{\rho_B}{\rho_w} + \varepsilon_{air}\frac{\rho_B}{B}\right)^2} \quad \text{Eq (IV.1)}$$

Because the different mineral additions do not impact the compressive strength the same way, an attempt was made to compute B from a weighted sum of the different constituents using coefficient experimentally fitted. The optimised formula reads:

$$B = (Q_{clinker} + 0.5Q_L + 0.7Q_S + 0.85Q_V + 1.5Q_{Mk} + 1.5Q_D) \quad \text{Eq (IV.2)}$$

164 datasets from the database with the 5 inputs are available and were used to verify Equation IV.1. The results are reported in Table IV-6, where the data are sorted according to the binder type. Another representation of the uncertainty is given in Figure IV-11 as a function of the W_{eff}/B_{tot} ratio for the modified Equation IV.1.

Table IV-6 Average differences between measured and computed values of f_c.

		Initial Equation I.104		Modified Equation IV.1	
Composition	Number of data	MAE (MPa)	MRE (%)	MAE (MPa)	MRE (%)
100% CEM I-based	28	6.2	12.8	7.2	14.8
Clinker + Filler	22	14.1	35.8	5.2	12.0
Clinker + Slag	32	8.2	19.5	10.3	19.4
Clinker + Fly ash	22	13.7	36.0	7.6	17.0
Clinker + Metakaolin	12	4.5	7.4	3.7	5.8
Clinker + Schist	2	14.9	16.1	13.2	14.3
Clinker + Silica fume	6	7.8	11.6	7.9	13.1
Clinker + Quartz	2	15.9	55.1	2.3	8.5
Clinker + Pozzolan	13	12.1	34.1	2.8	8.0
Ternary	25	14.1	29	10.4	18.1
Total	**164**	**10.5**	**24.6**	**7.5**	**14.8**

It can be observed that the modified equation leads to an average error reduction of 9.8 % and of 3 MPa. However, it can be observed that a high mean absolute error remains, specifically for ternary, slag, or schist-based concretes, for which additional verifications should be performed. This is rather a concern as these concrete mixes have become frequent nowadays, and an alternative model should be needed.

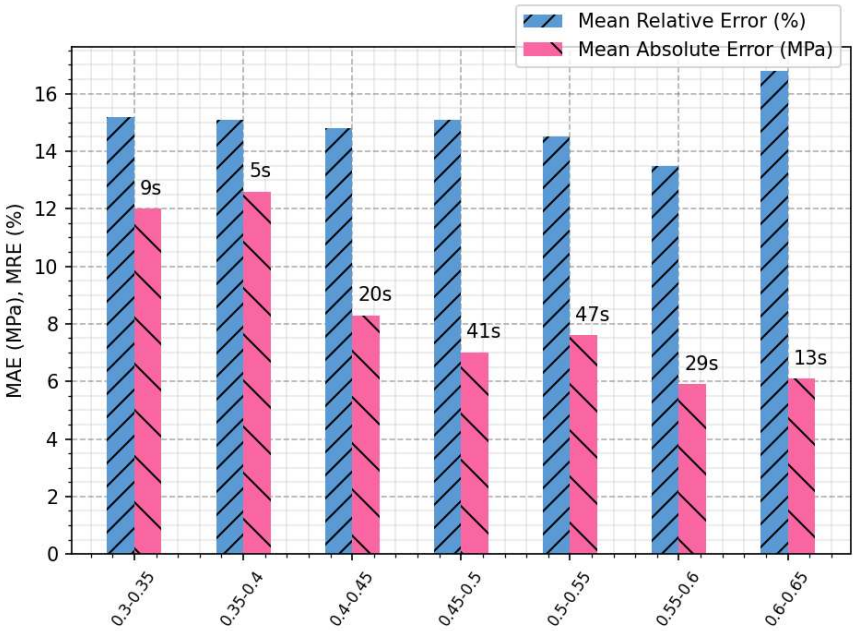

Figure IV-11 MAE and MRE versus W_{eff}/B_{tot} ranges obtained on the 164 results (Xs represents the number of specimens used for the computation).

It can be seen in Figure IV-11 that the mean absolute error decreases with an increase of W_{eff}/B_{tot} ratio. Since the mean relative error remains almost constant, it can be concluded that the drop of MAE is essentially due to the lower value of compressive strength obtained in average for higher water content in the formulation. However, warning should be added to the use of this model concerning W_{eff}/B_{tot} lower than 0.4, especially since only few specimens were available and that the results might not be representative.

The sensitivity analysis results are shown in Annex 3. As a general observation, it can be said that the highest impact is attributed to B_{tot} and W_{eff}. Though less important, the characteristic resistance of

cement f_{cem} also seems to impact significantly the concrete compressive strength. On the other hand, the small sensitivity observed for the air content and bulk density of cement show that their knowledge is less important for the compressive strength computation. Average value of cement bulk density could thus be taken instead of putting efforts in obtaining its precise value for each estimation. Value of ε_{air} could be estimated from the maximal diameter of the aggregates, as done by Papadakis (see Table I.17 in Section I.4.5.1).

IV.3.2.2. Porosity accessible to water models

Three models for computing the porosity accessible to water are compared in this subsection. Two of these models were developed by Papadakis in [289] and [66] and described in Annex 4. The third model, developed by Powers in [282], is detailed in section I.4.5.2.

While the model developed in [289] is specifically designed for silica fume-based concrete, and the model in [66] allows for the computation of paste porosity for silica fume and fly ash-based concrete, Powers' model was originally developed for CEM I-based concrete. However, as previously mentioned, Schmitt [6] validated this model for slag and filler-based concretes, taking into account the binder content rather than the quantity of cement. Therefore, in this section, the same approach is applied to all three models, enabling the computation of porosity for various types of concrete mixes.

The new equations for computing the cement paste porosity accessible to water are presented below as Equations IV.3 to IV.5 for [282], [289] and [66], respectively. In equation IV.4, the term "fly ash" (see Annex 4, [289]) is replaced by the content of pozzolanic and/or latent hydraulic additions, allowing for the consideration of different mineral additions.

$$\phi_0^p = \frac{\frac{W_{eff}}{B}}{\frac{W_{eff}}{B} + 0.32} - 0.53.\alpha.\left(1 - exp\left(-3.3.\frac{W_{eff}}{B}\right) - \frac{\frac{W_{eff}}{B}}{\frac{W_{eff}}{B} + 0.32}\right) \quad \text{Eq (IV.3)}$$

$$\phi = \varepsilon_{air} + \frac{W - 0.227(B - P) - 0.19P}{1000} \quad \text{Eq (IV.4)}$$

$$\phi_0^p = \varepsilon_{air} + \frac{W}{\rho_w} - (0.249(CaO - 0.7SO_3) + 0.191SiO_2 + 1.118Al_2O_3 - 0.357Fe_2O_3)\left(\frac{B}{1000}\right) \quad \text{Eq (IV.5)}$$

In all three cases, the porosity introduced by the aggregates is calculated using the equations specified in Section I.4.5.2, enabling the determination of the average porosity that is accessible to water within the concrete material.

The validation process is conducted on 143 datasets, where all 12 input data values are known. It is important to note that the conservation conditions before conducting the tests are not taken into account. The minimum conservation period for the utilised data is set at 28 days.

Table IV-7 Error obtained with the different models as a function of the concrete mix type.

		Equation IV.3 (Powers, [282])		Equation IV.4 (Papadakis, [289])		Equation IV.5 (Papadakis, [66])	
Composition	Number of data	MAE (%)	MRE (%)	MAE (%)	MRE (%)	MAE (%)	MRE (%)
100% CEM I-based	24	1.41	11.4	4.34	32.7	1.91	14.8
Clinker + Filler	27	0.88	7.0	1.98	14.8	3.06	22.5
Clinker + Slag	27	1.17	9.0	1.89	14.3	2.92	20.4
Clinker + Fly ash	11	1.05	8.6	1.73	12.9	2.47	17.9
Clinker + Metakaolin	13	0.58	4.3	2.03	14.8	2.51	18.7
Clinker + Schist	2	1.83	18.2	1.53	15.2	1.92	19.0
Clinker + Silica fume	3	1.81	13.6	3.31	22.3	1.75	15.2
Clinker + Quartz	2	0.43	2.6	7.12	43.7	1.33	8.2
Clinker + Pozzolan	2	0.24	1.5	4.9	29.7	0.97	5.9
Ternary	32	1.00	6.7	2.06	13.5	3.12	20.9
Total	**143**	**1.05**	**8.1**	**2.50**	**18.0**	**2.66**	**19.1**

The Powers' model appears more accurate for all types of materials, apart from silica fume where the second equation of Papadakis yields a lower mean absolute error. The performance observed in the Powers' model justifies its utilization for both inert and reactive additions unless evidence proves otherwise. Additionally, Figure IV-12 indicates the excellent performance of the Powers model across all ranges of the W_{eff}/B_{tot} ratio. It highlights an optimized error reduction for W_{eff}/B_{tot} values ranging between 0.4 and 0.45.

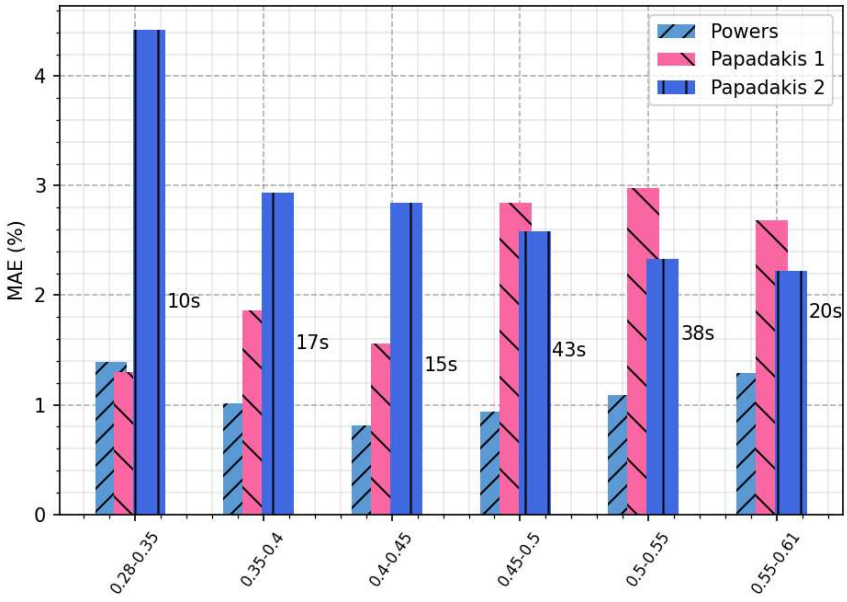

Figure IV-12 MAE versus W_{eff}/B_{tot} ranges obtained on the 143 data for each model (Xs represents the number of specimens used for the computation).

Due to its performance the sensitivity analysis presented in this section only refers to Powers' model. The sensitivity analyses carried out on the two other models can be found in Annex 3, as well as the variation ranges selected for the different parameters.

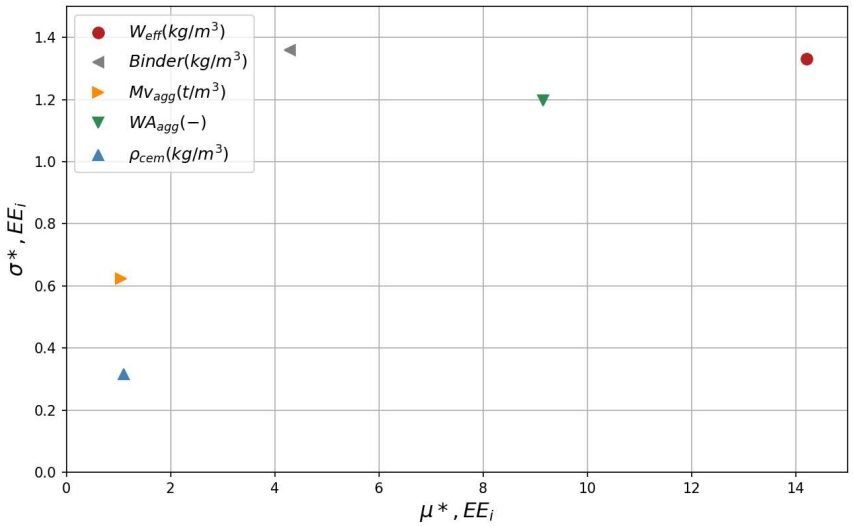

Figure IV-13 Results of the sensitivity analysis performed with the Morris method on the Powers' model for porosity accessible to water.

The porosity of the material is primarily influenced by the effective water content W_{eff} within the studied ranges. Additionally, the properties of the aggregates, including water absorption W_{agg}, have a significant impact on the results, followed by the binder content. The other parameters present a lower participation to the global sensitivity.

IV.3.2.3. Hydration models

One of the objectives of the tool is to enable predictions on concretes formulated with pozzolanic additions. One of the aspects to consider is the impact of the pozzolanic reaction on the content of portlandite and other hydrates. Therefore, it is crucial to assess the hydration models implemented, based on experimental measurements, and improve their accuracy for low-carbon concrete mixes. In this section, different methods for computing the portlandite content are compared.

First, the equation detailed in [109], which was originally developed for SF and CEM I-based paste, is used. Second, the equations detailed in [289] are also used for the sake of comparison. These equations were initially constructed for fly ash and silica fume-based concretes. Finally, the model of Kolani and Lacarrière [286], which is designed for regular Portland cement-based concrete, is used for estimating the portlandite content.

The interest in developing a unified tool during this Ph.D. led to a modification of the work of Kolani and Lacarrière. This modification assumes that the latent hydraulic and pozzolanic reactions occur in similar ways. Therefore, the same set of equations can be used for all reactive mineral additions with the application of a multiplication factor that depends on the type of addition. This unique modification led to the definition of Equations IV.6 and IV.7 for the computations of "equivalent pozzolanic" ($Q_{SCM_{eq}}$) and "equivalent clinker" ($Q_{K_{eq}}$) respectively.

$$Q_{SCM_{eq}} = Q_S + 1.2Q_V + 1.5Q_M + 3Q_{SF} + 2Q_P \quad \text{Eq (IV.6)}$$

$$Q_{K_{eq}} = Q_K - (0.2Q_V + 0.5Q_M + 2Q_{SF} + 1Q_P) \quad \text{Eq (IV.7)}$$

Table IV-8 Results of portlandite content estimation with the different equations and model, classified according to the binder type.

		Equation A.52 (AFGC, [109])		Equation A.53-A.58 (Papadakis, [289])		Section I.4.5.3 (Lacarrière and Kolani, [286])	
Composition	Number of data	MAE (%)	MRE (%)	MAE (%)	MRE (%)	MAE (%)	MRE (%)
100% CEM I-based	19	0.63	14.4	0.87	20.6	0.21	5.03
Clinker + Filler	12	0.49	17.7	1.28	49.0	0.65	26.8
Clinker + Slag	5	1.37	116	2.33	214	0.65	39.4
Clinker + Fly ash	20	1.86	68.1	1.74	75.0	1.09	31.6
Clinker + Metakaolin	12	1.44	76.3	2.37	140	0.64	33.5
Clinker + Silica fume	1	0.07	6.0	1.11	96.0	0.21	18.4
Clinker + Pozzolan	9	2.04	179	4.30	406	0.53	32.5
Ternary	12	1.11	75.6	1.74	126	0.49	28.1
Total	**90**	**1.23**	**65.2**	**1.86**	**117**	**0.62**	**25.5**

The obtained results demonstrate that the model of Lacarrière and Kolani exhibits a higher overall performance compared to the other two equations. Additionally, except for silica-fume and filler-based materials where the AFGC equation provides better results, the model of Lacarrière and Kolani shows the highest performance. Therefore, the latter model will be integrated into the final tool. In a subsequent step, the AFGC equation could be utilised for cross-validation when silica-fume and filler are employed. It is worth noting that considering the knowledge and inclusion of oxide compositions in the computations may enhance precision in the estimation. For instance, this study does not differentiate between low-calcium and high-calcium fly ash, despite their significant impact on hydration [289].

The results of the Morris sensitivity analysis are presented in Figure IV-14 and Figure IV-15. The variation ranges utilised for the different parameters are described in Annex 3.

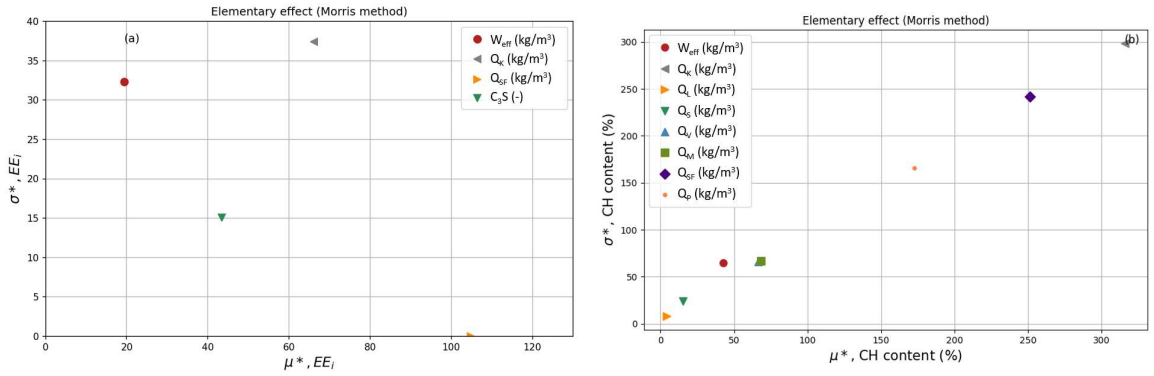

Figure IV-14 Morris's sensitivity analyses performed on the equation of the AFGC for portlandite content computation (a) and the hydration model of Lacarrière and Kolani with the integration of Equations IV.6 and IV.7 (b).

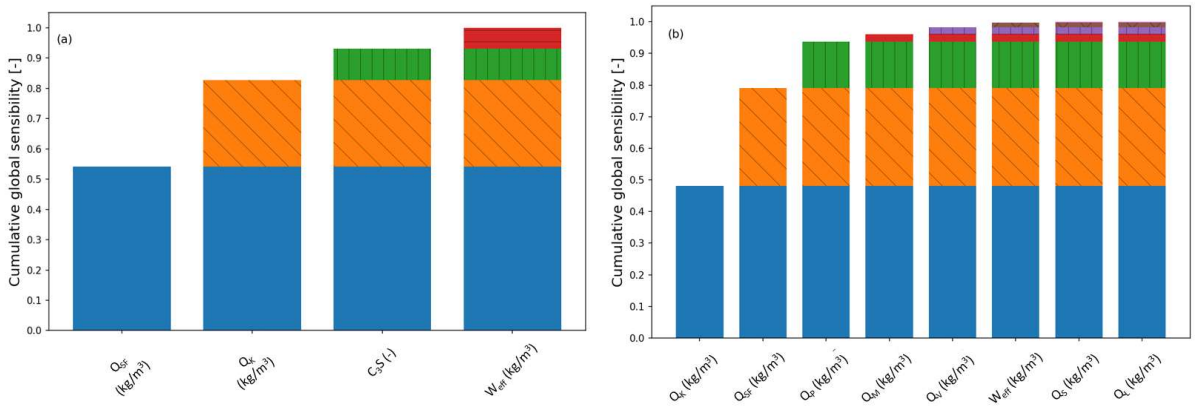

Figure IV-15 Cumulative sensitivity (Morris) obtained for the AFGC equation used for CH estimation (a) and the hydration model Lacarrière and Kolani with the integration of Equations IV.6 and IV.7 (b).

The results obtained on the AFGC equation show a high influence of the binder constituents, especially the Silica-fume. The influence of C_3S and effective water content, although lower, remains important in this model. Concerning the modified model of Lacarrière and Kolani, the clinker possesses the highest influence, followed by the Silica fume, which is close to the results obtained for the AFGC equation. Additionally, pozzolan demonstrates significant influence, whereas the remaining parameters have lesser impact on the results, according to the sensitivity analysis. It is crucial to bear in mind that the results of the sensitivity analysis are applicable only to the given variations presented in Annex 3, and that independent variations of different parameters need to be considered. The inclusion of co-dependency could yield more precise analyses in such cases.

IV.3.2.4. Ageing factor

The formula referenced in the FD P18-480 (2022) serves as the foundation for calculating the chloride ageing factor. This equation, provided in Section II.3.7, is utilised to predict the improvement factor of the chloride diffusion coefficient. Originally developed for mixtures that include clinker, slag, fly ash, silica fume, and/or metakaolin, it was determined that the formula does not account for the influence of the water-to-binder (W/B) ratio. Consequently, a modification was introduced based on data obtained from the HETEC report [152]. The collected data was analysed to establish Equation IV.8 that expresses the relationship between the W/B ratio and the reduction in the diffusion coefficient. Additionally, the impact of filler materials was incorporated into the equation, following a similar approach to the previous additions, and the equation's coefficients were adjusted using available experimental data. The finalized formula is presented in Equation IV.9.

$$k_{ae,W/B} = 0.709\left(W_{eff}/B_{tot}\right)^{-0.52} \quad \text{Eq (IV.8)}$$

$$ae = (0.22 - 0.148F_{\mathrm{L}} + min(0.75F_S; 0.35) + min(1.46F_V; 0.35) + min(1.1F_{SF}; 0.1))k_{ae,W/B} \quad \text{Eq (IV.9)}$$

The original and modified equations were tested against a dataset consisting of 93 experimental values. The results are presented in Table IV-9. The experimental ageing factors were computed using the Equation II.8 described in detail in Section II.3.7, where the diffusion coefficient D_{rcm} obtained from accelerated migration tests was used. Typically, the ageing factors should be computed using the apparent diffusion coefficients D_{app}. Hence, considering D_{rcm} certainly leads to additional discrepancies, which might explain why metakaolin was found to have no impact on ae.

Table IV-9 Results obtained with the two equations according to the mix type.

		Original Equation II.7 (FD P 18-480 (2022))		Modified Equation IV.9	
Composition	Number of data	MAE (-)	MRE (%)	MAE (-)	MRE (%)
100% CEM I-based	28	0.10	59	0.07	36
Clinker + Filler	14	0.14	142	0.10	91
Clinker + Slag	12	0.25	240	0.22	251
Clinker + Fly ash	21	0.11	18	0.08	13
Clinker + Metakaolin	5	0.19	173	0.08	77
Clinker + Schist	1	0.65	68	0.001	0.1
Clinker + Quartz	1	0.03	10	0.008	2.3
Ternary	11	0.23	55	0.17	50
Total	**93**	**0.15**	**91**	**0.11**	**70**

Compared to the previous version, the altered model improves slightly the accuracy as a small reduction is globally observed, of 0.04 for the mean absolute error (MAE) and of 21% for the relative error (MRE). Importantly, the reduction occurs for all compositions when using the new equations.

The use of accelerated migration coefficients instead of apparent diffusion coefficients was somehow a trick in the verification process. However, it did not impact the accuracy of the altered model. Hence, both models are proposed in the tool, with a recommendation to employ the original equation for calculations since it was based on D_{app} values, certainly closer to structures' properties.

Further improvements to better assess the ageing factor are still needed. Firstly, the consideration of the water-to-binder (W/B) ratio should be adjusted for each constituent, as each mineral addition may have a different impact. Additionally, not only the relative composition should be taken into account, but also the binder content.

Sensitivity analyses using the Morris method were conducted for both versions of the equation, considering the boundaries of input data outlined in Annex 3.

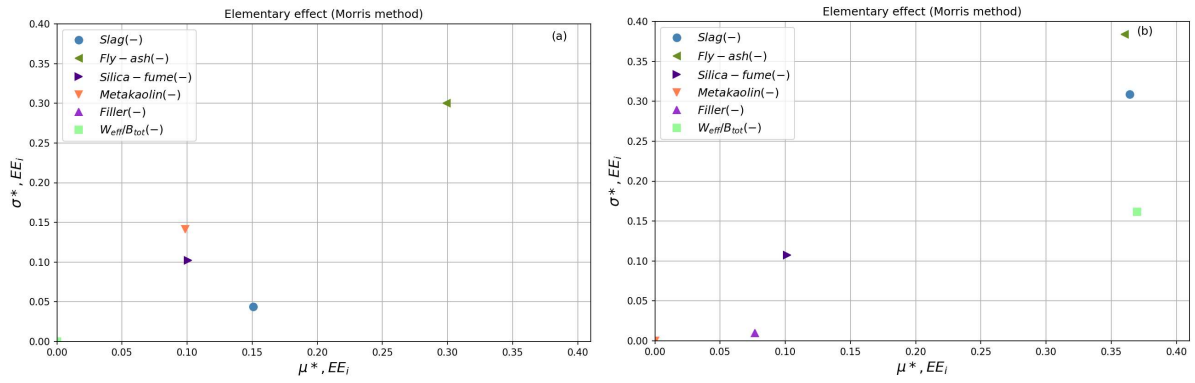

Figure IV-16 Results of the Morris sensitivity analyses on the original (b) and modified (a) equations for the ageing factor computation.

As expected by the weight associated to each mineral addition, a different order of influence is shown when comparing the two equations. First, the importance associated to slag is higher in the new Equation IV.9 than in the initial one. Second, the impact of the ratio W_{eff}/B_{tot} is categorized as important in the modified equation, highlighting the fact that this parameter should certainly be considered to accurate the ageing factor. The influence of filler is relatively low, certainly because a low coefficient (in absolute) of - 0.148 associated in Equation IV.9, in comparison with the other mineral additions considered.

IV.3.2.5. Conclusion

The results obtained in the previous sections help to define the capabilities of each empirical model. The objective is to assist the user of the tool in comprehending the limitations of each model, rather than prohibiting its use, and drawing attention to uncertainties affecting the output. These uncertainties lead to the standard deviation used within the context of the probabilistic approach. It is deemed that a model is acceptable for a specific application if the mean relative error (MRE) obtained (on a minimum of 5 specimens) is less than 40%.

Table IV-10 Overview of the analytical models for concrete properties determination.

Model	Modified Equation IV.9 for ageing factor [340]	Original Equation II.7 for ageing factor [340]	AFGC equation for CH content [109]	Hydration model with Equations IV.6 and IV.7 [286]	Model for porosity accessible to water [282]	Modified Equation IV.1 for mechanical resistance [278]
CEM I-based	Yes	Yes*	Yes	Yes	Yes	Yes
Filler-based	No	Yes*	Up to 30%	Up to 30%	Up to 40%	Up to 40%
Slag-based	No	Yes*	No	Up to 70%	Up to 70%	Up to 70%
Fly ash-based	Up to 50%	Up to 50%	No	Up to 50%	Up to 70%	Up to 70%
Silica-fume-based	No	No	?	?	?	Up to 15%
Metakaolin-based	No	Yes*	No	Up to 25%	Up to 25%	Up to 25%
Schist-based	No	No	?	?	?	?
Quartz-based	No	No	?	?	?	?
Ternary binder	No	Yes*	No	Yes	Yes	Yes
Min $\boldsymbol{W_{eff}/B_{tot}}$	0.4	0.45*	0.33	0.33	0.28	0.27
Max $\boldsymbol{W_{eff}/B_{tot}}$	0.59	0.55*	0.6	0.6	0.61	0.66
Min age	-	-	90	90	28	28
Max age	-	-	-	-	-	-
MAE on validated ranges	0.07	0.11	0.58	0.62	1.05	7.5
MRE on validated ranges	26	18	15.68	25.5	8.1	14.8
Most influent parameters (Account for more than 90% of the sensitivity)	$F_V, F_S, W_{eff}/B_{tot}$	F_V, F_M, F_S	Q_{SF}, Q_K, C_3S	Q_K, Q_{SF}, Q_P	W_{eff}, WA_{agg}	$f_{cem}, W_{eff}, Q_K, \varepsilon_{air}, Q_S, Q_V$
Less influent parameters	F_{SF}, F_L, F_M	$F_{SF}, F_L, W_{eff}/B_{tot}$	W_{eff}	$Q_M, Q_V, W_{eff}, Q_S, Q_L$	C, Mv_{agg}, ρ_{cem}	$Qz, \rho_{cem}, Q_L, Q_M, Q_{SF}, Q_D, Q_P$

*Validation performed by the initial author and not verified in this Ph.D.

IV.3.3. Experimental results database

In this study, a database of experimental results for various quantities (concrete formulation parameters, physical properties, etc.) needed as input parameters for durability models was built. The primary objective of building the database was, in the previous section, to verify and improve the empirical models providing the input parameters when all are not available by the user and must be derived from a limited input data. The second objective was to propose alternative learning models adequately using the available data. Two types of learning models, namely Polynomial Regression (PR) and Artificial Neural Network (ANN) were employed for this purpose. After completing the training and validation phases, the models obtained can estimate the needed quantities when provided with the required input data. It should be noted that a proper and accurate estimation requires a relatively large

amount of data for training and validation. The models are hence more efficient for well-studied types of concrete. For example, concretes formulated with slag, fly ash, and filler are in the scope of such models. However, for non-classical concretes like recent SCM-based ones, scarce data is a pitfall, and learning models fail to give relevant estimation.

For such a situation, it can be more attractive to search for a similar concrete formulation in the database. This was the purpose of a browsing technique developed in this Ph.D. work. It primarily involves quantifying the distance between a concrete formulation provided by the user and those present in the database, and then to define a similarity criterion. The technique covers de facto the usual concrete formulations.

Apart from utilizing the database for determining input parameters of durability models, further analysis was carried out to outline some trends, as discussed in subsection IV.3.3.3.

The database summary is presented in Annex 2, comprising of 1673 concrete mixes obtained from 57 references.

Computing some statistics reveals that most concrete mixes comprise clinker, slag, and fly ash. Other mineral additions have a smaller presence in this database, making it challenging to incorporate them into the development of learning-based models, for instance. This is why, in the subsequent section IV.3.3.1, certain datasets were omitted.

IV.3.3.1. Learning-based models

Polynomial regression and Artificial Neural Network were selected. They benefit from a wide usage within scientific research and the availability of open-source programming such as the Scikit-learn and Keras modules [315], [316].

The model validation is conducted using 25% of the experimental results database. A sensitivity analysis was performed using the Morris method, with 500 trajectories being employed, based on the same variation ranges utilised for the training phase. Main results regarding the validation and sensitivity analysis are reported in Annex 3.

The input data underwent standardization (regular normalisation) prior to their utilization in the models' creation and validation processes. It basically consists in subtracting the mean value et dividing by the standard deviation.

To appropriately account for the conservation of the sample prior to testing, the parameter $Cure$, resulting from an empirical process after several attempts, has been added as input data, as function of the temperature and moisture conditions:

$$Cure = \min\left(\max\left(0, \frac{\log(T_{cure})}{\log(20)}\right), 1.5\right)\left(\frac{RH_{cure}}{100}\right)^2\left(\frac{Age}{90}\right)^{0.25} \quad \text{Eq (IV.10)}$$

IV.3.3.1.1. Compressive strength f_c

Only concretes made exclusively with clinker, slag, and fly-ash were extracted from the database and considered in the learning-based models. 1594 datasets were used, out of which 75% (1196 datasets) were allocated for training purposes, while the remaining 25% (398 datasets) were reserved for validation.

The Artificial Neural Network model (ANN-CS) was constructed with settings as shown in Table IV-11, after an optimized iterative process aiming at minimizing the Mean Absolute Error (MAE) and Mean Relative Error (MRE). It should be noted that alternative configurations may exist, which could potentially yield superior outcomes.

Table IV-11 Setting of ANN-CS model.

Parameter	Hidden layer number	Maximal number of neurons	Decrease value of neuron	Loss	Validation split	Epochs	Activation function
Value	6	100	10	MSE	0.025	250	relu

The determination coefficients were 0.96 in the validation phase and 0.88 in the training phase. Mean Absolute Error (MAE) and Mean Relative Error (MRE) were 4.07 MPa and 10.43%, respectively, using the validation segment of the database.

Regarding the polynomial regression model (PR-CS), a maximal order of 2 was employed. The training and validation were conducted using the same distribution of the database, with 75% allocated for training and 25% for validation. The determination coefficients were 0.87 and 0.84 for the training and validation sets, respectively. Additionally, the validation database exhibited a mean absolute error (MAE) of 5.26 MPa and a mean relative error (MRE) of 14.02%. Both models provide an acceptable estimation of compressive strength and are therefore incorporated in the tool.

The results of the sensitivity analysis reveal a significant disparity between the two models, which can be attributed to their inherent differences. The influence is rather fairly shared among input data for ANN-CS compared to PR-CS. For both models W_{eff}/B_{tot} has the strongest impact on f_c, but they differ in their classification of the remaining input data. In ANN-CS, the characteristic strength of the cement is considered the second most influential factor, whereas the polynomial regression model disregards its significance. This discrepancy may suggest precarious behaviour in PR-CS. Due to the extensive distribution of influence in ANN-CS, it becomes challenging to identify non-influential parameters, with the exceptions of the slag content (Q_S), curing temperature (T_{cure}), and curing parameter ($Cure$). In contrast, the polynomial regression model indicates that the binder (consisting of $Q_{clinker}$, Q_S, and Q_V) and the effective water content (W_{eff}) exert the most influence. Additionally, PR-CS implies that the content and quality of the aggregates have a diminished impact compared to ANN-CS.

IV.3.3.1.2. Carbonation depth

This subsection investigates the determination of the carbonation depth using the artificial neural network model (ANN-CD). Polynomial regression was disregarded because less efficient.

Two ANN models are developed. The first model (ANN-CD1) is used to determine carbonation depth in natural conditions, while the second model (ANN-CD2) predicts carbonation depth in both natural and accelerated conditions. Furthermore, these models are utilised to calculate the carbonation rate (represented as K, mm.years-1 or mm.days-1 in natural and accelerated conditions respectively) under specific conditions. The calculation is based on the usual relationship:

$$Xc = K\sqrt{t} \qquad \text{Eq (IV.11)}$$

Two additional parameters were calculated to account for the sample preconditioning ($Precond$) and carbonation conditions ($Carbonation$), as represented by Equations IV.12 and IV.13. These functions were determined from an empirical process after several attempts. For the preconditioning function, it was assumed additionally that a 14-days preconditioning period leads to an almost moisture equilibrium. It is also assumed that a relative humidity of 60% during the preconditioning and during the carbonation process promotes maximum carbonation [92].

$$Precond = \mathrm{T}_{\mathrm{precond}}\left(-3.5\times10^{-6}RH_{precond}^{3} + 2\times10^{-4}RH_{precond}^{2} + 0.0153RH_{precond} + 0.1\right).\min\left(1.2, \left(\frac{t_{precond}}{14}\right)^{0.4}\right) \qquad \text{Eq (IV.12)}$$

$$Carbonation = T_{carbo}\left(-3.5 \times 10^{-6} RH_{carbo}^{3} + 2 \times 10^{-4} RH_{carbo}^{2} + 0.0153 RH_{carbo} + 0.1\right) P_{CO_2} \sqrt{t_{carbo}} \quad \text{Eq (IV.13)}$$

A total of 998 datasets were utilised for both training (75%, 749 datasets) and validation (25%, 249 datasets) of ANN-CD1. The distribution and statistical values of the database used are presented in Annex 3.

The optimal configuration of ANN-CD1 is presented in Table IV-12. The training and validation stages resulted in determination coefficients of 0.98 and 0.82, respectively. These coefficients indicate an overfitting of the model. However, the mean absolute error (MAE) and mean relative error (MRE) obtained during the validation phase, which were determined to be 1.03 and 20.62%, respectively, remain still satisfactory.

Table IV-12 Setting of ANN-CD1 and ANN-CD2.

Parameter	Hidden layer number	Maximal number of neurons	Decrease value of neuron	Loss	Validation split	Epochs	Activation function
Value	5	100	10	MSE	0.05	150	relu

ANN-CD2 was built using a total of 1727 datasets with the same settings as ANN-CD1. The training and validation phases resulted in determination coefficients of 0.98 and 0.88, respectively. During the validation stage, the model exhibited a MAE of 1.9 mm and a MRE of 25.49%. It is important to note that ANN-CD2 demonstrated lower efficiency compared to ANN-CD1. Nevertheless, it displayed remarkable capabilities in estimating carbonation depth under accelerated condition, particularly in the scenario presented earlier in Section II.3.5 corresponding to the recommendations of the XP P18-458 (2022). Consequently, these findings enable the determination of the durability indicator for the FD P18-480 (2022).

A sensitivity analysis is performed on both models using the method of Morris. The results are displayed in Annex 3. The parameters computed with Equations IV.10, IV.12 and IV.13 are left out of the analysis (using variation of 0). The variation used for the different input parameters are the minimal and maximal values displayed in Annex 3, covering the data ranges used for the models' construction.

The sensitivity analysis, despite some change of the parameters ranking, demonstrates a consistent trend. This outcome was expected, as both models were developed based on similar databases, with the second model considering wider ranges of conditions (accelerated carbonation). The analysis reveals that the most influential parameters are the composition (including parameters like $Q_{clinker}, Q_S, Q_V, W_{eff}$ and W_{eff}/B_{tot}), carbonation conditions (RH_{carbo} and $Time$ as well as $CO2_{carbo}$ for the second model) and conservation conditions (primarily the Age and RH_{cure}). While the content and types of aggregate, as well as the preconditioning conditions, have a relatively lower influence, the nature of the ANN-based models results in a significant distribution of influence observed across the parameters.

IV.3.3.1.3. Electrical resistivity

The lack of analytical models in the literature has led to propose the ANN model ANN-ER1. In addition to slag, fly ash, and clinker, ANN-ER also considers metakaolin and filler. The training set comprises 270 datasets (75% of the data), while the remaining 90 datasets (25%) are used for validation. There is a scarce amount of data available of electrical resistivity compared to carbonation depth and mechanical resistance. This discrepancy likely contributes to the lower accuracy level of ANN-ER1.

The determination coefficients equal to 0.98 and 0.93 for training and validation, respectively, indicate an over-fitting of the model, likely resulting from the limited amount of data available. The predictions

from the model on the validation datasets yielded a MAE of 39.2 Ohm.m and an MRE of 19.3%. These results suggest that the model is somehow poorly accurate. However, due to lack of consistent model elsewhere, ANN-ER1 is the best option available for now.

Table IV-13 Setting of ANN-ER1.

Parameter	Hidden layer number	Maximal number of neurons	Decrease value of neuron	Loss	Validation split	Epochs	Activation function
Value	6	100	10	MSE	0.05	200	relu

A second model ANN-ER2 is developed considering electrical resistivity values below 200 Ohm.m, which may improve the accuracy. The threshold value of 200 Ohm.m is chosen based on the distribution of available data (refer to Annex 3) and the threshold values recommended in the FD P 18-480 for XC exposure classes (100 and 175 Ohm.m, as mentioned in Section I.6.3). The objective is to focus on concretes presenting a rather low electrical resistivity for which differentiation between concrete mixes is critical for durability purpose.

ANN-ER2 is trained on the remaining 252 data points. The same distribution is used, resulting in 189 datasets for training and 63 datasets for validation. The range of variation in the database is presented in Annex 3.

The determination coefficients obtained are now equal to 0.92 and 0.61 for training and validation, respectively, hence lower than the values obtained for ANN-ER1. Similarly, the MAE and MRE values obtained on the validation datasets are 15.79 Ohm.m and 15.0%, which is satisfying for the application of this model.

The results of the sensitivity analysis performed on both models revealed a high influence of the parameters relative to the binder composition and the conservation conditions before testing (except for the temperature). The aggregate type and content have a lower influence on the results. It can be pointed out that higher results could have been expected for the effective water or W_{eff}/B_{tot} ratio.

IV.3.3.1.4. Conclusion

The determination coefficients together with the emphasized influential parameters from the sensitivity analyses conducted allowed to define and make the user aware of the limitations and potential errors in using the proposed ANN-based models, which are often considered black-boxes with mathematical parameters that are difficult to relate to physical meanings. To finally assist the user, Table IV-14 presents the limitations of each model and provides recommended application ranges.

Table IV-14 Overview of the learning-based models for concrete properties determination.

Model	ANN-ER2	ANN-ER1	ANN-CD2	ANN-CD1	PR-CS	ANN-CS
CEM I-based	Yes	Yes	Yes	Yes	Yes	Yes
Filler-based	Up to 40%	Up to 40%	Up to 35%	No	No	No
Slag-based	Up to 70%	Up to 70%	Up to 80%	Up to 80%	Up to 80%	Up to 80%
Fly ash-based	Up to 65%	Up to 70%	Up to 80%	Up to 80%	Up to 70%	Up to 70%
Metakaolin-based	Up to 20%	Up to 20%	No	No	No	No
Ternary binder	Filler, slag, fly ash and metakaolin	Filler, slag, fly ash and metakaolin	Filler, slag and fly-ash	Slag and fly-ash	Slag and fly-ash	Slag and fly-ash
Min $\boldsymbol{W_{eff}/B_{tot}}$	0.3	0.3	0.3	0.35	0.3	0.3
Max $\boldsymbol{W_{eff}/B_{tot}}$	0.55	0.55	0.65	0.65	0.8	0.8
Min age	28	28	1	1	7	7
Max age	90	90	365	365	365	365
Determination coefficient on validation	0.61	0.93	0.88	0.82	0.84	0.88
MAE on validated ranges	15.79	39.2	1.9	1.03	5.26	4.07
MRE on validated ranges (%)	15.0	19.3	25.5	20.6	14.0	10.4

An examination of the database reveals a lack of sufficient data on specific mineral additions, which raises concerns regarding the effectiveness of particular models. The limited availability of information regarding these minerals compromises the reliability of the chosen modelling methodology and is specified using a red font in the precedent table.

IV.3.3.2. Closest Formulations Selection Algorithm (CFSA)

The algorithm presented in this section enables a straightforward search within the database for a fair correspondence with a mix submitted by the user of the tool. The corresponding properties identified can be utilised as input for durability models or as a means of comparison with data acquired from other models or methods. This section solely elucidates the functionality of the algorithm, while the application in practical scenarios is discussed in Section IV.4.

The Closest Formulations Selection Algorithm (CFSA) operates by calculating the difference in composition between a mix provided by the user and the mixes in the database, where the desired property is known. This computation, denoted as (δ_{P,k_1,k_2}) involves a weighted sum of the relative differences in the composition parameters $C_{i,k}$, as expressed by Equation IV.14 for two mixes k_1 and k_2.The purpose of this calculation is to estimate the value of parameter P for the mix k_1.

$$\delta_{P,k_1,k_2} = \sum_{i=0}^{n} W_{P,i}\left(\frac{\left|C_{i,k_1} - C_{i,k_2}\right|}{C_{i,k_1}}\right) \qquad \text{Eq (IV.14)}$$

Where $W_{P,i}$ is the weight associated to the parameter P and to the i^{th} composition parameter C_i. A total of n composition parameters is considered, which depends on the parameter P to determine.

Due to limitations, it was not possible within the scope of this study to validate further the values assigned to $W_{p,i}$. Consequently, the weights are assumed to hold a constant value of $1/n_{parameters}$ for the next calculations, where $n_{parameters}$ denotes the number of composition parameters utilised during the search process. The methodology is however described to enable future improvements.

The utilization of a weighted sum that varies depending on the property (microstructural, mechanical, or durability) can be explained by the varying influence associated with each composition parameter on the output. For instance, it was demonstrated in Section IV.3.2.2 that the Powers' model has the capability to accurately calculate the water-accessible porosity of almost any type of binder by considering the binder content, effective water content, aggregate properties (water absorption and bulk density), and cement bulk density. The sensitivity (Figure IV-13) revealed that among these five parameters, the most influential factors were the effective water content, water absorption of aggregates, and binder content. This analysis suggests that the impact of aggregate and cement bulk density can be considered less significant for usual materials. Consequently, the influence of different composition parameters varies according to their type, which justifies the necessity of employing different weights.

However, the coefficients obtained from sensitivity analyses of the different models cannot be utilised because they could introduce a bias by the nature of the models. Therefore, the application domains of the CFSA differ from those of the models and derive from a Principal Component Analysis (PCA) performed onto the database (after the data has been centred and standardized). PCA, as detailed in Annex 4, allows do define new variables known as Principal Components (PCs). Although the PCs are vectors that can be expressed in terms of the initial parameters, they only hold mathematical significance. Each PC (denoted as PC_i) is associated with an eigen-value ($Eigen_{PC_i}$), which indicates its representativeness or explained variation. The sum of all the eigen-values is equal to 1. The higher the eigen-value, the more representative the PC is in the specific database. Therefore, only the first PCs are of interest for further analysis. In this study, the PCs were selected based on the eigen-value and must satisfy Inequation IV.15. Thus, only the PCs with greater influence than each individual initial parameter of the database were considered.

$$Eigen_{PC_i} > \left(\frac{1}{n_{parameters}}\right) \quad \text{Eq (IV.15)}$$

Weights can only be calculated for variables when enough data is available. Therefore, in this study, it was only possible to compute weights for four experimental parameters: D_{rcm}, Re, fc and φ_c^w.

The case of porosity accessible to water is taken as an example in this section. An ACP is carried out on the database, which includes the composition parameters and porosity accessible to water (comprising 143 sets of values). Figure IV-17 shows the coordinates of the three principal components (PCs) with the highest eigenvalues, complying with the criterion expressed in Equation IV.15. The absolute values of these coordinates are utilised since the sign is not relevant in this context.

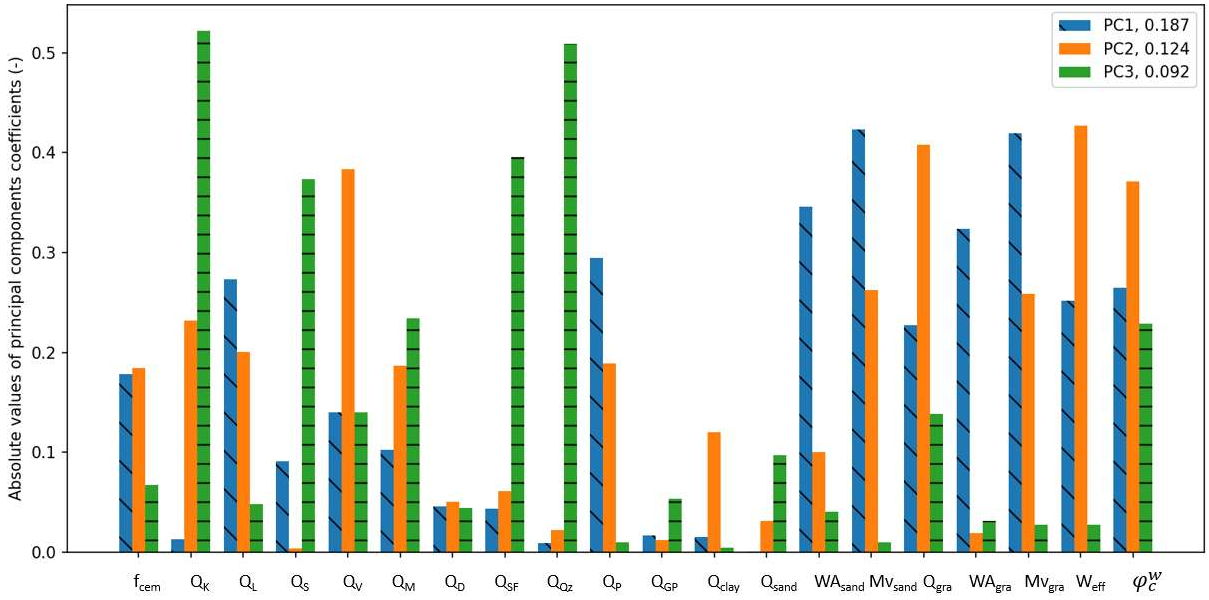

Figure IV-17 Representation of the principal components with highest explained variations obtained on the database with porosity.

A second filter is now defined to select the PCs presenting a sufficiently high coordinate for the quantity of interest (φ_c^w in this example), greater than a prescribed threshold, such as 0.2. The selected PCs remain the same in that case. Finally, for each selected PC after the second filter, a third filter is applied to eliminate parameters that do not display a strong role regarding the PC. This filter is set at a threshold value of 0.15 (chosen arbitrarily), as depicted in Figure IV-18 for the first PC. In this example, it leads to the elimination of 10 parameters considered negligible.

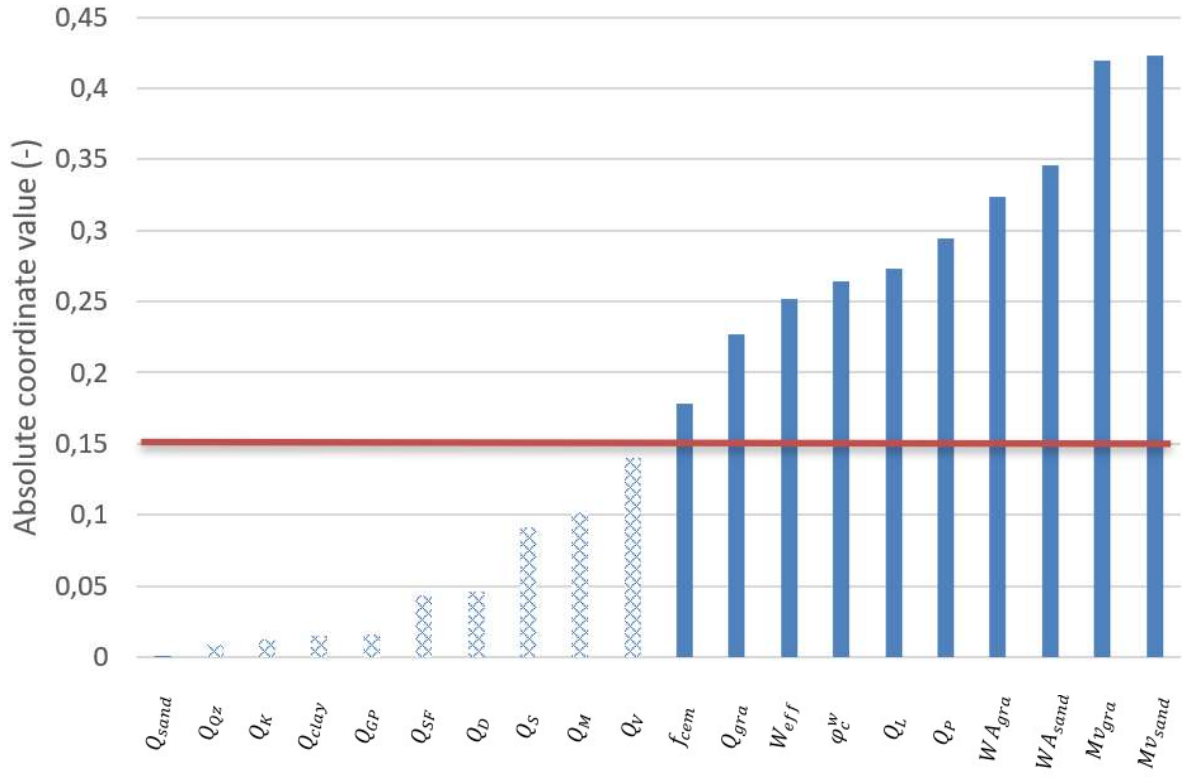

Figure IV-18 Absolute coordinates' values associated to the different parameters for the first principal component eigen-value of 0.187) obtained with the ACP on the database for the porosity accessible to water.

The remaining values, as shown in Figure IV-18 for porosity accessible to water, are utilised to determine the weights. The different principal components (PCs) selected are used, following Equation IV.16, where $Eigen_{PC_i}$ is the eigenvalue and C_{exp,PC_i} is the coordinate value associated with the experimental data considered. The coordinate representing the researched parameter is excluded.

$$W_{eig,PC_i} = Eigen_{PC_i} C_{exp,PC_i} \quad \text{Eq (IV.16)}$$

Finally, the sum of the weighted average coordinates' values is set to 1 by dividing the values relatively to their sum. These final values are the weights used in the CFSA to identify the proximity between two concrete mixes.

Table IV-15 Coordinates values of the selected PCs in the case of porosity accessible to water and resulting weights ($W_{P,i}$).

Property	PC1 (Eigen-value = 0.187)	PC2 (Eigen-value = 0.124)	PC3 (Eigen-value = 0.092)	Weight of the CFSA ($W_{P,i}$)
f_{cem}	0.178	0.184	0	0.054
Mv_{gra}	0.419	0.259	0	0.106
Mv_{sand}	0.423	0.262	0	0.108
W_{eff}	0.252	0.427	0	0.096
WA_{gra}	0.324	0	0	0.058
WA_{sand}	0.346	0	0	0.062
Q_{clay}	0	0	0	0
Q_D	0	0	0	0
Q_{GP}	0	0	0	0
Q_{gravel}	0.227	0.408	0	0.090
Q_K	0	0.232	0.522	0.074
Q_L	0.273	0.201	0	0.073
Q_M	0	0.187	0.234	0.043
Q_{Pz}	0.295	0.189	0	0.076
Q_{Qz}	0	0	0.509	0.045
Q_S	0	0	0.374	0.033
Q_{sand}	0	0	0	0.000
Q_{SF}	0	0	0.396	0.035
Q_V	0	0.383	0	0.046
Total	3	3.102	2.265	1

The same process was employed to assess the closeness regarding other properties serving as input parameters of durability models or being durability indicators as such. Not all the properties of interest could be examined because of the insufficient amount of data for some of them. The weighing coefficients obtained are presented in Table IV-16. It is worth noting that these coefficients were tailored to our specific database and may not be always applicable.

Table IV-16 Values of the weights ($W_{P,i}$) of the CFSA obtained for the different experimental properties.

Property	f_c	φ_c^w	Re	D_{rcm}
f_{cem}	0.086	0.054	0.078	0
Mv_{gra}	0	0.106	0.096	0
Mv_{sand}	0	0.108	0.059	0.124
W_{eff}	0.082	0.096	0.071	0.046
WA_{gra}	0.091	0.058	0.069	0.051
WA_{sand}	0.099	0.062	0.07	0.056
Q_{clay}	0.03	0	0	0.097
Q_D	0.048	0	0.007	0.032
Q_{GP}	0	0	0.014	0
Q_{gravel}	0.025	0.090	0.066	0.12
Q_K	0.077	0.074	0.099	0.027
Q_L	0.014	0.073	0.055	0.025
Q_M	0.067	0.043	0.017	0.045
Q_{Pz}	0.043	0.076	0	0
Q_{Qz}	0.078	0.045	0	0.097
Q_S	0.018	0.033	0.079	0.108
Q_{sand}	0.013	0.000	0.082	0.074
Q_{SF}	0.108	0.035	0.073	0.066
Q_V	0.120	0.046	0.065	0.031

In the final tool, different mixes of concrete are found having a good closeness, whenever possible, and the user is given the final choice in the selection process. Therefore, if a critical point is not taken into account by the selection algorithm, the user has the option to intervene and discard the concrete accordingly. The results are represented using a graph as depicted in Figure IV-19, which displays the relative difference obtained for each composition parameter. The graph also includes the sum of the average relative difference, as well as the weighted average relative difference for the parameters presented in Table IV-16. Additionally, the square root of the sum of squared relative differences is computed. This parameter is commonly used to measure the distance between two points (as is the case here) and allows for a third comparison.

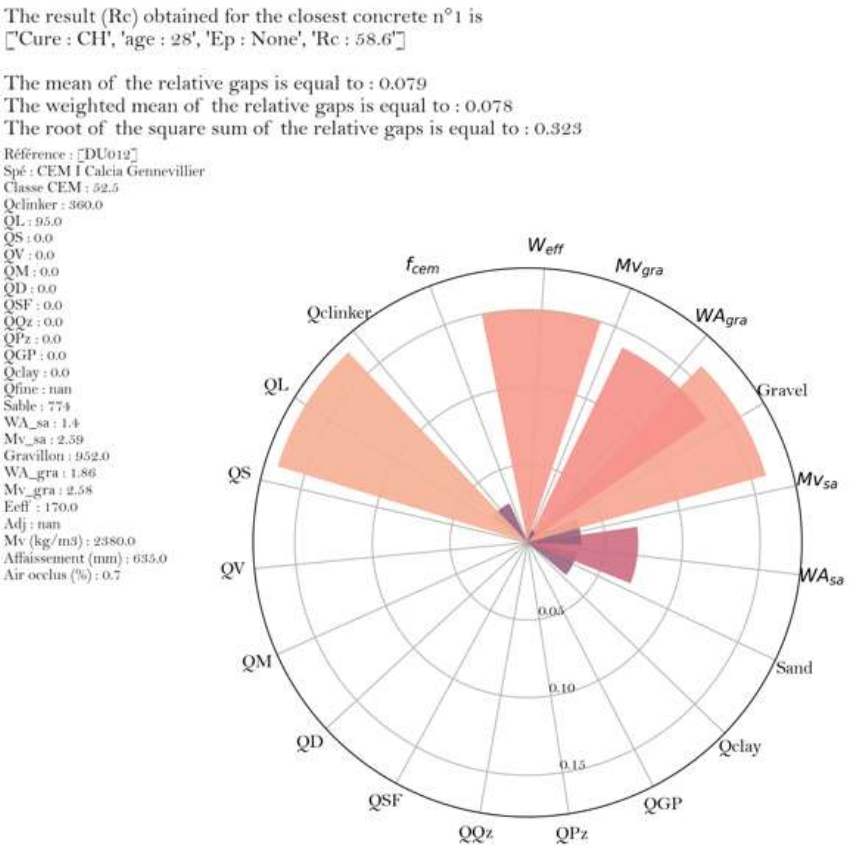

Figure IV-19 Example of comparison results obtained between a specified mix and the closest formulation of the database for fc estimation.

IV.3.3.3. Tendencies observed

The aim of this subsection is to draw global trends from the database. Specifically, the objective is to identify concrete compositions that exhibit higher levels of interest, both in terms of durability properties and environmental impact. In particular, the analysis focuses on the carbon footprint associated with a cubic meter of concrete. To assess this aspect, assumptions regarding the environmental impact of the various constituents are made based on information from the literature (refer to Table IV-17). These assumptions represent average values, considering solely the production process (transport is neglected). Additionally, although the database contains data on 1673 unique mixes, it cannot be considered as fully representative of the entire body of existing literature. Consequently, it is possible that more efficient mixes have already been discovered or are yet to be found, in relation to the properties examined in this study.

Table IV-17 Generic values of equivalent carbon (kgCO2eq/m3) for each constituent (Dec 2022).

K	L	S	V	M	Pz	SF - D	Qz	Water	Aggregate	Superplasticizer
765	39	100	27	139	239	354	120	0.132	2.74	1530
[344]	[32], [80]	[32], [80]	[32], [80]	[346]		[345]	[32], [80]	[349]	[348]	[347]

The graphical representations used in this section were inspired by Damineli [375]. These representations rely on indicators derived from measured properties such as compressive strength and electrical resistivity, as well as the equivalent carbon footprint associated with a concrete mix ($CO2_{eq}$, computed in kg of CO_2eq/m^3 of concrete). The purpose of these graphics is to enable an assessment of the properties in relation to their environmental impact.

For properties that need to be maximized to ensure better performance, the indicators are computed by dividing the equivalent carbon footprint by the property value. Conversely, for properties that need to be minimized for higher performance, the indicators are computed as the product of the property value with the equivalent carbon footprint. This approach allows for the visualization of optimal concrete mixes considering both environmental impact and the specific property being studied. Optimal properties can be identified as those closest to the origin on the graph.

In this study, the various indicators are calculated using Equations IV.17 to IV.21.

$$f_{c_{CO_2}} = CO2_{eq}/f_c \quad \text{Eq (IV.17)}$$

$$Re_{CO_2} = CO2_{eq}/Re \quad \text{Eq (IV.18)}$$

$$\varphi_{CO_2} = CO2_{eq}10^{-2}\varphi \quad \text{Eq (IV.19)}$$

$$D_{rcm,CO_2} = CO2_{eq}10^{10}D_{rcm} \quad \text{Eq (IV.20)}$$

$$K_{acc,CO_2} = CO2_{eq}K_{acc} \quad \text{Eq (IV.21)}$$

The relationship between mechanical strength and carbon footprint is firstly investigated in this study. Owing to the extensive dataset available, various graphs were constructed based on the binder type. These graphs are presented in Figure IV-21, where the influence of W_{eff}/B_{tot} is encapsulated using distinct marker shapes.

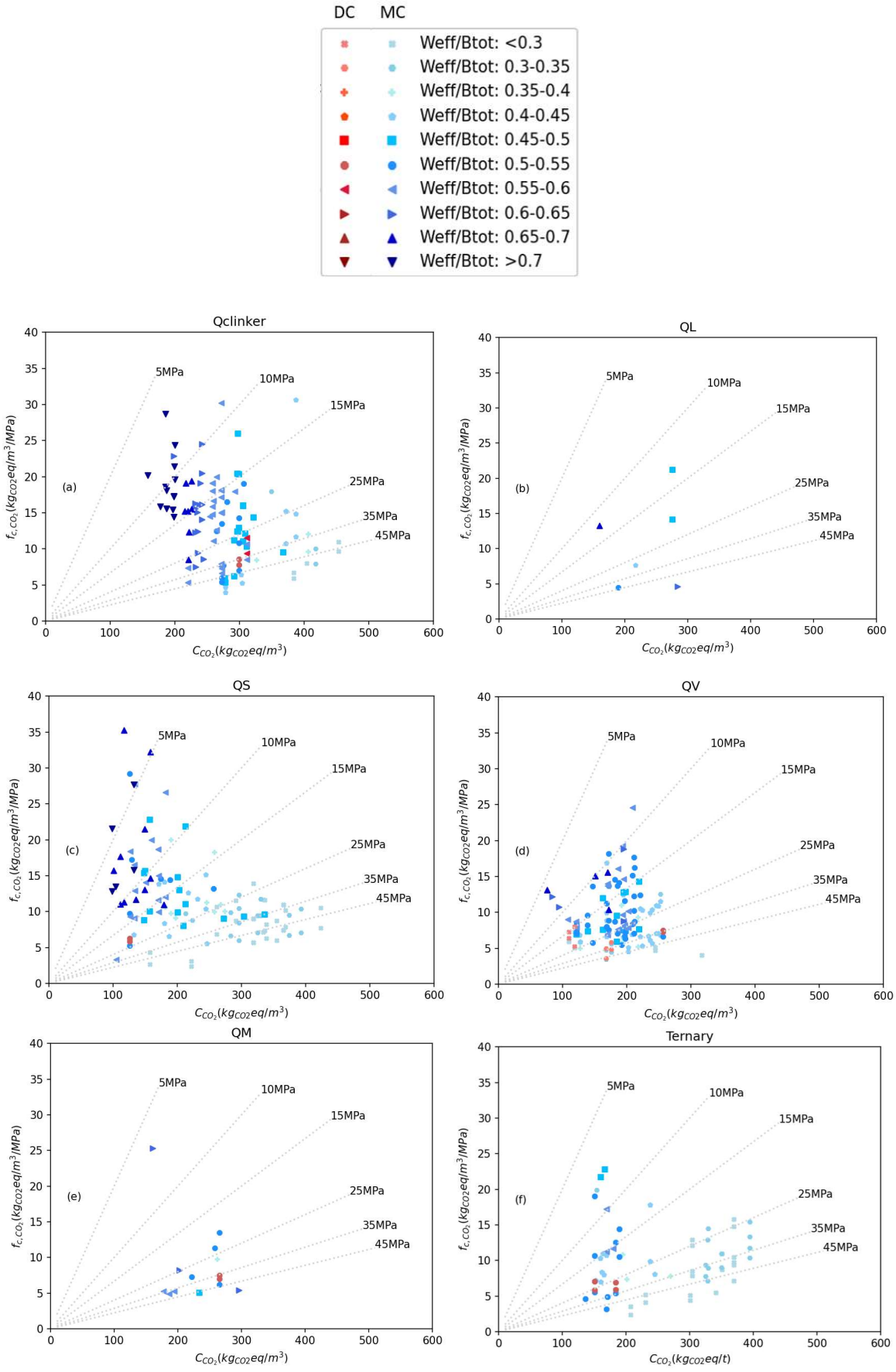

Figure IV-20 Compressive strength of concrete after 7 days of conservation for (a) CEM I-based concrete, (b) filler based concrete, (c) slag-based concrete, (d) fly ash-based concrete, (e) metakaolin based concrete and (f) ternary mixes.

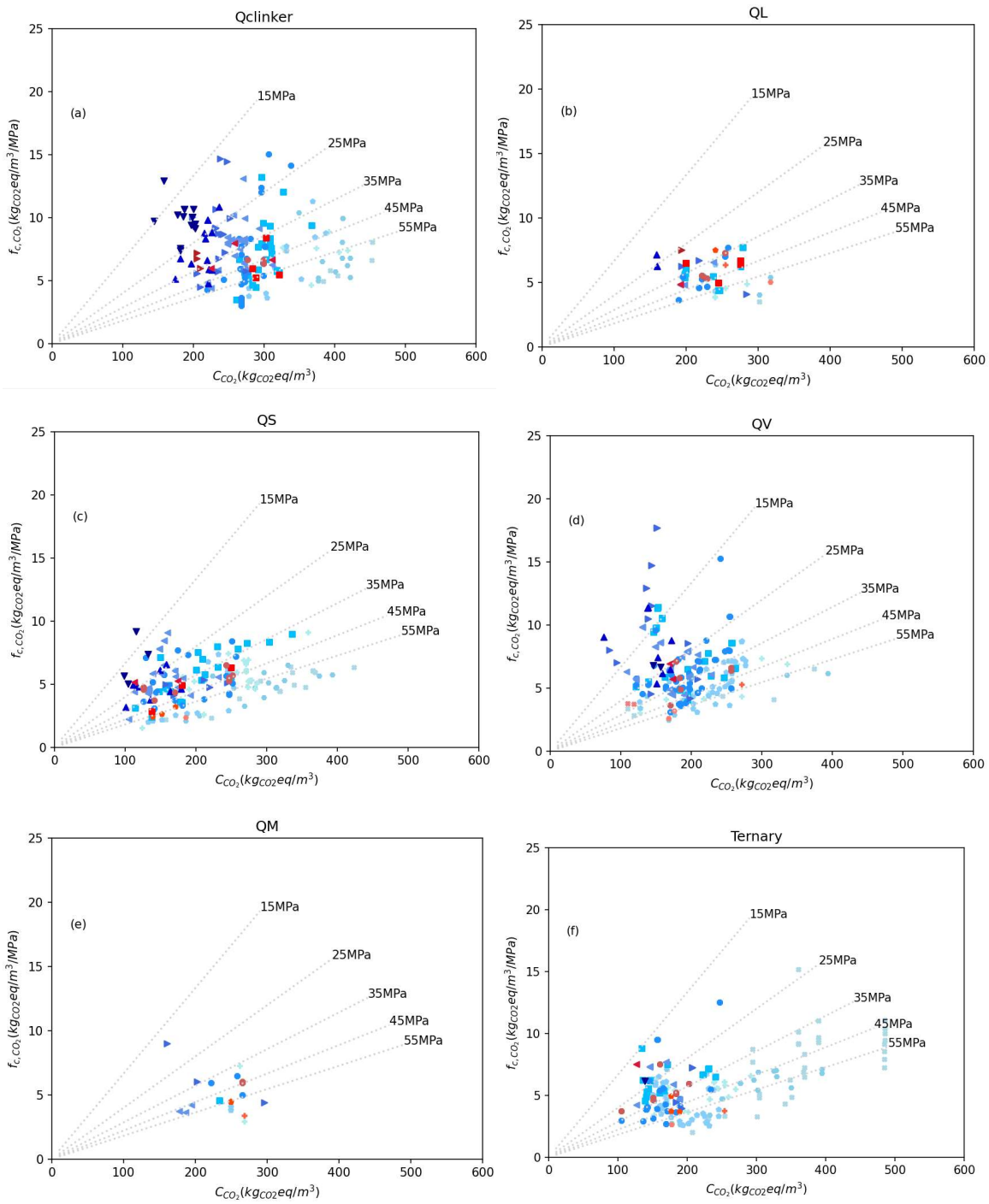

Figure IV-21 Compressive strength of concrete after 28 days of conservation for (a) CEM I-based concrete, (b) filler based concrete, (c) slag-based concrete, (d) fly ash-based concrete, (e) metakaolin based concrete and (f) ternary mixes.

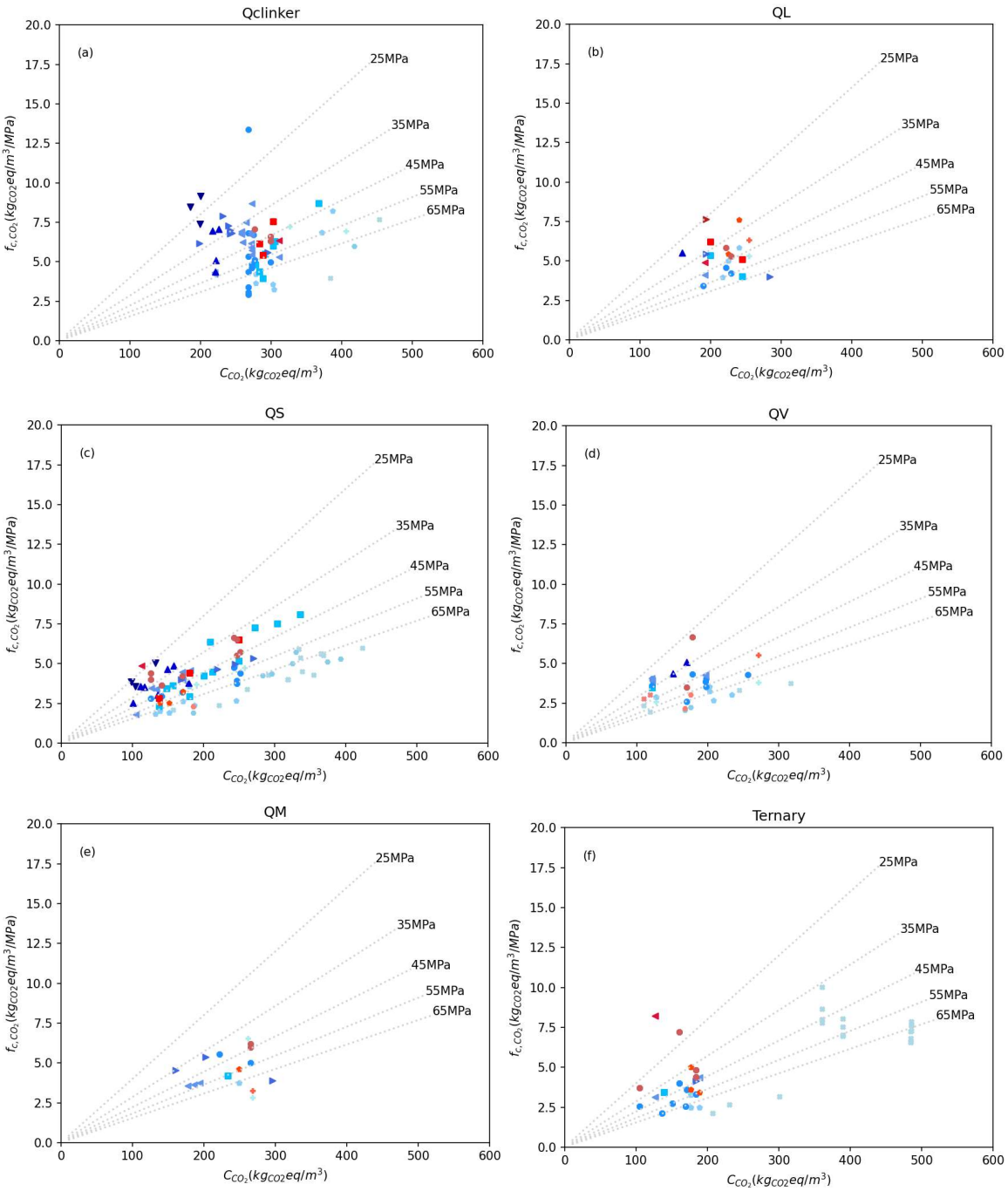

Figure IV-22 Compressive strength of concrete after 90 days of conservation for (a) CEM I-based concrete, (b) filler based concrete, (c) slag-based concrete, (d) fly ash-based concrete, (e) metakaolin based concrete and (f) ternary mixes.

The first general observation is that the carbon footprint increases as the W_{eff}/B_{tot} ratio decreases in the concrete composition. This can be attributed to the higher binder content in relation to the concrete volume when lower W_{eff}/B_{tot} ratios are used. However, a lower ratio value also results in higher compactness and, consequently, higher compressive strength. This trend can be observed in Figure IV-20, to Figure IV-22. Therefore, if a specific minimum compressive strength is desired for a given binder type (and considering a pre-established concrete design), there exists an optimal W_{eff}/B_{tot} ratio that fulfils the mechanical requirement while minimizing the carbon footprint.

When comparing the results obtained from samples conserved in Dry Conditions (DC) and Moist Conditions (MC), it is noticeable that there is a discrepancy due to the higher value of the indicator f_{cCO_2} in the case of DC. This is primarily due to lower mechanical resistance despite similar carbon footprints. This disparity is particularly obvious in Figure IV-22 (b) and (f), as well as in Figure IV-21 (b) and (e). This finding emphasizes the need to carry out an efficient hydration process on the concrete material to maximize its properties in relation to the carbon footprint.

A different way to observe this aspect is to compare the graphs obtained after 7 days, 28 days, and 90 days. For example, when examining the three graphs related to slag-based concretes (letter (c)), an increase in compressive strength over time prior to testing can be observed. This demonstrates the positive effect of conservation on the material properties and its final environmental impact. By extension, prolonging the conservation time could be utilised as a means to reduce the equivalent carbon footprint associated with a concrete mix. The inclusion of more pozzolanic additions in the concrete formulation could achieve similar mechanical strength as a CEM I-based concrete, given a longer conservation time. This would result in a lower carbon footprint and consequently, a lower f_{cCO_2} indicator. However, this scenario would require an extended conservation time and reduced production efficiency, which may not be easily feasible within an industrial context. These limitations provide the rationale behind exploring alternative methods such as thermal treatments.

Comparing the results obtained with Dry Conservation (DC, in red) and Moist Conservation (MC, in blue), it can be observed that a humid environment leads to a greater reduction in the CO2 indicator f_{cCO_2} for concrete with supplementary cementitious materials (SCM) when compared to CEM I-based concretes. This effect is particularly significant for ternary additions, where a clear reduction can be observed. Furthermore, comparing the graphs obtained for the same duration but different binder types, it is obvious that each addition studied here has its own potential.

The difference in CO2 indicator becomes noticeable after just 7 days of conservation and becomes more pronounced after 28 and 90 days. Figure IV-23 represents the time evolution of the average f_{cCO_2} indicator for each type of binder, as well as the difference compared to the 7-days values. It shows that the greatest reduction in the mean f_{cCO_2} indicator between 90 and 7 days is achieved with Slag-based, Fly-ash-based, and ternary binders. Additionally, for fly ash-based and ternary binders, there is a greater evolution between 28 and 90 days compared to the other mixes. This suggests a slower hydration kinetics on average for these types of binders. In comparison, most of the hydration for slag-based concrete likely occurs between 7 and 90 days, as the relative difference is greater than 50% compared to the other concrete types. Metakaolin hydration is even quicker and occurs within 7 days, which explains the low average f_{cCO_2} values even after just 7 days of MC.

Finally, it is worth noting that fly ash-based binders and ternary binders result in the lowest average f_{cCO_2} values after 90 days of MC.

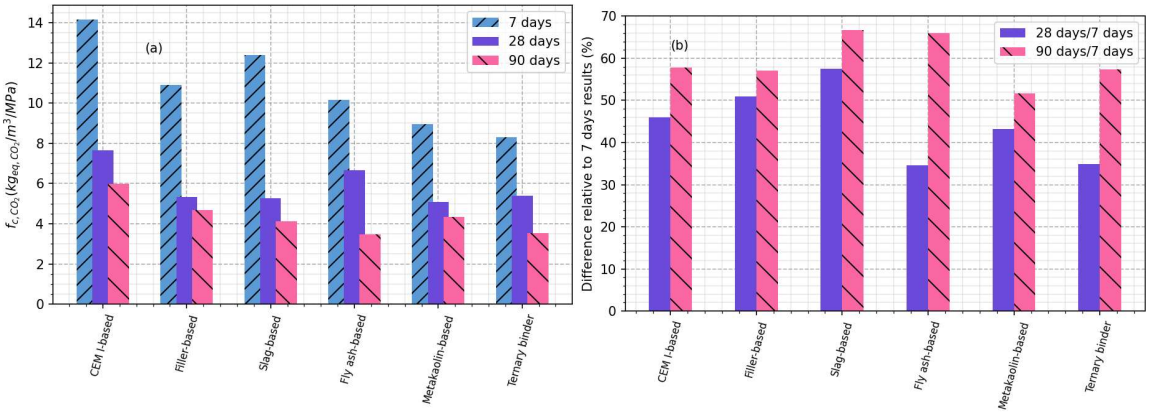

Figure IV-23 Mean values of f_{cCO_2} obtained after different conservation time for the different binder type in MC (a) and difference relative to the 7 days values (b).

In Figure IV-24 to Figure IV-30, the effect of the W_{eff}/B_{tot} ratio is not thoroughly investigated for the other properties or durability indicators as for the compressive strength. Hence, the marker shapes do not adhere to the same rules as Figure IV-20 to Figure IV-22, preventing the observation of the W_{eff}/B_{tot} ratio used for each data point. A crucial and debatable assumption is thus made for the rest of this section, assuming that this parameter remains consistent across different binder types and does not significantly affect the observable differences.

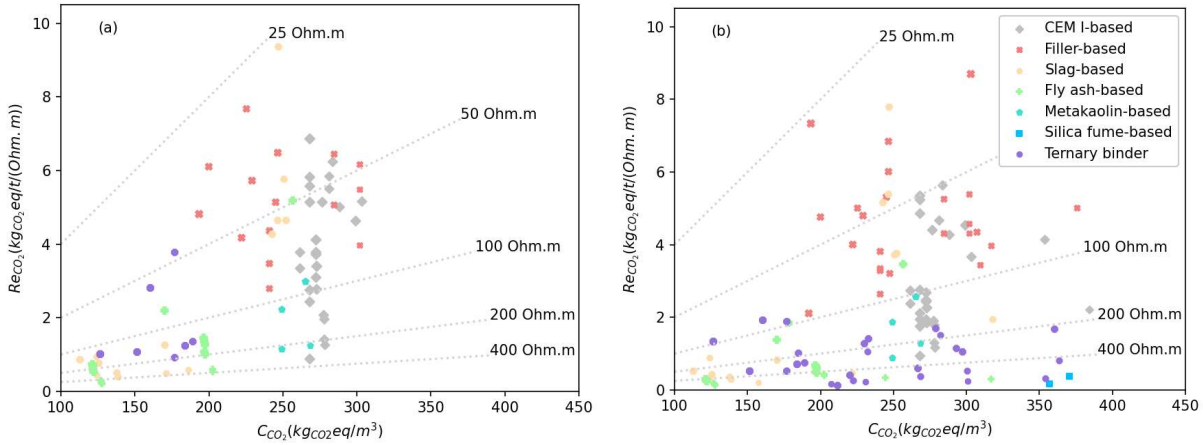

Figure IV-24 Electrical resistivity vs. equivalent carbon footprint of concrete by binder type for (a) 28 days, and (b) 90 days of moist conservation.

The Figure IV-24 represents the CO2 indicator for relative electrical resistivity (Re_{CO_2}). It is computed using Equation IV.18 and obtained for different types of binders at two measurement times: 28 and 90 days. Only Moist Conservation (MC) is considered due to a lack of data on alternative conservation environments.

Several observations can be made, especially with the assistance of Figure IV-25. Firstly, the mean values of Re_{CO_2} decrease between 28 and 90 days for all binder types, which can be attributed to the continued process of hydration. However, it is challenging to draw conclusions regarding the differences in hydration relative to binder type, primarily because most of the gain in electrical resistivity occurs before 28 days.

While it appears logical that the ternary binder benefits from a longer conservation time, the reduction in Re_{CO_2} achieved with CEM I-based concrete is higher than anticipated, particularly in comparison to the other binder types.

Filler-based concretes exhibit the lowest values of Re_{CO_2}, which highlights the durability limitations of this type of addition when used alone. Consequently, despite the reduction in equivalent carbon footprint associated with the replacement of clinker, the decrease in electrical resistivity caused by the incorporation of filler is significant.

Regarding concretes formulated with reactive additions, Figure IV-25 demonstrates clear advantages compared to CEM I-based concretes. Fly ash and ternary binders yield the most optimal compositions on average, based on the database results. They are followed by metakaolin and slag. It is challenging to draw conclusions regarding the interest in silica fume due to the limited availability of only two concrete mixes. However, it is worth noting the remarkably low values of Re_{CO_2} despite having relatively high C_{CO_2} values (see (b) Figure IV-24) according to the selected assumptions.

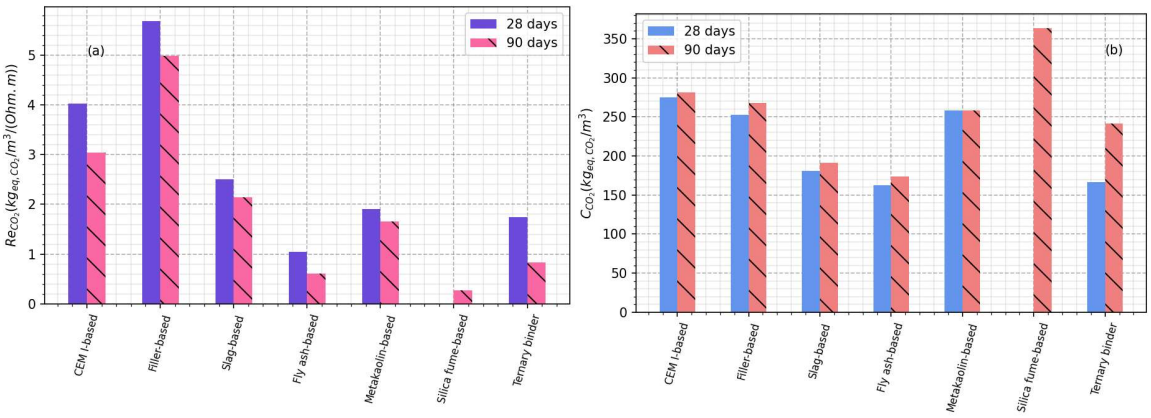

Figure IV-25 Mean Re_{CO_2} values (a) and mean C_{CO_2} values (b) obtained for 28 and 90 days of MC.

The results presented in this study indicate that the incorporation of pozzolanic and latent hydraulic mineral additions increases the electrical resistivity of the cementitious matrix. This enhancement can be attributed to both the chemical composition of the hydrates present in the matrix and physical effects. Particularly noteworthy are the results obtained for the ternary binder, which display significant improvements in electrical resistivity after 90 days of moist conservation (MC). This improvement may be attributed to an increased compactness of the binder, facilitated by a wider range of material fineness. According to De Larrard [33], optimal granular stacking can be achieved by distributing the granular particles more uniformly, which is typically achieved through the use of materials with a wider range of fineness. In the case of the ternary binder, the inclusion of three materials, as opposed to two or one, may provide the necessary range of fineness for improved granular stacking.

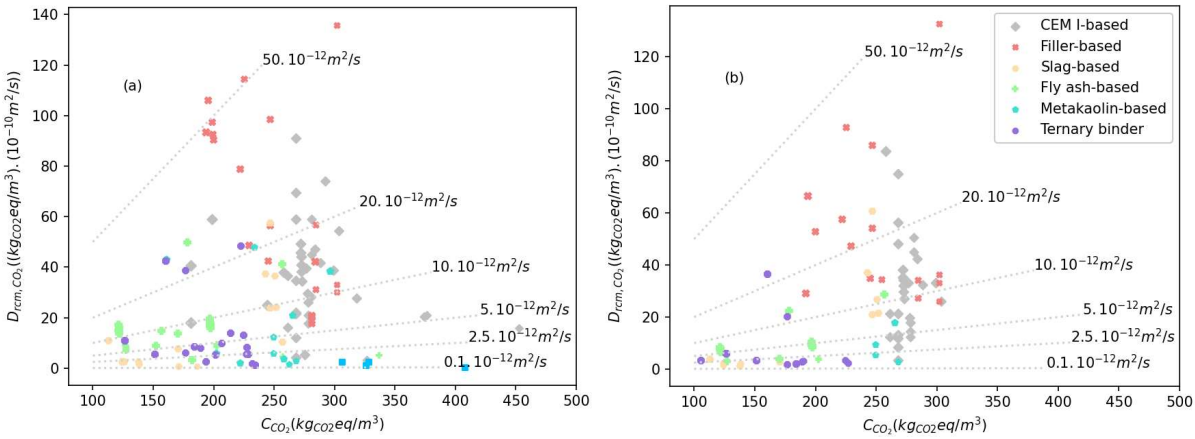

Figure IV-26 Chloride migration coefficient vs. equivalent footprint of concrete by binder for (a) 28 days, and (b) 90 days of moist conservation.

Similar results were obtained using the D_{rcm} indicator calculated with Equation IV.20. Filler-based materials consistently showed the poorest properties on average, followed by CEM I-based concretes. The replacement of clinker with supplementary cementitious materials (SCMs) demonstrated significant benefits, particularly when using fly ash, slag, and ternary binders. These alternatives allowed for the achievement of low D_{rcm,CO_2} values, with C_{CO_2}values less than 200 kg_{CO_2eq}/t. The results for silica fume-based binders were inconclusive due to limited data, but the available values exhibited low D_{rcm,CO_2} and high C_{CO_2} levels, indicating a remarkably low diffusion capacity for these binders.

The difference in results between the 28 and 90-days conservation showed similar increases resulting from extended hydration time, except for slag. The two graphs are constructed on different concrete mixes (dataset), which can complicate the conclusions.

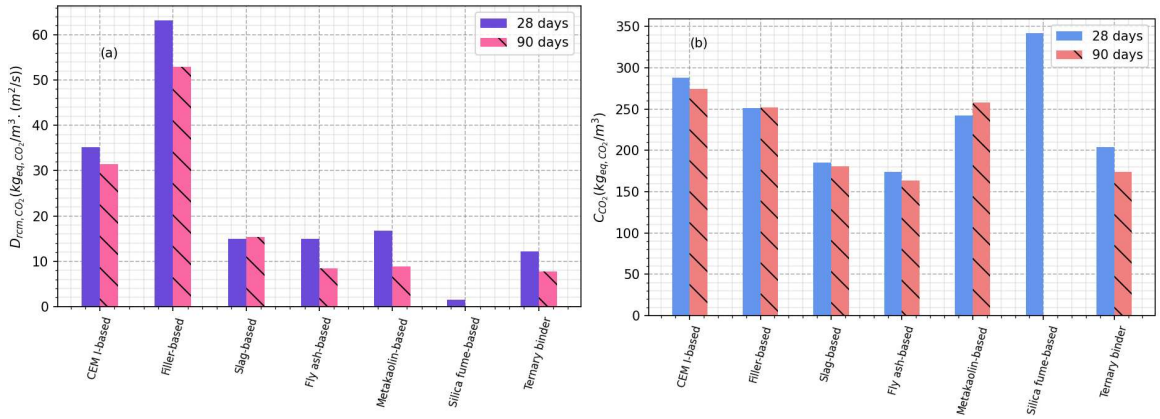

Figure IV-27 Mean D_{RCM,CO_2} values (a) and mean C_{CO_2} values (b) obtained for 28 and 90 days of moist conservation.

As demonstrated for Re_{CO_2}, ternary binders show slightly higher optimized values of D_{rcm,CO_2} compared to slag, fly ash, and metakaolin. This finding can be attributed to the variability in material particles' thinness, which leads to enhanced compactness and lower diffusion capacity of chloride. In contrast, the addition of other reactive substances when used alone with CEM I results in suboptimal granular stacking. However, the composition of the cementitious matrix, characterized by higher amounts of C-S-H and Afm, also plays a significant role in explaining the differences observed compared to CEM I-based binders.

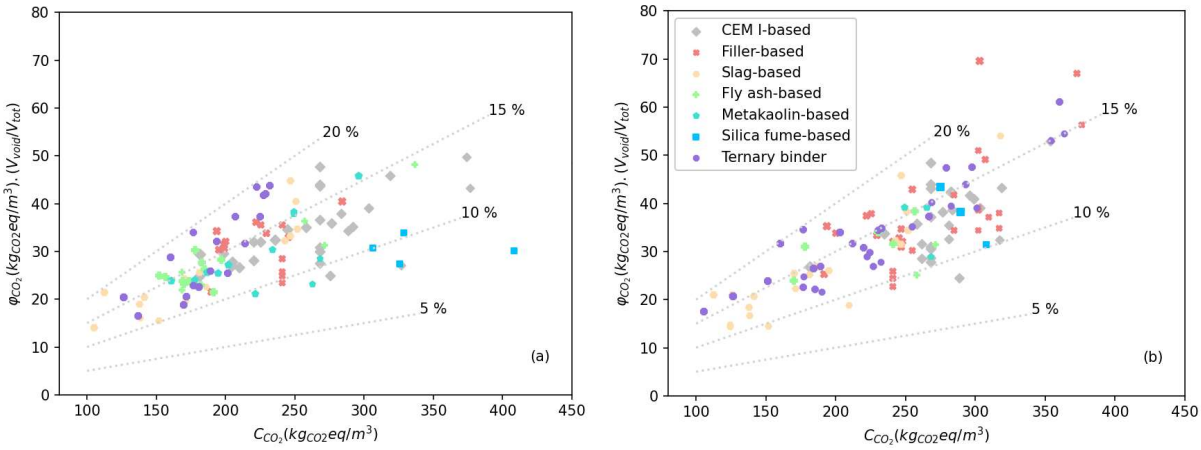

Figure IV-28 Porosity accessible to water vs. equivalent carbon footprint of concrete sorted by binder for (a) 28 days, and (b) 90 days of moist conservation.

The results obtained for the porosity accessible to water (φ_{CO_2}, computed with Equation IV.19), exhibit varying trends. For most of the concretes analysed in Figure IV-28, the porosity accessible to water falls within the range of 10 to 20%. Additionally, no clear distinction can be noticed between the different types of binders. This suggests that the reduction in C_{CO_2} values due to the incorporation of supplementary cementitious materials (SCMs) is feasible without significantly impacting the porosity accessible to water. As a result, the average values of φ_{CO_2} obtained are similar across most binder types. However, concrete mixtures containing slag and fly ash display notably lower values of this indicator.

Furthermore, the analysis of the difference between the two measurement times indicates that there is no distinct increase or decrease in the porosity accessible to water regardless of the binder types. This suggests that the evolution of φ_c^w with hydration likely occurs prior to 28 days for samples stored in moist conditions.

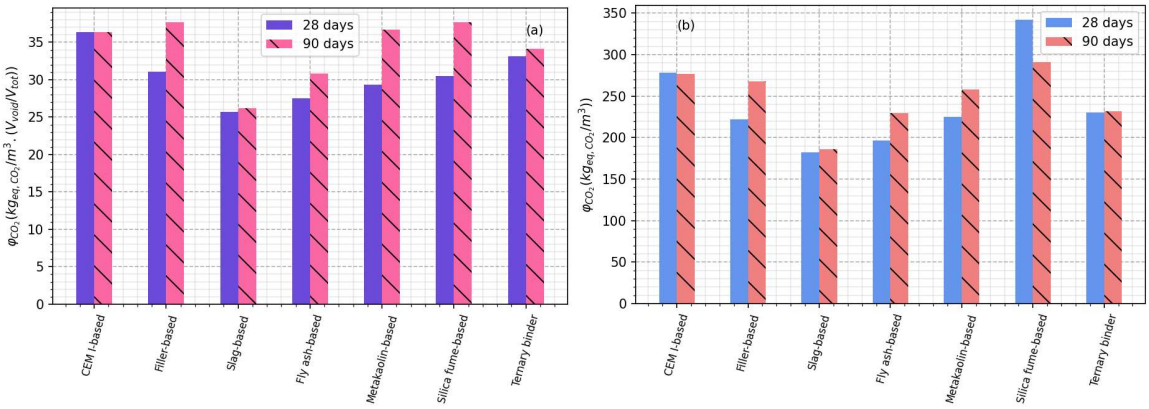

Figure IV-29 Mean φ_{CO_2} values (a) and mean C_{CO_2} values (b) obtained for 28 and 90 days of moist conservation.

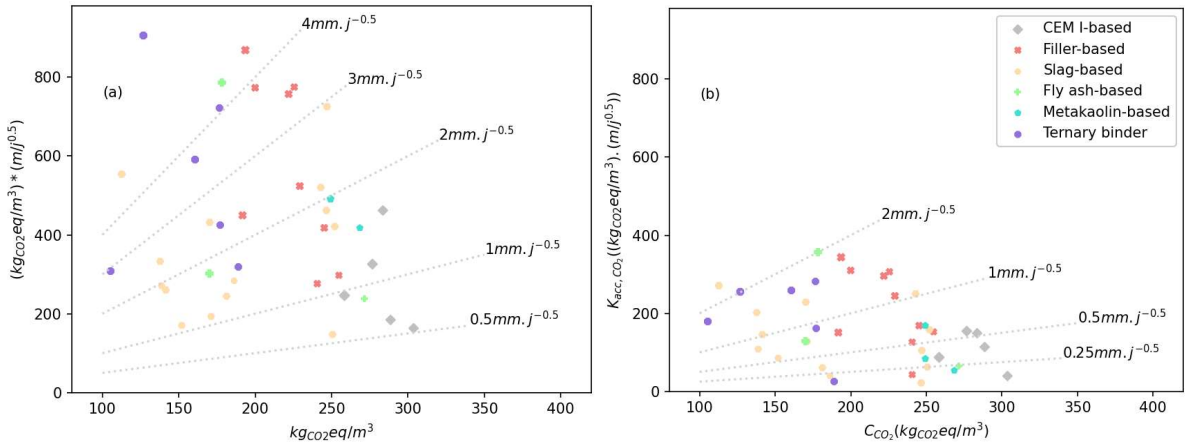

Figure IV-30 Accelerated carbonation (XP P18-458) carbonation rate vs. equivalent carbon footprint of concrete sorted by binder for (a) 90 days of dry conservation, and (b) 90 days of humid conservation.

The last indicator, K_{acc,CO_2}, is computed using Equation IV.21 and represents the accelerated carbonation, measured according to the XP P18-458 (2022), relative to the carbon footprint. The study deals with two conservation conditions as shown in Figure IV-30, while the conservation time prior to testing is held constant at 90 days. The results presented, along with the calculation of average values by binder type, demonstrate clear differences related to the conservation conditions.

The average values obtained from samples stored in DC indicate that, on average, concretes based on CEM I result in lower K_{acc,CO_2} despite having a higher environmental impact. This highlights the limit in using supplementary cementitious materials (SCMs) for clinker replacement in terms of carbonation resistance in the absence of sufficient conservation. However, when considering samples stored in MC for 90 days, a different trend is observed. In this case, the average K_{acc,CO_2} values are comparable among the different binders.

Both figures indicate that hydration significantly impacts carbonation resistance for all binders. Incorporating mineral additions in the mix leads to a greater reduction in the carbonation rate, K_{acc}, when comparing the values obtained in MC and in DC. Thus, the absolute differences calculated for average K_{acc,CO_2} values presented in Figure IV-31 demonstrate that a reduction of about 350 $kg_{eqCO_2}/m^3.(mm.j^{-0.5})$) can be achieved for metakaolin-based, filler-based, and ternary binders. Slag and fly-ash-based compositions also show an increase of the benefit linked to the favourable hydration compared to CEM I-based mix, with values superior to 220 $kg_{eqCO_2}/m^3.(mm.j^{-0.5})$) in average, compared to 167 $kg_{eqCO_2}/m^3.(mm.j^{-0.5})$) respectively. These observations highlight the potential for clinker replacement by SCMs in environments where carbonation is the primary aggressive phenomenon (XC exposure classes). However, the effectiveness of this replacement depends on the ability to impose appropriate conservation.

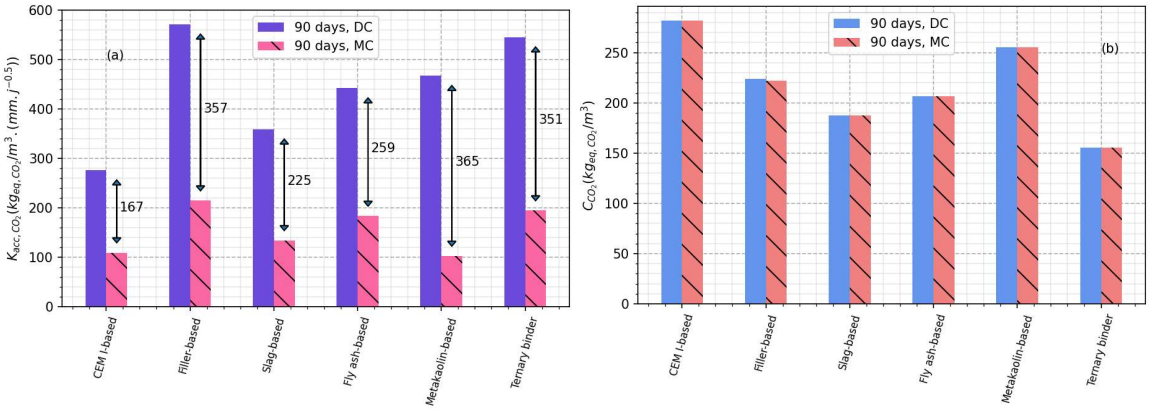

Figure IV-31 Mean K_{acc,CO_2} values(a) and mean C_{CO_2} values (b) obtained for 90 days of DC and MC.

This section explored the mechanical and durability properties of different Supplementary Cementitious Materials (SCMs) in relation to their environmental impact on concrete formulation. Due to the numerous and complex factors involved, only broad trends can be established.

However, there is interest in using mineral additions in concrete for two reasons. First, concretes with SCMs can achieve comparable mechanical strength to traditional CEM I-based concretes while reducing the environmental impact. Second, the durability properties of these concretes are particularly beneficial in chloride-induced corrosion environments (XS and XD exposure classes). The incorporation of pozzolanic and latent hydraulic additions in binders leads to lower chloride diffusion coefficient and higher electrical resistivity, resulting in enhanced performance and ecological benefits.

The findings regarding carbonation-induced corrosion environments (XC exposure classes) are less positive. Accelerated testing reveals that incorporating mineral additions in concrete mixtures can decrease the carbonation resistance, but this can be thwarted at some extent by an adequate conservation.

The economical aspect is not considered in this section, although it may be a limiting factor in using SCM-based formulations. Longer conservation times for these mixes can pose challenges. Therefore, alternative solutions to enhance the hydration of these concretes, such as thermal treatment or set accelerators, should be explored. However, it is important to note that these solutions also come with environmental costs.

The utilization of certain additions, which has been feasible for a few decades under specific conditions, remains inadequately exploited despite the significant benefits it can impart to concrete properties. The average clinker/cement ratio across the world is reported as 0.81 in [404], whereas values of 0.77 and 0.7 were recorded for France and Germany, respectively, in 2018 according to [405]. Consequently, the aim of the FD P 18-480 (2022) [340], as elaborated upon briefly in Section I.6.3, is to adopt a performance-based approach.

As a prospective avenue for further research, investigating the influence of different Supplementary Cementitious Materials (SCMs) on corrosion rate with the calculation of a comparable indicator related to carbon footprint would be interesting. The electrical resistivity values obtained already demonstrate the promising performance of pozzolanic- and slag-based concretes, which could signify a slower corrosion kinetics of steel reinforcing bars in these materials. For instance, it may substantiate the utilization of binders based on reactive mineral additions in XC environments, compensating for a shorter corrosion initiation stage with a more extensive propagation step. This aspect is indeed considered in the FD P18-480 (2022), where threshold values for accelerated carbonation rates are modulated by the concrete's electrical resistivity measurements.

Although the impact of aggregates is not addressed in this section, the use of Recycled Concrete Aggregates (RCA) represents a critical lever to reduce the carbon footprint that needs to be weighted up against durability properties.

IV.3.4. Confidence index ω

The developed tool proposes various ways to the user (analytical, ANN-based, PR-based models, as well as the CFSA) to estimate properties as input parameters of durability models, or durability indicators, from composition data he must define. In addition to usage precautions provided by the tool, this section introduces the concept of confidence index and outlines its calculation. The confidence index is utilised to further assists the user in assessing the convenience and accuracy of a model or method, facilitating the selection of the most suitable option. From a general viewpoint, the confidence index can also affect the input data, regardless of its origin (available in the design documentation, experimentally obtained, etc.), as well as the properties estimated from the data.

IV.3.4.1. Definition and use

The accuracy of a model or method is deemed according to the following ingredients:

- The values of input data with regard to the variation range, supposed consistent for applying the model or method.
- The closeness of the output from various models or methods for the same estimated property. However, the lack of time to verify this approach prevent its use in the present study. This aspect could be the subject of future work.
- The inherent lack of perfection affecting any experimental process to acquire data or a property.

The confidence index, ω, arbitrarily ranges from 0.25 (lowest confidence) to 1.1 (highest confidence). It affects the default uncertainty associated to an input data or a property. To this purpose, a default standard deviation ($\sigma_{default}$) is assigned to each input data, while the effective standard deviation (σ_{actual}) is determined using Equation IV.22:

$$\sigma_{actual} = \frac{\sigma_{default}}{\omega} \qquad \text{Eq (IV.22)}$$

A higher effective standard deviation results from a lower ω value, indicating a greater potential variability of the input data. The various values of $\sigma_{default}$ are presented in Table IV-18 and are dependent on the specific data or property being considered. These values are defined based on standards, documents, literature sources, and feedback. However, for steel rebar diameter, liquid permeability, hydrate contents, the initial chloride content, the depth of the convective zone, and ageing factor, a coefficient of variation (CoV) of 20% is chosen arbitrarily due to the unavailability of reliable sources.

In this document, the default standard deviations ($\sigma_{default}$) represent optimistic values, while the applied standard deviations (σ_{true}) reflect a more uncertain and pessimistic consideration of the variability. For example, the value of $\sigma_{default}$ that is defined for the total binder content can be expected for prefabricated concrete manufactured in a factory. However, this value is too low to account for the variability in constituents' contents in cast-in-place concrete, where the variability is higher. In the latter case, the confidence index is lower than 1.

Table IV-18 $\sigma_{default}$ values associated to the different parameters.

Parameter	$\sigma_{default}$	Unit	Reference
Content of cement ($\boldsymbol{Q_{CEM}}$)	0.04μ	Kg/m^3	[340], [406]
Effective water ($\boldsymbol{W_{eff}}$)	$\max(0.04\mu, 4)$	Kg/m^3	[340], [406]
Admixture ($\boldsymbol{Q_{adm}}$)	0.05μ	Kg/m^3	[340], [406]
Total binder ($\boldsymbol{Q_{binder}}$)	0.04	Kg/m^3	[340], [406]
Total aggregates ($\boldsymbol{Q_{agg}}$)	0.04μ	Kg/m^3	[340], [406]
Gravel ($\boldsymbol{Q_{gra}}$)	$\max(0.04\mu, 30)$	Kg/m^3	[340], [406]
Sand ($\boldsymbol{Q_{sa}}$)	$\max(0.04\mu, 30)$	Kg/m^3	[340], [406]
Reinforcing bar diameter ($\boldsymbol{D_{rebar}}$)	0.2μ	mm	-
Concrete cover ($\boldsymbol{C_{min}}$)*	3 - 6	mm	[6]
Cement composition in clinker and SCMs	2	%	Technical datasheets
SCMs and clinker composition in oxide	3	%	Technical datasheets
Bulk density on fresh concrete ($\boldsymbol{Mv_{fresh}}$)	10.2	Kg/m^3	[407]
Slump value ($\boldsymbol{Slump}$)	9	mm	[408]
Air content ($\boldsymbol{\varepsilon_{air}}$)	0.45	%	[409]
Compressive strength ($\boldsymbol{f_c}$)	0.05	MPa	[410]
Porosity accessible to water ($\boldsymbol{\varphi}$)	0.6	%	[411]
Bulk density ($\boldsymbol{M_v}$)	17	Kg/m^3	[411]
Gas permeability ($\boldsymbol{K_{gaz}}$)	0.2μ	m^2	[412]
Liquid permeability ($\boldsymbol{K_{liq}}$)	0.2μ	m^2	-
Portlandite content ($\boldsymbol{CH}$)	0.08μ	wt.% binder	Experimental measurement
C-S-H content ($\boldsymbol{CSH}$)	0.2μ		-
Afm content ($\boldsymbol{Afm}$)	0.2μ		-
Aft content ($\boldsymbol{Aft}$)	0.2μ		-
Chloride Apparent diffusion coefficient ($\boldsymbol{D_{app}}$)	0.33μ	m^2.s^{-1}	[413]
Initial chloride content ($\boldsymbol{C_0}$)	0.2μ	wt.% binder	-
Depth of the convective zone ($\Delta\boldsymbol{X}$)	0.2μ	mm	-
Chloride concentration ($\boldsymbol{Cs}$)	0.19μ	wt.% binder	[413]
Chloride migration coefficient ($\boldsymbol{D_{rcm}}$)	0.24μ	m^2.s^{-1}	[414]
Electric resistivity ($\boldsymbol{Re}$)	0.2μ	Ohm.m	[415]
Ageing factor ($\boldsymbol{ae}$)	0.2μ	-	-
Natural carbonation rate ($\boldsymbol{K_{nat}}$)	0.25μ	mm.years$^{-0.5}$	[416]
Accelerated carbonation rate ($\boldsymbol{K_{acc}}$)	0.25	mm.days$^{-0.5}$	[417]
Annual mean relative humidity ($\boldsymbol{RH_{mean}}$)	5	%	Meteorological database
Annual mean variation of relative humidity ($\Delta\boldsymbol{RH}$)	2.5	%	
Annual mean temperature ($\boldsymbol{T_{mean}}$)	5	°C	
Annual mean variation of temperature ($\Delta\boldsymbol{T}$)	2.5	°C	
Mean partial pressure of CO_2 ($\boldsymbol{P_{CO_2 mean}}$)	5	Pa	[418]
Mean variation of CO_2 partial pressure ($\Delta\boldsymbol{P_{CO_2}}$)	2.5	Pa	[418]
Mean chloride concentration ($\boldsymbol{Cl_{mean}}$)	0.04μ	g/L	[419], [420]
Critical concentration ($\boldsymbol{C_{crit}}$)	0.2μ/0.15	wt.% binder	[20], [191], [236]
Annual salting period ($\boldsymbol{t_{salting}}$)	0.2μ	days	-
Annual ratio of rainy day ($\boldsymbol{ToW}$)	0.2μ	-	-
Probability of driving rain ($\boldsymbol{Pdr}$)	0.2μ	-	-

*The standard deviation for the concrete cover can be adjusted by the user based on their confidence in the manufacturing process. A default value of 6mm is suggested, but it can be decreased to 3mm [6].

IV.3.4.2. Experimental measurements

The experimental measurement of an input data or a property remains the most rigorous way to estimate it. The computation of the confidence index is performed through a step-by-step process:

1) The initial value is set to $\omega_0 = 1$.
2) An adjusting factor λ_{test} is then applied depending on the accuracy of the testing technique, as proposed in Table IV-19. If only one kind of test exists for determining the parameter, λ_{test} is set to a constant value of 1, and the precision of the test is directly considered in the value of $\sigma_{default}$.

$$\omega_1 = \lambda_{test}\, \omega_0 \qquad \text{Eq (IV.23)}$$

3) The value can be adjusted by the user based on the condition of the measurement. If the experimental test is conducted by a certified operator (according to an official certification system), or conversely, if the measurement results from a rounded value, or averaging over multiple measurement locations, a corrective factor $\lambda_{condition}$ can be applied to ω_1 using Equation IV.24, where $\lambda_{condition}$ is ranges from 0.75 (indicating a decrease in confidence) to 1.1 (indicating the highest increase in confidence).

$$\omega_{tot} = \lambda_{condition}\, \omega_1 \qquad \text{Eq (IV.24)}$$

Table IV-19 λ_{test} values for the different experimental tests.

Parameter	Test	λ_{test}	Reference
Constituent content	Weighting	1	-
	Evaluation of the binder nature and content by chemical analyses	0.9	-
Cement composition	Technical sheet information	1	-
	Average value on datasheet	0.9	-
Oxide composition of SCM and clinker	Technical sheet information	1	-
	Average value on datasheet	0.9	-
Concrete cover	Prescription	1	-
	Pachometer*	1	-
Compressive strength	Test on laboratory samples	1	[410]
	Test on core samples	0.98	[421]
	Pundit -ultrasound measurement	0.95	[422]
	Sclerometer - Bouncing value	0.95	[423]
Electrical resistivity	Measure on sample	1	[415]
	Measure on structure	1.1	[424]
Environmental parameter ($\boldsymbol{RH}, \boldsymbol{T}, \boldsymbol{P_{CO_2}}, \boldsymbol{Cl^-}$)	Measure with device (meteorological station, Rotronic…)	1	-
	Average of standard or documentation	0.95	-

*Pachometer measurements provide a distribution of values, making it advisable to allow the tool to define its own distribution. However, it is possible to utilize the average value measured along with the standard deviation to employ an alternative distribution law. In this case, the user should manually set this value instead of relying on the current method.

IV.3.4.3. Literature model

The literature models discussed in Section IV.3.2 provide an alternative approach for determining the desired properties. In that case the confidence index is computed using the following process:

1) The initial value of ω_0 is set to 1.
2) If one input data is outside the supposed consistent range (as defined for all literature models in Section IV.3.2), ω_i is set to 0.25. If all the input data stay within the consistent range, ω_i is

computed using Equation IV.25. This calculation takes into account the Mean Relative Error (MRE, %) obtained from the database and presented in Table IV-10.

$$\omega_{tot} = \left(1 - \frac{MRE}{100}\right)\omega_0 \qquad \text{Eq (IV.25)}$$

IV.3.4.4. Regression and Artificial Neural Network

A similar procedure as described in the previous Section IV.3.4.3. for a literature-referenced model is adopted for PR and ANN-Models. All details are thoroughly presented in Section IV.3.3.1.

IV.3.4.5. Closest formulation selection algorithm

The closest formulation selection algorithm (CFSA), outlined in Section IV.3.3.2, enables the determination of the desired property from a concrete with a similar composition. The confidence index associated with this method is calculated through the following process, which takes into consideration the relative difference between the compositions of the two concretes:

1) The initial value of ω_0 is assigned as 1.
2) The second step involves employing the calculations explained in Section IV.3.3.2. The Mean of Relative Differences (MRD, %), computed based on the composition of the concrete mix in the database and the one inputted by the user, is utilised in Equation IV.26 to compute the value of ω_1. It accounts for the impact of the two concrete mixes' proximity on the result confidence.

$$\omega_{tot} = \left(1 - \frac{MRD}{100}\right)\omega_0 \qquad \text{Eq (IV.26)}$$

IV.4. Engineering modelling

A comparative analysis of various analytic models was conducted in [425]. The study proposes a novel method for determining the cost-benefit ratio of a given model based on its input variables, taking into consideration both the time and cost associated with acquiring each input. As a result, the models under investigation are classified not only based on their performance, but also according to their cost.

In the present study, the costs associated to the input acquisitions, or the experimental measurements are not taken into account. The tool utilised in this research allows for the prediction of every input parameter. Consequently, the primary focus of this research lies solely on evaluating the performance of each model implemented within the tool. The calculations of this section therefore acknowledge and account for the presence of uncertainties associated with the overall methodology, which approximates the input parameters in cases where experimental data is unavailable.

IV.4.1. Model selection and deterministic results

Various engineering models are implemented in the developed tool, analytical models presented in Annex 4, as well as the surrogate models based on SDReaM-Crete (refer to Section III.6.2), for carbonation and chloride-induced corrosion initiation. It is needed to the user to identify the models that exhibit the highest convenience with respect to the exposure class. Where data was available, a comparison with experimental measurement on structures was conducted to assess the ability of SDReaM-Crete to simulate real applications.

Sensitivity analyses are systematically performed for all models to quantify the impact of the different parameters on the output.

IV.4.1.1. Carbonation models

In this study, the exposure classes XC1, XC2, XC3, and XC4 are considered. The following carbonation models have been investigated:

- The meta-model built on the model SDReaM-crete using a polynomial chaos expansion and presented in Section III.6.2. **(SC)**
- The analytic models presented in Annex 4:
  - The model PerfDuB for carbonation detailed in [323] **(PE)**
  - The model developed by Demis in [27] **(DE)**
  - The model developed by the Japan society of Civil Engineers (JSCE) in [196] **(JA)**
  - The model developed by Parrott and detailed in [180] **(PA)**

The availability of multiple models provides users with a better means for adapting to specific situations.

As experimental result for structures exposed to XC1, XC2, and XC3 environments was not available, the models were utilised to predict the carbonation depth under laboratory conditions. For this purpose, various sources, including references [73], [370], [426], [427], were utilised. The different inputs available for each exposure class are summarized in Annex 2, while a concise summary of the data is provided in Table IV-20. In total, 28, 38, and 84 experimental results and datasets of inputs were available for XC1, XC2, and XC3, respectively.

Table IV-20 Abstract of the tables provided in Annex 2 for carbonation depth computations.

Name	Q_K (kg/m³)	Q_L (kg/m³)	Q_S (kg/m³)	Q_V (kg/m³)	W_{eff}/B_{tot} (-)	Q_{Agg} (kg/m³)	RH_{env} (%)	T_{env} (°C)	t_{tot} (year)
XC1_1	260	0	0	0	0.63	1949	50	20.00	1.0
XC1_2	207	0	0	89	0.55	1908	50	20.00	1.0
XC2_1	105	0	244	0	0.50	1825	95	20.00	0.1
XC2_2	52	0	295	0	0.50	1821	95	20.00	0.1
XC3_1	300	0	0	0	0.57	1870	65	20.00	2.0
XC3_2	271	0	0	48	0.51	1868	65	20.00	2.0

In order to compensate the missing information and data from employed sources, the following was considered:

- The hydration model proposed by Lacarrière and Kolani [286], as discussed in Section I.4.5.3 with the modification presented in Section IV.3.2.3, enables determining the calcium carbonation capacity within the hydrate of the cementitious paste.
- It is assumed that the bulk density of cement is 3100 kg/m³ which allows for the computation of the paste volume. The fines content is considered equal to 0 kg/m³.
- The porosity accessible to water is computed using the model of Powers [282] detailed in Section I.4.5.2. In cases where aggregate properties are unavailable, a water absorption of 1.1% and a bulk density of 2600 kg/m³ were considered.
- The coefficients of natural carbonation are computed utilizing the ANN-CD1 model developed in Section IV.3.3.1.2.
- The following values are assumed to be constant:
  - $\Delta RH = 0.02\ \%$
  - $P_{CO_2} = 40\ Pa$
  - $\varepsilon_{air} = 1.5\ \%$
  - ToW_{10} is 0

Regarding the exposure class XC4, a comparison with experimental measurement from existing structures was afforded, under confidentiality agreement with the owner. It is important to note that most of the binders used are predominantly clinker-based, with low content of Supplementary Cementitious Materials (SCMs) when present. Available information from documents and meteorological data are reported in Annex 2. For example, the input data for the first structure, S1, are shown in Table IV-21. The structures are also taken into consideration in the probabilistic computation (refer to Section IV.4.2).

Table IV-21 Extract of the Input parameters of the different structures' parts available for the carbonation models' verifications in XC4, available in Annex 2.

Name	Cement type	Cement content (kg/m³)	W_{eff}/C (-)	RH_{env} (%)	T_{env} (°C)	ToW_{10} (-)	φ_c^w (%)	t_{tot} (year)
S1P1	CEM I	400	0.37	71	13.9	0.023	12.2	43
S1P2	CEM I	475	0.34				12.6	
S1P3	CEM I	490	0.36				14.5	

In order to compensate the missing information and data, the following was considered:

- The hydration model of Lacarrière and Kolani [286], is employed.
- Due to the absence of the datasheet for the cements, average values are employed for the clinker, slag, and fly ash content, as well as the oxides present in each of the constituents. This enables the determination of the CaO_r content, which impacts the use of the hydration model and ultimately the contents of the binder constituents. The paste volume is calculated based on the binder and water content, with a cement bulk density of 3100 kg/m^3.
- The natural carbonation rates ($Knat$, mm/years$^{-0.5}$) are estimated using the CFSA defined in Section IV.3.3.2.
- The curing parameters of $Cure$ = 0.6, k_c = 2, and a curing time (t_c) of 2 days are utilised.
- Average values are applied for the other parameters:
  - The total aggregate content $Q_{Agg} = 1800\ kg/m^3$
  - The bulk density of aggregate $\rho_{Agg} = 2600\ kg/m^3$
  - The entrained air $\varepsilon_{air} = 1.5\ \%$
  - Variation of the relative humidity $\Delta RH = 10\%$
  - Mean value of CO_2 partial pressure $P_{CO_2} = 40\ Pa$

The modelling results are compared to the experimental measurements conducted during the inspection of the structures exposed to XC4 environments. The measurements represent average values rounded to 2.5 mm. It is important to note that, at times, the minimum and maximum values differ from 10 mm, which may explain some of the discrepancies observed. However, the experimental measurements used for the other XC environments are more precise.

An example of results is presented in Figure IV-32 for the structural component S8P1. This visualization tool enables the user to select the most appropriate model for the case study from the available options. Additionally, comparing the results obtained from different models aids in identifying any issues related to parameter settings and assists the user in resolving them.

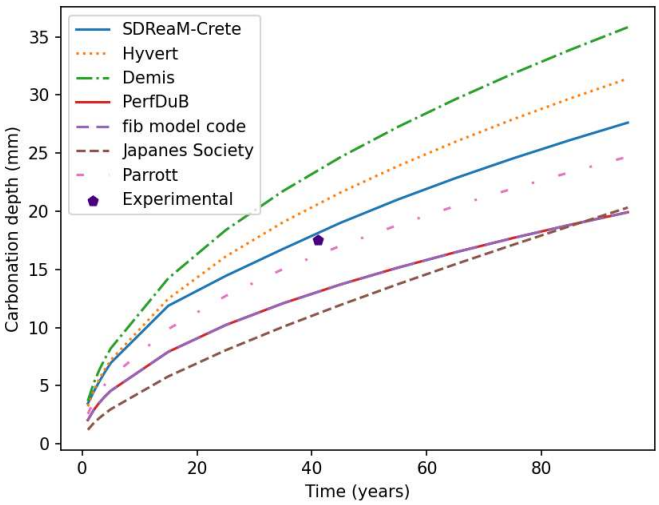

Figure IV-32 Application screenshot of the data visualisation for carbonation obtained for S8P1 in XC4.

The mean errors obtained for each exposure class are presented in Table IV-22, while the results from each model are plotted against the experimental measurements in Figure IV-33. In addition to that, a line with a slope of 1 is plotted on the figures, along with a variation of 5 mm around that line. This variation represents the minimum ΔC_{dev} value recommended by the national annex of the Eurocode 2.

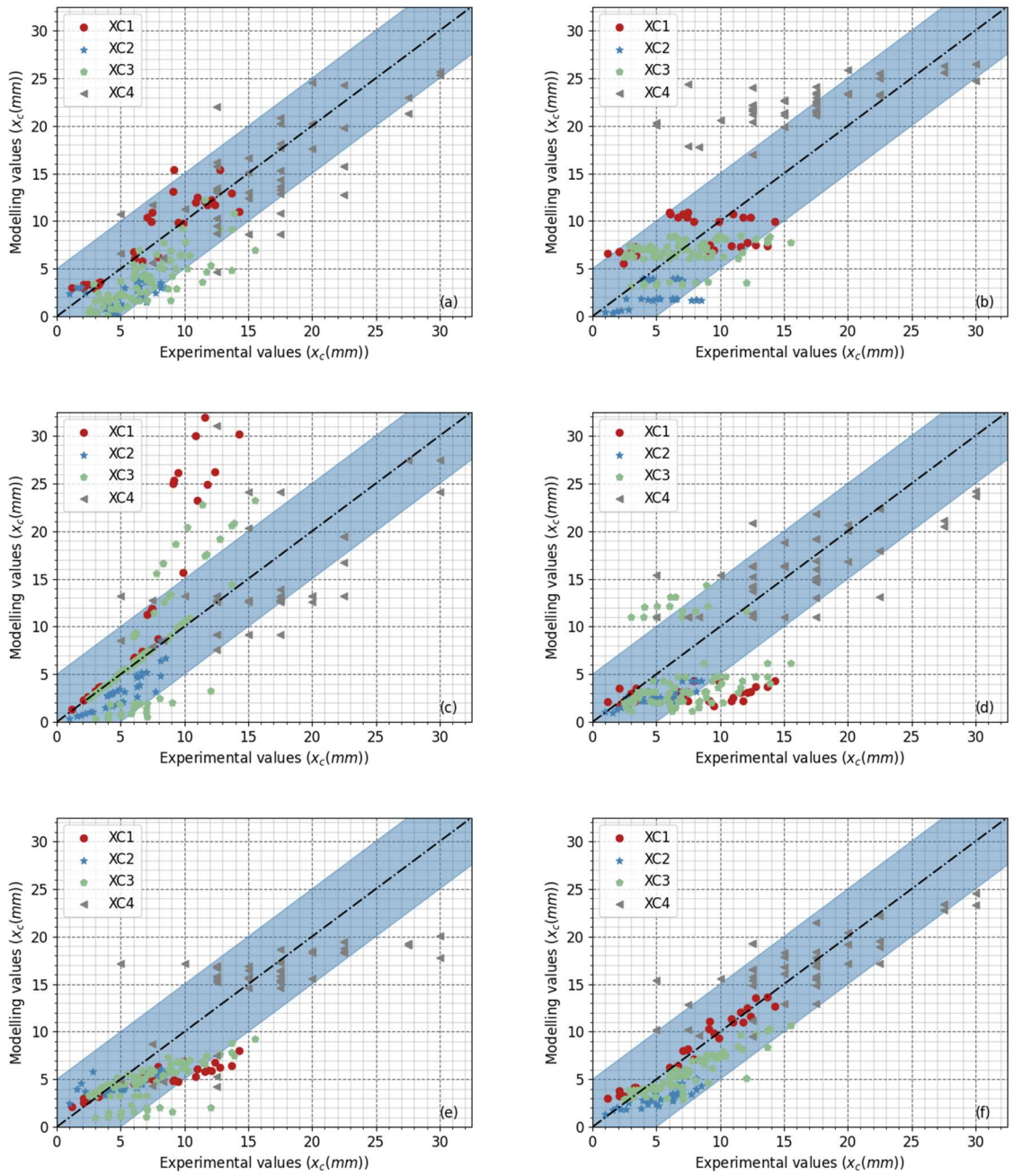

Figure IV-33 Modelling results vs. experimental results obtained in the different environments for (a) SDReaM-Crete surrogate model, (b) Demis model, (c) the PerfDuB model for carbonation, (d) the JSCE model, (e) the model of Parrott, (f) the mean of the models.

The results obtained from the comparison indicate that the SDReaM-Crete surrogate model and Parrott's model yield more satisfactory results in the XC1 environments. The other models result in higher average errors, which can be attributed to an incorrect consideration of the low relative humidity in XC1 environments. However, the mean of the five models yields very satisfactory results.

In the XC2 environment, the Parrott and the PerfDuB models produce better results based on the MAE and MRE values. Nonetheless, the MRE values obtained remain elevated, particularly for the PerfDuB model. SDReaM-Crete yields the lowest accuracy, likely due to an incorrect consideration of the carbonation in high relative humidity (certainly correlated to the functions used to compute the liquid permeability and the desorption isotherm). This can be observed in Table IV-22, where SDReaM-Crete

produces a negative mean error (ME), indicating that the predicted carbonation depth is lower than the experimental measurements. The proximity between the mean error and the mean absolute error suggests a minimal variation between the modelling and experimental results. Therefore, SDReaM-Crete likely requires a correction of -3 mm for the datasets considered in these studies [73], [370]. Other models show similar trends, indicating a lack of consideration for these conditions in the models.

Similar conclusions can be drawn for XC3 when considering the surrogate model based on SDReaM-Crete. Demis, Parrott, and PerfDuB models demonstrate slightly improved results. However, it should be noted that the overall mean of the models yields lower errors compared to each individual model.

For structures exposed to XC4 environments for a period of approximately 40 years, the models that yield better results are Parrott, SDReaM-Crete, and JSCE. The Demis model appears to be less suitable for the situations studied. It is worth mentioning that the overall mean of the different models results in the lowest errors.

All verifications conducted in XC1, XC2, and XC3 environments are based on low exposure durations (less than 2 years). Therefore, additional verifications should be carried out using results from structure inspections.

Table IV-22 Errors obtained for the different models on the different conditions.

XC class	Model	SDReaM-Crete surrogate model	Demis model	PerfDuB model	JSCE model	Parrott model	Mean of models
XC1 (28)	ME (mm)	0.88	0.65	8.37	-4.93	-2.82	0.42
	MAE (mm)	1.42	3.42	8.37	5.11	3.06	0.77
	MRE (%)	24.7	77.1	78.6	57.3	34.5	19.8
	Best option	X					X
XC2 (38)	ME (mm)	-3.01	-2.74	-1.65	-2.39	-0.73	-2.10
	MAE (mm)	3.32	2.74	1.73	2.39	1.41	2.15
	MRE (%)	66.7	51.3	38.1	41.7	36.0	37.8
	Best option			X		X	X
XC3 (84)	ME (mm)	-3.20	-0.57	0.70	-2.43	-2.41	-1.58
	MAE (mm)	3.24	2.30	2.87	4.39	2.58	1.68
	MRE (%)	48.3	37.7	36.6	61.9	34.1	21.4
	Best option		X	X		X	X
XC4 (44)	ME (mm)	-1.56	5.87	-1.34	-0.32	-1.42	-0.24
	MAE (mm)	3.69	6.53	4.20	3.56	3.77	3.20
	MRE (%)	24.9	58.5	30.0	27.2	27.0	25.8
	Best option	X			X	X	X
Total (194)	ME (mm)	-2.20	0.64	0.89	-2.31	-1.91	-0.98
	MAE (mm)	3.09	3.51	3.74	3.91	2.69	1.98
	MRE (%)	43.2	50.8	41.4	49.4	32.9	25.4

The results of this section demonstrate the limitations of the various models based on different environmental conditions. The comparisons provide insights into the average misestimations that can be expected from each model and highlight the precautions to be taken when predicting carbonation depth. The function computing the mean of the carbonation depth (using the 5 models) appears to be a suitable option for all exposure classes. Therefore, this function will also be employed in the probabilistic calculations conducted in Section IV.4.2 on structures exposed to XC4 environment.

Morris' sensitivity analyses are also utilised to determine the order of influence and global influence of each input parameter involved in the carbonation computation. All the parameters utilised in the models are listed in Annex 3, along with their minimum and maximum variations.

Based on the results of the sensitivity analyses, a summary table (Table IV-23) collects the most influential parameters of each model responsible for more than 90% of the global sensitivity. Additionally, a sensitivity analysis of the function calculating the average carbonation depth (of the five models) was conducted. The same variation ranges are employed as in the preceding sensitivity analyses.

Table IV-23 Most influent parameters of the carbonation models.

Model	Parameters
Carbonation model SDReaM-Crete	φ_c^w, t_{tot}, RH_{env}, T_{env}
PerfDuB model	K_{nat}, t_{tot}, RH_{env}
JSCI model	Q_K, W_{eff}, Q_S, t_{tot}
Parrott model	t_{tot}, CaO_r, RH_{env}
Demis model	RH_{env}, t_{tot}, P_{CO_2}
Means of models	t_{tot}, RH_{env}, K_{nat}, φ_c^w, $Binder$, Q_K

The obtained results demonstrate that the carbonation time (t_{tot}) is a highly influential parameter in the carbonation models. Additionally, the relative humidity exhibits a significant influence on the carbonation depth. Lastly, the material's resistance to carbonation, described by K_{nat} or as a function of other material parameters (φ_c^w, Q_K, CaO_r), is identified as the final parameter of utmost importance among the influential inputs.

Furthermore, the sensitivity analysis performed on the model that calculates the average of the five previous models validates the previous findings regarding the parameters' influence.

The results verifications presented may not be sufficient to qualify the models. It would certainly be useful to compare the distribution of the computed and experimental data. In addition to the mean value, the deviation and dispersion needs to be similar as well. Moreover, Monte Carlo simulations could have been used to measure the confidence ranges of each model, to check if they integrate the experimental values used.

IV.4.1.2. Chloride penetration models

We address herein chloride ingress in the XS and XD environments, as specified in the NF EN 206/CN (2022) standard. Additionally, the subclasses XS3e, XS3m, XD3f, and XD3tf, as introduced in the FD P18-480 (2022) document, are also taken into account when feasible.

The experimental measurements pertain to structures that were investigated during the PerfDuB project [428] or obtained from the Arcadis archives, under confidentiality agreements.

The meta-models developed in Section III.6.2 for the different exposure conditions are utilised accordingly. Furthermore, the model employed in the PerfDuB project [323] and the chloride penetration computation model from the *fib* code [20] are also utilised.

The default values for each environmental parameter are proposed in Table IV-24, based on the exposure classes considered. These values are utilised only when there is a lack of information available for a specific structure. However, obtaining mean relative humidity and temperature values from the meteorological station has always been feasible. Therefore, these values are specified for each case.

Table IV-24 Environmental parameters' default values defined for the different exposure class for chloride-induced corrosion.

Exposure class	C_{env} (g/L)	RH_{env} (%)	ΔRH (%)	T_{env} (K)	$t_{salting}$ (days)	Δx (mm)
XS1	16	75	10	289	-	5
XS2	22	100	0	289	-	0
XS3e	19	83	10	289	-	15
XS3m	22	83	20	289	-	20
XD3	10	75	20	289	5	15
XD3f	15	75	20	289	15	15
XD3tf	20	75	20	289	30	15

The Mean Absolute Error (MAE) and Mean Relative Error (MRE) are calculated for each set of experimental results. However, when the chloride concentration is equal to 0 wt.% binder, a relative error of 100% is obtained (except if the model predicted 0 as well). Therefore, a second MRE, denoted as MRE_{w0}, is calculated without considering the zero experimental values.

Next, the modeling results are graphed against the experimental measurements. A line originating from the origin with a slope of 1 is consistently plotted. Additionally, deviations of 0.2 wt.% binder are plotted around this central line to account for variations and were chosen arbitrarily.

IV.4.1.2.1. Reinforced concrete of the BHP 2000 project [428]

A consequential experimental campaign was conducted on reinforced concrete walls subjected to varying aggressive conditions. For the chloride exposure, two specific exposure classes were considered in this study:

- XS3m: This environment involves tidal variations, resulting in a mean annual relative humidity of 77.5 % and a mean temperature of 286.65 K. The remaining environmental parameters were kept at default values.
- XD3tf: In this environment, the concretes are exposed to annual deicing salt application. The mean annual temperature recorded is 281.3K, while the mean annual relative humidity is 74.5%.

In this investigation, a total of nine different concrete mixes were thoroughly examined, utilizing combinations of CEM I, fly ash, and silica fume. The specific compositions and properties of these mixes can be found in Table IV-25.

Table IV-25 Composition and properties of the BHP 2000 mixes.

Name	B (kg/m³)	W_{eff}/B_{tot} (-)	F_{SF} (wt.% binder)	F_V (wt.% binder)	φ_c^w (%)	$D_{rcm,90}$ (10^{-12} m²/s)	ae_{480} (-)
M25CV	243	0.77	0	20	15.7	9.5	0.52
M25	230	0.84	0	0	16.1	30	0.30
M30CV	318	0.52	0	30	12.8	1.7	0.60
M50CV	404	0.45	0	20	15	1.8	0.52
M50	410	0.48	0	0	14.7	8.7	0.30
M75	461	0.32	0	0	11.4	5.6	0.30
M75FS	382	0.36	5	0	10	0.8	0.36
M100FS	453	0.3	9	0	8.4	0.3	0.40
M120FS	516	0.23	12	0	7.4	0.04	0.40

Most of the required input properties were already available. However, the ageing factor (ae) and the hydrate content were estimated using the FD P18-480 (2022) formula (Equation II.7, [340]) and the hydration model proposed by Lacarrière and Kolani (Sections I.4.5.3 and IV.3.2.3, [286]).

The concentrations of free chloride were measured at depths ranging from 0 to 80 mm after 19 years of exposure. The chloride concentration was calculated using various models for each data point, resulting in the mean errors presented in Table IV-26.

Table IV-26 Errors obtained with the different models on the BHP 2000 measurements.

Model		*fib* model code	PerfDuB model	SDReaM-Crete meta-models	Mean of models
XS3m (66 values)	MAE (wt.% cement)	0.626	0.483	0.473	0.33
	MRE (%)	43	39	40	31
	MRE_{w0} (%)	42	36	36	29
XD3tf (44 values)	MAE (wt.% cement)	0.099	0.129	0.142	0.096
	MRE (%)	33	41	41	35
	MRE_{w0} (%)	29	41	33	32

The provided graphics present an overview of the distribution of results, comparing the modelling and experimental values for each model.

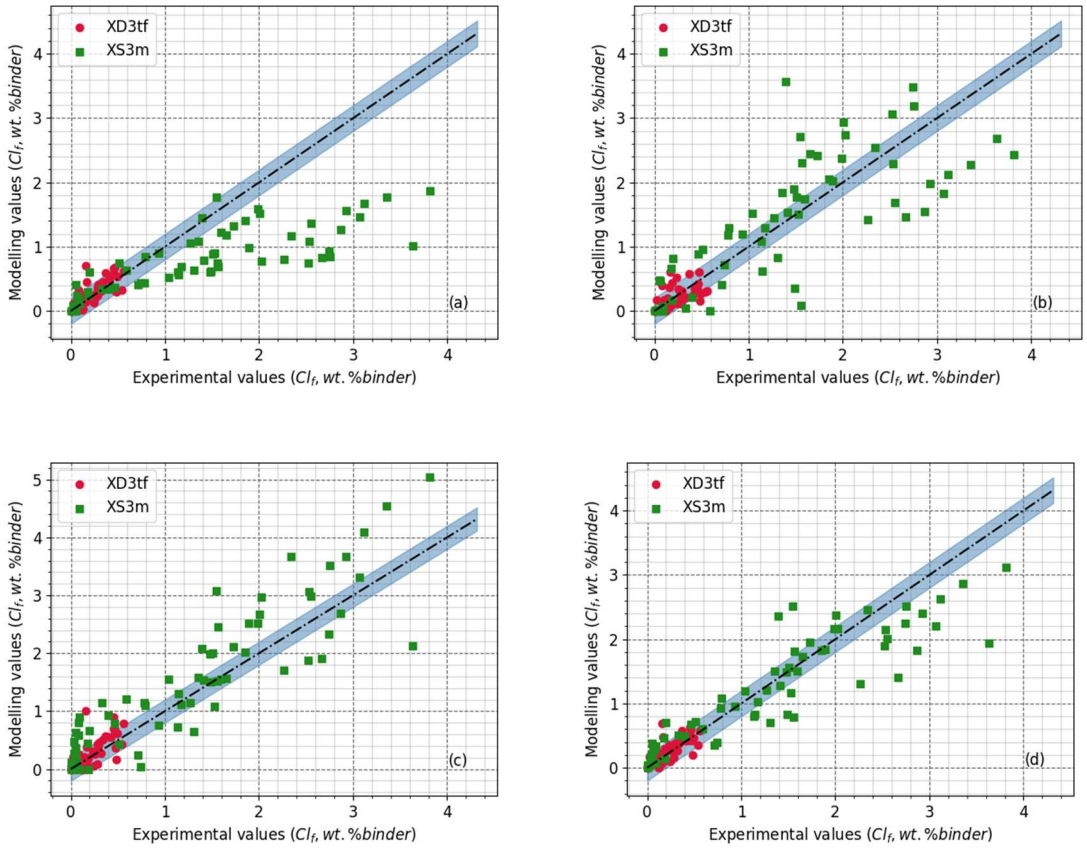

Figure IV-34 Comparison of the different model on the BHP 2000 results for XS3 and XD3. (a) fib model code, (b) PerfDuB model, (c) SDReaM-Crete meta-models, (d) Mean of the different models.

Different observations can be made on these graphics:

- The *fib* code model appears to inaccurately predict certain values for the XS3m environment. The concentration values computed with this model are lower than those computed with the other models, leading to significant underestimations, particularly for low depth where a high chloride concentration can be obtained experimentally. However, the predictions of concentrations in the XD3tf environment are more accurate than those obtained with the other model, as shown by the lower errors in Table IV-26.
- The PerfDuB model predicts concentration in XS3m environment with higher precision. However, substantial variations can be observed around the desired line with a slope of 1 for all measured depths. In the XD3tf environment, the predictions are less accurate than those of the *fib* code model, resulting in higher errors.
- More conservative results are obtained with the surrogate-model based on SDReaM-Crete. The mean errors obtained in the XS3m environment are close to those obtained with the PerfDuB model. Nevertheless, it can be observed in Figure IV-34 that the model predicts excessively high concentrations for high depths, where chloride concentrations are close to 0 wt.% binder. In the XD3tf environment, the model adequately predicts chloride concentrations, even though the values are generally higher than those obtained experimentally.
- The mean concentrations of the three models are computed. The results obtained demonstrate lower mean errors and better predictions compared to the individual models for both XS3m and XD3tf environments. The conservative results of SDReaM-Crete likely offset the results of the *fib* code model, resulting in a good approximation of the experimental concentration values. However, the results obtained for XS3m are non-conservative, leading to lower values than expected.

IV.4.1.2.2. Structures investigated in the PerfDuB project [428]

Two specific structures investigated in the framework of the PerfDuB project were investigated:

- The bridge of Ré Island (France, Atlantic Ocean): This structure serves to connect the island to the mainland of France and is directly exposed to the ocean. For this structure, only inspection data of fully submerged concretes were available, which led to categorize it under the XS2 exposure class (T_{mean} = 285 K).
- The bridge of Pirou (France, English Channel): This structure is considered to be exposed to deicing salts and marine airborne salt, owing to its close proximity to the English Channel. Therefore, it was assigned to the XD3f and XS1 exposure classes ($T_{mean} = 284\text{K}$, $RH_{mean} = 80\%$, $\Delta RH = 20\%$). In order to account for the cross-influence of the chloride sources (marine and non-marine), an increase of the default Cl_{env} up to 20 g/L was chosen arbitrarily.

The compositions and main properties of the different concrete mixes are exposed in Table IV-27.

Table IV-27 Compositions and properties associated to the concrete of the different PerfDuB structures.

Name	$Binder$ (kg/m^3)	W_{eff}/B_{tot} (-)	Fs (%)	$D_{rcm,90}$ (m^2/s)	φ_c^w (%)	ae_{480} (-)
Re	370	0.56	10	6.8×10^{-12}	12.1-15.3	0.32
Pirou	400	0.46	0	9.0×10^{-12}	11.9	0.3

One issue addressed in this study is the lack of comprehensive data on the properties of different zones within the structures. With only one or two measurements of the properties, the variability of composition and parameters is not fully captured in the predictions, which may contribute to the observed errors.

As previously, most of the parameters were available, but the ageing factor (ae) and the hydrate content were estimated using the FD P18-480 (2022) formula (Equation II.7, [340]) and the hydration model proposed by Lacarrière and Kolani (Sections I.4.5.3 and IV.3.2.3, [286]).

The computations performed using various models resulted in the mean errors presented in Table IV-28.

Table IV-28 Errors obtained with the different models on the measurements for the PerfDuB structures.

Model		*fib* model code	PerfDuB model	SDReaM-Crete meta-models	Mean of models
XS2 (23 values)	MAE (wt.% cement)	0.255	0.174	0.343	0.159
	MRE (%)	44	37	42	26
	MRE_{w0} (%)	44	37	40	26
XD3/XS1 (44 values)	MAE (wt.% cement)	0.121	0.091	0.203	0.127
	MRE (%)	39	45	48	45
	MRE_{w0} (%)	36	42	46	43

A graphical representation of the results is presented in Figure IV-35. The results demonstrate the following:

- The *fib* code model accurately predicts the results in XD3f environment. However, like the XS3m environment, the model results in XS2 environments are significantly lower than the experimental measurements.
- The PerfDuB model provides good predictions for the chloride concentration in both XS2 and XD3f environments. However, there are still discrepancies between the modelling and experimental results, particularly when predicting low concentrations in XS2.
- The SDReaM-Crete surrogate models generally yield conservative values. This model exhibits the highest MAE (Mean Absolute Error) for both XS2 and XD3f environments.
- The mean of the results yields reliable predictions, and even outperformed the PerfDuB model in XS2 environments.

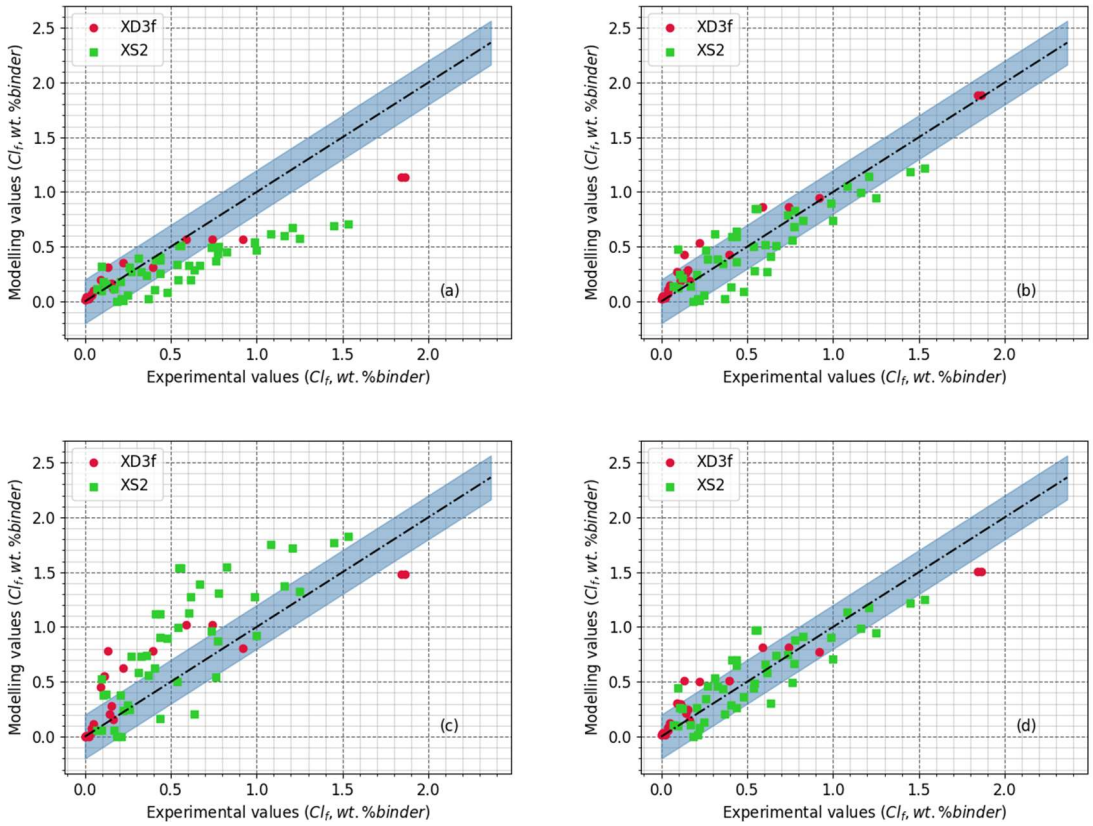

Figure IV-35 Comparison of the different model on the PerfDuB results for XS2 and XD3f. (a) fib model code, (b) PerfDuB model, (c) SDReaM-Crete meta-models, (d) Mean of the different models.

IV.4.1.2.3. Arcadis' maritime structure

Data on a maritime structure directly exposed to the sea were available and subjected to a confidential agreement. The exposure classes considered were XS2 (T_{mean} = 284.6 K) and XS3e (T_{mean} = 287 K, $HR_{mean} = 79$ %).

The composition and parameters obtained from the studied concretes are summarized in Table IV-29.

Table IV-29 Composition and properties of the Arcadis' maritime structure.

Name	Cement type	φ_c^w (%)	D_{rcm} (m^2/s)	ae_{480} (-)	CH (mol/m^3)	CSH (mol/m^3)	Afm (mol/m^3)	Aft (mol/m^3)	t_{ini} (years)
S1	CEM V/A (S-V)	15.7	3.4×10^{-12}	0.59	306	1820	206	191	41
S2	CEM III/A		9.9×10^{-12}	0.3	1071	1602	397	299	34
S3	CEM I		2.6×10^{-12}	0.42	230	1762	160	163	17

The available data for this study consisted of the cement type, which was determined through Scanning Electron Microscope (SEM) analysis at the same time of inspection of the structure. Assumptions were made for each zone as follows:

- The total binder content was assumed to be 350 kg/m^3. This assumption is justified based on the construction period.
- The W_{eff}/B_{tot} ratio was taken to be 0.5. This assumption is also justified based on the construction period.

- Regular aggregates with a total content of 1800 kg/m^3 were considered, with a bulk density of 2600 kg/m^3 and an average water absorption (WA) of 1.1%.
- The initial chloride content was assumed to be 0 wt.% of the binder.
- The curing factor for SDReaM-Crete was assumed to be 0.9 (structure in an environment with high relative humidity or immersed in water).

To estimate the different parameters, various models were utilised:

- The model of Powers [282] is used to estimate φ_c^w.
- The model of Lacarrière and Kolani [286] is used for the hydrate contents.
- The Equation II.7 from the FD P18-480 (2022) is used to compute the ageing factor.
- The CFSA (refer to Section IV.3.3.2) is used to define the value of D_{rcm} used for each zone.

The results obtained with the different models are plotted in Figure IV-36, while the mean errors are reported in Table IV-30.

Table IV-30 Errors obtained with the different models on the measurements for the Arcadis marine structure.

Model		*fib* model code	PerfDuB model	SDReaM-Crete meta-models	Mean of models
XS3e (29 values)	MAE (wt.% cement)	0.093	0.090	0.110	0.088
	MRE (%)	61	61	76	63
	MRE_{w0} (%)	40	37	39	40
XS2 (14 values)	MAE (wt.% cement)	0.278	0.156	0.213	0.195
	MRE (%)	57	48	67	55
	MRE_{w0} (%)	39	24	31	35

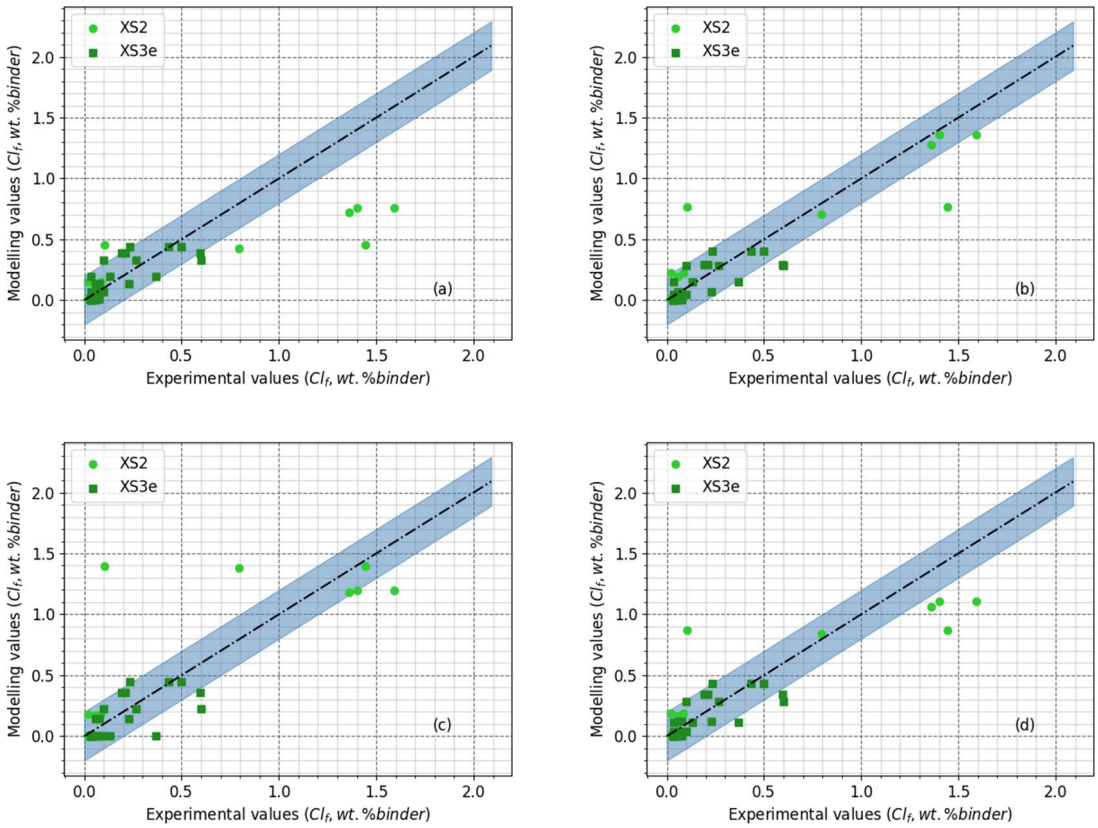

Figure IV-36 Comparison of the different model on Arcadis' maritime structure for XS2 and XS3e. (a) fib model code, (b) PerfDuB model, (c) SDReaM-Crete meta-models, (d) Mean of the different models.

The comparisons of the modelling and experimental results show different trends:

- Firstly, the *fib* code model in the XS3e environment exhibits a good predictive capability, with low absolute errors. However, in the XS2 environment, the values predicted by the model are generally lower than the experimental values.
- Furthermore, the PerfDuB model provides an even better prediction for both XS2 and XS3e environments, with differences below 0.2 wt.% of binder.
- On the other hand, the surrogate models SDReaM-Crete yield less satisfactory results, as they display higher errors.
- However, when considering the mean of the three models, the overall performance is still satisfactory. The mean errors are comparable to those of the PerfDuB model, albeit slightly higher in the case of the XS2 environment. This discrepancy can be attributed to the inaccurate values obtained from both the SDReaM-Crete surrogate model and the *fib* model code.

IV.4.1.2.4. Arcadis' road structures exposed to deicing salts

Chloride ion profiles were evaluated on the road structures examined in Section IV.4.1.1 to determine carbonation depth. The awareness of the structures' locations enabled estimation of the frequency of deicing salt application. Therefore, most structures can be categorized as being in environment XD3. The composition and properties of the available concrete mixes, as well as the environmental conditions considered, are presented in Table IV-21.

The modelling results yielded the average errors documented in Table IV-31. All the values obtained are plotted in Figure IV-37.

Table IV-31 Errors obtained with the different models on the measurements for the Arcadis' road structures.

Model		*fib* model code	PerfDuB model	SDReaM-Crete meta-models	Mean of models
XD3 (247 values)	MAE (wt.% cement)	0.201	0.187	0.188	0.157
	MRE (%)	31	30	31	27

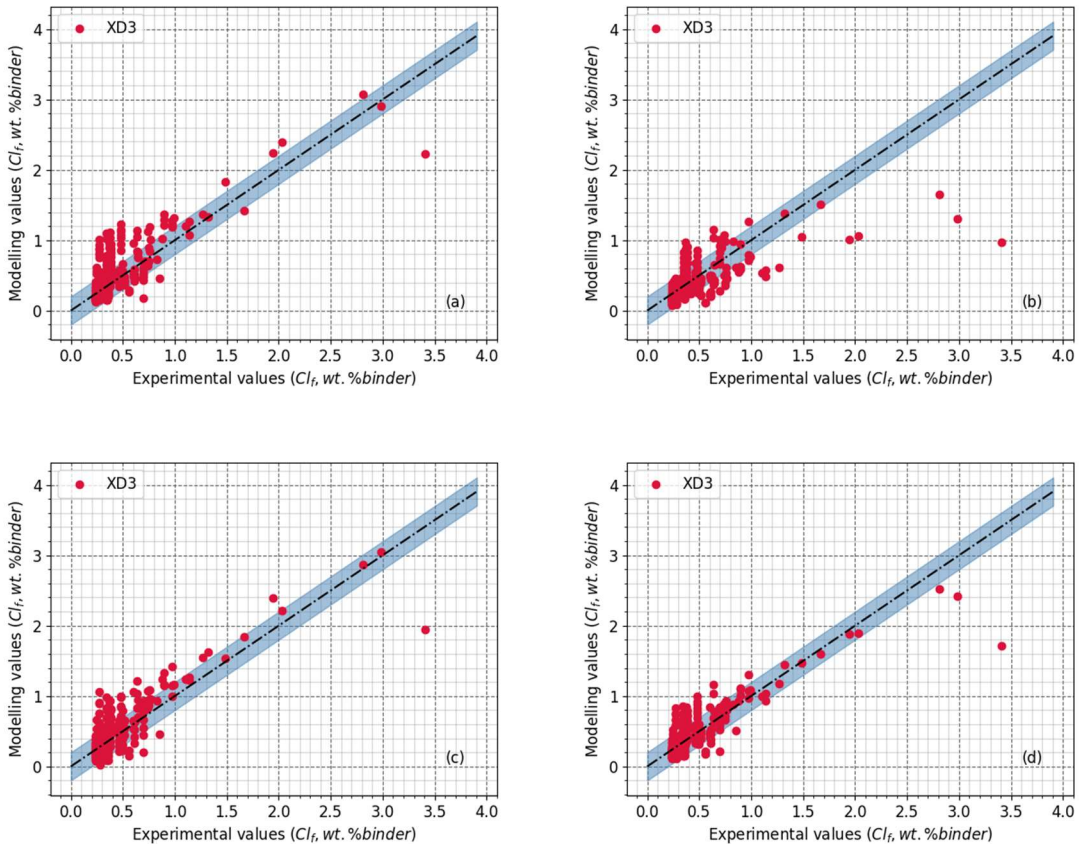

Figure IV-37 Comparison of the different model on Arcadis' bridges for XD3. (a) fib model code, (b) PerfDuB model, (c) SDReaM-Crete meta-models, (d) Mean of the different models.

The results obtained on the structures exposed to XD3 environments demonstrate the following:

- The *fib* code model generally overestimates the concentration values, indicating a conservative approach. This trend is particularly pronounced for high concentrations.
- The PerfDuB model displays fewer conservative predictions compared to the other models, especially for high concentrations.
- The SDReaM-Crete surrogate model yields conservative predictions.
- Combining the predictions from all three models leads to higher precision in the results. This approach yields the lowest mean errors, as presented in Table IV-31.

It should be noted that the measured concentrations values are low, which can be attributed to the specific environmental conditions under consideration. Additionally, there is a high variability observed among all the prediction models, resulting in a significant deviation of results ranging from 0 to 0.75 wt.% binder. This variability is likely due to an inaccurate representation of the environmental conditions, particularly in terms of chloride concentration. Estimating the precise concentration values to be applied is challenging, as there are usually no annual measurements available for structure exposed to deicing salts. Consequently, the XD3 exposure classes are less precise than the XS2 and XS3 classes in this regard. It is plausible that the different structures considered in this section were exposed

to varying periods of salting, with different annual variations, which were not taken into account in the modeling process and thus explaining some of the obtained errors.

IV.4.1.2.5. Conclusions

Table IV-32 summarizes the efficiency of each model according to the exposure class considered.

Table IV-32 Validation results obtained on the different models according to the exposure class.

Exposure class	Criteria	*fib* code model	PerfDuB model	SDReaM-Crete meta-models	Mean of the models
XS2 (37 values)	MAE (wt.% binder)	0.264	0.167	0.294	0.173
	MRE_{w0} (%)	42	32	37	29
	Recommended method		X		X
XS3e (29 values)	MAE (wt.% binder)	0.093	0.090	0.110	0.088
	MRE_{w0} (%)	40	37	39	40
	Recommended method		X		X
XS3m (66 values)	MAE (wt.% binder)	0.626	0.483	0.473	0.33
	MRE_{w0} (%)	42	36	36	29
	Recommended method				X
XD3 (291 values)	MAE (wt.% binder)	0.189	0.172	0.190	0.152
	MRE_{w0} (%)	32	32	33	29
	Recommended method				X
XD3tf (44 values)	MAE (wt.% binder)	0.099	0.129	0.142	0.096
	MRE_{w0} (%)	29	41	33	32
	Recommended method	X			X
Total (467 values)	MAE (wt.% binder)	0.242	0.207	0.229	0.170
	MRE_{w0} (%)	34	34	34	30

The results indicate that better predictions can be achieved by considering the mean of the three models used. By using all the models, an equilibrium can be found, although the modelling results obtained using this method are sometimes lower than the experimental ones.

One major challenge that contributes to elevated errors in predicting the durability of structures is the lack of data available for most concrete zones. Consequently, the values obtained from core samples taken from one location of the structure can only offer an approximation of values for other parts of the structure. This limitation leads to imprecise estimations. It is crucial to consider this variability in the computations, which justifies the use of probabilistic computation techniques to accurately predict the durability of the structure.

The *fib* model code encountered difficulties in estimating high concentrations, which were addressed in the PerfDuB model by introducing an enrichment factor. This explains why certain cases, such as in the XS3m environment, yield high errors. However, the model can still be effective in predicting low concentrations at greater depths, as the value of interest is the one obtained at the reinforcing bar surface. The model is deemed efficient when the concrete cover exceeds 30 mm. Another approach could consist in measuring the efficiency of the models in computing adequately the range of critical concentrations leading to corrosion onset.

The PerfDuB model demonstrates the lowest mean errors compared to the other two models, except for XD3tf environments, where the *fib* model code yielded better results. This highlights the potential of analytical models for operational applications when finite element models are not easily applicable.

SDReaM-Crete surrogate models exhibit lower precision compared to alternative computations. This could be attributed to various factors affecting the calculations:

- First, the absence of variability consideration may have a greater impact on the surrogate models. For example, input data predicted by a hydration model, which heavily relies on composition parameters, may be required. However, the exact composition is often unknown, leading to uncertainties in the estimation of hydrates content. Additionally, it has been demonstrated in Section IV.3.2.3 that the hydration model has limitations and may introduce errors in certain cases, even when the precise composition is known. However, the sensitivity analyses (refer to Table IV-33) show that these parameters have certainly few impacts on the results.
- Second, uncertainties also arise from the initial finite element model used for training the meta-model. The method employed to estimate liquid permeability and desorption isotherm, with functions of porosity and the W_{eff}/B_{tot}, may be responsible for errors when the convective process influences chloride ingress. This issue could be addressed by directly utilizing the finite element model or adopting alternative approaches for estimating these parameters, but it would require the acquisition of experimental data on structure.
- Third, the convection may not be adequately accounted for in the model. Notably, this phenomenon primarily depends on relative humidity and its variations, while the model only considers annual averages of these values. This likely explains the excessive chloride concentrations observed in most cases with SDReaM-Crete when XS3 and XD3 exposure classes are considered. To overcome this problem, introducing weekly or daily variations in hydrologic conditions, which better reflect the real environment, could be beneficial. However, such an approach would significantly increase computational time and was not feasible within the scope of this study.

Morris's sensitivity analyses were conducted on the different models to identify the key parameters. The selected parameters and their corresponding ranges of variation are presented in Annex 4. The influential parameters, responsible for 90% of the global sensitivity, are listed in Table IV-33.

Table IV-33 Parameters responsible for 90% of the influence on the results in the models used for chloride ingress computation.

Exposure class	*fib* model code	PerfDuB model	SDReaM-Crete surrogate models	Mean of models
XS1-XS3	D_{rcm}, Cl_{env}, CC	$D_{rcm}, \varphi_c^w, Binder, Cl_{env}$	$\varphi_c^w, CC, Cl_{env}, D_{rcm}$	$D_{rcm}, Cl_{env}, \varphi_c^w, Binder$
XS2	D_{rcm}, CC, Cl_{env}	$D_{rcm}, \varphi_c^w, Binder, Cl_{env}$	$CC, ae, Cl_{env}, D_{rcm}, t_{tot}$	D_{rcm}, CC, Cl_{env}
XD3	D_{rcm}, Cl_{env}, CC	$D_{rcm}, \varphi_c^w, Binder, Cl_{env}$	CC, t_{tot}, HR_{mean}	$D_{rcm}, Cl_{env}, Binder, \varphi_c^w, CC$

The results demonstrate different trends among the models analysed:

- The *fib* code model relies mainly on three parameters regardless of the exposure conditions: D_{rcm}, representing the material properties; Cl_{env}, accounting for the environment; and CC, reflecting the system design. However, this model has limitations, particularly in its consideration of the convective process, which is only taken into account through the Δx parameter. It was expected that the exposure time, t_{tot}, would be among the influential parameters for this model.
- In contrast, the PerfDuB model is primarily influenced by four parameters, irrespective of the exposure class. D_{rcm} and Cl_{env} have also a high influence in this model, but the binder content and φ_c^w also have a significant impact. This is likely due to the computation of the convective zone and the enrichment factor in this model. The influence of the concrete cover is relatively

low for the chosen range of variations, and t_{tot} does not figure among the most influential parameters.

- The SDReaM-Crete model displays a different order of influence. The environmental chloride concentration is present in the XS surrogate models but absent in the XD3 surrogate model. This discrepancy may be attributed to an excessive washing of chloride ions in the initial model, causing a substantial drop in concentration regardless of the Cl_{env} value applied during the short period of t_{salt}. However, this phenomenon does not appear in the previous results shown. The difference between XS2 and XS1-XS3 environments reflects a change in the governing phenomenon of chloride ingress. In fully submerged structures, diffusion of chloride ions is the primary mechanism and is defined by D_{rcm} and ae in the model. Conversely, in concrete subjected to wetting-drying cycles, convection of chloride ions becomes more significant than diffusion within the variation range of this sensitivity analysis. This explains the inclusion of φ_c^w as one of the controlling parameters for convection.

It should be noted that the sensitivity analyses for SDReaM-Crete were conducted on a specific surrogate model for each exposure condition, while only one model was used for all environmental conditions in both analytical models. This may explain the larger differences in influential parameters obtained using SDReaM-Crete.

IV.4.1.3. Corrosion models

As a conservative viewpoint, corrosion propagation is assumed to begin as soon as corrosion has been initiated. Due to the different nature of corrosion propagation, carbonation and chloride-induced corrosion are not considered with the same models. However, the overall computational framework remains the same. Initially, the corrosion current (i_{corr}, µA/cm^2) is calculated using a first model. The average value obtained from this calculation is then used to determine the time of propagation leading to a critical point, which is the formation of the first crack in the concrete cover.

The analytical models employed in this section for i_{corr} computation do not directly account for the oxygen concentration at the reinforcing bar surface, excepted for Nguyen's model [261]. Furthermore, Yalcyn et al.'s model [271] does not take into consideration the saturation degree or relative humidity. Therefore, there is no factor considering the accessibility of oxygen and water content at the steel surface. To address this limitation, the surrogate model presented in Section III.6.2.4 is utilised to calculate the saturation degree at the reinforcing bar surface. This, in turn, enables the estimation of the probability of active corrosion (P_{ac}, as shown in Equation III.81), which is integrated into Yalcyn et al.'s model as a multiplication factor affecting i_{corr}. This modification requires the computation of the values at each time-step, leading to an increase of the computational cost. The value of P_{ac} is also used as input in the model of Nguyen.

Even if the parameter P_{ac} is not applied to all models, each one considers the saturation degree at the reinforcing bar surface. Hence, the SDReaM-Crete-based surrogate model is used for each model to allow the transition between the relative humidity of the environment (RH_{env}) and the saturation degree (Sr) of the concrete material at the steel surface (thus considering the concrete cover CC value). A CEM I-based regular concrete ($Binder$ = 380 kg/m^3, W_{eff}/B_{tot} = 0.5) was considered for the computations of the saturation degree.

IV.4.1.3.1. Carbonation-induced corrosion

In the case of carbonation induced corrosion, two model are chosen for i_{corr} computation:

- The model developed by Nguyen [261] used in the work of Schmitt [6] who verified its functioning on the results of Vu [165]. The model is described in Section I.4.4.1 **(NG)**.
- The model used during the PerfDuB project based on [266] and detailed in Annex 4 **(PE_XC)**

Then, the propagation time is computed using one of the following models which compute the corrosion time require to cause the cracking of the concrete cover:

- The model proposed in the PerfDuB project based on [429] and detailed in Annex 4 **(PE_XCcr)**.
- The model of Maaddawy developed in [430] and detailed in Annex 4 **(MA)**.
- The model of Morinaga detailed in [193] and presented in Annex 4 **(MO)**.

The different parameters of the models are presented in Table IV-34 for the i_{corr} estimation and in Table IV-35 for the propagation time computation. These models are generally fitted on accelerated test and do not always represent adequately the real phenomenon occurring in a structure. The results of the sensitivity analyses are presented in a following Section (IV.4.1.3.3) and compared to the results obtained on the models for chloride-induced corrosion propagation.

Table IV-34 Variation ranges of the models' parameters for the corrosion current computation in XC environments.

Parameter	Symbol	Minimal boundary	Maximal boundary	Reference	Model
Propagation time (years)	t_{prop}	1	70	Arbitrarily chosen	NG
Saturation degree (-)	Sr	0.35	1	-	NG, PE_XC
Average temperature (°C)	T_{env}	5	25	Weather station	PE_XC
Electrical resistivity (Ohm.m)	Re	20	1500	Database	PE_XC
Ratio of corrosion products diffusing (-)	α_{TM}	0.05	0.4	Arbitrarily chosen	NG
Probability of active corrosion (-)	P_{ac}	0.2	1	Arbitrarily chosen	NG
Concrete cover (mm)	CC	10	80	-	NG

Table IV-35 Variation ranges of the models' parameters for the propagation time estimation in XC environments.

Parameter	Symbol	Minimal boundary	Maximal boundary	Reference	Model
Reinforcing bar diameter (mm)	D_{rebar}	8	36	-	All
Concrete cover (mm)	CC	10	80	-	All
Corrosion current (µA/cm^2)	i_{corr}	0.01	2	[166]	All
Compressive strength of concrete (MPa)	f_c	15	105	Database of results	MA

A comparison with experimental measurements was not feasible due to the lack of available data on structures. Accurate tracking of structures is crucial for detecting the timing of depassivation and the initiation of corrosion propagation. Nevertheless, various computations were performed using the models.

Initially, propagation times up to 50 years were assumed to calculate the average values of i_{corr}, aiming to evaluate the evolution of this parameter as predicted by Nguyen's model (refer to Figure IV-38). These values were then compared with the constant values obtained from the PerfDuB model, which does not consider the propagation time as an input. A concrete cover of 40 mm is considered for the computation of the saturation degree.

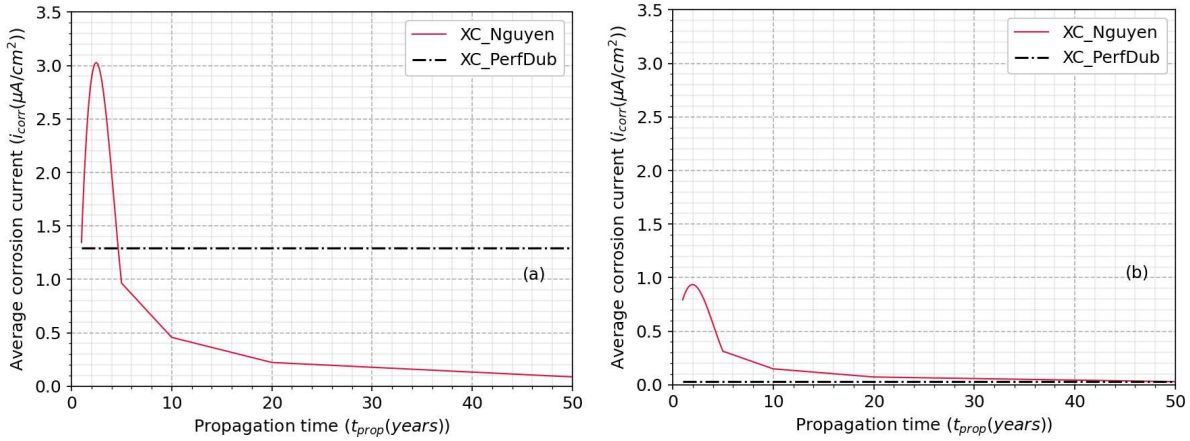

Figure IV-38 Average value of corrosion current as a function of total propagation time for (a) HR_{env} = 95 % and (b) HR_{env} = 50 %.

Based on the results presented in Figure IV-38, it is obvious that the two corrosion models employed exhibit distinct behaviour. The PerfDuB model yields a lower corrosion current value compared to the Nguyen model at a relative humidity of 50%. However, in environments with high relative humidity, the model of Nguyen provides lower current values than the PerfDuB model.

This discrepancy certainly indicates that the PerfDuB model was specifically calibrated to derive an average propagation time. In environments characterized by a relative humidity of approximately 95%, the propagation time considered is typically short, around 5 years [323]. Conversely, in dry environments, the propagation time can extend to 45 years or beyond. Consequently, the overlapping observed in Figure IV-38 (a) can be attributed to this aspect and the propagation time utilised in fitting the PerfDuB model. The low corrosion current value depicted in Figure IV-38 (b) corresponds to the incorporation of a lengthy propagation time (where the overlapping between the two models takes place after 50 years of corrosion propagation).

In order to simplify the subsequent computations, only the PerfDuB model was utilised to calculate the corrosion current in this study. The use of the Nguyen model, which necessitates knowledge of the propagation time, would have required the application of a time-consuming dichotomy method.

To determine the propagation time of corrosion prior to the emergence of the initial crack in the concrete cover, the default conditions outlined for the XC exposure classes (refer to Table IV-4 Section IV.3.1) were adopted. The prescribed values provided in the PerfDuB documentation were compared to the values obtained from the three available models (PE_XCcr, MO, MA). Analyses were performed considering a reinforcement bar diameter of 20 mm and a compressive strength of 45 MPa. The concrete cover thicknesses utilised were those specified by the EC2 for a structure class S6 (25 mm for XC1, 35 mm for XC2 and XC3, and 40 mm for XC4). The electrical resistivity values employed for the corrosion current calculations were 50, 100, and 175 Ohm.m, aiming to obtain the most conservative values permitted by the modulation on electrical resistivity. The resulting corrosion currents are presented in Table IV-36, while the propagation times obtained using the three different models and conditions are displayed in Table IV-4.

Table IV-36 Corrosion current (µA/cm2) computed using the PerfDuB's model for carbonation induced corrosion.

	i_{corr} (µA/cm²)			
Resistivity (Ohm.m)	XC1	XC2	XC3	XC4
< 100	0.155	2.898	0.596	0.313
100 – 175	0.078	1.449	0.298	0.156
> 175	0.044	0.828	0.170	0.089

Table IV-37 Propagation times associated to each XC classes for different concrete electrical resistivity values according to the models and considering the corrosion current computed with PerfDuB's model.

	t_{prop} (years)											
Resistivity (Ohm.m)	XC1			XC2			XC3			XC4		
Model	PE	MA	MO	PE	MA	MO	PE	MA	MO	PE	MA	MO
< 100	6.4	3.5	7.6	0.4	0.2	0.6	2.0	1.1	2.8	4.0	2.3	6.1
100 – 175	12.8	7.0	15.2	0.8	0.5	1.1	3.9	2.2	5.6	8	4.6	12.1
> 175	22.5	12.3	26.7	1.4	0.8	2.0	6.8	3.9	9.8	14	8	21.3

It can first be noted that the three different models compute propagation time with fairly similar order of magnitude.

However, the computed values of propagation time are significantly lower than those specified in the PerfDuB documentation ([323] see Table IV-4 in Section IV.3.1). Two main factors contribute to the discrepancy between the computed values and those recommended.

- Firstly, the conservative consideration of electrical resistivity results in a reduction of the maximum propagation time that the reinforced concrete system can sustain. However, even when considering higher electrical resistivity, it is not possible to obtain equivalent values.
- Secondly, the models employed in this study were calibrated under accelerated test conditions, assuming aggressive corrosion propagation and favourable environmental conditions for propagation, while disregarding any dormant period. Consequently, extremely low propagation times were predicted. The sensitivity analysis of the mechanical models indicates that i_{corr} is the most influential input on the results (refer to Table IV-43). Therefore, the precise prediction of i_{corr} is a major concern in these models. The predicted values are notably higher than the current values obtained, resulting in overly conservative predictions for the propagation time. As a result, Table IV-38 presents the corrosion current values that lead to the expected propagation time, which are lower than those previously obtained in Table IV-36.

Table IV-38 Corrosion current required to obtain the values of propagation time prescribed by the PerfDuB recommendations, with the different models.

	i_{corr} (µA/cm²)											
Resistivity (Ohm.m)	XC1			XC2			XC3			XC4		
Model	PE	MA	MO	PE	MA	MO	PE	MA	MO	PE	MA	MO
< 100	0.009	0.01	0.004	0.1	0.11	0.06	0.05	0.06	0.03	0.21	0.23	0.12
100 – 175	0.009	0.01	0.004	0.07	0.08	0.04	0.04	0.05	0.02	0.05	0.06	0.03
> 175	0.009	0.01	0.004	0.04	0.06	0.03	0.03	0.04	0.02	0.03	0.04	0.02

Even though a complete follow-up was not conducted, corrosion current values were obtained on structures during the PerfDuB project. For instance, the Blondel Bridge, a reinforced concrete structure exposed to XC4/XS1 environments for 50 years, showed instantaneous corrosion current ranging from 0.003 to 0.120 µA/cm² [428]. These values, although not directly comparable with the average values computed in Table IV-38, provide an estimate of the expected values for this type of structure and environment. The concrete used is CEM I-based and likely has low electrical resistivity. Hence, the value of 0.313 µA/cm² obtained with the PerfDuB model for estimating the corrosion current is likely overestimated and indicates the limitation of the model.

To improve the accuracy of the models, it is essential to gather more numerous and reliable data on corrosion propagation behaviour in structures. However, this is a recurring challenge due to the

variability of the phenomenon and the associated cost of a comprehensive setup. The PerfDuB project addressed this issue by monitoring the condition of reinforcing bars in reinforced concrete walls exposed to carbonation (CERIB, Epernon) and marine chloride in tidal zones (LaSiE, La Rochelle).

The same analysis is now being conducted for chloride-induced corrosion propagation.

IV.4.1.3.2. Chloride-induced corrosion

The chloride-induced corrosion current, i_{corr}, is computed using three models (detailed in Annex 4):

- The model proposed by Balafas et al. in [270] **(**referred to as **BA)**,
- The model of Yalçyn et al. detailed in [271] **(YA)**,
- The model used in the national project PerfDuB detailed in [272] **(PE_Cl)**,

The various parameters of these models are presented in Table IV-39, along with the selected ranges of variation for the subsequent Morris sensitivity analysis.

To calculate the time taken for the first crack to form, the analytical model proposed by Alonso et al. was utilised [431] (referred to as **PE_Clcr**). The functioning of this model is further described in Annex 4, and the input values and ranges selected for the sensitivity analysis are provided in Table IV-35.

Table IV-39 Variation ranges of the models' parameters for the corrosion current computation in XS/XD environments.

Parameter	Symbol	Minimal boundary	Maximal boundary	Reference	Model
Propagation time (years)	t_{prop}	0	100	-	YA, BA
Initial corrosion current (µA/cm^2)	i_0	0	0.1	[271]	YA
Corrosion constant (days^{-1})	C	0.0005	0.002	-	YA
Chloride content (wt.% binder)	[Cl$^-$]	0	4		BA, PE_Cl
Saturation degree (-)	Sr	0.35	1	-	BA, PE_Cl
Average temperature (K)	T_{env}	278	298	Weather station	PE_Cl
Electrical resistivity (Ohm.m)	Re	20	1500	Database	PE_Cl
Critical concentration (wt.% binder)	C_{crit}	0.2	2	[6]	PE_Cl
Probability of active corrosion (-)	P_{ac}	0.2	1	-	YA

The study aimed to investigate the chloride-induced corrosion propagation in reinforced concrete structures. The unavailability of follow-up measurements on structures exposed to chloride did not allow for experimental verifications. Therefore, the presented computations only show a comparison of the different models among themselves and with the values prescribed by the PerfDuB project [323].

Firstly, the average corrosion current was computed using three models for various propagation times. Assumptions were made for the remaining inputs: the initial corrosion current (i_0) was set to a value of 0.5 µA/cm², and the corrosion constant (C) was set to 0.0011 (days^{-1}), as mentioned in [271] . The chloride content at the reinforcing bar was considered to be 2 wt.% of binder, while the critical concentration was set to 0.6 wt.% of binder. The temperature was assumed to be 287 K, and the concrete material had an electrical resistivity of 100 Ohm.m.

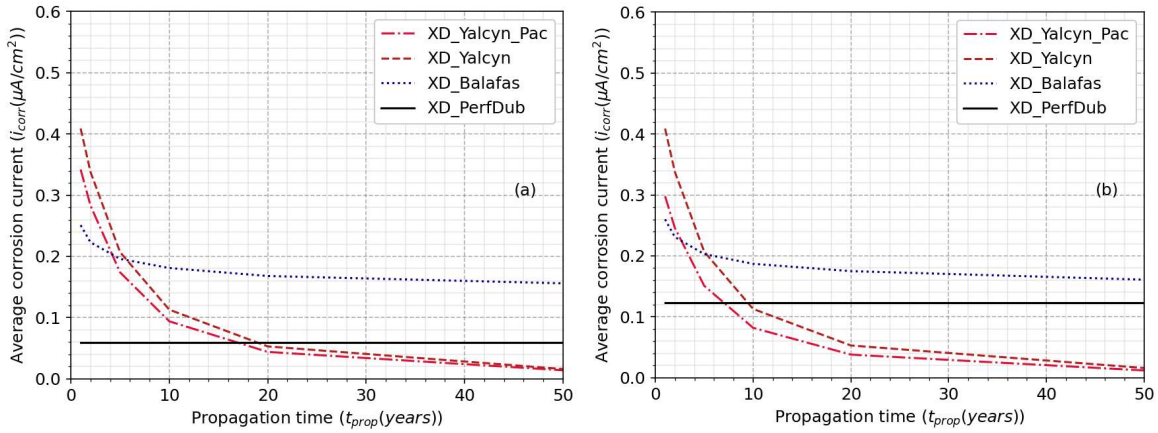

Figure IV-39 Average corrosion current vs propagation time estimated with the different model for chloride-induced corrosion for (a) RH_{env} = 0.75 and (b) RH_{env} = 0.9.

The results obtained in this study demonstrate a certain level of variability in the corrosion current. However, the range of this variability remains relatively limited. It should be noted that the PerfDuB model is time independent, while the other two models take into account the corrosion current's evolution over time. Despite both the Yalçyn and Balafas models showing a decrease in the initial value, they yield different average i_{corr} values. Interestingly, after 18 and 10 years, the mean value provided by the PerfDuB model falls within the range of values produced by the other models.

Both versions of the Yalçyn models, the original and the one incorporating active corrosion probability (P_{ac}), present only minor differences in value for the two relative humidity levels examined. However, the importance of considering the P_{ac} parameter is noticeable at lower relative humidity levels. For instance, an environmental relative humidity of 50% leads to a more significant global decrease of 58%.

It is important to note that the previous computations assumed a constant concentration of chloride. However, in most cases, this concentration tends to increase as aggressive ions penetrate the material or when bound chlorides are released due to a decrease in the interstitial solution's pH (caused by the corrosion phenomenon). Due to this reason, graphics illustrating the evolution of i_{corr} values as a function of chloride concentration are provided below (assuming a constant propagation time of 20 years).

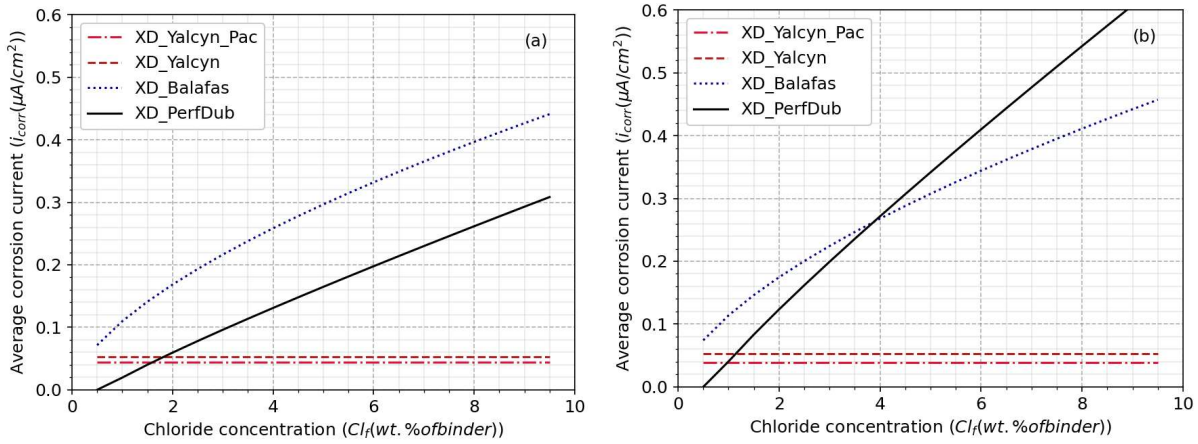

Figure IV-40 Average corrosion current vs free chloride content estimated with the different model for chloride-induced corrosion for (a) RH_{env} = 0.75 and (b) RH_{env} = 0.9.

The results of this study indicate that it is important to consider both the appropriate values for chloride concentration and the total length of propagation time when conducting future computations. The

Yalçyn model should be excluded from these computations. Although the Balafas and PerfDuB models demonstrate similar tendencies, they exhibit different evolutions based on the chloride concentration and relative environment. Therefore, the model used in the PerfDuB project, is selected for the next computation. This choice is primarily due to the ease of incorporating the computation of propagation time, which is not included as an input in the model.

For each exposure class, the values are determined using the default environmental values provided in the

Table IV-5 of Section IV.3.1, the concrete cover specified by the EC2 (refer to Section I.6.4), and a reinforcing bar diameter of 20 mm. Although the recommended values from the PerfDuB documentation do not consider the modulation of propagation time with electrical resistivity, three values for $\boldsymbol{Re}$ are tested to assess its influence on the results. This consideration is important as the influence of $\boldsymbol{Re}$ has been demonstrated in the literature [263].

The chloride concentration is adjusted to 5 wt.% of binder to get closer to the recommended values. The use of 2 wt.% of binder concentration at the rebar resulted in excessively high tolerable propagation times except for XS2. This discrepancy found for XS2 can be attributed to the erroneous consideration of a high saturation degree in the PerfDuB model, which is responsible for the i_{corr} computation.

Table IV-40 Corrosion current (µA/cm²) associated to each XS/XD exposure classes [323].

Class	XS1	XS2	XS3e	XS3m	XD1	XD2	XD3f	XD3tf
$\boldsymbol{RH_{env}}$ (%)	75	100	80	83	75	90	75	75
$\boldsymbol{Re}$ = 50 Ohm.m	0.313	0.989	0.405	0.470	0.313	0.649	0.313	0.313
$\boldsymbol{Re}$ = 100 Ohm.m	0.157	0.495	0.203	0.235	0.157	0.325	0.157	0.157
$\boldsymbol{Re}$ = 175 Ohm.m	0.089	0.283	0.116	0.134	0.089	0.185	0.089	0.089

Hence, one criticism that can be addressed to this model is its erroneous assumption that relative humidity is always equal to 100%. This assumption overlooks the potential limiting factor of oxygen access in the model, leading to an exaggerated erroneous corrosion current value assigned to a relative humidity value of 100%. This aspect of the model can explain the discrepancy in the values obtained for XS2, as shown in Table IV-41.

Subsequently, the i_{corr} values obtained are utilised as input in the model proposed by Alonso et al. [431]. The resulting propagation time values are presented in the following table, along with the recommended values.

Table IV-41 Propagation times (years) recommended [323] and obtained with the PerfDuB model, leading to cracking of the concrete material.

Class	XS1	XS2	XS3e	XS3m	XD1	XD2	XD3f	XD3tf
Recommended values (years)	10	30	2	2	15	5	5	5
$\boldsymbol{Re}$ = 50 Ohm.m	9	3	8	7	9	5	11	11
$\boldsymbol{Re}$ = 100 Ohm.m	18	6	16	14	18	10	21	21
$\boldsymbol{Re}$ = 175 Ohm.m	32	11	29	25	32	17	38	38

A close correlation can be seen between the recommended and computed values when considering electrical resistivity in the range of 50 and 100 Ohm.m. XS2 environment, however, exhibits an obvious error due to the i_{corr} value computed by the previous model. Nevertheless, the remaining values closely align with each other, and any variation observed among them is likely due to the similar chloride concentrations considered for all exposure classes. The lower recommended values for XS3 and XD3 suggest that a higher concentration of chloride should be taken into account when computing the i_{corr}.

Conversely, XD1 demonstrates the opposite trend, indicating the need for a lower concentration value in the computation, certainly due to the slower penetration rate of chloride in XD1 when compared to XD2 and XD3.

It should be noted that the utilization of 5 wt.% of binder is excessively high and has not typically been reached in previous computations and measurements (refer to Section IV.4.1.2). Consequently, additional calibration of the PerfDuB model for corrosion current computation might be necessary to adequately account for the chloride concentration at the reinforcing bar.

However, this aspect of the model presents a challenge as it requires precise knowledge of the chloride concentration at the reinforcing bar. As demonstrated by the prior predictions in Section IV.4.1.2, this value is not constant over time and is likely to increase during the whole propagation, resulting in an increase in corrosion current (rather than the decrease observed in Figure IV-39). Therefore, the PerfDuB model needs to be modified to calculate corrosion current for different time periods, considering the evolution of chloride concentration.

Another factor that could contribute to the deviation between computed and recommended values is the use of default values for each exposure class (refer to Section IV.3.1). These values, and those recommended by PerfDuB for propagation times, are generic and do not encompass all scenarios for these exposure classes. Thus, variations in the final values are expected and support the need to develop models capable of accurately considering environmental and material inputs.

The considerable variation caused by the evolution of electrical resistivity, which can reach higher ranges of values in low carbon concrete, also highlights the limitations of the prescribed values that were likely established for regular Portland cement-based concretes. However, due to the lack of experimental results in this study regarding this aspect, no definitive conclusions can be drawn. Further investigation is needed to determine if the model properly accounts for the influence of electrical resistivity on the i_{corr} value.

IV.4.1.3.3. Conclusions

The comparison of corrosion currents obtained with the models for carbonation and chloride-induced corrosion showed a significant difference in magnitude. It appears that the model used for carbonation predicts higher corrosion currents compared to the model used for chloride-induced corrosion. This difference accurately reflects the disparity between the two corrosion phenomena. In the case of carbonation, the uniform corrosion consumes a larger amount of steel compared to pitting corrosion, but the failure criteria are reached more slowly than in chloride-induced corrosion, resulting in a higher section loss of the steel. This justifies the need to consider different mechanical models for the computation of propagation times, as different failure criteria must be taken into account based on the nature of the depassivation phenomena.

The models referred to as "PerfDuB models" were selected by the PerfDuB project despite their limited capacity to consider time dependency. Tests conducted within the Applet project [432], for example, demonstrated that the most effective models to represent the results obtained on slab were Morinaga's model for carbonation-induced corrosion and Balafas' model for chloride-induced corrosion.

The absence of consideration for electrical resistivity in the recommended values for chloride-induced corrosion propagation time is a limiting factor for the development of low-carbon binders, which generally have higher electrical resistivity than ordinary Portland concretes and thus have a greater potential for resisting corrosion. However, the absence of modulation may be a conservative decision considering the uncertain impact of concrete electrical resistivity on corrosion propagation. Additionally, this study showed that pozzolanic and latent hydraulic-based binders exhibit better performance in terms of chloride ingress resistance (see Section II.2.7 and Section IV.3.3.3). Therefore,

the benefits of using these types of low-carbon binders are already considered during the initiation stage of corrosion if a performance-based approach is considered (refer to FD P18-480 (2022) explicated in Section I.6.3).

It should be noted that the models for corrosion current computation do not consider the properties of the steel. However, literature has shown that different steel compositions may lead to different corrosion resistance ([146], [433] see Section I.3.4). Hence, it would be useful to include a correcting factor in the models to account for this aspect, which has a certain impact on the time to failure.

Morris's sensitivity analyses were conducted and provided the parameters responsible for more than 90% of the overall cumulative sensitivity on the output, as shown in Table IV-42.

Table IV-42 Parameters responsible for 90% of the influence of i_{corr} according to the Morris sensitivity analysis.

Model	NG	PE_XC	YA	BA	PE_Cl
Influent parameters	t_{prop}, P_{ac}	Re , Sr	i_0, P_{ac}	t_{prop}, Sr, Cl_f	Re , Sr, Cl_f

The parameters influencing the computation of the corrosion current (i_{corr}) are:

- The relative humidity, in both carbonation and chloride-induced corrosion. This influence is accounted for in the model either through the consideration of Sr (surface relative humidity), or through the computation of P_{ac} (corrosion activation probability)
- The chloride concentration reaching the steel in Balafas and PerfDuB models. This highlights the significance of accurately predicting this variable at the surface of the reinforcing bar.
- The electrical resistivity in PerfDuB model. This parameter, which is absent in other models, appears to have a noteworthy impact on the corrosion current.

To develop an effective predictive model for corrosion, it is important to consider the time dependence demonstrated by factors such as propagation time length, saturation degree, and chloride concentration at the steel surface. Hence, an improvement to the current corrosion consideration could involve directly integrating its computation into the initiation model. As a result, a simple analytical equation could be integrated into SDReaM-Crete finite element model to directly output the corrosion current. Surrogates could then be created to directly provide the i_{corr} value.

Table IV-43 Parameters responsible for 90% of the influence of t_{prop} according to the Morris sensitivity analysis.

Model	PE_XCcr	MO	MA	PE_Clcr
Influent parameters	i_{corr}, D_{rebar}	i_{corr}	i_{corr}	i_{corr}, D_{rebar}

The results obtained from the models calculating the propagation time exhibit consistent observations of the parameters, primarily focusing on the sensitivity associated with the corrosion current and reinforcing bar diameter values. Furthermore, the comparable patterns observed provide an explanation for the similar orders of magnitude obtained with the different models used for the computation of the propagation time for carbonation-induced corrosion (refer to Table IV-4).

IV.4.2. Probabilistic approach

The previous section demonstrated the efficacy of various models in accurately representing the durability of reinforced concrete structures in a majority of XC, XS, and XD3 environments. Additionally, it provided a foundation for selecting a model based on performance criteria. However, it is crucial to consider the variability of parameters and the inherent uncertainties associated with the different methods employed for determining input.

Hence, probabilistic calculations are being conducted on various structures exposed to XC4 and XS2/XS3 environments. The objective is to determine the probabilities associated with critical times corresponding to the onset of corrosion and the propagation of corrosion leading to crack formation. The models used are the ones that have been identified as the most consistent during deterministic calculations. However, based on the findings from Section IV.4.1, it has been observed that computing the mean of multiple models generally yields better results for the initiation phase, rather than relying on a single model alone. Therefore, this approach has been adopted for the computation of the initiation period as well and is demonstrated for XC4 environments. Tables, which include the input data and distribution parameters, can be found in Annex 2.

IV.4.2.1. Carbonation induced corrosion (XC) – depassivation probability

In this section, probabilistic computations were performed on the various bridge structures provided by Arcadis (exposed to XC4 environments), using the First Order Reliability Method (FORM). The standard deviations used for the computations were set according to Table IV-18, which defines default values for different parameters. Additionally, the confidence indices were determined based on the rules described in Section IV.3.4.

The probability distributions of the input parameters considered random variables were either derived from existing literature or carefully selected to ensure acceptable variation ranges. Consequently, most of the parameters have a beta or lognormal distribution, as shown in Annex 2. Although some of the variables may be stochastically dependent, for the sake of simplicity, it was assumed that variables are not correlated.

In Section IV.4.1.1, three models (SDReaM-Crete metamodel, JSCE [196] model and Parrott [194] model) were identified as being more effective in XC4 environments, along with the function computing the mean of the five models presented. Therefore, the four methods were utilised in this section for performing the various probabilistic computations.

The investigation has focused on specific zones of interest of the bridge structures to assess their condition state regarding durability. The distribution of the concrete cover in each zone was estimated using a pachometer. The measurements were then used to calculate the depassivation probabilities associated with each zone.

The design service life of the bridge is 100 years, as recommended in Eurocodes. However, for the purpose of this study, only the initiation period is taken into consideration. In accordance with the recommendations of the PerfDuB documentation [323], a propagation time of 5 years is assumed for structures exposed to XC4 environments (i.e., electrical resistivity of the concrete is less than 100 Ohm.m). Therefore, the structure must be able to withstand an initiation period (t_{ini}) of 95 years.

The limit state function $G(X)$ is defined as: $G(X) = x_c - CC$.

Instead of considering the whole measurements of the concrete cover, and the derived probability distribution for each zone, probabilities were first calculated for different mean values of concrete cover, ranging from 5 to 80 mm. A standard deviation of 2.5 mm was considered, taking into account the uncertainties of the pachometer measurements available, rounded to the nearest 5 mm. The parameter was assumed to follow a normal distribution. The distributions of the concrete cover measured experimentally are used afterward in the computation of the corrosion activity.

The pachometer measurements revealed a wide variation in the concrete cover. To further investigate this aspect, the analysis focused on two specific structures: S2 (consisting of CEM I-based concrete) and S7 (composed of CEM II/A-S-based concrete). The results obtained for each part (or zone) are displayed in Figure IV-41 and Figure IV-42.

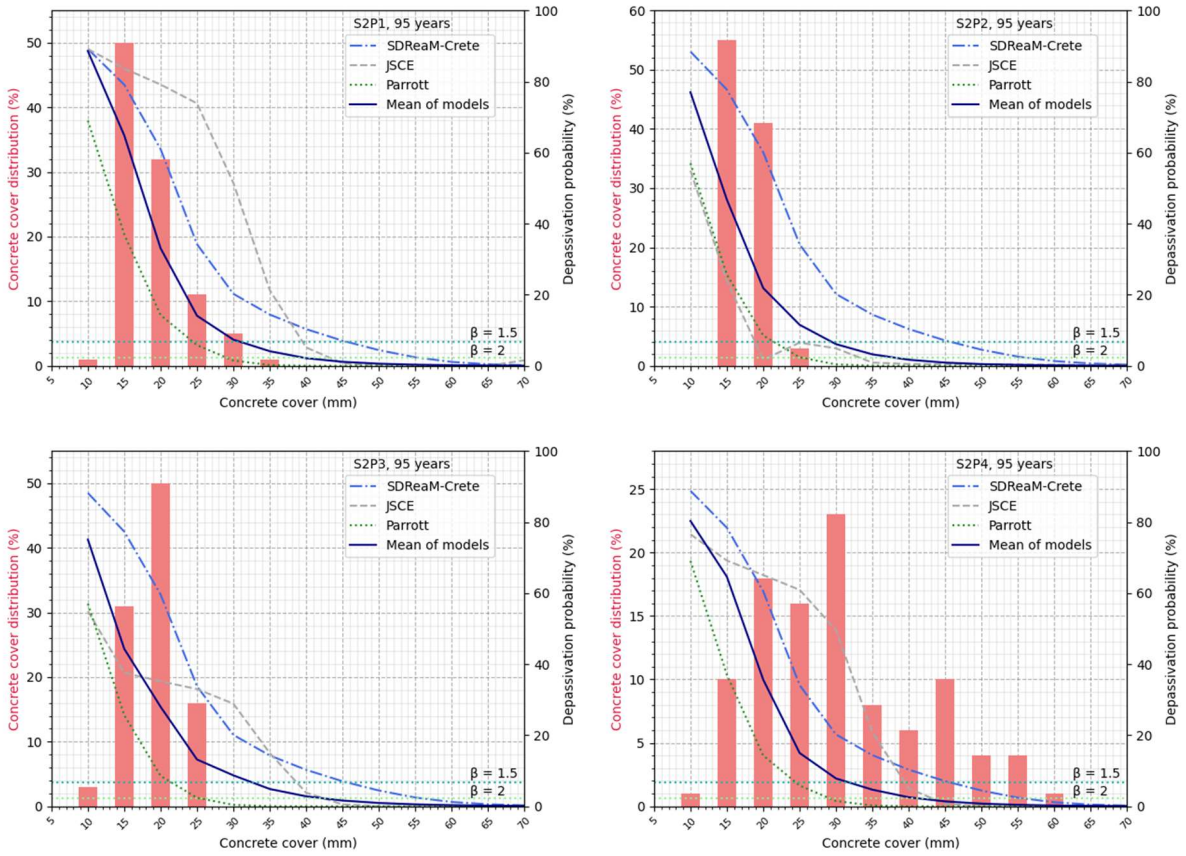

Figure IV-41 Representation of the pachometer results and the depassivation probability computed with each model for the different zone of the structure S2 (CEM I-based concretes exposed to XC4 environment).

After a service life of 43 years, the average carbonation depths in various zones of the structure were measured to be 7.5 mm, 5 mm, 12.5 mm, and 12.5 mm. Utilizing the simple square time, it is expected that the carbonation depths after 95 years should be approximately 11.6 mm, 7.7 mm, 19.3 mm, and 19.3 mm. These values are only used as a comparison basis in this study. However, it could be interesting to implement a method to update the computed probability (refer to [434]).

With respect to the carbonation models a high dispersion in computed probabilities is exhibited. This discrepancy can be attributed to the probability distributions of the input parameters used in each model.

The SDReaM-Crete surrogate model yields the highest probability of depassivation. It is important to note that the same trend is observed across all four zones. The sensitivity analysis conducted in Section IV.4.1.1 identified four key parameters encompass more than 90% of the overall sensitivity: $\varphi_c^w, t_{tot}, RH_{env}$ and T_{env}. Among these parameters, only the porosity differs among the zones, and the observed variations between the four zones are less than 3%. This explains the limited variation in the computed depassivation probability using this model.

The JSCE model results in a higher fluctuation of the results depending on the zone considered. This model takes into account the composition parameters as input. The difference between the average values of binder content and effective water content in each zone is higher, reaching up to 10% and 8% respectively. This difference can explain the variation in probability obtained between each zone. It is worth noting that the trends of the P_{dep} vs. CC curve differ from the general trends obtained with the other models.

The Parrott model predicts a lower depassivation probability. The input parameters, especially the coefficient of D_{air}, are challenging to calibrate as a function of concrete, which inevitably leads to errors. However, in the different zones, the model predicts the reaching of the first threshold ($\beta = 1.5$, P_{dep} = 6.68 %) for concrete values below 20 or 25 mm. This matches with the measurements taken on the structure (and considering the hypothesis of a square root law of time) which showed maximum values of 19.3 mm for this structure after 95 years of exposure.

The computation of the depassivation probability, using the mean of the models, results in slightly higher values than the Parrott model. These values range from 30 mm to 35 mm when considering the β threshold of 1.5. This method can be considered more conservative and is used for the predictions on the overall set of structures in this section.

The second structure, S7, used CEM II/A-S cement. The predictions made using the four different models are presented in Figure IV-42, considering an initiation period of 95 years. It is worth noting that due to the nature of the binder (presence of slag), a higher electrical resistivity can be expected. This should result in a lower propagation rate (higher propagation time tolerable), allowing for the consideration of an 80-year initiation period [323]. However, since there are no results available regarding this parameter, the most conservative value is used for the computations.

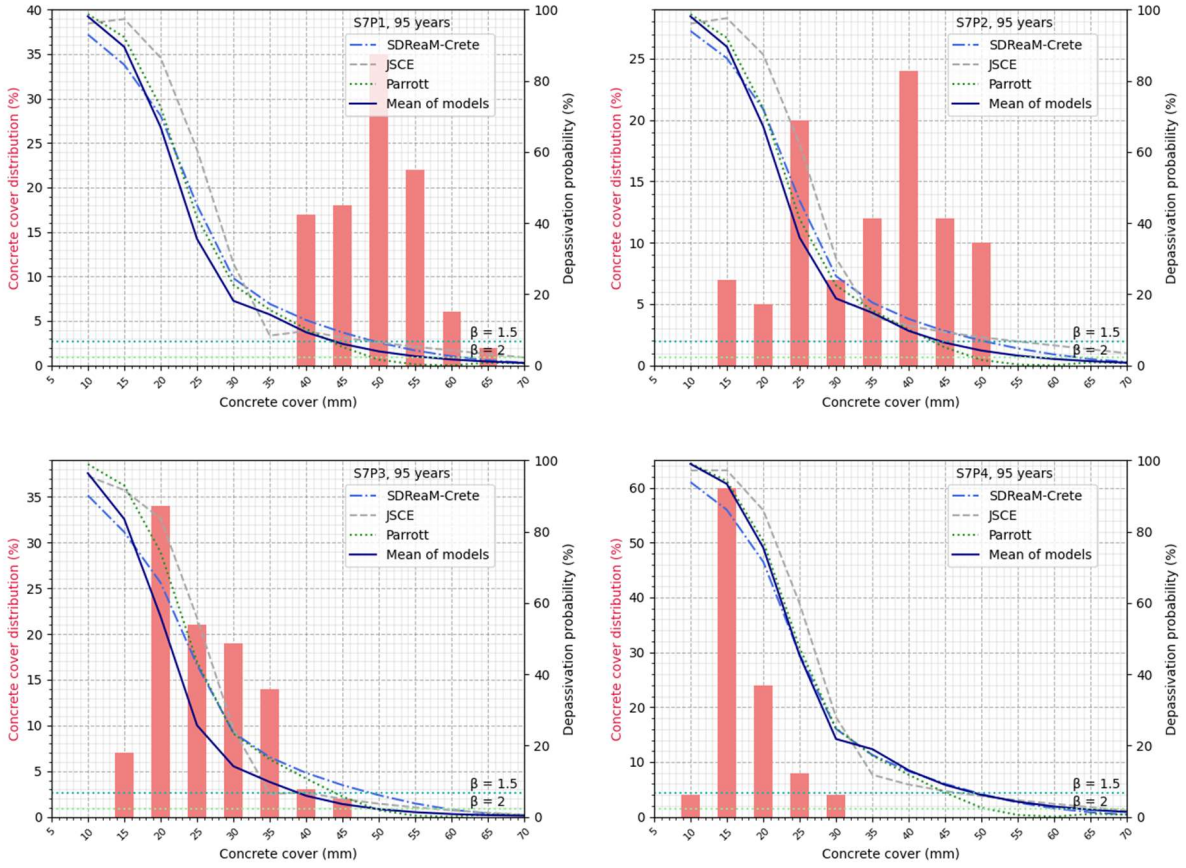

Figure IV-42 Schematic representation of the pachometer results and the depassivation probability computed with each model for the different zone of the structure S7 (CEM II/A-S-based concretes exposed to XC4 environment).

The experimental results obtained on S7 during the inspection (after 39 years) yielded carbonation depths of 17.5, 12.5, 15, and 30 mm. By extrapolating these values using the square time law equation to a time of 95 years, carbonation depths of 27, 19.3, 23.1, and 46.2 mm are estimated for the structures.

The probabilistic calculations conducted with different models show very thin differences in the probability values. All models predict concrete cover values between 40 and 50 mm to achieve a reliability index of 1.5 after 95 years of exposure. This suggests that the models consider the uncertainties of the material and environment similarly, despite using different distributions and input parameters. However, acquiring these equivalences between the different distribution can be complicated and may explain the discrepancy in the results obtained for structure S2 (refer to Figure IV-41). This latter aspect requires careful consideration of factors such as the influence of each parameter on the models' output and the correlation between different material parameters and properties. Sometimes, the present methodology and tool developed may not adequately account for these factors due to invalid mathematical methods or varying ranges of input parameters. As a result, discrepancies between the probabilities estimated by different models are expected, and a further thorough analysis of the results should be carried out to decide the appropriate value for each case.

The computed values for structures S2 and S7 indicate that, for most of the considered areas, the threshold probability value of 6.68% is exceeded after 95 years. This is supported by the significant variation in concrete cover measurements obtained from these structures using a pachometer, with some concrete cover values below 20 mm. As a result, active corrosion has already been detected in certain parts of the structures during inspections. Therefore, a prediction of corrosion activity is proposed below, using the function computing the mean of the five models (refer to Section IV.4.1.1).

First, the depassivation probability is computed for every structure zone at different exposure times. The results are presented in Figure IV-43, where a threshold value of 6.68% was used for better readability of the data.

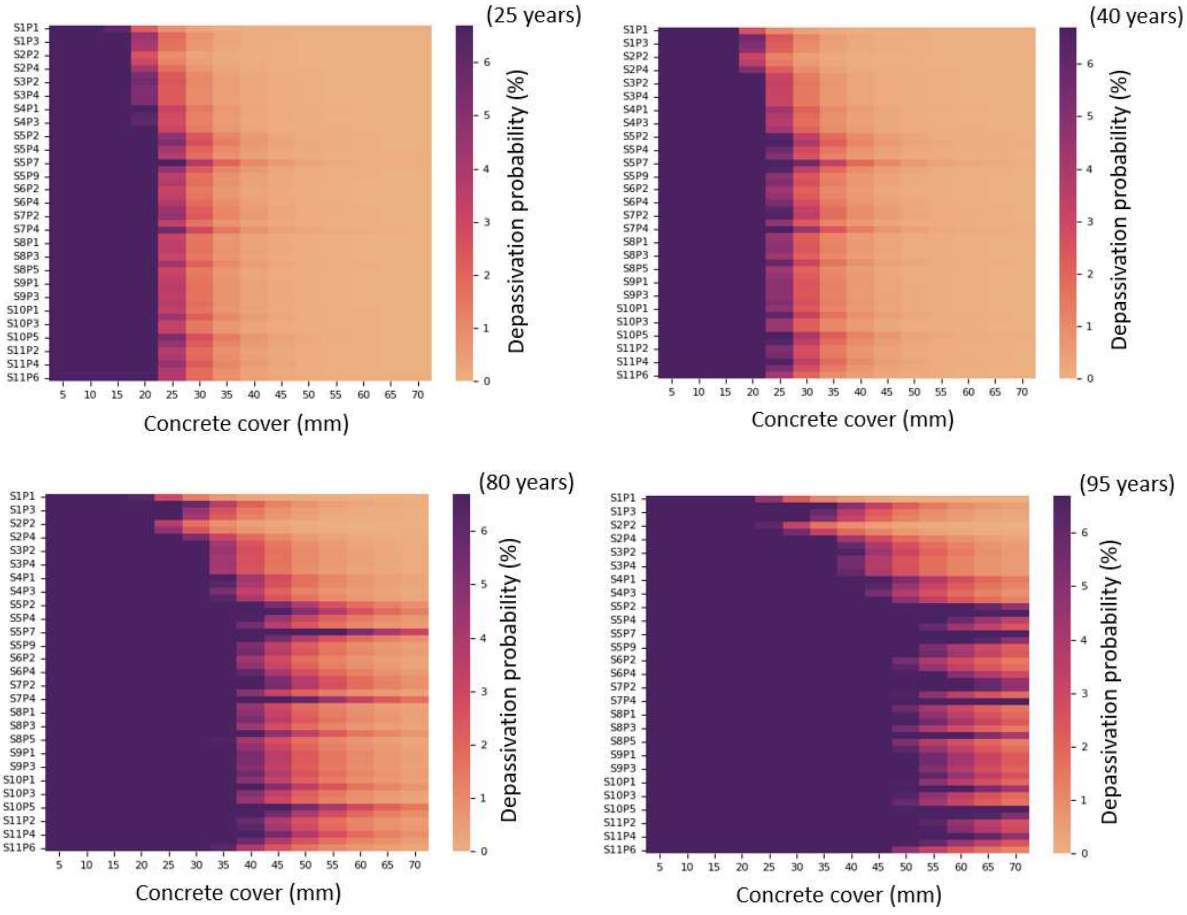

Figure IV-43 Depassivation probability of the different Arcadis' road structures ($\beta_{threshold} = 1.5, P_{dep,threshold} = 6.68\%$) computed with the mean of the models for 25, 50, 80 and 95 years.

The results indicate an anticipated increase in the probability of depassivation with increasing duration of exposure. Therefore, it is necessary to compare the data obtained after a 40-year exposure period, which closely aligns with the inspection times for all structures and the pachometer measurements. The experimental measurements are presented in the form of a histogram, which illustrates the distribution probability of concrete cover in each respective zone. The heatmaps, depicted in Figure IV-44, showcase the probability and cumulative distribution of concrete cover depths. They show that the probabilities obtained for the different exposure times (refer to Figure IV-43) exceed the threshold value of 6.68% in most zones of the structures according to these computations.

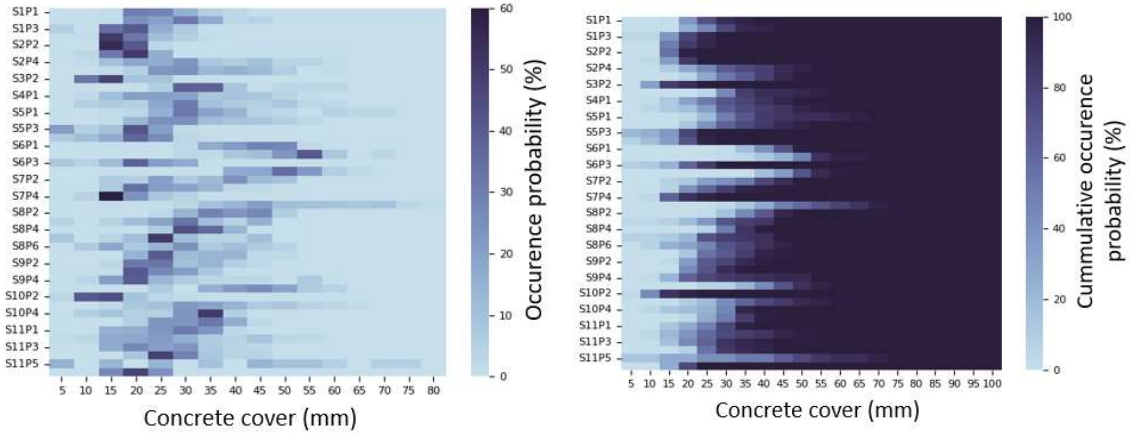

Figure IV-44 Heatmaps used for the representation of the probability and cumulative probability of concrete cover occurrence in each zone.

The next step involves predicting the extent of the potentially depassivated zone in terms of its degree or ratio. The previously used threshold of 6.68% is considered highly reliable. However, it is likely that corrosion only initiates when the depassivation probability is higher. Therefore, a value of 25% is considered as the threshold to define the onset of corrosion. The ratio of the zone where the depassivation probability exceeds 25% is then calculated. If this ratio is greater than 0.5 (which means that more than 50% of the structure has a depassivation probability greater than 25%), the corrosion is deemed active. The previously mentioned threshold values were found to be the most effective in predicting the condition state of the reinforcing bars regarding corrosion. Less effective threshold values are also presented in the subsequent tables.

Table IV-44 shows the ratios obtained for S2 and S7, along with the conclusion drawn from the active corrosion measurements.

Table IV-44 Corrosion activity and ratios of S2 and S7 zones corresponding to different depassivation probability.

Name	Active corrosion according to measurement	Ratio of the zone where $P_{dep} > 6.67\%$	Ratio of the zone where $P_{dep} > 25\%$	Ratio of the zone where $P_{dep} > 50\%$	Ratio of the zone where $P_{dep} > 75\%$
S2P1	YES	0.99	0.51	0	0
S2P2	NO	0.96	0	0	0
S2P3	YES	1	0.34	0	0
S2P4	YES	0.68	0.11	0	0
S7P1	NO	0.7	0	0	0
S7P2	YES	0.97	0.97	0.39	0.07
S7P3	YES	1	0.95	0.41	0
S7P4	NO	1	0.96	0.64	0

The computed ratios are now compared with threshold values. If a ratio exceeds the threshold, then corrosion is considered active; otherwise, it is considered non-initiated. The latter ratios are optimized to achieve maximum prediction accuracy and are assigned values of 0.98, 0.5, 0.05, and 0.05 for the four thresholds mentioned above. The prediction success rates are presented in Table IV-45. The most satisfactory results are obtained when using a depassivation probability threshold of 25%.

Table IV-45 Success of prediction obtained according to the threshold conditions.

Ratio of the zone	Ratio threshold	Success	Success in predicting active corrosion	Success in predicting inactive corrosion
$P_{dep} > 6.67\%$	0.98	68%	63%	75%
$P_{dep} > 25\%$	0.5	73%	75%	70%
$P_{dep} > 50\%$	0.05	66%	71%	60%
$P_{dep} > 75\%$	0.05	59%	88%	25%

This method could be improved by considering different P_{dep} thresholds simultaneously. Furthermore, it is important to note that the uncertainties associated with the experimental testing procedure are not taken into account and could also contribute to erroneous estimations.

These calculations are performed solely to illustrate the method. However, it could be decided to utilize the carbonation depth measurements from the inspection to adjust the various parameters of the models. This could also justify manually reducing the standard deviations and thereby increasing the precision in the determination.

An alternative approach to the calculations performed could have been to consider a beta distribution fitted to the pachometer distribution. This would have allowed for the computation of a global probability to encompass the entire zone. However, the precise locations of the measurements within each zone are unknown. The experimental distribution obtained does not correspond to a spatial distribution, but rather to a general "count" of the concrete cover depths in a zone. Therefore, computing a "global probability" would likely be challenging to analyse and utilize. Nevertheless, examples of the results obtained are presented in the following table for structures S2 and S7. The calculations are performed considering the confidence indices computed during the acquisition of the input parameters and assuming that all parameters are "safely assessed", corresponding to confidence indices of 1. This comparison provides insight into the influence of the process and how it affects the probabilistic estimations. The model that computes the mean of the models is used to calculate the following probabilities. The probability displayed in red indicates zones where active corrosion was measured.

Table IV-46 Beta distribution and depassivation probability obtained on the different zones of S2 and S7.

Name	μ	σ	Min	Max	$P_{dep,40years}$	$P_{dep,95years}$	$P_{dep,40years}$	$P_{dep,95years}$
	(mm)				Confidence indices computed		Confidence indices set to 1	
S2P1	18.6	3.8	19	35	8.3%	10.2%	9.5%	13.4%
S2P2	17.2	2.6	15	25	5.2%	12.4%	4.2%	6.6%
S2P3	19.0	3.0	10	25	5.1%	11.1%	4.4%	6.4%
S2P4	30.6	9.1	10	60	13.6%	27.9%	14.2%	28.5%
S7P1	49.4	4.8	40	65	5.9%	6.2%	7.6%	8.3%
S7P2	33.4	8.7	15	50	8.3%	18.4%	21.4%	48.1%
S7P3	25.8	5.8	15	45	7.1%	18.4%	14.0%	35%
S7P4	17.4	3.5	10	30	7.3%	14.4%	13.4%	24.3%

The results indicate a relatively high probability of depassivation in most zones of the bridge structures, particularly after a depassivation time of 95 years. Even after 40 years, the depassivation probabilities consistently exceed the reliability threshold commonly used, which is 6.68%. However, it is challenging to establish a clear relationship between this global depassivation probability and corrosion activity when comparing to experimental measurements.

The inclusion of computed confidence indices significantly affects the obtained probabilities, particularly for the second structure. These deviations are likely attributed to the nature of the binder material. Structure S2 incorporates CEM I-based binder, while structure S7 utilizes CEM II/A-S-based binder, leading to lower carbonation resistance. However, due to the unavailability of detailed information about the precise nature and composition of the cement used, the confidence index for the content of slag and clinker is low. To account for this uncertainty, a beta distribution is considered with fixed minimum and maximum values prescribed by NF EN 197-1 (2011) for CEM II/A-S. Consequently, a higher deviation on the slag content, which may result in a lower carbonation rate, is considered when confidence indices are low, specifically in the case of S7. A similar effect applies to other parameters. It is worth noting that smaller differences are observed for S2, likely due to fewer uncertainties in the definition of the binder, leading to higher computed confidence indices.

IV.4.2.2. Carbonation-induced corrosion (XC) – Corrosion-induced cracking probability

In the previous probabilistic computation, only the depassivation time was considered probabilistically, while the propagation time was assumed to be constant (with values recommended in the PerfDuB conclusions [323]). An alternative method is proposed in this study, which incorporates the computation of the probability of exceeding the time prior to cracking, taking into account the propagation time using a corrosion model (refer to Section IV.4.1.3). To simplify the computational process, three models are considered, each for the different prediction steps required:

- The initiation stage is considered using the SDReaM-Crete surrogate model for carbonation. The output of this model is transformed to compute the required time for corrosion initiation. A square root law of time is applied to transform the carbonation depth into a carbonation rate, which is then used to determine the initiation time (t_{ini}).
- The models used in the PerfDuB project for the computation of the corrosion current (i_{corr}) (PE_XC) and the computation of the propagation time (t_{prop}, years) (PE_XCcr) are employed (as described in Annex 4 and Section I.4.4).

A function is then defined to compute the sum of the initiation and propagation time. The limit state function becomes:

$$G(X) = t_{tot} - \left(t_{ini} + t_{prop}\right) \geq 0 \qquad \text{Eq (IV.27)}$$

The main purpose is to apply a methodology to determine the cracking probability while verifying that the predicted outcomes align with the previous findings. Various mean values are considered for the concrete cover, which has a normal distribution with a standard deviation of 2.5 mm.

The diameter of the reinforcing bars is assumed to be 12 mm and is also subject to a normal distribution with a standard deviation of 2 mm. The electrical resistivity is initially assessed using a Beta distribution. For all zones of CEM I-based structures, a Beta distribution with parameters of μ = 65 Ohm.m, σ = 10 Ohm.m, min = 40 Ohm.m, and max = 150 Ohm.m is employed. Conversely, for CEM II/A-S and CEM II/A-V structures, a Beta distribution with parameters of μ = 100 Ohm.m, σ = 10 Ohm.m, min = 60 Ohm.m, and max = 200 Ohm.m is utilised. This differentiation is based on the superior electrical properties of slag-based concrete in comparison to CEM I-based material [374]. The following plots illustrate the progression of the probability of corrosion-induced cracking in the structures.

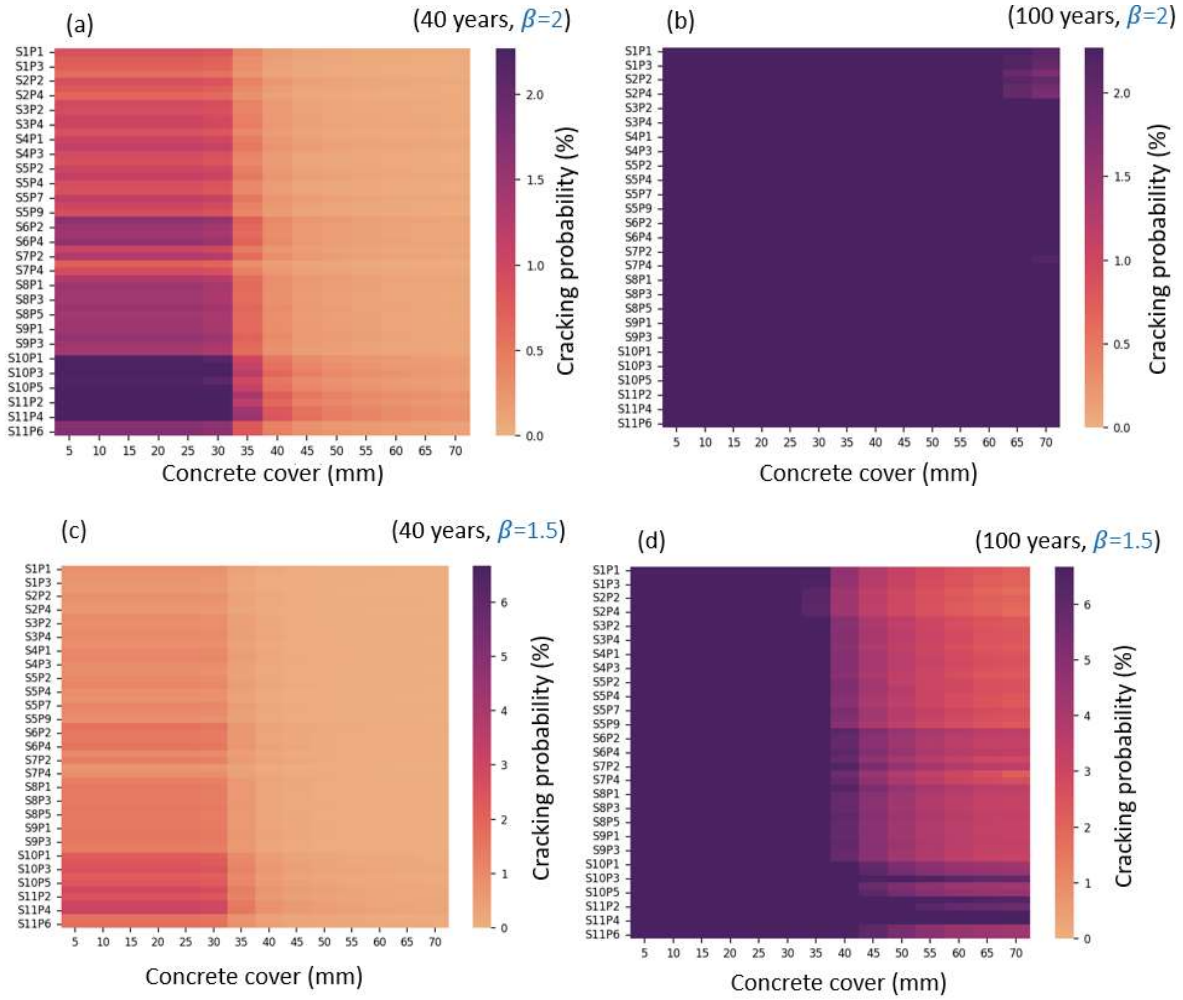

Figure IV-45 corrosion-induced cracking probability obtained after 40 and 100 years of exposure, considering a threshold of 2.27% (β=2, a and b) and 6.68% (β=1.5, c and d).

After 100 years, the obtained probabilities exceed the threshold of 2.27% at 70 mm for all zones (refer to Figure IV-45 (b)). At 30 mm, a crack probability of at least 6.68% is obtained (refer to Figure IV-45 (d)). This threshold is associated with a very low reliability index of 1.5, which is insufficient for the present application. As mentioned in Section I.5.2, a reliability index of 3.8 (P_f = 0.007%) can be considered to ensure an adequate level of safety for the structure with regards to ultimate limit states. However, this reliability index is not met in the current calculations, as the formation of a crack does not rely to a structural failure, so a reliability index of 2 is chosen instead. To enhance the accuracy of the computed value for the time to failure, the time to spalling could be included in the calculations. It is important to note that the structural limit (mechanical resistance insufficiency) should be considered in the computation. However, the methodology currently lacks an integrated model. Hence, it would be necessary to conduct a time-dependent analysis, incorporating the critical time as a random variable, rather than the time-wise analysis conducted in the present study.

The model proposed by Stewart and Suo in (detailed in Annex 4) is utilised to calculate the time to spalling (t_{sp}, in years). It is important to note that this model was originally developed for pitting corrosion and is only used here to illustrate the significance of considering an additional phase of corrosion in the computation of failure probability. The inputs for this model include the water-to-binder ratio, concrete cover, corrosion current, and crack opening (in millimetres). It is assumed that the crack width (also in millimetres) follows a Beta (μ = 0.5, σ = 0.05, min = 0.3, max = 0.9) distribution. The remaining parameters are known. The limit state function is now defined as:

$$G(X) = t_{tot} - \left(t_{ini} + t_{prop} + t_{sp}\right) \geq 0$$ Eq (IV.28)

The results obtained for 40 and 100 years are shown in Figure IV-46.

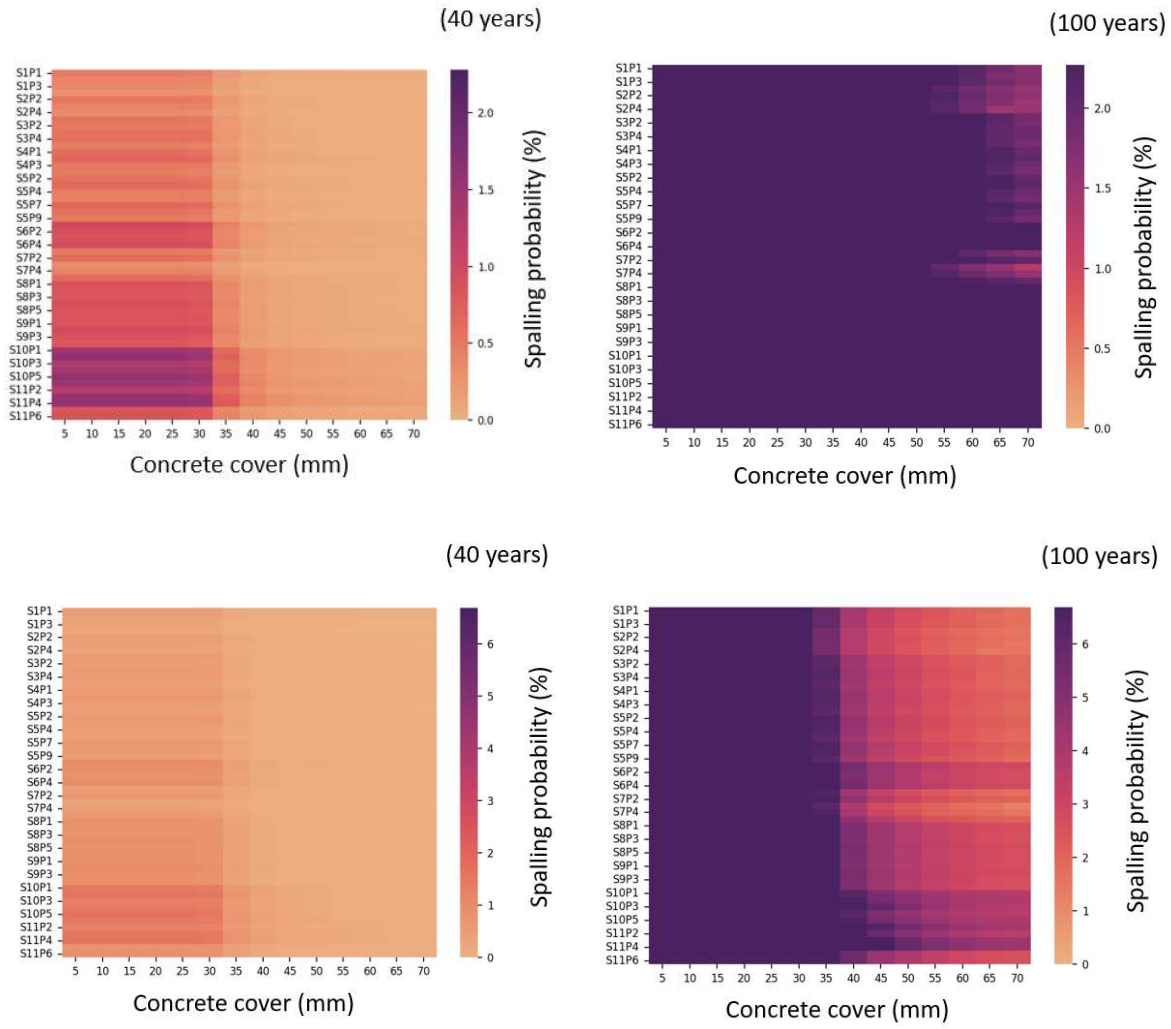

Figure IV-46 Corrosion-induced spalling probability obtained after 40 and 100 years of exposure, considering a threshold of 2.27% (β=2) and 6.68% (β=1.5).

The results obtained for the cracking and spalling probability demonstrate a close correspondence. It is noteworthy that the spalling probability yields slightly lower values, which can be attributed to the consideration of t_{sp}.

Since the spalling model is typically used for chloride induced corrosion, only the cracking probability is taken into account. The obtained values reveal that:

- After 100 years of exposure, the probability of cracking exceeds 2.27% (reliability index of 2) for all structural zones. Additionally, the cracking probability exceeds 6.68% (reliability index of 1.5) for concrete cover greater than 30 mm. These results indicate that the structures do not meet the specified reliability requirement of 2, nor 1.5. It is important to note that SDReaM-Crete leads to a higher probability of depassivation compared to the other models (refer to Figure IV-41), which partially explains the obtained probabilities. However, the inspection and results obtained after 40 years of service do not rule out the possibility of crack and spalling formation

in the structure after 100 years of service. Therefore, although certainly conservative, these results are considered acceptable.

- Considering the results obtained for a 40-year exposure period, the reliability index of 2 is achieved for all structures and zones. These results align with the observations made during the same period. Despite the presence of active corrosion in certain reinforcing bars, no cracking was identified, likely because the duration of active corrosion was insufficient to induce cracking of the concrete cover.

IV.4.2.3. Chloride induced corrosion (XS) – Depassivation probability

The present study focuses on chloride-induced corrosion and investigates the structure harbour provided by Arcadis. In order to conduct a probabilistic computation, three zones of the structure are considered, which are exposed to XS2 or XS3e environments. The design objective is to ensure the structure can endure 100 years of exposure. The propagation times for XS2 and XS3e are stated as 30 years and 3 years respectively, as outlined in the PerfDuB documentation [323]. Mean and standard deviation values are computed using the methods described earlier in Section IV.3. Confidence indices are also calculated for the different parameters, and they are used to adjust the standard deviation. The selected distributions and their corresponding values are presented in Annex 2.

Contrary to the inspection conducted on the bridge structures, distribution of concrete cover were not available in the precise location considered for prediction. However, various concrete cover values were measured for each zone, enabling the acquisition of minimum, maximum, and mean values (grouped together for each of the three zones).

The model utilised in this study is the PerfDuB model and the probabilistic approach is performed using the FORM algorithm.

Table IV-47 Concrete covers measurements realised in the different maritime structures.

Concrete cover	S1	S2	S3
XS	XS2	XS3e	XS3e
Binder type	CEM V/A (S-V)	CEM III/B	CEM I
t_{tot}	41	34	17
Mean	39	37	53
Minimal	33	24	33
Maximal	48	47	61

A beta distribution could be considered as an option for evaluating the depassivation probability of the overall zone. However, this method may be inadequate as it does not account for weak spots. In order to address this limitation, an alternative approach is proposed: considering the mean, minimal, and maximal values as average values for the distribution of the concrete cover. For this parameter, a Gaussian distribution with a standard deviation of 3 mm (assumed to be lower than the uncertainties of the pachometer test) is assumed. This enables the computation of the depassivation probability as a function of time displayed in Figure IV-47.

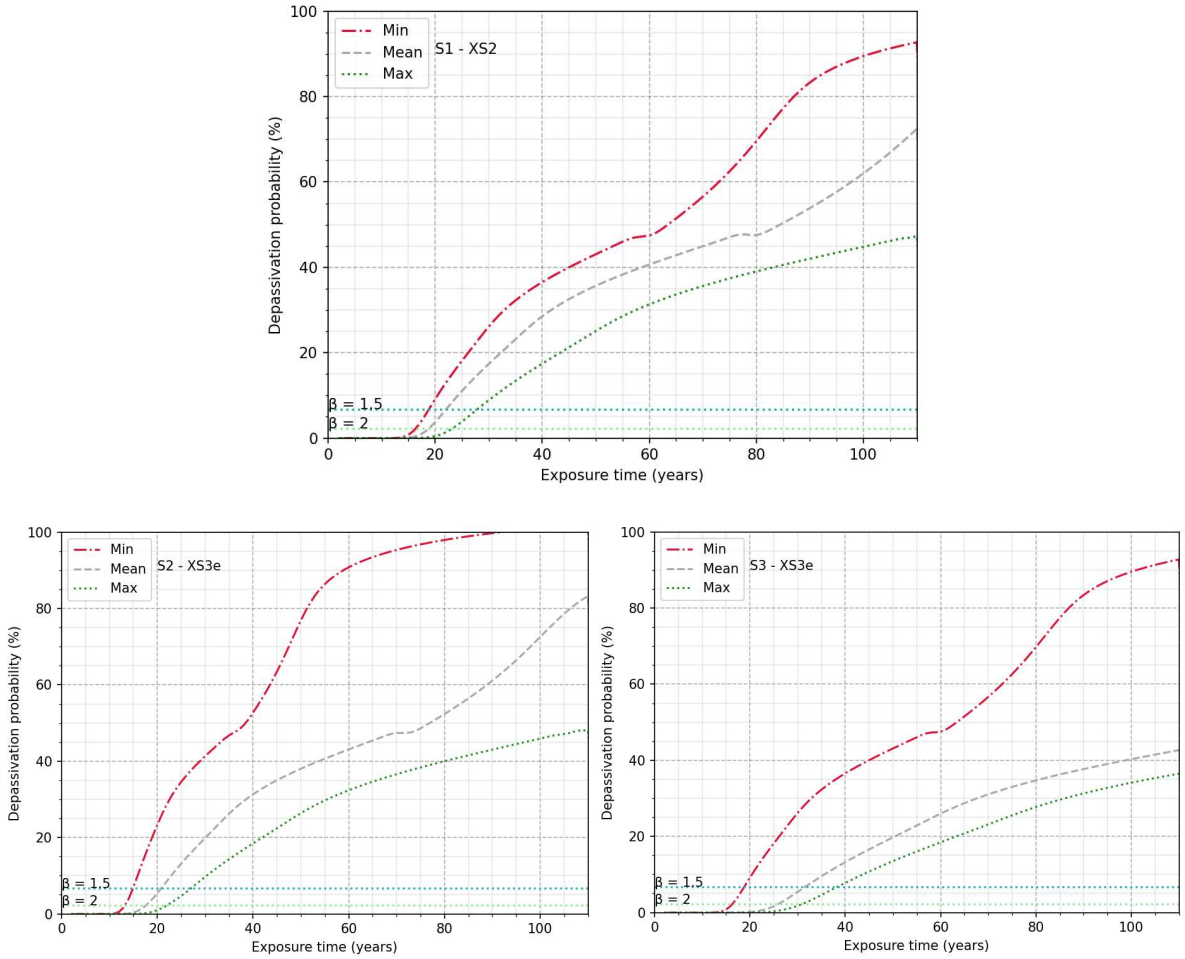

Figure IV-47 Depassivation probability as a function of exposure time with minimal, maximal, and mean concrete values.

The obtained data present complexities in their analysis and attributing a conclusion on the state of the structure is also challenging. However, it is clear that the depassivation probability exceeds the threshold value of 6.67%. In XS2 environments, considering the S1 minimal concrete cover, this value is reached after 19 years (while a value of 70 years is expected). In XS3e, for S2 and S3, the same analysis indicates times of 15 and 19 years, respectively (while the value expected is 97 years). On the other hand, when considering the maximal concrete cover, the times exceed 27, 26, and 39 years. Although these times do not correspond to the initiation of corrosion in the structure, they are expected to represent the desired duration for the structure to withstand aggression before depassivation, thus ensuring sufficient reliability. The results demonstrate that the current concrete cover is insufficient to meet the desired service life, given the assumptions made. These assumptions were based on limited data, which resulted in a high standard deviation that accounts for probable errors in the average values estimated using the different methods of the tool.

In the case of carbonation-induced corrosion, a method was employed to estimate the corrosion activity by calculating the depassivation probability and the distribution of concrete cover. It was determined that if more than 50% of the zone had a depassivation probability exceeding 25%, the corrosion would be considered active. In this study, the concrete cover distribution data was not provided. However, it can be assumed that the mean is similar to the median, and by considering this value, approximately 50% of the structure is affected. Therefore, the time required to reach a depassivation probability of 25% would correspond to the initiation of corrosion in that zone. Using this approach, corrosion initiation times of 35, 35, and 55 years were calculated for structures S1, S2, and S3, respectively. These values are relatively low compared to the expected service life and imply that maintenance and/or

repair would be necessary for these structures. Nevertheless, the validity of these results could not be verified due to the unavailability of corrosion activity data.

The mean and maximal values of concrete cover measured for S1 and S2 are similar (refer to Table IV-47). However, the environments considered for these structures are different, with S1 being exposed to XS2 and S2 being exposed to XS3e. The estimated depassivation probabilities for both structures are close to each other, with a slightly higher value obtained for S1. It is known that XS3e is more aggressive than XS2, which suggests that it should lead to a higher depassivation probability. The binder nature, specifically CEM V/A (S-V) for S1 and CEM III/B for S2, may be responsible for this discrepancy. It is hypothesized that the chloride resistance is better in the case of S2. However, further insight should be needed to compare the different exposure classes on similar materials and see if the environment is not erroneously considered.

IV.5. Conclusion and recommendations

The different computations, both deterministic and probabilistic, in this section demonstrate the practical application of the various models presented in Section I.4 (in conjunction with Annex 4), as well as the meta-model based on the finite element model SDReaM-Crete (refer to Section III.6.2).

The proposed methodology in this study is intricate, necessitating a comprehension of concrete material and its durability, as well as proficiency in various mathematical methods. Although the different parts of the methodology are thoroughly described in the manuscript, mastery and proper utilization may require significant time investment. Furthermore, additional verifications are always necessary as the methodology is not completely accurate.

Nevertheless, the implementation of an automated Python-based tool in this research allows users to successfully execute the various stages detailed in Section IV, ranging from input acquisition to probabilistic calculations. Additionally, this tool offers a basic checking system described in Section IV.2, that enables the reduction of error occurrences. However, it is important to note that users remain responsible for assessing the fairness of the final output.

The complexity of the methodology arises from two primary factors.

- Firstly, the consideration of complex phenomena and the highly variable nature of the concrete material necessitates the development of various models and algorithms that can adapt to each specific situation. Additionally, the introduction of new materials in concrete manufacturing adds to the complexity of predicting properties and durability in reinforced concrete. The incorporation of these novel materials necessitates the verification and adaptation of previously employed models.
- Secondly, when using this methodology in an operational context, where information regarding materials, geometry, and the environment may be lacking, it is necessary to develop a self-sufficient method capable of estimating the input parameters of major durability models when they are unknown to the user. The objective is to enable predictions with minimal input provided by the user while ensuring safety. This aspect often requires the use of assumptions, which can impact the final predictions. Thus, it is essential to measure and consider the uncertainties introduced in the computations. One attempt to address this issue is the definition of a confidence index.

The two main types of results obtained, deterministic and probabilistic, jointly allow for the visualization of the state of a reinforced concrete system as a function of time or design. However, it is crucial to carefully consider the results obtained when making decisions regarding maintenance. In general, a conservative approach is recommended in predictions, where the aim is to determine the time before

corrosion initiation to prevent it. However, to extend the lifespan estimation of the system, the propagation of corrosion can also be taken into account. If the propagation stage is integrated into the computations, the reliability level of the analysis must be increased as the consequences of the phenomenon can be more critical than simple depassivation and must be prevented.

To enhance the accuracy of predictions, inspections on structures are highly recommended. Specifically, it is crucial to assess durability parameters by examining core samples if the composition of the concrete utilised in the structure is unknown. This step ensures that the predictions are not flawed. For example, in the case of Arcadis' marine structure, the precise composition was unknown, and no durability indicators or properties were accessible. Merely knowing the nature of the binder was insufficient to estimate the parameters, thereby necessitating the use of assumptions to define the binder content for each zone. These assumptions negatively impact the accuracy of the predictions and should be avoided whenever possible, to ensure the most precise outputs.

The environmental conditions for the structure are generally easily obtainable as the location is typically known. Consequently, meteorological station data can be utilised to accurately define the environmental conditions. However, assessing the design and configuration of the structure part may prove more complex, leading to a decrease in the precision of the environmental parameters. This aspect, therefore, necessitates a thorough understanding of the structural weak spots to ensure accurate failure prediction in each of these locations. Specifically, it is imperative to measure the concrete cover or have precise knowledge of its value to facilitate meaningful predictions.

Non-destructive testing (NDT) techniques, although not always sufficient to fully assess the necessary parameters, can still provide valuable additional information that can facilitate the use of the tool. With a wide range of methodologies available for properties determination, such as artificial neural network (ANN)-based models, literature-based models, and the Closest Formulation Selection Algorithm (CFSA) defined in Section IV.3.2 and IV.3.3, it is often possible to capitalize on any additional measurements obtained through NDT. For example, conducting NDT to measure the mechanical resistance of a structure can aid in identifying similar compositions within the experimental results database and improve accuracy in predicting durability through model inputs.

The overall methodology and tool described in this document represent an initial version and are not completely foolproof. They may have certain limitations in assessing the structural durability and should be used with caution. Additionally, the output generated by these methods necessitate additional interpretation to make informed decisions regarding inspection and maintenance. Consequently, it is foreseeable that the integration of various modules and updates will be required. For instance, incorporating a more precise understanding of the mechanical aspect, such as considering the potential deterioration of mechanical strength due to corrosion, would present numerous advantages.

Furthermore, most supplementary cementitious materials (SCMs) that are being utilised in concrete materials remain incompletely understood. Therefore, to successfully incorporate these materials into the current developed tool, it is essential for the methodology itself to be adaptable and amendable. Various research investigations are presently being conducted on this subject. When experimental results, as well as new equations and models, become available, it will be imperative to update the tool to incorporate these new components into the model.

GENERAL CONCLUSIONS AND PERSPECTIVES

The construction sector is currently encountering two primary challenges. Firstly, within the context of global warming, there is a need for changes in construction methods, to reduce the environmental impact of this sector. This has led to the development of new materials for reinforced concrete productions, specifically low-carbon concretes that are likely to be utilised in the near future. Consequently, there is an increasing need for the accurate prediction and modelling of these low-carbon concretes, which are still not well understood. Secondly, structures that were built following the great war and during the thirty glorious years are now reaching a long service life and suffering from degradation, necessitating appropriate actions. Lengthening their service life constitutes an important lever for the reduction of the construction carbon footprint. Addressing both challenges requires efficient predictions and a precise methodology to assist civil engineering professionals in making informed decisions.

The objective of this research was to participate in the development of a methodology for the reduction of the financial and ecological impact of structures while ensuring performance and safety. Therefore, the first chapter of this document presented a literature review on the durability and modelling of reinforced concrete. It explored different approaches to reduce the carbon footprint, particularly the use of mineral additions, whether inert or reactive. The impact of these SCMs on the concrete microstructure and the durability of reinforced concrete against carbonation and chloride-induced corrosion was addressed. The findings highlighted the complexity of these phenomena but demonstrated real possibilities for producing decarbonized concretes. The literature data still need to be completed, especially for these newer cement types. However, the implementation of these new solutions can't be delayed because of the emergency of the sector decarbonation. This point also motivated the development of an experimental campaign for this PhD project, including durability measurements on low-carbon binders and cement + SCMs solutions.

Additionally, a literature review on the various methods available for predicting concrete properties, depassivation induced by carbonation or chloride, and corrosion propagation was presented. Each model has specific features and considers different inputs, as they are generally tailored to specific situations. This aspect complicates the durability prediction, particularly when the application ranges of the models are unclear. Therefore, it was necessary to identify suitable models according to the environment and the type of material. In order to increase the flexibility of the methodology for considering carbonation and chloride ingress, various literature models were selected and tested. However, these models need to be faced experimental measurements conducted in different environments or exposure classes (defined in NF EN 206/CN (2022)), and for different types of binders. The scarcity in the literature of available models for hydration and durability prediction for low clinker-based concretes motivated certain choices in the experimental design, such as the manufacturing of metakaolin and fly ash-based concrete for hydration studies, and CEM III/B and CEM V/A-based concrete for durability studies.

The second chapter of this document focused on the experimental measurements carried out on the microstructure and durability of new binders. These results obtained were essential for considering these binders in the finite element model developed and the final methodology. Six concrete mixes were defined: a reference mix based on CEM I, two mixes with 15 wt.% of mineral additions (metakaolin and fly ash), a concrete mix based on CEM III/B, a concrete mix based on CEM V/A (S-V), and a recomposed mix based on CEM VI (S-V) using the two preceding cements. The main differentiation between these mixes was the type of binder used, while the binder content, water to binder ratio, aggregate type, and content were similar for all mixes. Therefore, most of the variation in the results can be attributed to the nature of the binder.

The results obtained from concrete and mortars containing metakaolin, fly ash, and slag have partially validated and improved the predictions made in the third and fourth chapters. They not only served for modelling and improving predictions, but also provided various insights. Firstly, it was observed that concrete mixes incorporating reactive mineral additions required longer conservation periods for being efficient, particularly in relation to carbonation rate, electrical resistivity, chloride diffusion coefficient, as well as gas and liquid permeabilities. These findings highlighted the limitations of the materials formulated in the present study (W_{eff}/B_{tot} = 0.5). It is crucial to note that other levers than conservation and curing exist and allow higher performances in SCMs-based concretes to develop. The reduction of the W_{eff}/B_{tot} ratio, the use of thermal treatment and the optimisation of the granular skeleton can be efficient ways to favour good durability in these concretes. The work realised in Section IV.3.3 and the indices of Daminelli especially showed the high societal interest of these solutions.

Secondly, the results aligned with the existing literature when it comes to the performance of pozzolanic and latent hydraulic additions. Concrete with higher clinker contents demonstrated improved resistance to carbonation, indicating the intrinsic relationship between portlandite content and carbonation rate. Mixes with increased levels of pozzolanic and latent hydraulic additions displayed enhanced performance in terms of chloride resistance and electrical characteristics, suggesting the potential benefits of these new binder materials.

Thirdly, the mechanical properties of the concrete generally matched the expectations based on the technical data sheets of the cement, except for the F2 and F6 mixes. The low mechanical strength observed in F2_CEMIII/B_0.49_35, both in mortar and concrete, can likely be attributed to a batch of defective cement and the low cement characteristic strength of 32.5 MPa. On the other hand, F6_CEMVI_0.5_48*, which consisted of a combination of CEM V/A (S-V) 42.5N and CEM III/B 32.5N, exhibited higher mechanical performance, almost at the level of F5_CEMV/A_0.49_51. This superiority can be attributed to several factors: firstly, the fineness of the cements used in F6 was different, potentially enabling better compaction of the mixture. Secondly, the high slag content in CEM III/B necessitates an activator (portlandite) for proper hydration. It is likely that the clinker content in the initial cement was insufficient to fully hydrate the slag. However, the higher clinker content in CEM V/A allowed for the hydration of the remaining slag, resulting in increased mechanical strength. The results obtained, also in terms of carbonation and chloride penetration resistance, give promising sight of the possibility to mix different cements, with potential increase of the material performances.

In the third chapter, the focus shifted to the durability model SDReaM-Crete, which was modified and validated. This Finite Element Model, initially developed using Comsol by Mai-Nhu [7], underwent improvements during Schmitt's Ph.D. [6]. These enhancements included the incorporation of slag and filler-based concretes in the model, as well as the creation of surrogate models based on the results from the finite element model. The modifications made in the present study encompassed the following aspects:

- Addition of conservation and curing consideration in the model, based primarily on the experimental results obtained from samples conserved under dry, external, and moist conditions.
- Fitting of equations to new binders containing metakaolin, fly ash, and ternary binders. This was done to accommodate low-carbon concretes.
- Enhancement of the modelling of partial pressure of CO_2 (for accelerated testing) and hydrologic transfers, by developing new methods for determining water permeability and desorption isotherms.
- Modification of the pH equation for natural carbonation, in order to better account for low-carbon concretes with lower portlandite contents.

- Improvement in the modelling of chloride convection, allowing for the consideration of XS3 and XD3 exposure classes.

The model validation was based on results obtained from the concretes dedicated to this Ph.D. study as well as existing literature results, specifically the PerfDuB investigations on carbonation. This validation process confirmed the accuracy of most parts of the model, but also highlighted the need for further improvements.

Adequately considering the different binders was tricky, particularly for acquiring the input parameters. The model encompasses numerous input parameters, which in turn present a challenge in defining their accurate values adaptable to specific situations. This justified developing an efficient tool capable of automatically predicting the inputs based on the composition and environmental parameters. While the current version of the model and tool perform within certain limitations in terms of composition, further attention should be given to enable the consideration of alternative binders or binders with high contents of Supplementary Cementitious Materials (SCMs).

To enhance the model, it is suggested to focus on improving the calculation of liquid permeability and desorption isotherms, possibly by taking into account the influence of mineral additions. The transfer of moisture has indeed a significant impact on both carbonation and chloride ingress and should be adequately accounted for in the model. A sharpened criticism that can be addressed to the model is the absence of hysteresis for the sorption/desorption isotherm. Currently, only the desorption isotherm is considered, which could lead to erroneous estimations, particularly in the case of cyclic variations in relative humidity. Therefore, modifications need to be made to the model's equations to better account for this aspect and to consider certain environments, such as XD3 and XS3 exposure classes.

Additionally, it is necessary to investigate the binding of chloride, which was not assessed in this Ph.D. study and was solely based on one literature source in previous studies using SDReaM-Crete. This aspect of the model affects the diffusion of chloride in the material and cannot be neglected.

The computation of pH could be further improved by either replacing the equations or considering the actual composition of the interstitial solutions with the presence of different alkaline species. However, this would require extensive work and increase computational time.

Due to the lengthy computation process, the model was not directly suitable for operational use. To address this issue, the building of meta-models through polynomial chaos expansion (PCE) was investigated. PCE was preferred over artificial neural networks (ANN) as it yielded better results for this specific application. However, alternative methods to PCE could potentially yield improved performance and should be explored. The surrogate models developed using PCE allowed almost instantaneous computation with minimal loss of precision. Separate surrogate models were created for carbonation and chloride ingress to facilitate quicker computations in the final tool, as well as enable probabilistic analysis. The validation of the model and surrogate models was conducted by using laboratory results in Section III.

The final chapter presented a tool and methodology developed based on the three previous sections. The objective of this tool was to predict the condition state of a reinforced concrete structure exposed to carbonation and chloride ingress. The output of this tool should enable the user to assess the overall structure state, as well as identify weak spots and singularities. The methodology consisted of several defined steps:

First, the user must enter the available data into the application, which is then transforms into inputs to the durability models. The goal is to efficiently utilize the available data, regardless of its type, in order to accurately predict the structure current and future condition state. Various techniques have been employed to process the data in order to achieve this goal. The literature has been extensively utilised

as a primary resource, because it contains numerous data and models for computing different properties based on the concrete composition. Some of these models have been improved to consider new mineral additions that were not originally accounted for in the initial works.

Additionally, an experimental results database was created during this PhD research and used to estimate model inputs when efficient literature methods were not available. The tool applies two main methods: learning-based models and the Closest Formulation Selection Algorithm (CFSA). Both methods allow the estimation of these inputs according to composition parameters of the mix considered.

Regardless of the method employed to estimate input parameters, it is necessary to measure the uncertainties associated with the prediction. Therefore, a confidence index was defined within the framework of this study, ranging between 0.25 and 1.25. This index serves to inform the user about the consistency of the parameter prediction method, as well as to influence the probabilistic computations by adjusting the value of the standard-deviation for the parameter associated. Default standard-deviations were established for all input parameters of the durability models, then affected by the confidence index. This approach intended to account for potential estimation errors in the average parameter value. It should be noted that only a few tests have been conducted on this method, and additional verifications will be necessary. These verifications will likely result in some modifications to balance the calculation of the confidence index for each parameter acquisition method.

Once the input parameters and the associated confidence indices are obtained, the user is presented with various durability models. The objective was to develop an application capable of considering carbonation and chloride-induced corrosion from initiation to critical mechanical loss. Currently, the application has implemented initiation models (based on literature and SDReaM-Crete surrogate models) as well as propagation models able to predict concrete cover cracking. Several comparisons were conducted with both laboratory and on-field experimental data. These tests led to specific recommendations regarding the models' performance based on the exposure class and binder nature considered.

The tool allows for the implementation of deterministic and probabilistic computations according to the need. Although more enhanced reliability methods exist, FORM was selected due its easy and efficient connection to the tool, allowing:

- The automated computation of standard deviation and distribution parameters of random variables, based on experimental results, literature, and standards. It leads to a fair estimation of variability, that remains adaptable by the user.
- The ability to associate depassivation and propagation predictions, enabling the stacking of different models to predict a single value instead of predicting individual values for each stage of the corrosion process.

This document presents the initial version of the tool, which requires numerous modifications and validations to ensure a relevant and versatile functioning in all scenarios. To facilitate continuous improvement, a second database of results has been established. This database includes data from structural archives and inspections, as well as the tool's prediction results. The purpose is to record feedback on the tool's utilization, to avoid repeating errors and enable verification of results with previous cases. It is important to note that relying solely on a comparison of the tool's output is insufficient. Each step of the tool's utilization, from input computation to probabilistic computations, must be thoroughly analysed.

Although several verifications were conducted on existing structures in the present work, no predictions were made for new structures using the performance-based approach. Therefore, it is necessary to

apply the tool in such cases to determine if reliable predictions can be obtained using the models based on accelerated indicators of the FD P18-480 (2022) and compositions alone.

Future versions of the application should incorporate the consideration of specific factors, such as cracking. The presence of coating, which is commonly used maintenance/repair solution in bridge structures, must also be taken into account. However, further verification is required, including the acquisition of experimental results on structures. Additionally, the service life of the coating, which is estimated to be around 20 years, must be considered. One possible approach could involve the development of a surrogate model based on SDReaM-Crete finite element model to encompass these considerations.

From a global perspective, the concrete construction sector will continue to undergo evolution, including the development of new recommendations, particularly regarding the use of low carbon binders and innovative mixes. The ability of numerical tools to adapt to these new guidelines and incorporate them into their functionality will remain an advantage. The decision to develop the present tool using an open-source programming language was influenced by this need, with the aim of making it more flexible and easily modifiable.

Furthermore, other aspects need to be modified in the tool. The algorithms developed should be improved to minimize the time taken for different mathematical processes, such as the FORM algorithm. Additionally, time and accuracy could be improved by creating lighter surrogate models such as sparse PCE. Therefore, further improvements in the creation of surrogate models are necessary. A Latin Hypercube Sampling (LHS) method was employed instead of a crude Monte-Carlo method. However, it was subsequently discovered that alternative approaches, like using pseudo random sequences (e.g., Sobol), could reduce computation time and still produce reliable surrogate models. Therefore, investigating these alternative methods would be valuable in increasing the efficiency of creating new surrogate models, particularly when modifications are made to the initial finite element model.

The remaining parts of the tool, including the computation of the confidence index and the CFSA, need to be validated using additional results. This may induce slight modifications to the implemented methods. Furthermore, acquiring new experimental results in the database will be essential for the effective functioning of the search algorithm and the development of learning-based models. This aspect is particularly important for low carbon concretes with high SCM contents. It could also offer a reliable method for estimating the chloride diffusion coefficient, which is not always well considered in the current version of the tool.

The current version of the tool only accepts results from structure inspections for comparison in deterministic computations. This feature assists users in selecting the most efficient models. However, there is room for further improvement, specifically in creating an automatic update mechanism for predictions to enhance reliability. Additionally, maintenance and repairs should also be considered as they can modify the structure's capability to endure aggressive environments. This aspect has been addressed in previous studies [435], [436] and is mandatory for the present tool's improvement. Acquisition of experimental measurements on structures would be necessary for this purpose. Moreover, it is crucial to consider defects and singularities, such as cracks, which can significantly increase the degradation of reinforced concrete systems. Utilizing three-dimensional modelling that accounts for specific zones could be a valuable option, despite the increased prediction time. Although the study does not account for the impact of global warming, the models and the tool already allow for the consideration of induced temperature increases.

Although refinement and further development of the tool, together with complementary validation phases, are still needed, the main milestones, logical and numerical architecture of a methodology have been proposed and comfortably established in the present work, aiming at contributing to the required transformation of the concrete construction sector facing its future challenges.

The French construction ministry has set a national low carbon strategy aiming for carbon neutrality by 2050. Achieving this target relies heavily on the construction sector's ability to replace harmful components with new eco-friendly materials while ensuring the reliability and safety of constructions. The study of reinforced concrete system durability falls within this scope, and additional research is required to enable accurate predictions and constructions. The recent boom of artificial intelligence in society may also play a decisive role in influencing this field, as it does in many other domains.

BIBLIOGRAPHY

[1] IEA, « Global Status Report for Buildings and Construction 2019 ». https://www.iea.org/reports/global-status-report-for-buildings-and-construction-2019, License: CC BY 4.0, 2019.

[2] « Accueil », PERFDUB. Consulté le: 18 janvier 2023. [En ligne]. Disponible sur: https://www.perfdub.fr/

[3] Conseil national de l'industrie, « Décarbonatation de l'industrie - Feuille de route de la filière ciment (mai 2021) ». 2021.

[4] A. D'Alessandro, C. Fabiani, A. L. Pisello, F. Ubertini, A. Materazzi, et F. Cotana, « Innovative concretes for low carbon constructions: a review », *Int. J. Low-Carbon Technol.*, mai 2016, doi: 10.1093/ijlct/ctw013.

[5] R. Polder, W. H. A. Peelen, M. Raupach, et K. Reichling, « Economic effects of full corrosion surveys for aging concrete structures », *Mater. Corros.*, vol. 64, févr. 2013, doi: 10.1002/maco.201206709.

[6] L. Schmitt, « Durabilité des ouvrages en béton soumis à la corrosion: optimisation par une approche probabiliste », Thèse de doctorat, LMDC, INSA Toulouse, 2019.

[7] J. Mai-Nhu, « Corrosion des armatures du béton : couplage carbonatation-chlorures en présence de cycles hydriques », Thèse de doctorat, LMDC, INSA Toulouse, 2013.

[8] « Cement – Analysis », IEA. Consulté le: 18 janvier 2023. [En ligne]. Disponible sur: https://www.iea.org/reports/cement

[9] « TecEco - Home ». Consulté le: 18 janvier 2023. [En ligne]. Disponible sur: https://www.tececo.com/

[10] L. Linger, L. Boutillon, et G. Thomas, « - L'EMPREINTE CO2 DU BETON ».

[11] « Cement: production ranking top countries 2021 », Statista. Consulté le: 18 janvier 2023. [En ligne]. Disponible sur: https://www.statista.com/statistics/267364/world-cement-production-by-country/

[12] CEMBUREAU, « 2021 Activity Report ». 2021.

[13] M. S. Imbabi, C. Carrigan, et S. McKenna, « Trends and developments in green cement and concrete technology », *Int. J. Sustain. Built Environ.*, vol. 1, n° 2, p. 194-216, déc. 2012, doi: 10.1016/j.ijsbe.2013.05.001.

[14] « Home », FastCarb. Consulté le: 20 mars 2023. [En ligne]. Disponible sur: https://fastcarb.fr/en/home/

[15] B. Hou, *The Cost of Corrosion in China*. 2019. doi: 10.1007/978-981-32-9354-0.

[16] U. Angst, « Challenges and opportunities in corrosion of steel in concrete », *Mater. Struct.*, vol. 51, févr. 2018, doi: 10.1617/s11527-017-1131-6.

[17] L. Yan, W. Deng, N. Wang, X. Xue, J. Hua, et Z. Chen, « Anti-Corrosion Reinforcements Using Coating Technologies—A Review », *Polymers*, vol. 14, n° 21, Art. n° 21, janv. 2022, doi: 10.3390/polym14214782.

[18] V. S. Bhatia, « 2017 ASCE Infrastructure Report Card ». Consulté le: 16 mars 2023. [En ligne]. Disponible sur: https://blog.envirosight.com/2017-asce-infrastructure-report-card

[19] « NF EN 206/CN », Afnor EDITIONS. Consulté le: 18 janvier 2023. [En ligne]. Disponible sur: https://www.boutique.afnor.org/fr-fr/norme/nf-en-206-cn/beton-specification-performance-production-et-conformite-complement-nationa/fa185553/1463

[20] M. Bartholomew *et al.*, « fib Bulletin 76. Benchmarking of deemed-to- satisfy provisions in standards: Durability of reinforced concrete structures exposed to chlorides », fib. The International Federation for Structural Concrete, Éd., in fib Bulletins. fib. The International Federation for Structural Concrete, mai 2015. doi: 10.35789/fib.BULL.0076.

[21] Normes Internationales ISO, « ISO 13824:2020 Bases for design of structures - General principles on risk assessment of systems involving structures ». 2020.

[22] Normes Internationales ISO, « ISO 2394:2015 Principes généraux de la fiabilité des constructions ». 2015.

[23] O. Gooranorimi et K. N. Shiu, « Maintenance and Repair Costs for Different Types of Parking Structures ».
[24] B. Bary et A. Sellier, « Coupled moisture—carbon dioxide–calcium transfer model for carbonation of concrete », *Cem. Concr. Res.*, vol. 34, nº 10, p. 1859-1872, oct. 2004, doi: 10.1016/j.cemconres.2004.01.025.
[25] J. Mai-Nhu *et al.*, « Probabilistic approach for durable design of concrete cover: Application to carbonation », *Eur. J. Environ. Civ. Eng.*, vol. 16, p. 264-272, mars 2012, doi: 10.1080/19648189.2012.667705.
[26] J. Mai-Nhu, A. Sellier, P. Rougeau, et F. Duprat, « Numerical tool for durability assessment of concrete structures subjected to aggressive environment, Numerical Modelling, Strategies for Sustainable Concrete Structures », Aix-en-Provence, 2012.
[27] S. Demis, M. P. Efstathiou, et V. G. Papadakis, « Computer-aided modeling of concrete service life », *Cem. Concr. Compos.*, vol. 47, p. 9-18, mars 2014, doi: 10.1016/j.cemconcomp.2013.11.004.
[28] « PlotDigitizer: Extract Data from Graph Image Online », PlotDigitizer. Consulté le: 5 juillet 2023. [En ligne]. Disponible sur: https://plotdigitizer.com/
[29] « Welcome to Python.org », Python.org. Consulté le: 19 janvier 2023. [En ligne]. Disponible sur: https://www.python.org/
[30] « Matplotlib — Visualization with Python ». Consulté le: 5 juillet 2023. [En ligne]. Disponible sur: https://matplotlib.org/
[31] Saloma, A. Nasution, I. Imran, et M. Abdullah, « Improvement of Concrete Durability by Nanomaterials », *Procedia Eng.*, vol. 125, p. 608-612, 2015, doi: 10.1016/j.proeng.2015.11.078.
[32] CERIB, « Ressources minérales pour les liants des bétons décarbonés : disponibilité, perspectives d'évolution et innovations ». 2022.
[33] F. De Larrard, *Concrete Mixture Proportioning: A Scientific Approach*. London: CRC Press, 1999. doi: 10.1201/9781482272055.
[34] « NF P18-545 », Afnor EDITIONS. Consulté le: 20 mars 2023. [En ligne]. Disponible sur: https://www.boutique.afnor.org/fr-fr/norme/nf-p18545/granulats-elements-de-definition-conformite-et-codification/fa164857/37796
[35] A. Osouli, R. Chaulagai, E. Tutumluer, et H. Shoup, « Strength characteristics of crushed gravel and limestone aggregates with up to 12% plastic fines evaluated for pavement base/subbase applications », *Transp. Geotech.*, vol. 18, p. 25-38, mars 2019, doi: 10.1016/j.trgeo.2018.10.004.
[36] M. Naderi et A. Kaboudan, « Experimental study of the effect of aggregate type on concrete strength and permeability », *J. Build. Eng.*, vol. 37, p. 101928, mai 2021, doi: 10.1016/j.jobe.2020.101928.
[37] S. Yehia, A. Abdelfatah, et D. Mansour, « Effect of Aggregate Type and Specimen Configuration on Concrete Compressive Strength », *Crystals*, vol. 10, nº 7, Art. nº 7, juill. 2020, doi: 10.3390/cryst10070625.
[38] R. K. Dhir, J. de Brito, R. V. Silva, et C. Q. Lye, « 10 - Recycled Aggregate Concrete: Durability Properties », in *Sustainable Construction Materials*, R. K. Dhir, J. de Brito, R. V. Silva, et C. Q. Lye, Éd., in Woodhead Publishing Series in Civil and Structural Engineering. , Woodhead Publishing, 2019, p. 365-418. doi: 10.1016/B978-0-08-100985-7.00010-8.
[39] V. Carević, I. Ignjatović, et J. Dragaš, « Model for practical carbonation depth prediction for high volume fly ash concrete and recycled aggregate concrete », *Constr. Build. Mater.*, vol. 213, p. 194-208, juill. 2019, doi: 10.1016/j.conbuildmat.2019.03.267.
[40] M. Gomes et J. de Brito, « Structural concrete with incorporation of coarse recycled concrete and ceramic aggregates: durability performance », *Mater. Struct.*, vol. 42, nº 5, p. 663-675, juin 2009, doi: 10.1617/s11527-008-9411-9.
[41] G. Kumar et S. S. Mishra, « Effect of recycled concrete aggregate on mechanical, physical and durability properties of GGBS–fly ash-based geopolymer concrete », *Innov. Infrastruct. Solut.*, vol. 7, nº 4, p. 237, mai 2022, doi: 10.1007/s41062-022-00832-w.

[42] R. Kurda, J. D. Silvestre, J. de Brito, et H. Ahmed, « Optimizing recycled concrete containing high volume of fly ash in terms of the embodied energy and chloride ion resistance », *J. Clean. Prod.*, vol. 194, p. 735-750, sept. 2018, doi: 10.1016/j.jclepro.2018.05.177.
[43] K. McNeil et T. H.-K. Kang, « Recycled Concrete Aggregates: A Review », *Int. J. Concr. Struct. Mater.*, vol. 7, n° 1, Art. n° 1, mars 2013, doi: 10.1007/s40069-013-0032-5.
[44] M. Etxeberria, E. Vázquez, A. Marí, et M. Barra, « Influence of amount of recycled coarse aggregates and production process on properties of recycled aggregate concrete », *Cem. Concr. Res.*, vol. 37, n° 5, p. 735-742, mai 2007, doi: 10.1016/j.cemconres.2007.02.002.
[45] K. K. Sagoe-Crentsil, T. Brown, et A. H. Taylor, « Performance of concrete made with commercially produced coarse recycled concrete aggregate », *Cem. Concr. Res.*, vol. 31, n° 5, p. 707-712, mai 2001, doi: 10.1016/S0008-8846(00)00476-2.
[46] I. Maruyama, M. Sogo, et T. Sogabe, « Flexural properties of reinforced recycled concrete beams », *Proc. Int. RILEM Conf. Use Recycl. Mater. Build. Struct.*, p. 8-11, janv. 2004.
[47] Afnor EDITIONS, « NF P18-513 Addition pour béton hydraulique - Métakaolin - Spécifications et critères de conformité ». 2012.
[48] D. K. Panesar, « 3 - Supplementary cementing materials », in *Developments in the Formulation and Reinforcement of Concrete (Second Edition)*, S. Mindess, Éd., in Woodhead Publishing Series in Civil and Structural Engineering. , Woodhead Publishing, 2019, p. 55-85. doi: 10.1016/B978-0-08-102616-8.00003-4.
[49] Ž. Michal, V. Tomáš, et L. Ingrisova, « Dosage of Metakaolin in High Performance Concrete », *Key Eng. Mater.*, vol. 722, p. 311-315, déc. 2016, doi: 10.4028/www.scientific.net/KEM.722.311.
[50] J. J. Chen, Q. H. Li, P. L. Ng, L. G. Li, et A. K. H. Kwan, « Cement Equivalence of Metakaolin for Workability, Cohesiveness, Strength and Sorptivity of Concrete », *Materials*, vol. 13, n° 7, p. 1646, avr. 2020, doi: 10.3390/ma13071646.
[51] J. Khatib, « Metakaolin concrete at a low water to binder ratio », *Constr. Build. Mater. - CONSTR BUILD MATER*, vol. 22, p. 1691-1700, août 2008, doi: 10.1016/j.conbuildmat.2007.06.003.
[52] ASTM, « ASTM C618-19 Standard Specification for Coal Fly Ash and Raw or Calcined Natural Pozzolan for Use in Concrete ». 2022.
[53] AFNOR, « NF EN 450-1 Cendres volantes pour béton - Partie 1 : définition, spécifications et critères de conformité ». 2012.
[54] S. Diamond, « Effects of two Danish flyashes on alkali contents of pore solutions of cement-flyash pastes », *Cem. Concr. Res.*, vol. 11, n° 3, p. 383-394, mai 1981, doi: 10.1016/0008-8846(81)90110-1.
[55] M. J. McCarthy et T. D. Dyer, « Pozzolanas and pozzolanic materials », in *Lea's Chemistry of Cement and Concrete*, Elsevier, 2019, p. 363-467. doi: 10.1016/B978-0-08-100773-0.00009-5.
[56] « ASTM C989-05 Standard Specification for Ground Granulated Blast-Furnace Slag for Use in Concrete and Mortars ». 2017. Consulté le: 18 janvier 2023. [En ligne]. Disponible sur: https://www.astm.org/c0989-05.html
[57] « NF EN 15167-1 », Afnor EDITIONS. Consulté le: 18 janvier 2023. [En ligne]. Disponible sur: https://www.boutique.afnor.org/fr-fr/norme/nf-en-151671/laitier-granule-de-hautfourneau-moulu-pour-utilisation-dans-le-beton-mortie/fa137602/28082
[58] A. Zelwer et A. Le Roux, « MATERIAUX SPECIFIQUES DE GENIE CIVIL - LA PHASE LIQUIDE DU CIMENT HYDRATE. PERSPECTIVES POUR LA REACTION ALCALI-SILICE », *ETUDES Rech. 1990 RESEAU LPC*, 1991, Consulté le: 18 janvier 2023. [En ligne]. Disponible sur: https://trid.trb.org/view/1010600
[59] M. Moranville-Regourd et S. Kamali-Bernard, « 10 - Cements Made From Blastfurnace Slag », in *Lea's Chemistry of Cement and Concrete (Fifth Edition)*, P. C. Hewlett et M. Liska, Éd., Butterworth-Heinemann, 2019, p. 469-507. doi: 10.1016/B978-0-08-100773-0.00010-1.
[60] P. Smarzewski, « Influence of silica fume on mechanical and fracture properties of high performance concrete », *Procedia Struct. Integr.*, vol. 17, p. 5-12, janv. 2019, doi: 10.1016/j.prostr.2019.08.002.

[61] M. F. M. Zain, M. Safiuddin, et H. Mahmud, « Development of high performance concrete using silica fume at relatively high water–binder ratios », *Cem. Concr. Res.*, vol. 30, n° 9, p. 1501-1505, sept. 2000, doi: 10.1016/S0008-8846(00)00359-8.
[62] A. Mansor, A. Hamed, et R. Borg, « Effect of Silica Fume on High Performance Concrete Strength », mars 2016.
[63] A. T. Tabereaux et R. D. Peterson, « Chapter 2.5 - Aluminum Production », in *Treatise on Process Metallurgy*, S. Seetharaman, Éd., Boston: Elsevier, 2014, p. 839-917. doi: 10.1016/B978-0-08-096988-6.00023-7.
[64] « Opportunities for use of bauxite residue in cement », International Aluminium Institute. Consulté le: 18 janvier 2023. [En ligne]. Disponible sur: https://international-aluminium.org/resource/opportunities-for-use-of-bauxite-residue-supplementary-cementitious/
[65] International Aluminium Institute, « Opportunities for use of bauxite residue in special cements ». World Aluminium.
[66] V. G. Papadakis, « Experimental investigation and theoretical modeling of silica fume activity in concrete », *Cem. Concr. Res.*, vol. 29, n° 1, p. 79-86, janv. 1999, doi: 10.1016/S0008-8846(98)00171-9.
[67] M. Adjoudj, « Effet des additions minérales et organiques sur le comportement rhéologique du béton ».
[68] H. Elçi, N. Türk, et I. işintek, « Limestone dimension stone quarry waste properties for concrete in Western Turkey », *Arab. J. Geosci.*, vol. 8, mars 2015, doi: 10.1007/s12517-015-1838-z.
[69] « Blast Furnace Slag – IspatGuru ». Consulté le: 21 mars 2023. [En ligne]. Disponible sur: https://www.ispatguru.com/blast-furnace-slag/
[70] L. Courard, A. Darimont, M. Schouterden, F. Ferauche, X. Willem, et R. Degeimbre, « Durability of mortars modified with metakaolin », *Cem. Concr. Res.*, vol. 33, n° 9, p. 1473-1479, sept. 2003, doi: 10.1016/S0008-8846(03)00090-5.
[71] C. Perlot et P. Rougeau, « Intérêt des métakaolins dans les bétons », *Monogr. Cent. DÉtudes Rech. Ind. Béton*, janv. 2007.
[72] K. A. Gruber, T. Ramlochan, A. Boddy, D. Hooton, et M. D. A. Thomas, « Increasing Concrete Durability With High-Reactivity Metakaolin », *Cem. Concr. Compos.*, vol. 23, p. 479-484, déc. 2001, doi: 10.1016/S0958-9465(00)00097-4.
[73] M. D. A. Thomas et J. D. Matthews, « Carbonation of fly ash concrete », *Mag. Concr. Res.*, n° 1, p. 12, 1992.
[74] Z. Liu, D. Xu, et Y. Zhang, « Experimental Investigation and Quantitative Calculation of the Degree of Hydration and Products in Fly Ash-Cement Mixtures », *Adv. Mater. Sci. Eng.*, vol. 2017, p. 1-12, 2017, doi: 10.1155/2017/2437270.
[75] « Rheology and setting of high volume fly ash mixtures », *ResearchGate*, doi: 10.1016/j.cemconcomp.2010.01.008.
[76] Y. Liu et Y. Wei, « Effect of calcined bauxite powder or aggregate on the shrinkage properties of UHPC », *Cem. Concr. Compos.*, vol. 118, p. 103967, avr. 2021, doi: 10.1016/j.cemconcomp.2021.103967.
[77] B. Alsubari, « Influence of fly ash and GGBFS on the pH value of cement mortar in different curing conditions », *Adv. Concr. Constr.*, juin 2021, doi: 10.12989/acc.2021.11.5.419.
[78] *Dossier 2005: référentiel des matériaux d'un stockage de déchets à haute activité et à vie longue. Tome 2, Matériaux cimentaires*. in Collection Les Rapports - ANDRA. Châtenay-Malabry: ANDRA, 2005.
[79] F. R. Andriolo et B. C. Sgaraboza, « Proceedings of the 7th International Conference of AAR », p. 66-70, 1985.
[80] « Infociments : la base documentaire de référence sur les ciments et bétons ». Consulté le: 21 mars 2023. [En ligne]. Disponible sur: https://www.infociments.fr/
[81] P. Suraneni, A. Hajibabaee, S. Ramanathan, Y. Wang, et J. Weiss, « New insights from reactivity testing of supplementary cementitious materials », *Cem. Concr. Compos.*, vol. 103, p. 331-338, oct. 2019, doi: 10.1016/j.cemconcomp.2019.05.017.

[82] AFNOR, « NF EN 197-1 Ciment - Partie 1 : composition, spécifications et critères de conformité des ciments courants ». 2012. Consulté le: 18 janvier 2023. [En ligne]. Disponible sur: https://www.boutique.afnor.org/fr-fr/norme/nf-en-1971/ciment-partie-1-composition-specifications-et-criteres-de-conformite-des-ci/fa149898/1234
[83] « NF EN 197-5 Ciment - Partie 5 : ciment Portland composé CEM II/C-M et Ciment composé CEM VI ». 2021. Consulté le: 6 février 2023. [En ligne]. Disponible sur: https://www.boutique.afnor.org/fr-fr/norme/nf-en-1975/ciment-partie-5-ciment-portland-compose-cem-ii-cm-et-ciment-compose-cem-vi/fa200094/264804
[84] J. W. Bullard *et al.*, « Mechanisms of cement hydration », *Cem. Concr. Res.*, vol. 41, n° 12, p. 1208-1223, déc. 2011, doi: 10.1016/j.cemconres.2010.09.011.
[85] J. Duchesne et E. J. Reardon, « Measurement and prediction of portlandite solubility in alkali solutions », *Cem. Concr. Res.*, vol. 25, n° 5, p. 1043-1053, juill. 1995, doi: 10.1016/0008-8846(95)00099-X.
[86] « Microstructure and microanalysis of hardened cement pastes involving ground granulated blast-furnace slag | SpringerLink ». Consulté le: 19 janvier 2023. [En ligne]. Disponible sur: https://link.springer.com/article/10.1007/BF01133772
[87] S. Stephant, « Étude de l'influence de l'hydratation des laitiers sur les propriétés de transfert gazeux dans les matériaux cimentaires », 2015. doi: 10.13140/RG.2.1.1665.4483.
[88] M. I. C. Sousa et J. H. da S. Rêgo, « Effect of nanosilica/metakaolin ratio on the calcium alumina silicate hydrate (C-A-S-H) formed in ternary cement pastes », *J. Build. Eng.*, vol. 38, p. 102226, juin 2021, doi: 10.1016/j.jobe.2021.102226.
[89] A. C. A. Muller, K. L. Scrivener, J. Skibsted, A. M. Gajewicz, et P. J. McDonald, « Influence of silica fume on the microstructure of cement pastes: New insights from 1H NMR relaxometry », *Cem. Concr. Res.*, vol. 74, p. 116-125, août 2015, doi: 10.1016/j.cemconres.2015.04.005.
[90] Z. Shi *et al.*, « Experimental studies and thermodynamic modeling of the carbonation of Portland cement, metakaolin and limestone mortars », *Cem. Concr. Res.*, vol. 88, p. 60-72, oct. 2016, doi: 10.1016/j.cemconres.2016.06.006.
[91] R. Snellings, G. Mertens, et J. Elsen, « Supplementary Cementitious Materials », *Rev. Mineral. Geochem.*, vol. 74, n° 1, p. 211-278, janv. 2012, doi: 10.2138/rmg.2012.74.6.
[92] S. von Greve-Dierfeld *et al.*, « Understanding the carbonation of concrete with supplementary cementitious materials: a critical review by RILEM TC 281-CCC », *Mater. Struct.*, vol. 53, n° 6, p. 136, oct. 2020, doi: 10.1617/s11527-020-01558-w.
[93] B. Lothenbach, K. Scrivener, et R. D. Hooton, « Supplementary cementitious materials », *Cem. Concr. Res.*, vol. 41, n° 12, p. 1244-1256, déc. 2011, doi: 10.1016/j.cemconres.2010.12.001.
[94] W. Li *et al.*, « Influence of metakaolin on the hydration and microstructure evolution of cement paste during the early stage », *Appl. Clay Sci.*, vol. 229, p. 106674, nov. 2022, doi: 10.1016/j.clay.2022.106674.
[95] K. Weng, « Influence of silica fume and fly ash on hydration, microstructure and strength of cement based mixtures », p. xiv, 141 leaves : ill.; 30 cm., 1992, doi: 10.11575/PRISM/18566.
[96] J. Shao, J. Gao, Y. Zhao, et X. Chen, « Study on the pozzolanic reaction of clay brick powder in blended cement pastes », *Constr. Build. Mater.*, vol. 213, p. 209-215, juill. 2019, doi: 10.1016/j.conbuildmat.2019.03.307.
[97] M. Luna, D. Arcos, L. Duro, Spain, et S. Kärnbränslehantering, « Effects of grouting, shotcreting and concrete leachates on backfill geochemistry », janv. 2023.
[98] M. J. McCarthy et T. D. Dyer, « 9 - Pozzolanas and Pozzolanic Materials », in *Lea's Chemistry of Cement and Concrete (Fifth Edition)*, P. C. Hewlett et M. Liska, Éd., Butterworth-Heinemann, 2019, p. 363-467. doi: 10.1016/B978-0-08-100773-0.00009-5.
[99] J. E. Szulejko, P. Kumar, A. Deep, et K.-H. Kim, « Global warming projections to 2100 using simple CO2 greenhouse gas modeling and comments on CO2 climate sensitivity factor », *Atmospheric Pollut. Res.*, vol. 8, n° 1, p. 136-140, janv. 2017, doi: 10.1016/j.apr.2016.08.002.
[100] M. Thiery, « Modélisation de la carbonatation atmosphérique des matériaux cimentaires : prise en compte des effets cinétiques et des modifications microstructurales et hydriques »,

These de doctorat, Marne-la-vallée, ENPC, 2005. Consulté le: 19 janvier 2023. [En ligne]. Disponible sur: https://www.theses.fr/2005ENPC0014
[101] D. A. Kulik, « Improving the structural consistency of C-S-H solid solution thermodynamic models », *Cem. Concr. Res.*, vol. 41, n° 5, p. 477-495, mai 2011, doi: 10.1016/j.cemconres.2011.01.012.
[102] R. Bucher, P. Diederich, G. Escadeillas, et M. Cyr, « Service life of metakaolin-based concrete exposed to carbonation », *Cem. Concr. Res.*, vol. 99, p. 18-29, sept. 2017, doi: 10.1016/j.cemconres.2017.04.013.
[103] A. AL-Ameeri, M. I. Rafiq, et O. Tsioulou, « Influence of cracks on the carbonation resistance of concrete structures », juill. 2018.
[104] N. Hyvert, A. Sellier, F. Duprat, P. Rougeau, et P. Francisco, « Dependency of C–S–H carbonation rate on CO2 pressure to explain transition from accelerated tests to natural carbonation », *Cem. Concr. Res.*, vol. 40, n° 11, p. 1582-1589, nov. 2010, doi: 10.1016/j.cemconres.2010.06.010.
[105] N. Hyvert, « Application de l'approche probabiliste à la durabilité des produits préfabriqués en béton », These de doctorat, Toulouse 3, 2009. Consulté le: 18 janvier 2023. [En ligne]. Disponible sur: https://www.theses.fr/2009TOU30030
[106] J.-P. Ollivier et A. Vichot, *La durabilité des bétons. Bases scientifiques pour la formulation de bétons durables dans leur environnement*. Consulté le: 19 janvier 2023. [En ligne]. Disponible sur: https://www.decitre.fr/livres/la-durabilite-des-betons-9782859784348.html
[107] M. I. Khan et C. J. Lynsdale, « Strength, permeability, and carbonation of high-performance concrete », *Cem. Concr. Res.*, vol. 32, n° 1, p. 123-131, janv. 2002, doi: 10.1016/S0008-8846(01)00641-X.
[108] S. Collepardi, V. Corinaldesi, G. Moriconi, G. Bonora, et M. Collepardi, « DURABILITY OF HIGH-PERFORMANCE CONCRETES WITH POZZOLANIC AND COMPOSITE CEMENTS », présenté à Fifth CANMET/ACI International Conference on Durability of ConcreteCanada Centre for Mineral and Energy Technology (CANMET) of Natural Resources Canada, Ottawa; American Concrete Institute; and Japan Concrete Institute., 2000. Consulté le: 18 janvier 2023. [En ligne]. Disponible sur: https://trid.trb.org/view/656162
[109] « Conception des bétons pour une durée de vie donnée des ouvrages - Maîtrise de la durabilité vis-à-vis de la corrosion des armatures et de l'alcali-réaction », AFGC. Consulté le: 18 janvier 2023. [En ligne]. Disponible sur: https://www.afgc.asso.fr/publication/conception-des-betons-pour-une-duree-de-vie-donnee-des-ouvrages-maitrise-de-la-durabilite-vis-a-vis-de-la-corrosion-des-armatures-et-de-lalcali-reaction/
[110] Ph. Turcry, L. Oksri-Nelfia, A. Younsi, et A. Aït-Mokhtar, « Analysis of an accelerated carbonation test with severe preconditioning », *Cem. Concr. Res.*, vol. 57, p. 70-78, mars 2014, doi: 10.1016/j.cemconres.2014.01.003.
[111] T. Chaussadent, « Etat des lieux et reflexions sur la carbonatation du beton arme », *ETUDES Rech. Lab. PONTS CHAUSSEES - Ser. OUVRAGES ART*, n° OA 29, sept. 1999, Consulté le: 18 janvier 2023. [En ligne]. Disponible sur: https://trid.trb.org/view/958956
[112] R.- Dheilly et J. Tudo, « ETUDE DU SYSTEME CAO-H2O-CO2 POUR UN STOCKAGE OPTIMAL DE LA CHAUX », *Cim. Betons Platr. Chaux*, n° 820, mars 1996, Consulté le: 18 janvier 2023. [En ligne]. Disponible sur: https://trid.trb.org/view/992010
[113] E. Drouet, S. Poyet, P. Le Bescop, J.-M. Torrenti, et X. Bourbon, « Carbonation of hardened cement pastes: Influence of temperature », *Cem. Concr. Res.*, vol. 115, p. 445-459, janv. 2019, doi: 10.1016/j.cemconres.2018.09.019.
[114] F. Wang, J. Xu, Y. Xu, L. Jiang, et G. Ma, « A comparative investigation on cathodic protections of three sacrificial anodes on chloride-contaminated reinforced concrete », *Constr. Build. Mater.*, vol. 246, p. 118476, juin 2020, doi: 10.1016/j.conbuildmat.2020.118476.
[115] U. A. Birnin-Yauri et F. P. Glasser, « Friedel's salt, Ca2Al(OH)6(Cl,OH)·2H2O: its solid solutions and their role in chloride binding », *Cem. Concr. Res.*, vol. 28, n° 12, p. 1713-1723, déc. 1998, doi: 10.1016/S0008-8846(98)00162-8.

[116] A. K. Suryavanshi, J. D. Scantlebury, et S. B. Lyon, « The binding of chloride ions by sulphate resistant portland cement », *Cem. Concr. Res.*, vol. 25, n° 3, p. 581-592, avr. 1995, doi: 10.1016/0008-8846(95)00047-G.
[117] X. Wang, « Modelling of multi-species transport within possibly carbonated concrete in saturated or non saturated condition », phdthesis, Université Paris-Est, 2012. Consulté le: 18 janvier 2023. [En ligne]. Disponible sur: https://theses.hal.science/tel-00730834
[118] V. S. Ramachandran, R. C. Seeley, et G. M. Polomark, « Free and combined chloride in hydrating cement and cement components », *Matér. Constr.*, vol. 17, n° 4, p. 285-289, juill. 1984, doi: 10.1007/BF02479084.
[119] E. M. Theissing, P. v. Hest-Wardenier, et G. de Wind, « The combining of sodium chloride and calcium chloride by a number of different hardened cement pastes », *Cem. Concr. Res.*, vol. 8, n° 6, p. 683-691, nov. 1978, doi: 10.1016/0008-8846(78)90077-7.
[120] J. J. Beaudoin, V. S. Ramachandran, et R. F. Feldman, « Interaction of chloride and C□S□H », *Cem. Concr. Res.*, vol. 20, n° 6, p. 875-883, nov. 1990, doi: 10.1016/0008-8846(90)90049-4.
[121] « T47. Guide de prescription des ciments pour des constructions durables », Infociments. Consulté le: 19 janvier 2023. [En ligne]. Disponible sur: https://www.infociments.fr/ciments/t47-guide-de-prescription-des-ciments-pour-des-constructions-durables
[122] ARLIGUIE G et HORNAIN N., « GranDuBé - Grandeurs associées à la Durabilité des Bétons », AFGC. Consulté le: 18 janvier 2023. [En ligne]. Disponible sur: https://www.afgc.asso.fr/publication/grandube-grandeurs-associees-a-la-durabilite-des-betons/
[123] K. O. Ampadu, K. Torii, et M. Kawamura, « Beneficial effect of fly ash on chloride diffusivity of hardened cement paste », *Cem. Concr. Res.*, vol. 29, n° 4, p. 585-590, avr. 1999, doi: 10.1016/S0008-8846(99)00047-2.
[124] R. K. Dhir, M. A. K. El-Mohr, et T. D. Dyer, « Developing chloride resisting concrete using PFA », *Cem. Concr. Res.*, vol. 27, n° 11, p. 1633-1639, nov. 1997, doi: 10.1016/S0008-8846(97)00146-4.
[125] M. Thomas, « Chloride thresholds in marine concrete », *Cem. Concr. Res.*, vol. 26, n° 4, p. 513-519, avr. 1996, doi: 10.1016/0008-8846(96)00035-X.
[126] B. H. Oh, S. Y. Jang, et Y. S. Shin, « Experimental investigation of the threshold chloride concentration for corrosion initiation in reinforced concrete structures », *Mag. Concr. Res.*, vol. 55, n° 2, p. 117-124, avr. 2003, doi: 10.1680/macr.2003.55.2.117.
[127] C. Arya, N. R. Buenfeld, et J. B. Newman, « Factors influencing chloride-binding in concrete », *Cem. Concr. Res.*, vol. 20, n° 2, p. 291-300, mars 1990, doi: 10.1016/0008-8846(90)90083-A.
[128] C. LARSEN, « Chloride binding in concrete, Effect of surrounding environment and concrete composition », Norwegian University of Science and Technology.
[129] C. L. Page et Ø. Vennesland, « Pore solution composition and chloride binding capacity of silica-fume cement pastes », *Matér. Constr.*, vol. 16, n° 1, p. 19-25, janv. 1983, doi: 10.1007/BF02474863.
[130] R. Liu *et al.*, « The effect of carbonate and sulfate ions on chloride threshold level of reinforcement corrosion in mortar with/without fly ash », *Constr. Build. Mater.*, vol. 113, p. 90-95, juin 2016, doi: 10.1016/j.conbuildmat.2016.03.018.
[131] J. M. R. Dotto, A. G. de Abreu, D. C. C. Dal Molin, et I. L. Müller, « Influence of silica fume addition on concretes physical properties and on corrosion behaviour of reinforcement bars », *Cem. Concr. Compos.*, vol. 26, n° 1, p. 31-39, janv. 2004, doi: 10.1016/S0958-9465(02)00120-8.
[132] M. Manera, Ø. Vennesland, et L. Bertolini, « Chloride threshold for rebar corrosion in concrete with addition of silica fume », *Corros. Sci.*, vol. 50, n° 2, p. 554-560, févr. 2008, doi: 10.1016/j.corsci.2007.07.007.
[133] H. Ye, N. Jin, X. Jin, et C. Fu, « Model of chloride penetration into cracked concrete subject to drying–wetting cycles », *Constr. Build. Mater.*, vol. 36, p. 259-269, nov. 2012, doi: 10.1016/j.conbuildmat.2012.05.027.

[134] H. Ye, Y. Tian, N. Jin, X. Jin, et C. Fu, « Influence of cracking on chloride diffusivity and moisture influential depth in concrete subjected to simulated environmental conditions », *Constr. Build. Mater.*, vol. 47, p. 66-79, oct. 2013, doi: 10.1016/j.conbuildmat.2013.04.024.
[135] H. Ye, C. Fu, N. Jin, et X. Jin, « Influence of flexural loading on chloride ingress in concrete subjected to cyclic drying-wetting condition », *Comput. Concr.*, vol. 15, n° 2, p. 183-198, févr. 2015, doi: 10.12989/CAC.2015.15.2.183.
[136] H. Ye, X. Jin, C. Fu, N. Jin, Y. Xu, et T. Huang, « Chloride penetration in concrete exposed to cyclic drying-wetting and carbonation », *Constr. Build. Mater.*, vol. 112, p. 457-463, juin 2016, doi: 10.1016/j.conbuildmat.2016.02.194.
[137] K. K. Sagoe-Crentsil et F. P. Glasser, « "Green rust", iron solubility and the role of chloride in the corrosion of steel at high pH », *Cem. Concr. Res.*, vol. 23, n° 4, p. 785-791, juill. 1993, doi: 10.1016/0008-8846(93)90032-5.
[138] G. S. Frankel, « Pitting Corrosion of Metals: A Review of the Critical Factors », *J. Electrochem. Soc.*, vol. 145, n° 6, p. 2186, juin 1998, doi: 10.1149/1.1838615.
[139] P. Sandberg, « Critical evaluation of factors affecting chloride initiated reinforcement corrosion in concrete », Licentiate Thesis, Division of Building Materials, LTH, Lund University, 1995.
[140] F. Hunkeler, « 1 - Corrosion in reinforced concrete: processes and mechanisms », in *Corrosion in Reinforced Concrete Structures*, H. Böhni, Éd., in Woodhead Publishing Series in Civil and Structural Engineering. , Woodhead Publishing, 2005, p. 1-45. doi: 10.1533/9781845690434.1.
[141] U. Angst, B. Elsener, C. K. Larsen, et Ø. Vennesland, « Critical chloride content in reinforced concrete — A review », *Cem. Concr. Res.*, vol. 39, n° 12, p. 1122-1138, déc. 2009, doi: 10.1016/j.cemconres.2009.08.006.
[142] G. K. Glass, B. Reddy, et N. R. Buenfeld, « The participation of bound chloride in passive film breakdown on steel in concrete », *Corros. Sci.*, vol. 42, n° 11, p. 2013-2021, nov. 2000, doi: 10.1016/S0010-938X(00)00040-8.
[143] B. Reddy, G. K. Glass, P. J. Lim, et N. R. Buenfeld, « On the corrosion risk presented by chloride bound in concrete », *Cem. Concr. Compos.*, vol. 24, n° 1, p. 1-5, févr. 2002, doi: 10.1016/S0958-9465(01)00021-X.
[144] G. K. Glass et N. R. Buenfeld, « The influence of chloride binding on the chloride induced corrosion risk in reinforced concrete », *Corros. Sci.*, vol. 42, n° 2, p. 329-344, févr. 2000, doi: 10.1016/S0010-938X(99)00083-9.
[145] M. Pourbaix, « Thermodynamics and corrosion », *Corros. Sci.*, vol. 30, n° 10, p. 963-988, janv. 1990, doi: 10.1016/0010-938X(90)90205-J.
[146] H. Arup, « Corrosion of reinforcing steel in concrete - an overview », *Semin. Fail. Repair Corroded Reinf. Concr. Struct. Oyes Lond.*, 1984.
[147] C. Alonso, C. Andrade, M. Castellote, et P. Castro, « Chloride threshold values to depassivate reinforcing bars embedded in a standardized OPC mortar », *Cem. Concr. Res.*, vol. 30, n° 7, p. 1047-1055, juill. 2000, doi: 10.1016/S0008-8846(00)00265-9.
[148] Y. Cao, C. Gehlen, U. Angst, L. Wang, Z. Wang, et Y. Yao, « Critical chloride content in reinforced concrete — An updated review considering Chinese experience », *Cem. Concr. Res.*, vol. 117, p. 58-68, mars 2019, doi: 10.1016/j.cemconres.2018.11.020.
[149] Jens. M. Frederiksen, « Chloride threshold values for service life design », *RILEM Int. Workshop TMC*, 2000.
[150] P. K et S. P., « Chloride threshold levels and corrosion rates in cracked high performance concrete exposed in a marine environment. », *Present. 4th CANMETACI Int Conf Durab. Concr. Syd. Aust.*, août 1997.
[151] K. Pettersson, « CORROSION THRESHOLD VALUE AND CORROSION RATE IN REINFORCED CONCRETE », *CBI Rep. 292*, 1992, Consulté le: 15 mars 2023. [En ligne]. Disponible sur: https://trid.trb.org/view/501279
[152] *HETEK: A System for Estimation of Chloride Ingress Into Concrete : Theoretical Background*. Danish Road Directorate, 1997.

[153] A. K. Suryavanshi et R. Narayan Swamy, « Stability of Friedel's salt in carbonated concrete structural elements », *Cem. Concr. Res.*, vol. 26, n° 5, p. 729-741, mai 1996, doi: 10.1016/S0008-8846(96)85010-1.
[154] P. FRANCISCO, « Fiche 25 - Additions : Définitions, types, utilisations ». CERIB. Memento Production, 2008.
[155] A. J. Sedriks, *Corrosion of Stainless Steels.*, vol. 2nd Edition. in Wiley-Interscience, vol. 2nd Edition. New-York, 1996.
[156] E. Medina, J. M. Medina, A. Cobo, et D. M. Bastidas, « Evaluation of mechanical and structural behavior of austenitic and duplex stainless steel reinforcements », *Constr. Build. Mater.*, vol. 78, p. 1-7, mars 2015, doi: 10.1016/j.conbuildmat.2015.01.008.
[157] J. Jiang *et al.*, « The Passive Film Growth Mechanism of New Corrosion-Resistant Steel Rebar in Simulated Concrete Pore Solution: Nanometer Structure and Electrochemical Study », *Materials*, vol. 10, n° 4, p. 412, avr. 2017, doi: 10.3390/ma10040412.
[158] F. Presuel, J. Scully, et S. Sharp, « Literature Review of Commercially Available Alloys That Have Potential as Low-Cost, Corrosion-Resistant Concrete Reinforcement », *Corrosion*, vol. 66, août 2010, doi: 10.5006/1.3479955.
[159] C.-O. A. Olsson et D. Landolt, « Passive films on stainless steels—chemistry, structure and growth », *Electrochimica Acta*, vol. 48, n° 9, p. 1093-1104, avr. 2003, doi: 10.1016/S0013-4686(02)00841-1.
[160] A. Machet *et al.*, « XPS and STM study of the growth and structure of passive films in high temperature water on a nickel-base alloy », *Electrochimica Acta*, vol. 49, n° 22, p. 3957-3964, sept. 2004, doi: 10.1016/j.electacta.2004.04.032.
[161] Z. Wei *et al.*, « Chapter 18 - Failure mechanisms and modes analysis of vehicle exhaust components and systems », in *Handbook of Materials Failure Analysis with Case Studies from the Aerospace and Automotive Industries*, A. S. H. Makhlouf et M. Aliofkhazraei, Éd., Boston: Butterworth-Heinemann, 2016, p. 393-432. doi: 10.1016/B978-0-12-800950-5.00018-1.
[162] S. Papavinasam, « Chapter 6 - Modeling – Internal Corrosion », in *Corrosion Control in the Oil and Gas Industry*, S. Papavinasam, Éd., Boston: Gulf Professional Publishing, 2014, p. 301-360. doi: 10.1016/B978-0-12-397022-0.00006-6.
[163] C.-O. A. Olsson, « Wet Corrosion of Stainless Steels and Other Chromium-Bearing Alloys », in *Encyclopedia of Interfacial Chemistry*, K. Wandelt, Éd., Oxford: Elsevier, 2018, p. 535-542. doi: 10.1016/B978-0-12-409547-2.13583-8.
[164] Z. Ahmad, « CHAPTER 9 - SELECTION OF MATERIALS FOR CORROSIVE ENVIRONMENT », in *Principles of Corrosion Engineering and Corrosion Control*, Z. Ahmad, Éd., Oxford: Butterworth-Heinemann, 2006, p. 479-549. doi: 10.1016/B978-075065924-6/50010-6.
[165] N. tru Vu, « Contribution à l'étude de la corrosion par carbonatation du béton armé : approche expérimentale et probabiliste », These de doctorat, Toulouse, INSA, 2011. Consulté le: 18 janvier 2023. [En ligne]. Disponible sur: https://www.theses.fr/2011ISAT0008
[166] C. Andrade, C. Alonso, J. Gulikers, R. B. Polder, et R. Cigna, « Recommendations of RILEM TC-154-EMC: "Electrochemical techniques for measuring metallic corrosion" Test methods for on-site corrosion rate measurement of steel reinforcement in concrete by means of the polarization resistance method ». Materials and Structures, 2004.
[167] G. Sergi, « Corrosion of steel in concrete: Cement matrix variables », Aston University, 1986.
[168] A. F. A. Fuhaid et A. Niaz, « Carbonation and Corrosion Problems in Reinforced Concrete Structures », *Buildings*, vol. 12, n° 5, Art. n° 5, mai 2022, doi: 10.3390/buildings12050586.
[169] M. Arreola-Sanchez, E. M. Alonso-Guzman, W. Martinez-Molina, A. A. Torres-Acosta, H. L. Chavez-Garcia, et J. M. Ponce-Ortega, « Reinforced Concrete Structure Performance in Marine Structures: Analyzing Durability Indexes to Obtain More Accurate Corrosion Initiation Time Predictions », *Materials*, vol. 14, n° 24, Art. n° 24, janv. 2021, doi: 10.3390/ma14247662.
[170] K. Tuutti, « Corrosion of steel in concrete », *Swedish Cement and Concrete Research Institute*, Stockholm, 1982.

[171] S. Lapuerta, « Etude de la corrosion du fer à l'interface de différents milieux (eau, air) soumis à l'irradiation de protons », phdthesis, Université Claude Bernard - Lyon I, 2005. Consulté le: 18 janvier 2023. [En ligne]. Disponible sur: https://theses.hal.science/tel-00011671
[172] P. Barnes, « An Investigation into the Corrosion Fatigue Behaviour of High Strength Carbon Steel Tensile Armour Wires », 2014. doi: 10.13140/RG.2.1.1863.0883.
[173] A. Nasser, « La corrosion des aciers dans le béton à l'état passif et par carbonatation : prise en compte des courants galvaniques et des défauts d'interface acier-béton », These de doctorat, Toulouse 3, 2010. Consulté le: 18 janvier 2023. [En ligne]. Disponible sur: https://www.theses.fr/2010TOU30248
[174] V. L'Hostis, D. Neff, L. Bellot-Gurlet, et P. Dillmann, « Characterization of long-term corrosion of rebars embedded in concretes sampled on French historical buildings aged from 50 to 80 years », *Mater. Corros.*, vol. 60, n° 2, p. 93-98, févr. 2009, doi: 10.1002/maco.200805019.
[175] Rochelle M. Cornell et Udo Schwertmann, « The Iron Oxides: Structure, Properties, Reactions, Occurrences and Uses, 2nd, Completely Revised and Extended Edition | Wiley », Wiley.com. Consulté le: 18 janvier 2023. [En ligne]. Disponible sur: https://www.wiley.com/en-us/The+Iron+Oxides%3A+Structure%2C+Properties%2C+Reactions%2C+Occurrences+and+Uses%2C+2nd%2C+Completely+Revised+and+Extended+Edition-p-9783527606443
[176] W.-J. Chitty, P. Dillmann, V. L'Hostis, et C. Lombard, « Long-term corrosion resistance of metallic reinforcements in concrete—a study of corrosion mechanisms based on archaeological artefacts », *Corros. Sci.*, vol. 47, n° 6, p. 1555-1581, juin 2005, doi: 10.1016/j.corsci.2004.07.032.
[177] R. Zhang, A. Castel, et R. François, « The corrosion pattern of reinforcement and its influence on serviceability of reinforced concrete members in chloride environment », *Cem. Concr. Res.*, vol. 39, n° 11, p. 1077-1086, nov. 2009, doi: 10.1016/j.cemconres.2009.07.025.
[178] Y. Wang, A. Mukherjee, et A. Castel, « Detection of Top-Bar Effect in Reinforced Concrete Using Guided Ultrasonic Waves », *J. Struct. Eng.*, vol. 147, n° 4, p. 04021032, avr. 2021, doi: 10.1061/(ASCE)ST.1943-541X.0002950.
[179] Q. Qiu, « A state-of-the-art review on the carbonation process in cementitious materials: Fundamentals and characterization techniques », *Constr. Build. Mater.*, vol. 247, n° Complete, [En ligne]. Disponible sur: http://resolver.scholarsportal.info/resolve/09500618/v247icomplete/nfp_asrotccmfact.xml
[180] A. B. Revert, K. De Weerdt, K. Hornbostel, et M. R. Geiker, *State-of-the-art report: Service life modelling, carbonation of concrete and corrosion in carbonated concrete.* NTNU, 2017. Consulté le: 26 janvier 2023. [En ligne]. Disponible sur: https://ntnuopen.ntnu.no/ntnu-xmlui/handle/11250/2480580
[181] J. Khunthongkeaw, S. Tangtermsirikul, et T. Leelawat, « A study on carbonation depth prediction for fly ash concrete », *Constr. Build. Mater.*, vol. 20, n° 9, p. 744-753, nov. 2006, doi: 10.1016/j.conbuildmat.2005.01.052.
[182] D. NIU, Z. Dong, et J. Pu, « Random model of predicting the carbonated concrete depth », *Industrial Construction*, 1999.
[183] X. Zhang, X. Zhou, H. Zhou, K. Gao, et Z. Wang, « Studies on forecasting of carbonation depth of slag high performance concrete considering gas permeability », *Appl. Clay Sci.*, vol. 79, p. 36-40, juill. 2013, doi: 10.1016/j.clay.2013.02.020.
[184] A. Ju, « Concrete carbonation and durability of reinforced concrete », *Concrete*, 1992.
[185] L. X. Jiang, Y. Zhang, Y. Q. Liu, X. Zhang, H. F. Xie, et J. Wang, « Experimental study and calculation formula of carbonation depth », *Concrete*, 1996.
[186] L. Jiang, B. Lin, et Y. Cai, « A model for predicting carbonation of high-volume fly ash concrete », *Cem. Concr. Res.*, vol. 30, n° 5, p. 699-702, mai 2000, doi: 10.1016/S0008-8846(00)00227-1.
[187] X.-Y. Wang et H.-S. Lee, « A model for predicting the carbonation depth of concrete containing low-calcium fly ash », *Constr. Build. Mater.*, vol. 23, n° 2, p. 725-733, févr. 2009, doi: 10.1016/j.conbuildmat.2008.02.019.

[188] X.-Y. Wang et H.-S. Lee, « A model predicting carbonation depth of concrete containing silica fume », *Mater. Struct.*, vol. 42, n° 6, p. 691-704, juill. 2009, doi: 10.1617/s11527-008-9413-7.
[189] V. Papadakis, C. Vayenas, et M. N. Fardis, « Fundamental modelling and experimental investigation of concrete carbonation », *Materials Journal*, 1991.
[190] K. Sisomphon et L. Franke, « Carbonation rates of concretes containing high volume of pozzolanic materials », *Cem. Concr. Res.*, vol. 37, n° 12, p. 1647-1653, déc. 2007, doi: 10.1016/j.cemconres.2007.08.014.
[191] P. Schiessl *et al.*, *fib Bulletin 34. Model Code for Service Life Design*. in fib Bulletins. fib. The International Federation for Structural Concrete, 2006. doi: 10.35789/fib.BULL.0034.
[192] M. Guiglia et M. Taliano, « Comparison of carbonation depths measured on in-field exposed existing r.c. structures with predictions made using fib-Model Code 2010 », *Cem. Concr. Compos.*, vol. 38, p. 92-108, avr. 2013, doi: 10.1016/j.cemconcomp.2013.03.014.
[193] S. Morinaga, « Prediction of service lives of reinforced concrete buildings based on rate of corrosion of reinforcing steel. », *Rport No 23 Shimizu Corp*, 1988.
[194] L. J. Parrott, « A study of carbonation-induced corrosion », *Mag. Concr. Res.*, vol. 46, n° 166, p. 23-28, mars 1994, doi: 10.1680/macr.1994.46.166.23.
[195] P. Bamforth, « Enhancing reinforced concrete durability: Guidance on selecting measures for minimising the risk of corrosion of reinforcement in concrete ». T. C. Society Ed, vol 61, 2004.
[196] T. Uomoto *et al.*, « Standard Specifications for Concrete Structures-2007 by Japan Society of Civil Engineers », *Concr. J.*, vol. 46, p. 3-14, janv. 2008, doi: 10.3151/coj1975.46.7_3.
[197] L. Czarnecki et P. Woyciechowski, « Concrete Carbonation as a Limited Process and Its Relevance to Concrete Cover Thickness », *Mater. J.*, vol. 109, n° 3, p. 275-282, mai 2012, doi: 10.14359/51683817.
[198] A. Silva, R. Neves, et J. de Brito, « Statistical modelling of carbonation in reinforced concrete », *Cem. Concr. Compos.*, vol. 50, p. 73-81, juill. 2014, doi: 10.1016/j.cemconcomp.2013.12.001.
[199] S. von Greve-Dierfeld et C. Gehlen, « Performance based durability design, carbonation part 1 - Benchmarking of European present design rules », *Struct. Concr.*, vol. 17, n° 3, p. 309-328, sept. 2016, doi: 10.1002/suco.201600066.
[200] T. P. Hills, F. Gordon, N. H. Florin, et P. S. Fennell, « Statistical analysis of the carbonation rate of concrete », *Cem. Concr. Res.*, vol. 72, p. 98-107, juin 2015, doi: 10.1016/j.cemconres.2015.02.007.
[201] A. Schiessi, « Zur Frage de zulässigen rissbreite und der erforder lichen betondeckung im stahlbetonbau- unter besonderer berücksichtigung der karbonatisierung des betongs. » Technical University of Munich, 1976.
[202] G. C. Bouquet, « Carbonation induced corrosion of reinforcement », in *Challenges of Concrete Construction: Volume 3, Repair, Rejuvenation and Enhancement of Concrete*, Thomas Telford Publishing, 2002, p. 465-475. doi: 10.1680/rraeoc.31753.0047.
[203] C. Andrade et R. D'Andrea, « Electrical resistivity as microstructural parameter for the calculation of reinforcement service life », *Microstruct. Relat. Durab. Cem. Compos.*, vol. 1, p. 1483-1490, janv. 2008.
[204] B. G. Salvoldi, H. Beushausen, et M. G. Alexander, « Oxygen permeability of concrete and its relation to carbonation », *Constr. Build. Mater.*, vol. 85, p. 30-37, juin 2015, doi: 10.1016/j.conbuildmat.2015.02.019.
[205] A. Steffens, D. Dinkler, et H. Ahrens, « Modeling carbonation for corrosion risk prediction of concrete structures », *Cem. Concr. Res.*, vol. 32, n° 6, p. 935-941, juin 2002, doi: 10.1016/S0008-8846(02)00728-7.
[206] A. V. Saetta et R. V. Vitaliani, « Experimental investigation and numerical modeling of carbonation process in reinforced concrete structures: Part I: Theoretical formulation », *Cem. Concr. Res.*, vol. 34, n° 4, p. 571-579, avr. 2004, doi: 10.1016/j.cemconres.2003.09.009.

[207] B. Bary et C. Mügler, « Simplified modelling and numerical simulations of concrete carbonation in unsaturated conditions », *Rev. Eur. Génie Civ.*, vol. 10, p. 1049-1072, nov. 2006, doi: 10.1080/17747120.2006.9692905.
[208] A. Morandeau, M. Thiery, P. Dangla, et C. White, « Accelerated carbonation modelling of fly ash-blended cement paste », oct. 2014. doi: 10.13140/2.1.5091.0723.
[209] C. Perlot, B. Caprad, et P. Rougeau, « Mieux maîtriser la durabilité des bétons par l'approche performantielle ». Les éditions du CERIB, 2007.
[210] R. Miragliotta, « Modélisation des processus physico-chimiques de la carbonatation des bétons préfabriqués : prise en compte des effets de paroi », These de doctorat, La Rochelle, 2000. Consulté le: 29 juin 2023. [En ligne]. Disponible sur: https://www.theses.fr/2000LAROS046
[211] V. Baroghel-Bouny, M. Thiéry, et X. Wang, « Modelling of isothermal coupled moisture–ion transport in cementitious materials », *Cem. Concr. Res.*, vol. 41, n° 8, p. 828-841, août 2011, doi: 10.1016/j.cemconres.2011.04.001.
[212] O. Burkan Isgor et A. G. Razaqpur, « Finite element modeling of coupled heat transfer, moisture transport and carbonation processes in concrete structures », *Cem. Concr. Compos.*, vol. 26, n° 1, p. 57-73, janv. 2004, doi: 10.1016/S0958-9465(02)00125-7.
[213] Y. Kellouche, B. Boukhatem, M. Ghrici, R. Rebouh, et A. Zidol, « Neural network model for predicting the carbonation depth of slag concrete », *Asian J. Civ. Eng.*, vol. 22, n° 7, p. 1401-1414, nov. 2021, doi: 10.1007/s42107-021-00390-z.
[214] « Fundamental Modeling and Experimental Investigation of Concrete Carbonation », *ACI Mater. J.*, vol. 88, n° 4, 1991, doi: 10.14359/1863.
[215] B. Hunt et N. Cooke, « Thermal Calculations for Bridge Design », *J. Struct. Div.*, vol. 101, n° 9, p. 1763-1781, sept. 1975, doi: 10.1061/JSDEAG.0004153.
[216] Y. Xi, Z. P. Bažant, et H. M. Jennings, « Moisture diffusion in cementitious materials Adsorption isotherms », *Adv. Cem. Based Mater.*, vol. 1, n° 6, p. 248-257, nov. 1994, doi: 10.1016/1065-7355(94)90033-7.
[217] X. Zhu, G. Zi, W. Lee, S. Kim, et J. Kong, « Probabilistic analysis of reinforcement corrosion due to the combined action of carbonation and chloride ingress in concrete », *Constr. Build. Mater.*, vol. 124, p. 667-680, oct. 2016, doi: 10.1016/j.conbuildmat.2016.07.120.
[218] D. Conciatori, F. Laferrière, et E. Brühwiler, « Comprehensive modeling of chloride ion and water ingress into concrete considering thermal and carbonation state for real climate », *Cem. Concr. Res.*, vol. 40, n° 1, p. 109-118, janv. 2010, doi: 10.1016/j.cemconres.2009.08.007.
[219] R. Cherif, « Etude de l'effet de la composition de la solution interstitielle des matériaux cimentaires sur les interactions multi-espèces lors des transferts de chlorures », phdthesis, Université de La Rochelle, 2018. Consulté le: 5 juillet 2023. [En ligne]. Disponible sur: https://theses.hal.science/tel-01906062
[220] T. Ishida et K. Maekawa, « Modeling of pH profile in pore water based on mass transport and chemical equilibrium in theory », *Translation from proceedings of JSCE, No, 648/V-47, may 2000*.
[221] Z. Liu, Y. Wang, J. Wang, C. Liu, J. Jiang, et H. Li, « Experiment and simulation of chloride ion transport and binding in concrete under the coupling of diffusion and convection », *J. Build. Eng.*, vol. 45, p. 103610, janv. 2022, doi: 10.1016/j.jobe.2021.103610.
[222] L.-O. Nilsson, « A model for convection of chloride », *Model Convect. Chlorides*, p. 47-68, janv. 1997.
[223] A. Soive, « Recensement des modèles de durbailité des bétons armés exposés aux ions chlorure ». ANR Modevie, 2017.
[224] Q. L. Zhao et Y. Z. Zhang, « Concentration Distribution of Chloride Ion under the Influence of the Convection-Diffusion Coupling », *Adv. Mater. Sci. Eng.*, vol. 2017, p. e2076986, juin 2017, doi: 10.1155/2017/2076986.
[225] E. Poulsen, « Diffusion of Chloride in Concrete », CRC Press, avr. 2014. doi: 10.1201/9781482295108.
[226] EuroLightCon, « Technical report - Chloride penetration into concrete with lightweight aggregates ». EuroLightCon document, 1999.

[227] A. Lindvall, « DURACRETE – PROBABILISTIC PERFORMANCE BASED DURABILITY DESIGN OF CONCRETE STRUCTURES ».
[228] J. Mai-Nhu, P. Rougeau, L. Linger, P.-E. Denis, et S. Magné, *THE NEW COASTAL ROAD ON REUNION ISLAND (FRANCE): APPLICATION OF DURABILITY MODEL TO A REAL CASE*. 2015.
[229] « Projet ANR MODEVIE », PERFDUB. Consulté le: 22 février 2023. [En ligne]. Disponible sur: https://perfdub.fr/programme/projet-anr-modevie/
[230] T. Luping, « Engineering expression of the ClinConc model for prediction of free and total chloride ingress in submerged marine concrete », *Cem. Concr. Res.*, vol. 38, n° 8, p. 1092-1097, août 2008, doi: 10.1016/j.cemconres.2008.03.008.
[231] S. Nanukuttan, C. Green, M. Basheer, D. Robinson, J. McCarter, et G. Starrs, « Key performance indicators – A new approach for specifying concrete and assessing state of health of concrete structure », *RILEM Int. Workshop Perform.-Based Specif. Control Concr. Durab.*, vol. 89, p. 301-308, 2013.
[232] A. Soive, T. Van Quan, et V. Baroghel-Bouny, « Requirements and possible simplifications for multi-ionic transport models – Case of concrete subjected to wetting-drying cycles in marine environment », *Constr. Build. Mater.*, vol. 164, p. 799-808, mars 2018, doi: 10.1016/j.conbuildmat.2018.01.015.
[233] Life-365 Consortium III, « Life-365TM Service Life Prediction ModelTM and Computer Program for Predicting the Service Life and Life-Cycle Cost of Reinforced Concrete Exposed to Chlorides ». 2020.
[234] L. Y. Li et C. L. Page, « Finite element modelling of chloride removal from concrete by an electrochemical method », *Corros. Sci.*, vol. 42, n° 12, p. 2145-2165, déc. 2000, doi: 10.1016/S0010-938X(00)00044-5.
[235] « STADIUM® Overview », SIMCO Technologies. Consulté le: 29 juin 2023. [En ligne]. Disponible sur: https://www.simcotechnologies.com/what-we-do/stadium-technology-portfolio/stadium-overview/
[236] E. Bastidas-Arteaga, « Contribution for sustainable management of reinforced concrete structures subjected to chloride penetration », sept. 2010.
[237] N. Ukrainczyk et E. Koenders, « Numerical Model for Chloride Ingress in Cement Based Materials: Method of Lines Implementation for Solving Coupled Multi-species Diffusion with Binding », vol. 1, p. 109-119, nov. 2016.
[238] Task Group 5.6, *Model Code for Service Life Design - bulletin 34*. 2006.
[239] Q. Liu, L. Li, D. Easterbrook, et J. Yang, « Multi-phase modelling of ionic transport in concrete when subjected to an externally applied electric field », *Eng. Struct.*, vol. 42, p. 201-213, sept. 2012, doi: 10.1016/j.engstruct.2012.04.021.
[240] N. Benkemoun, M. N. Hammood, et O. Amiri, « Embedded finite element formulation for the modeling of chloride diffusion accounting for chloride binding in meso-scale concrete », *Finite Elem. Anal. Des.*, vol. 130, p. 12-26, août 2017, doi: 10.1016/j.finel.2017.03.003.
[241] *Dictionnaire de physique (4e édition) - Richard Taillet, Loïc Villain, Pascal Febvre - De Boeck Superieur - Grand format - Dalloz Librairie PARIS*. Consulté le: 14 mars 2023. [En ligne]. Disponible sur: https://www.librairiedalloz.fr/livre/9782807307445-dictionnaire-de-physique-4e-edition-richard-taillet-loic-villain-pascal-febvre/
[242] A. Lindvall, « Chloride ingress data from field and laboratory exposure – Influence of salinity and temperature », *Cem. Concr. Compos.*, vol. 29, n° 2, p. 88-93, févr. 2007, doi: 10.1016/j.cemconcomp.2006.08.004.
[243] E. Koenders, K. Imamoto, et A. Soive, Éd., *Benchmarking Chloride Ingress Models on Real-life Case Studies—Marine Submerged and Road Sprayed Concrete Structures: State-of-the-Art Report of the RILEM TC 270-CIM*, vol. 37. in RILEM State-of-the-Art Reports, vol. 37. Cham: Springer International Publishing, 2022. doi: 10.1007/978-3-030-96422-1.
[244] H. Hirao, K. Yamada, H. Takahashi, et H. Zibara, « Chloride Binding of Cement Estimated by Binding Isotherms of Hydrates », *J. Adv. Concr. Technol.*, vol. 3, n° 1, p. 77-84, 2005, doi: 10.3151/jact.3.77.

[245] G. Sergi, S. W. Yu, et C. L. Page, « Diffusion of chloride and hydroxyl ions in cementitious materials exposed to a saline environment », *Mag. Concr. Res.*, vol. 44, n° 158, p. 63-69, mars 1992, doi: 10.1680/macr.1992.44.158.63.
[246] T. Luping et L.-O. Nilsson, « Chloride binding capacity and binding isotherms of OPC pastes and mortars », *Cem. Concr. Res.*, vol. 23, n° 2, p. 247-253, mars 1993, doi: 10.1016/0008-8846(93)90089-R.
[247] S. H. Maron, J. B. Lando, et C. F. Prutton, *Fundamentals of physical chemistry*. New York: Macmillan, 1974. Consulté le: 18 janvier 2023. [En ligne]. Disponible sur: http://catalog.hathitrust.org/api/volumes/oclc/724229.html
[248] G. K. Glass, N. M. Hassanein, et N. R. Buenfeld, « Neural network modelling of chloride binding », *Mag. Concr. Res.*, vol. 49, n° 181, p. 323-335, déc. 1997, doi: 10.1680/macr.1997.49.181.323.
[249] L. O. Nilsson, M. Massat, et L. Tang, « Effect of Non-Linear Chloride Binding on the Prediction of Chloride Penetration Into Concrete Structures », *Spec. Publ.*, vol. 145, p. 469-486, mai 1994, doi: 10.14359/4554.
[250] Rasheeduzzafar, S. S. Al-Saadoun, A. S. Al-Gahtani, et F. H. Dakhil, « Effect of tricalcium aluminate content of cement on corrosion of reinforcing steel in concrete », *Cem. Concr. Res.*, vol. 20, n° 5, p. 723-738, sept. 1990, doi: 10.1016/0008-8846(90)90006-J.
[251] M. DECTER, N. R. SHORT, C. L. PAGE, et D. D. HIGGINS, « Chloride ion penetration into blended cement pastes and concretes. Fly Ash, Silica Fume, Slag. and Natural Pozzolans in Concrete », Detroit, p. 1399-1411, 1989.
[252] P. SANDBERG et L. LARSSON, « Chloride binding in cement pastes in equilibrium with synthetic pore solutions », Goteborg, p. 98-107, 1993.
[253] J. Tritthart, « Chloride binding in cement II. The influence of the hydroxide concentration in the pore solution of hardened cement paste on chloride binding », *Cem. Concr. Res.*, vol. 19, n° 5, p. 683-691, sept. 1989, doi: 10.1016/0008-8846(89)90039-2.
[254] E. Samson et J. Marchand, « Modeling the transport of ions in unsaturated cement-based materials », *Comput. Struct.*, vol. 85, n° 23, p. 1740-1756, déc. 2007, doi: 10.1016/j.compstruc.2007.04.008.
[255] B. Johannesson, K. Yamada, L.-O. Nilsson, et Y. Hosokawa, « Multi-species ionic diffusion in concrete with account to interaction between ions in the pore solution and the cement hydrates », *Mater. Struct. Constr.*, vol. 40, p. 651-665, juill. 2006, doi: 10.1617/s11527-006-9176-y.
[256] V. Q. Tran *et al.*, « Effect of temperature on the chloride binding capacity of cementitious materials », *Mag. Concr. Res.*, vol. 73, n° 15, p. 771-784, août 2021, doi: 10.1680/jmacr.19.00484.
[257] M. Achour, O. Amiri, F. Bignonnet, et E. Rozière, « Modelling of Coupling of Chloride and Carbonation in Concrete », janv. 2017.
[258] S. J. H. Meijers, J. M. J. M. Bijen, R. de Borst, et A. L. A. Fraaij, « Computational results of a model for chloride ingress in concrete including convection, drying-wetting cycles and carbonation », *Mater. Struct.*, vol. 38, n° 2, p. 145-154, mars 2005, doi: 10.1007/BF02479339.
[259] W. Puatatsananon et V. Saouma, « Nonlinear Coupling of Carbonation and Chloride Diffusion in Concrete », *J. Mater. Civ. Eng. - J MATER Civ. ENG*, vol. 17, juin 2005, doi: 10.1061/(ASCE)0899-1561(2005)17:3(264).
[260] X. Shen, W. Jiang, D. Hou, Z. Hu, J. Yang, et Q. Liu, « Numerical study of carbonation and its effect on chloride binding in concrete », *Cem. Concr. Compos.*, vol. 104, p. 103402, nov. 2019, doi: 10.1016/j.cemconcomp.2019.103402.
[261] H. Nguyen, B. Bary, et T. Larrard, « Coupled carbonation-rust formation-damage modeling and simulation of steel corrosion in 3D mesoscale reinforced concrete », *Cem. Concr. Res.*, vol. 74, p. 95-107, août 2015, doi: 10.1016/j.cemconres.2015.04.008.

[262] C. Alonso, C. Andrade, et J. A. González, « Relation between resistivity and corrosion rate of reinforcements in carbonated mortar made with several cement types », *Cem. Concr. Res.*, vol. 18, n° 5, p. 687-698, sept. 1988, doi: 10.1016/0008-8846(88)90091-9.
[263] J. Gulikers, « Theoretical considerations on the supposed linear relationship between concrete resistivity and corrosion rate of steel reinforcement », *Mater. Corros.*, vol. 56, n° 6, p. 393-403, 2005, doi: 10.1002/maco.200403841.
[264] H. W. Song, H. J. Kim, S. J. Kwon, C. H. Lee, K. J. Byun, et C. K. Park, « Prediction of service life in cracked reinforced concrete structures subjected to chloride attack and carbonation », Yonsei University, Korea.
[265] P. Ghods, O. b. Isgor, et M. Pour-Ghaz, « A practical method for calculating the corrosion rate of uniformly depassivated reinforcing bars in concrete », *Mater. Corros.*, vol. 58, n° 4, p. 265-272, 2007, doi: 10.1002/maco.200604010.
[266] A. El Farissi, « Prédiction de la durée d'utilisation des ouvrages en béton armé par une approche performantielle dans le cas de la corrosion induite par la carbonatation ou l'attaque des ions chlorure », These de doctorat, La Rochelle, 2020. Consulté le: 20 juin 2023. [En ligne]. Disponible sur: https://www.theses.fr/2020LAROS025
[267] K. A. T. Vu et M. G. Stewart, « Structural reliability of concrete bridges including improved chloride-induced corrosion models », *Struct. Saf.*, vol. 22, n° 4, p. 313-333, janv. 2000, doi: 10.1016/S0167-4730(00)00018-7.
[268] R. Landolfo, L. Cascini, et F. Portioli, « Modeling of Metal Structure Corrosion Damage: A State of the Art Report », *Sustainability*, vol. 2, n° 7, Art. n° 7, juill. 2010, doi: 10.3390/su2072163.
[269] D. E. Klinesmith, R. H. McCuen, et P. Albrecht, « Effect of Environmental Conditions on Corrosion Rates », *J. Mater. Civ. Eng.*, vol. 19, n° 2, p. 121-129, févr. 2007, doi: 10.1061/(ASCE)0899-1561(2007)19:2(121).
[270] I. Balafas et C. Burgoyne, « Modeling the Structural Effects of Rust in Concrete Cover », *J. Eng. Mech.-Asce - J ENG MECH-ASCE*, vol. 137, janv. 2010, doi: 10.1061/(ASCE)EM.1943-7889.0000215.
[271] H. Yalçyn et M. Ergun, « The prediction of corrosion rates of reinforcing steels in concrete », *Cem. Concr. Res.*, vol. 26, n° 10, p. 1593-1599, oct. 1996, doi: 10.1016/0008-8846(96)00139-1.
[272] C. Chalhoub, « Study of the initiation and propagation phases of chloride induced corrosion in reinforced concrete structures », These de doctorat, Toulouse 3, 2020. Consulté le: 20 juin 2023. [En ligne]. Disponible sur: https://www.theses.fr/2020TOU30311
[273] T. Liu et R. W. Weyers, « Modeling the Dynamic Corrosion Process in Chloride Contaminated Concrete Structures », *Cem. Concr. Res.*, vol. 28, n° 3, p. 365-379, mars 1998, doi: 10.1016/S0008-8846(98)00259-2.
[274] S. Ahmad, « Empirical modelling of indicators of chloride-induced rebar corrosion », vol. 27, p. 195-207, janv. 2000.
[275] G. Ji et O. Isgor, « ON THE NUMERICAL SOLUTION OF LAPLACE'S EQUATION WITH NONLINEAR BOUNDARY CONDITIONS FOR CORROSION OF STEEL IN CONCRETE », janv. 2006.
[276] O. B. Isgor et A. G. Razaqpur, « Advanced modelling of concrete deterioration due to reinforcement corrosion », *Can. J. Civ. Eng.*, vol. 33, n° 6, p. 707-718, juin 2006, doi: 10.1139/l06-007.
[277] M. Pour-Ghaz, O. Burkan Isgor, et P. Ghods, « The effect of temperature on the corrosion of steel in concrete. Part 2: Model verification and parametric study », *Corros. Sci.*, vol. 51, n° 2, p. 426-433, févr. 2009, doi: 10.1016/j.corsci.2008.10.036.
[278] V. L. TA, S. Bonnet, T. Senga Kiessé, et A. Ventura, « A new meta-model to calculate carbonation front depth within concrete structures », *Constr. Build. Mater.*, vol. 129, nov. 2016, doi: 10.1016/j.conbuildmat.2016.10.103.
[279] V. G. Papadakis et S. Demis, « Estimation and Validation of Concrete Strength and Service Life Using Software Packages based on Predictive Models. », *DBMC*, Porto - Portugal, 2011.

[280] F. de Larrard, *Structures granulaires et formulation des bétons*. Paris, France: Laboratoire Central des Ponts et Chaussées, 2000.
[281] R. Feret, *Sur la compacité des mortiers hydrauliques*, vol. Série 7, Volume 4. in Annales des Ponts et Chaussées, vol. Série 7, Volume 4.
[282] T. C. Powers, « A discussion of cement hydration in relation to the curing of concrete », *Highw. Res. Board Proc.*, vol. 27, 1948, Consulté le: 26 janvier 2023. [En ligne]. Disponible sur: https://trid.trb.org/view/102345
[283] D. C. Park, « Carbonation of concrete in relation to CO2 permeability and degradation of coatings », *Constr. Build. Mater.*, vol. 22, nº 11, p. 2260-2268, nov. 2008, doi: 10.1016/j.conbuildmat.2007.07.032.
[284] Portland Cement Association, *Permeability of Portland cement paste / by T.C. Powers ... [et al.]*. Portland Cement Association, 1955. Consulté le: 18 janvier 2023. [En ligne]. Disponible sur: http://archive.org/details/PermeabilityOfPortlandCementPasteByT.c.Powers...etAl.
[285] V. Waller, « Relationship between mix design of concrete, generation of heat during hydration and compressive strength », phdthesis, Ecole des Ponts, 1999. Consulté le: 18 janvier 2023. [En ligne]. Disponible sur: https://hal-enpc.archives-ouvertes.fr/tel-01223803
[286] B. Kolani, L. Buffo-Lacarriere, A. Sellier, L. Boutillon, et L. Linger, « Hydration of slag-blended cements », *Cem. Concr. Compos.*, vol. 34, nº 9, p. 1009, 2012, doi: 10.1016/j.cemconcomp.2012.05.007.
[287] B. Kolani, « Comportement au jeune âge des structures en béton armé à base de liants composés aux laitiers », These de doctorat, Toulouse 3, 2012. Consulté le: 18 janvier 2023. [En ligne]. Disponible sur: https://www.theses.fr/2012TOU30204
[288] L. Buffo-Lacarrière, « Prévision et évaluation de la fissuration précoce des ouvrages en béton ».
[289] V. G. Papadakis, « Effect of supplementary cementing materials on concrete resistance against carbonation and chloride ingress », *Cem. Concr. Res.*, vol. 30, nº 2, p. 291-299, févr. 2000, doi: 10.1016/S0008-8846(99)00249-5.
[290] F. Adenot, « Durabilite du beton : caracterisation et modelisation des processus physiques et chimiques de degradation du ciment », These de doctorat, Orléans, 1992. Consulté le: 18 janvier 2023. [En ligne]. Disponible sur: https://www.theses.fr/1992ORLE2001
[291] W. Chen, « Hydration of slag cement: theory, modeling and application ».
[292] H. J. H. Brouwers, « The work of Powers and Brownyard revisited: Part 1 », *Cem. Concr. Res.*, vol. 34, nº 9, p. 1697-1716, sept. 2004, doi: 10.1016/j.cemconres.2004.05.031.
[293] C. Andrade, « Calculation of chloride diffusion coefficients in concrete from ionic migration measurements », *Cem. Concr. Res.*, vol. 23, nº 3, p. 724-742, mai 1993, doi: 10.1016/0008-8846(93)90023-3.
[294] Nordtest method, « NT BUILD 492 - Concrete mortar and cement-based repair materials: Chloride migration coefficient from non-steady-state migration experiments », 1999.
[295] Q. Yuan, D. Deng, C. Shi, et G. De Schutter, « Chloride binding isotherm from migration and diffusion tests », *J. Wuhan Univ. Technol.-Mater Sci Ed*, vol. 28, nº 3, p. 548-556, juin 2013, doi: 10.1007/s11595-013-0729-y.
[296] P. Spiesz et H. J. H. Brouwers, « The apparent and effective chloride migration coefficients obtained in migration tests », *Cem. Concr. Res.*, vol. 48, p. 116-127, juin 2013, doi: 10.1016/j.cemconres.2013.02.005.
[297] D. P. Bentz, O. M. Jensen, A. M. Coats, et F. P. Glasser, « Influence of silica fume on diffusivity in cement-based materials: I. Experimental and computer modeling studies on cement pastes », *Cem. Concr. Res.*, vol. 30, nº 6, p. 953-962, juin 2000, doi: 10.1016/S0008-8846(00)00264-7.
[298] Jens. M. Frederiksen, « Report N° 123 - Chloride penetration into concrete manual ». HETEK, 1993.
[299] D. P. Bentz, « Influence of silica fume on diffusivity in cement-based materials: II. Multi-scale modeling of concrete diffusivity », *Cem. Concr. Res.*, vol. 30, nº 7, p. 1121-1129, juill. 2000, doi: 10.1016/S0008-8846(00)00263-5.

[300] J. Lizarazo-Marriaga et P. Claisse, « Determination of the concrete chloride diffusion coefficient based on an electrochemical test and an optimization model. »
[301] AFNOR, « FD P18-480 Béton - Justification de la durabilité des ouvrages en béton par méthode performantielle ». 2022. [En ligne]. Disponible sur: https://norminfo.afnor.org/consultation/fd-p-18-480/justification-de-la-durabilite-des-ouvrages-en-beton-par-methode-performantielle/123737
[302] B. Sudret, « Global sensitivity analysis using polynomial chaos expansion », *Reliab. Eng. Syst. Saf.*, vol. 93, p. 964-979, juill. 2008, doi: 10.1016/j.ress.2007.04.002.
[303] G. Blatman, « Adaptive sparse polynomial chaos expansions for uncertainty propagation and sensitivity analysis », These de doctorat, Clermont-Ferrand 2, 2009. Consulté le: 5 mai 2023. [En ligne]. Disponible sur: https://www.theses.fr/2009CLF21955
[304] E. Torre, S. Marelli, P. Embrechts, et B. Sudret, « Data-driven polynomial chaos expansion for machine learning regression », *J. Comput. Phys.*, vol. 388, p. 601-623, juill. 2019, doi: 10.1016/j.jcp.2019.03.039.
[305] R. G. Ghanem et P. D. Spanos, *Stochastic Finite Elements: A Spectral Approach*. New York, NY: Springer, 1991. doi: 10.1007/978-1-4612-3094-6.
[306] R. Ghanem et P. D. Spanos, « Polynomial Chaos in Stochastic Finite Elements », *J. Appl. Mech.*, vol. 57, n° 1, p. 197-202, mars 1990, doi: 10.1115/1.2888303.
[307] E. Novak et K. Ritter, « Simple Cubature Formulas with High Polynomial Exactness », *Constr. Approx.*, vol. 15, p. 499-522, déc. 1999, doi: 10.1007/s003659900119.
[308] I. Babuška, F. Nobile, et R. Tempone, « A Stochastic Collocation Method for Elliptic Partial Differential Equations with Random Input Data », *SIAM Rev.*, vol. 52, n° 2, p. 317-355, janv. 2010, doi: 10.1137/100786356.
[309] G. Blatman et B. Sudret, « Adaptive sparse polynomial chaos expansion based on least angle regression », *J. Comput. Phys.*, vol. 230, n° 6, p. 2345-2367, mars 2011, doi: 10.1016/j.jcp.2010.12.021.
[310] M. Berveiller, B. Sudret, et M. Lemaire, « Stochastic finite element: a non intrusive approach by regression », *Eur. J. Comput. Mech.*, vol. 15, n° 1-3, p. 81-92, janv. 2006, doi: 10.3166/remn.15.81-92.
[311] G. Blatman et B. Sudret, « Principal component analysis and Least Angle Regression in spectral stochastic finite element analysis », juill. 2011. doi: 10.1201/b11332-101.
[312] N. Lüthen, S. Marelli, et B. Sudret, « Sparse Polynomial Chaos Expansions: Literature Survey and Benchmark », *SIAMASA J. Uncertain. Quantif.*, vol. 9, n° 2, p. 593-649, janv. 2021, doi: 10.1137/20M1315774.
[313] « OpenTURNS ». Consulté le: 20 février 2023. [En ligne]. Disponible sur: https://openturns.github.io/www/index.html
[314] « UQLab - The Framework for Uncertainty Quantification », uqlab. Consulté le: 18 janvier 2023. [En ligne]. Disponible sur: https://www.uqlab.com
[315] « sklearn.neural_network.MLPRegressor », scikit-learn. Consulté le: 20 février 2023. [En ligne]. Disponible sur: https://scikit-learn/stable/modules/generated/sklearn.neural_network.MLPRegressor.html
[316] « Keras: Deep Learning for humans ». Consulté le: 1 juin 2023. [En ligne]. Disponible sur: https://keras.io/
[317] Comité Européen du Béton, « Manuel Sécurité des Structures - Concepts généraux - Charges et action ». Bulletin d'information 106 et 107, 1975.
[318] Cominté Européen du Béton, « General principles on Reliability for Structures ». Bulletin d'information 191, 1988.
[319] AFNOR, « NF EN 1990 Eurocodes structuraux - Bases de calcul des structures ». 2011. Consulté le: 18 janvier 2023. [En ligne]. Disponible sur: https://www.boutique.afnor.org/fr-fr/norme/nf-en-1990/eurocodes-structuraux-bases-de-calcul-des-structures/fa102408/21211
[320] AFNOR, « NF EN 1992-2 Eurocode 2 - Calcul des structures en béton - Partie 2 : ponts en béton - Calcul des dispositions constructives ». 2006. Consulté le: 19 janvier 2023. [En ligne].

Disponible sur: https://www.boutique.afnor.org/fr-fr/norme/nf-en-19922/eurocode-2-calcul-des-structures-en-beton-partie-2-ponts-en-beton-calcul-de/fa114140/27287
[321] ISO/TC 98/SC 2 Fiabilité des structures, « ISO 2394 Principes généraux de la fiabilité des constructions ». 2015.
[322] C.C.T.G., « Fascicule 65 (2018) - Exécution des ouvrages de génie civil en béton ». 2018. [En ligne]. Disponible sur: https://www.infociments.fr/fascicule-65-presentation-generale
[323] M. Carcassès, F. Cussigh, et F. Toutlemonde, « Synthesis report PerfDuB GT2B - Definition of performance thresholds according to exposure classes. » 2021.
[324] Task Group 8.6, *Bulletin 76 : Benchmarking of deemed-to-satisfy provisions in standards: Durability of reinforced concrete structures exposed to chlorides*. 2015.
[325] F. Pedrosa et C. Andrade, « Corrosion induced cracking: Effect of different corrosion rates on crack width evolution », *Constr. Build. Mater.*, vol. 133, p. 525-533, févr. 2017, doi: 10.1016/j.conbuildmat.2016.12.030.
[326] D. Chen et S. Mahadevan, « Chloride-induced reinforcement corrosion and concrete cracking simulation », *Cem. Concr. Compos.*, vol. 30, n° 3, p. 227-238, mars 2008, doi: 10.1016/j.cemconcomp.2006.10.007.
[327] S. T. Yang, K. F. Li, et C. Q. Li, « Numerical determination of concrete crack width for corrosion-affected concrete structures », *Comput. Struct.*, vol. 207, p. 75-82, sept. 2018, doi: 10.1016/j.compstruc.2017.07.016.
[328] A. Strauss *et al.*, « Probabilistic and Semi-Probabilistic Analysis of Slender Columns Frequently Used in Structural Engineering », *Appl. Sci.*, vol. 11, n° 17, Art. n° 17, janv. 2021, doi: 10.3390/app11178009.
[329] J. Duchaine, M. Wahl, D. Markel, et H. Bouchard, « A probabilistic approach for determining Monte Carlo beam source parameters: II. Impact of beam modeling uncertainties on dosimetric functions and treatment plans », *Phys. Med. Biol.*, vol. 67, n° 4, p. 045006, févr. 2022, doi: 10.1088/1361-6560/ac4efb.
[330] G.-D.-P. F. Mbetmi, « Fiabilité résiduelle des ouvrages en béton dégradés par réaction alcali-granulat: application au barrage hydroélectrique de Song Loulou ».
[331] R. Rackwitz et B. Flessler, « Structural reliability under combined random load sequences », *Comput. Struct.*, vol. 9, n° 5, p. 489-494, nov. 1978, doi: 10.1016/0045-7949(78)90046-9.
[332] « Fiabilité des structures : couplage mécano-fiabiliste statique LEMAIRE Maurice, CHATEAUNEUF Alaa, MITTEAU Jean-Claude », Librairie Lavoisier. Consulté le: 18 janvier 2023. [En ligne]. Disponible sur: https://www.lavoisier.fr/livre/genie-civil-BTP/fiabilite-des-structures-couplage-mecano-fiabiliste-statique/lemaire/descriptif-9782746210578
[333] E. ARDILLON, « Méthode FORM, rapport établi lors des discussion du groupe de travail Sécurité et sureté des structures de l'IMdR ». 2014.
[334] A. M. HASOFER et M. C. LIND, « An Exact and Invariant First Order Reliability Format », *Journal of Engineering Mechanics*, p. 111-121, 1974.
[335] AFNOR, « NF EN 1992-1-1 Eurocode 2 - Calcul des structures en béton - Partie 1-1 : règles générales et règles pour les bâtiments ». 2005. Consulté le: 18 janvier 2023. [En ligne]. Disponible sur: https://www.boutique.afnor.org/fr-fr/norme/nf-en-199211/eurocode-2-calcul-des-structures-en-beton-partie-11-regles-generales-et-reg/fa039724/25784
[336] LCPC, « Guide technique : Recommandations pour la prévention des désordres dus à la réaction sulfatique interne ». Techniques et méthodes des laboratoires des ponts et chaussées.
[337] LCPC, « Guide technique : Recommandations pour la durabilité des bétons durcis soumis au gel ». Techniques et méthodes des laboratoires des ponts et chaussées.
[338] AFNOR, « NF EN 13369 Règles communes pour les produits préfabriqués en béton ». 2006. Consulté le: 18 janvier 2023. [En ligne]. Disponible sur: https://www.boutique.afnor.org/fr-fr/norme/nf-en-13369/regles-communes-pour-les-produits-prefabriques-en-beton/fa188565/1763

[339] E. Rozière, « Étude de la durabilité des bétons par une approche performantielle », These de doctorat, Nantes, 2007. Consulté le: 18 janvier 2023. [En ligne]. Disponible sur: https://www.theses.fr/2007NANT2125
[340] AFNOR, « FD P18-480 - Béton — Justification de la durabilité des ouvrages en béton par méthode performantielle ». octobre 2022.
[341] AFNOR, « NF EN 196-1 Méthodes d'essais des ciments - Partie 1 : détermination des résistances ». 2016. [En ligne]. Disponible sur: https://www.boutique.afnor.org/fr-fr/norme/nf-en-1961/methodes-dessais-des-ciments-partie-1-determination-des-resistances/fa184622/57803
[342] « (PDF) Perméabilité à l'eau des bétons : développement d'une méthode alternative par séchage ». Consulté le: 3 février 2023. [En ligne]. Disponible sur: https://www.researchgate.net/publication/327285593_Permeabilite_a_l'eau_des_betons_developpement_d'une_methode_alternative_par_sechage
[343] E.-P. Mbemba-Kiele, « Influence of Drying on the Behaviour of Concrete at Very Early-Age », phdthesis, Université de Nantes ; Ecole Centrale de Nantes (ECN), 2010. Consulté le: 30 janvier 2023. [En ligne]. Disponible sur: https://theses.hal.science/tel-00726153
[344] « Ciments et LHR : analyse et inventaire du cycle de vie (ACV/ICV), déclaration environnementale produit (DEP) », Infociments. Consulté le: 30 janvier 2023. [En ligne]. Disponible sur: https://www.infociments.fr/ciments/ciments-declaration-environnementale-inventaire-analyse-du-cycle-de-vie
[345] Y. Zhang, « Assessment of CO2 emissions and cost of fly ash concrete », oct. 2014.
[346] « Constituants du béton ». Consulté le: 30 janvier 2023. [En ligne]. Disponible sur: http://www.diogen.fr/index.php/constituants-du-beton
[347] « Plasticisers and superplasticisers EPD 2015 | EFCA ». Consulté le: 30 janvier 2023. [En ligne]. Disponible sur: https://www.efca.info/download/plasticisers-and-superplasticisers-epd-2015/
[348] « Analyse de cycle de vie des granulats | UNPG ». Consulté le: 30 janvier 2023. [En ligne]. Disponible sur: https://www.unpg.fr/accueil/dossiers/environnement/analyse-de-cycle-de-vie-des-granulats/
[349] « Documentation Base Carbone ». Consulté le: 30 janvier 2023. [En ligne]. Disponible sur: https://bilans-ges.ademe.fr/documentation/UPLOAD_DOC_FR/index.htm?eau_de_resseau.htm
[350] AFNOR, « NF EN 12390-3 (2019) Essais pour béton durci - Partie 3 : Résistance à la compression des éprouvettes ». 2019. Consulté le: 30 janvier 2023. [En ligne]. Disponible sur: https://www.boutique.afnor.org/fr-fr/norme/nf-en-123903/essais-pour-beton-durci-partie-3-resistance-a-la-compression-des-eprouvette/fa190566/83462
[351] A. Neville, « Consideration of durability of concrete structures: Past, present, and future », *Mater. Struct.*, vol. 34, n° 2, p. 114-118, mars 2001, doi: 10.1007/BF02481560.
[352] AFNOR, « NF P18-459 Béton - Essai pour béton durci - Essai de porosité et de masse volumique ». 2022. Consulté le: 30 janvier 2023. [En ligne]. Disponible sur: https://www.boutique.afnor.org/fr-fr/norme/nf-p18459/beton-essai-pour-beton-durci-essai-de-porosite-et-de-masse-volumique/fa160729/34961
[353] AFNOR, « XP P18-458 (2022) Essai sur béton durci - Essai de carbonatation accélérée ». 2022. Consulté le: 1 février 2023. [En ligne]. Disponible sur: https://www.boutique.afnor.org/fr-fr/norme/xp-p18458/essai-pour-beton-durci-essai-de-carbonatation-acceleree-mesure-de-lepaisseu/fa158331/32271
[354] AFNOR, « XP P18-462 (2022) Essai sur béton durci - Essai accéléré de migration des ions chlorure en régime non-statinnaire - Détermination du coefficient de diffusion apparent des ions chlorure ». 2022. [En ligne]. Disponible sur: https://www.boutique.afnor.org/fr-fr/norme/xp-p18462/essai-sur-beton-durci-essai-accelere-de-migration-des-ions-chlorure-en-regi/fa203053/340441

[355] V. Turgeon-Mallette, « Durabilité du béton fibré à ultra-haute performance : effet de la présence de microfissures sur la migration des ions chlorure », 2019, Consulté le: 2 avril 2023. [En ligne]. Disponible sur: http://hdl.handle.net/20.500.11794/67730
[356] C. Andrade, M. Castellote, et R. d'Andrea, « Measurement of ageing effect on chloride diffusion coefficients in cementitious matrices », *J. Nucl. Mater. - J NUCL MATER*, vol. 412, p. 209-216, mai 2011, doi: 10.1016/j.jnucmat.2010.12.236.
[357] V. Baroghel-Bouny *et al.*, « Ageing and durability of concrete in lab and in field conditions: Investigation of chloride penetration », *J. Sustain. Cem.-Based Mater.*, vol. 2, juin 2013, doi: 10.1080/21650373.2013.797938.
[358] « XP P18-481 », Afnor EDITIONS. Consulté le: 1 février 2023. [En ligne]. Disponible sur: https://www.boutique.afnor.org/fr-fr/norme/xp-p18481/essai-sur-beton-durci-mesure-de-la-resistivite-electrique/fa203059/340444
[359] C. Andrade et M. Castellote, « Chloride Aging Factor of Concrete Measured by Means of Resistivity », 2011.
[360] G. Villain et G. Platret, « Two Experimental Methods to Determine Carbonation Profiles in Concrete », *Mater. J.*, vol. 103, n° 4, p. 265-271, juill. 2006, doi: 10.14359/16610.
[361] Q. Zhou et F. P. Glasser, « Thermal stability and decomposition mechanisms of ettringite at <120°C », *Cem. Concr. Res.*, vol. 31, n° 9, p. 1333-1339, sept. 2001, doi: 10.1016/S0008-8846(01)00558-0.
[362] V. S. Ramachandran, R. M. Paroli, J. J. Beaudoin, et A. H. Delgado, « 11 - Gypsum and Gypsum Products », in *Handbook of Thermal Analysis of Construction Materials*, V. S. Ramachandran, R. M. Paroli, J. J. Beaudoin, et A. H. Delgado, Éd., Norwich, NY: William Andrew Publishing, 2002, p. 449-490. doi: 10.1016/B978-081551487-9.50013-X.
[363] G. Villain, M. Thiery, et G. Platret, « Measurement methods of carbonation profiles in concrete: Thermogravimetry, chemical analysis and gammadensimetry », *Cem. Concr. Res.*, vol. 37, n° 8, p. 1182-1192, août 2007, doi: 10.1016/j.cemconres.2007.04.015.
[364] W. A. Klemm, *Ettringite and Oxyanion-substituted Ettringites, Their Characterization and Applications in the Fixation of Heavy Metals: A Synthesis of the Literature*. Portland Cement Association, 1998.
[365] J. M. Rivas-Mercury, P. Pena, A. H. de Aza, et X. Turrillas, « Dehydration of Ca3Al2(SiO4)y(OH)4(3−y) (0 », *J. Eur. Ceram. Soc.*, vol. 28, n° 9, p. 1737-1748, janv. 2008, doi: 10.1016/j.jeurceramsoc.2007.12.038.
[366] N. Collier et N. Milestone, « The encapsulation of Mg(OH) 2 sludge in composite cement », *Cem. Concr. Res. - CEM CONCR RES*, vol. 40, p. 452-459, mars 2010, doi: 10.1016/j.cemconres.2009.10.007.
[367] M. Kök et W. Smykatz-Kloss, « Thermal Characterization of Dolomites », *J. Therm. Anal. Calorim.*, vol. 64, p. 1271-1275, juin 2001, doi: 10.1023/A:1011521802817.
[368] F. Kontoleontos, P. Tsakiridis, A. Marinos, N. S. Katsiotis, V. Kaloidas, et M. Katsioti, « Dry-grinded Ultrafine Cements Hydration. Physicochemical and Microstructural Characterization », *Mater. Res.*, vol. 16, p. 404-416, avr. 2013, doi: 10.1590/S1516-14392013005000014.
[369] L. Mosser, E. Garcia-Diaz, P. Rougeau, et F. Jacquemot, « Bétons bas carbone à base de liants ternaires : propriétés rhéologiques, mécaniques et de durabilité », in *NOMAD 2022 - 4e conférence internationale francophone Nouveaux Matériaux et Durabilité*, Montpelier, France: IMT Mines Alès and LMGC and LIFAM, nov. 2022. Consulté le: 13 juillet 2023. [En ligne]. Disponible sur: https://hal.science/hal-03879255
[370] E. Gruyaert, P. Van den Heede, et N. De Belie, « Carbonation of slag concrete: Effect of the cement replacement level and curing on the carbonation coefficient – Effect of carbonation on the pore structure », *Cem. Concr. Compos.*, vol. 35, n° 1, p. 39-48, janv. 2013, doi: 10.1016/j.cemconcomp.2012.08.024.
[371] A. M. Abd El Fattah et I. N. A. Al-Duais, « Modeling of Chloride Binding Capacity in Cementitious Matrices Including Supplementary Cementitious Materials », *Crystals*, vol. 12, n° 2, Art. n° 2, févr. 2022, doi: 10.3390/cryst12020153.

[372] V. Baroghel-Bouny, X. Wang, M. Thiery, M. Saillio, et F. BARBERON, « Prediction of chloride binding isotherms of cementitious materials by analytical model or numerical inverse analysis », *Cem. Concr. Res.*, vol. 42, p. 1207-1224, sept. 2012, doi: 10.1016/j.cemconres.2012.05.008.
[373] L. Doussang, G. Samson, F. Deby, B. Huet, E. Guillon, et M. Cyr, « Durability (General Transfer Properties and Chloride Penetration Resistance) of Three Low-Carbon Concretes (Low Clinker, Alkali-Activated Slag and Supersulfated Cement) ». Rochester, NY, 2 mai 2023. doi: 10.2139/ssrn.4436149.
[374] M. Achrafi, G. Villain, et S. Bonnet, « Monitoring chloride diffusion in BFS concrete using an Electrical Resistivity Tomography device », *E-J. Nondestruct. Test.*, vol. 27, sept. 2022, doi: 10.58286/27281.
[375] B. L. Damineli, F. M. Kemeid, P. S. Aguiar, et V. M. John, « Measuring the eco-efficiency of cement use », *Cem. Concr. Compos.*, vol. 32, n° 8, p. 555-562, sept. 2010, doi: 10.1016/j.cemconcomp.2010.07.009.
[376] H. Ranaivomanana, « Tranferts dans les milieux poreux réactifs non saturés : application à la cicatrisation de fissure dans les matériaux cimentaires par carbonatation », These de doctorat, Toulouse 3, 2010. Consulté le: 18 janvier 2023. [En ligne]. Disponible sur: https://www.theses.fr/2010TOU30268
[377] M. Thiery, V. Baroghel-Bouny, N. Bourneton, G. Villain, et C. Stéfani, « Modélisation du séchage des bétons », *Rev. Eur. Génie Civ.*, vol. 11, n° 5, p. 541-577, mai 2007, doi: 10.1080/17747120.2007.9692945.
[378] T. Q. Nguyen, « Modélisations physico-chimiques de la pénétration des ions chlorures dans les matériaux cimentaires », These de doctorat, Marne-la-vallée, ENPC, 2007. Consulté le: 18 janvier 2023. [En ligne]. Disponible sur: https://www.theses.fr/2007ENPC0730
[379] M. Van Genuchten, « A Closed-form Equation for Predicting the Hydraulic Conductivity of Unsaturated Soils1 », *Soil Sci. Soc. Am. J.*, vol. 44, sept. 1980, doi: 10.2136/sssaj1980.03615995004400050002x.
[380] S. Oh, Y. K. Kim, et J.-W. Kim, « A Modified van Genuchten-Mualem Model of Hydraulic Conductivity in Korean Residual Soils », *Water*, vol. 7, n° 10, Art. n° 10, oct. 2015, doi: 10.3390/w7105487.
[381] R. J. Millington, « Gas Diffusion in Porous Media », *Science*, vol. 130, n° 3367, p. 100-102, juill. 1959, doi: 10.1126/science.130.3367.100-a.
[382] M. J. Mitchell, O. E. Jensen, K. A. Cliffe, et M. M. Maroto-Valer, « A model of carbon dioxide dissolution and mineral carbonation kinetics », *Proc. R. Soc. Math. Phys. Eng. Sci.*, vol. 466, n° 2117, p. 1265-1290, déc. 2009, doi: 10.1098/rspa.2009.0349.
[383] A. V. Saetta, R. V. Scotta, et R. V. Vitaliani, « Analysis of Chloride Diffusion into Partially Saturated Concrete », *Mater. J.*, vol. 90, n° 5, p. 441-451, sept. 1993, doi: 10.14359/3874.
[384] H. Akita, T. Fujiwara, et Y. Ozaka, « A practical procedure for the analysis ofmoisture transfer within concrete due to drying », *Mag. Concr. Res.*, vol. 49, n° 179, p. 129-137, juin 1997, doi: 10.1680/macr.1997.49.179.129.
[385] « Thermal Properties and Transient Thermal Analysis of Structural Members During Hydration », *ACI Mater. J.*, vol. 95, n° 3, 1998, doi: 10.14359/373.
[386] I. Asadi, P. Shafigh, Z. F. B. Abu Hassan, et N. B. Mahyuddin, « Thermal conductivity of concrete – A review », *J. Build. Eng.*, vol. 20, p. 81-93, nov. 2018, doi: 10.1016/j.jobe.2018.07.002.
[387] Q. Wu, T. Rougelot, N. Burlion, et X. Bourbon, « Experimental investigation of the first desorption isotherm of a high performance concrete with thin sliced samples », *Constr. Build. Mater.*, vol. 72, p. 389-397, déc. 2014, doi: 10.1016/j.conbuildmat.2014.09.032.
[388] J. Liu, « Etude expérimentale de la perméabilité relative des matériaux cimentaires et simulation numérique du transfert d'eau dans le béton », These de doctorat, Ecole centrale de Lille, 2011. Consulté le: 13 février 2023. [En ligne]. Disponible sur: https://www.theses.fr/2011ECLI0018

[389] H. Ranaivomanana, J. Verdier, A. Sellier, et X. Bourbon, « Toward a better comprehension and modeling of hysteresis cycles in the water sorption–desorption process for cement based materials », *Cem. Concr. Res.*, vol. 41, n° 8, p. 817-827, août 2011, doi: 10.1016/j.cemconres.2011.03.012.
[390] M. Lion et J. Sanahuja, « Perméabilité à l'eau des bétons : développement d'une méthode alternative par séchage », nov. 2018.
[391] A. Bordy, « Influence des conditions thermo-hydriques de conservation sur l'hydratation de matériaux cimentaires à base d'une fine recyclée », phdthesis, Université de Cergy Pontoise, 2016. Consulté le: 18 mai 2023. [En ligne]. Disponible sur: https://theses.hal.science/tel-01644803
[392] « Current weather data - OpenWeatherMap ». Consulté le: 11 juin 2023. [En ligne]. Disponible sur: https://openweathermap.org/current#name
[393] Y. Gao, J. Zhang, S. Zhang, et Y. Zhang, « Probability distribution of convection zone depth of chloride in concrete in a marine tidal environment », *Constr. Build. Mater.*, vol. 140, p. 485-495, juin 2017, doi: 10.1016/j.conbuildmat.2017.02.134.
[394] C. Zeeb et P. J. Burns, « A Comparison of Failure Probability Estimates by Monte Carlo Sampling and Latin Hypercube Sampling », janv. 1998.
[395] R. Hirata, A. Ooi, E. Tada, et A. Nishikata, « Influence of the degree of saturation on carbon steel corrosion in soil », *Corros. Sci.*, vol. 189, p. 109568, août 2021, doi: 10.1016/j.corsci.2021.109568.
[396] N. Kabashi, C. Krasniqi, A. Sadikaj, S. Bublaku, M. Ali, et H. Morina, « CORROSION IN CONCRETE UNDER SULPHATE AND CHLORIDE ATTACKS », avr. 2017.
[397] R. Folic et D. Zenunović, « Durability design of concrete structures, Part 2: Modelling and structural assessment », *Facta Univ. - Ser. Archit. Civ. Eng.*, vol. 8, janv. 2010, doi: 10.2298/FUACE1001045F.
[398] E. Chavez Ulloa, R. Camacho-Chab, M. Sosa-Baz, P. Castro-Borges, et T. López Pérez, « Corrosion Process of Reinforced Concrete by Carbonation in a Natural Environment and an Accelerated Test Chamber », *Int. J. Electrochem. Sci.*, vol. 8, p. 9015-9029, juill. 2013, doi: 10.1016/S1452-3981(23)12946-4.
[399] « sklearn.inspection.permutation_importance », scikit-learn. Consulté le: 20 février 2023. [En ligne]. Disponible sur: https://scikit-learn/stable/modules/generated/sklearn.inspection.permutation_importance.html
[400] « tkinter — Interface Python pour Tcl/Tk », Python documentation. Consulté le: 26 mai 2023. [En ligne]. Disponible sur: https://docs.python.org/3/library/tkinter.html
[401] « Carbon dioxide now more than 50% higher than pre-industrial levels ». Consulté le: 11 juin 2023. [En ligne]. Disponible sur: https://www.noaa.gov/news-release/carbon-dioxide-now-more-than-50-higher-than-pre-industrial-levels
[402] « scipy.stats.kstest — SciPy v1.11.1 Manual ». Consulté le: 30 juillet 2023. [En ligne]. Disponible sur: https://docs.scipy.org/doc/scipy/reference/generated/scipy.stats.kstest.html#scipy-stats-kstest
[403] T. Mayra de Oliveira, M. Farage, L. Goliatt, et T. BITTENCOURT, « Analysis and validation of correlation curves between sclerometry and compression tests for the evaluation of compressive strength of concretes », *Rev. IBRACON Estrut. E Mater.*, vol. 11, p. 779-809, août 2018, doi: 10.1590/s1983-41952018000400008.
[404] « Clinker replacement | Climate Technology Centre & Network | Tue, 11/08/2016 ». Consulté le: 5 juin 2023. [En ligne]. Disponible sur: https://www.ctc-n.org/technologies/clinker-replacement
[405] The carbon transition think tank, « Décarboner la filière ciment-béton - Dans le cadre du plan de transformation de l'économie Française - The shift project ». 2022.
[406] C.C.T.G., « Fascicule n°65 - Ecécution des ouvrages de génie civil en béton ». 2017.
[407] AFNOR, « NF EN 12350-6 (2019) Essais pour béton frais - Partie 6 : Masse volumique ». 2019.

[408] AFNOR, « NF EN 12350-2 (2019) Essais pour béton frais - Partie 2 : Essais d'affaissement ». 2019.
[409] AFNOR, « NF EN 12350-7 (2019) Essais pour béton frais - Partie 7 : Teneur en air - Méthode de la compressibilité ». 2019.
[410] AFNOR, « NF EN 12390-3 (2019) Essais pour béton durci - Partie 3 : Résistance à la compression des éprouvettes ». 2019.
[411] AFNOR, « NF P18-459 (2022) Béton - Essai pour béton durci - Essai de porosité et de masse volumique ». 2022.
[412] AFNOR, « XP P18-463 (2011) Essai de perméabilité aux gaz sur béton durci ». 2011.
[413] AFNOR, « NF EN 12390-11 Essais pour béton durci - Partie 11 : Détermination de la résistance du béton à la pénétration des chlorures, diffusion unidirectionnelle ». 2015.
[414] AFNOR, « XP P18-462 (2022) Essai sur béton durci - Essai accéléré de migration des ions chlorure en régime non-statinnaire - Détermination du coefficient de diffusion apparent des ions chlorure ». 2022.
[415] AFNOR, « XP P18-481 (2022) Essai sur béton durci - Mesure de la résistivité électrique ». 2022.
[416] AFNOR, « NF EN 12390-10 (2018) Essais pour bton durci - Partie 10 : Détermination de la résistance à la carbonatation du béton à des niveaux atmosphériques de dioxyde de carbone ». 2018.
[417] AFNOR, « XP P18-458 (2022) Essai sur béton durci - Essai de carbonatation accélérée ». 2022.
[418] I. R. Kennedy, J. W. Runcie, S. Zhang, et R. J. Ritchie, « A New Look at Physico-Chemical Causes of Changing Climate: Is the Seasonal Variation in Seawater Temperature a Significant Factor in Establishing the Partial Pressure of Carbon Dioxide in the Earth's Atmosphere? », *Thermo*, vol. 2, n° 4, Art. n° 4, déc. 2022, doi: 10.3390/thermo2040028.
[419] « Salinity Distribution at the Ocean Surface - Sea Surface Salinity - Remote Sensing ». Consulté le: 13 juin 2023. [En ligne]. Disponible sur: http://www.salinityremotesensing.ifremer.fr/sea-surface-salinity/salinity-distribution-at-the-ocean-surface
[420] T. Soukissian *et al.*, « Marine Renewable Energy in the Mediterranean Sea: Status and Perspectives », *Energies*, vol. 10, sept. 2017, doi: 10.3390/en10101512.
[421] AFNOR, « NF EN 12504-1 (2019) Essais pour béton dans les structures - Partie 1 : Carottes - Prélèvement, examen et essais en compression ». 2019.
[422] AFNOR, « NF EN 12504-4 (2021) Essais pour béton dans les structures - Partie 4 : Détermination de la vitesse de propagation des ultrasons ». 2021.
[423] AFNOR, « NF EN 12504-2 (2021) Essais pour béton dans les structures - Partie 2 : Essais non destructifs - Détermination de l'indice de rebondissement ». 2021.
[424] AFNOR, « EN 12390-19 Essais pour béton durci - Détermination de la résistivité électrique ». 2023.
[425] N. Rakotovao Ravahatra, T. de Larrard, F. Duprat, E. Bastidas-Arteaga, et F. Schoefs, « A Cost-Benefit Methodology for Selecting Analytical Reinforced Concrete Corrosion Onset Models », *Adv. Civ. Eng.*, vol. 2020, p. 3286721, 2020, doi: 10.1155/2020/3286721.
[426] E. Rozière, A. Loukili, et F. Cussigh, « A performance based approach for durability of concrete exposed to carbonation », *Constr. Build. Mater.*, vol. 23, n° 1, p. 190-199, janv. 2009, doi: 10.1016/j.conbuildmat.2008.01.006.
[427] S. Boualleg, M. Bencheikh, L. Belagraa, A. Daoudi, et M. A. Chikouche, « The Combined Effect of the Initial Cure and the Type of Cement on the Natural Carbonation, the Portlandite Content, and Nonevaporable Water in Blended Cement », *Adv. Mater. Sci. Eng.*, vol. 2017, p. e5634713, mars 2017, doi: 10.1155/2017/5634713.
[428] B. Godart et M. Dierkens, « PN PerfDuB - Synthesis Report of GT2a - Analysis of Data obtained on existing structures ». 2022.
[429] A. Torres-Acosta et A. Sagues, « Concrete cracking by localized steel corrosion - Geometric effects », *ACI Mater. J.*, vol. 101, p. 501-507, nov. 2004.

[430] T. El Maaddawy et K. Soudki, « A model for prediction of time from corrosion initiation to corrosion cracking », *Cem. Concr. Compos.*, vol. 29, n° 3, p. 168-175, mars 2007, doi: 10.1016/j.cemconcomp.2006.11.004.
[431] C. Alonso, C. Andrade, J. Rodriguez, et J. M. Diez, « Factors controlling cracking of concrete affected by reinforcement corrosion », *Mater. Struct.*, vol. 31, n° 7, p. 435-441, août 1998, doi: 10.1007/BF02480466.
[432] V. L'Hostis, « Non destructive evaluation for the prediction of structure degradation and the monitoring optimization - T4_1.2 - Synthesis of simplified models for steel corrosion. » 15 septembre 2012.
[433] C. L. Page, « 5 - Corrosion and protection of reinforcing steel in concrete », in *Durability of Concrete and Cement Composites*, C. L. Page et M. M. Page, Éd., in Woodhead Publishing Series in Civil and Structural Engineering. , Woodhead Publishing, 2007, p. 136-186. doi: 10.1533/9781845693398.136.
[434] F. Perrin, « Prise en compte des données expérimentales dans les modèles probabilistes pour la prévision de la durée de vie des structures », These de doctorat, Clermont-Ferrand 2, 2008. Consulté le: 2 août 2023. [En ligne]. Disponible sur: https://www.theses.fr/2008CLF21823
[435] E. Bastidas-Arteaga et F. Schoefs, « Stochastic improvement of inspection and maintenance of corroding reinforced concrete structures placed in unsaturated environments », *Eng. Struct.*, vol. 41, p. 50-62, août 2012, doi: 10.1016/j.engstruct.2012.03.011.
[436] E. Bastidas-Arteaga et F. Schoefs, « Sustainable maintenance and repair of RC coastal structures », *Proc. Inst. Civ. Eng. - Marit. Eng.*, vol. 168, n° 4, p. 162-173, déc. 2015, doi: 10.1680/jmaen.14.00018.
[437] A. Lindvall, « Environmental actions on concrete exposed in marine and road environments and its response ».
[438] Y. Wang, L. Wu, Y. Wang, Q. Li, et Z. Xiao, « Prediction model of long-term chloride diffusion into plain concrete considering the effect of the heterogeneity of materials exposed to marine tidal zone », *Constr. Build. Mater.*, vol. 159, p. 297-315, janv. 2018, doi: 10.1016/j.conbuildmat.2017.10.083.
[439] F. Legeron et P. Paultre, « Prediction of Modulus of Rupture of Concrete », *Mater. J.*, vol. 97, n° 2, p. 193-200, mars 2000, doi: 10.14359/823.
[440] Canadian Standards Association, « Canadian Standards Association, (CSA) A23.3-94. Design of concrete structures. » 1994.
[441] M. G. Stewart et Q. Suo, « Extent of spatially variable corrosion damage as an indicator of strength and time-dependent reliability of RC beams », *Eng. Struct.*, vol. 31, n° 1, p. 198-207, janv. 2009, doi: 10.1016/j.engstruct.2008.08.011.
[442] M. D. McKay, R. J. Beckman, et W. J. Conover, « A Comparison of Three Methods for Selecting Values of Input Variables in the Analysis of Output from a Computer Code », *Technometrics*, vol. 21, n° 2, p. 239-245, 1979, doi: 10.2307/1268522.
[443] S. Wold, K. Esbensen, et P. Geladi, « Principal component analysis », *Chemom. Intell. Lab. Syst.*, vol. 2, n° 1, p. 37-52, août 1987, doi: 10.1016/0169-7439(87)80084-9.
[444] I. T. Jolliffe et J. Cadima, « Principal component analysis: a review and recent developments », *Philos. Trans. R. Soc. Math. Phys. Eng. Sci.*, vol. 374, n° 2065, p. 20150202, avr. 2016, doi: 10.1098/rsta.2015.0202.
[445] L. Journaux, « UNIVERSITE DE BOURGOGNE SCIENCES ET TECHNIQUES ANALYSE MULTISPECTRALE D'IMAGES SATELLITAIRES ET ANALYSE MULTI-TABLEAUX : APPLICATION A LA REPARTITION DES POPULATIONS D'OISEAUX ET A LA STRUCTURE DU PAYSAGE », 2006. doi: 10.13140/2.1.1542.4641.
[446] N. D. Lawrence, « Sensitivity Analysis », nov. 2022, Consulté le: 5 mai 2023. [En ligne]. Disponible sur: https://mlatcl.github.io/mlphysical/lectures/05-01-sensitivity-analysis.html

ANNEXES

Annex 1 – Constituents (Section II)

FICHE TECHNIQUE PRODUIT — **CIMENTS**

LAFARGE Construire des villes meilleures

USINE DU TEIL

CEM I 52,5 N - SR 5 CE PM-CP2 NF HTS

NF EN 197-1 NF P 15-317 NF P 15-318

Déclaration de Performance n° 0333-CPR-1203

SERVICES EXCLUSIFS
Centre de Relation Clientèle :
0 825 888 425 Service 0,15 € / min + prix appel

CARACTERISTIQUES PHYSIQUES ET MECANIQUES

	DP (min)	Stabilité (mm)	Résistances mécaniques (MPa) 2 jours	28 jours			MV (g/cm3)	SSB (cm²/g)	Demande en eau (%)	L*		
Val. moyenne	166	1	33,4	66,1			3,16	3670	26,6	64,1		
Val. garantie	> 60	< 5	> 18	> 50								

CARACTERISTIQUES CHIMIQUES

	Valeur moyenne	Valeur garantie		Valeur moyenne
SO3 (%)	2,2	≤ 2,5	Alcalins équivalents [Na2O + 0,658 K2O] (%)	0,2
Chlorures Cl- (%)	0,03	≤ 0,1	Alcalins actifs [suivant la norme NF P 18-454] (%)	0,2
Perte au feu 950°C (%)	1,5	≤ 3	Vc coefficient de variation des alcalins actifs	0,13
Insolubles (%)	0,35	≤ 0,75		
S-- (%)	0	≤ 0,2		

CONSTITUANTS PRINCIPAUX ET SECONDAIRES :

Clinker Portland LE TEIL	**97,0%**			**Constituants secondaires**	**3,0%**
C3S + C2S (%)	84			Calcaire	
CaO/SiO2	2,8			Fines de cuisson	
MgO (%)	0,8			Laitier de haut fourneau	
C3S (%)	67				
C2S (%)	17				
C3A (%)	4			**Total des constituants**	
C4AF (%)	7			**100%**	

AUTRES CONSTITUANTS

Gypse (%)	2,5
Agent de mouture AMA 32E - Teneur sous forme d'extrait sec (%)	0,04

LIVRAISON EN VRAC

A member of LafargeHolcim

ISO 9001 BUREAU VERITAS Certification

ISO 14001 BUREAU VERITAS Certification

Date de révision : **11/01/2017**

Direction Commerciale
Assistance
et Prescription Clients
Tél. : 01 34 77 78 81
Fax : 01 30 98 73 50

Ciments Calcia
HEIDELBERGCEMENT Group

Version du : 26/02/2020
N° DoP : 0333-CPR-2105

Fiche produit

COUVROT

CEM II/A-LL 42.5 R CE CP2 NF

Caractéristiques physiques et mécaniques

Compression en MPa				Eau pâte pure en %	Début de prise en mn	Stabilité en mm	Masse volumique en g/cm³	Surface Blaine en cm²/g	Chaleurs en J/g		L*
1j	2j	7j	28j						41h	120h	
-	35	49	57	27.6	3H14	0	3.05	4824	335	-	67

Composition élémentaire (%)	
Perte au feu	6.8
SiO_2	17.8
Al_2O_3	4.5
Fe_2O_3	2.4
TiO_2	-
MnO	-
CaO	63.8
MgO	0.9
SO_3	3.3
K_2O	0.87
Na_2O	0.16
P_2O_5	0.1
S--	<0,02
Cl-	0.01
Insoluble	0.2
Na_2O eq.	0.74
Na_2O eq. Actif	0.65
C_3A	-
$C_3A+0.27xC_3S$	-
$C_4AF+2xC_3A$	-

Constituants (%)	
Principaux	
Clinker (K) de Couvrot	87.0
Calcaire (L)	12.0
Secondaires	1.0
BPD (%)	
Sulfate de calcium	
Gypse	5.4
Anhydrite	-
Additifs	
Agent de mouture	0.037
Agent réducteur de Cr VI	0.20

Etablissement	Vrac	Big bag	Sac 25 kg	Sac 35 kg
Usine de Couvrot	Oui	Non	Non	Non
Dépôt de Bruneseau	Oui	Non	Non	Non
Dépôt de Strasbourg	Oui	Non	Non	Non

Caractéristiques des constituants

Nature	Caractéristiques		
Clinker (K) de Couvrot	CaO/SiO_2	-	3.1
	C_3S+C_2S (%)	-	78
	MgO (%)	-	1.0
	Al_2O_3 (%)	-	-
	C_3S (%)	-	68.6
	C_2S (%)	-	9.8
	C_3A (%)	-	9.8
	C_4AF (%)	-	8.3
Calcaire (L ou LL)	$CaCO_3$ (%)		100.0
	Vb (g/100g)		0.1
	TOC (%)		0.15
Laitier (S)	Laitier vitreux (%)		-
	$(CaO+MgO)/SiO_2$		-
	$CaO+MgO+SiO_2$ (%)		-
Cendres (V)	PF (%)		-
	CaO réactive (%)		-
	SiO_2 réactive (%)		-
Fumées de silice (D)	SiO_2 amorphe (%)		-
	PF (%)		-
	Aire massique BET (m^2/kg)		-

Ces valeurs ne sont données qu'à titre indicatif. Les résultats d'auto-contrôle sont disponibles sur demande à la Direction Commerciale Assistance et Prescription Clients

afaq ISO 9001 Qualité
AFNOR CERTIFICATION

Siège social :
Rue des Technodes
78930 Guerville
Tél. : 01 34 77 78 00
Fax : 01 34 77 79 06

SAS au capital de 593 836 525 €
Siren 654 800 689 RCS Versailles

Direction Commerciale
Assistance
et Prescription Clients
Tél. : 01 34 77 78 81
Fax : 01 30 98 73 50

Ciments Calcia
HEIDELBERGCEMENT Group

version du: 21/02/22
N° DoP : 0333-CPR-2207

Fiche produit

ROMBAS

CEM III/B 32,5 N-LH/SR CE PM-CP1 NF "SPM"

Caractéristiques physiques et mécaniques

Compression en MPa				Eau pâte pure en %	Début de prise en mn	Stabilité en mm	Masse volumique en g/cm³	Surface Blaine en cm²/g	Chaleurs en J/g		L*
1j	2j	7j	28j						41h	120h	
-	9	23	42	29,9	3h54	1	2,97	3497	188	-	73

Indice de concentration d'activité I	0,56

Composition élémentaire (%)		Constituants (%)	
Perte au feu	1,4	**Principaux**	
SiO_2	31	Clinker (K) COUVROT (%)	29,0
Al_2O_3	8,7		
Fe_2O_3	1,2		
TiO_2	-	Laitier (S)	71,0
MnO	-		
CaO	48		
MgO	4,9	**Secondaires**	
SO_3	2,9		
K_2O	0,66		
Na_2O	0,21		
P_2O_5	-		
S--	0,55		
Cl-	0,03		
		Sulfate de calcium	
Insoluble	0,5	Gypse	-
		Anhydrite	4,9
Na_2O eq.	0,64		
Na_2O eq. Actif	-	**Additifs**	
C_3A	-	Agent réducteur de Cr VI	0,15
$C_3A+0.27xC_3S$	-		
$C_4AF+2xC_3A$	-		

Etablissement	Vrac	Big bag	Sac 25 kg	Sac 35 kg
Usine de Rombas	Oui	Non	Non	Non

Caractéristiques des constituants

Nature	Caractéristiques		
			K
Clinker (K) COUVROT (%)	CaO/SiO_2	-	3,1
	C_3S+C_2S (%)	-	78
	MgO (%)	-	1,0
	Al_2O_3 (%)	-	-
	C_3S (%)	-	68
	C_2S (%)	-	9,3
	C_3A (%)	-	9,9
	C_4AF (%)	-	8,4
Calcaire (L ou LL)	$CaCO_3$ (%)		-
	Vb (g/100g)		-
	TOC (%)		-
Laitier (S)	Laitier vitreux (%)		98
	$(CaO+MgO)/SiO_2$		1,3
	$CaO+MgO+SiO_2$ (%)		84
Cendres (V)	PF (%)		-
	CaO réactive (%)		-
	SiO_2 réactive (%)		-
Fumées de silice (D)	SiO_2 amorphe (%)		-
	PF (%)		-
	Aire massique BET (m^2/kg)		-

Ces valeurs ne sont données qu'à titre indicatif. Les résultats d'auto-contrôle sont disponibles sur demande à la Direction Commerciale.

Siège social :
Rue des Technodes
78930 Guerville
Tél. : 01 34 77 78 00
Fax : 01 34 77 79 06

SAS au capital de 593 836 525 €
Siren 654 800 689 RCS Versailles

Direction Commerciale
Tour Alto
4 Place des Saisons
92400 Courbevoie
Tél : 01 40 89 51 00

Ciments Calcia
HEIDELBERGCEMENT Group

version du: 01/08/22
N° DoP : 0333-CPR-5006

Fiche produit

AIRVAULT

CEM V/A (S-V) 42,5 N CE PM-ES-CP1 NF "PMF3"

Caractéristiques physiques et mécaniques

Compression en MPa				Eau pâte pure en %	Début de prise en mn	Stabilité en mm	Masse volumique en g/cm³	Surface Blaine en cm²/g	Chaleurs en J/g		L*
1j	2j	7j	28j						41h	120h	
-	22	31	52	30,5	5h19	0	2,92	4971	291	-	59

Indice de concentration d'activité I	0,49

Composition élémentaire (%)		Constituants (%)	
Perte au feu	1,5	**Principaux**	
SiO_2	31	Clinker (K) AIRVAULT (%)	58,0
Al_2O_3	10		
Fe_2O_3	4,0		
TiO_2	-	Laitier (S) (%)	22,0
MnO	-	Cendres (V) (%)	20,0
CaO	46		
MgO	2,5	**Secondaires**	
SO_3	2,7	Calcaire (LL) (%)	
K_2O	1,3		
Na_2O	0,37		
P_2O_5	0,36		
S--	0,16	FDEC (%)	
Cl-	<0,007		
		Sulfate de calcium	
Insoluble	-	Gypse	3,1
		Anhydrite	-
Na_2O eq.	1,2		
Na_2O eq. Actif	0,74	**Additifs**	
		Agent de mouture	0,048
C_3A	-	Agent réducteur de Cr VI	0,43
$C_3A+0.27xC_3S$	-		
$C_4AF+2xC_3A$	-		

Etablissement	Vrac	Big bag	Sac 25 kg	Sac 35 kg
Usine d'Airvault	Oui	Non	Non	Oui

Caractéristiques des constituants

Nature	Caractéristiques		
			K
Clinker (K) AIRVAULT (%)	CaO/SiO_2	-	3,1
	C_3S+C_2S (%)	-	78
	MgO (%)	-	1,4
	Al_2O_3 (%)	-	-
	C_3S (%)	-	68
	C_2S (%)	-	10
	C_3A (%)	-	6,9
	C_4AF (%)	-	10
Calcaire (L ou LL)	$CaCO_3$ (%)		94
	Vb (g/100g)		0,33
	TOC (%)		0,05
Laitier (S)	Laitier vitreux (%)		99
	$(CaO+MgO)/SiO_2$		1,4
	$CaO+MgO+SiO_2$ (%)		86
Cendres (V)	PF (%)		4,0
	CaO réactive (%)		<10
	SiO_2 réactive (%)		40
Fumées de silice (D)	SiO_2 amorphe (%)		-
	PF (%)		-
	Aire massique BET (m^2/kg)		-

Ces valeurs ne sont données qu'à titre indicatif. Les résultats d'auto-contrôle sont disponibles sur demande à la Direction Commerciale.

Siège social
Tour Alto
4 Place des Saisons
92400 Courbevoie
Tél : 01 40 89 51 00

SAS au capital 593 836 525 euros
Siren 654 800 689 en cours de transfert au RCS de Nanterre

argeco DEVELOPPEMENT

FICHE TECHNIQUE PRODUIT

argicem®

METAKAOLIN (NF P 18-513) A - F_M - W_M

CARACTERISTIQUES CHIMIQUES

Exigences chimiques	Norme appliquée	Valeur garantie	Valeur moyenne
Silice (SiO_2) + Alumine (Al_2O_3)	NF EN 196-2	> 90,0 %	92,45 %
Chlorures	NF EN 196-2	< 0,1 %	0,002 %
Sulfates	NF EN 196-2	< 1,0 %	0,20 %
Oxyde de calcium (CaO) libre	NF EN 451-1	< 1,0 %	0,322 %
Teneur en alcalins totaux (Na_2O équivalent)	NF EN 196-2	-	0,251 %
Oxyde de magnesium (MgO)	NF EN 196-2	< 4,0 %	0,19 %
Perte au feu	NF EN 196-2	< 4,0 %	1,30 %
Valeur au bleu MB_F	NF EN 933-9	< 10 g/kg	7,48 g/kg
Fixation de l'hydroxyde de calcium ($Ca(OH)_2$)	Essai Chapelle modifié	> 700 mg/g	773,9 mg/g

Les valeurs moyennes, données à titre indicatif, sont les valeurs des douze derniers mois

CARACTERISTIQUES PHYSIQUES

Exigences physiques	Norme appliquée	Valeur garantie	Valeur moyenne
Masse volumique des particules	NF EN 196-6 NF EN 197-7	2500 kg/m3 ± 200 kg/m3	2551 kg/m3
Finesse	NF EN 933-1	Passant à 0.063 mm ≥ 70 % (Catégorie F_M)	74,6 %
Indice d'activité à 28 jours	NF EN 196-1	> à 100 % (Type A)	i_{28} = 101,93 %
Demande en eau	NF EN 196-3	≤ 1,15 (Catégorie W_M)	1,08
Temps de début de prise	NF EN 196-3	< 25 %	3,40 %
Stabilité	NF P 18-513	Si (CaO) libre < 1%	N.A.
Surface spécifique BET	NF ISO 9277	-	15,65 m²/g

Les valeurs moyennes, données à titre indicatif, sont les valeurs des douze derniers mois

Date de révision : 13/07/2016

SURSCHISTE

SILICOLINE®

- Cendre volante silico-alumineuse certifiée EN 450.
- La Silicoline® est disponible sèche ou humide, en vrac ou conditionnée en big bag, et se transporte par camion-citerne pulvérulent ou par bateau.

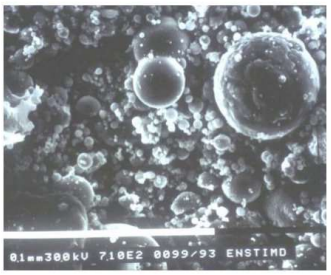

ANALYSES PHYSIQUES			
Perte au feu Taux de carbone	%	EN 196-2 à 950° 1 heure NF P 10-694	2 à 7
Masse Volumique apparente - en vrac			
séche non tassée	t/m3		0,6 à 0,8
séche tassée	t/m3		0,8 à 1,00
humide	t/m3		1,00 à 1,20
Masse Volumique réelle des grains	t/m3	EN 196-6	2,00 à 2,40
Masse Volumique absolue de la matière	t/m3		2,06 à 2,80
Granulométrie			
passants à 45 µm	%	EN 451-2 ou Alpine	65 à 75
passants à 80 µm	%	méthode Alpine	75 à 90
passants à 200 µm	%	méthode Alpine	96 à 99
passants à 315 µm	%	méthode Alpine	100
Blaine		g/cm2	2300 à > 5000
Indices d'activité			selon les cendres
28 j	%	EN 196-1	> 75 - > 80 -> 83
90 j	%	EN 196-1	> 85 - > 90 -> 95
ANALYSES CHIMIQUES			
SiO2	%	ICP ou FLUO X	50 à 55
Al2O3	%	ICP ou FLUO X	20 à 25
Fe2O3	%	ICP ou FLUO X	8,5
MgO	%	ICP ou FLUO X	3
MnO2	%	ICP ou FLUO X	0,5
CaO Total	%	ICP ou FLUO X	1 à 6
CaO Libre	%	EN 451-1	0,15 à 1
SO3	%	EN 196-2	0,3 à 2
TiO2	%	ICP ou FLUO X	1
Chlore T	%	EN 196-2	0,04
P2O5	%	ICP ou FLUO X	0,25
Na2O	%	ICP ou FLUO X	0,6
K2O	%	ICP ou FLUO X	0,8 à 4

PROPRIETES POUZZOLANIQUES

BETON
Selon la norme EN 196.1
Détermination résistances mécaniques
Indice activité à 28 jours en % = 75* à > 90
Indice activité à 90 jours en % = 85* à >100
*minimum exigé par EN 450-1 2012

ROUTE
Selon norme NF P 98 111
Essais de réactivité des cendres silico-alumineuses à la chaux.
Indice pouzzolanique :
à 60 jours MPa > 3.5 et à 360 jours MPa >10

REGLEMENTATION

CIMENT
Spécifications dans la norme NF P 15 301 et NF EN 197-1

ROUTE

NF P 11 300	Classification des sols
NF EN 14227-XX	Mélanges traités aux liants hydrauliques
EN 13282	Liants hydrauliques routiers

BETON

EN 450-1 2012	Cendres volantes pour béton, spécifications et critères de conformités
EN 450-2	Cendres volantes pour béton, Evaluation de la conformité
EN 206-1	Béton – Spécification – Performance

SURSCHISTE SIEGE
ZI LA CROISETTE
33 Rue Auguste Mariette
62300 LENS

Tél : 03 21 45 73 73
Fax : 03 21 45 73 70
Mail : siege@surschiste.com
Site internet : www.surschiste.com

Carrières du Boulonnais
Tél : 03.21.99.67.00
Fax : 03.21.99.67.10

S.A.S. CARRIERES DU BOULONNAIS
62250 FERQUES
R.C. CALAIS B 541 750 550 - APE 142A

Fiche Technique Produit

GRAVILLON lavé 4/12 mm (GL0412)

Référence normative	NF P 18-545, Article 10 Code : A
Nature Pétrographique	Calcaire viséen dur compact
Utilisation	Granulats pour bétons hydrauliques

AFNOR CERTIFICATION
11, rue Francis de Pressensé
93571 LA PLAINE ST DENIS Cedex

Spécifications contractuelles :

	2D	1.4D	D	D/1,4	d	d/2	f	FI	LA
Tamis (mm)	25	18	12,5	9	4	2			
Vss			99.0	70.0	10.0	5.0	4.00	20	30
Vsi	100.0	98.0	90.0	40.0					
Vss + U			100.0	76.0	15.0	6.0	4.30	24	33
Vsi - U		97.0	85.0	34.0					
Sf max				9.09					

Résultats : Granularité et propreté : Période du 05/05/12 au 05/11/12 (6 mois)
Autres caractéristiques : Période du 05/11/10 au 05/11/12 (24 mois)

	2D	1.4D	D	D/1,4	d	d/2	f	FI	LA
Tamis (mm)	25	18	12,5	9	4	2			
maxi			97.0	74.5	4.3	2.4	1.33	14	26
Xf+1,25 Sf			96.2	69.4	3.4	1.7	0.81		25.2
moyenne Xf	**100.0**	**100.0**	**93.6**	**61.3**	**2.4**	**1.1**	**0.54**	**12.8**	**23.7**
Xf - 1,25 Sf	100.0	100.0	91.0	53.3					
mini	100.0	100.0	87.0	42.4					
Ecart type Sf	0.00	0.00	2.08	6.46	0.79	0.42	0.220		1.20
nb. valeurs	51	51	51	51	51	51	51	10	24

Fuseau de régularité **de fabrication** **Moyenne de fabrication**

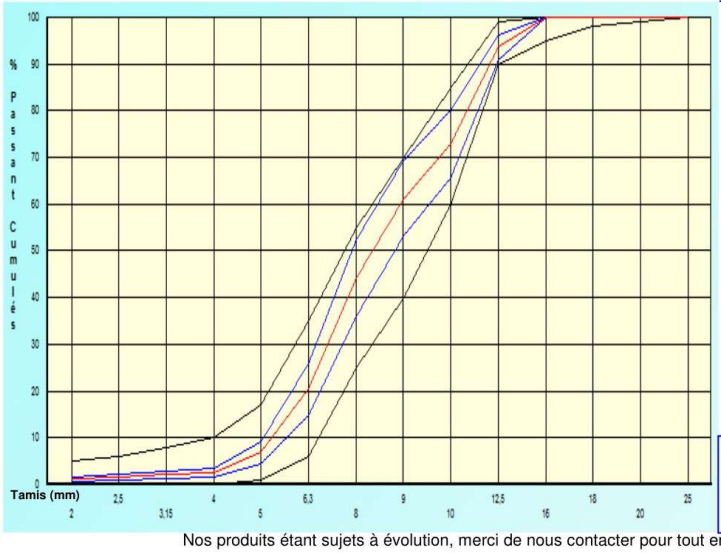

Autres Caractéristiques

	Valeur	Dernier Essai
MVR	2,67 t/m3	03/09/12
WA24	0,7 %	03/09/12
Na2O équi.	5,6 mg/kg	16/01/12
S total	0,03 %	16/01/12
Cl-	<0,0002%	16/01/12
MBF	1,9 g/kg	11/10/12
ImP	Néant	25/10/12
A R	NR	16/01/12

Sensibilité au gel-dégel: GA.
Boulettes d'argile : Néant (25/10/2012)
Présence éventuelle de nodules ferreux.

Date et visa du responsable contrôle qualité
05/11/12

Fiche n°: 1238

Nos produits étant sujets à évolution, merci de nous contacter pour tout engagement ou durée de validité

Carrières du Boulonnais

Tél : 03.21.99.67.00
Fax : 03.21.99.67.10

S.A.S. CARRIERES DU BOULONNAIS
62250 FERQUES
RCS BOULOGNE-SUR-MER B 541 750 550

Fiche Technique Produit

SABLE lavé 0/4 mm à 7 % de fines (SL0704)

Référence normative	NF P 18-545,article 10 Code : A
Lieu de production	FERQUES
Site de production	CARRIERES DU BOULONNAIS
Nature Pétrographique	Calcaire viséen dur compact
Utilisation	Granulats pour bétons hydrauliques

AFNOR CERTIFICATION
11, rue Francis de Pressensé
93571 LA PLAINE ST DENIS Cedex

Spécifications contractuelles : Engagement producteur du 28/05/15 au 28/11/15

	2D	1.4D	D	2	1	0,5	0,25	0,125	f	FM	MB
Tamis (mm)	8	5,6	4	2	1	0,500	0,250	0,125	0,063		
Vss			99.0		64.0		37.0		10.0	3.15	1.50
Vsi	100.0	95.0	89.0		50.0		23.0		4.0	2.55	
Vss + U			100.0		68.0		41.0		12.0	3.30	2.00
Vsi - U		94.0	87.0		46.0		19.0		2.0	2.40	
Sf max					4.24		4.24			0.180	

Résultats : Granularité et propreté : Période du 28/11/14 au 28/05/15 (6 mois)
Autres caractéristiques : Période du 28/11/14 au 28/05/15 (6 mois)

	2D	1.4D	D	2	1	0,5	0,25	0,125	f	FM	MB
Tamis (mm)	8	5,6	4	2	1	0,500	0,250	0,125	0,063		
maxi			96.0		62.3		36.3		9.0	3.02	0.60
Xf+1,25 Sf			95.9		60.0		34.3		8.0	2.94	0.43
moyenne Xf	**100.0**	**100.0**	**94.9**	**74.1**	**57.3**	**44.1**	**31.6**	**16.8**	**6.1**	**2.81**	**0.34**
Xf - 1,25 Sf	100.0	100.0	94.0		54.5		28.9		4.3	2.68	
mini	100.0	100.0	93.0		51.9		27.6		4.0	2.57	
Ecart type Sf	0.00	0.00	0.76	2.26	2.19	2.35	2.15	1.86	1.45	0.100	0.080
nb. valeurs	47	47	47	47	47	47	47	47	47	47	47

Fuseau de régularité **de fabrication** **Moyenne de fabrication**

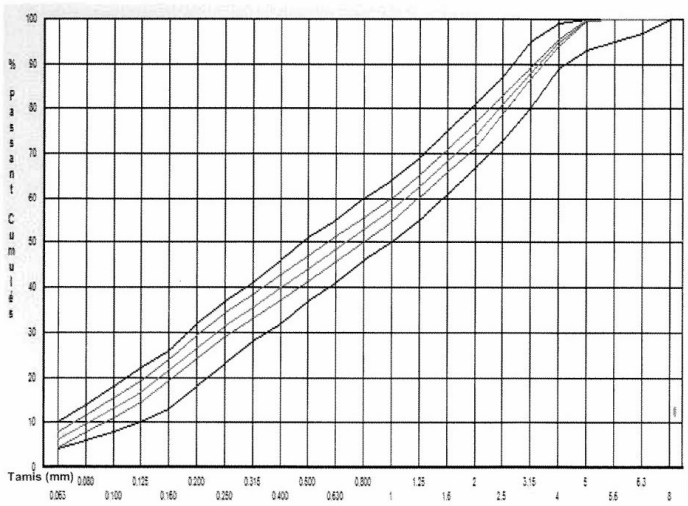

Autres Caractéristiques

	Valeur	Dernier Essai
WA24	0.53%	19/01/15
S total	0,08 %	02/02/15
Cl-	0,0007%	24/01/14
Na2O équi.	23.3mg/kg	19/01/15
MVR	2,66 t/m3	19/01/15
A R	NR	02/02/15
PO	Négatif	02/02/15
ImP	Néant	11/05/15
SO3	<0.04%	02/02/15

Date et visa du responsable contrôle qualité
28/05/15

Fiche n° : 1464

Nos produits étant sujets à évolution, merci de nous contacter pour tout engagement ou durée de validité

Annex 2 – Numerical values (Sections II – III – IV)

Experimental measurements (Sections II.3.4 – III.5.1)

Table 0-1 Statistical values of the environmental parameters for the 90 days periods of mass monitoring for each mix.

Mix name	F1_CEMI_ 0.49_55	F2_CEMIII/B_ 0.49_35	F3_CEMI_ 0.52_V15%_52	F4_CEMI_ 0.49_M15%_53	F5_CEMV/A_ 0.49_51	F6_CEMVI/A_ 0.5_48*
μ_{RH} (%)	**33.1**	**33.1**	**37.4**	**33.1**	**40.6**	**37.7**
CoV_{RH} (%)	14.1	14.1	21.5	14.1	16	18.4
min_{RH} (%)	23.5	23.5	24.3	23.5	27.1	22.5
max_{RH} (%)	47.9	47.9	60.6	47.9	60.5	67.4
μ_T (°C)	**23.6**	**23.6**	**20.4**	**23.6**	**23.7**	**25.1**
CoV_T (°C)	9.3	9.3	2.5	9.3	3.68	9.9
min_T (°C)	19.9	19.9	18.3	19.9	21.8	19.7
max_T (°C)	30.1	30.1	26	30.1	30.2	32.6

*This formulation was recomposed using two different cements.

Experimental results database (Section IV.3.3)

Table 0-2 Statistical values computed over the composition of the 1673 concrete mixes.

Constituent	Unit	Min	Max	25%	50%	75%	mean	CoV (%)	Number
$Qclinker$	Kg/m^3	52	856	212	280	357	289	37	1673
QL	Kg/m^3	0	208	0	0	0	6	429	145
QS	Kg/m^3	0	359	0	0	115	55	148	1169
QV	Kg/m^3	0	599	0	0	109	58	159	1353
QM	Kg/m^3	0	172	0	0	0	1	746	67
QD	Kg/m^3	0	554	0	0	0	6	909	23
QSF	Kg/m^3	0	172	0	0	0	1	662	63
QQz	Kg/m^3	0	276	0	0	0	0	2508	3
QPz	Kg/m^3	0	225	0	0	0	1	1002	25
QGP	Kg/m^3	0	135	0	0	0	0	2891	2
$Qclay$	Kg/m^3	0	450	0	0	0	6	797	28
$Qfine$	Kg/m^3	0	11	0	0	0	0	967	23
$QSable$	Kg/m^3	0	1800	710	783	856	783	24	1671
WA_{sa}	%	0.1	8	0.53	0.85	1.28	1.38	116	257
Mv_{sa}	Kg/m^3	0.9	2.71	2.58	2.6	2.65	2.54	12	291
$Qgravel$	Kg/m^3	0	1334	882	967	1047	916	29	1671
WA_{gra}	%	0.21	16.3	0.73	1.11	2.02	1.89	112	289
Mv_{gra}	Kg/m^3	0.97	2.77	2.57	2.59	2.66	2.53	13	307
$Weff$	Kg/m^3	150	300	162	182	193	183	16	1671
Adj	Kg/m^3	0	13	0	2	8	4	129	1330

Input data used for carbonation depth computation (Section IV.4)

Table 0-3 Composition and properties of the concrete exposed to XC1 environment [73], [426].

Name	Q_K (kg/m³)	Q_L (kg/m³)	Q_S (kg/m³)	Q_V (kg/m³)	W_{eff}/B_{tot} (-)	Q_{Agg} (kg/m³)	RH_{env} (%)	T_{env} (°C)	$f_{c,28}$ (MPa)	Age (t_{tot}, year)
XC1_1	260	0	0	0	0.63	1949	50	20.00	48	1.0
XC1_2	207	0	0	89	0.55	1908	50	20.00	40	1.0
XC1_3	207	0	0	89	0.55	1818	50	20.00	35	1.0
XC1_4	260	0	0	0	0.63	1858	50	20.00	38	1.0
XC1_5	260	0	0	0	0.63	1717	50	20.00	38	1.0
XC1_6	280	0	0	0	0.58	1937	50	20.00	52	1.0
XC1_7	223	0	0	95	0.51	1893	50	20.00	53	1.0
XC1_8	223	0	0	95	0.51	1948	50	20.00	38	1.0
XC1_9	260	0	0	0	0.63	1949	50	20.00	36	1.1
XC1_10	207	0	0	89	0.55	1908	50	20.00	31	1.1
XC1_11	207	0	0	89	0.55	1818	50	20.00	25	1.1
XC1_12	260	0	0	0	0.63	1858	50	20.00	31	1.1
XC1_13	260	0	0	0	0.63	1717	50	20.00	29	1.1
XC1_14	280	0	0	0	0.58	1937	50	20.00	39	1.1
XC1_15	223	0	0	95	0.51	1893	50	20.00	39	1.1
XC1_16	223	0	0	95	0.51	1948	50	20.00	33	1.1
XC1_17	300	0	0	0	0.57	1870	40	20.00	42	2.0
XC1_18	271	0	0	48	0.51	1868	40	20.00	45	2.0
XC1_19	242	0	0	104	0.45	1856	40	20.00	46	2.0
XC1_20	196	0	0	196	0.37	1831	40	20.00	42	2.0
XC1_21	300	0	0	0	0.57	1870	40	20.00	42	2.0
XC1_22	271	0	0	48	0.51	1868	40	20.00	45	2.0
XC1_23	242	0	0	104	0.45	1856	40	20.00	46	2.0
XC1_24	196	0	0	196	0.37	1831	40	20.00	42	2.0
XC1_25	300	0	0	0	0.57	1870	40	20.00	42	2.0
XC1_26	271	0	0	48	0.51	1868	40	20.00	45	2.0
XC1_27	242	0	0	104	0.45	1856	40	20.00	46	2.0
XC1_28	196	0	0	196	0.37	1831	40	20.00	42	2.0

Table 0-4 Composition and properties of the concrete exposed to XC2 environment [73], [370].

Name	Q_K (kg/m³)	Q_L (kg/m³)	Q_S (kg/m³)	Q_V (kg/m³)	W_{eff}/B_{tot} (-)	Q_{Agg} (kg/m³)	RH_{env} (%)	T_{env} (°C)	$f_{c,28}$ (MPa)	Age (t_{tot}, year)
XC2_1	105	0	244	0	0.50	1825	95	20.00	-	0.1
XC2_2	52	0	295	0	0.50	1821	95	20.00	-	0.1
XC2_3	105	0	244	0	0.50	1825	95	20.00	-	0.2
XC2_4	52	0	295	0	0.50	1821	95	20.00	-	0.2
XC2_5	105	0	244	0	0.50	1825	95	20.00	-	0.3
XC2_6	52	0	295	0	0.50	1821	95	20.00	-	0.3
XC2_7	300	0	0	0	0.57	1870	80	20.00	42	2.0
XC2_8	271	0	0	48	0.51	1868	80	20.00	45	2.0
XC2_9	242	0	0	104	0.45	1856	80	20.00	46	2.0
XC2_10	196	0	0	196	0.37	1831	80	20.00	42	2.0
XC2_11	300	0	0	0	0.57	1870	80	20.00	42	2.0
XC2_12	271	0	0	48	0.51	1868	80	20.00	45	2.0
XC2_13	242	0	0	104	0.45	1856	80	20.00	46	2.0
XC2_14	196	0	0	196	0.37	1831	80	20.00	42	2.0
XC2_15	300	0	0	0	0.57	1870	80	20.00	42	2.0
XC2_16	271	0	0	48	0.51	1868	80	20.00	45	2.0
XC2_17	242	0	0	104	0.45	1856	80	20.00	46	2.0

Name	Q_K (kg/m3)	Q_L (kg/m3)	Q_S (kg/m3)	Q_V (kg/m3)	W_{eff}/B_{tot} (-)	Q_{Agg} (kg/m3)	RH_{env} (%)	T_{env} (°C)	$f_{c,28}$ (MPa)	Age (t_{tot}, year)
XC2_18	196	0	0	196	0.37	1831	80	20.00	42	2.0
XC2_19	300	0	0	0	0.57	1870	90	20.00	42	2.0
XC2_20	271	0	0	48	0.51	1868	90	20.00	45	2.0
XC2_21	242	0	0	104	0.45	1856	90	20.00	46	2.0
XC2_22	196	0	0	196	0.37	1831	90	20.00	42	2.0
XC2_23	300	0	0	0	0.57	1870	90	20.00	42	2.0
XC2_24	271	0	0	48	0.51	1868	90	20.00	45	2.0
XC2_25	242	0	0	104	0.45	1856	90	20.00	46	2.0
XC2_26	196	0	0	196	0.37	1831	90	20.00	42	2.0
XC2_27	300	0	0	0	0.57	1870	90	20.00	42	2.0
XC2_28	271	0	0	48	0.51	1868	90	20.00	45	2.0
XC2_29	242	0	0	104	0.45	1856	90	20.00	46	2.0
XC2_30	196	0	0	196	0.37	1831	90	20.00	42	2.0
XC2_31	300	0	0	0	0.57	1870	90	20.00	42	2.0
XC2_32	271	0	0	48	0.51	1868	90	20.00	45	2.0
XC2_33	242	0	0	104	0.45	1856	90	20.00	46	2.0
XC2_34	196	0	0	196	0.37	1831	90	20.00	42	2.0
XC2_35	300	0	0	0	0.57	1870	80	5.00	42	2.0
XC2_36	271	0	0	48	0.51	1868	80	5.00	45	2.0
XC2_37	242	0	0	104	0.45	1856	80	5.00	46	2.0
XC2_38	196	0	0	196	0.37	1831	80	5.00	42	2.0

Table 0-5 Composition and properties of the concrete exposed to XC3 environment [73], [427].

Name	Q_K (kg/m³)	Q_L (kg/m³)	Q_S (kg/m³)	Q_V (kg/m³)	W_{eff}/B_{tot} (-)	Q_{Agg} (kg/m³)	RH_{env} (%)	T_{env} (°C)	$f_{c,28}$ (MPa)	Age (t_{tot}, year)
XC3_1	300	0	0	0	0.57	1870	65	20.00	42	2.0
XC3_2	271	0	0	48	0.51	1868	65	20.00	45	2.0
XC3_3	242	0	0	104	0.45	1856	65	20.00	46	2.0
XC3_4	196	0	0	196	0.37	1831	65	20.00	42	2.0
XC3_5	242	0	0	104	0.45	1856	65	20.00	50	2.0
XC3_6	242	0	0	104	0.45	1856	65	20.00	47	2.0
XC3_7	250	0	0	0	0.68	1912	65	20.00	33	2.0
XC3_8	226	0	0	40	0.61	1921	65	20.00	33	2.0
XC3_9	202	0	0	87	0.54	1916	65	20.00	35	2.0
XC3_10	162	0	0	162	0.44	1904	65	20.00	33	2.0
XC3_11	202	0	0	87	0.54	1916	65	20.00	34	2.0
XC3_12	202	0	0	87	0.54	1916	65	20.00	34	2.0
XC3_13	350	0	0	0	0.49	1822	65	20.00	50	2.0
XC3_14	314	0	0	55	0.44	1818	65	20.00	50	2.0
XC3_15	280	0	0	120	0.39	1802	65	20.00	53	2.0
XC3_16	226	0	0	226	0.32	1771	65	20.00	48	2.0
XC3_17	280	0	0	120	0.39	1802	65	20.00	51	2.0
XC3_18	280	0	0	120	0.39	1802	65	20.00	51	2.0
XC3_19	350	0	0	0	0.49	1822	65	20.00	50	2.0
XC3_20	314	0	0	55	0.44	1818	65	20.00	50	2.0
XC3_21	280	0	0	120	0.39	1802	65	20.00	53	2.0
XC3_22	226	0	0	226	0.32	1771	65	20.00	48	2.0
XC3_23	280	0	0	120	0.39	1802	65	20.00	51	2.0
XC3_24	280	0	0	120	0.39	1802	65	20.00	51	2.0
XC3_25	300	0	0	0	0.57	1870	65	20.00	42	2.0
XC3_26	271	0	0	48	0.51	1868	65	20.00	45	2.0

Name	Q_K (kg/m³)	Q_L (kg/m³)	Q_S (kg/m³)	Q_V (kg/m³)	W_{eff}/B_{tot} (-)	Q_{Agg} (kg/m³)	RH_{env} (%)	T_{env} (°C)	$f_{c,28}$ (MPa)	Age (t_{tot}, year)
XC3_27	242	0	0	104	0.45	1856	65	20.00	46	2.0
XC3_28	196	0	0	196	0.37	1831	65	20.00	42	2.0
XC3_29	242	0	0	104	0.45	1856	65	20.00	50	2.0
XC3_30	242	0	0	104	0.45	1856	65	20.00	47	2.0
XC3_31	250	0	0	0	0.68	1912	65	20.00	33	2.0
XC3_32	226	0	0	40	0.61	1921	65	20.00	33	2.0
XC3_33	202	0	0	87	0.54	1916	65	20.00	35	2.0
XC3_34	162	0	0	162	0.44	1904	65	20.00	33	2.0
XC3_35	202	0	0	87	0.54	1916	65	20.00	34	2.0
XC3_36	202	0	0	87	0.54	1916	65	20.00	34	2.0
XC3_37	350	0	0	0	0.49	1822	65	20.00	50	2.0
XC3_38	314	0	0	55	0.44	1818	65	20.00	50	2.0
XC3_39	280	0	0	120	0.39	1802	65	20.00	53	2.0
XC3_40	226	0	0	226	0.32	1771	65	20.00	48	2.0
XC3_41	280	0	0	120	0.39	1802	65	20.00	51	2.0
XC3_42	280	0	0	120	0.39	1802	65	20.00	51	2.0
XC3_43	300	0	0	0	0.57	1870	65	20.00	42	2.0
XC3_44	271	0	0	48	0.51	1868	65	20.00	45	2.0
XC3_45	242	0	0	104	0.45	1856	65	20.00	46	2.0
XC3_46	196	0	0	196	0.37	1831	65	20.00	42	2.0
XC3_47	242	0	0	104	0.45	1856	65	20.00	50	2.0
XC3_48	242	0	0	104	0.45	1856	65	20.00	47	2.0
XC3_49	250	0	0	0	0.68	1912	65	20.00	33	2.0
XC3_50	226	0	0	40	0.61	1921	65	20.00	33	2.0
XC3_51	202	0	0	87	0.54	1916	65	20.00	35	2.0
XC3_52	162	0	0	162	0.44	1904	65	20.00	33	2.0
XC3_53	202	0	0	87	0.54	1916	65	20.00	34	2.0
XC3_54	202	0	0	87	0.54	1916	65	20.00	34	2.0
XC3_55	350	0	0	0	0.49	1822	65	20.00	50	2.0
XC3_56	314	0	0	55	0.44	1818	65	20.00	50	2.0
XC3_57	280	0	0	120	0.39	1802	65	20.00	53	2.0
XC3_58	226	0	0	226	0.32	1771	65	20.00	48	2.0
XC3_59	280	0	0	120	0.39	1802	65	20.00	51	2.0
XC3_60	280	0	0	120	0.39	1802	65	20.00	51	2.0
XC3_61	300	0	0	0	0.57	1870	65	5.15	42	2.0
XC3_62	271	0	0	48	0.51	1868	65	5.15	45	2.0
XC3_63	242	0	0	104	0.45	1856	65	5.15	46	2.0
XC3_64	196	0	0	196	0.37	1831	65	5.15	42	2.0
XC3_65	242	0	0	104	0.45	1856	65	5.15	50	2.0
XC3_66	242	0	0	104	0.45	1856	65	5.15	47	2.0
XC3_67	300	0	0	0	0.57	1870	65	5.15	42	2.0
XC3_68	271	0	0	48	0.51	1868	65	5.15	45	2.0
XC3_69	242	0	0	104	0.45	1856	65	5.15	46	2.0
XC3_70	196	0	0	196	0.37	1831	65	5.15	42	2.0
XC3_71	242	0	0	104	0.45	1856	65	5.15	50	2.0
XC3_72	242	0	0	104	0.45	1856	65	5.15	47	2.0
XC3_73	450	0	0	0	0.50	1350	65	20.00	51	1.1
XC3_74	360	90	0	0	0.50	1350	65	20.00	45	1.1
XC3_75	315	0	135	0	0.50	1350	65	20.00	37	1.1
XC3_76	450	0	0	0	0.50	1350	65	20.00	51	1.1
XC3_77	360	90	0	0	0.50	1350	65	20.00	45	1.1
XC3_78	315	0	135	0	0.50	1350	65	20.00	37	1.1
XC3_79	450	0	0	0	0.50	1350	65	20.00	51	1.1

Name	Q_K (kg/m³)	Q_L (kg/m³)	Q_S (kg/m³)	Q_V (kg/m³)	W_{eff}/B_{tot} (-)	Q_{Agg} (kg/m³)	RH_{env} (%)	T_{env} (°C)	$f_{c,28}$ (MPa)	Age (t_{tot}, year)
XC3_80	360	90	0	0	0.50	1350	65	20.00	45	1.1
XC3_81	315	0	135	0	0.50	1350	65	20.00	37	1.1
XC3_82	450	0	0	0	0.50	1350	65	20.00	51	1.0
XC3_83	360	90	0	0	0.50	1350	65	20.00	45	1.0
XC3_84	315	0	135	0	0.50	1350	65	20.00	37	1.0

Table 0-6 Input parameters of the different structures' parts available for the carbonation models' verifications in XC4.

Name	Cement type	Cement content (kg/m³)	W_{eff}/C (-)	RH_{env} (%)	T_{env} (°C)	$ToW_{2.5}$ (-)	$f_{c,28}$ (MPa)	φ_c^w (%)	Age (t_{tot}, year)
S1P1	CEM I	400	0.37	71	13.9	0.23	45	12.2	43
S1P2	CEM I	475	0.34				45	12.6	
S1P3	CEM I	490	0.36				59	14.5	
S2P1	CEM I	475	0.37	67	13.2	0.19	49	13.5	43
S2P2	CEM I	350	0.41				36	15	
S2P3	CEM I	365	0.42				37	13	
S2P4	CEM I	415	0.39				45	14	
S3P1	CEM I	390	0.45	64	14.8	0.16	62	13.1	39
S3P2	CEM I	395	0.4				56	12	
S3P3	CEM I	395	0.4				56	12	
S4P1	CEM I	370	0.48	62	15.1	0.17	45	12.9	42
S4P2	CEM I	360	0.45				48	13.1	
S5P1	CEM I	445	0.49	66	15	0.17	50	14.1	42
S5P2	CEM I	375	0.61				43	15.7	
S5P3	CEM I	490	0.46				36	14.8	
S5P4	CEM I	425	0.49				39	13.3	
S6P1	CEM I	365	0.59	66	14.8	0.18	52	17.2	39
S6P2	CEM I	420	0.51				43	17.1	
S6P3	CEM I	385	0.56				41	16	
S7P1	CEM II/A-S	400	0.57				34	16.7	
S7P2	CEM II/A-S	490	0.46				36	15.9	
S7P3	CEM II/A-S	415	0.61				30	19	
S7P4	CEM II/A-S	375	0.52				45	11.7	
S8P1	CEM I	425	0.52				44	17.7	
S8P2	CEM I	450	0.48				37	16.2	
S8P3	CEM I	460	0.48				45	16.1	
S8P4	CEM I	415	0.56				37	18.1	
S8P5	CEM I	455	0.47				44	16.4	
S8P6	CEM I	420	0.51				44	16.4	
S9P1	CEM I	420	0.49				37	16	38
S9P2	CEM I	375	0.52				39	16.7	
S9P3	CEM I	425	0.51				41	17	
S9P4	CEM I	480	0.51				39	17.3	
S10P1	CEM I	410	0.47	66	15	0.17	40	14.1	42
S10P2	CEM I	365	0.58				41	15.3	
S10P3	CEM II/A-V	385	0.43				44	13.2	
S10P4	CEM I	395	0.5				47	14.8	
S10P5	CEM I	360	0.57				29	18	
S11P1	CEM II/A-S	335	0.54				33	15.1	43
S11P2	CEM II/A-S	350	0.5				37	13	
S11P3	CEM II/A-S	330	0.55				45	15.7	
S11P4	CEM II/A-S	325	0.59				42	15.8	
S11P5	CEM II/A-S	385	0.57				49	17.1	
S11P6	CEM II/A-S	390	0.48				48	16	

Data associated to probabilistic computations (Section IV.4.2)

Carbonation-induced depassivation

Table 0-7 Distribution chosen for the different parameters used in the carbonation models.

Parameter	Symbol	Distribution	Ref	Model
Clinker content (kg/m³)	$Q_{clinker}$	Beta (μ, σ, 200, 450)	-	JA
Slag content (kg/m³)	Q_S	Lognormal or Constant	-	JA
Fly ash content (kg/m³)	Q_V	Lognormal or Constant	-	JA
Silica fume content (kg/m³)	Q_{SF}	Lognormal or Constant	-	JA
Aggregate content (kg/m³)	Q_{Agg}	Beta (μ, σ, 1500, 2100)	-	DE
Bulk density of aggregate (kg/m³)	ρ_{Agg}	Beta (μ, σ, 2000, 2700)	-	DE
Effective water content (kg/m³)	W_{eff}	Beta (μ, σ, 150, 250)	-	JA
$\boldsymbol{W_{eff}/B_{tot}}$ (-)	W_{eff}/B_{tot}	Beta (μ, σ, 0.35, 0.65)	-	SC
Ca content able to carbonate in CH (mol/m³)	Ca_{CH}	Beta (μ, σ, 200, 1300)	[6]	SC, HY, DE
Ca content able to carbonate in CSH (mol/m³)	Ca_{CSH}	Beta (μ, σ, 1000, 2200)	[6]	SC, HY, DE
Ca content able to carbonate in Afm (mol/m³)	Ca_{Afm}	Beta (μ, σ, 150, 600)	[6]	SC, HY
Ca content able to carbonate in Aft (mol/m³)	Ca_{Aft}	Beta (μ, σ, 150, 500)	[6]	SC, HY
Reactive CaO content (kg/m³)	CaO_r	Beta (μ, σ, 40, 250)	-	PA
Paste volume	V_{paste}	Beta (μ, σ, 0.2, 0.4)	-	HY
Air diffusion coefficient (10^{-18} m2/s)	D_{air}	Lognormal	-	PA
Entrapped air (%)	ε_{air}	Lognormal	-	DE
Porosity accessible to water (-)	φ	Beta (μ, σ, 0.1, 0.2)	[6]	SC, DE
Compressive strength 28 days (MPa)	Fc_{28days}	Lognormal		HY
Natural carbonation rate	$Knat$	Lognormal	[199]	PE, FI
Curing parameter for SDReaM-crete (-)	$Cure$	Constant	-	SC
Curing parameter for PerfDuB (-)	k_c	Constant	-	PE
Duration of the curing (days)	t_{cure}	Constant	[191]	FI
Mean relative humidity (-)	RH_{mean}	Beta (μ, σ, 0.55, 0.8)	[191]	SC, DE, PE, FI, PA
Variation of relative humidity (-)	ΔRH	Beta (μ, σ, 0.1, 0.3)	[191]	SC
Mean temperature (K)	T_{mean}	Normal	[20], [191]	SC, HY
Partial pressure of CO_2 (Pa)	P_{CO_2}	Lognormal	-	SC, HY, DE, FI
Number of days with rain ratio (>10mm, -)	ToW_{10}	Lognormal	-	PE
Number of days with rain ratio (>2.5mm, -)	$ToW_{2.5}$	Lognormal	-	FI
Probability of driving rain (-)	Pdr	Lognormal	-	FI
Concrete cover (mm)	CC	Normal	[20], [199]	All
Exposure time (s)	t_{tot}	Constant	-	All

Chloride-induced depassivation

Table 0-8 Distribution selected for the different parameters of the model used to compute the chloride concentration.

Parameter	Symbol	Distribution	Ref	Model
Porosity accessible to water (-)	φ	Beta (μ, σ, 0.1, 0.2)	[6]	SC, PE
Chloride migration coefficient (m2/s)	D_{rcm}	Normal	[20]	All
Initial free chloride concentration (wt.% binder)	Cl_0	Lognormal	[20]	FI, PE
Environmental chloride concentration (g/L)	Cl_{env}	Lognormal	[20]	All
Critical concentration (wt.% binder)	C_{crit}	Beta (0.6, 0.15, 0.2, 2)	[20]	SC
Ageing factor (-)	ae	Beta	[20]	All
Exposure time (years)	t_{tot}	Constant	-	All
Binder content (kg/m³)	$Binder$	Beta (μ, σ, 200, 600)	-	PE
Convective zone depth (mm)	Δx	Beta (10, 5, 0, 50) or constant	[20]	FI
Mean temperature (K)	T_{env}	Normal	[20]	SC
Curing parameter for SDReaM-crete (-)	$Cure$	Beta (μ, σ, 0.5, 1)	-	SC
Partial pressure of CO_2	P_{CO_2}	Lognormal	-	SC
Ca content able to carbonate in CH (mol/m³)	Ca_{CH}	Beta (μ, σ, 200, 1300)	[6]	SC

Parameter	Symbol	Distribution	Ref	Model
Ca content able to carbonate in CSH (mol/m³)	Ca_{CSH}	Beta (μ, σ, 1000, 2200)	[6]	SC
Ca content able to carbonate in Afm (mol/m³)	Ca_{Afm}	Beta (μ, σ, 150, 600)	[6]	SC
Ca content able to carbonate in Aft (mol/m³)	Ca_{Aft}	Beta (μ, σ, 150, 500)	[6]	SC
$\boldsymbol{W_{eff}/B_{tot}}$ (-)	W_{eff}/B_{tot}	Beta (μ, σ, 0.35, 0.65)	-	SC
Mean relative humidity (%)	RH_{env}	Beta (μ, σ, 0.55, 0.8)	[191]	SC
Mean annual variation of the relative humidity (%)	ΔRH	Beta (μ, σ, 0.1, 0.3)	[191]	SC
Salting period (days)	t_{salt}	Beta (μ, σ, 5, 30)	-	SC

Annex 3 – Sensitivity analyses (Section IV)

Table 0-9 Variation ranges of the different parameters used for the sensitivity analyses.

Parameter	Symbol	Minimal boundary	Maximal boundary	Reference
Binder content (kg/m³)	B	250	675	Database
Binder bulk density (kg/m³)	ρ_B	2600	3200	Technical data sheets
Clinker content (kg/m³)	C	140	600	Database
Cement bulk density (kg/m³)	ρ_C	2800	3300	Technical data sheets
Filler content (kg/m³)	Q_L	0	200	Database
Filler relative content (-)	L	0	0.41	
Slag content (kg/m³)	Q_S	0	400	
Slag relative content (-)	S	0	0.85	
Fly ash content (kg/m³)	Q_V	0	360	
Fly ash relative content (-)	FA	0	0.7	
Metakaolin content (kg/m³)	Q_M	0	170	
Metakaolin relative content (-)	M	0	0.25	
Silica fume content (kg/m³)	Q_{SF}	0	170	
Silica fume content (-)	SF	0	0.3	
Schist content (kg/m³)	Q_D	0	100	
Quartz content (kg/m³)	Q_{Qz}	0	250	
Pozzolan content (kg/m³)	Q_{Pz}	0	225	
Glass powder content (kg/m³)	Q_{GP}	0	135	
Clay content (kg/m³)	Q_{Clay}	0	100	
SCMs content (kg/m³)	Q_{SCM}	0	400	
SCMs bulk density (kg/m³)	ρ_{SCM}	2000	3100	Technical data sheets
Aggregate content (kg/m³)	Q_{Agg}	1200	2000	Database
Water absorption aggregate (%)	WA_{Agg}	0.1	6	
Bulk density aggregate (kg/m³)	ρ_{Agg}	2200	2750	
Effective water content (kg/m³)	W_{eff}	125	300	
$\boldsymbol{W_{eff}/B_{tot}}$ (-)	W_{eff}/B_{tot}	0.28	0.7	
$\boldsymbol{C_3S}$ (-)	C_3S	0.3	0.6	Technical data sheets
Entrapped air (%)	ε_{air}	0.3	9	Database
Porosity accessible to water (-)	φ	0.05	0.25	
Age before chloride testing (days)	t_{rcm}	7	730	
Characteristic strength (MPa)	f_{cem}	30	55	
Relative humidity (-)	RH	0.35	0.95	Meteorological station
SiO_2 weight ratio (-)	SiO_2	0.57	0.67	Technical data sheets
SO_3 weight ratio (-)	SO_3	0.01	0.031	Technical data sheets
CaO weight ratio (-)	CaO	0.154	0.25	Technical data sheets
Al_2O_3 weight ratio (-)	Al_2O_3	0.03	0.08	Technical data sheets
Fe_2O_3 weight ratio (-)	Fe_2O_3	0.005	0.06	Technical data sheets

Literature models for input parameters calculations (Section IV.3.2)

Mechanical resistance computation

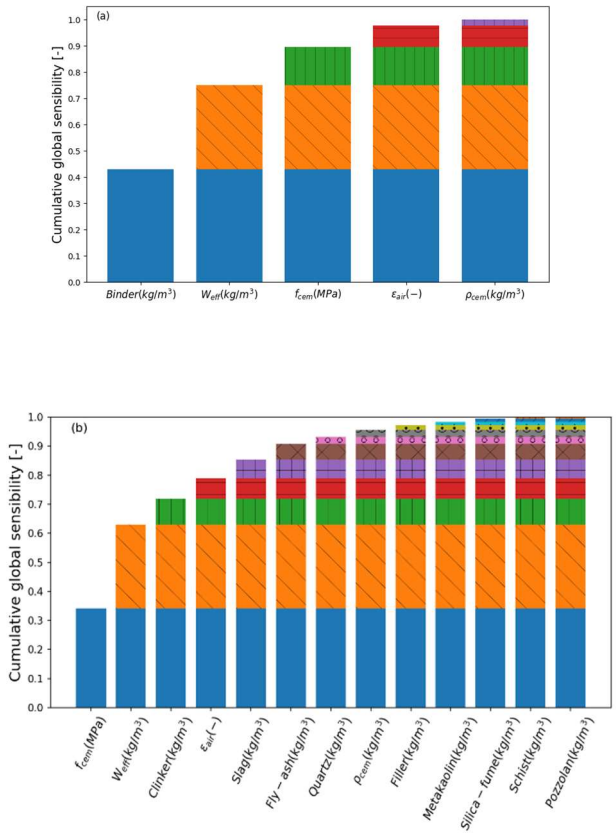

Figure 0-1 Cumulative global sensitivity obtained with the Morris method on Papadakis Equation I.104 (a) and the modified Papadakis Equation IV.1 (b) [278].

Water porosity models

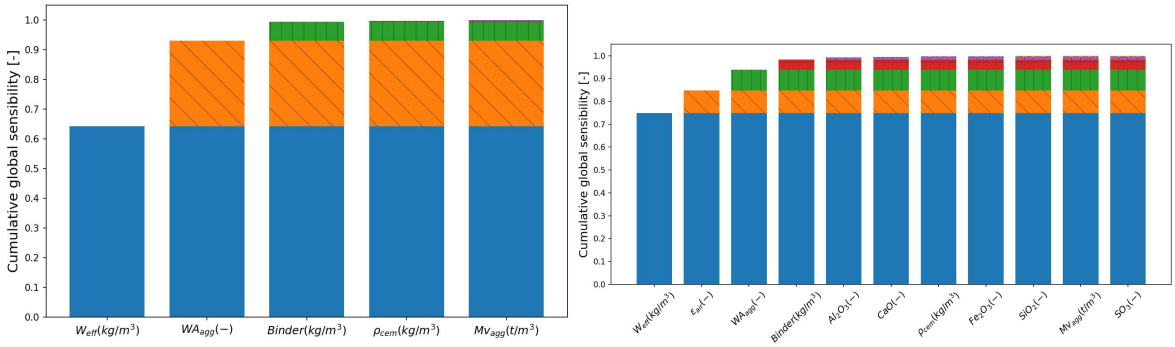

Figure 0-2 Results of Morris sensitivity analyses realised on Power's porosity model [282] and. Papadakis' porosity model [66].

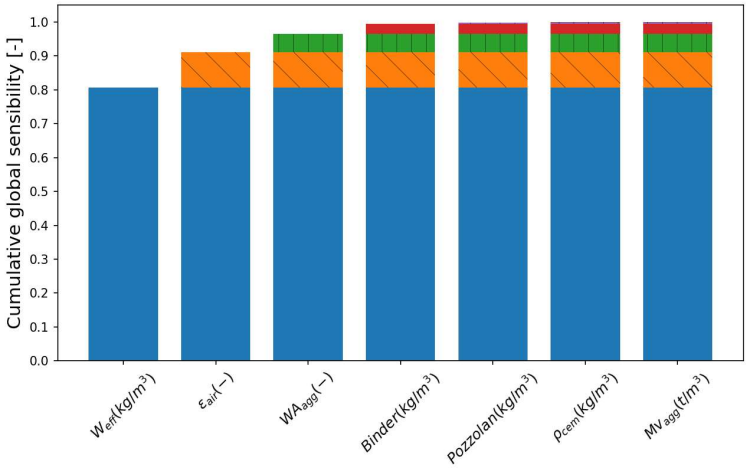

Figure 0-3 Cumulative sensitivities of Papadakis' porosity model [289].

Hydration models

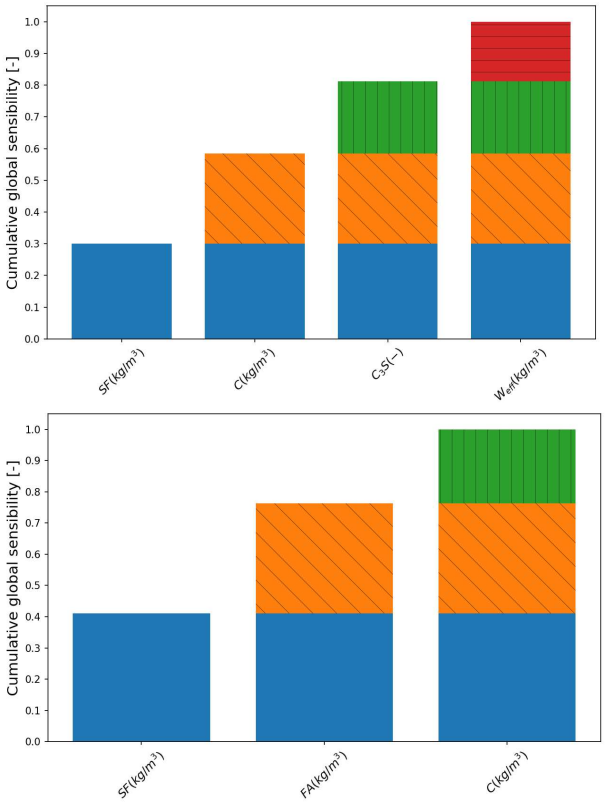

Figure 0-4 Cumulative sensitivities (Morris) obtained for the hydration equation of the AFGC [109] and the hydration model of Papadakis [289].

Learning-based models for properties computation (Section IV.3.3)

Compressive strength f_c

Table 0-10 Statistic repartition of the database used for the training and validation of the models for f_c determination.

Parameters	Mean	Std	Min	25%	50%	75%	Max
f_{cem}	44.22	4.34	32.50	42.50	42.50	42.50	52.50
$Qclinker$	270.86	98.59	83.00	194.70	260.90	346.50	786.00
QS	55.34	82.25	0.00	0.00	0.00	114.00	359.40
QV	51.70	69.26	0.00	0.00	0.00	105.00	280.00
$Qsand$	779.98	136.15	0.00	714.30	783.00	847.00	1382.00
WA_{sa}	1.51	1.23	0.10	1.40	1.40	1.40	8.00
Mv_{sa}	2.58	0.07	2.22	2.59	2.59	2.59	2.66
$Qgravel$	970.92	171.28	0.00	907.00	968.00	1048.00	1334.00
WA_{gra}	1.80	0.79	0.46	1.86	1.86	1.86	5.13
Mv_{sa}	2.58	0.05	2.37	2.58	2.58	2.58	2.77
W_{eff}/B_{tot}	0.48	0.12	0.24	0.40	0.49	0.56	0.95
Age	70.19	174.98	1.00	14.00	28.00	90.00	2534.00
T_{cure}	20.01	0.64	16.00	20.00	20.00	20.00	27.00
RH_{cure}	92.10	11.92	45.00	95.00	95.00	95.00	100.00
W_{eff}	177.03	23.22	112.00	161.85	178.00	192.00	262.80

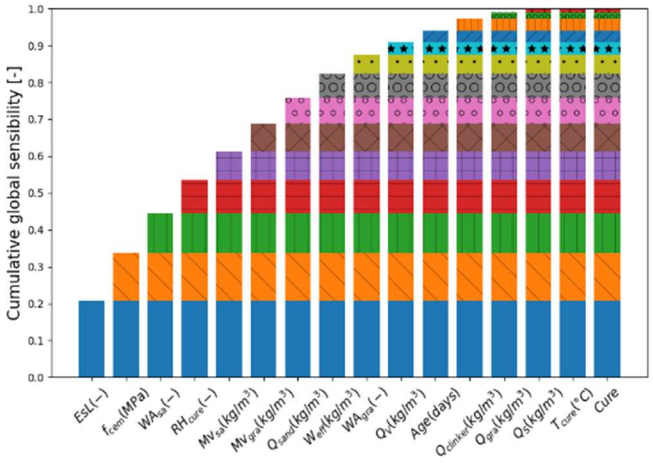

Figure 0-5 Results of the Morris sensitivity analysis performed on the ANN model for the determination of the compressive strength.

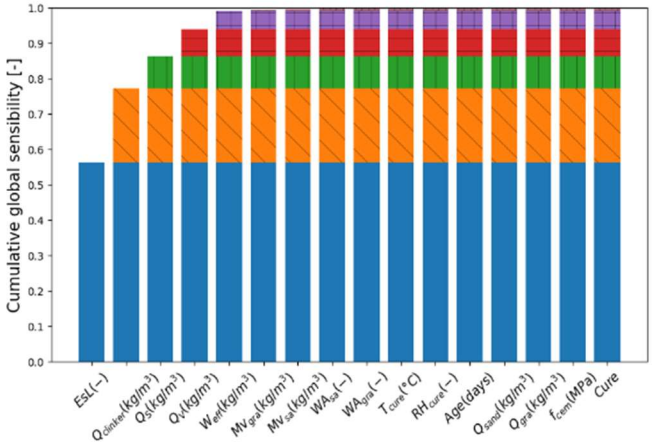

Figure 0-6 Results of the Morris sensitivity analysis performed on the polynomial model for the determination of the compressive strength.

Carbonation depth

Table 0-11 Statistic repartition of the database used for the training and validation of the models for natural carbonation depth determination.

Parameters	Mean	Std	Min	25%	50%	75%	Max
f_{cem}	50.45	4.19	32.50	52.50	52.50	52.50	52.50
$Qclinker$	261.09	64.35	52.00	217.00	263.50	289.00	460.00
QS	27.52	50.15	0.00	0.00	0.00	46.50	295.00
QV	39.45	53.07	0.00	0.00	0.00	62.00	276.00
$Qsand$	890.34	149.69	514.00	844.00	932.00	1002.00	1350.00
WA_{sa}	0.98	0.24	0.53	0.85	0.85	1.20	1.40
Mv_{sa}	2.58	0.01	2.57	2.58	2.58	2.58	2.66
$Qgravel$	934.29	171.53	0.00	850.00	877.00	940.00	1314.00
WA_{gra}	1.15	0.39	0.54	0.98	0.98	0.98	2.10
Mv_{sa}	2.59	0.01	2.56	2.59	2.59	2.59	2.67
W_{eff}/B_{tot}	0.52	0.07	0.32	0.45	0.50	0.55	0.68
Age	39.18	69.80	0.00	3.25	28.00	35.00	540.00
$\sqrt{Time}$	28.09	8.79	5.29	19.10	27.02	32.09	42.72
T_{cure}	20.00	0.00	20.00	20.00	20.00	20.00	20.00
RH_{cure}	95.77	4.62	50.00	95.00	95.00	95.00	100.00
W_{eff}	167.07	17.11	140.00	155.00	162.00	182.00	225.00
T_{carbo}	0.93	0.15	0.54	0.86	0.97	1.00	1.12
RH_{carbo}	70.50	7.88	40.00	66.10	71.10	73.90	95.00
$CO2_{carbo}$	0.04	0.00	0.04	0.04	0.04	0.04	0.05

Table 0-12 Statistic repartition of the database used for the training and validation of the models for natural carbonation depth determination.

Parameters	Mean	Std	Min	25%	50%	75%	Max
f_{cem}	47.90	5.12	32.50	42.50	52.50	52.50	52.50
$Qclinker$	267.31	76.81	52.00	210.00	270.00	314.50	486.00
QL	30.00	42.3	0.00	0.00	0.00	36.00	156.00
QS	23.57	53.02	0.00	0.00	0.00	63.00	295.00
QV	55.12	68.25	0.00	0.00	28.00	104.00	280.00
$Qsand$	821.31	180.75	0.00	677.50	862.00	976.00	1350.00
WA_{sa}	1.32	1.29	0.10	0.85	0.85	1.40	8.00
Mv_{sa}	2.57	0.08	2.22	2.58	2.58	2.59	2.66
$Qgravel$	973.41	198.06	0.00	861.00	910.00	1147.00	1314.00
WA_{gra}	1.44	0.90	0.21	0.98	0.98	1.86	5.00
Mv_{sa}	2.59	0.06	2.39	2.58	2.59	2.59	2.77
W_{eff}/B_{tot}	0.50	0.08	0.28	0.45	0.50	0.55	0.70
Age	48.71	76.04	0.00	14.00	28.00	37.50	540.00
$\sqrt{Time}$	19.01	12.83	1.00	5.48	19.10	27.02	42.72
T_{cure}	20.13	0.92	20.00	20.00	20.00	20.00	27.00
RH_{cure}	94.66	8.57	45.00	95.00	95.00	95.00	100.00
W_{eff}	169.91	19.29	112.00	155.00	170.00	185.00	225.00
T_{carbo}	0.97	0.14	0.54	0.97	1.00	1.00	1.27
RH_{carbo}	68.06	7.84	40.00	65.00	68.90	73.20	95.00
$CO2_{carbo}$	6.80	14.90	0.04	0.04	0.04	5.00	100.00

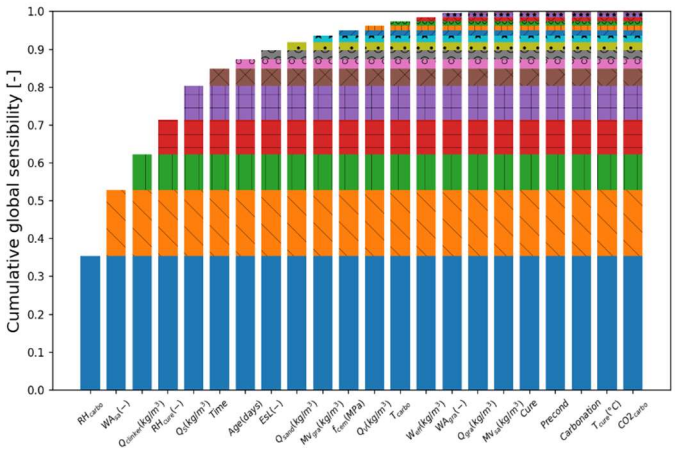

Figure 0-7 Results of the Morris sensitivity analysis on the ANN model for natural carbonation depth computation.

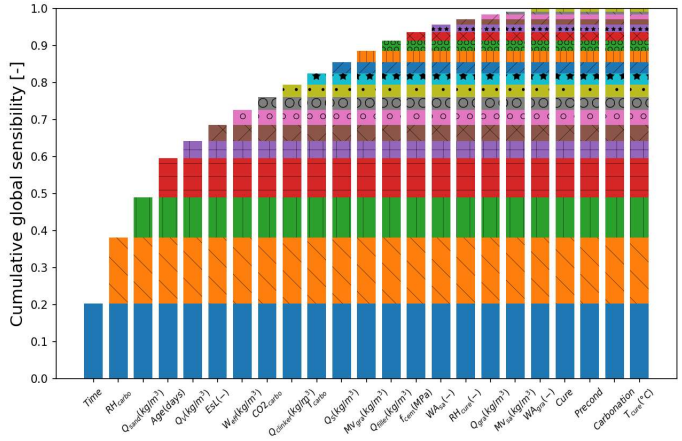

Figure 0-8 Results of the Morris sensitivity analysis on the ANN model for carbonation depth computation (in natural and accelerated conditions).

Electrical resistivity

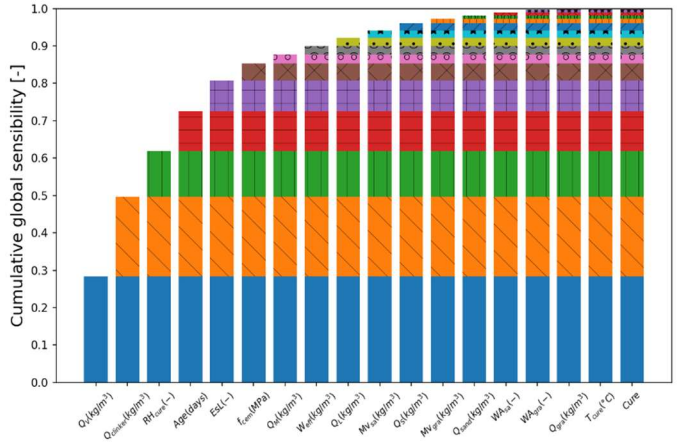

Figure 0-9 Results of the sensitivity analysis of Morris for the ANN model used for the electrical resistivity determination without threshold.

Table 0-13 Statistic repartition of the database used for the training and validation of the models for electrical resistivity determination.

Parameters	Mean	Std	Min	25%	50%	75%	Max
f_{cem}	45.36	5.27	32.50	42.50	42.50	52.50	52.50
$Qclinker$	276.45	91.41	110.20	206.64	304.38	350.00	485.00
QL	17.17	37.74	0.00	0.00	0.00	0.00	190.00
QS	37.43	76.77	0.00	0.00	0.00	0.00	340.00
QV	41.82	70.22	0.00	0.00	0.00	83.60	210.00
QM	3.54	14.76	0.00	0.00	0.00	0.00	76.00
$Qsand$	793.22	236.70	0.00	774.00	831.00	936.00	1186.98
WA_{sa}	2.11	2.35	0.45	0.53	1.28	2.33	8.00
Mv_{sa}	2.56	0.14	2.22	2.57	2.60	2.66	2.71
$Qgravel$	845.53	245.81	0.00	839.25	876.50	965.00	1166.67
WA_{gra}	1.94	1.43	0.46	1.10	1.58	1.86	5.00
Mv_{sa}	2.58	0.10	2.39	2.56	2.58	2.67	2.74
W_{eff}/B_{tot}	0.47	0.07	0.29	0.41	0.50	0.50	0.61
Age	129.46	121.50	2.00	28.00	90.00	180.00	365.00
T_{cure}	20.01	1.20	16.00	20.00	20.00	20.00	22.00
RH_{cure}	90.74	13.62	45.00	95.00	95.00	95.00	100.00
W_{eff}	173.38	21.46	126.00	157.50	175.00	190.00	270.00

Table 0-14 Variation ranges of the different parameters used for the ANN model creation considering only values of Re inferior to 200 Ohm.m.

Parameters	Mean	Std	Min	25%	50%	75%	Max
f_{cem}	46.03	5.63	32.50	42.50	42.50	52.50	52.50
$Qclinker$	305.34	81.52	110.20	270.90	323.00	350.00	485.00
QL	23.44	43.09	0.00	0.00	0.00	42.53	190.00
QS	32.11	70.37	0.00	0.00	0.00	0.00	269.80
QV	15.79	38.48	0.00	0.00	0.00	0.00	210.00
QM	3.85	14.92	0.00	0.00	0.00	0.00	76.00
$Qsand$	788.81	255.14	0.00	786.00	845.00	936.00	1186.98
WA_{sa}	1.82	2.04	0.45	0.53	1.28	1.40	8.00
Mv_{sa}	2.58	0.12	2.22	2.59	2.60	2.66	2.71
$Qgravel$	825.26	266.38	0.00	829.50	864.00	953.28	1148.33
WA_{gra}	1.70	1.20	0.46	0.70	1.58	1.86	5.00
Mv_{sa}	2.58	0.09	2.39	2.56	2.58	2.58	2.74
W_{eff}/B_{tot}	0.47	0.07	0.29	0.45	0.50	0.50	0.61
Age	109.62	113.67	2.00	28.00	90.00	90.00	365.00
T_{cure}	19.92	1.36	16.00	20.00	20.00	20.00	22.00
RH_{cure}	88.69	15.83	45.00	95.00	95.00	95.00	100.00
W_{eff}	177.03	19.01	129.00	167.00	175.00	190.00	270.00

Models for carbonation depths computation (Section IV.4.1)

Table 0-15 Input parameters of the different carbonation models and variation ranges used for the sensitivity analyses.

Parameter	Symbol	Minimal boundary	Maximal boundary	Reference	Model
Clinker (kg/m³)	$Q_{clinker}$	140	600	Database	JA
Slag (kg/m³)	Q_S	0	400		JA
Fly ash (kg/m³)	Q_V	0	360		JA
Silica fume (kg/m³)	Q_{SF}	0	170		JA
Aggregate (kg/m³)	Q_{Agg}	1200	2000		DE
Bulk density of aggregate (kg/m³)	ρ_{Agg}	1800	2700	Datasheet	DE
Effective water (kg/m³)	W_{eff}	125	300	Databased	JA
$\boldsymbol{W_{eff}/B_{tot}}$ (-)	W_{eff}/B_{tot}	0.28	0.7		SC
Ca content able to carbonate in CH (mol/m³)	Ca_{CH}	200	1300	Test of Lacarrière and Kolani model on database	SC, DE
Ca content able to carbonate in CSH (mol/m³)	Ca_{CSH}	1000	2200		SC, DE
Ca content able to carbonate in Afm (mol/m³)	Ca_{Afm}	150	600		SC
Ca content able to carbonate in Aft (mol/m³)	Ca_{Aft}	150	500		SC
Reactive CaO content (kg/m³)	CaO_r	40	250	Database	PA
Entrapped air (%)	ε_{air}	0.3	9		DE
Porosity accessible to water (-)	φ_c^w	0.05	0.25		SC, DE
Natural carbonation rate	K_{nat}	0.4	8.2		PE
Curing parameter for SDReaM-crete (-)	$Cure$	0.5	1	Section III.5.1	SC
Curing parameter for PerfDuB (-)	k_c	1	2.5	[191]	PE
Mean relative humidity (-)	RH_{env}	0.35	0.95	Metrological station	SC, DE, PE, PA
Variation of relative humidity (-)	ΔRH	0	0.2		SC
Mean temperature (K)	T_{env}	285	293		SC
Partial pressure of CO_2 (Pa)	P_{CO_2}	25	60		SC, DE
Number of days with rain ratio (>10mm, -)	ToW_{10}	0	0.1		PE
Exposure time (s)	t_{tot}	1	100	-	All

Models for chloride penetration computation (Section IV.4.1)

Table 0-16 Input parameters of the different models for chloride concentration computation and variation ranges associated.

Parameter	Symbol	Exposure class	Minimal boundary	Maximal boundary	Reference	Model
Porosity accessible to water (-)	φ	All	0.05	0.25	Database of experimental results	SC, PE
Chloride migration coefficient (m2/s)	D_{rcm}	All	10^{-14}	5×10^{-11}		All
Initial free chloride concentration (wt.% binder)	Cl_0	All	0	0.2	[19]	FI, PE
Environmental chloride concentration (g/L)	Cl_{env}	XS1-XS3	10	40		All
		XS2	18	30		
		XD3	10	40		
Critical concentration (wt.% binder)	C_{crit}	XS1-XS3	0.2	1.2	-	SC
		XS2	0.6	2		
		XD3	0.2	1.2		
Ageing factor (-)	ae	All	0.3	0.6	[340]	All
Exposure time (years)	t_{tot}	All	10	100	-	All
Binder content (kg/m³)	$Binder$	All	200	650	Database of results	PE
Convective zone depth (mm)	ΔX	XS1-XS3	0	30	[236], [257], [258], [393]	FI
		XS2	0	5		
		XD3	0	20		
Mean temperature (K)	T_{env}	All	278.15	303.15	Meteorological station	SC
Curing parameter for SDReaM-crete (-)	$Cure$	All	0.5	1	Section III.5.1	SC
Partial pressure of CO_2	P_{CO_2}	XS1-XS3	0	60	-	SC
		XD3	0	60		
Ca content able to carbonate in CH (mol/m³)	Ca_{CH}	All	200	1300	Test of Lacarrière and Kolani model on database	SC
Ca content able to carbonate in CSH (mol/m³)	Ca_{CSH}	All	1000	2200		SC
Ca content able to carbonate in Afm (mol/m³)	Ca_{Afm}	All	150	600		SC
Ca content able to carbonate in Aft (mol/m³)	Ca_{Aft}	All	150	500		SC
$\boldsymbol{W_{eff}/B_{tot}}$ (-)	W_{eff}/B_{tot}	All	0.28	0.7	Database of results	SC
Mean relative humidity (%)	RH_{env}	XS1-XS3	0.35	0.95	Meteorological station	SC
		XD3	0.35	0.95		
Mean annual variation of the relative humidity (%)	ΔRH	XS1-XS3	0	0.4		SC
		XD3	0	0.4		
Salting period (days)	t_{salt}	XD3	5	30	[19], [340]	SC
Concrete cover (mm)	CC	All	5	80	-	All

Annex 4 – Literature and models (Sections I – III – IV)

Analytic models for carbonation-induced corrosion (Section IV.4)

Model of Von-Greve and Gehlen [199]

This empirical time-dependent model is based on the *fib* code model [191]. The equation has been modified by substituting the inverse of effective carbonation resistance, R_{NAC}^{-1} with the term K_{nat}, and replacing the CO_2 concentration in air with the function k_a.

$$x_c(t) = K_{nat}\sqrt{k_e k_c k_a}\sqrt{t}W(t) \qquad \text{Eq (A.1)}$$

$$k_a = \frac{P_{CO_2}}{P_{CO_2,ref}}$$ Eq (A.2)

Where:

- K_{nat} is the natural carbonation rate (mm.year$^{-0.5}$) measured according to the NF EN 12390-10.
- k_a is a function accounting for the effect of CO_2 concentration in the ambient air.
- P_{CO_2} is the carbon dioxide concentration in the environment to which the structure is exposed (%.vol).
- $P_{CO_2,ref}$ is the carbon dioxide concentration of reference fixed at a value of 0.04%.vol.

The interests of these two modifications are a simplification of the equation and a better consideration of the partial pressure impact on the results. However, it does not solve the problem related to the consideration of low relative humidity.

Demis model [27]

In their work, Demis and Al. proposed a concrete service life estimation tool able to estimate:

- The concrete strength,
- The service life with respect to carbonation
- The service life with respect to chloride penetration

Finally, it enables the user to compute the cost and environmental aspects of the construction. The methodology developed presents the interest to give a global vision of the concrete durability as a function of its financial and environmental costs. A method with similar goals is developed in this study, and considers the work previously performed by the authors.

The estimation of the depassivation time related to carbonation exposure is detailed in this section. The integration and solution of the non-linear differential equations proposed by Papadakis et al. are used [214]. They permit the computation of the carbonation depth (x_C, m) at a given time (t, s) as well as the estimation of the critical time ($t_{cr,carb}$, s) required for the carbonation front to reach the reinforcement located at a distance corresponding to the concrete cover size CC expressed in mm (refer to Equations A.4 and A.5 respectively). The correctness of these equations was demonstrated for ordinary Portland cement (OPC) and for cases involving the inclusion of supplementary cementing materials (SCM).

The material variability is accounted for through the parameters Ca_{CH} and Ca_{CSH} which correspond to the calcium hydroxide and calcium-silicate-hydrate content in concrete (kg/m3), respectively. Additionally, the effective diffusivity of CO_2 in carbonated concrete, D_{CO_2}(m^2/s), is calculated using Equation A.3, with consideration to a given relative humidity, RH_{env}, expressed as a percentage.

$$D_{CO_2} = 6.1 \times 10^{-6} \left(\frac{\varphi_c^w - \varepsilon_{air}}{1 - \frac{Q_{agg}}{\rho_{agg}} - \varepsilon_{air}} \right) \left(1 - \frac{RH_{env}}{100} \right)^{2.2}$$ Eq (A.3)

Where φ_c^w is the porosity accessible to water of the carbonated concrete (-), ε_{air} the volume fraction of entrapped or entrained air in concrete (-), Q_{agg} the aggregate content in concrete volume (kg/m^3) and ρ_{agg} the aggregate average density (kg/m^3).

$$x_c = \sqrt{\frac{2D_{CO_2}\left(\frac{P_{CO_2}}{100}\right)t}{0.33Ca_{CH} + 0.214Ca_{CSH}}}$$ Eq (A.4)

$$t_{cr,carb} = \frac{(0.33Ca_{CH} + 0.214Ca_{CSH})CC^2}{2D_{CO_2}\left(\frac{P_{CO_2}}{100}\right)}$$ Eq (A.5)

One drawback of this model is the consideration of low relative humidity. When RH_{env} is higher than 65%, the calculated carbonation depth decreases, which aligns with findings in the literature [110]. However, for lower values of relative humidity, the carbonation depth continues to increase, indicating a failure to account for the dependence between saturation degree and CO_2 dissolution capacity. This limitation restricts the applicability of the model for scenarios with low relative humidity. Additionally, the absence of the temperature in the equations further hinders its accuracy and comprehensiveness. Moreover, the simplification of considering only two hydrates (C-S-H and C-A-S-H) neglects the carbonation potential of Afm and Aft, thereby oversimplifying the chemical complexity of cementitious materials.

However, this model also presents numerous advantages. Firstly, it allows for the calculation of carbonation depth for various CO_2 partial pressure (P_{CO_2} , %.vol) values, enabling the consideration of accelerated carbonation tests. Secondly, despite the need to utilize hydrate quantities (for Ca_{CH} and Ca_{CSH}), the required parameters are straightforward. Lastly, this model has been demonstrated to be highly effective for a diverse range of cement types, which is a valuable feature.

Carbonation model of the Japan Society of Civil Engineers (JSCE) [196]

The Japan Society of Civil Engineers (JSCE) has proposed a validated analytical model in [196]. The model is founded on composition parameters and includes a time-dependent aspect that adheres to a square root relationship, as depicted by Equation A.6.

$$x_c = (-3.57 + 9\left(\frac{W_{eff}}{C + k_{SCM}Q_{SCM}}\right)\sqrt{t} \qquad \text{Eq (A.6)}$$

Where :

- x_c is the carbonation depth (mm).
- W_{eff} is the effective water content (kg/m^3).
- C is the cement content (kg/m^3).
- k_{SCM} is the efficiency of the supplementary cementitious material. It is traduced with a coefficient of 0.6, 0.05 and -0.2 for slag, fly-ash and Silica-fume.
- Q_{SCM} is the content of SCM in the binder (kg/m^3).
- t is the exposure time expressed in years.

The model is validated using different experimental measurements in Section IV.4.1 and is then integrated into the final scientific tool. This highlights the significance of considering multiple material parameters, specifically the binder type, along with the prerequisite knowledge of the k_{SCM} value for the respective materials. However, it is important to note that the model does not account for the influence of environmental factors such as relative humidity and temperature, nor does it consider the effects of preconditioning and curing. Hence, the equation can only offer accurate predictions for carbonation under the specific natural exposure conditions utilised for its calibration.

Carbonation model of Parrott [194]

A model for carbonation estimation was proposed by Parrott in [194]. It considers only 4 parameters and is expressed with Equation A.7:

$$x_c = 64\, D_{air}^{0.4} \frac{t^n}{CaO_r^{0.5}} \qquad \text{Eq (A.7)}$$

Where :

- x_c is the carbonation depth (mm).
- D_{air} is the air permeability coefficient of the concrete cover (expressed in 10^{-16} m^2.years^{-1}).
- n is the time exponent which is function of the relative humidity (RH, %) and computed with Equation A.8.

- CaO_r is the amount of reactive CaO contained in the cementitious matrix (kg/m^3).
- t is the exposure time (years).

$$n = 0.02536 + 0.01785RH - 0.0001623RH^2 \quad \text{Eq (A.8)}$$

The dependence on environmental parameters is considered by taking into account the relative humidity (RH, -). A value close to 0.5 is observed for relative humidity levels ranging from 50% to 70%. Regarding the material properties, both the diffusion of CO_2 and the quantity of reactive material are taken into consideration. This only requires the use of a simple assumption for calculating CaO_r relative to the binder composition. The determination of the parameter D_{air} can be performed through a gas permeability test (refer to Section II.3.3), but further verification is needed. This model is applied in Section IV.4 and integrated into the final tool.

PerfDuB Model [266]

The model used in PerfDuB is based on the model developed in the Modevie project and the work conducted by El Farissi [266] on SCM-based concretes. In order to determine the carbonation depth, the following Equation A.9 is employed:

$$x_c(t) = K_{nat} k_{RH} \sqrt{t_{eff}} \quad \text{Eq (A.9)}$$

The unique material parameter is the natural carbonation rate K_{nat} (mm.year$^{-0.5}$). The environment is considered with 2 functions: k_{RH} which represents the effect of relative humidity on the carbonation rate (see Equation A.10) and t_{eff} which is the effective time of carbonation (years) considering the wetting/drying cycles (see Equation A.11).

$$k_{RH} = 1.1\left(1 - \left(\frac{RH_{env} - 50}{50}\right)^2\right) \quad \text{Eq (A.10)}$$

$$t_{eff} = t - (t_w + t_d) = (1 - (1 + \beta_w)ToW_{10})t \quad \text{Eq (A.11)}$$

With:

- t the total exposure time (year).
- t_w the time of total humidification due to the rain (year).
- t_d the time required for the "drying depth" reaches the one of the carbonation (year).
- β_w is a constant relative to the rain equal to 1.5.
- ToW_{10} is the ratio of rainy days in a year where the rain height is superior to 10 mm (instead of 2.5 mm in the *fib* code model). A recommended value of 0.05 is given for XC4 while a value of 0 is prescribed for the other exposures classes.
- RH_{env} is the relative humidity expressed in %.

In the framework of the PerfDuB project, a comprehensive database was established to compile results pertaining to various types of concretes. Both natural and accelerated carbonation rates were quantified. The measurements were conducted in accordance with the standards XP P18-458 (2022) for the accelerated test, while natural carbonation was performed under controlled conditions (RH = 50%, T = 20°C). The results indicated a linear relationship between the accelerated and natural carbonation rate with a coefficient of 3.03. Consequently, the rate of accelerated carbonation obtained using the particular methodology (refer to Section II.3.5) can be employed to approximate the natural carbonation rate (K_{nat}). Additionally, El Farissi [266], reported coefficients of 3.66 (R2 = 0.72) for dry curing (DC) and 2.91 (R2 = 0.69) for moist curing (MC) in his research.

In further works, the impact of the curing process should be considered through a parameter k_c. In the work of El Farissi [266], it was fitted on experimental measurements such as :

$$k_c = c\frac{\left(1 - 0.17\left(\frac{f_{c,t}}{f_{c,28}}\right)\right)^{1.4}}{\left(\frac{f_{c,t}}{f_{c,28}}\right)^{0.5}}$$ Eq (A.12)

Where c is a constant equal to 0.65 for dry curing and 1.47 for moist curing.

Analytic models for chloride-induced corrosion (Section IV.4)

fib code model [20]

The model proposed by the "Fédération Internationale du Béton" (*fib – International Concrete Association)*) is derived from the second Fick's law (Equation I.69), but with additional modifications incorporated (as seen in Equation A.13):

$$Cl_t\,(x,t) = Cl_0 + \left(Cl_{S,\Delta x} - Cl_0\right)\operatorname{erf}\left(1 - \frac{x - \Delta x}{\sqrt{4D_{app}.t}}\right)$$ Eq (A.13)

The apparent chloride diffusion coefficient D_{app} in $m^2.s^{-1}$ (as expressed in Equation A.14), is modified to incorporate the concept of convective transport in addition to diffusive transport. The parameter Δx represents the depth, in mm, up to which ionic transport is not only diffusive but also convective. $Cl_{S,\Delta x}$ denotes the chloride concentration in kg/m^3 of concrete at a depth equal to the convection zone Δx.

These modifications to the second Fick law enable the consideration of convection resulting from variations in the hydrologic conditions at the surface of the concrete. For depths greater than Δx, the concrete is presumed to be fully saturated, with constant hydrologic conditions. Consequently, ionic species only migrate through diffusion. The apparent diffusion coefficient is mathematically expressed as:

$$D_{app} = k_e D_{RCM,t0}\left(\frac{t_0}{t}\right)^{ae}$$ Eq (A.14)

The environmental parameter, denoted as k_e accounts for the temperature effect on chloride ingress. Additionally, the material ageing factor, represented by ae, reflects the evolution of the concrete's microstructure during its service life. The diffusion coefficient, $D_{RCM,t0}$, measured through accelerated tests at time t_0 (days), is used to quantify chloride ingress (in m^2/s).

The ageing factor, ae, ranges between 0 and 1 and plays a crucial role in the model, particularly when the concrete incorporates binary or ternary binders with lower hydration kinetics than CEM I cement. The *fib* Model Code serves as a pre-standard document for concrete structure design, offering ease of use, especially for standard CEM I based concrete, while also incorporating material variability through the chloride diffusion coefficient and the ageing factor.

However, the increasing use of new additions in concrete, coupled with limited knowledge regarding their effects on concrete properties, leads to increased uncertainty in the model. The *fib* Code Model was primarily developed based on results obtained with CEM I concrete. Therefore, it is necessary to accurately measure the impact of additions on model parameters, such as $Cl_{S,\Delta x}$ or ae , in order to adjust and improve them.

Recently, the PerfDuB project [2], [428] concluded, aiming to develop an advanced analytical model for durability, specifically considering concretes containing diverse additions. This improved model is directly inspired by the *fib* Code Model [191].

PerfDuB and ANR Modevie model [2], [229]

The model developed in the Modevie and PerfDuB projects is used to calculate the time it takes for rebar corrosion to initiate when chloride ions penetrate the material. This model is based on the *fib* model and aims to improve the consideration of new binder types.

In this model, the modified solution of the second Fick's law (Equation A.13) is employed. It takes into account an average diffusion coefficient $D_m(t)$ (equation A.18) and a depth Δx, which represents the maximum chloride content assumed to remain constant after a long exposure time. The depth Δx is determined using an empirical expression (equation A.15) [232], [357], [393], [437], [438].

$$\Delta x = 0.45\left(\frac{\varphi_c^w}{11.5}\right)^5 \Delta x_0 \qquad \text{Eq (A.15)}$$

Where φ_c^w is the water-accessible porosity (%) and Δx_0 the reference depth equal to 10mm.
The maximal chloride ions concentration $Cl_{S,\Delta x}$ (at depth Δx) is stated as:

$$Cl_{S,\Delta x} = E\ Cl_{f,sat} \qquad \text{Eq (A.16)}$$

Where E is an enrichment coefficient, $Cl_{f,sat}$ the free chlorides concentration in saturated condition determined with the equation A.17.

$$Cl_{f,sat} = \varphi_c^w \frac{Cl_{f,env}}{Q_{binder}} \qquad \text{Eq (A.17)}$$

With Q_{binder} the binder content in kg/m^3 of concrete and $Cl_{f,env}$ the environmental free chloride content in wt.% relative to the binder mass.

The chloride content in a specific depth (Δx) is understood to have a higher value compared to the environmental content as a result of the capillary action occurring during wetting-drying cycles [232]. Beyond this depth, the chloride profile is governed by the Fick diffusion in this model, assuming a fully saturated material.

Ultimately, the average diffusion coefficient $D_m(t)$ can be calculated using Equation A.18, taking into account the chloride ions migration value measured at t_0 through an accelerated migration test.

$$D_m(t) = k_e\left(\frac{t_0}{t_{th}}\right)^{ae}\left[\frac{(1-ae)t + \alpha t_{th}}{(1-ae)t}\right] D_{RCM,t_0} \qquad \text{Eq (A.18)}$$

Where D_{rcm,t_0} is the migration coefficient measured at the age t_0, t_{th} is the threshold time equal to 10 years (beyond which the diffusion coefficient is supposed constant), ae is the ageing coefficient, k_e is the same parameter than in the *fib* code model and translates the effect of temperature.

Analytic model for carbonation-induced corrosion propagation (Section IV.4)

PerfDuB model for carbonation induced corrosion propagation [2]

The propagation stage of carbonation-induced corrosion is analysed in the PerfDuB model. In the initial step, the current density of corrosion, denoted by i_{corr} (µA.cm^{-2}), is calculated using the Equation A.19.

$$i_{corr} = V_0 \frac{k_{RH} k_T}{Re_{sat}} \qquad \text{Eq (A.19)}$$

Where:

- V_0 is a constant equal to 168.9 µA.Ω.m.cm^{-2}.
- Re_{sat} represents the electrical resistivity of the concrete in saturated conditions (Ω.m). It is specified in the report of the project that the electrical resistivity needs to be multiplied by 10 in XC1 environment to account for the dry environment.
- k_T is a function accounting for the influence of the temperature defined with the Equation A.20. The temperature T is expressed in K.
- k_{RH} is a function accounting for the influence of the relative humidity defined with the Equation A.21. The relative humidity RH is expressed in %.

$$k_T = e^{-4220\left(\frac{1}{T}-\frac{1}{293.15}\right)}$$ Eq (A.20)

$$k_{RH} = \frac{1}{\left(\frac{RH-95}{6}\right)^2 + 1}$$ Eq (A.21)

The corrosion rate V_{corr} (µm.year^{-1}) is then computed using the Faraday law expressed in Equation A.22:

$$V_{corr} = \frac{\Delta s}{\Delta t} = \frac{M_{Fe}}{\rho_s F z_{Fe}} i_{corr} = 11.61 i_{corr}$$ Eq (A.22)

Finally, the critical steel section loss X_{crit} (mm) leading to the cover cracking is computed with the Equation A.23 [429]:

$$X_{crit} = 11\left(\frac{CC}{D_{rebar}}\right)\left(\frac{CC}{L_a}+1\right)^2$$ Eq (A.23)

Where:

- CC refers to the concrete cover (mm)
- D_{rebar} represents the diameter of the reinforcing bar (mm)
- L_a denotes the anodic length (mm)

This model assumes a constant corrosion current; however, in real conditions, corrosion propagation is time dependent. Therefore, this model only calculates the average corrosion current and does not adequately account for the phenomenon. Nevertheless, this model incorporates various factors that influence corrosion in reinforced concrete, such as material properties controlled by electrical resistivity, environmental conditions represented by relative humidity and temperature, and the geometry represented by the concrete cover and reinforcing bar diameter. The anodic length L_a was revealed a prominent parameter, imposed during experimental tests accompanying the fitting of the model. However, in real reinforcing cage layout already depassivated, this parameter is almost impossible to estimate.

Morinaga [193]

A model for the computation of the propagation time leading to cracking $t_{prop,cr}$ (year) is proposed by Morinaga in [193] and corresponds to the Equation A.24:

$$t_{prop,cr} = 0.602 \frac{D_{rebar}\left(1+2\left(\frac{CC}{D_{rebar}}\right)\right)^{0.85}}{i_{corr}}$$ Eq (A.24)

Where:

- CC is the concrete cover (mm)
- D_{rebar} the reinforcing bar diameter (mm)
- i_{corr} the corrosion current (expressed here in 10^{-4} g/cm^2/years)

The models presented for the acquisition of the corrosion current generally yield a value expressed in µA/cm^2. The conversion between these two units is achieved by utilizing the bulk density of steel ($\rho_s = 7.85$g/cm^3) and the relation defined in Equation A.25, based on Faraday's law.

$$\frac{1mA}{m^2} = 1.16\frac{\mu m}{year} \quad or \quad 1\mu A = \frac{1mm^3}{year}$$ Eq (A.25)

Morinaga's model is founded upon a mechanical assumption, which incorporates the consideration of acceptable internal stresses dependent on both the diameter of the reinforcing bar and the concrete cover. It is essential to acknowledge that the model does not encompass the mechanical properties of concrete, thus presenting a limitation.

Maaddawy [430]

In [430], Maaddawy et al. present a model for predicting the propagation time leading to concrete cover cracking. The model is derived from several carefully considered assumptions and is summarized by the following equation:

$$t_{prop,cr} = \left(\frac{7117.5D'(1+v+\Psi)}{i_{corr}E_{ef}}\right)\left(\frac{2CCf_t}{D_{rebar}} + \frac{2\delta_0 E_{eff}}{(1+v+\Psi)D'}\right)$$ Eq (A.26)

Where :

- D_{rebar} is the diameter of the reinforcing bar (mm)
- v is the Poisson' ratio of concrete (0.18)
- δ_0 is the thickness of the porous zone (in the range of 10-20 µm)
- i_{corr} is the current density (µA/cm^2)
- $\Psi = \frac{D'^2}{2C(CC+D')}$
- $D' = D_{rebar} + 2\delta_0$
- $f_t = 0.94\sqrt{f_c}$ MPa [439] is the modulus of rupture
- $E_{eff} = \frac{E_c}{1+\psi_{cr}}$ is the effective elastic modulus of concrete [430]
- ψ_{cr} is the creep coefficient (2.35) [440]
- $E_c = 4500\sqrt{f_c}$ MPa [440] is the elastic modulus
- CC is the concrete cover thickness (mm)

Analytic model for chloride-induced corrosion propagation (Section IV.4)

Balafas and Burgoyne [270]

The model proposed by Balafas and Burgoyne in [270] is built upon the earlier research conducted by Liu and Weyers [273]. The latter involved a comparison of the model's outcomes with accelerated tests performed on concrete slabs subjected to varying chloride concentrations.

$$i_{corr} = 0.92\exp\left(8.37 + 0.618\,ln(1.69Cl_f) - \frac{3034}{T} - 0.000105R_{Ohm} + 2.35t^{-0.215}\right)$$ Eq (A.27)

Where:

- i_{corr} is the current density (µA/cm^2).
- Cl_f is the chloride concentration at the interface concrete steel (kg/m^3).
- T is the temperature (K).
- R_{Ohm} is the resistivity of the concrete (Ohm) approximated with Equation A.28.
- t is the time of active corrosion (years).

$$R_{Ohm} = 90.537RH^{-7.2548}\left[1 + \exp\left(5 - 50(1-RH)\right)\right]$$ Eq (A.28)

With RH the relative humidity (-).

It should be noted that this model does not explicitly consider the concrete cover of the material. However, it could be incorporated by calculating the resistivity, R_{Ohm}, using the lineic electrical resistivity (R_e, Ohm.m) and the value of concrete cover (CC, m) utilizing the following equation:

$$R = \frac{Re}{CC} \quad \text{Eq (A.29)}$$

The model presented in this study was developed based on a specific set of measurements conducted under accelerated conditions. Therefore, in order to ensure its reliability and applicability for maintenance predictions, it is necessary to validate this model using data obtained from real conditions or actual structures.

Yalcyn and Ergun [271]

The model developed by Yalcin and Ergun [271] enables the calculation of the corrosion current of reinforced concrete exposed to chlorides. To empirically validate the model, the authors conducted a verification study using i_{corr} results obtained through a linear polarisation resistance method. The concrete specimens used in the verification study were composed of 90% clinker and 10% pozzolan.

The corrosion current is computed using Equation A.30:

$$i_{corr} = i_0 . \exp(-C . t) \quad \text{Eq (A.30)}$$

Where:

- i_0 is the initial current density (µA/cm^2),
- C is a corrosion constant defined equal to 1.1.10^{-3} j^{-1},
- t is the time of corrosion propagation (in days).

This model is a simplified representation based on accelerated tests where chlorides were directly introduced into the concrete mixing water during manufacturing. Environmental and material parameters were not explicitly included as input variables. However, assuming constant conditions and the absence of any changes in material composition throughout corrosion progression, these parameters can be implicitly considered through the unique parameter i_0. It should be noted that this type of model is not easily applicable for maintenance prediction on real structures due to the frequently unknown value of this parameter.

PerfDuB model for chloride induced corrosion propagation [2]

In the case of chloride induced corrosion, the propagation phase is modelled according to a different set of equations compared to carbonation induced corrosion. First, the corrosion current i_{corr} (A/m^2) is computed using the Equation A.31:

$$i_{corr} = Y_{Cl} \frac{k_{Cl} k_{C/A} k_{O_2}}{Re} \quad \text{Eq (A.31)}$$

Where:

- k_{Cl} is a function representing the contamination to free chloride (see Equation A.32)
- $k_{C/A}$ is a parameter linked to the C/A ratio and is considered constant with a value of 4 (justified by the experimentations of Chahloub [272]).
- k_{O_2} accounts for the oxygen availability and is equal to 1 except for the XS2 where it needs to be determined as a function of the immerged steel part and the cathodic length.
- Re is the electrical resistivity (Ω.m) computed with the Equation A.33.

$$k_{Cl} = \frac{\left(\left|Cl_f - C_{crit}\right| + Cl_f - C_{crit}\right)^{0.89}}{0.08} \quad \text{Eq (A.32)}$$

$$Re = Re_{sat}\left(\left(\frac{100}{RH}\right)^4\right)^d \quad \text{Eq (A.33)}$$

With Cl_f the final concentration in free chloride (wt.% of binder), C_{crit} the critical concentration in free chloride considered constant and equal to 0.6 wt.% of the binder, Re_{sat} the electrical resistivity measured in fully saturated concrete and a temperature of 20°C (Ω.m) and d a factor linked to the drying period.

The steel section loss S_a (mm²) can then be computed using the empirical model of Alonso et al. [262] with the Equation A.34:

$$S_a = A_S\left(1-\left(1-\frac{2Pr_{O_2}pf_g}{D_{rebar}}\left(7.53+9.32\frac{CC}{D_{rebar}}\right)10^{-3}\right)^2\right) \quad \text{Eq (A.34)}$$

Where:

- D_{rebar} is the nominal diameter of the reinforcing bar (m)
- A_S is the transversal section of the reinforcing bar (m²)
- CC is the concrete cover thickness (m)
- pf_g is a pitting factor.
- Pr_{O_2} is a factor linked to the pressure of the corrosion products and depends on the availability of oxygen. It is equal to 1 for the exposure classes XS1 and XS3, while it goes up to 2.5 for XS2.

Finally, the propagation time is computed using the Equation A.35:

$$t_{prop} = \mu\left(\frac{S_a}{D_{rebar}}\right)\left(\frac{1}{k_i i_{corr}}\right) \quad \text{Eq (A.35)}$$

Where μ is defined using the Faraday law (see Equation A.36), k_i is a factor generally equal to 0.5 that define the capacity of the corrosion current to penetrate in depth and its participation to the lateral extension of the anodic zone.

$$\mu = \frac{\rho_S z_{Fe} F}{2M_{Fe}\tan(\theta_s)} = 1629\ A.year.m^{-3} \quad \text{Eq (A.36)}$$

With θ_s the half angle of opening limiting the section loss S_a considered equal to 0.2618 radian.

Stewart and Suo [441]

Stewart and Huo define a model to compute the time of corrosion propagation leading from cracking to spalling. The model considered four main inputs:

- The water to cement ratio (W/B, -)
- The concrete cover (CC, mm)
- The corrosion current "experimentally measured" (i_{corr}, µA/cm²)
- The width of the crack formed (w, mm)

First, the authors defined a function to compute the corrosion current at the beginning of the corrosion and the corrosion current at a specific point of time:

$$i_{corr,1} = \frac{27\left(1-\frac{W}{B}\right)^{-1.64}}{CC} \quad \text{Eq (A.37)}$$

$$\boldsymbol{i_{corr,t} = i_{corr,1}0.85(t-t_{ini})^{-0.3}} \quad \text{Eq (A.38)}$$

Then, three coefficients are computed:

- A and B, which account for the crack width influence and are computed with Equations A.39 and A.40 respectively.
- kR defines the influence of the corrosion current and is computed with Equation A.41.

$$A = \frac{700 - 65}{1 - 0.3} w - 207.143 \quad \text{Eq (A.39)}$$

$$B = \frac{0.23 - 0.45}{1 - 0.3} w + 0.544 \quad \text{Eq (A.40)}$$

$$kR = 0.95 \left(\exp\left(-0.3 \left(\frac{i_{corr,exp}}{i_{corr_t}} \right) \right) - \left(\frac{i_{corr,exp}}{2500 i_{corr,t}} \right) + 0.3 \right) \quad \text{Eq (A.41)}$$

Finally, the spalling time is computed with the following equation:

$$t_{sp} = kR \left(\frac{0.0114}{i_{corr,0}} \right) \left(A \left(\frac{C}{W/B} \right)^B \right) \quad \text{Eq (A.42)}$$

This model is a simple approximation of the pitting corrosion consequence in reinforced concrete. It can be noted that it requires the computation of the estimation of the crack width in order to operate, as well as a method to measure or estimate the $i_{corr,exp}$ value. The formula used to compute i_{corr_t} is hence subjected to criticism since important parameters are absent from Equations A.37 and A.38, such as the electrical resistivity (which accounts for the binder nature among other parameters).

It can also be noted that the concrete strength does not appear in this model, despite its evident impact on the final time. It certainly comes from the assumptions made by the authors who compute the crack width from the mechanical strength of the concrete material.

Analytical models for concrete properties estimation (Sections III.5 – IV.4)

Porosity

Porosity accessible to water in sound concrete including silica fume Papadakis [66]

To obtain the Equation A.43 given in [66], Papadakis et al. use the following equation with diverse assumptions:

$$\varphi_p^w = \varepsilon_{air} + \frac{W_{eff}}{\rho_w} - \left(\Delta\varphi_{hyd} + \Delta\varphi_{poz} + \Delta\varphi_{car} \right) \quad \text{Eq (A.43)}$$

W_{eff} is the water content (kg/m^3), ρ_w is the bulk density of water equal to 981 kg/m^3, ε_{air} is the entrapped or entrained air ratio (-) and $\Delta\varphi_{hy}$, $\Delta\varphi_{poz}$, $\Delta\varphi_{car}$ are the porosity reductions associated to the hydration of the Portland cement, the pozzolanic activity and the carbonation of the hydrates.

It is then explained that, given the values of molar volumes differences ($\Delta\bar{V}_x$, shown in Table 0-17) between solid reactants (x) and products of the hydration:

- The porosity reductions caused by the pozzolanic reaction of silica fume can be neglected ($\Delta\varphi_{poz} \approx 0$);
- The porosity reduction caused by the hydration of Portland cement, given in Equation A.43, leads to the Equation A.44 for non-carbonated concrete.

$$\Delta\varphi_{hyd} = (C_3S)\Delta\bar{V}_{C_3S} + (C_2S)\Delta\bar{V}_{C_2S} + (C_3A)\Delta\bar{V}_{C_3A} + (C_4AF)\Delta\bar{V}_{C_4AF} \quad \text{Eq (A.44)}$$

Table 0-17 Differences in molar volumes computed for the different species intervening in the hydration reaction of Portland cement and silica fume [66].

Constituent	Species	Differences in molar volumes ($\Delta\bar{V}_x$, 10^{-3} m³/kg)
Portland Cement	C3S	0.2334
	C2S	0.2285
	C3A	0.5769
	C4AF	0.2321
Silica Fume	S	-0.0032

$$\varphi_p^w = \varepsilon_{air} + \frac{W_{eff}}{\rho_w} - (0.249(CaO - 0.7SO_3) + 0.191SiO_2 + 1.118Al_2O_3 - 0.357Fe_2O_3)\left(\frac{C}{1000}\right) \quad \text{Eq (A.45)}$$

Where $CaO, SO_3, SiO_2, Al_2O_3$ and Fe_2O_3 are the weight ratio (-) of calcium oxide, sulphur oxide, silicon oxide, aluminium oxide and iron oxide contained in the CEM I cement. C is the cement content (kg/m3).

Porosity accessible to water of carbonated paste, Papadakis equations [289]

In this study, Papadakis uses three sets of equations to compute the porosity accessible to water depending on the SCM used for clinker replacement. Two porosity values are computed: the first, φ_p^w corresponds to the total porosity of the sound material while the second, $\varphi_{p,car}^w$, corresponds to the porosity accessible to water for carbonated cement paste. Only Silica fume (Q_{SF}, kg/m³) and fly ash ($Q_{V,L}$ for low-calcium and $Q_{V,H}$ for high calcium fly ash, kg/m³) are considered.

For cement paste containing silica fume ($Q_{SF} < 0.18B$):

$$\varphi_p^w = \varepsilon_{air} + (W_{eff} - 0.226Q_K)/1000 \quad \text{Eq (A.46)}$$

$$\varphi_{p,car}^w = (W_{eff} - 0.267Q_K - 0.0278Q_{SF})/1000 \quad \text{Eq (A.47)}$$

For cement paste containing low calcium fly ash ($Q_{V,L} < 0.23B$):

$$\varphi_p^w = \varepsilon_{air} + (W_{eff} - 0.227Q_K - 0.188Q_{V,L})/1000 \quad \text{Eq (A.48)}$$

$$\varphi_{p,car}^w = (W_{eff} - 0.268Q_K - 0.177Q_{V,L})/1000 \quad \text{Eq (A.49)}$$

For cement paste containing high calcium fly ash ($Q_{V,H} < 0.58B$):

$$\varphi_p^w = \varepsilon_{air} + (W_{eff} - 0.226Q_K - 0.193Q_{V,H})/1000 \quad \text{Eq (A.50)}$$

$$\varphi_{p,car}^w = (W_{eff} - 0.267Q_K - 0.203Q_{V,H})/1000 \quad \text{Eq (A.51)}$$

Where ε_{air} is the air content brought by the aggregates (-). W_{eff} and Q_K are the effective water and clinker content respectively (expressed in kg/m³).

It is important to note that these equations are defined for the SCM used in Papadakis's work and rely on the measure of the oxide content. Modifications of the constant values are supposed needed for different types of silica fume and fly ash.

One drawback of the methodology for modelling is that many equations and conditions are required to compute the value of porosity according to the compositions of the binder. It is always more appreciated to have a unique equation able to compute the results for all cases. Here, because all equations have been fitted on paste containing one SCM only, it is difficult to conclude on the possibility to regroup all

the equations in one using the same coefficients, since pairing effects of the different additions might lead to erroneous estimations in case of ternary binder.

Hydrate contents

Portlandite content, AFGC equation [109]

The formula presented by Baroghel-Bouny in the document of the AFGC [109] allows the portlandite content (CH, kg/m^3) after 28 days of hydration to be estimated under the hypothesis that C_3S (expressed as a weight ratio, -) is the only source of portlandite formation.

$$CH = \max\left(0, 0.422C \times C_3S \min\left(1; \frac{1}{0.418}\frac{W_{eff}}{C}\right) - 0.617Q_{SF}\right) \quad \text{Eq (A.52)}$$

Where C is the cement content (kg/m3) and Q_{SF} the silica fume content (kg/m^3). 0.418 corresponds to the W_{eff}/C ratio required for a complete hydration of the C_3S. 0.422 is the proportion of portlandite formed with the consumption of one unit mass of C_3S. 0.617 is the proportion of portlandite consumed after 28 days by the pozzolanic reaction.

It is specified that this equation can only be used with CEM I cement type, which explains the absence of a sink term linked to the pozzolanic reaction (responsible for the consumption of portlandite). Therefore, the flaws of this equation are linked to the absence of C_2S consideration and the inability to consider cement different than CEM I.

Portlandite and C-S-H contents, Papadakis equations [289]

In this study, Papadakis uses three sets of equations depending on the SCM used for clinker replacement for portlandite and C-S-H computations. The quantities are given in kg/m^3 under the hypothesis that complete hydration has been achieved. Only Silica fume (Q_{SF}, kg/m^3) and fly ash ($Q_{V,L}$ for low-calcium and $Q_{V,H}$ for high calcium fly ash, kg/m^3) are considered.

For cement paste containing silica fume ($Q_{SF} < 0.18B$):

$$CH = 0.29Q_K - 1.62Q_{SF} \quad \text{Eq (A.53)}$$

$$CSH = 0.57Q_K + 2.49Q_{SF} \quad \text{Eq (A.54)}$$

For cement paste containing low calcium fly ash ($Q_{V,L} < 0.23B$):

$$CH = 0.3Q_K - 1.3Q_{V,L} \quad \text{Eq (A.55)}$$

$$CSH = 0.57Q_K + 1.25Q_{V,L} \quad \text{Eq (A.56)}$$

For cement paste containing high calcium fly ash ($Q_{V,H} < 0.58B$):

$$CH = 0.29Q_K - 0.5Q_{V,H} \quad \text{Eq (A.57)}$$

$$CSH = 0.57Q_K + 0.79Q_{V,H} \quad \text{Eq (A.58)}$$

Where W_{eff} and Q_K are the effective water and clinker content respectively (expressed in kg/m^3).

Statistical methods (Sections III.6 – IV.3.2)

Latin Hypercube Sampling (LHS) and Principal Component Analysis (PCA) are discussed in this section. LHS is employed to generate the data required for constructing surrogate models, ensuring a well-distributed input and minimizing the computational burden associated with the original Finite Element Method (FEM) model. On the other hand, PCA is utilised for preprocessing the database and identifying correlations among various parameters.

Latin Hypercube Sampling (LHS)

Latin hypercube sampling (LHS) is utilised as an alternative to crude Monte-Carlo sampling in this study for dataset preparation. The objective of this approach is to optimize the distribution of the datasets in order to minimize the amount of data while ensuring a fair representation of each parameter within their respective ranges. The use of LHS enables a more uniform spread of the sample points across the defined range values. This is achieved by dividing the support axes of probability distributions into n intervals of equal probability. Subsequently, one unique sample is randomly selected from each interval or "stratification" (as depicted in Figure 0-10 for the case of n = 20).

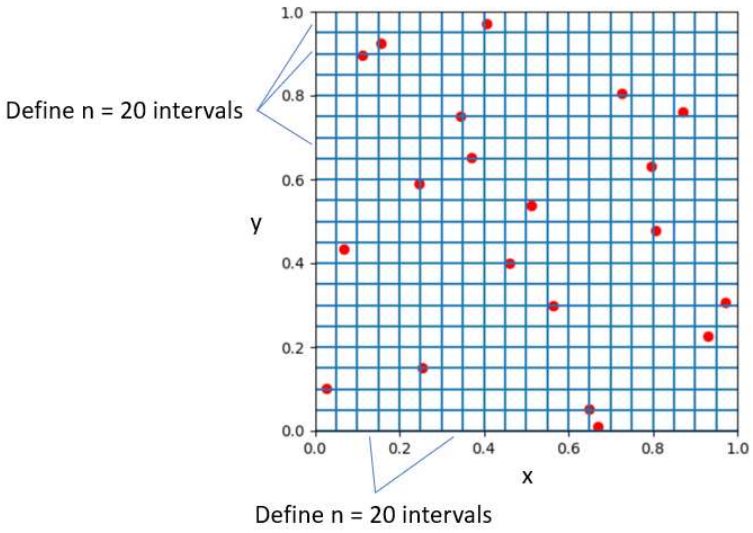

Figure 0-10 Latin hypercube sampling method applied for a two-dimension system cut in n = 20 intervals.

In the context of statistical sampling, a Latin Square refers to a square grid containing sample positions where there is only one sample in each row and each column. This concept can be extended to multiple dimensions, known as a Latin Hypercube, where each sample is the only one in each axis-aligned hyperplane containing it.

In crude Monte Carlo sampling, new samples are generated without considering the previous sample points, following a memoryless method. On the other hand, Latin Hypercube Sampling takes into account the rows and columns that have already been selected for the next sample selections. This approach requires fewer samples to recreate the input distribution, resulting in reduced computation time for tasks like surrogate model creation [442].

However, it has been demonstrated in previous studies [394] that when important interactions exist between design parameters, Latin Hypercube Sampling may not provide a significant advantage compared to crude Monte Carlo sampling. In such cases, alternative methods like using a pseudo random sequence of Sobol could potentially yield higher performance.

Principal Component Analysis (PCA)

Principal Component Analysis (PCA) is a statistical technique utilised for multivariate data analysis. It aims to describe the dataset by calculating the principal directions (or eigen vectors) of correlation. The dataset can be represented as p-dimensional vectors x_1, …, x_p or alternatively as the data matrix X [443]. Here, p represents the number of numerical variables, and n represents the size of the dataset.

The direction of correlation is a linear combination of X columns (corresponding to the vectors x_j for $j \in [1, p]$) explaining the maximum variance that can be expressed as:

$$\sum_{j=1}^{p} a_j x_j = XA \qquad \text{Eq (A.59)}$$

Where A is a vector of constants a_1, …, a_p. The variance is maximized when A satisfies the Equation A.60, where S is the sample covariance matrix associated to X.

$$Var(XA) = A^T SA \qquad \text{Eq (A.60)}$$

To address this problem efficiently and effectively, it is necessary to impose a constraint wherein unit-norm vectors are used. This restriction entails finding matrix A such that $A^T A = 1$. Consequently, the problem becomes equivalent to the maximization of $A^T SA - l(A^T A - 1)$, where l represents a Lagrange multiplier. Differentiating with respect to A yields the following outcome:

$$SA - LA = 0 \qquad \text{Eq (A.61)}$$

In the context of a covariance matrix S, the vector L represents the eigenvalues λ_i, where $i \in [1, p]$. Each eigenvalue λ_i corresponds to the variance of the respective eigenvector a_i's linear combination. These linear combinations, known as principal components (PC) of the dataset, are denoted by Xa_i. The product Xa_1, which corresponds to the largest eigenvalue λ_1, represents the most important correlation between the parameters X and serves as the most representative component of the dataset. Usually, only the two or three most significant principal components are considered for data analysis [444]. The goal is to identify the principal components representative of the datasets and depends on the eigenvalues difference.

The values of a_i, expressed as linear combinations of the x_j variables (for j ranging from 1 to p), can be utilised to depict the correlation between the different parameters according to the datasets used. The correlations obtained, particularly for the top eigenvalues, serve as indicators of the interdependency of the variables and can also be employed for tasks such as determining the correlation matrix. Figure 0-11 depicts an instance of the three highest eigenvalues acquired through Principal Component Analysis (PCA) on a database of results on composition and mechanical strength (as outlined in Section IV.3.3).

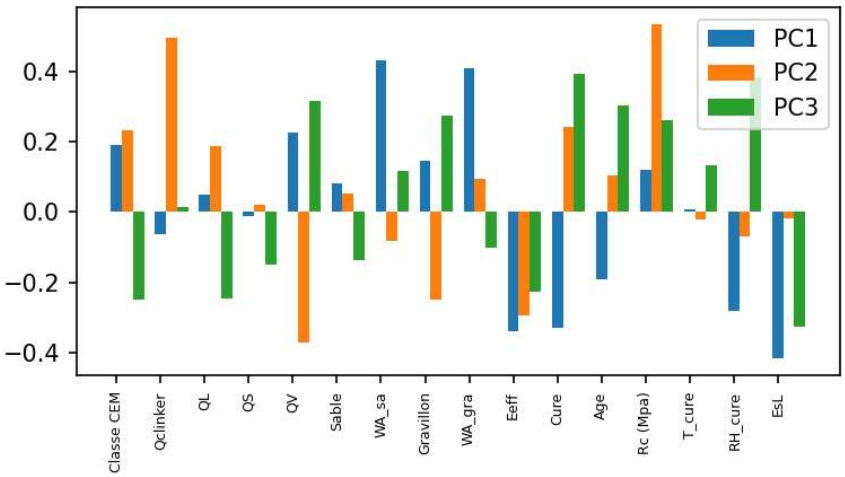

Figure 0-11 Representation of the weight of each parameter in the three highest principal components for the database.

In Figure 0-11, high absolute values indicate a significant impact of the parameter on other parameters. On the contrary, values close to zero suggest low correlations with other parameters.

PCA serves various purposes in scientific research, including problem simplification, data reduction, variable selection, and classification, among others. One notable application of PCA results involves the graphical representation of a pair (or three for three-dimensional representation) of principal components (an example is provided in Figure 0-12). This visualization facilitates the identification of various dataset trends, including cluster and group formations. Additionally, it aids in the detection of outlier values that may arise from assessment issues.

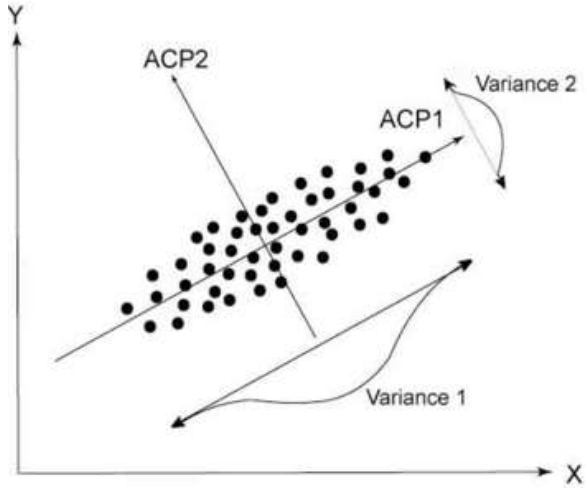

Figure 0-12 Example of graphical representation for principal component analysis exploitation [445].

Sensitivity analysis (Section III.6 – IV.3 – IV.4)

Sensitivity analyses are valuable tools for assessing the impact of specific input parameters on the results of a given model or equation. These methods involve evaluating the extent to which variations in individual input parameters affect the overall outcome, either independently or in relation to other parameters. In this section, two specific methods are presented. They are utilised in Section III.6 and Section IV.

Morris sensitivity analysis

In the Morris' method, the Elementary Effect (EE_i) (as shown in Equation A.62) of an input parameter on the model output is calculated. In other words, the impact of each parameter (x_i) on the model results can be obtained and compared. To begin with, the range of variation for each input parameter needs to be defined in order to obtain their "trajectories". The number of computations required for each trajectory is equal to the number of variables (n) to be tested plus one. Within a given trajectory, each input parameter changes only once throughout the calculations, while only one parameter changes between each successive computation (refer to the example presented in Table 0-18). Therefore, each trajectory provides a single value of the elementary effect of each input parameter, which can be determined using the following equation A.62.

$$EE_i = \frac{f(X_1, \dots, X_i + \Delta_i, \dots, X_n) - f(X_1, \dots, X_i, \dots, X_n)}{\Delta_i} \qquad \text{Eq (A.62)}$$

Where Δ_i is the perturbation in the interval defined for the considered input.

Hence, one trajectory alone has no real sense, but the realization of many trajectories allows to compute statistic on the elementary effects of the parameters. Between each trajectory, different parameters are randomly changed:

- The initial point of the trajectory.
- The order of variation of the parameters between each computation of the trajectory.
- The direction of the variation (the parameter can increase or decrease) and its exact value.

Table 0-18 Example of input values for one trajectory [6].

	1st parameter	2nd parameter	3rd parameter
1st computation	0.2	1.5	3.4
2nd computation	0.3	1.5	3.4
3rd computation	0.3	1.5	2.6
4th computation	0.3	1.8	2.6

The trajectory number to obtain a fair accuracy, must be superior or equal to k times the product of the variables number with the computation number of one trajectory ($r \geq kn(n+1)$). The standard deviation (σ_i) and mean of absolute values (μ_i^*) of each elementary effect hold:

$$\mu_i^* = \frac{\sum_{j=1}^{r} |EE_{i,j}|}{r} \qquad \text{Eq (A.63)}$$

$$\sigma_i = \sqrt{\frac{1}{r-1}\sum_{j=1}^{r}\left(EE_{i,j} - \mu_i\right)^2} \qquad \text{Eq (A.64)}$$

From the values of these parameters the following findings can be drawn. First, the higher the average μ_i^*, the higher the impact of the parameter on the output result is. Second, the deviation σ_i helps highlighting the presence of interaction between different parameters or to show a nonlinear effect on the result (see Figure 0-13).

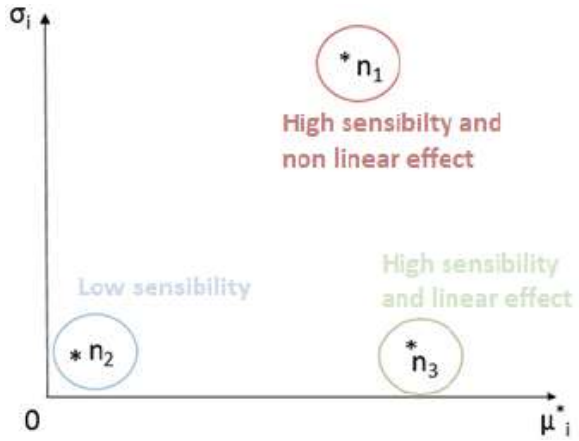

Figure 0-13 Results example of a sensitivity analysis realised with the Morris method [6].

The global sensitivity (Gi*) is then calculated to rank the different parameters (see Equation A.65).

$$G_i^* = \frac{G_i}{\sum_{i=1}^{n} G_i} \qquad \text{Eq (A.65)}$$

Where G_i can be obtained for each parameter i with Equation A.66:

$$G_i = \mu_i^{*2} + \sigma_i^2 \qquad \text{Eq (A.66)}$$

Parameters are then listed in ascending order of global sensitivity. The overall cumulative sensitivity calculated according to this ranking order enables to identify parameters with negligible influence, which makes a small contribution above a certain overall cumulative sensitivity threshold, usually stated at 0.95.

Also, ranking the parameters helps the user of a given model to cease the importance of each parameter on the output and select the parameters that can be taken constant without over-impacting the result(s).

Sobol sensitivity analysis

Sobol sensitivity analysis, also known as Sobol method or Sobol indices, is a statistical technique used for sensitivity analysis of a computational model. It helps in understanding the relationships between input variables and the output of a model and quantifies the relative importance of these input variables in in the variance of the output.

The Sobol analysis decomposes the total variance in the output of the model into individual variances attributed to each input variable and their interactions. An interest of this method compared to the Morris sensitivity analysis is the possibility to assess the combined influence of one parameter paired with one or various other parameters. This way, the precise coupling effects of the parameters can be determined in addition to the impacts of individual parameters.

Different indices are defined for this method [446]:

- The First Order Sobol Indices (S_i) corresponds to a measure of the input variable x_i first order sensitivity, which is the impact of the sole input x_i variation on the result(s) variation. This index is computed using the Equation A.67. This value is standardized relatively to the total variance, thus, the sum of all first order Sobol indices equals 1.

$$S_i = \frac{var\big(f(x_i)\big)}{var\big(f(x)\big)} \qquad \text{Eq (A.67)}$$

  Where $var\big(f(x_i)\big)$ is the variance of the conditional mean (when only the variable x_i varies), and $var\big(f(x)\big)$ the global variance of the function.
- The Total Order Sobol Indices (S_{Ti}). It corresponds to the contribution on the output variance of a parameter x_i including the variance caused by the variable alone and its interactions with every other input considered.

$$S_{Ti} = \frac{\int_0^1 var(x_i)p(x_i)dx_i}{var\big(f(x)\big)} \qquad \text{Eq (A.68)}$$

  Where $p(x_i)$ is the probability density associated to x_i. Each parameter probability density is considered uniformly distributed.

The total variance is computed to be the sum of the n different parameters variance (see Equation A.69)

$$var(f(x)) = \sum_{i=0}^{n} var\big(f(x_i)\big) \qquad \text{Eq (A.69)}$$